Universidade do Minho
Escola de Engenharia

Georgios Karanikoloudis

Experimental methods for investigating the effects of soil settlements and vibrations in cultural heritage buildings, induced by underground structures

abril de 2023

Experimental methods for investigating the effects of soil settlements and vibrations in cultural heritage buildings, induced by underground structures
Georgios Karanikoloudis
UMinho | 2023

Universidade do Minho
Escola de Engenharia

Georgios Karanikoloudis

Experimental methods for investigating the effects of soil settlements and vibrations in cultural heritage buildings, induced by underground structures

Tese de Doutoramento
Engenharia Civil

Trabalho efetuado sob a orientação do(a)
Professor Doutor Paulo José Brandão Barbosa Lourenço
Investigador Principal Doutor João Bilé Serra

abril de 2023

STATEMENT OF INTEGRITY

I hereby declare having conducted this academic work with integrity. I confirm that I have not used plagiarism or any form of undue use of information or falsification of results along the process leading to its elaboration.

I further declare that I have fully acknowledged the Code of Ethical Conduct of the University of Minho.

ACKNOWLEDGEMENTS

Reflecting towards the end of my PhD, it has been a remarkable and worthwhile journey, that grossly shaped me as a structural and conservation engineer. Far and foremost, I would like to express my sincere gratitude to my supervisor Professor Paulo B. Lourenço, for entrusting me with a demanding experimental campaign, and always offering his guidance and support. I have gained greatly from his expertise in every computational, analytical and experimental aspect related to masonry. I feel extremely lucky to have gained a life-long mentor and a role model of integrity and humbleness.

I would also like to extend my gratitude to my co-supervisor P.I. Dr. João Bilé Serra. I benefited greatly from his guidance, support, and vast knowledge in geotechnics. Throughout the many challenges during my PhD, I found great support from the Post-doc Researcher Dr. Nuno Mendes, who practically taught me most of my computational and experimental skills. Also, my sincere thanks to Professor Graça Vasconcelos, Professor Daniel Oliveira and Dr. Rui Silva for their help on many experimental challenges on the way.

My experimental research would not have been possible without the tremendous support from the technical personnel of the ISISE Laboratory of the Civil Engineering Department of the University of Minho, and in particular Marco Jorge and António Matos. Also, my gratitude to my favorite mason Sr. Manuel, and to Carlos, Mr. Goncalves, Cesar, and Luciano for all their help and support. This experimental work would not have been possible without the generous support from Secil and Kerakoll construction material companies, which have gracefully offered their line of products.

I want to thank all my friends and colleagues, for a journey fun and worthwhile; Giorgia, Giorgos, Marina, Pilar, Susana, Maria Pia, Elena, Elesban, Meera, Telma, Rafa, Joao, Ton, Nikoleta, Carolina, Sandri, Chiara, Carla, Antonio, Lelsie, Alberto and many more. Lastly, to my family, I dedicate my whole effort, together with my endless joy for the love and support I received.

This work has been part of the ‘Analysis and Mitigation of Risks in Infrastructures – InfraRisk’ Doctoral Programme and the provided scholarship was funded by the Portuguese Science and Technology Foundation (FCT).

Experimental methods for investigating the effects of soil settlements and vibrations in cultural heritage buildings, induced by underground structures.

ABSTRACT

Structural assessment for cultural heritage structures, in the proximity of operating underground railways is twofold, by induced soil movements, from tunneling construction, and by fatigue, through induced ground-borne vibrations, from railway operations. Both hazards are found interacting, with effects on durability. Yet, a multi-hazard response assessment remains an open challenge, since many constitutive material models do not account for cyclic deterioration.

This thesis is focused on field monitoring, experimental testing and analytical applications, with the aim of obtaining a clear knowledge on the in-plane capacity and damage, in simulated, historic, brick masonry and lime mortar specimens. First, fatigue tests in diagonal compression in wallets, replicated different levels of cyclic and static loading. Second, in-plane tests on a differential displacement uplift were conducted in piers and spandrel masonry specimens and the effectiveness of repair and strengthening, namely of grouting injections and a Fiber Reinforced Cementitious Matrix system (FRCM), were assessed.

Considering the fatigue tests in diagonal compression, under medium to high amplitudes of induced ground-borne vibrations and high static loads, they have resulted in cracking, at relatively low number of cycles. As for the experimental works on the in-plane behavior in piers and spandrel specimens, under a vertical uplift, a sequential in-plane failure is identified through flexural and shear cracking in the spandrel, together with a final, sliding, shear crack in one of the piers, while the repair and strengthening schemes, both were tested effective, providing sufficient shear capacity and displacement ductility.

Key words: Unreinforced brick masonry; Piers and spandrel specimens; Soil settlements; Induced ground-borne vibrations; Monitoring; Fatigue; Fiber Reinforced Cementitious Matrix systems; Grouting injections.

Métodos experimentais para investigar os efeitos de subsidência do solo e vibrações em edifícios de patrimônio arquitetónico, induzidos por estruturas subterrâneas.

RESUMO

O avaliação estrutural do património arquitetónico, nas proximidades das ferrovias subterrâneas em operação, é duplo, seja por subsidência do solo devido à construção de túneis, seja pela fadiga, provocada por vibrações induzidas no solo, por operações ferroviárias. Ambos os perigos estão interagindo, com efeitos na durabilidade. No entanto, uma avaliação da resposta a múltiplos perigos é um desafio em aberto, dado muitos modelos constitutivos de materiais não considerarem a deterioração cíclica.

Esta tese foca-se nas campanhas de monitoramento e experimental, e em aplicações analíticas, com o objetivo de obter um conhecimento claro sobre a resistência no plano e dano, em provetes de alvenaria de tijolo e argamassa de cal históricos. A primeira relativa a ensaios de compressão diagonal com fadiga em muretes, com diferentes níveis de carga cíclica e estática. Na segunda campanha, foram realizados ensaios no plano com assentamento diferencial de elevação em provetes representativos de nós coluna-viga de paredes de alvenaria, e foi avaliada a eficácia de reparação e reforço, nomeadamente de injeções de calda e de sistemas de matriz cimentícia reforçada com fibras (FRCM).

Considerando os ensaios de compressão diagonal com fadiga, sob amplitudes médias a altas de vibrações induzidas no solo e elevadas cargas estáticas, ocorreu fissuração a um número de ciclos relativamente baixo. Relativamente à campanha experimental sobre o comportamento no plano dos provetes pilar-coluna, sob deslocamento de elevação, observou-se uma sequência de falhas, através de fissuras por flexão e corte nas vigas, em conjunto com uma fissura final, deslizante, devido a corte, num dos pilares, enquanto as soluções de reparação e reforço, ambos provaram ser eficazes, proporcionando resistência ao corte e ductilidade suficientes.

Palavras-chave: Alvenaria de tijolo não armada; Provetes de coluna-viga; Subsidência do solo; Vibrações induzidas no solo; Monitoramento; Fadiga; Sistemas de matriz cimentícia reforçada com fibras; Injeções de calda.

To my father

Contents

ACKNOWLEDGEMENTS ..... **IV**

ABSTRACT ..... **V**

RESUMO ..... **VI**

LIST OF FIGURES ..... **XIII**

LIST OF TABLES ..... **XXVII**

CHAPTER 1. INTRODUCTION **1**

1.1. Background and motivation 1

1.2. Thesis objectives 4

1.3. Research methodology 5

1.4. Outline and organization 9

CHAPTER 2. INDUCED SOIL SETTLEMENTS AND VIBRATIONS FROM UNDERGROUND STRUCTURES **11**

2.1. Introduction 11

2.2. Tunneling in soft ground 13

2.3. Induced soil settlements from underground structures 16

2.3.1. Damage criteria 16

2.3.2. Analytical models 18

2.3.3. FE modelling approach 33

2.4. Induced vibrations from underground railway traffic 39

2.4.1. Wave propagation in the elastic half-space 39

2.4.2. Vibrations from underground railway tunnels 40

2.4.3. FE modelling approach 43

2.4.4. Mitigation measures 46

2.5. Conclusions 47

CHAPTER 3. MATERIAL CHARACTERIZATION FOR SIMULATED HISTORIC MASONRY, REPAIR AND RETROFIT 48

3.1. Introduction 48

3.2. Reference façade and brickwork of the 19th-20th centuries 49

3.3. Experimental research on simulated historic masonry 58

3.3.1. In plane failure in brick masonry under monotonic loading 58

3.3.2. Capacity tests in uniaxial and diagonal compression, testing protocols and monitoring under cyclic loading 65

3.4. Compressive and flexure tests on simulated historic masonry constituents, repair and retrofit material 69

3.4.1. Hydraulic lime mortar 70

3.4.2. Solid fired bricks 77

3.4.3. High performance hydraulic lime-based render and fluid binder 82

3.5. Mechanical tests on simulated historic masonry assemblies 84

3.5.1. Uniaxial cyclic compression tests 87

3.5.2. Diagonal monotonic compression tests 92

3.6. Analytical stress-strain expressions from experimental data 96

3.7. Conclusions 99

CHAPTER 4. FIELD MONITORING OF INDUCED GROUND-BORNE VIBRATIONS 101

4.1. Introduction 101

4.2. Criteria and aspects from international standards 103

4.2.1. General framework 103

4.2.2. Data acquisition planning 106

4.3. Field monitoring in the Church of the Angels 110

4.3.1. Historic perspective 110

4.3.2. Ambient vibration tests 111

4.3.3. Acquisitions of induced vibrations with geophones 115

4.3.4. Coupling acquisitions of induced vibrations with geophones and seismographers 127

4.4. Conclusions 135

CHAPTER 5. FATIGUE TESTS ON MASONRY WALLETS UNDER DIAGONAL COMPRESSION 137

5.1. Introduction 138

5.2. Experimental research for fatigue loading on masonry 139

5.3. Experimental fatigue tests on masonry specimen, under high static diagonal compression and medium-low stress ratios 148

5.3.1. Introduction 148

5.3.2. Test specimen configuration and initial material properties under a monotonic diagonal compression loading test 149

5.3.3. Static diagonal compression cyclic preload, initial stiffness monitoring and estimated initial material properties from analytical curve fitting 156

5.3.4. Diagonal compression fatigue test setup, preparation, instrumentation and data acquisition 158

5.4. Conclusions 183

CHAPTER 6. TESTS OF DIFFERENTIAL SETTLEMENTS ON PIERS AND SPANDREL SPECIMENS, REPAIR AND RETROFIT APPLICATIONS 187

6.1. Introduction 187

6.2. Theoretical background on structural interaction of piers and spandrels and abacus of kinematic-static in-plane mechanisms under differential settlements 189

6.3. Experimental investigation for capacity tests on masonry assemblies, composed by piers and spandrels 190

6.4. Building codes mechanical strength models on dominant failure modes for piers and spandrels 194

6.5. Experimental works on masonry piers and spandrel assemblies under a vertical displacement field 203

6.5.1. Masonry assemblies, setup implementation and testing protocols 203

6.5.2. Experimental results 211

6.5.3. Application of mechanical strength models for masonry spandrels UN1 and UN2 244

6.6. Conclusions 254

CHAPTER 7. CONCLUSIONS AND FUTURE RESEARCH 257

7.1. Introduction 257

7.2. Summary of conclusions 258

7.2.1. Implementation and processing aspects on field monitoring of induced ground-borne vibrations 258

7.2.2. Evaluation of structural damage and failure in masonry, under long-term fatigue loading 258

7.2.3. Quantitative interpretations from tests of differential settlements on piers and spandrel specimens, and the effect of repair and retrofit applications 262

7.2.4. Structural assessment of buildings of cultural heritage, under multitude actions and long-term effects from differential settlements and ground-borne vibrations 264

7.3. Future research 266

REFERENCES 268

ANNEXES 284

ANNEX A 285

List of Figures

Figure 1. Flow chart of the thesis outline, with the research background, basis and activities comprising the thesis. 10

Figure 2. Volume losses during tunneling excavation with a TBM. 16

Figure 3. Greenfield conditions: (a) schematic of a 3-layered soil strata; (b) distribution of the horizontal strain in the transverse direction, together with the settlement trough; (c) distribution of the horizontal strain in the longitudinal direction, together with the settlement trough; (d) configuration of the settlement trough in the 3D space. 21

Figure 4. Distribution of the horizontal strain in the transverse direction, together with the settlement troughs, for different types of soil, with K values in the range of 0.2-0.7. 22

Figure 5. Distribution of the horizontal strain in the transverse direction, together with the settlement troughs, for an arbitrary twin tunnel configuration and a chosen K value of 0.2. 22

Figure 6. Quality of Gaussian fitting compared with real measuring data: (a) schematic of a twin metro construction and overlying Felice aqueduct in Rome [Amorosi et al. 2014]; (b) settlement trough in transverse section, measured at base [Amorosi et al. 2014] and greenfield profile, with width parameter K in the range of 0.4–0.6, and according to soil layer properties from Amorosi et al. 2014; (c) corresponding regression in left and right part of settlement trough. 23

Figure 7. The Limiting Tensile Strain method: (a) building division in hogging (L_h) and sagging (L_s) zones, at point of inflection; (b) tensile strain components in equivalent beam. 25

Figure 8. Estimation of equivalent bending and axial stiffness in 2D: (a) system of a masonry wall; (b) system of a masonry building with foundation, piers, spandrels and timber floors. Note the abbreviations for the relevant geometrical properties. 29

Figure 9. Equivalent 2D beam. Design curves for modification factors under plane strain conditions of: (a) deflection ratios; (b) maximum horizontal strains [Potts and Addenbrooke 1997]. 31

Figure 10. Equivalent 3D shell. Design curves for modification factors of: (a) deflection ratios; (b) maximum horizontal strains [Franzius et al. 2006]. 31

Figure 11. Vertical settlement troughs from tunneling: (a) variation of axial stiffness a*, with a chosen p* equal to 0.518 m^{-1}; (b) variation of bending stiffness p*, with chosen a* equal to 48.6 [Potts and Addenbrooke 1997]. 32

Figure 12. Damage categories association graphs, of horizontal strain, with angular distortion (a) and deflection ratios (b). Adapted from Boscardin and Cording 1989 and Potts and Addenbrooke 1997. 32

Figure 13. Initial and final configuration of the tunnel's section, according to the gap parameter: (a) construction sequence and intermediate steps; (b) resulting nodal displacement vectors at last step, based on Amorosi et al. 2014. 35

Figure 14. Sequential tunnel construction progress and calibration, under greenfield conditions, employed for FE analyses [Rampello et al. 2012]. 36

Figure 15. Soil-structure coupling approach, with solids of equivalent mass and stiffness characteristics [Rampello et al. 2012]. 38

Figure 16. Pandrol Fastclip fastening connection, with flexible rail pads [Thompson et al. 2009]. 41

Figure 17. Floating slab track system: (a) typical cross section [Thompson et al. 2009]; (b) implemented system in built tunnel [Vibration from Underground Railways Pipe-in-Pipe software – New Release 2013]. 41

Figure 18. Underground railway induced vibrations: (a) mechanism of rolling noise and vibration in a railway track [Thompson et al. 2009]; (b) propagation through the soil half-space continuum; (c) vibration pattern of a concrete tunnel lining at 100 Hz [Jones et al. 2002]; (d) instantaneous displacement field in the soil around an unlined tunnel, at 100 Hz [Jones et al. 2002]. 42

Figure 19. FE modelling of track system, supported on sleepers, with: (a) an equivalent wheel-rail track interaction model [Thompson et al. 2009]; (b) an equivalent wheel-rail track interaction model for modelling a moving train [Ntotsios et al. 2015]. 44

Figure 20. Coupled approach of finite elements and boundary elements. Boundary elements are presented with normal vectors, pointing to the soil medium [Thompson et al. 2009]. 45

Figure 21. The 2.5 method: (a) train-rail track model [Yang et al. 2010]; (b) 2D near field profile, of tunnel lining and surrounding soil, in half-space [Yang et al. 2010]. 46

Figure 22. Brick masonry multi-story residential building of the 19th and 20th centuries: (a) elevation and section of the façade of Maison En Brique of 1881 by Buysschaert M., in Brussels, [Chabat 1886]; (b) exposed sidewall, of a residential building of the 19th century in Valladolid, of a composite timber frame and brick masonry infills (calle Doctor Cazalla) [Camino Olea 2001]; (c) brick masonry façades from 1880s (calle de la Estación, Valladolid) [Camino Olea 2001]; (d) and

(e) typical construction details of spandrel, side piers and timber floors, of a residential building of the 20th century in Valladolid [Camino Olea 2001]; (f) plan, elevation and half-section of the reference building of the early 20th century in Valladolid [Camino Olea 2001]. 53

Figure 23. Foundation system for brick masonry residential buildings: (a) typical section of foundation footing for brick masonry façades, of residential buildings of the 17th-19th centuries in Madrid. Typical dimensions based on Castilian feet (~0,28 m) [González-Redondo et al. 2003]; Pombalino buildings of the 18th century in Lisbon: (b) trench of regular stone masonry footings and a grid of timber piles, for weak soil substrates and high seismicity areas [Cardoso et al. 2014]; (c) brick masonry groin vault system at basement level [Cardoso et al. 2014]. 54

Figure 24. Schematic representation of the reference brick masonry building, used for constructing the laboratory testing assemblies, adapted from González-Redondo et al. 2003, Chabat 1886 and Camino Olea 2001: (a) 3D view; (b) details for arch configuration, brick patterns for piers and constituents. 56

Figure 25. 2D schematic representation of the reference brick masonry building, used for constructing the laboratory testing assemblies. Note the façade, floor configuration, roof, internal timber frame system and sidewalls, as adapted from González-Redondo et al. 2003, Chabat P. 1886 and Camino 2001. 57

Figure 26. Masonry typical crack pattern and representation of stresses in a localized area of the specimen under: (a) uniaxial compression. Note the layer separation in section, following the alignment of head joints; (b) diagonal compression. 60

Figure 27. Material models of unconfined compression, based on concrete inelastic behavior: (a) Hognestad 1951 parabola; (b) parabolic curve according to Feenstra 1993; (c) inelastic curve of §3.1.5 EN 1992-1-1 2004; (d) the Thorenfeldt et al. 1987 curve [Diana user's manual. 2020]. 60

Figure 28. Material models of linear tension until tensile strength ft and predefined softening for: (a) linear tension softening; (b) nonlinear exponential tension softening; (c) nonlinear tension softening according to Hordijk 1991 [Diana user's manual. 2020]. 63

Figure 29. Indicative stress-strain curves, showing the tensile and compressive behavior and the area equal to the fracture energy. [Diana user's manual. 2020]. 64

Figure 30. Monitoring of stiffness degradation, with the damage indicator $\mathrm{dj,k}$, under cyclic uniaxial loading in compression (a) and tension (b) [ABAQUS 2009]. 66

Figure 31. Material characterization of hydraulic lime mortar M4: (a) flow table test; (b) three-point loading test for flexural capacity; (c) compression strength test; (d) test for Young's modulus and compressive strength. 72

Figure 32. Stress-strain curves for flexure, of the M4 hydraulic lime mortar prisms, at different curing periods. 74

Figure 33. Stress-strain curves for compression, of the M4 hydraulic lime mortar prisms, at different curing periods. 75

Figure 34. M4 hydraulic lime mortar prisms: (a) and (b) boxplot, whisker chart and mean curve of strength evolution in time, for the three-point loading flexure test and uniaxial compression test respectively; (c) and (d) respective normalized curves for the flexural and compressive strength at 365 days. 75

Figure 35. Young's modulus evolution in time, of the M4 hydraulic lime mortar cylinders, with a boxplot, a whisker chart and a mean curve 76

Figure 36. Solid fired bricks: (a) schematic representation of a brick unit with cut cubes and prism specimen for uniaxial compression and Young's modulus tests; (b) stack of cubes and prisms from 6 bricks. 78

Figure 37. Three-point loading test for flexural capacity characterization of solid fired bricks: (a) front view; (b) back view. Note the flexural crack at mid-span. 80

Figure 38. Stress-strain curves, of the tested solid fired bricks for flexural strength (a), and uniaxial compressive strength normal to the bed (b) and header face (c). 80

Figure 39. Material characterization of solid fired brick prisms: (a) Young's modulus and fracture patterns (b) and (c), under uniaxial compression normal to the bed face; (d) Young's modulus and fracture patterns (e) and (f), under uniaxial compression normal to the header face. 82

Figure 40. Stress-strain curves for flexure at 28 days of curing: (a) hydraulic lime-based render M15; (b) hydraulic lime-based fluid binder M15. 83

Figure 41. Stress-strain curves for compression at 28 days of curing: (a) hydraulic lime-based render M15; (b) hydraulic lime-based fluid binder M15. 84

Figure 42. Building process of brick masonry wallets for UC and DC tests. Note the flemish bond pattern of 1½ brick thickness. 86

Figure 43. Geometry, instrumentation and setup of uniaxial compression tests on brick masonry wallets with lime mortar (UC_i). Note the range of the initial measuring lengths of the LVDTs, from all four UC_i wallets. 88

Figure 44. Stress-strain curves for axial and lateral strains of wallet UC1, tested monotonically under uniaxial compression. Here, the 2D maximum principal strain distribution plots are presented at five stress states, from DIC acquisitions. 88

Figure 45. Stress-strain curves for axial and lateral strains of wallets UC2-4 tested under cyclic uniaxial compression. Note the force and displacement time-history pattern and the six stress states. Here, for display purposes, the absolute values of the compressive strains of LVDT-1 and LVDT-2 were chosen. Note the selected stress state points, for the corresponding DIC plots..... 90

Figure 46. 2D maximum principal strain distribution plots at five stress states, from DIC acquisitions, of wallets UC2-4 tested under cyclic uniaxial compression. Note the ¨x¨ symbol for failed DIC acquisitions. 91

Figure 47. Graphic representations: (a) Young's modulus and compressive strength relation from uniaxial compressive tests in UC1-4 wallets and other sources; (b) propagation of elastic (el.) and plastic (pl.) axial strains for each cycle, of tested wallets UC2-4, under cyclic uniaxial compression; (c) linear regression analysis of the secant stiffness versus the vertical total strain at peak of each cycle i, normalized with the total strain at peak. Note the sole value for the ultimate secant stiffness and normalized strain for UC3, here not included in the regression analysis. 92

Figure 48. Geometry, instrumentation and setup of diagonal compression tests on brick masonry wallets with lime mortar. Note the range of the initial measuring lengths of the LVDTs, from all four DCi wallets. 93

Figure 49. Force/translation time-histories, shear stress-strain curves and failure at last stage, of wallets tested under monotonic (DC1 and DC2) and cyclic (DC3 and DC4) diagonal compression. Note that the loading cycles for DC4 are not distinguishable, due to high noise. 94

Figure 50. 2D maximum principal strain distribution plots at five stress states, from DIC acquisitions, of wallets DC1, DC2 and DC4 tested under uniaxial compression. Note the DIC acquisition for the DC3 the failure was sudden and was not captured. 96

Figure 51. Envelope stress-strain curves from cyclic uniaxial compression tests of UC2, UC3 and UC4: (a) stress-strain curves versus envelope curves from Equation 28, Equation 29 and Equation 30, Equation 31 and Equation 32. Note the dashed curve, after the maximum obtained strain; (b)

linear regression graph of test stress data for $0.05\mathrm{fc}$, $0.33\mathrm{fc}$, $0.75\mathrm{fc}$, $0.90\mathrm{fc}$, fc and $\mathrm{fc,ult}$. Note the test and prediction data in x-x and y-y axis respectively..... 98

Figure 52. Envelope stress-strain curves from monotonic and cyclic diagonal compression tests of DC1, DC3 and DC4: (a) shear stress-strain curves versus envelope curves from Equation 28, Equation 29 and Equation 30, Equation 31 and Equation 32. Note the dashed curve, after the maximum obtained strain; (b) linear regression graph of test stress data for $0.05\mathrm{ft}$, $0.33\mathrm{ft}$, $0.75\mathrm{ft}$, $0.90\mathrm{ft}$, ft and $\mathrm{ft,ult}$. Note the test and prediction data in x-x and y-y axis respectively. 98

Figure 53. Church of the Angels: (a) view of the front façade [SIPA 2011]; (b) side view of the staircase, leading to the main entrance of the church, with evident signs of settlements; (c) plan view of the church [SIPA 2011]; (d) view of the nave and altar, looking east. 111

Figure 54. Measuring equipment: (a) seismographers in the three windows of the main façade, in Setup 1; (b) close view of seismographer SO3 (Setup 1) placed in the south-west window of the main façade. 113

Figure 55. Disposition of seismographers in the performed setups, at the transept and chapels of the Church of the Angels..... 114

Figure 56. Mode shapes obtained from the SSI-UPC Method, of the first six modes, with interpolation [SVS 2019]. 114

Figure 57. Different monitoring points, uncorrelated in time, at the basement and at intermediate heights in the front end of the Church of the Angels. Note the reference point near the source of vibration, at the level of the sidewalk. 117

Figure 58. Isolated, uncorrelated signals of passing underground trains, recorded in the level of the sidewalk (a), the basement (b) and the middle span of the choir loft floor (c). Note the vectorial components, the different sampling rates (sps) in color coding and the difference between maximum values. 117

Figure 59. Data acquisition at the Church of the Angels, in the level of the sidewalk: (a) unfiltered triaxial velocity components of one acquisition (30min) and the corresponding spectrograms; (b) spectrograms of all unfiltered signals in three directions, during the entire acquisition (3.5 h), corresponding squared Welsh power spectral density graphs and band-pass Butterworth Chebyshev type II filter; (c) velocity-time history 3D plots, after filtering, for all three directions and velocity vectors VR, for all setups. Note the absolute maximum ppv from the empirical cumulative distribution function and chosen quantile. 121

Figure 60. Data acquisition in the front end of the Church of the Angels, at the level of the basement: (a) spectrograms of all unfiltered signals in three directions, during the entire acquisition (6.5 h), corresponding squared Welsh power spectral density graphs and band-pass Butterworth Chebyshev type II filter. Note the division in 0.5 h increments, between acquisitions during operational passing trains (1-9) and during no operation (10-13), divided by a dashed line in PSD graphs; (b) velocity-time history 3D plots, after filtering, for all three directions, for all setups. Note the absolute maximum ppv from the empirical cumulative distribution function and chosen quantile. 123

Figure 61. Data acquisition in the front end of the Church of the Angels, at the level of the ground floor. Comparative unfiltered velocity-time histories (30 min) plots in three locations of the ground floor; the left gate (a), the middle gate (b) and the right gate (c); (d) spectrograms of unfiltered signals (acquisitions 1-5), in the middle gate floor, in three directions, squared Welsh power spectral density graphs and band-pass Butterworth Chebyshev type II filter; (e) velocity-time history plots, after filtering, for all three directions, for all setups, in the middle gate floor. Note the absolute maximum ppv from the empirical cumulative distribution function and chosen quantile. 124

Figure 62. Data acquisition, in the facade of the Church of the Angels, at the level of the first floor and after vectorial rotation; (a) spectrograms of all unfiltered signals in three directions, corresponding squared Welsh power spectral density graphs and band-pass Butterworth Chebyshev type II filter. Note the division between different acquisition locations, i.e., the middle windowsill (1) (Date/Time 1-3) and the left windowsill (2) (Date/Time 4), divided by a dashed line in PSD graphs; (b) velocity-time history 3D plots, after filtering, for all three directions, of all setups. Note the absolute maximum ppv from the empirical cumulative distribution function and chosen quantile. 125

Figure 63. Data acquisition in the front end of the Church of the Angles, at the mid-span of the choir loft floor; (a) unfiltered velocity-time histories plots of an hourly signal in three directions, corresponding spectrograms, squared Welsh power spectral density graphs and band-pass Butterworth Chebyshev type II filter; (b) velocity-time history 3D plots, after filtering, for all three directions and velocity vectors VR. Note the absolute maximum ppv from the empirical cumulative distribution function and chosen quantile. 126

Figure 64. Coupled, synchronized recordings with geophones and seismographers at the Church of the Angels: (a) acquisition points in elevation, at the basement, the middle gate at ground floor

and at the level of the 1st floor (left façade window); (b) correlation between integration schemes of accelerations in the time and frequency domain. 132

Figure 65. Data acquisition at the basement of the Church of the Angels, from coupled velocity and acceleration recordings of setup S01; (a) acceleration-time history plots of a 4.5 h signal in three directions, under different filtering and an initial squared Welsh PSD graph; (b) synchronized velocity-time history 3D plots, after filtering, for all three directions, from non-spurious velocity signals and integrated accelerations. Note the empirical cumulative distribution function plot and chosen quantiles for each case. 133

Figure 66. Data acquisition at the ground floor of the Church of the Angels, from coupled velocity and acceleration recordings of setup S02; (a) acceleration-time history plots of a 1.5 h duration signal in three directions, under different filtering and an initial squared Welsh PSD graph; (b) synchronized velocity-time history 3D plots, after filtering, for all three directions, from non-spurious velocity signals and integrated accelerations. Note the empirical cumulative distribution function plot and chosen quantiles for each case. 134

Figure 67. Data acquisition at the 1st floor façade of the Church of the Angels, from coupled velocity and acceleration recordings of setup S03; (a) acceleration-time history plots of a 0.5 h duration signal in three directions, under different filtering and an initial squared Welsh PSD graph; (b) synchronized velocity-time history 3D plots, after filtering, for all three directions, from non-spurious velocity signals and integrated accelerations. Note the empirical cumulative distribution function plot and chosen quantiles for each case. 135

Figure 68. Equivalent fatigue loading under a constant amplitude, cyclic sinusoidal pattern, with the associated abbreviations. Note the higher mean stress σm, compared to the stress range $\Delta\sigma$, for testing masonry specimens under compressive or tensile stresses. 141

Figure 69. Stages of fatigue life: (a) indicative load patterns of fatigue tests, under different static stress levels σmi, in MPa, vs. cycles, and safety factor relation of a known fatigue stress combination; (b) cumulative life expectancy of a fatigue regime, linked to the different cyclic stress amplitudes σai and number of cycles Nfi, based on the Miner´s rule. 143

Figure 70. Three stages of fatigue strain, under constant fatigue stress: a rapid increase of Stage I, steady Stage II and a tertiary Stage III, until failure. Note the indicative percentage of each stage, with respect to the fatigue life Nf, as established from fatigue studies. 145

Figure 71. Correlation between the local state of stress and the initiation of cracking, from single and double flat jack tests in historic brick masonry buildings. Note that stress data over the correlation line exceed the state of the first crack, while the rest are below the onset of cracking. Adapted from Binda et al. 2007. 147

Figure 72. Accelerated fatigue experimental tests, under continuous cyclic vibrations, versus an intermittent, transient and pseudo steady state vibration regime. 148

Figure 73. Geometry and instrumentation setup of the diagonal compression cyclic fatigue tests on brick masonry wallets, with lime mortar joints and plaster (DCfi-j). 151

Figure 74. Monotonic diagonal compression test of wallet DCf1: (a) shear stress-strain curve until ultimate step. Note the chosen initial maximum shear amplitude of 200 kN for the fatigue tests of wallets DCfi-j; (b) lateral strains in time, from horizontal LVDTs and strain gauges attached in masonry and in plaster; (c) closeup on shear diagonal crack, with the splitting of plaster and without detachment from the substrate; failure of at last stage, as shown from the front (d) and the back side (e). Note the relative location of strain gauges SG1 and SG2..... 153

Figure 75. Diagonal compression tests of DCf1, DC1, DC3 and DC4: (a) linearized piecewise functions of shear stress-strain curves until peak; (b) normalized shear stress-strain curves until peak and average fit at each designated point. 156

Figure 76. Preliminary cyclic diagonal compression tests for wallets DCf2 (a), DCf3 (b) and DCf4 (c), with fit envelope curves until peak; (d) linearized shear stress-strain curves of wallets DCf1, DC1, DC3, DC4, DCf2, DCf3 and DCf4; (e) normalized shear stress-strain curves until peak, of wallets DCf1, DC1, DC3, DC4, DCf2, DCf3 and DCf4 and average fit at each designated point. 157

Figure 77. Load rate scheme on loading-fatigue-unloading branches of performed diagonal compression fatigue tests. Note the constant stress range $\Delta\sigma$ and the steady increase of static stress increment σi, for each consecutive fatigue test, until the failure of the wall specimen. . 162

Figure 78. Diagonal compression fatigue load-time histories for wallets DCf4 (a) DCf2 (b) and DCf3 (c), and respective failure modes (d), (e) and (f). Note the presented order of the tested specimens, according to the chosen progressive amplitude of the fatigue diagonal compression loading... 165

Figure 79. Temperature variation in displacement acquisition data for testing conditions of DCfi wallets. Displacement and temperature time histories from respective LVDTs, strain gauges and

temperature sensors, for a 48h recording period, and without external loading. Correlation graphs of displacement and temperature data and linear trends. 168

Figure 80. Process diagram for temperature compensation of large time series fatigue displacement raw data, from LVDTs and strain gauges. Note the equal condition for the samples per sec (sps) of temperature and displacement data. 168

Figure 81. Raw data and temperature detrending of fatigue cyclic shear tests in diagonal compression for wallet DCf4: (a) and (b) shear strain in masonry; (c) and (d) shear strain in render; (e) and (f) lateral strain from strain gauge, attached in masonry. Note the temperature evolution in the secondary vertical axis, the failure point and the average fatigue strain in magenta. 169

Figure 82. Raw data and temperature detrending of fatigue cyclic shear tests in diagonal compression for wallet DCf2: (a) and (b) shear strain in masonry; (c) and (d) shear strain in render; (e) and (f) lateral strain from strain gauge-1, attached in masonry; (g) and (h) lateral strain from strain gauge-2, attached in masonry. Note the temperature evolution in the secondary vertical axis, the failure point and the average fatigue strain in magenta. 170

Figure 83. Raw data and temperature detrending of fatigue cyclic shear tests in diagonal compression for wallet DCf3: (a) and (b) shear strain in masonry; (c) and (d) shear strain in render; (e) and (f) lateral strain from strain gauge, attached in masonry. Note the temperature evolution in the secondary vertical axis, the failure point and the average fatigue strain in magenta. 171

Figure 84. Fatigue acquisition data after temperature detrending, for wallet DCf2 in diagonal compression: (a) diagonal compression stress-strain curve in masonry surface, superposed with the shear elastic and secant modulus, normalized to the initial respective values from the first static loading branch; (b) and (c) average shear strain evolution and first derivative, with respect to fatigue cycles N; (d) and (e) average shear secant stiffness and first derivative, with respect to fatigue cycles N. Note the positive and negative trends for shear strain and stiffness respectively, indicative of fatigue softening. 177

Figure 85. Fatigue acquisition data after temperature detrending, for wallet DCf3 in diagonal compression: (a) diagonal compression stress-strain curve in masonry surface, superposed with the shear elastic and secant modulus, normalized to the initial respective values from the first static loading branch; (b) and (c) average shear strain evolution and first derivative, with respect to fatigue cycles N; (d) and (e) average shear secant stiffness and first derivative, with respect to fatigue

cycles N. Note the positive and negative trends for shear strain and stiffness respectively, indicative of fatigue softening. 178

Figure 86. Fatigue acquisition data after temperature detrending, for wallet DCf4 in diagonal compression: (a) diagonal compression stress-strain curve in masonry surface, superposed with the shear elastic and secant modulus, normalized to the initial respective values from the first static loading branch; (b) and (c) average shear strain evolution and first derivative, with respect to fatigue cycles N; (d) and (e) average shear secant stiffness and first derivative, with respect to fatigue cycles N. Note the positive and negative trends for shear strain and stiffness respectively, indicative of fatigue softening. 179

Figure 87. Exponential decay curve fitting of the normalized secant shear stiffness versus the normalized shear strain of the last fatigue loading branch, leading to failure, for wallets DCf3 and DCf4. 180

Figure 88. Fatigue loading data fitting with a reverse Gompertz curve for: (a) and (b) the fatigue average shear strain and average secant shear stiffness for DCf3-3 respectively; (c) and (d) the fatigue average shear strain and average secant shear stiffness for DCf4-6 respectively. 182

Figure 89. End to end linear piecewise function for normalized secant shear stiffness evolution and normalized cycles, for fatigue branches DCf3-3 and DCf4-6. 183

Figure 90. Abaqus of probable in-plane failure modes in a system of masonry piers and spandrels, subjected to an asymmetric vertical deformation; (a) configuration of spandrels with a timber lintel and a masonry arch at the intrados, and representation of in-plane failure modes in the spandrel, with a potential prioritization of bending failure (b), diagonal shear failure (c), and sliding shear failure in one of the piers (d). 194

Figure 91. Flexural strength verification, through shear interaction of interlocking bricks, bead and collar joints, at the interface of spandrels with piers. Adapted from FEMA 306 1998. 198

Figure 92. Experimental tests: (a) details of UN1 and UN2 twin assemblies, side by side, as a portion of the reference façade of Figure 24, and phases during construction (b) and (c). Note the segmental masonry arch and timber lintel, configured each, at a half of the spandrel's thickness, the material constituents and the Flemish bond, with a thickness of two bricks. 205

Figure 93. Preliminary FEM static nonlinear phased analysis of the reference façade, under service loads. Plots of vertical stresses in MPa. For the boundary conditions, note the simply supported beams of the roof and floors and the pinned supports at the base of the masonry façade. 206

Figure 94. Schematic representation in elevations and perspective views, of the experimental setup arrangement for UN1 and UN2 piers and spandrel masonry assemblies. 209

Figure 95. View of the axial roller bearings, part of the lateral, in-plane restrain system for the uplifting frame and pier. 209

Figure 96. Front and back views of the experimental setup for UN1 and UN2 masonry assemblies (a) and configuration of the grid of extension rods and LVDTs (b). 211

Figure 97. Masonry assemblies UN1-US (a) and UN2-US (b): time histories of the averaged monotonic vertical displacements from the actuators, the top LVDTs and the in-plane rotation of the non-moving and moving piers. 212

Figure 98. Experimental shear-displacement curves for the spandrels of the masonry assemblies UN1-US (a) and UN2-US (b). Note the relative vertical displacement of the spandrel at x-axis, and the corresponding parts (UNi-DS-Part-j) of documented damage assessment, in Figure 100 and Figure 101. 213

Figure 99. Cracked spandrel from the part of the timber lintel (left) and arch (right) for UN1-US. 214

Figure 100. Masonry assembly UN1-US: Damage State (DS) assessment at the end of each partial testing setup, of the monotonic, differential uplift. Note the arrows corresponding to the direction of the monotonic differential uplift, from each elevation side of the assembly, the differentiation of structural cracks in terms of width and color. 215

Figure 101. Cracked spandrel from the part of the timber lintel (left) and arch (right) for UN2-US. 215

Figure 102. Masonry assembly UN2-US: Damage State (DS) assessment at the end of each partial testing setup, of the monotonic, differential uplift. Note the arrows corresponding to the direction of the monotonic differential uplift, from each elevation side of the assembly, the differentiation of structural cracks in terms width and color. 216

Figure 103. UN1-DS-GR: (a) scheme of damaged state and crack filling locations; (b) cracked spandrel from the part of the timber lintel (left) and arch (right); (c) perforations at crack interfaces, insertion of tubes and sealing with mortar; (d) influx of water; (e) grout injection; (f) sealing of tubes. 221

Figure 104. Masonry assembly UN2-DS-GR-FRCM and schematic representation of the damaged state, crack filling locations, and implementation stages of the FRCM retrofitting system. 223

Figure 105. Masonry assembly UN2-DS-GR-FRCM (a) grouting injections of cracked masonry. Note the drilling holes for the adhesive in-plane anchors; (b) implementation stages of the FRCM system, involving the laying of the first layer of render, the placement of the fiber mesh, the insertion of the fiber mesh grid for the in-plane anchors, together with grouting, and the final layer of render; (c) retrofitted masonry assembly with a FRCM system after curing of 28 days..... 224

Figure 106. Masonry assemblies UN1-DS-GR (a) and UN2-DS-GR-FRSM (b): time histories of the averaged monotonic vertical displacements from the actuators, the top LVDTs and the in-plane rotation of the fixed and moving piers..... 226

Figure 107. Experimental shear-displacement curves for the spandrels of the masonry assemblies UN1-DS-GR (a) and UN2-DS-GR-FRSM (b), superposed with UN1-US and UN2-US respectively. Note the relative vertical displacement of the spandrel at the plot's x-axis, and the corresponding parts (UN1-DS-GR-Part-j and UN2-DS-GR-FRSM-Part-j) of documented damage assessment, corresponding to Figure 107, Figure 108 and Figure 109..... 228

Figure 108. Masonry assembly UN1-DS-GR: Damage State (DS) assessment at the end of each partial testing setup, of the monotonic, differential uplift. Note the arrows corresponding to the direction of the monotonic differential uplift, from each elevation side of the assembly, the differentiation of structural cracks in terms width, and under different contours..... 231

Figure 109. Masonry assembly UN2-DS-GR-FRSM (Setups 1-4): Damage State (DS) assessment at the end of each partial testing setup, of the monotonic, differential uplift. Note the arrows corresponding to the direction of the monotonic differential uplift, from each elevation side of the assembly, the differentiation of structural cracks in terms width, and under different contours. 232

Figure 110. Masonry assembly UN2-DS-GR-FRSM (Setups 5-8): Damage State (DS) assessment at the end of each partial testing setup, of the monotonic, differential uplift. Note the arrows corresponding to the direction of the monotonic differential uplift, from each elevation side of the assembly, the differentiation of structural cracks in terms width, and under different contours. 233

Figure 111. Testing of UN2-DS-GR-FRCM: close view of crack patterns at the intrados of the spandrel close to the fixed pier, from the side of the timber lintel (a) and of the arch (b)..... 234

Figure 112. View of testing masonry assembly of UN1-DS-GR, during an AVT Setup..... 236

Figure 113. Disposition of accelerometers in the performed Setups for: (a) UN1-US; (b) UN1-DS, and (c) UN1-DS-GR, with identified modes of vibration obtained from the SSI-UPCX method, and deformed mode shapes, with linear interpolation. 237

Figure 114. Disposition of accelerometers in the performed Setups for: (a) UN2-US; (b) UN2-DS, and (c) UN2-DS-GR-FRCM, with identified modes of vibration obtained from the SSI-UPCX method, and deformed mode shapes, with linear interpolation. 238

Figure 115. Data driven stabilization diagrams, with the poles selection of the SSI-UPCX method, for (a) UN1-US; (b) UN1-DS; (c) UN1-DS-GR; (d) UN2-US; (e) UN2-DS, and (f) UN2-DS-GR-FRCM. Note the Nyquist frequency of 100 Hz [SVS 2019]. 239

Figure 116. Evolution of frequencies for the undamaged state (US), the damaged state (DS), and the repair and retrofitted state (R&R) of the pier and spandrel masonry assemblies UN1 and UN2. 244

List of Tables

Table 1. Cracking damage categories, with correlation on induced vertical settlements [Day 1999 and Boscardin et al. 1989]. 17

Table 2. Formulation of the LTS method and the greenfield settlement profile [Netzel 2006, Burland and Wroth 1974, Boscardin and Cording 1989 and Timoshenko 1957]. Note the representation for bending diagonal, horizontal and combined strain in Figure 7b. 26

Table 3. Graphic representation of main brick bond patterns, at corner interlocking and for various wall thicknesses. Note the cut bricks in red to accommodate the brick interlocking at corners. Adapted from Chabat 1886 and Lacroux et al. 1878. 50

Table 4. Geometric aspects and typological characteristics of brick masonry façades, of residential brick masonry buildings, from the beginning of the 20th century, in Valladolid, Spain [Camino Olea 2001]. Note the geometrical features of the reference façade (Ref.). 55

Table 5. Testing protocols in selected experimental campaigns of uniaxial compression of masonry specimens, with focus on loading or displacement control, monotonic or cyclic, and capacity range. 68

Table 6. Testing protocols in selected experimental campaigns of diagonal compression of masonry specimens, with focus on loading or displacement control, monotonic or cyclic, and capacity range. 69

Table 7. Flow rate test results for hydraulic lime mortar mixes with different water percentage. 71

Table 8. Physical and mechanical properties of M4 NHL mortar, i.e., mass density, compressive strength, flexural strength and Young's modulus. 74

Table 9. Physical and mechanical properties of fired bricks, i.e., mass density, water absorption, mean porosity, compressive strength, flexural strength and Young's modulus. 79

Table 10. Physical and mechanical properties of M15 hydraulic lime-based render and fluid binder, i.e., mass density, compressive strength, flexural strength and Young's modulus. 83

Table 11. Physical and mechanical properties of M4 hydraulic lime-based mortar prisms, collected during construction and cured at ambient environmental conditions in the laboratory, i.e., mass density, compressive strength, flexural strength and Young's modulus. 87

Table 12. Mechanical properties of UC1-4 brick masonry wallets with lime mortar M4 tested in uniaxial compression, i.e., compressive strength, Young's modulus, $EMOD\sigma max$ ratio and maximum axial strain..... 91

Table 13. Cyclic diagonal compression test variations in peak shear stress and strain, for wallets DC3 and DC4..... 94

Table 14. Mechanical properties of DC1-4 brick masonry wallets with lime mortar M4, tested in diagonal compression, i.e., tensile strength, shear strain at peak, shear modulus and ratio with compressive strength..... 95

Table 15. Goodness of fit from linear regression analysis, for selected stress values from tests of UC and DC, corresponding to 5%, 0.33%, 0.75%, 90%, 100% of the strength and at ultimate stage, with the predicted stress values from Equation 28, Equation 29 and Equation 30, Equation 31 and Equation 32..... 99

Table 16. Average mechanical properties accounted for the characterization of simulated historic brick masonry with M4 NHL mortar, based on mechanical laboratory testing and literature.... 100

Table 17. Peak particle velocity limits for historic structures from various standards..... 107

Table 18. Distinction between cracks, regarding their width w [SN 604312A:1992]. 110

Table 19. Frequencies and damping ratios of the first six modal shapes with the SSI-UPC Method [SVS 2019]..... 115

Table 20. Ground-borne vibration levels and attenuation compared within the building. Note the reference of zero VdB at the level of the sidewalk. 118

Table 21. Evolution of shear stress, shear strain and shear stiffness, during the monotonic diagonal compression test of wallets DCf1, DC1, DC2, DC3, DC4. 155

Table 22. Evolution of shear stress, shear strain and shear stiffness, for rendered wallets DCf2, DCf3 and DCf4, retrieved from the envelope curve of the preliminary cyclic diagonal compression tests and the envelope curve fit of Equation 29, until the peak. Note the predicted tensile strength, peak shear strain and shear modulus, according to the curve fitting process..... 158

Table 23. Fatigue ppv, ppd target amplitudes, with the corresponding shear force amplitudes for each wallet. 161

Table 24. Fatigue testing protocols for the three consecutive loading branches. 163

Table 25. Fatigue sign variables for diagonal compression, for each of the testing wallets (DCfi) and fatigue parts (j). 163

Table 26. Shear stiffness evolution during static (A_j) and fatigue (B_j) loading branches, for wallet DCf2. 173

Table 27. Shear stiffness evolution during static (A_j) and fatigue (B_j) loading branches, for wallet DCf3. 173

Table 28. Shear stiffness evolution during static (A_j) and fatigue (B_j) loading branches, for wallet DCf4. 173

Table 29. Mean and standard deviation of shear strain secant stiffness rate of Stage II fatigue, in B_j loading branches, for wallets DCf2, DCf3 and DCf4. Note the fatigue branches resulting to failure in red. Note the computation of the first derivative from the 9^{th} order polynomial fit for the average shear strains and secant shear stiffness of the fatigue cycles. 180

Table 30. Estimated fatigue cycles to failure for incomplete fatigue branches, according to the obtained end to end linear piecewise functions for fatigue, and under the hypothesis of constant fatigue failure properties, for each of the tested wallets DCf3 and DCf4. Note the deterministic fatigue cycles until failure for fatigue branches DCf3-3 and DCf4-6, in red. 183

Table 31. Experimental data collection of unreinforced masonry piers and spandrels from literature, considering aspects of shear capacity and drift ratio thresholds [Gattesco et al. 2015, Parisi et al. 2014, Graziotti et al. 2016 and Beyer and Dazio 2012]. 193

Table 32. Experimental testing on asymmetrical monotonic vertical uplift in masonry piers and spandrels: tested assemblies, types of boundary conditions and strengthening specifications. 204

Table 33. Preliminary material properties, cross-sections and spacing of floor and roof diaphragms. 207

Table 34. Experimental data collection of unreinforced and reinforced masonry wallets, with FRCM systems, tested under uniaxial compression [Carozzi et al. 2018, Prota et al. 2006 and Wang et al. 2019]. 219

Table 35. Certified material properties of sub-components of the FRCM system with adhesive anchors [GeoCalce FL Antisismico 2019, GeoCalce F Antisismico 2019, GeoSteel 600 2019 and GeoSteel Injector&Connector 2019]. 225

Table 36. Test results: spandrel maximum shear force and peak displacement, yield displacement and shear force ordinate, displacement ductility and hardening stiffness for UN1-US, UN1-DS-GR, UN2-US and UN2-DS-GR-FRCM. 228

Table 37. Frequencies, damping ratios and mode shape characteristics, under the SSI-UPCX method, for all the tested masonry assemblies [SVS 2019]. 240

Table 38. MAC values of principal in-plane and out-of-plane, in-phase modes between: (a) UN1-US; and UN1-DS; (b) UN1-US and UN1-DS-GR; (d) UN2-US and UN2-DS, and (e) UN2-US and UN2-DS-GR-FRCM. Note the color gradient and cell attributes in (c). 241

Table 39. Analytical formulations, with geometrical and mechanical parameters for prioritizing the in-plane strengths for the non-moving masonry piers of UN1-US, UN2-US, UN1-DS-GR and UN2-DS-GR-FRCM, according to FEMA 356 2000. 251

Table 40. Analytical formulations, with geometrical and mechanical parameters for the in-plane flexural strength in the spandrels of UN1-US, UN2-US, UN1-DS-GR and UN2-DS-GR-FRCM, according to FEMA 356 2000. 252

Table 41. Analytical formulations, with geometrical and mechanical parameters for the in-plane shear strength in the spandrels of UN1-US, UN2-US, UN1-DS-GR and UN2-DS-GR-FRCM, according to FEMA 356 2000 and NTC 2018. 253

Table 42. Correlation of displacement and temperature data with linear trending, for wallet DCf2.Note the relative locations of strain gauges, LVDTs and cracks. 285

Table 43. Correlation of displacement and temperature data with linear trending, for wallet DCf3.Note the relative locations of strain gauges, LVDTs and cracks. 290

Table 44. Correlation of displacement and temperature data with linear trending, for wallet DCf4.Note the relative locations of strain gauges, LVDTs and cracks. 292

CHAPTER 1. INTRODUCTION

CHAPTER 1. Outline

1.1. Background and motivation

1.2. Thesis objectives

1.3. Research methodology

1.4. Outline and organization

1.1. Background and motivation

Cultural heritage buildings are irreplaceable and highly complex, having evolved over time, and contain various heritage components and systems. Given their low mechanical properties, weak connections between parts and fragile failure modes, heritage buildings are highly susceptible to changes on their foundations and, in particular, unprecedented transformation processes in cities due to tunneling. In fact, the demand for tunnel constructions in over-concentrated urban networks emerges when no other means of transferring people or materials are applicable or adequate, in terms of efficacy, time transferring needs and obstruction. Tunneling constructions and subsequent underground railway operations, pose a significant impact on overlying structures, and, in particular, on highly sensitive historic masonry structures.

In general, the challenges involved in processes of structural safety assessment, repair and retrofit of cultural heritage buildings are manifold. These are related to the defined values of cultural heritage assets and acceptable damage levels, which must address crack initiation and cannot be only defined at ultimate level or collapse prevention. In case of valuable finishings, such as frescoes, tiles, timber marquetry or others, the definition of threshold damage values is particularly complex. As stated in ISO 13822:2010, the performance criteria for historic structures aim on securing the integrity of historic assets, both structural and non-structural, through additional serviceability limit states, and under more strict thresholds of vibration levels.

One of the main effects of tunneling construction is the induced soil movements during the excavation processes and the implication on the performance of surface neighboring structures, which remains a challenge at design and construction stages. In fact, the prediction of settlements for soil and overlying structures, either empirical, with analytical models, or complex nonlinear Finite Element (FE) models, coupled or uncoupled, is one of the main tasks in the design of

underground infrastructures, as it allows the estimation of the related induced damage, and provides a strategy to select the most appropriate mitigation techniques [Puzrin et al. 2012, Mair and Taylor 1997 and Amorosi et al. 2014].

In a following stage, underground railway induced vibrations are considered, caused by quasi-static and dynamic axial loads from moving trains, which are transmitted through the soil continuum and reach the foundation level of the buildings of interest. Here, geotechnical parameters, design and construction processes, as well as operational use characteristics, are among the parameters that define the amplitude and severity of induced vibrations in historic buildings [Thompson et al. 2009]. The effect of ground-borne vibrations is material deterioration and cracking, through frequently repeated actions, defined as fatigue [FIB Model Code 2013]. Under the current framework, vibration limits of kinetic quantities (i.e. vibration levels), are present in international standards, and aim on minimizing the possibility of immediate or fatigue damage for serviceability limit states, with strict threshold values for cultural heritage buildings, yet variable in different standards [ISO 4866:1990/Amd 2:1996 2010, BS 7385-2:1993, DIN 4150-3 2016, SN 640312A 1992 and GB/T 50452 2008]. In addition, monitoring protocols of ground-borne vibrations in buildings, present in many standards, define among others, the periodicity and locations of acquisitions, the sampling frequencies, the wave propagation limits within the building, the appropriateness of geophones for data collection and the direct measurement of velocities and post-processing protocols, involving filtering and integration schemes [SN 640312A:1992, DIN 45669-2:1995-06, DIN 4150-3 2016, ISO 4866:1990/Amd 2:1996 2010, BS 5228-2:2009+A1:2014 and BS 7385-2:1993].

Thus, the process of structural reliability and damage for cultural heritage structures in the proximity of operating underground railways is twofold and interrelated, namely by accidental damage through settlements and the progressive structural deterioration through fatigue. Both phenomena are time dependent and repetitive (or cyclic), and thus, monitoring of structural conditions or actions, under continuous and long-term observation periods, is considered essential and linked to the knowledge of structural response [ISO 13822:2010].

In addition to the above, deterioration models and hysteretic force-displacement relations are often not incorporated in complex FE modelling, e.g., nonlinear 3D homogeneous FE models under a smeared crack approach, and thus, the process of structural assessment through the use of nominal values for material properties can be unrealistic, especially under adverse effects of

severe environmental fluctuations, improper operation and fatigue actions [ISO 13822:2010]. Simplifications in existing nonlinear material models, and present knowledge on material data and computational restrictions, pose unavoidable constraints in conducting a full multi-hazard structural response assessment. Additionally, in numerical models, many simplifications, such as the use of equivalent monotonically increasing loads [Lourenco 1996], instead of dynamically induced ones, reflect on the accuracy of a sequential nonlinear response. This has a direct impact on cumulative damage propagation and the corresponding ductility capacity. Instead, the use of corrective coefficients on the nominal material properties, accounting for structural deterioration in areas, over a specific timeframe, and based on experimental results, is considered more achievable. As also stated in ISO 13822:2010, time variating material properties are defined under probabilistic distribution functions over time.

Furthermore, considering the structural assessment of masonry cultural heritage buildings, in the proximity of underground railways, at a given point of the service life, and unless extensive long-term monitoring periods have preceded, it is rather difficult to associate structural damage in buildings, solely to settlements or ground-borne vibrations. Crack formation may be initiated by settlements, earthquakes, or accidental actions, but, additionally, continuous ground-borne vibrations of high amplitudes may further increase existing cracks or introduce new ones. The different hazards will unavoidably interact, such as earthquakes and settlements, which can introduce additional discontinuities and changes in load paths that result locally to stress intensities close to the ultimate capacity, where fatigue actions appear more destructive. Thus, in masonry structures, long-term effects on ductility, durability, stiffness and strain increase, under the presence of various hazards, have not been fully investigated.

Experimental studies on accelerated fatigue in masonry involve mostly static loading conditions and equivalent fatigue cyclic loading, with the ultimate fatigue strength and number of cycles (S-N curves) being of interest, as presented in Casas 2009, Casas 2010, Koltsida et al.2018A, Koltsida et al.2018B, Carpinteri et al. 2014, Melbourne et al. 2004, Roberts et al. 2006 and Ronca et al. 2005. Yet, a clear knowledge of the evolution of the fracture parameters, stiffness properties and the rate of deterioration in historic masonry, under realistic combinations of static stress paths and ground-borne vibration fatigue is not clearly established. Besides, fatigue experimental testing of masonry wallets is of particular complexity, given the large testing durations and restrictions in terms of the specimen's size, load application and instrumentation.

Experimental in-plane capacity tests in masonry perforated walls, composed by piers and a spandrel, have proven the significant contribution of the spandrel in the overall in-plane capacity, with a combination of flexural and diagonal shear cracking in the spandrel, as seen in Augenti et al. 2016, Gattesco et al. 2015, Gattesco et al. 2008, Parisi et al. 2014 and Beyer and Dazio 2012. Issues of increased complexity involve the definition and application of vertical and axial prestress levels, in the piers and spandrels, respectively, with the later contributing on the spandrel's shear capacity and ductility, as demonstrated in Beyer and Dazio 2012 and Graziotti et al. 2016. Structural reintegration techniques on damaged piers and spandrel systems, by means of grouting, near surface inorganic matrix-grid systems with mortar coatings, and external steel fiber-reinforced polymer ties, have been evaluated experimentally in Augenti et al.2016 and Gattesco et al. 2015.

1.2. Thesis objectives

The effect of soil settlements and vibrations induced by underground structures on the safety of neighboring masonry cultural heritage buildings is an open challenge. Hence, the process of obtaining reliable experimental data, for the assessment and prediction of settlement-vibration induced damages on masonry specimens, simulating historic masonry, and investigating the performance of engineered repair and retrofit applications, are the main objectives of the current work, which intend to contribute with sufficient knowledge to this field of study. The approach is considered of high complexity, since the mutual influence of soil settlements and induced ground-borne vibrations is not easily incorporated experimentally. Thus, each action is experimentally investigated as independent, in different types of specimens, with the acquired results meant to be incorporated to future FE modelling applications. For this purpose, the thesis will address the following issues:

(a) Compile information regarding the typology of historical brick masonry residential buildings of the 19^{th} and 20^{th} centuries in Europe, with focus on masonry facades (configuration and materials) and characterize physically and mechanically material constituents and assemblies, used for the experimental tests on differential settlements and fatigue for induced ground-borne vibrations;

(b) construction characteristics of tunnels in urban environment, with focus on soft soil conditions, and the nature of induced ground-borne vibrations;

(c) the value of cultural heritage and their structural and mechanical characteristics, together with damage classification thresholds, methods and processes, aimed at assessing induced soil settlement and ground-borne vibrations;

(d) design and application of field monitoring strategies, in order to acquire data for ground-borne vibration in a real case study of a cultural heritage building and diagnose inherent challenges in acquisition and processing;

(e) add new experimental data on the study and monitoring of fatigue loading applications in simulated historic masonry specimens, replicating realistic combinations of static and fatigue loading, and focusing on material deterioration and stiffness degradation;

(f) add new experimental data on the study and monitoring of in-plane differential settlements, in simulated historic masonry specimens, and quantify the nonlinear in-plane response, damage mechanisms, structural interactions between piers and spandrels. In addition, assess the effectiveness and performance of up-to-date structural repair and retrofit techniques on pier and spandrel systems, under a differential displacement field, that have suffered extensive cracking;

(g) in terms of analytical processes, to correlate testing results with analytical formulations for fatigue, also considering strain and stiffness parameters. For the testing results on differential settlements, to implement capacity prediction and types of failure, according to existing macro-element capacity models, present in building codes, also accounting for boundary conditions, repair, and retrofitting, and

(h) involve non-destructive testing methods for damage and stiffness evolution in the experimental laboratory campaign of differential settlements and fatigue.

1.3. Research methodology

Considering the research background, motivation and objectives, as established in previous sections, the current thesis focuses on experimental tests in simulated historic masonry assemblies, with solid low fired bricks and lime mortar, and replicating the effect of soil settlements and ground-borne vibrations, with focus on monitoring the development of cracks and strains in masonry.

The reference configuration for constructing the masonry assemblies was set in the facades of brick masonry residential buildings, with weak horizontal timber diaphragms, dating between the 19th-20th centuries in Europe and in particular in the Iberia Peninsula, described thoroughly in Chabat P. 1886, Lacroux et al. 1878, Camino Olea 2001, Apolo and Martínez-Luengas 1995, González-Redondo et al. 2003, Cardoso et al. 2014 and Mascarenhas 1996. Here, the main characteristic for the spandrels are a combination of a segmental brick masonry arch and a set of timber beams equally placed in their thickness. For the choice of material constituents to simulate historic masonry, the goal was set on reaching a medium to low compressive strength f_c and Young's modulus, with the respective ranges of 2.6-8.0 MPa and (200:550) f_c, according to NTC 2018, Tomazevic 1999 and FEMA 306 1998. Solid bricks, fired at low temperatures, from the Cenol manufacturing company in Amarante, Portugal, and a ready lime mortar premix, with classification of M4 and CS II, from SecilTek, a Portuguese construction material company, were used [BS EN 998-2:2003, EN 998-1:2016, REABILITA CAL CS 2019]. Additionally, two modern repair and retrofit materials for masonry were used, a high-performance hydraulic lime-based fluid binder M15, for crack filling, and a Fiber Reinforced Cementitious Matrix system (FRCM), with a hydraulic lime-based premix render, of class M15, from KERAKOLL construction material company [GeoCalce FL Antisismico 2019 and GeoCalce F Antisismico 2019]. Material characterization tests were conducted on mortar flow rate, mass density, brick water absorption and mean porosity, three-point loading tests for flexural capacity, compression strength tests and tests for Young's modulus. After a curing period of around 200 days, a series of constructed masonry wallets with a Flemish bond and a 1½ brick thickness were tested under cyclic uniaxial and diagonal compression, according to BS EN 1052-1-1999 and ASTM E519/E519M-20, in order to obtain reference values on strength and the evolution of stiffness and energy dissipation at incremental steps, also documented with Digital Image Correlation (DIC) acquisitions. As a last step, the obtained data were checked under a set of analytical stress-strain expressions from literature and the best envelope fits were identified, serving as a reference for capacity prediction of wallets, during the fatigue experimental campaign.

Next, accelerated fatigue experimental tests, assuming the scenario of ground-borne vibrations, were designed under diagonal compression loading regimes, in masonry wallets, considering also the presence of a lime-based render in one side. Loading protocols were set under a high static shear stress and low to medium stress reversals, considering realistic scenarios of direct shear stress concentrations at specific locations of a façade, with the masonry at a highly

nonlinear state, a small capacity margin and relatively close to failure. Also, for each tested wallet, instead of an independent loading regime for fatigue, an alternative scenario was investigated, under time-based variations of static stress and strain, which, according to Binda 2008, are common in the course of time, for many historic structures, mainly from environmental and anthropogenic influences.

The statistical results from the in-situ monitoring campaign of induced vibrations in the Church of the Angels in Lisbon, were here used partly as a reference, in order to move from the targeted peak particle velocity (ppv) values, under the measured wave frequency range, to the targeted displacement and corresponding force amplitudes of the fatigue loading. For each specimen, under a specified number of cycles, corresponding to a period of passing trains of around 1.5 years, static diagonal compression amplitudes were progressively increased, with a constant fatigue range, and until failure was reached.

Here, a reference diagonal compression capacity curve was obtained by testing a specimen under monotonic diagonal compression. Subsequent envelope curves of diagonal compression, for each of the specimens tested under fatigue, were constructed partly from preliminary quasi-static, cyclic loading, and partly from curve fitting, under the statistically normalized stress-strain relationships, from both rendered and unrendered wallets.

For each masonry wallet, tested under diagonal compression fatigue, and until failure occurred after N_f cycles, shear strain-time histories were found temperature dependent, following complex contractions and dilations, and thus, were linearly compensated by means of simultaneous readings from temperature sensors. Following, fatigue data were processed individually for each loading combination, based on shear strain (γ_t) relaxation and secant shear stiffness (G_{sec}) softening, and fatigue curves of γ_t-N_f, G_{sec}-N_f and $G_{sec,norm}$-$\gamma_{t,norm}$ were constructed, for monitoring plastic deformations, shear strain and stiffness evolution, and associate fatigue life estimates, according to Dowling 2007, Glinka 1985 and Hu et al. 2021.

Finally, results from complete fatigue tests, in terms of the average shear strain γ_t and secant shear stiffness G_{sec}, were fitted with a reversed non-symmetrical sigmoid function of the Gompertz equation, under a high achieved correlation. Considering the hypothesis of Holmen 1982, of equal fatigue failure properties, end-to-end linear piecewise functions of normalized fatigue

properties were used to estimate the fatigue life of the various, fatigue stress states, where failure was not reached.

For the experimental campaign of an asymmetrical monotonic vertical displacement, two identical real scale specimens were constructed in the ISISE Laboratory of the Civil Engineering Department of the University of Minho (Portugal), comprised by masonry piers and a spandrel, under the abovementioned reference brick masonry façade. The boundary conditions, were configured under a constant, vertical stress field in the piers, replicating gravitational loads, equivalent to the 2nd story of the reference façade. For the lateral restrain, two different conditions were applied, i.e., one of free rotations and a restrain of lateral supports for the uplifting pier, by means of axial roller bearings and diagonal prestressed rods, tied to the reaction wall. Regarding the horizontal axial restrain in the spandrels, no axial prestress was applied, accounting for uniform spans and spacing of piers, and the absence of strengthening axial elements. By means of a steel testing frame, an equivalent vertical uplift was applied in one of the piers, by means of two electro-mechanic actuators, and until fully formed cracks in the spandrel and piers were reached. Subsequent surface deformations were measured by means of 44 linear variable differential transformers (LVDTs). Test results were produced in terms of global displacement and rotation-time histories, shear force-vertical displacement capacity curves in the spandrels, while crack mapping was conducted in various intermediate testing increments.

Furthermore, for the damaged specimen's, the effectiveness of two strengthening techniques was investigated, i.e., a simple reintegration of the internal crumbling and fragmentations, by means of lime-based grouting, and a comprehensive strengthening strategy with grouting and a Fiber Reinforced Cementitious Matrix system (FRCM), with in-plane FRCM anchors, under a total of four testing applications, under the same loading regime. Testing results are compared with the ones of the undamaged specimens, in terms of shear force, shear stiffness, yield displacement, peak displacement and corresponding ductility. Besides, under a series of ambient vibration testing (AVT), conducted prior to each test, damage assessment is attempted from the resulted vibration signatures (frequencies, mode shapes and damping).

Finally, the collection of experimental data for the tested piers and spandrel, masonry assemblies, is compared with code analytical expressions, of expected failure modes and nominal capacities, under the framework of FEMA 274 1997, FEMA 356 2000, FEMA 306 1998 and NTC 2018. Here, a hierarchical step-by-step evaluation of the in-plane capacities is performed,

accounting for the documented damage progression, and considering that load trajectories are not significantly altered by prior failure modes. Considering the contribution of strengthening elements, the in-plane capacity component of the FRCM system is incorporated according to ACI 549.4R-13 2013 and CNR-DT 215/2018 2020.

1.4. Outline and organization

The thesis provides a quantitative approach, analysis and processing for the effect of soil settlements and fatigue from induced ground-borne vibrations, in historic masonry buildings, under equivalent experimental testing in replicas of historic masonry specimens, and field monitoring applications in a real case study. The respective tasks are divided in five chapters, besides the introduction (Chapter 1) and the chapter of conclusions and future works (Chapter 7). The chapters are given in (Figure 1) and configured as followed:

- **Chapter 1 – Introduction**: presents the research background and motivation, the main objectives associated with the developed work, the research methodology followed and the outline organization of the thesis.
- **Chapter 2 – Induced soil settlements and vibrations from underground structures**: reviews the research background in the field of induced settlements and ground-borne vibrations in soft ground, together with damage evaluation criteria, numerical and analytical applications.
- **Chapter 3 – Material characterization for simulated historic masonry, repair and retrofit**: contains the configuration of the brick masonry residential buildings, dating between the 19^{th}-20^{th} centuries in Europe, used as reference for the experimental campaign of differential settlements and fatigue from ground-borne vibrations, together with mechanical and physical characterization tests of replicas of historic constituents, masonry specimens, as well as repair and retrofit materials.
- **Chapter 4 – Field monitoring of induced ground-borne vibrations**: evaluates the current framework for the assessment and monitoring of ground-borne induced vibrations and demonstrates the applicability, post-processing and appropriateness of coupled instrumentation, through monitoring in a cultural heritage building, in close proximity to a metro line, with perceivable ground-borne vibrations.

- **Chapter 5 – Fatigue tests on masonry wallets under diagonal compression**: contains results and analytical applications for accelerated fatigue experimental tests in masonry wallets, simulating the effect of ground-borne vibrations, under diagonal compression loading regimes.
- **Chapter 6 – Tests of differential settlements on piers and spandrel specimens, repair and retrofit applications**: contains results and analytical applications from experimental tests on asymmetrical monotonic vertical displacements, in masonry specimens composed by piers and a spandrel, together with the assessment of two strengthening techniques, i.e., a structural reintegration by means of lime-based grouting and a comprehensive strengthening with grouting and a Fiber Reinforced Cementitious Matrix system (FRCM), with in-plane FRCM anchors.
- **Chapter 7 – Conclusions and future research**: presents the main conclusions from the developed experimental research and proposes topics for future research and development, based on the concept of numerical modelling of multi-hazard analysis for induced soil settlements and ground-borne vibrations in cultural heritage buildings.

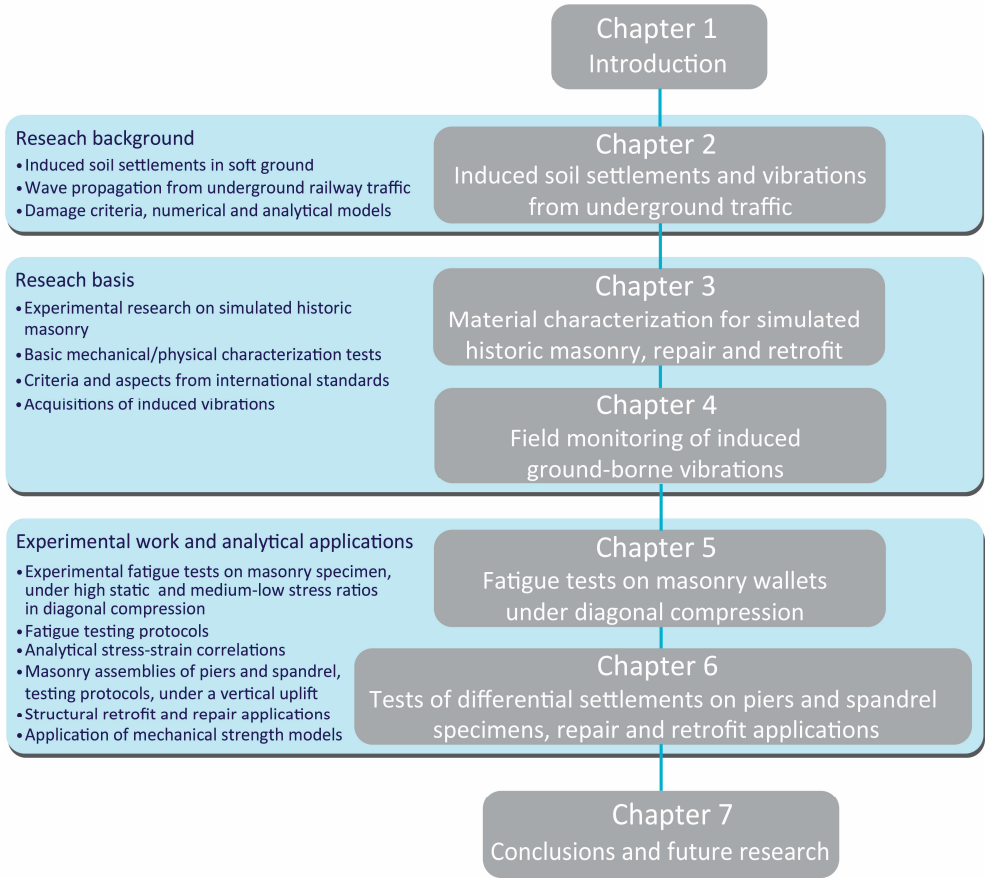


Figure 1. Flow chart of the thesis outline, with the research background, basis and activities comprising the thesis.

CHAPTER 2. INDUCED SOIL SETTLEMENTS AND VIBRATIONS FROM UNDERGROUND STRUCTURES

CHAPTER 2. Outline

2.1. Introduction

2.2. Tunneling in soft ground

2.3. Induced soil settlements from underground structures

2.3.1. Damage criteria

2.3.2. Analytical models

2.3.2.1. Greenfield deformations

2.3.2.2. Limiting Tensile Strain Method

2.3.3. FE modelling approaches

2.4. Induced vibrations from underground railway traffic

2.4.1. Wave propagation in the elastic half-space

2.4.2. Vibrations from underground railway tunnels

2.4.3. FE modelling approaches

2.4.3.1. Semi-analytical models

2.4.3.2. The Boundary Element method in 2D and 3D

2.4.3.3. The 2.5D method

2.4.4. Mitigation measures

2.5. Conclusions

2.1. Introduction

During the design, implementation and execution process of a tunnel, actions should be undertaken in order to mitigate the potential risks [Bickel and Kuesel 1982]. The prediction of settlements is one of the main tasks in the design of urban underground infrastructures, as it allows the estimation of the related damage, induced on surface structures, and provides a key ingredient to select the most appropriate mitigation techniques to be adopted. Here, masonry historic structures are the main focus of interest. Among the challenges for damage assessment are the uncertainty on material parameters, the damage and deterioration due to weathering and

environmental actions, the highly non-linear behavior of masonry, known by its quasi-brittle fracture and cracking, the consequent stress redistribution, and the important effect of soil–structure interaction.

The conventional approach to evaluate possible induced damage due to soil settlements is based on the empirical prediction of the subsidence curve under free-field (also known as greenfield) conditions [Peck 1969 and Fargnoli et al. 2013]. The building is represented by a simple, weightless, two-dimensional (2D) deep elastic beam, undergoing sagging and hogging modes of deformation according to the soil displacement profile. The onset of cracking is related to the critical tensile strain within the beam, associated with shear and bending. Extension of this approach to a three-dimensional (3D) space has been performed recently, adopting an analytical thick plate model to include the effect of both in-plane and out-of-plane ground movements [Namazi and Mohamad 2013]. These so-called uncoupled approaches do not consider the interaction between soil and structure, in terms of additional stiffness and weight, on the tunneling-related displacement field. Thus, pre-assessments frequently lead to over-estimated differential settlements and, consequently, damage predictions are more severe than what is typically observed in real cases [Amorosi et al. 2014 and Giardina et al. 2013]. The coupled effect of building weight and stiffness, the soil characteristics, the ground properties and the type of foundations play a fundamental role in the structural response, affecting the settlement profile and the resulting building damage. In Potts and Addenbrooke 2017, a coupled 2D finite element model is used to study the influence of a surface structure on the ground movement due to tunneling. Their numerical results showed that the presence of the surface structure has a significant influence on the ground movement.

In case of masonry structures, only a few numerical studies have been performed, considering the soil-structure interaction in 2D or 3D space and assuming nonlinear material models for both soil and masonry, see e.g. in Amorosi et al. 2014, Giardina et al. 2013 and Burd et al. 2000. On the other hand, only very few experiments have been published on complex masonry structures subjected to ground displacements, see e.g. Giardina et al. 2012. Moreover, the lack of accurate crack measurements makes the validation of numerical models difficult. The development of suitable numerical models and reliable experimental results are therefore essential at this stage for obtaining a deep insight into the failure mechanisms in masonry buildings, which will lead to reliable assessment and strengthening methods.

In the proximity of underground subway lines, induced vibrations are mostly concerned during operational time, but can also be considered important during construction, especially since construction periods involve large time spans. Vibration levels are assessed through different national standards and against criteria for damage on structural and non-structural components [Thompson et al. 2009]. Issues of importance, but also of increased complexity, are determining the effects on load-bearing capacity, mostly regarding fatigue, under certain number of cycles, and on the damage of non-structural components. Mostly, the assessment is carried through in situ measurements, but the definition of acceptable vibration levels is also conflicting when using different international regulations, particularly in the case of cultural heritage buildings. An advanced assessment should account for analytical and numerical modelling. A key aspect is the propagation of waves, through the elastic non-homogeneous soil continuum. Thus, theoretical models of wave propagation are of use [Thompson et al. 2009].

FE models can serve as an assessment and prediction tool for induced vibrations, on soil-structure interaction problems, by means of dynamic analysis of moving loads, with time integration. However, certain restrictions apply, mainly on the wave-propagation characteristics. Conventional FE models cannot replicate adequately the wave propagation, mainly due to unavoidable spurious reflections on the artificial boundaries of the model. In order for the soil to be modelled as an infinite medium or 'free field', an appropriate combination of springs and dashpots is necessary, along with bodies of great mass and rigidity [Diana user's manual 2020]. Other approaches, involve the Boundary Element method (BE), with focus only on discretization of internal boundaries, versus the domain discretization of the FE method. Thus, the soil is represented with an infinite extent, and boundary values of physical quantities are obtained through interpolation functions. Yet, the BE method requires vast computational resources [Thompson et al. 2009]. Lastly, through the '2.5-dimensional' method, a 3D response can be obtained efficiently, by applying Fourier transformation techniques in 2D FE models of tunnel sectional profiles [Yang and Hung 2001 and Ghangale et al. 2019].

2.2. Tunneling in soft ground

The demand of constructing a tunnel emerges when no other means of transferring people or materials are applicable or adequate, considering also aspects of efficacy, time transferring needs and obstruction, for over-concentrated, above ground, urban networks. Tunneling works are

highly dependent on design and construction characteristics, reflecting also completion times and high costs.

The current work will be focused on the tunneling in soft ground, i.e., in sandy to silty clay soils, and the assessment of settlements and vibrations, at the level of foundation of surface infrastructure and particularly monuments, thus, in approximation, settlements and vibrations at surface level. The specification of soft ground might differ in accordance with a geotechnical or tunneling engineering perspective, but in general it can be defined as the type of soil that requires any form of support, so as to prevent ground instabilities, both in short and long term. Tunneling construction in soft ground is usually the one producing ground movements, with relatively high magnitudes. Thus, having an estimation on the expected settlement profile, prior to construction, is crucial, which will also determine the construction procedure and the implementation of settlement control measures in specified areas. The methodology of the settlement profile is associated with the settlement volume and normalized volume loss [Bickel and Kuesel 1982]. The main volume loss, and corresponding induction of settlements, is due to the radial deformations of the tunnel's face, soon after the excavation and before the installation of the tunnel lining and grouting [Mair and Taylor 1997]. Also of relevance is the applied pressure on the tunnel's face, which controls the magnitude of rapid inward face displacements [ITA/AITES Report 2006]. The prediction and assessment of ground movements, prior to construction, is influenced by stratigraphy, the construction method, the type of tunneling and the overlying structures. Prior to construction, the parameters that have a high level of uncertainty and are known to a limited extent are those related with the geological conditions, the effective foundation conditions and geometry. In particular, detailed characterization of surface and subsurface conditions has a significant effect on the accuracy and magnitude of predicted settlements. A geotechnical investigation is essential for the level of knowledge of soil conditions, prior to the design and execution of tunneling. It mainly involves deep boreholes and cross-hole tests, cone penetration tests with a piezocone, down-hole tests and dilatometer tests. Additionally, triaxial compression and tensile tests can determine the shear stiffness of soil layers [Rampello et al. 2012]. The mechanical properties of soil layers that overlay a tunnel structure, and are essential for design purposes, are the density, the shear strength, the Young's modulus, the Poisson's ratio and the permeability. All properties are referred to undrained soil conditions and for soft ground tunneling, with the actual field soil properties strictly associated with ground water conditions [Mair and Taylor 1997].

Tunnel excavation techniques in the urban environment are divided between two main categories, i.e., bored tunneling versus cut-and-cover tunnels. For bored tunneling, which is the focus of the current study, temporary support, during excavation is provided by shield support, compressed air, slurry machine, earth pressure balance machine (EPB) or shotcrete. Permanent support (lining) is usually implemented by precast wedged blocks of concrete, or reinforced shotcrete. The lining is constructed or fabricated just behind the temporary shield, whereas the shield is projected along the line by means of reaction jacks against the completed parts of the lining. In use of Tunnel Boring Machines (TBM), closed face head cutters are propelled by cutting rotation. Controlling face thrust counteracts the front soil pressures (Earth Pressure Balance) [Esveld 2001 and Potts and Zdravkovic 2001].

Under these conditions, the induced stress release causes soil movements towards the opening, or else volume losses, and the main design requirement is limiting ground deformations. In summary, the total short-term settlement profile, induced by the tunneling, can be divided in the following and is presented in Figure 2 [Esveld 2001 and Potts and Zdravkovic 2001]:

- *Face loss*. By counteracting with applied pressure in the plane of the cutter head, the induced settlement can be controlled and minimized.
- *Radial loss in shield*. Contractions in the shield are mostly due to its conical shape. By the use of Earth Pressure Balance (EPB), the soil pressure in the circumference of the boring machine can be reduced.
- *Radial loss behind the shield (tail void)*. If the lining is constructed immediately behind the shield, then a portion of the face is unsupported and radial deformations evolve. Regardless of where the immediate lining segments are placed, a gap is always present between the tunnel lining and the soil, which is actively deformable. It is common practice to directly fill the gap by injecting grout under pressure, which can keep the deformation of the tunnel's face within certain limits.

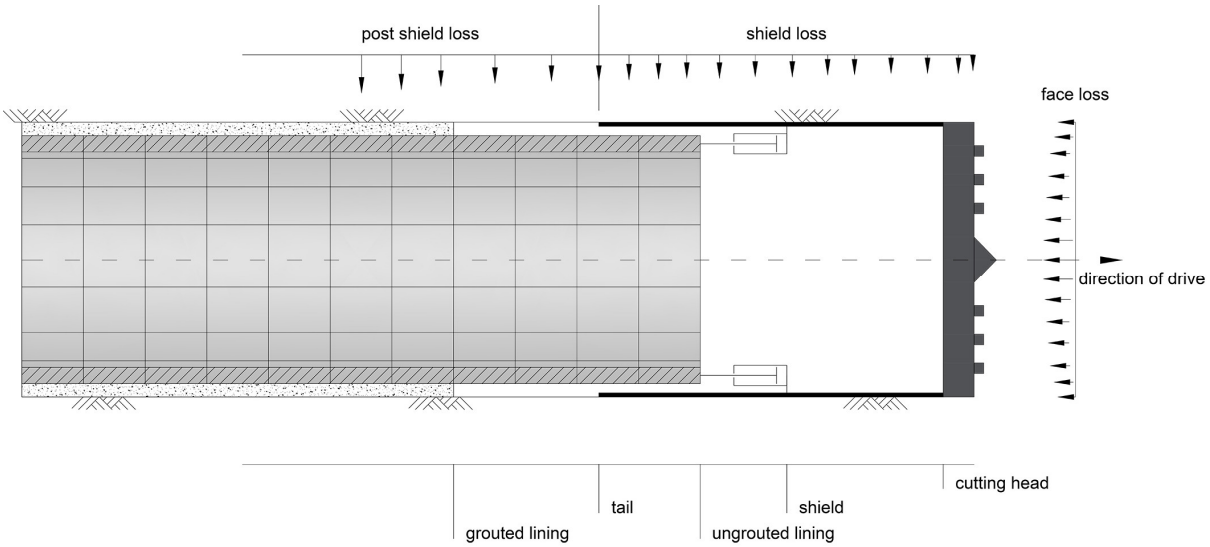


Figure 2. Volume losses during tunneling excavation with a TBM.

2.3. Induced soil settlements from underground structures

As previously discussed, tunneling construction unavoidably induces settlements to the overlying structures. Heritage buildings, due to their low mechanical properties, quasi-brittle failure, and valuable non-structural assets, are highly susceptible to changes in the substrate. Qualitative and quantitative indicators are part of a damage classification process, within the grand objective of associating overall damage levels to measured values of the deformed configuration. Also, extensive monitoring of the settlement progression and magnitude during construction, in the proximity of overlying historical buildings, together with crack monitoring, can serve to optimize settlement mitigation in real time.

2.3.1. Damage criteria

Damage classification in heritage buildings is a valuable documentation tool for inspection and diagnosis. Damage categories are usually based on the work of Burland and Wroth 1974 and Boscardin and Cording 1989, with typical maximum tensile strains and crackwidths for various damage risk categories, under induced settlements in brick and stone masonry structures. In total, six damage categories are defined (from 0 to 5). In progressive magnitude, tensile damage is classified in terms of visual or aesthetic appearance (0-2), serviceability (3-4) and structural stability (5) and are described in Table 1 [Day 1999]. Here, it can be noted that for masonry structures, the range of tensile strains is between 0.05% and 1% [Day 1999]. Yet, damage due to settlements can highly differ, depending on many structural and architectural characteristics. Thus, the current damage chart should not be followed blindly.

Table 1. Cracking damage categories, with correlation on induced vertical settlements [Day 1999 and Boscardin et al. 1989].

Damage Category	Damage Degree	Description of typical damage and form of repair	Typical crack widths (mm)	Description of cracks	Maximum tensile strain %	Δ^* cm	Δ/L^{**}	β^{***} ($\times 10^{-3}$)
0	Negligible	Hairline cracks of less than about 0.1 mm width.	0-0.1	Hairline	0-0.05	<3	$< 1/300$	0-1.1
1	Very slight	Fine cracks which can easily be treated during normal decoration. Perhaps isolated slight fracturing in building. Cracks in external brickwork visible on close inspection.	0.1-1	Fine to medium	0.05-0.075	3-4	$1/300$ *to* $1/240$	1.1-1.6
2	Slight	Cracks easily filled. Redecoration probably required. Several slight fractures inside the building. Exterior cracks visible; some repointing may be required for weather-tightness. Doors and windows may stick slightly.	1-5	Wide to open	0.075-0.15	4-5	$1/240$ *to* $1/175$	1.6-3.3
3	Moderate	Cracks may require cutting out and patching. Recurrent cracks can be masked by suitable linings. Repointing and possibly replacement of a small amount of exterior brickwork may be required. Doors and windows sticking. Utility services may be interrupted. Weather tightness often impaired.	5-15	Open	0.15-0.3	5-8	$1/175$ *to* $1/120$	3.3-6.7
4	Severe	Extensive repair involving removal and replacement of sections of walls, especially over doors and windows required. Windows and door frames distorted. Floor slopes noticeably. Walls lean or bulge noticeably, some loss of bearing in beams. Utility services disrupted.	15-25		0.3-1.0	8-13	$1/120$ *to* $1/70$	>6.7
5	Very severe	Major repair required involving partial or complete reconstruction. Beams lose bearing, walls lean badly and require shoring. Windows broken by distortion. Danger of instability.	>25			>13	$> 1/70$	

*Maximum vertical differential settlement. (Figure 7)

**Deflection slope; Δ is the relative deflection, between two corresponding points, with a distance L. (Figure 7)

***Angular distortion (Figure 7)

2.3.2. Analytical models

A first stage preliminary assessment of induced soil settlements, in terms of magnitude, distribution, and tensile damage, can be performed by means of empirical and analytical methods, namely the greenfield deformations and the Limiting Tensile Strain Method (LTS Method).

2.3.2.1. Greenfield deformations

A first preliminary assessment of induced soil settlements in the 3D ground displacement field, in terms of magnitude and distribution, can be made by means of empirical and analytical methods. In O'Reilly and New 1982, predictive equations were developed, for the settlement profile in the 2D and 3D overlying space. Parameters of control are the soft soil type, the tunneling geometry and configuration, while no structure or other kind of infrastructure on the surface is accounted. The equations are basically normal distribution function curves, which have been validated, through a large number of case studies and observations [Attewell and Woodman 1982].

In the 2D configuration, Equation 1 is describing the vertical settlement distribution, of the Gaussian error function, in the presence of one tunnel and along a perpendicular section to the tunnel's main axis. Here, $S_v(x)$ is the vertical displacement at a horizontal distance x from the tunnel axis, $S_{v,max}$ is the maximum vertical settlement, measured above the tunnel axis, i_x is the horizontal distance between the vertical axis and the point of inflection, known as trough width parameter and is approximately configured as a linear function of the depth, of the tunnel's center line z_o (Rankin 1988 and Lake et al. 1992). K is a dimensionless constant, known as soil constant, depending on the soil type. For sandy to silty clay soils, the K parameter ranges from 0.20 to 0.70 respectively [Mair and Taylor 1997 and Lee et al. 2013]. Lastly, z_o is the tunnel depth and z is the depth of the subsurface settlement trough, below the soil surface, where obviously at the upper soil surface z=0 [Cheng et al. 2006]. In the case of a multi-layered soil, the i_x parameter is configured according to Equation 2, where K_i is the soil constant of each soil layer and z_i is the thickness of each layer, as shown in Figure 3.

$$S_v(x) = S_{v,max} \cdot e^{-\frac{x^2}{2 \cdot i_x^2}}$$

Equation 1

$$i_x = K \cdot (z_o - z)$$

$$i_x = \sum K_i \, z_i$$

Equation 2

The vertical settlement trough can be also described by the volume loss ratio V_L (%), a factor associated to tunneling techniques, such as induced face pressure, in particular, for closed face tunneling EPB (Equation 3). Lower and upper bounds of estimated volume loss values are assigned, as well as values for the width parameter K, according to experience and literature, under similar soil conditions and construction methods. V_s is the volume of the settlement trough per unit length and D is the tunnel's diameter.

$$V_S = \int_{-\infty}^{+\infty} S_v(x)dx = \sqrt{2\pi} \cdot i_x \cdot S_{v,max}$$

$$V_L = \frac{V_S}{\pi \cdot D^2/_4} = \sqrt{\frac{32}{\pi}} \frac{i_x S_{v,max}}{D^2}$$

Equation 3

$$S_v(x) = \sqrt{\frac{\pi}{2}} \cdot \frac{V_L \cdot D^2}{4 \cdot i_x} \cdot e^{-\frac{x^2}{2 \cdot i_x^2}}$$

The horizontal displacements in the transverse direction are directed towards the tunnel's axis. Out of a simple approach, the horizontal component of the settlement vector in the 2D space $S_h(x)$ and the horizontal strain in the transverse direction $\varepsilon_{hx}(x)$, are considered as a function of the vertical settlement:

$$S_h(x) = S_v(x) \cdot \frac{x}{z_o}$$

$$\varepsilon_{hx}(x) = \frac{S_v(x)}{z_o} \cdot \left(\frac{x^2}{i_x^2} - 1 \right)$$

Equation 4

Graphically, settlement components and horizontal strain are presented in Figure 3b. Regarding the progression of a tunnel line, the greenfield displacements evolve in the 3D space. Figure 3d presents the 3D configuration of the settlement troughs in transverse and longitudinal sections. Settlement profiles in the longitudinal direction, with respect to the tunnel's main axis, affect mostly the area in proximity to the tunnel's face. Longitudinal troughs can cause damage to overlying structures, according to their relative position and orientation, with respect to the

progression of the tunnel. Here, the vertical settlement profile is described by a function of the cumulative probability curve Φ, of the Gaussian distribution function, described by Equation 5, with a mean value equal to $S_{v,max}$ and a standard deviation equal to the width parameter i_y [Attewell and Woodman 1982 and Attewell et al. 1986]. As shown in Figure 3c, right above of the tunnel's face (y=0) the vertical settlements are equal to $0.5 \cdot S_{v,max}$, if no face support is considered. In case of closed face tunneling, the expected settlement above the tunnel face ranges from 25% to 30% of $S_{v,max}$. The width parameter in the y-y axis can be set equal to the one in the transversal direction, i.e., $i_x = i_y$ [Attewell and Woodman 1982 and Attewell et al. 1986]. The horizontal displacement of the longitudinal settlement trough is that of a Gaussian normal distribution curve, described in Equation 6 [Attewell and Woodman 1982 and Attewell et al. 1986]. By differentiating $S_h(y)$ with respect to y, the horizontal strain in the longitudinal direction is given by Equation 7. Here, positive values of strain are ahead of the tunnel's face and correspond to tension, whereas behind the tunnel's face the strains are negative and are compressive (Figure 3c).

$$S_v(y)_{x=0} = S_{v,max}\Phi\left(\frac{y}{i_y}\right) \qquad \text{Equation 5}$$

$$S_h(y)_{x=0} = \frac{V_L \cdot D^2}{8 \cdot z_o} \cdot e^{-\frac{y^2}{2 \cdot i_y^2}} \qquad \text{Equation 6}$$

$$\varepsilon_h(y)_{x=0} = -y\frac{V_L \cdot D^2}{8 \cdot i_y^2 \cdot z_o} \cdot e^{-\frac{y^2}{2 \cdot i_y^2}} \qquad \text{Equation 7}$$

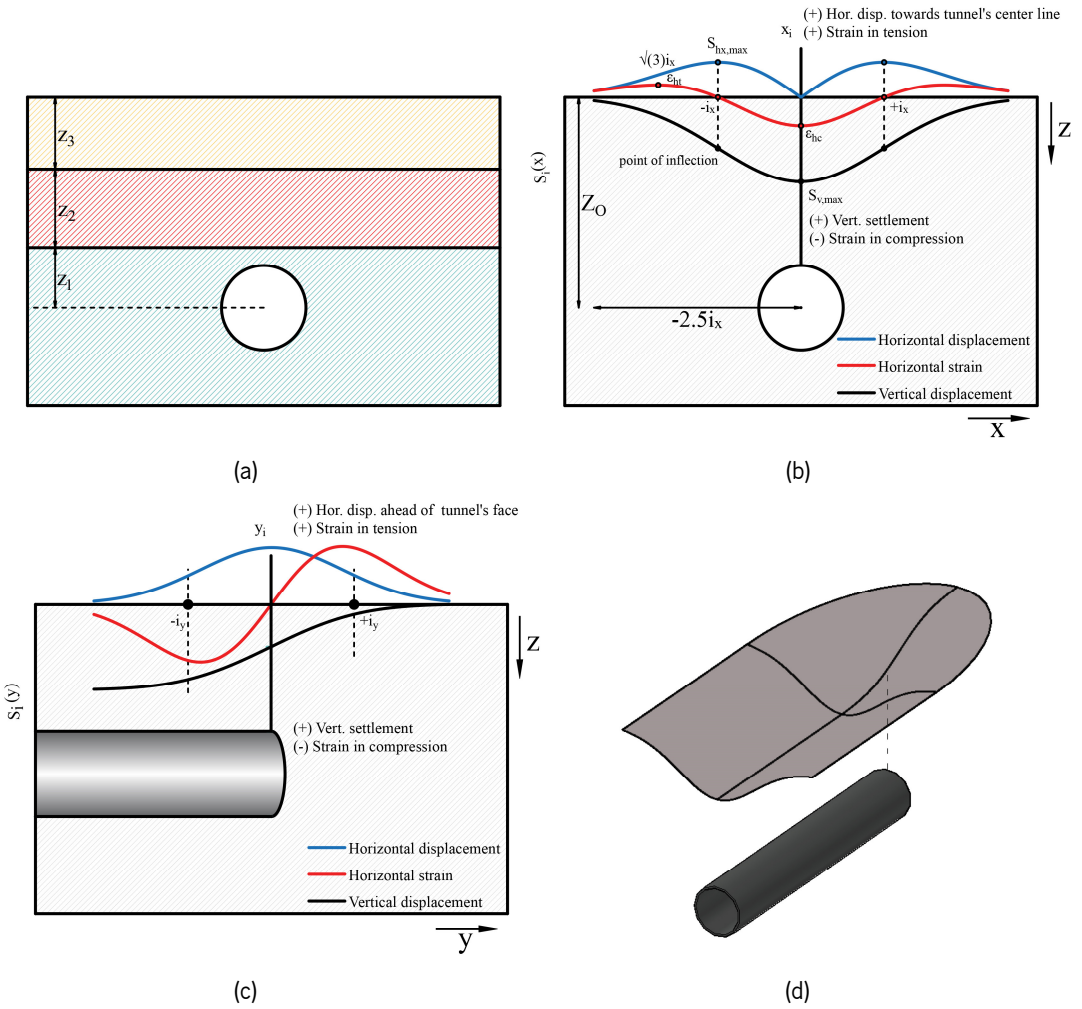


Figure 3. Greenfield conditions: (a) schematic of a 3-layered soil strata; (b) distribution of the horizontal strain in the transverse direction, together with the settlement trough; (c) distribution of the horizontal strain in the longitudinal direction, together with the settlement trough; (d) configuration of the settlement trough in the 3D space.

Considering the aspect of induced settlements in geotechnical terms, for shallow tunnel construction in soft soils, during excavation, a redistribution of pore pressures and stresses occurs, initiating in the proximity of the tunnel opening, which can either be positive or negative. For coarse soils, pore pressure tends to reduce, and yielded stress zones appear in the circumference of the side walls, propagating towards the surface. Since the strength of those soils is governed by frictional forces, the soil above the tunnel does not yield, but deforms as a rigid block downwards. On the other hand, in cohesive soils the yield zone surrounds uniformly the tunnel and expands outwards. Thus, induced settlements from tunnels in coarse soils tend to be more localized, with higher magnitudes, than in cohesive soils. Also, associated with higher, more localized, soil deformation of the subsurface, the trough tends to be smaller for cohesionless soils and larger in cohesive ones [Wong and Kaiser 1987]. A parametric graphic representation on the effect on the settlement trough, regarding the type of soil is shown in Figure 4.

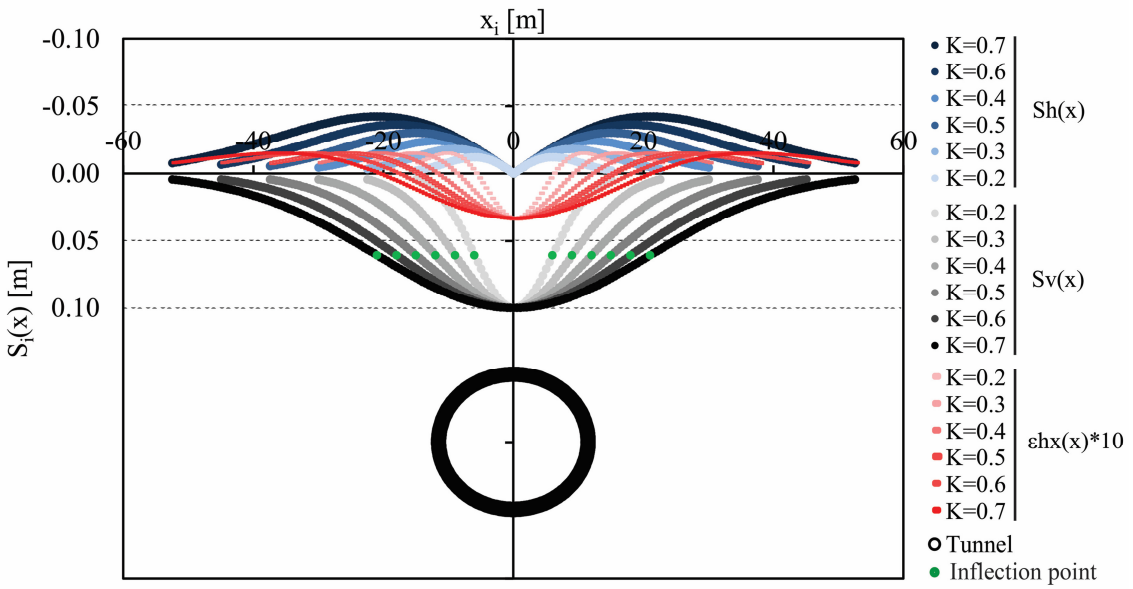


Figure 4. Distribution of the horizontal strain in the transverse direction, together with the settlement troughs, for different types of soil, with K values in the range of 0.2-0.7.

In the presence of more than one tunnel with a relative depth and distance from center points, the dimensional equations change accordingly [O'Reilly and New 1982]. They can be more complex, but the settlement trough is derived as the superposition of troughs from single tunnels, as shown in Figure 5. Yet, the construction process of several tunnels is almost never simultaneous, which lowers the quality of Gaussian fitting, as shown from the superposition of real and analytical data in Figure 6 [Amorosi et al. 2014]. The vertical settlement distribution $S_v(x)$, the horizontal component $S_h(x)$ and horizontal strain $\varepsilon_{hx}(x)$, in the presence of two tunnels, along a perpendicular section to the tunnels main axis is given by Equation 8, Equation 9 and Equation 10 respectively. Here, d is the distance from the tunnels center points.

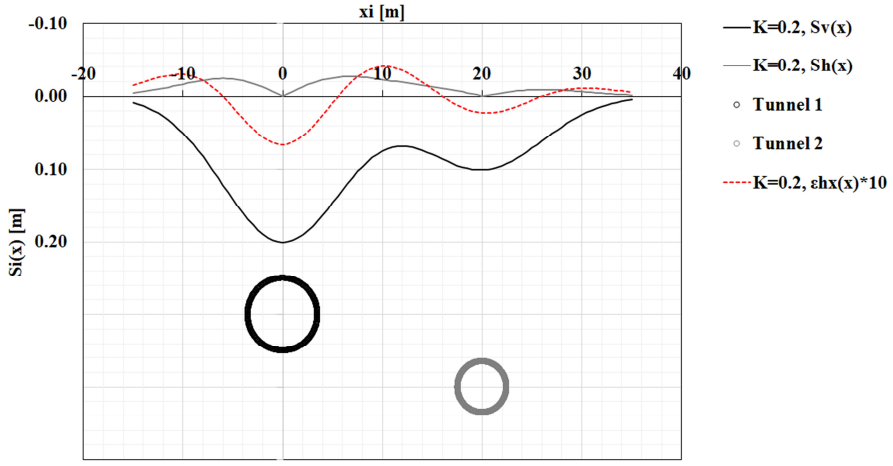


Figure 5. Distribution of the horizontal strain in the transverse direction, together with the settlement troughs, for an arbitrary twin tunnel configuration and a chosen K value of 0.2.

$$S_v(x) = S_{v,max1} \cdot e^{-\frac{x^2}{2 \cdot i_{x1}^2}} + S_{v,max2} \cdot e^{-\frac{(x-d)^2}{2 \cdot i_{x2}^2}}$$

Equation 8

$$S_v(x) = \sqrt{\frac{\pi}{2}} \cdot \frac{V_{L1} \cdot D_1^2}{4 \cdot i_{x1}} \cdot e^{-\frac{x^2}{2 \cdot i_{x1}^2}} + \sqrt{\frac{\pi}{2}} \cdot \frac{V_{L1} \cdot D_2^2}{4 \cdot i_{x2}} \cdot e^{-\frac{(x-d)^2}{2 \cdot i_{x2}^2}}$$

$$S_h(x) = S_{v1}(x) \cdot \frac{x}{z_{o1}} + S_{v2}(x) \cdot \frac{x-d}{z_{o2}}$$

Equation 9

$$\varepsilon_{hx}(x) = \frac{S_{v1}(x)}{z_{o1}} \cdot \left(\frac{x^2}{i_{x1}^2} - 1\right) + \frac{S_{v2}(x)}{z_{o2}} \cdot \left(\frac{(x-d)^2}{i_{x2}^2} - 1\right)$$

Equation 10

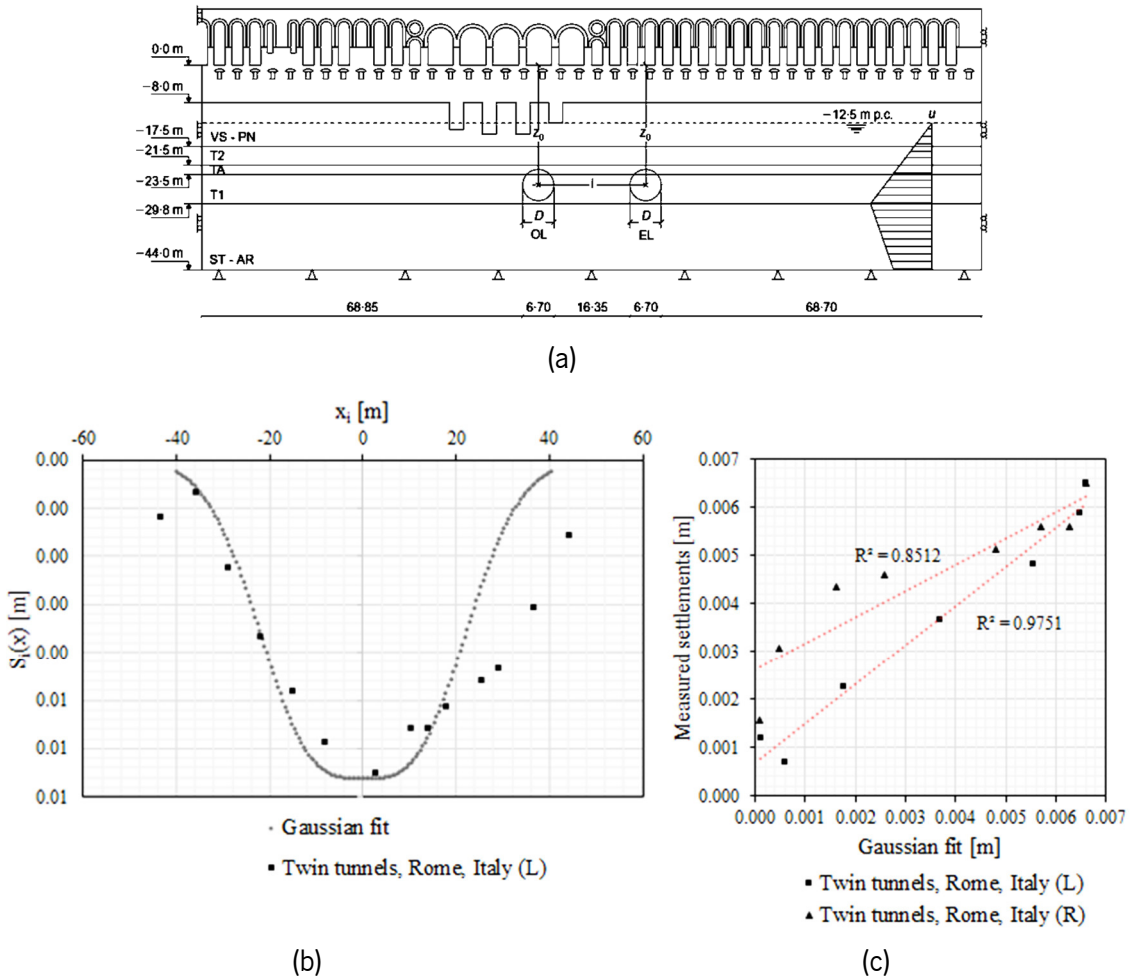


Figure 6. Quality of Gaussian fitting compared with real measuring data: (a) schematic of a twin metro construction and overlying Felice aqueduct in Rome [Amorosi et al. 2014]; (b) settlement trough in transverse section, measured at base [Amorosi et al. 2014] and greenfield profile, with width parameter K in the range of 0.4–0.6, and according to soil layer properties from Amorosi et al. 2014; (c) corresponding regression in left and right part of settlement trough.

2.3.2.2. Limiting Tensile Strain Method

In urban areas, a preliminary assessment of the tensile damage in surrounding buildings, due to induced foundation settlements, can be performed through an empirical-analytical process, known as Limiting Tensile Strain Method (LTS Method). The method was developed by Burland and Wroth 1974 and Boscardin and Cording 1989. By simplified calculations on simple beams, representative of the structure's geometry and stiffness, angular distortion and deflection ratios are obtained, as well as tensile strain resultants, under the effect of deformation patterns. Next, values of tensile strains are associated to tensile strain limits and corresponding damage categories [Boscardin and Cording 1989 and Day 1999]. Note that the associated damage is dependent on the geometrical characteristics of the structure and the lateral distance from the tunnel's main axis [Shin et al. 2007]. Yet, the level of simplification cannot reflect on the diversity of the structure and the irregularity of the near settlement field.

Given the fact that the LTS Method does not account for the soil-structure interaction, it provides upper bound limits of strain values and thus, a conservative estimate [Netzel 2006]. An initial calculation of the greenfield settlement profile is performed (see section 2.3.2.1) and applied as boundary conditions, in the relative position of a simplified 2D model of the structure, a linear elastic beam, of equivalent bending and shear stiffness. Only the part of the building inside the vertical settlement influence area, until a far field limit of vertical settlements of 1mm is analyzed and is divided at the point of inflection (width parameter i from the tunnel's center line), in two parts [Mair and Taylor 1996]. Each part is analyzed separately, according to subjected hogging and sagging deformations, with corresponding cracking, due to direct and diagonal tensile strains (Figure 7). Induced building strains are based on analytical beam equations and plane strain conditions, of a simply supported beam, at both ends, by use of the Timoshenko beam theory (Table 2) [Timoshenko 1957].

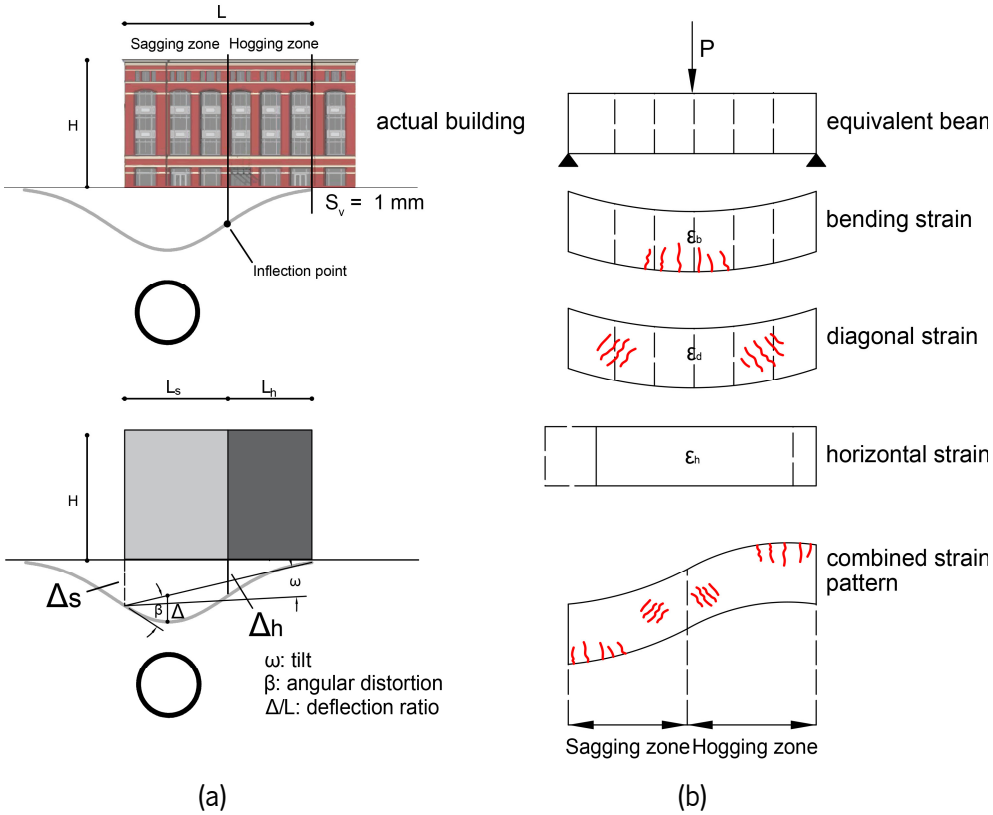


Figure 7. The Limiting Tensile Strain method: (a) building division in hogging (L_h) and sagging (L_s) zones, at point of inflection; (b) tensile strain components in equivalent beam.

Table 2. Formulation of the LTS method and the greenfield settlement profile [Netzel 2006, Burland and Wroth 1974, Boscardin and Cording 1989 and Timoshenko 1957]. Note the representation for bending diagonal, horizontal and combined strain in Figure 7b.

Derivation of sagging and hogging parts	$H, {}^{\Delta_s}/_{L_s}$ $H, {}^{\Delta_h}/_{L_h}$	H: Height of equivalent beam L: Length of equivalent beam Δ: Relative deflection s: Sagging part h: Hogging part E: Young Modulus G: Shear Modulus v: Poisson's ratio I: Moment of inertia P: Fictitious vertical point load at mid-span F: Shear form factor (rectangular section) F=1.2 [Renton 1991 and Cowper 1966] F=1.5 [Timoshenko 1957] A: Cross section area
Material parameters: Stiffness ratio Assuming for massive masonry walls, with a Poisson ration of 0.3 [Burland and Wroth 1974]	$E/G = 2.6$	
Deflection ratio of a fictitious point loaded beam for both shear and bending [Timoshenko 1957]	$\frac{\Delta}{L} = \frac{P \cdot L^2}{48 \cdot EI} + \frac{P \cdot F}{4 \cdot G \cdot A}$	
Bending strain in sagging zone for the neutral axis at the middle of the beam [Burland and Wroth 1974] * Shear factor F=1.2	$\varepsilon_{b,max} = {}^{\Delta}/_{L} \cdot \left[\frac{6 \cdot \frac{L}{H}}{\left(\frac{L}{H}\right)^2 + 1.2^* \frac{E}{G}}\right]$	
Diagonal strain in sagging zone for the neutral axis at the middle of the beam * Shear factor F=1.2 [Gere and Timoshenko 1972]	$\varepsilon_{d,max} = {}^{\Delta}/_{L} \cdot \left[\frac{3 \cdot \frac{E}{G}}{2 \cdot \left(\frac{L}{H}\right)^2 + 2 \cdot 1.2^* \frac{E}{G}}\right]$	
Bending strain in hogging zone for the neutral axis at the bottom of the beam [Burland et al 1974] * Shear factor F=1.2	$\varepsilon_{b,max} = {}^{\Delta}/_{L} \cdot \left[\frac{3 \cdot \frac{L}{H}}{0.25 \cdot \left(\frac{L}{H}\right)^2 + 1.2^* \frac{E}{G}}\right]$	
Diagonal strain in sagging zone for the neutral axis at the bottom of the beam * Shear factor F=1.2 [Gere and Timoshenko 1972]	$\varepsilon_{d,max} = {}^{\Delta}/_{L} \cdot \left[\frac{3 \cdot \frac{E}{G}}{0.5 \cdot \left(\frac{L}{H}\right)^2 + 2 \cdot 1.2^* \frac{E}{G}}\right]$	
Horizontal strain	$\varepsilon_h = {}^{\Delta L}/_{L}$	
Resultant extreme fiber bending and diagonal strain [Boscardin and Cording 1989] [Gere and Timoshenko 1972]	$\varepsilon_{br} = \varepsilon_{bmax} + \varepsilon_h$ $\varepsilon_{dr} = \varepsilon_h \frac{1-v}{2} + \sqrt{\varepsilon_h{}^2 \left(\frac{1-v}{2}\right)^2 + \varepsilon_{dmax}^2}$	Highest value chosen

Based on a combination of settlement profiles from in-situ measurements, greenfield troughs and numerical analysis, actual induced settlements in adjacent buildings present smaller curvatures, than those of the corresponding greenfield troughs. The stiffness of the buildings, in the proximity of the tunnel, tends to flatten the curvature of the settlement profile and in accordance, the sagging and hogging modes of deformation. In Potts and Addenbrooke 1997, modification factors M are suggested, based on greenfield deformations. Those are applied on the deflection ratios in order to account for the stiffness of both the building and the soil, to the settlement profile.

For this purpose, in the 2D space, the relative bending stiffness p^* and relative axial stiffness a^* of the soil-structure system are given by Equation 11. Here, B corresponds to the building's length, perpendicular to the tunnel's main axis, I is the moment of inertia A is the area of the cross section of the equivalent beam, E_S is the secant stiffness of the soil at 0.1‰ axial strain, as obtained from triaxial tests and E is the Young's Modulus of the equivalent beam [Potts and Addenbrooke 1997]. The self-weight of the building, even though it can potentially affect the stress conditions of the underlying soil, is not considered, in order to simplify the analytical formulations.

Instead, in the 3D space, the structure is represented by an equivalent plate, under the same concept. The 3D relative stiffness expressions, as proposed by Franzius et al. 2006, include the building's length L, longitudinal to the tunnel axis, the tunnel's depth z_o and are depicted in Equation 12.

$$p_{2d}^* = \frac{E \cdot I}{E_s \cdot \left(\frac{B}{2}\right)^4}, a_{2d}^* = \frac{E \cdot A}{E_s \cdot \frac{B}{2}} \qquad \text{Equation 11}$$

$$p_{3d}^* = \frac{E \cdot I}{E_s \cdot z_o \cdot B^2 \cdot L}, a_{3d}^* = \frac{E \cdot A}{E_s \cdot B \cdot L} \qquad \text{Equation 12}$$

Here, different kinds of formulations are applicable, accounting for the relative axial and bending stiffness of masonry structures in 2D or 3D configurations, found in Timoshenko 1995, Mair and Taylor 2001 and Goh and Mair 2014. Geometric properties can be affected by the presence of openings and the contribution of timber diaphragms or slabs.

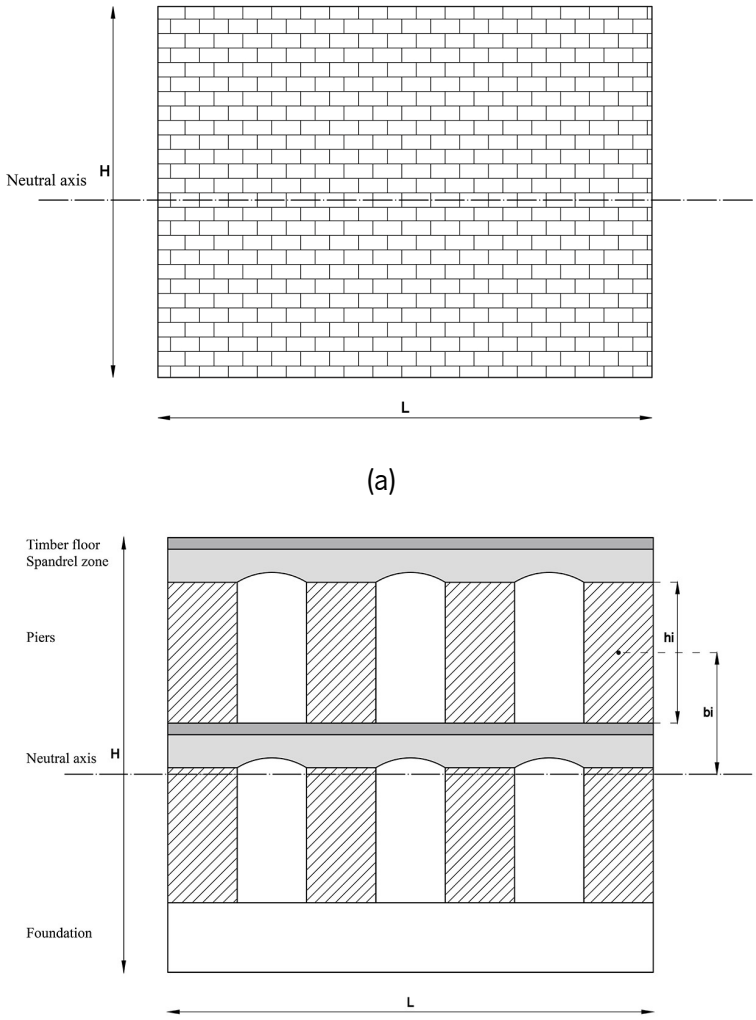
According to the parallel axis theorem in Timoshenko 1955, the relative moment of inertia I of a rectangular section (e.g. wall, floor etc.), refers to the building's neutral axis. The bending stiffness of a single wall (Figure 8a) is given in Equation 13. Instead, the bending stiffness of a structure, decomposed into several floors, and relative to the structure's neutral axis is depicted in Equation 14 (Figure 8b). It only accounts for the contribution of each slab, increased, depending on the distance from the neutral axis. Thus, an overestimated value of I is obtained, since the formulation is based on rigidly connected slabs. Instead, an algebraic sum for the stiffness of each floor slab was adopted in Mair and Taylor 2001, for a 10-storey reinforced concrete building, which disregards the axial stiffness of the slabs, led to a good correlation with field measurements (Equation 15). For framed buildings and perfect rigid connections, the stiffening effect of the

columns, in the in-plane bending stiffness, was accounted by Meyerhof 1953 and adjusted in Goh and Mair 2014, given in Equation 16. Under the hypothesis of bays of equal span, with respect to the total span L of the building in sagging or hogging mode, and the height h of the columns, an increase in the algebraic sum of bending stiffness is introduced by a column-stiffening factor C. Here K_{LC}, K_{UP} and K_B is the average stiffness of the columns in the lower and upper floor, and a connecting beam or spandrel respectively [Goh and Mair 2014]. Regarding unreinforced masonry structures, it can be assumed that timber floors, spandrels and floor beams are weakly connected to piers and walls. Their contribution to bending stiffness is lower and the flexural rigidity of the foundation would be mostly accounted for. In particular, the bending stiffness of the walls is greatly influenced by the percentage of openings. As shown in Son 2015, from results of parametric numerical analyses, the correlations between bending stiffness and window percentage area in masonry façades, and for various ratios of shear and normal stiffness, present a similar reduction.

The axial stiffness in unreinforced masonry buildings accounts for the contribution of horizontal structural elements, i.e., the spandrels and floor beams. It can be computed in sections at the mid span of openings, with the lower value chosen, according to Equation 17.

A numerical process can be adopted, accounting for the exact geometry of a masonry building with timber floors. Equivalent elastic bending and axial stiffness values are evaluated by applying bending and axial stresses, under the linear formulations of Gere and Timoshenko 1972 (Equation 18). Regarding boundary and loading conditions, the building is subjected to a bending moment M_O and an axial load P_O, with the corresponding deflection and axial elongation δ_{max}, at midspan. Accounting for cracked conditions in a conservative approach, stiffness values of masonry structural elements can be reduced by a factor of 0.5, according to §4.3.1(7) of EN 1998-1:2004.

Both for the 2D and 3D configuration, a conversion of stiffness and geometric properties is required, according to the fictitious thickness t_{fe} of the beam or the plate, shown in Equation 19 [Franzius et al. 2006 and Son 2015].



L: length of structure

H: height of structure

l_i: length of component

h_i: height of component

t_i: width of component

b_i: distance from neutral axis of structure

E_i: Young's modulus of component

A_i: area of component

I, I_i: moment of inertia

Figure 8. Estimation of equivalent bending and axial stiffness in 2D: (a) system of a masonry wall; (b) system of a masonry building with foundation, piers, spandrels and timber floors. Note the abbreviations for the relevant geometrical properties.

$$I_{wall} = \frac{t \cdot H^3}{12}, \qquad A_{wall} = t \cdot H \qquad \text{Equation 13}$$

$$(EI)_{structure} = \left(\sum_i [E_i(I_i + A_i b_i^2)]\right)_{floors} = \sum_i \left[E_i\left(\frac{t_i \cdot {h_i}^3}{12} + t_i \cdot h_i \cdot b_i^2\right)\right] \qquad \text{Equation 14}$$

$$(EI)_{structure} = \left(\sum_i (E_i \cdot I_i)\right)_{floors} = \sum_i \left[E_i\left(\frac{t_i \cdot {h_i}^3}{12}\right)\right] \qquad \text{Equation 15}$$

$$(\mathrm{EI})_{\mathrm{frame}} = \left(\sum_{\mathrm{i}} (\mathrm{E_i} \cdot \mathrm{I_i} \cdot \mathrm{C})\right)_{\mathrm{columns}}, \mathrm{C} = 1 + \left(\frac{\mathrm{L}}{\mathrm{l}_i}\right)^2 \left(\frac{\mathrm{K_{LC}} + \mathrm{K_{UC}}}{\mathrm{K_{LC}} + \mathrm{K_{UC}} + \mathrm{K_B}}\right)$$

Equation 16

$$\mathrm{K_{LC}} = \left(\frac{\mathrm{EI}}{\mathrm{h}_i}\right)_{\mathrm{LC}}, \quad \mathrm{K_{UC}} = \left(\frac{\mathrm{EI}}{\mathrm{h}_i}\right)_{\mathrm{UC}}, \quad \mathrm{K_B} = \left(\frac{\mathrm{EI}}{\mathrm{l}_i}\right)_{\mathrm{B}}$$

$$(\mathrm{EA})_{\mathrm{structure}} = \left(\sum_{\mathrm{i}} \mathrm{E_i} \cdot \mathrm{A_i}\right)_{\mathrm{floors}}$$

Equation 17

$$(\mathrm{EI})_{\mathrm{structure}} = \frac{\mathrm{M_o} \cdot \mathrm{L}^2}{8 \cdot \delta_{\max}}, (\mathrm{EA})_{\mathrm{structure}} = \frac{\mathrm{P_o} \cdot \mathrm{L}}{\delta_{\max}}$$

Equation 18

$$\mathrm{t_{fe}} = \sqrt{\frac{12(\mathrm{EI})_{\mathrm{structure}}}{(\mathrm{EA})_{\mathrm{structure}}}}, \quad \mathrm{E_{fe}} = \frac{(\mathrm{EA})_{\mathrm{structure}}}{1 \cdot \mathrm{t_{fe}}}, \quad \mathrm{A_{ef}} = 1 \cdot \mathrm{t_{fe}}, \mathrm{I_{fe}} = \frac{1 \cdot \mathrm{t_{fe}^3}}{12}$$

Equation 19

Modification factors M act as multipliers on the greenfield deflection ratios $\mathrm{DR^{GF}}$ and greenfield strains $\varepsilon^{\mathrm{GF}}$, at foundation level, both for sagging and hogging modes according to Potts and Addenbrooke 1997:

$$\mathrm{DR_{sag}} = \mathrm{M}^{\mathrm{DR_{sag}}} \cdot \mathrm{DR_{sag}^{GF}}$$

Equation 20

$$\mathrm{DR_{hog}} = \mathrm{M}^{\mathrm{DR_{hog}}} \cdot \mathrm{DR_{hog}^{GF}}$$

Equation 21

$$\varepsilon_{hc} = \mathrm{M}^{\varepsilon_{hc}} \cdot \varepsilon_{hc}^{\mathrm{GF}}$$

Equation 22

$$\varepsilon_{ht} = \mathrm{M}^{\varepsilon_{ht}} \cdot \varepsilon_{ht}^{\mathrm{GF}}$$

Equation 23

By assigning eccentricity normalized ratios $\frac{\mathrm{e}}{\mathrm{L}}$ for the building's design process, curves that associate modification factors with values of relative bending p^* and axial a^* stiffness can be defined, as shown in Figure 9 and Figure 10. Here, e is the distance between the building's and the tunnel's center axes. Potts and Addenbrooke 1997 conducted a parametric 2D FE analysis on

the influence of the axial and bending stiffness of a reference building, to the vertical settlement trough, induced by tunneling. The building was modelled as a weightless equivalent beam and the results are presented in Figure 11. Values of updated deflection ratios, horizontal strains and angular distortion, from the equivalent beam approach of Boscardin and Cording 1989 are associated graphically with damage categories of Table 1, as shown in Figure 12.

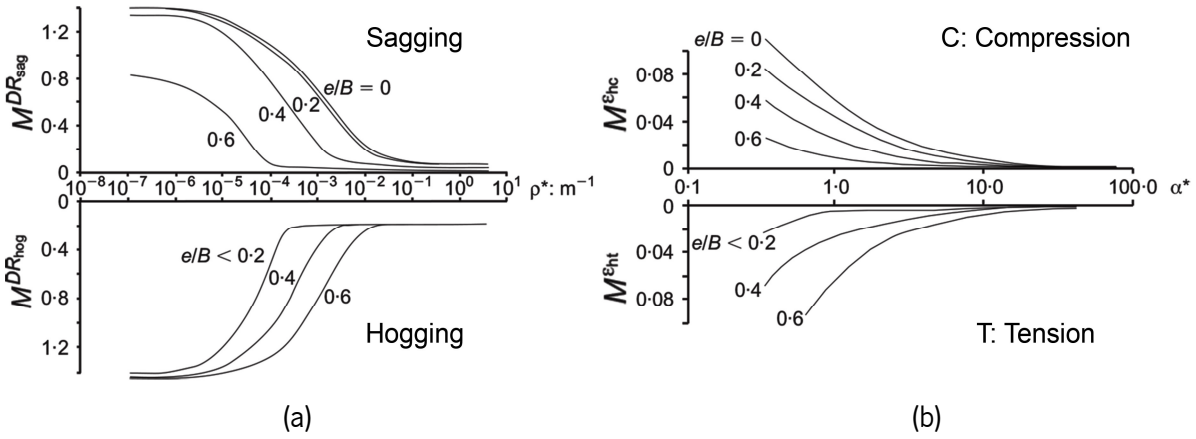


Figure 9. Equivalent 2D beam. Design curves for modification factors under plane strain conditions of: (a) deflection ratios; (b) maximum horizontal strains [Potts and Addenbrooke 1997].

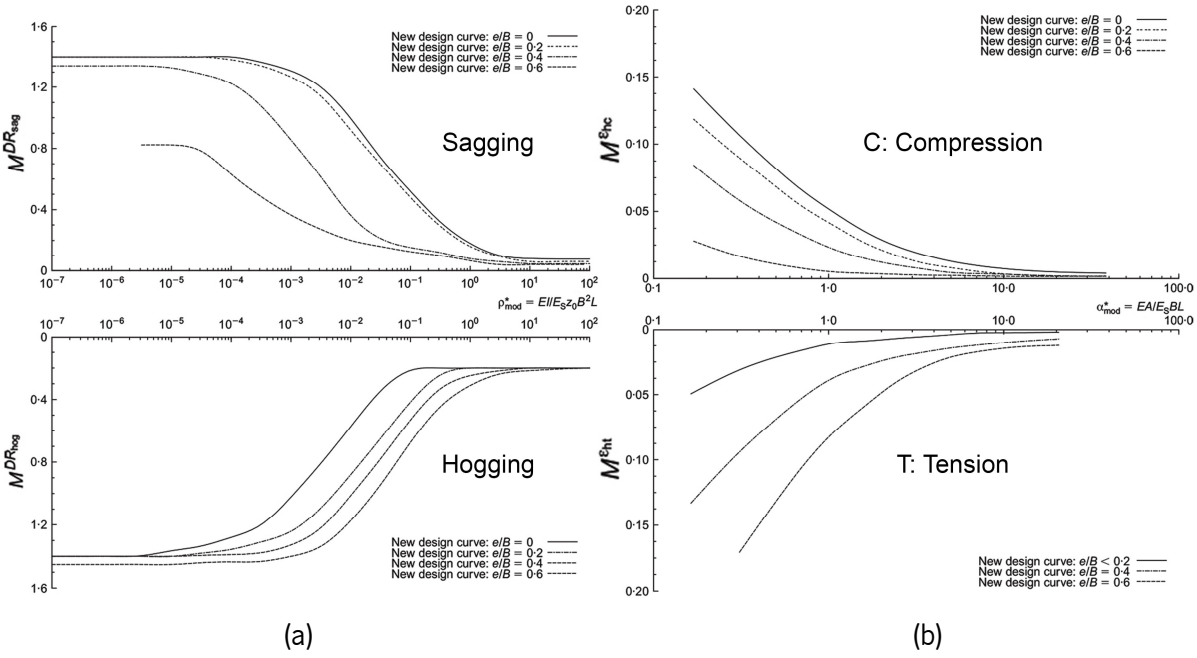


Figure 10. Equivalent 3D shell. Design curves for modification factors of: (a) deflection ratios; (b) maximum horizontal strains [Franzius et al. 2006].

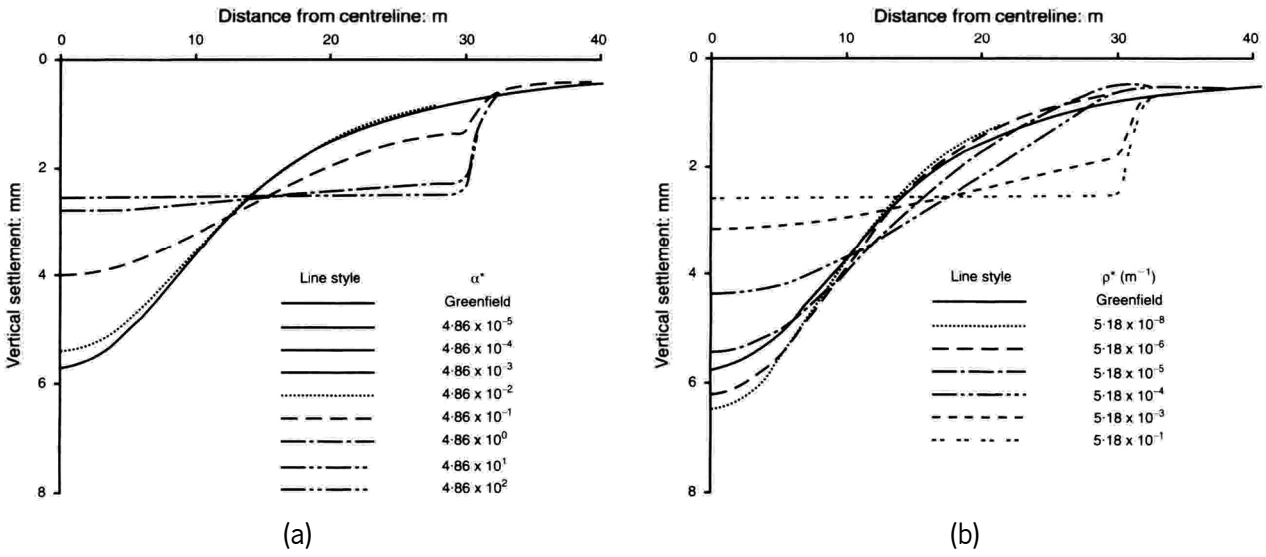


Figure 11. Vertical settlement troughs from tunneling: (a) variation of axial stiffness a*, with a chosen p* equal to 0.518 m^{-1}; (b) variation of bending stiffness p*, with chosen a* equal to 48.6 [Potts and Addenbrooke 1997].

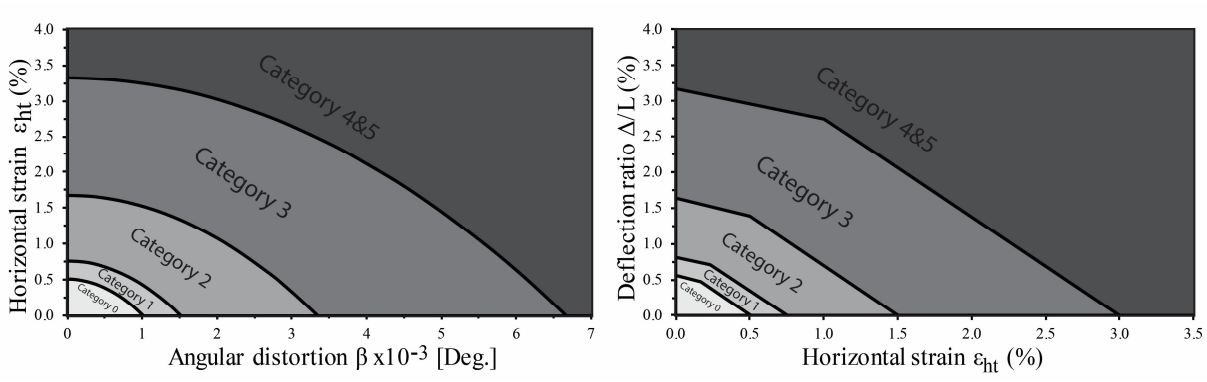


Figure 12. Damage categories association graphs, of horizontal strain, with angular distortion (a) and deflection ratios (b). Adapted from Boscardin and Cording 1989 and Potts and Addenbrooke 1997.

In summary, the analytical process of evaluating damage induced by settlements covers three levels:

1. Preliminary assessment (1st level): The greenfield settlement profile (vertical and horizontal deflections), based on the construction of a tunnel, with given diameter, depth and soil conditions. An assumed volume loss V_L(%) is the reference for accounting the magnitude of settlements at the surface. The output contains maximum deflection ratios and maximum compressive and tensile strains, for hogging and sagging zones, of a reference building. From interaction diagrams (Figure 12), the association to damage categories and threshold limits is made.

2. Preliminary assessment (2nd level): Contribution of the building's bending and axial stiffness (EI, EA), and soil stiffness (E_S). All structural elements are considered, i.e., wall, piers, spandrels, foundations and floors. Conversion in equivalent stiffness values in the 2D or 3D plane strain field, i.e., a simple supported beam and plate respectively, of fictitious thickness. Modification factors are derived from design curves, accounting also the relative position of the building with respect to the tunnel's centerline, based on numerical parametric analyses, as described in Potts and Addenbrooke 1997 and Franzius et al. 2006. The output contains updated settlements profiles, geometric indicators and maximum strains. Previous damage categories might change.

3. Detailed assessment (3rd level): Based on numerical analyses, accounting for the detailed representation of the foundations and soil-structure interaction, as given in section 2.3.3.

2.3.3. FE modelling approach

The Finite Element Method (FEM), in 2D or 3D space, allows the prediction of ground settlements, accounting for several parameters, such as the construction process (i.e. cut-and-cover, bored tunneling, earth pressure balance, etc.), the evolution of lining, the type of shield, the presence of more than one tunnel and the effect of overlying structures. Also, regarding the soil mechanical characteristics, material nonlinearity and anisotropic behavior can improve the predictions on the expected settlement profiles in a 3D displacement field.

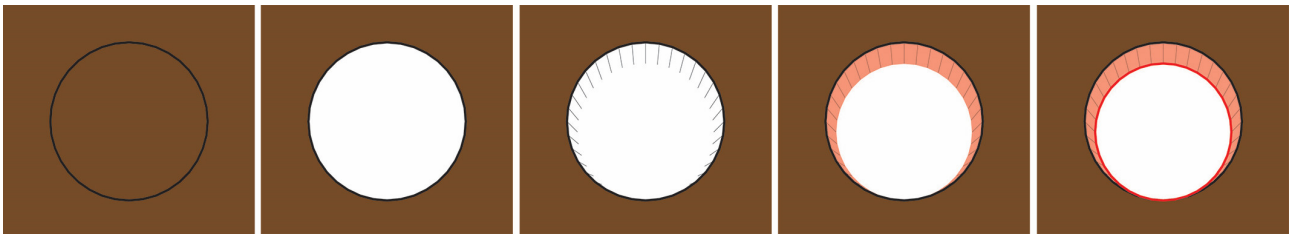
A 2D FE approach, can be accounted within a certain level of simplification. Under current restrictions, this analysis considers that the tunnel's lining is progressing perpendicularly to the principal plane of the building [Amorosi et al. 2014]. Plane strain boundary conditions are accounted for the soil. A thickness of the plane strain element (soil) is assigned, in terms of an equivalent thickness, to match the expected greenfield settlement profile, under self-weight conditions.

Under the current computational capabilities, advanced 3D FE analyses are also feasible and within acceptable limits of time and cost. The challenge arises on the way of assigning the displacement field, under the tunnel construction. Displacement fields at tunnel surface correspond to deformations of the subsurface continuum. Both fields induce volume changes in the tunnel face and ground surface, associated with the target volume loss V_L, under undrained conditions [Amorosi et al. 2014]. In most cases, surface settlement volumes and ground volume loss in the tunnel are considered equal [Son 2015]. Regarding also the soil-structure interaction, total

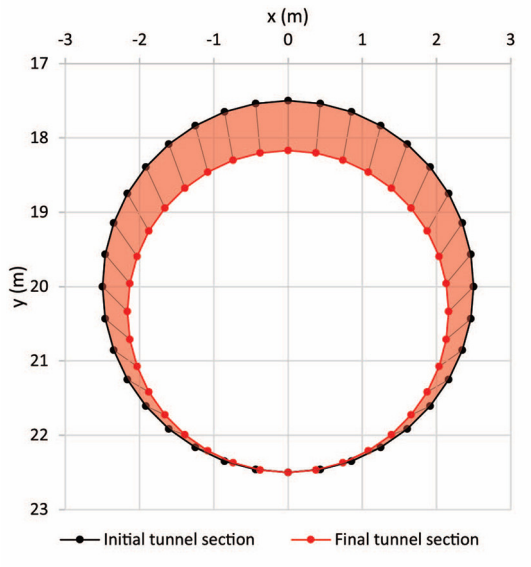
connectivity can either be assumed or instead, interface elements and translational springs are used, in order to model the interaction in terms of in-plane and tangential stiffness, with either linear or nonlinear properties.

First, the FE model needs to be calibrated, in order to match the displacements of the greenfield conditions, without the presence of the structure. A phased analysis is conducted by simulating construction steps; initially, the soil covering the tunnel section is deactivated in volumetric parts, defined by the tunnel construction geometric parameters; next, other elements are activated by forming the rings around the perimeter, corresponding to the shield temporary lining. Afterwards and in a sequential pattern, parts of the shield are deactivated, imposing deformation under overlying pressure, at the boundary nodes of the interior face, simulating the target volume loss V_L. An optimized deformation of the tunnel is assumed, according to Rowe et al. 1983, known as the gap parameter, which varies according to construction parameters (Figure 13) [Amorosi et al. 2014]. According to the gap parameter, the volume loss in the tunnel's intrados is under a displacement field of vertical and horizontal components. The displacement vector with the highest amplitude is on the top crown, while no displacements are considered in the lowest point (Figure 13b).

Thus, the partial deactivation of boundary soil tractions, will initiate nodal displacements, until reaching the target volume loss V_L. A sensitivity analysis is often necessary, regarding mostly the mechanical properties of the overlying masonry structure, the properties of the interface at foundation level and those of the soil, in order to obtain the target volume loss V_L. Usually, as an intermediate step, and just before the lining placement, a displacement field, induced at the tunnel's interior boundary nodes, can be applied in order to obtain the exact target volume loss value [Amorosi et al. 2014].



(a)



(b)

Figure 13. Initial and final configuration of the tunnel's section, according to the gap parameter: (a) construction sequence and intermediate steps; (b) resulting nodal displacement vectors at last step, based on Amorosi et al. 2014.

Elements representing the partial lining segments are then introduced under the new deformed configuration, while sectional deformations on that part, as prescribed from the gap parameter, are considered almost complete (Figure 14). Injected grouting can also be introduced by updating the material properties in the FE parts of the tunnel's perimeter [Diana user's manual. 2020]. The analysis progresses with more soil parts removed, in between the shield and lining, as the tunneling construction advances. At all times, in the tunnel's face, a support pressure is applied, counteracting the total horizontal stresses, acting on an influence zone, that can be calculated from activated soil volumes. At all intermediate load steps, the correlation between empirical and numerical sectional and longitudinal settlement profiles is checked and calibrated, first for simulating the greenfield three dimensional FE model, in terms of soil conditions, crown deflection and target volume loss. In the updated FE model, the overlying structures are then incorporated, after the calibration of the FE model, and final results are obtained [Rampello et al. 2012].

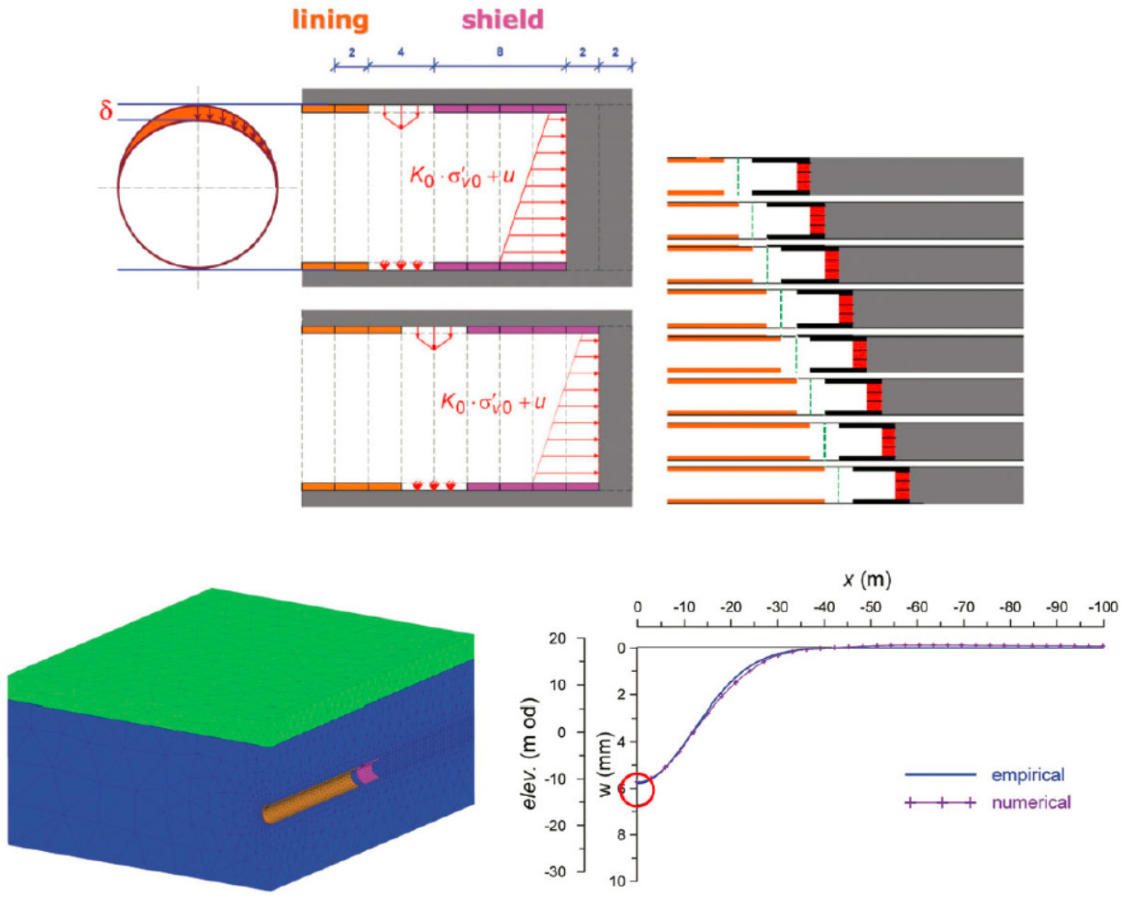


Figure 14. Sequential tunnel construction progress and calibration, under greenfield conditions, employed for FE analyses [Rampello et al. 2012].

Here it is noted that long-term effects, due to changes in hydraulic conditions in fine-grained soils, can affect the settlement distribution. Parameters of influence that need also to be considered are the initial pore water pressure distribution, the excess pore water pressure generated by the tunnel's construction, the soil compressibility and the ratio of permeability, between the tunnel's lining and the soil [Rampello et al. 2012].

In the next stage, for introducing the overlying structures, in a predefined area of influence, two different modelling approaches are then conducted, accounting for the level of geometrical representation of the building of interest and the surrounding structures. Current decisions are mostly dependent on the available computational resources. First, a simplified modelling approach involves mainly the surrounding structures. 3D equivalent solids of a simpler geometry, fully connected to the soil and with a linear elastic behavior, serve to introduce mass and stiffness equivalents (Figure 15). The updating parameter is the Young's Modulus, which will serve to match the distribution of nodal forces at the foundation level, compared to an accurately represented

structural model. The sum of overlying structures will potentially affect the displacement field at the foundation level and will introduce an updated settlement distribution, by the tunneling construction [Rampello et al. 2012]. Second, moving to a more detailed geometrical representation for the structure of interest, a decoupling modelling approach can assess the structural damage. The induced displacement field, from the tunneling construction can be implicitly assigned as boundary conditions at the foundation base, under a time incremental nonlinear analysis.

Modelling results from similar studies have shown that the displacement field, with and without the soil structure interaction present similar magnitudes, but completely different deflection patterns, which in historic structures of low mechanical properties can strongly affect the sagging and hogging deformations and therefore, the distribution and localization of tensile damage. In fact, in many cases, the consideration of the soil-structure interaction can even result in settlements of higher magnitude, compared to those from empirical formulations [Wong and Kaiser 1987]. Thus, the stiffness of the overlying structures is of relevance.

Computed results, in terms of principal strains can be compared with bounds of limiting tensile strains from codes and literature, in order to identify categories of corresponding damage. Though, through a more realistic representation and modelling of the structure, direct distribution plots of maximum principal tensile strains and principal crackwidths can offer a detailed distribution of damage.

As far as the size of the soil volume is concerned, modelling should encounter the soil below all the buildings of interest. The extension of the mesh, transversally to the tunnel's center axis, should be in such a way so as to cover the volumes of greenfield settlements of at least 2.5i, from either side, where i is the distance from the tunnel's axis until the point of inflection. The step size and relative element activation and deactivation, during the phased analysis depends on the time progression of the excavation and segmental placing of the lining (indicative of ~1.0m) and needs to be adjusted according to field data and construction time schedules. In general, the time evolution of settlements in a specified point is dependent on the relative position of the cutter head and can last for several days [Zheng et al. 2015]. Documented fluctuations on the surface settlements start when the cutter face distance is in the order of 1D behind the monitoring point, where D is the diameter of the tunnel and are stabilized at an advancing distance in the order of ~5D [Zheng et al. 2015].

At far field conditions, side soil boundaries are modelled with roller supports, whereas the soil base is modelled as pinned. Hydrostatic water pressure can be assigned as a surface pressure distributed load on the lateral surfaces of the soil.

From the case study of the Tianjin Metro Line 2, as studied by Zheng et al. 2015, the shield is modelled either as solid or shell ring shaped element, of representative thickness (~10cm) and of a type of steel material. The implemented lining is of reinforced concrete of around 35cm of thickness, while in between the face and lining, an interface according to the Mohr Coulomb yield criterion is implemented. Grouting prior to the placement of the lining can also be modeled as an additional ring shape element in the circumference of the face [Zheng et al. 2015].

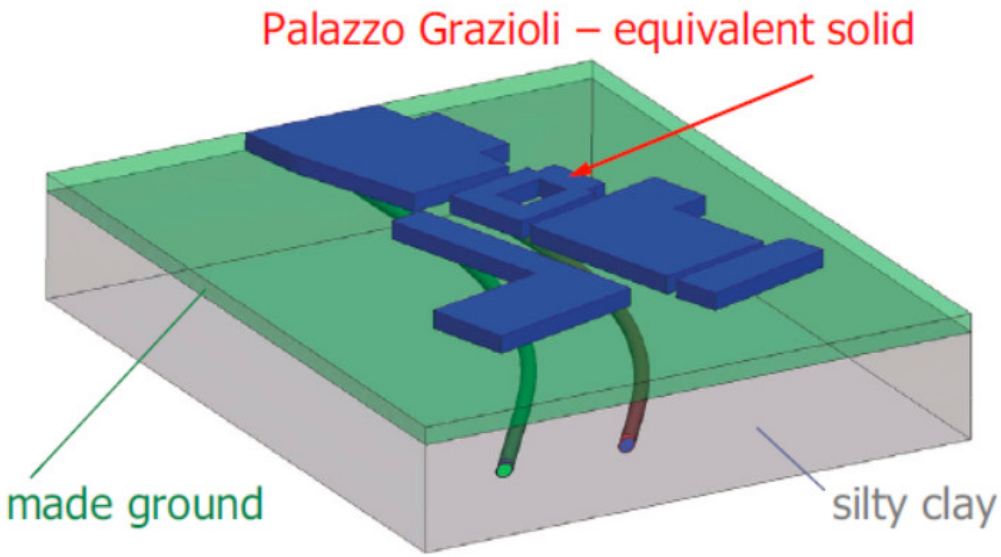


Figure 15. Soil-structure coupling approach, with solids of equivalent mass and stiffness characteristics [Rampello et al. 2012].

In conclusion, advanced numerical tools offer a coupling approach, by considering both surface and subsurface conditions. The complexity of a tunnel construction with many assigned geometrical irregularities and the interactions with overlying structures, means that it is not possible to address the problem with empirical and elastic response solutions, especially when the objective is set on the assessment of historical structures [Potts and Zdravkovic 2001].

In detail, issues of increased complexity, dealt by FE modelling can involve [Potts and Zdravkovic 2001]:

- Tunnel construction sequence and techniques.
- Multiple tunnel construction.
- Arbitrary alignment between the tunnel's main axis and the structures of interest.
- Complex soil stratigraphy and hydraulic conditions.
- Local ground treatments (i.e. grouting).
- Adjacent overlying structures and services.
- Long term settlement conditions.

2.4. Induced vibrations from underground railway traffic

2.4.1. Wave propagation in the elastic half-space

Considering elastic soil properties and an infinite half-space, vibrations propagate through compression and shear waves defined as P-wave and S-waves respectively. Each wave is characterized by a wave speed, associated to the material properties of each soil strata and given by Equation 24-Equation 27. Here c_1 and c_2 are the fundamental wave speeds for P-wave and S-wave respectively, with $c_1 > c_2$, λ and μ are the Lamé constants, E is the Young's modulus, v is the Poisson's ratio and p is the material density.

$$c_1 = \sqrt{\frac{\lambda + 2\mu}{\rho}} \quad (P - Wave) \qquad \text{Equation 24}$$

$$c_2 = \sqrt{\frac{\mu}{\rho}} \quad (S - Wave) \qquad \text{Equation 25}$$

$$\lambda = \frac{vE}{(1+v)(1-2v)} \qquad \text{Equation 26}$$

$$\mu = \frac{E}{1+v} \qquad \text{Equation 27}$$

When vibration waves reach the ground surface, they also propagate along the free boundary, with a combination of shear and compressive deformations, namely as Rayleigh waves. Rayleigh waves

are the slowest waves, with speeds from 100 m/s to 300 m/s for soft and stiff soil respectively and are usually carrying the highest wave energy [Thompson et al. 2009].

2.4.2. Vibrations from underground railway tunnels

The final configuration of a railway tunnel is concluded with the construction of the railway track system. A conventional configuration comprises a system of rails, fastened on a series of transverse sleepers made of concrete, steel or mixed. The whole system is configured by varying layers of crushed stones, called ballast, in a normal depth of around 30 to 40 cm. The lower base supporting system, the subgrade, rests on the tunnel invert boundaries [Thompson et al. 2009].

Additional specifications and more recent applications can cover aspects, such as:

(a) The type of fasteners, mostly involving the reduction of impact loads and cracking, especially when concrete sleepers are used, by means of clipped connection, with greater elasticity (Figure 16) [Thompson et al. 2009].

(b) The use of a reinforced concrete slab track, instead of a ballasted track. A slab track requires lower maintenance, lower costs and construction times, lower weights and a lower total height [Esveld 2001].

(c) In case of slab tracks, the use of prefabricated reinforced concrete track panels, with pockets, for the insertion of twin-block booted sleepers can simplify the construction process and lessen significantly the construction costs. With addition of elastomeric interface layers (pads), the system provides a flexible rail support and reduces resonance frequencies and ground-borne vibrations [Thompson et al. 2009 and Esveld 2001]. The system is depicted in Figure 17 and forms a floating slab track.

A complete isolation of the railing track system is the one where the slab track system rests on the tunnel invert by soft elastomeric supports, i.e., steel coil springs. The system, defined as ‘floating slab track’, is used as a base isolator, thus, reducing coupled resonance frequencies (Figure 17). Yet, the construction cost is high [Thompson et al. 2009].

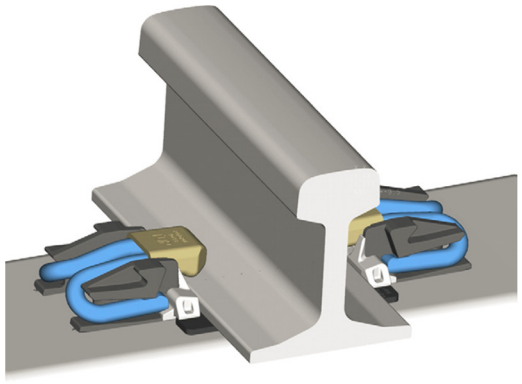


Figure 16. Pandrol Fastclip fastening connection, with flexible rail pads [Thompson et al. 2009].

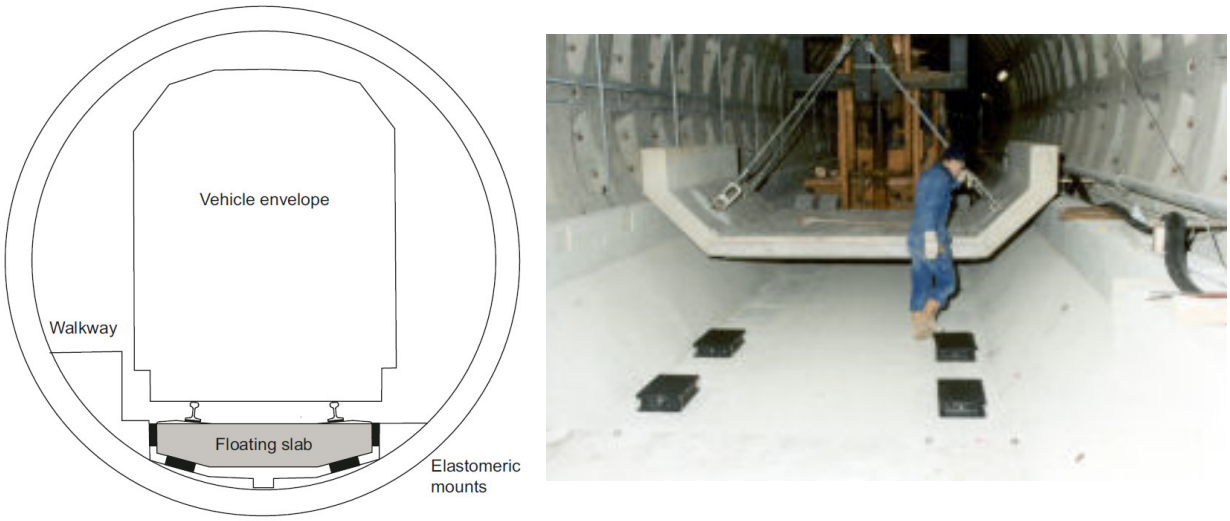


Figure 17. Floating slab track system: (a) typical cross section [Thompson et al. 2009]; (b) implemented system in built tunnel [Vibration from Underground Railways Pipe-in-Pipe software – New Release 2013].

Railway induced vibrations are produced through quasi-static and dynamic axle loads. They exhibit an arbitrary time variation, duration and periodicity. In moving trains, the principal mechanism is the dynamic excitation due to the unevenness of wheels and track lines, but also from irregularities, causing impact excitation in rail joints and wheel flats (Figure 19a). The vibration wavelength is considered broad-band. The energy and frequency content are also highly dependent on the characteristics of the moving train, i.e., the speed and weight [Thompson et al. 2009].

Vibrations induced from trains running in tunnels are transmitted through intermediate soil strata, in the 3D space, thus controlling the wave propagation (Figure 18b). Even though the highest amount of energy is transmitted downwards, the main interest is on the propagation of waves towards the surface and at the foundation level of the buildings of interest. Those vibrations are mainly P-waves, rather than S-waves or surface waves [Jones et al. 2002]. Vibrations propagate

first through the tunnel's lining (i.e. concrete rings), in a similar way as Rayleigh waves, as shown in Figure 18c and mostly influence vibrations on the surface, directly above the lining. Next, at lower angles, the wave propagation adopts a cylindrical wave-front shape, as shown in Figure 18d [Thompson et al. 2009 and Jones et al. 2002].

The vibration signal that reaches a neighboring structure is then defined as ground-borne vibration. It contains a higher frequency content that normally ranges from 30 to 250 Hz. Though, frequencies up to 100 Hz are to be considered as relevant for induced structural or aesthetic damage [ISO 4866:1990/Amd 2:1996 2010, DIN 4150-3 2016, BS 7385-2:1993 and Xia and Calçada 2013]. In a range distance of around 100 m and according to amplitude and intensity characteristics, ground railway vibrations can be also perceivable by building occupants [Thompson et al. 2009]. Following, in section 4.2, the assessment and monitoring process of ground-borne vibrations is explained, together with a field monitoring exercise, based on criteria from international standards.

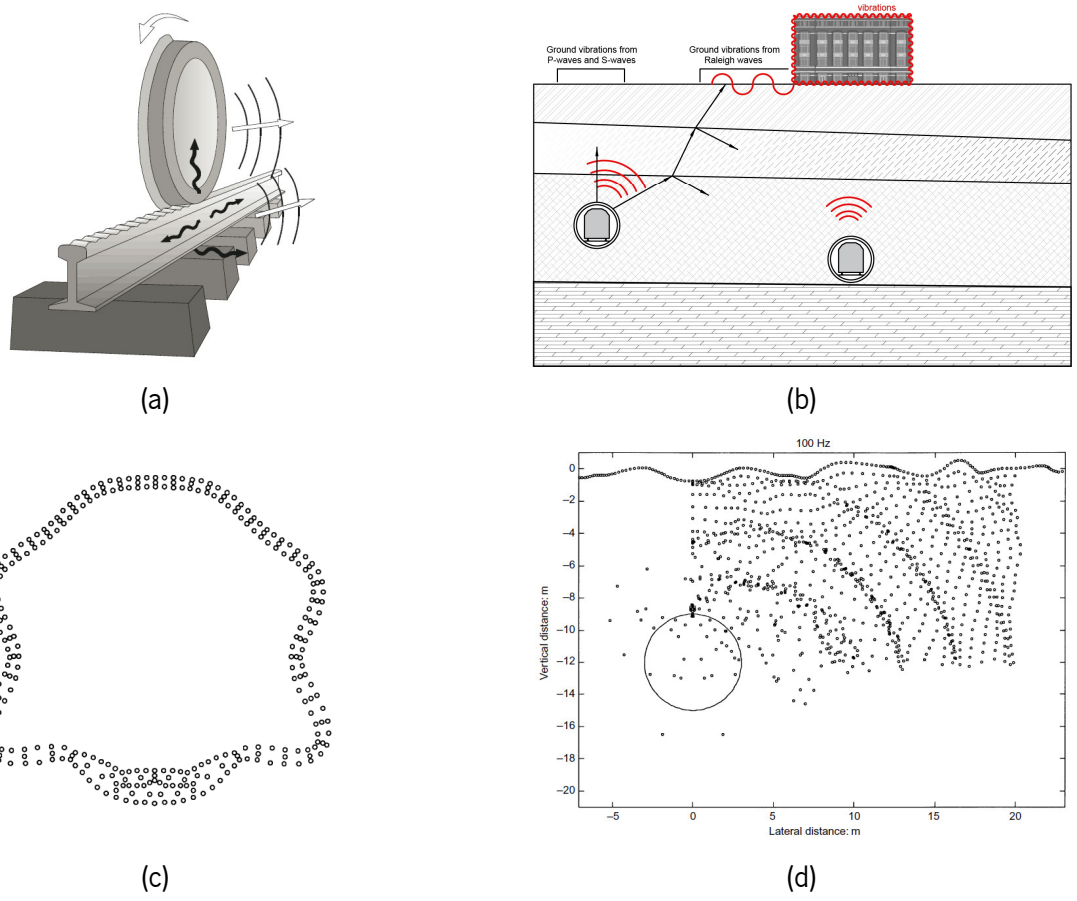


Figure 18. Underground railway induced vibrations: (a) mechanism of rolling noise and vibration in a railway track [Thompson et al. 2009]; (b) propagation through the soil half-space continuum; (c) vibration pattern of a concrete tunnel lining at 100 Hz [Jones et al. 2002]; (d) instantaneous displacement field in the soil around an unlined tunnel, at 100 Hz [Jones et al. 2002].

2.4.3. FE modelling approach

Finite Element (FE) models can serve as an efficient assessment and prediction tool for induced vibrations on soil-structure interaction problems. Numerical analyses are performed by means of dynamic moving loads with time integration. However, certain restrictions apply, mainly on the wave-propagation characteristics and boundary conditions. If a coupled approach is followed, the analysis is comprised of three models; the dynamic analysis under moving loads, for the train-track-tunnel-soil interaction model; the tunnel-soil-structure interaction model and the model for the dynamic propagation of vibrations inside the structure.

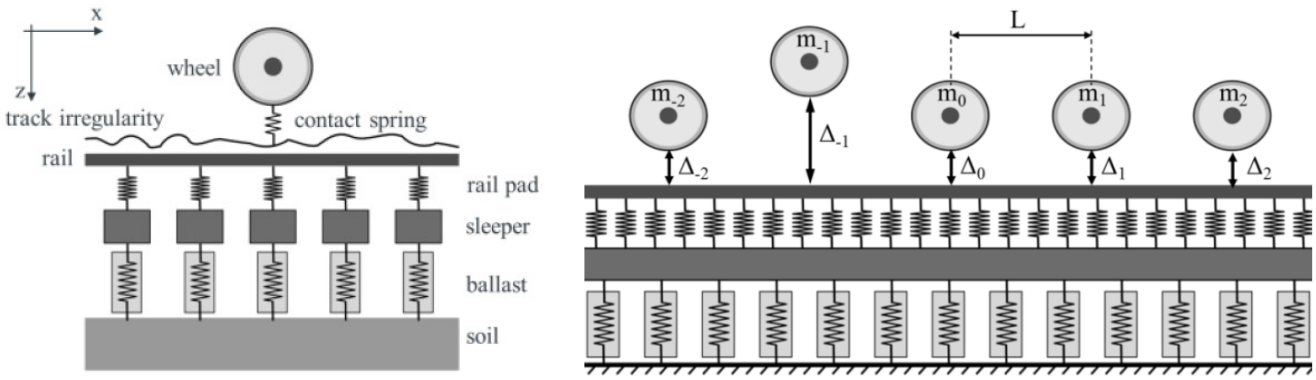
2.4.3.1. Semi-analytical models

As described in Section 2.4.2, the rail track system is supported on sleepers, with resilient rail pads. Further beneath, the sleepers rest on the ballast. The whole system, considering the single system of one wheel, can be modelled in 2D as a continuous Euler-Bernoulli beam, with a Winkler foundation, comprised by a series of springs, with intermediate elements, representing the sleepers (Figure 19a). Here, for the rail track, E is the Young's modulus, I is the moment of inertia of the cross-section, with a mass per unit length $\mathrm{m'_r}$. The normal stiffness per unit length of the pad and ballast is $\mathrm{s_p}$ and $\mathrm{s_b}$ respectively, while $\mathrm{m'_s}$ and $\mathrm{m'_b}$ is the mass of the sleeper and ballast respectively [Thompson et al. 2009]. If more layers are present (i.e. a floating slab), they are modelled the same way as the ballast [Ntotsios et al. 2015]. All components are assigned with damping properties, by means of a constant loss factor n, in the stiffness of each spring and the Young's modulus. Thus, $\mathrm{s_i}$ is replaced by $\mathrm{s}(1+\mathrm{in})$ and E is replaced by $\mathrm{E}(1+\mathrm{in_r})$, where $\mathrm{n_r}$ is the loss factor from the rail. Here is noted that for low values of damping, the amplification in terms of force transmissibility is larger [Thompson et al. 2009].

In the process of modelling the moving train, each wheel can be represented by a concentrated mass M, in series with a spring of normal stiffness K. In between the two systems, a Hertzian contact is introduced. The wheel-rail track system induces vibration signals that are constant in the longitudinal direction of the rail tracks (Figure 19a). By means of Fourier transformations, vibrations in the frequency-wavenumber domain are calculated from the 2D semi-analytical model. Results are finally transformed in the frequency-space domain, using an inverse Fourier transformation [Ntotsios et al. 2015]. Input parameters are moving axle loads, either moving constant or harmonic and the wheel-rail track irregularities, as an irregular wavenumber

along the rail-track. Outputs provide dynamic forces and kinetic quantities in the wheel-rail track interface and the ground [Ntotsios et al. 2015].

In the case of underground trains, the process is the Pipe-in-Pipe (PiP) model, developed by Forrest and Hunt 2006 and by Hussein and Hunt 2007. Despite the whole wheel-rail track system, the tunnel and surrounding soil layers are modelled as concentric cylindrical shells. Similar to the surface rail track system, the tunnel lining and the surrounding soil are considered constant in the longitudinal direction. The train is modelled by a distinctive number of wheel masses, with a constant distance L, as shown in Figure 19b. The moving axle load function can be derived from the superposition of the harmonic function of each wheel [Ntotsios et al. 2015 and Hunt and Hussein 2007]. The wheel-rail track irregularities are modelled through relative displacements Δ_i. Vibrations through the tunnel-soil system are calculated through transfer functions.



(a) (b)

Figure 19. FE modelling of track system, supported on sleepers, with: (a) an equivalent wheel-rail track interaction model [Thompson et al. 2009]; (b) an equivalent wheel-rail track interaction model for modelling a moving train [Ntotsios et al. 2015].

2.4.3.2. The Boundary Element method in 2D and 3D

Semi-analytical models for vibration propagation in the 'free field' are rather limited, given certain restrictions, such as the regular tunnel lining and homogeneous soil conditions. Thus, numerical methods are more suitable [Thompson et al. 2009].

The Boundary Element method (BE) is a coupled approach and requires the combination of solid or shell finite elements, representing internal boundaries, i.e., the tunnel structure, and boundary elements for the boundaries of the soil medium (Figure 20). In specific, since only the free field and tunnel boundaries need to be modelled, the medium is considered infinite. The propagation of vibration waves is calculated by means of Green's functions, for shear and

compression waves, and is explained in detail in Dominguez 1993. Yet, BE models in 2D are mostly used for evaluating the influence of specific parameters on the tunnel and structure, rather than predicting the absolute vibration values. The induced vibrations at source, from the moving train is clearly a three-dimensional problem, with three-dimensional wave propagation in the soil medium. However, 3D BE models require vast computational resources [Thompson et al. 2009, Hunt and Hussein 2007 and Andersen and Jones 2006].

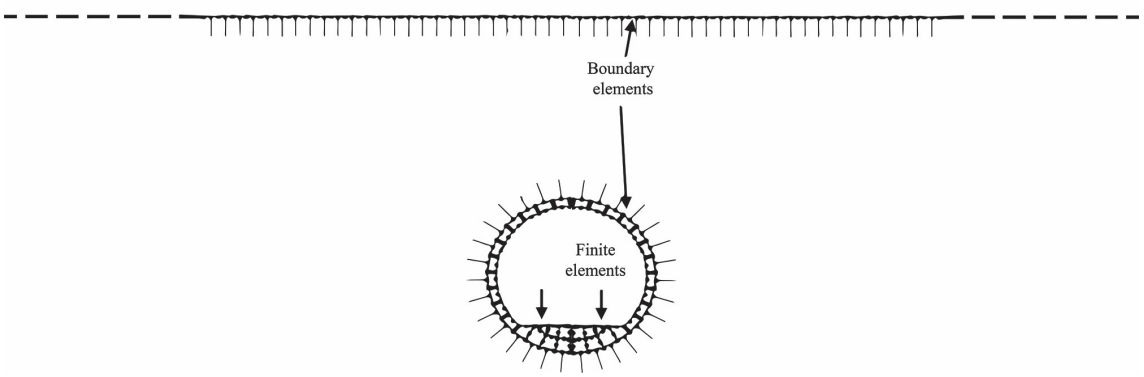


Figure 20. Coupled approach of finite elements and boundary elements. Boundary elements are presented with normal vectors, pointing to the soil medium [Thompson et al. 2009].

2.4.3.3. The 2.5D method

Through the '2.5-Dimensional' method, a 2D FE and BE model is solved a number of times, for different wavelengths and a 3D response is obtained, by applying Fourier transformation techniques [Thompson et al. 2009, Yang and Hung 2001 and Ghangale et al. 2019]. The soil layers and tunnel geometry are assumed uniform along the tunnel's center axis.

Initially, the 2D FE model contains the part of the near field, i.e., the soil layers and tunnel structure, and the far field, representing the soil medium and simulated by infinite elements. All elements are considered in plane-strain state. As described in section 2.4.3.1, a moving train is modelled as a series of wheels, in interaction with the rail-track, as shown in Figure 21a. The total response in the time-space domain contains information regarding the 2D profile and the load-moving direction, as shown in Figure 21b [Yang and Hung 2001 and Yang et al. 2010].

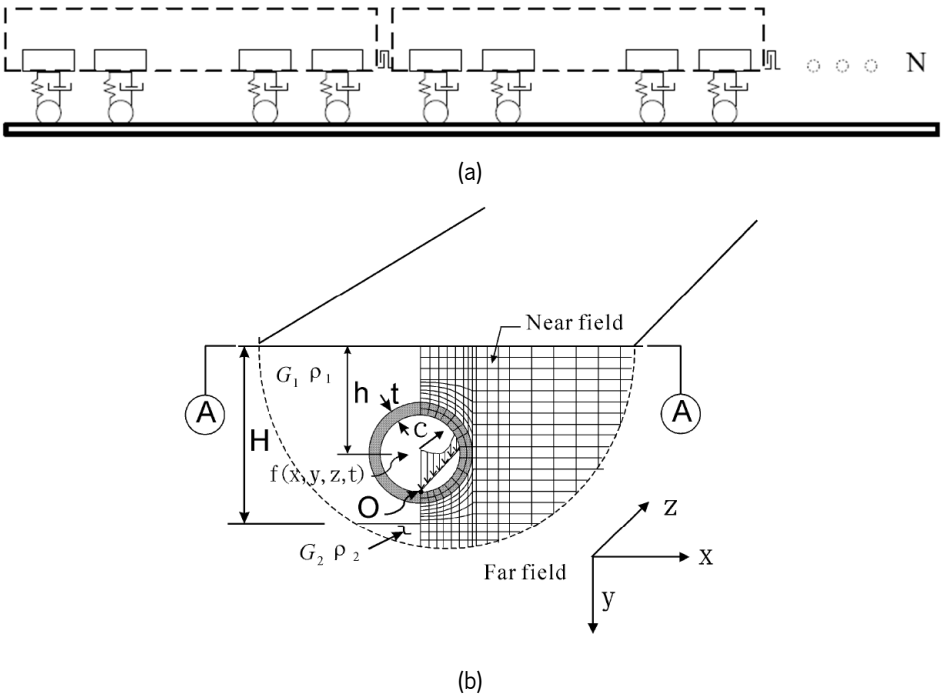


Figure 21. The 2.5 method: (a) train-rail track model [Yang et al. 2010]; (b) 2D near field profile, of tunnel lining and surrounding soil, in half-space [Yang et al. 2010].

2.4.4. Mitigation measures

Mitigation measures on induced vibrations from railways in tunnels can be divided into two categories, those that involve measures at source, i.e., wheel and rail track unevenness, and measures along the transmission path, i.e., buried soft barriers.

As described in section 2.1, measures applied in the track-ground interface, i.e., type of fasteners, booted sleepers, can have significant results on the amplitude of induced vibrations [Thompson et al. 2009]. A complete isolation of the railing track system, by a 'floating slab track', with elastomeric supports is considered the most efficient measure for reducing induced ground-borne vibrations, although, under significant construction costs (Figure 17) [Thompson et al. 2009].

Regarding measures along the transmission path, the main focus is on impeding the propagation of elastic waves in the soil medium and before they reach the structure of interest. The use of in-filled trenches or buried walls is based on concepts of diffraction, reflection and scattering of wave energy, but can reduce mostly the transmission of surface waves.

Regarding the type, a trench with no infill (open trench) would be the most effective, since no waves of any kind propagate in voids. Yet, many complexities in construction arise, mainly due

to issues of stability and large depth. Instead, trenches with bentonite-slurry infills can be used [Richart et al. 1970]. According to Richart et al. 1970, for a target reduction of 25% in the vertical vibration component, the ratio between the depth and the R-wave length L_R, for a continuous circular trench, with a radius at least $10L_R$, is equal to 0.6. Yet, design criteria, regarding the depth of the trench and the relative distance from the vibration source and the building of interest, should be verified for each case and validated through numerical models [Thompson et al. 2009].

Lastly, in the presence of very soft soils, surrounding the tunnel or adverse ground-borne vibrations, which urge immediate protective measures for cultural heritage buildings, soil stabilization, by means of injection grouting, can stiffen the soil and foundations, and also reduce ground-borne vibration amplitudes [Hunt and Hussein 2007].

2.5. Conclusions

Tunneling construction in soft ground is responsible for induced soil settlements, on the surface of neighboring structures. Induced ground-borne vibrations are the result of underground subway lines, during the operational time of passing trains. Both phenomena consist in a twofold complex problem, for the structural assessment and damage evaluation in historic masonry structures, in close proximity to underground subway lines.

Under current conventional approaches, subsidence curves of empirical prediction and analytical models can only serve as preliminary evaluation scenarios. Regarding the propagation of waves, from the tunnel's lining to the foundation base of the reference building, theoretical models of wave propagation are of use. Field monitoring strategies can acquire subsidence and vibration acquisition data, of use as input in numerical studies.

Advanced 3D FE models for settlement and vibration assessment, in order to be reliable, should cover several aspects, i.e., the tunnel's construction characteristics, the soil substrate, the soil-structure interaction, the 'free field' wave propagation etc. Considering also the need for a detailed representation of historic buildings, in order to capture accurately the stress paths and crack patterns, the resulting FEM and FEA are bound to become increasingly large, with large computational times. Thus, coupled approaches are considered appropriate, where the settlement or vibration fields, as outputs from FEA, of a FEM that contains a soil-tunnel system, with crude overlying buildings, are assigned as input in the more sophisticated FE model of the building of interest.

CHAPTER 3. MATERIAL CHARACTERIZATION FOR SIMULATED HISTORIC MASONRY, REPAIR AND RETROFIT

CHAPTER 3. Outline

3.1. Introduction

3.2. Reference façade and brickwork of the 19th-20th centuries

3.3. Experimental research on simulated historic masonry

3.3.1. In plane failure in brick masonry under monotonic loading

3.3.2. Capacity tests in uniaxial and diagonal compression, testing protocols and monitoring under cyclic loading

3.4. Compressive and flexure tests on simulated historic masonry constituents, repair and retrofit material

3.4.1. Hydraulic lime mortar

3.4.2. Solid fired bricks

3.4.3. High performance hydraulic lime-based render and fluid binder

3.5. Mechanical tests on simulated historic masonry assemblies

3.5.1. Uniaxial cyclic compression tests

3.5.2. Diagonal monotonic compression tests

3.6. Analytical stress-strain expressions from experimental data

3.7. Conclusions

3.1. Introduction

Historic brick masonry is inherently characterized by heterogeneity, anisotropy of properties, nonlinearity and a significantly different response under loading in tension and compression. The type of failure, crack pattern, strength and stress-strain evolution of brick masonry are interrelated with the geometrical and mechanical characteristics of its constituents, i.e., thickness of mortar joints, brick size, bond pattern and interlocking, strength and stiffness of bricks and mortar etc. [Como 2016]. The current chapter covers the architectural and structural configuration of brick masonry residential buildings, dating between the 19th-20th centuries in Europe and in particular in the Iberia Peninsula. An extensive experimental campaign was

performed, by constructing brick masonry wallets from modern material, simulating historic ones, in order to characterize mechanically load-bearing brick masonry perforated walls, followed by testing under the effect of settlements and vibrations.

3.2. Reference façade and brickwork of the 19th-20th centuries

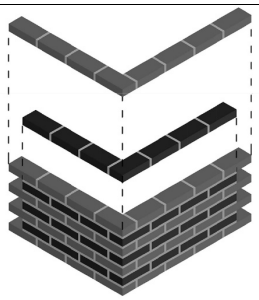
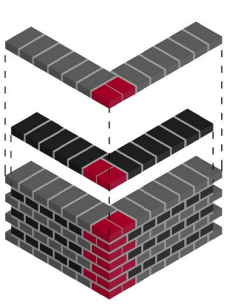
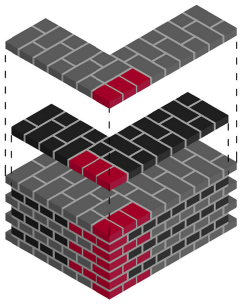
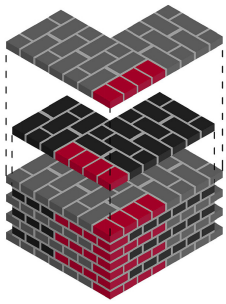
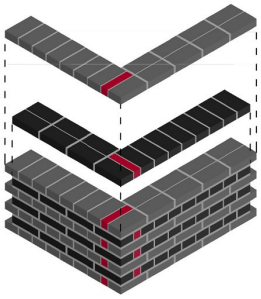
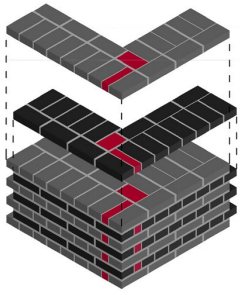
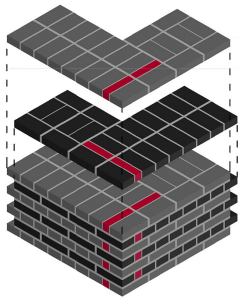
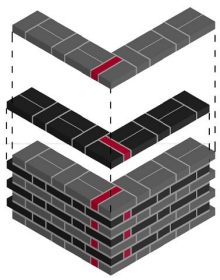
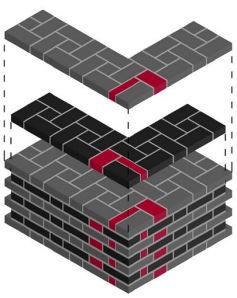
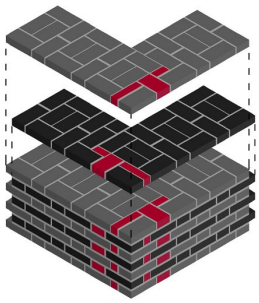
Brick architectural works, prevailed between the middle of the 19th century and the beginning of the 20th century in Europe, with buildings reaching up to six floors. Associated with the beginning of the industrial revolution, brick architecture materializes in residential projects, and brick production, being greatly increased, moves towards a more standardized and industrialized manner [Adell Argilés 1992]. From an architectural perspective, prevailing styles were revivals of earlier architectural movements, i.e., the Greek Revival (1800-1900), the Gothic Revival (1810-1900), the Romanesque Revival (1840-1880). These spread across Europe, but also worldwide [Benovolo 1971, Bergdoll 2000 and Ching et al. 2017].

Regarding brick shapes and sizes, they tend to unify, in many cases by law, and proportions are established around the 1:2:(4-5) ratio, for the height, width and length respectively. In order for the brick arrangement to accommodate thick bed joints (≥1cm) the brick's length is fairly equal to twice the width, with an additional tolerance of one joint [Chabat P. 1886]. The mortar joint is mostly lime mortar, with a typical mix ratio of parts per volume equal to 3:2:1, for the sand, lime and water respectively. Yet, lime was used mostly slaked, often not matured enough to become lime putty, and thus the mix ratio per volume is 3:2 for sand and lime respectively, with no extra water added, from that already contained in lime putty [Camino Olea 2001]. This is somewhat different from hydraulic lime mortars, as defined by modern building codes, which specify the class of hydraulic lime (NHL 2, NHL 3.5 and NHL 5) and a volume ratio of (3-4.5):1 for the sand and lime respectively, depending on the target strength class of the mortar [BS EN 459-1:2010 and NA to BS EN 1996-1-1:2005].

Moving to the construction site, interlocking is implemented rigorously, in order to achieve connectivity in the wall's thickness and elevation, under different bond patterns and wall thicknesses. Many of the established bond patterns in the 19th century Europe, are presented in textbooks of the time, as in Lacroux et al. 1878 and are associated to respective geographic practices, i.e., English, Flemish, Belgian, Spanish, American etc. Depending on the orientation and sequence of header and stretcher brick faces, the main geometrical rule is for the head joints to

correspond in the middle of the brick's length, placed directly above and below (Table 3) [Lacroux et al. 1878]. For the purposes of the experimental campaign and the replicas of historic masonry, the Flemish bond was chosen, which provides a consistent interlocking both in section and elevation, together with a limited number of cut bricks.

Table 3. Graphic representation of main brick bond patterns, at corner interlocking and for various wall thicknesses. Note the cut bricks in red to accommodate the brick interlocking at corners. Adapted from Chabat 1886 and Lacroux et al. 1878.

	Thickness			
Bond	½ Brick	1 Brick	1 ½ Bricks	2 Bricks
Stretcher		–	–	–
Header	–			
English	–			
Flemish	–			

From a structural perspective, the brick masonry buildings of the 19th century are composed by load bearing walls, with the main façade being the emblematic architectural element, incorporating decorative features, many of which with unplastered brickwork patterns, different

brick colors, and brick projections, as described in Chabat 1886 (Figure 22a, c and e). The openings are often closed with arches, where the brickwork is more elaborate and often serving as decoration, i.e., segmental, flat and circular arches. Many openings, according to Chabat 1886 and Chabat 1989, were configured under a combined system of a brick masonry arch, covering half the exterior thickness, and the interior half was bridged with a system of timber beams (Figure 22a).

The internal skeleton, in most cases, is a lighter timber frame, with timber floors and posts, while transversal walls, sidewalls and staircase walls were configured as a composite system of an internal timber frame of horizontal, vertical and diagonal timber elements and crude masonry infills, as described in Camino Olea 2001 and González-Redondo et al. 2003 (Figure 22b). The transversal walls were in some cases party walls, considering that many of the buildings were aligned within blocks. Their thickness varied from 0.21-0.28 m, according to González-Redondo et al. 2001, and were constructed, similarly to the internal walls, of a composite system of a timber frame and masonry infills, although evolving progressively to plain brick masonry walls, by the end of the 19th century, and according to fire provision regulations, as the ones implemented in Madrid and elsewhere in Spain [González-Redondo et al. 2003]. As explained in Camino Olea 2001, the façades of residential buildings in Valladolid, Spain, between 1884 and 1926, had the external claddings with solid or frogged bricks molded by mechanical pressure, which made them more water resistant and flattened the external faces, whereas the inner layers were with ordinary solid bricks. Yet, the façade of a 19th century residential multistory building is considered as a uniform structural element, primarily due to projecting bricks, or else toothing [Adell Argilés 1992]. As described in González-Redondo et al. 2003, the foundations of residential buildings in Madrid, dating between the 17th and the 19th centuries, were continuous wall footings, of extended width of 0.9-1.20 m and a depth of around 3 m, to accommodate a basement, with consecutive layers of brick courses and rubble stone masonry with lime mortar (Figure 23a). In the presence of a basement or a cellar, the ceiling on top was often configured with barrel or groin masonry vaults, of either brick or stone (Figure 23c) [González-Redondo et al. 2003]. In cases of a high phreatic level and weak soil substrates, the masonry foundation was configured over a grid of timber piles, hammered by impact that reached depths higher than 12 m. Depending on their length, the piles could either serve compacting the underlying soil (<6 m) or serve as friction piles (>12 m) [Apolo and Martínez-Luengas 1995]. Such foundation piles are also typical in the much earlier Pombalino buildings of the 18th century in Lisbon (Figure 23b) [Cardoso et al. 2014].

Generic geometrical features of brick masonry façades of multistory residential buildings from the early 20th century in Valladolid are presented in Table 4 [Camino Olea 2001]. Here, the thickness of the façade walls at ground floor varies from 0.75 m (4-stories) to 0.45 m (2-stories), which according to local brick sizes, corresponds to a brick bond pattern with a thickness ranging from 3 to 2½, and 2 bricks respectively [Camino Olea 2001]. For the upper stories, the façade is configured with a thickness of 0.45-0.55 m, thus a thickness of two bricks [Camino Olea 2001]. The length of continuous vertical masonry piers and that of the openings are in the range 0.80-1.90 m and 1.10-1.25 m respectively [Camino Olea 2001]. At the last floor, a double pitched roof is configured, with the ridge beam parallel to the façade. In many cases the upper spandrel-cornice of the façade is extended up to 1 m high, which converts the upper roof space into an attic (Figure 22f).

From the historic building database of Camino Olea 2001, a historic brick masonry façade is used as reference (Table 4 and Figure 22f), in order to reproduce reliable experimental data on the cracking behavior of load-bearing brick masonry perforated walls, under the effect of settlements and vibrations. The configuration of the reference façade, part of residential 4-story building (3-stories and attic) of the early 20th century in Valladolid (Calle de la Asuncion 11, 1908, Table 4 and Figure 22f) was chosen as reference for the current experimental work, mostly due to the regularity in elevation, piers, spandrels and openings.

According to Chabat 1886 and Chabat 1989, the spandrels, instead of flat or segmental full-thickness arches, were configured with a segmental brick masonry arch in the half-outer thickness, and with a set of timber beams placed in the half-inner part of the façade system (Figure 22a).

The floors, which are typically around 5-7m in span, consist of principal timber beams, perpendicular to the main façade, embedded until half the thickness, and resting on continuous timber beams (wall plates), of similar size (Figure 22d and f). The floor beam size, according to González-Redondo et al. 2001 can be either 20x14, 16x12 or 12x9 cm^2 (height x width). On the other side, the beams are embedded in the composite timber frame wall, parallel to the façade. A typical distance between sides of two adjacent floor beams is equal to the actual width of the beam, according to González-Redondo et al. 2001. The space in between was covered with a system of nailed planks or crude masonry and an arched extrados [González-Redondo et al. 2003]. The double-pitched roof system was built similarly to the floors, with a main system of timber rafters,

perpendicular to the façade, resting on a wall plate, and a secondary system of smaller size beams nailed perpendicular to the main ones. Next, a system of planks is configured and a final layer of tiles or metal plates of steel, lead or zinc, is placed [González-Redondo et al. 2003].

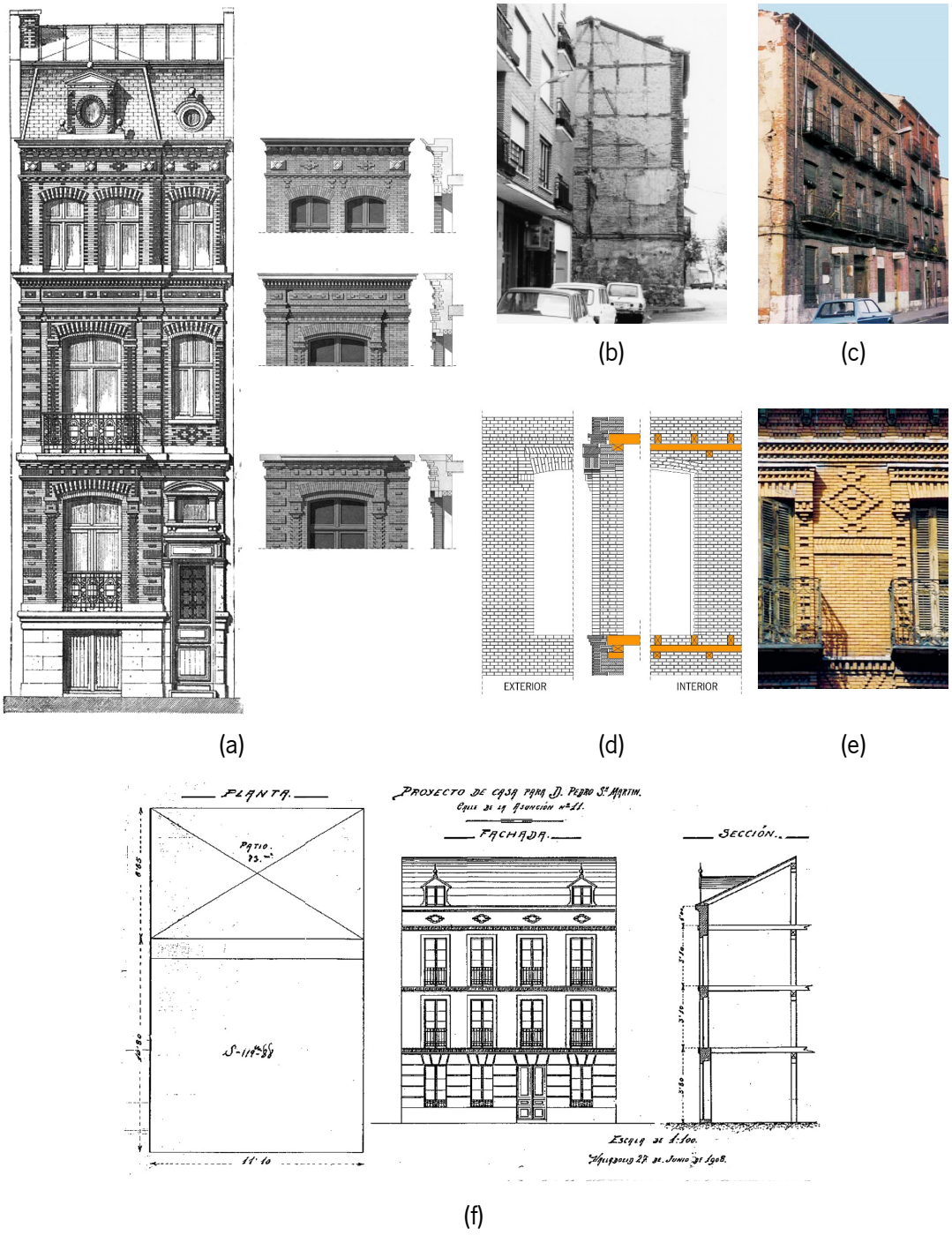


Figure 22. Brick masonry multi-story residential building of the 19th and 20th centuries: (a) elevation and section of the façade of Maison En Brique of 1881 by Buysschaert M., in Brussels, [Chabat 1886]; (b) exposed sidewall, of a residential building of the 19th century in Valladolid, of a composite timber frame and brick masonry infills (calle Doctor Cazalla) [Camino Olea 2001]; (c) brick masonry façades from 1880s (calle de la Estación, Valladolid) [Camino Olea 2001]; (d) and (e) typical construction details of spandrel, side piers and timber floors, of a residential building of the 20th century in Valladolid [Camino Olea 2001]; (f) plan, elevation and half-section of the reference building of the early 20th century in Valladolid [Camino Olea 2001].

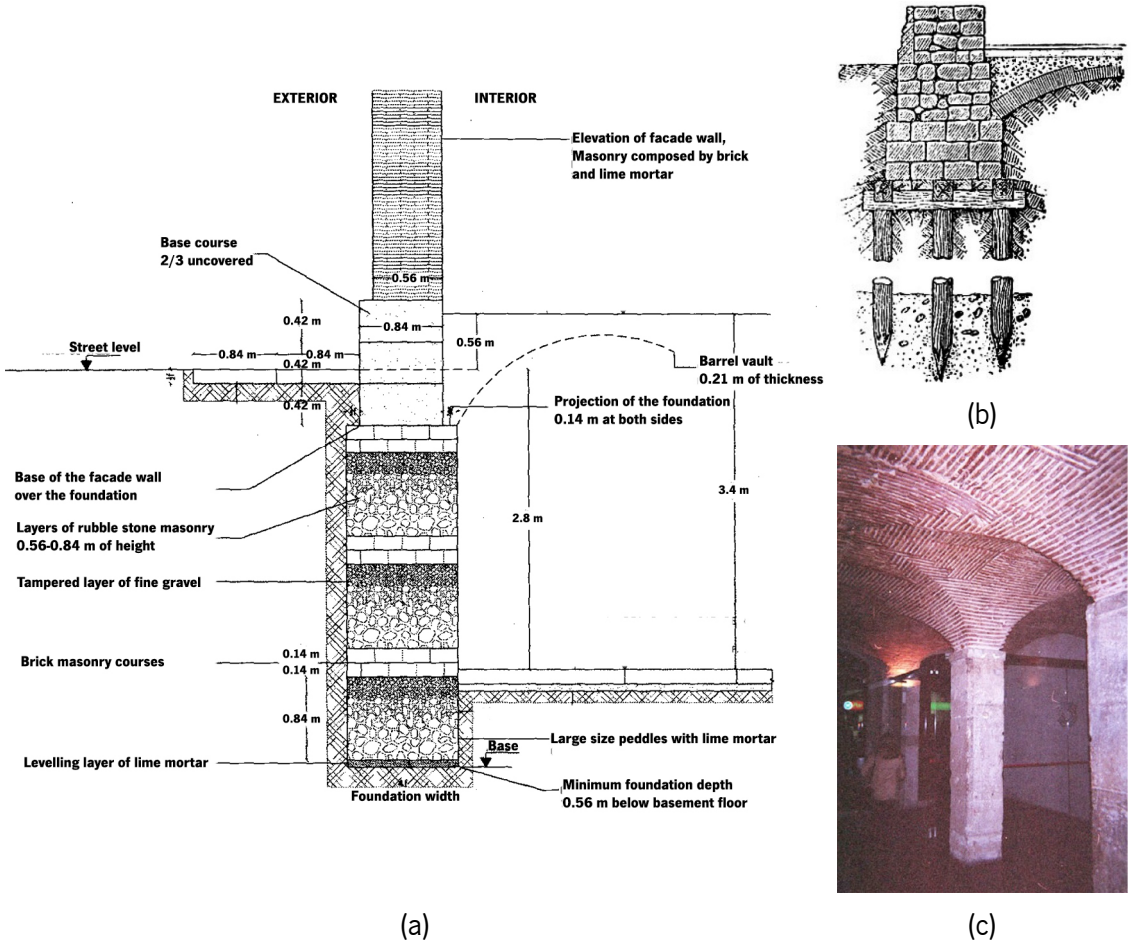


Figure 23. Foundation system for brick masonry residential buildings: (a) typical section of foundation footing for brick masonry façades, of residential buildings of the 17th-19th centuries in Madrid. Typical dimensions based on Castilian feet (~0,28 m) [González-Redondo et al. 2003]; Pombalino buildings of the 18th century in Lisbon: (b) trench of regular stone masonry footings and a grid of timber piles, for weak soil substrates and high seismicity areas [Cardoso et al. 2014]; (c) brick masonry groin vault system at basement level [Cardoso et al. 2014].

Table 4. Geometric aspects and typological characteristics of brick masonry façades, of residential brick masonry buildings, from the beginning of the 20th century, in Valladolid, Spain [Camino Olea 2001]. Note the geometrical features of the reference façade (Ref.).

Building facade (Location, Construction, Architect)	Length/ Height (m)	Floors (#)	Openings per floor (#)	Height of 1st floor (m)	Height of 2nd floor (m)	Height of 3rd floor (m)	Height of 4th floor (m)	Height of cornice (m)	Wall thickness of ground floor (m)	Wall thickness of upper floors (m)	Wall thickness of top floor (m)	Corner/ Inner piers (m)	Size of openings (m)
Calle Francos 15, 1904, Modesto Coloma	12.6/ 11.4	3	2	4.00	3.70	3.70	-	-	0.70	0.55	0.55	1.25/ 1.90	1.10
Calle de las Angustias 46 a 58, 1904, E. Repullés y Vargas	17.2/ 15.0	4	3	4.25	3.75	3.50	3.50	-	0.70	0.55	0.50	1.80/ 1.80	1.25
A la calle Mendizabal, 1907, Antonio Ortiz de Urbina	9.4/ 14.5	4	3	4.10	3.30	3.30	3.20	0.60	0.60	0.45	0.45	1.50/ 1.50	1.25
A la calle de la Alegría, 1907, Antonio Ortiz de Urbina	26.8/ 14.5	4	2	4.10	3.30	3.30	3.20	0.60	0.60	0.45	0.45	1.50/ 1.60	1.25
Calle de la Mantería, 45 y 47, 1907, Modesto Coloma	14.5/ 10.8	3	2	3.90	3.50	3.40	-	-	0.70	0.55	0.55	1.03/ 1.55	1.25
Calle del Jabón 3 y 5, 1908, Antonio Ortiz de Urbina	10.8/ 15.3	4	3	4.50	3.50	3.40	3.40	0.50	0.60	0.45	0.45	1.40/ 2.08	1.25
Calle del Jabón 1, 1908, Antonio Ortiz de Urbina	5.7/ 13.8	4	2	4.10	3.40	3.15	2.90	0.20	0.60	0.45	0.45	0.90/ 1.35	1.25
Calle de la Asuncion 11, 1908, Antonio Ortiz de Urbina (Ref.)	10.8/ 11.0	3	4	3.80	3.10	3.10	-	1.00	0.6	0.45	0.45	1.20/ 1.20	1.20
Average CoV (%)	13.85 45.4% / 13.61 12.2%	4 12.2%	2 20.4%	4.14 4.3%	3.49 4.7%	3.39 4.8%	3.24 6.4%	0.48 34.5%	0.64 7.7%	0.49 10.0%	0.49 9.1%	1.34 21.2% / 1.68 14.0%	1.23 4.3%

A schematic representation of the reference building, with no basement, a brick masonry façade, a timber floor configuration, a timber roof, an internal timber frame system and composite sidewalls is shown in Figure 24 and Figure 25, as adapted from González-Redondo, et al. 2003, Chabat 1886 and Camino Olea 2001. This configuration will be the base reference for the laboratory testing assemblies. In total, two assemblies were built and tested in this work, representative of the geometry and loading conditions of the reference façade, and are located at the 2nd story (Figure 25).

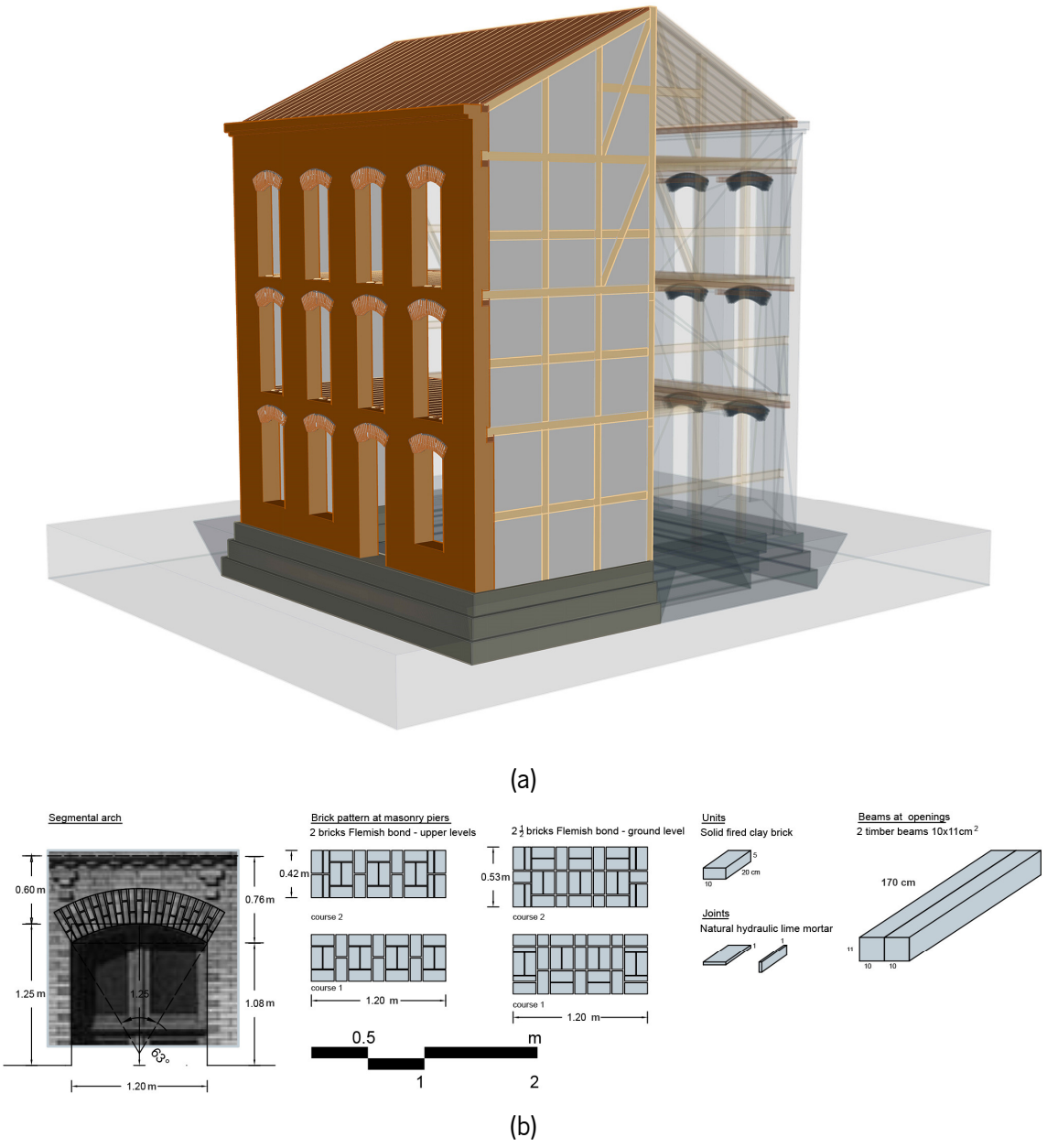


Figure 24. Schematic representation of the reference brick masonry building, used for constructing the laboratory testing assemblies, adapted from González-Redondo et al. 2003, Chabat 1886 and Camino Olea 2001: (a) 3D view; (b) details for arch configuration, brick patterns for piers and constituents.

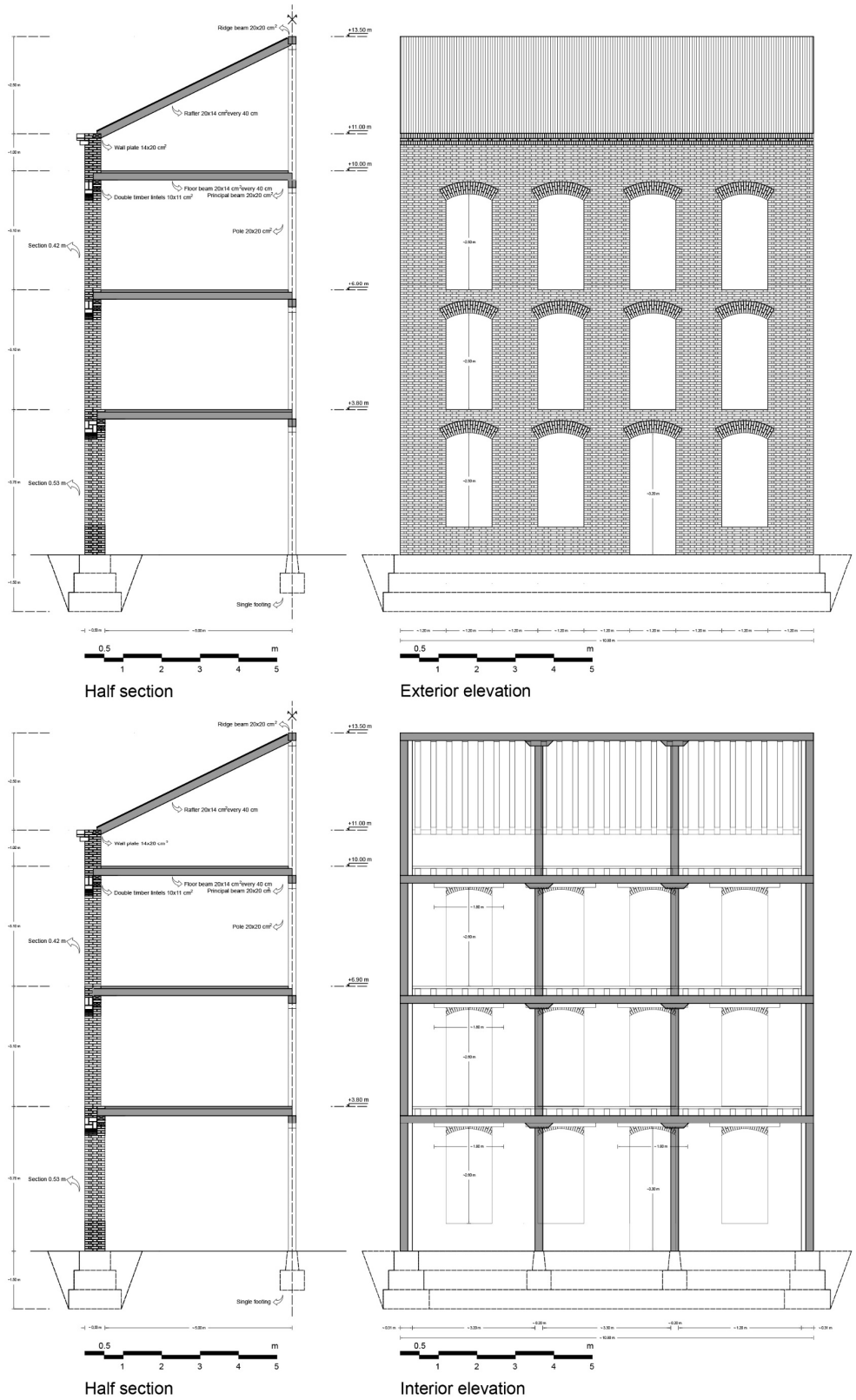


Figure 25. 2D schematic representation of the reference brick masonry building, used for constructing the laboratory testing assemblies. Note the façade, floor configuration, roof, internal timber frame system and sidewalls, as adapted from González-Redondo et al. 2003, Chabat P. 1886 and Camino 2001.

3.3. Experimental research on simulated historic masonry

Brick masonry is a quasi-brittle heterogeneous material, composed by brick units and mortar, under many possible geometrical characteristics and unit arrangements. The different stiffness and strength of masonry constituents are responsible for a complex nonlinear response, even at early stages of loading. Masonry uniformity and regularity, when present, lay on the constant arrangement of bricks within patterns, the presence of toothing and interlocking of layers, together with the consistency of mortar joint thickness and material supply. In terms of computational specifications, the process of structural assessment and characterization of masonry at a building scale may be governed by a homogenization approach, particularly suitable for three-dimensional solid models [Lourenço 2002]. Thus, masonry is usually studied as a composite material of a homogeneous averaged nature, which is coupled with experimental tests on medium to large size masonry specimens [Lourenço 1996]. Regarding the evolution of damage upon loading, constitutive models that describe the transition from smeared cracking to localized macro-cracks are used [Lourenço 1996]. Macro-cracks are formed close to the peak load and for the post-peak response to be observed the load needs to be reduced, under displacement control techniques [Lourenço 1996]. Yet, the knowledge of the mechanics of the microstructure is inherent for understanding damage propagation in masonry, and homogenized constitutive models implicitly account for the discontinuum elements [Lourenço 1998, Angelillo et al. 2014 and Lourenço 1996].

3.3.1. In plane failure in brick masonry under monotonic loading

The compressive strength of a historic solid fired clay brick can vary between 5-25 MPa, depending mostly on the type and quantity of clay and the uniformity and attainment of firing temperatures [Como 2015]. In general, higher and more uniform firing temperatures tend to produce bricks of higher compressive strength. Yet, firing temperatures of historic bricks were usually in the order of 1000ºC [Fernandes et al. 2009]. As presented in Fernandes et al. 2009, physical properties of fired bricks dated within the 12^{th}-18^{th} centuries, namely the porosity, apparent density and water absorption are within the range 12%-43% in volume, 16.80-18.70 kN/m^3 and 6%-32% in weight respectively. Furthermore, the tensile strength of the brick, which most of times is determined by flexure tests, and the Young's modulus, vary in the range of 3%-13.5% and 125-1400 times of the uniaxial compression strength respectively [Fernandes et al. 2009].

The typical component of historic mortars is lime, either slaked or hydraulic, usually with pozzolanic additives. Additional components to a historic lime mortar mix are sand, aggregates and water, the latter in proportions of 15-20% in mass [Como 2015]. Their uniaxial compression strength is within the range of 0.5-2.5 MPa, and under modern code specifications, historic mortars can be designated as (iv) and (iii), M2 and M4 class respectively (Table NA-2 of NA to BS EN 1996-1-1: 2005) or even as CS I category mortar (Table 1 of EN 998-1:2010).

Regarding the behavior of brick masonry, under uniaxial compression, as explained in Como 2016 and Kaushik et al. 2007, the vertical stresses σ_z are uniform and equal with the vertical stresses $\sigma_{z,b}$ and $\sigma_{z,m}$, for the bricks and mortar respectively. In the lateral directions, the bricks are usually stretched, while the mortar joints are compressed, and both lateral forces must be balanced (Figure 26a) [Zucchini et al. 2006]. By considering the local stress field in both constituents, it is obvious that the failure of brick masonry in uniaxial compression is triggered by the vertical compression and lateral stretching of bricks, causing vertical, splitting cracks, along the thickness and faces (Figure 26a) [Como 2016 and Kaushik et al. 2007]. In terms of magnitude, the compressive strength of masonry is always lower than of the bricks, but statistically presents a high variation, depending on the relative height, the stiffness and the Poisson ratio of the brick courses and bed joints [Como 2016]. According to the Italian building code NTC 2018, the compressive strength of fired clay brick masonry with lime or cementitious mortar is in the range of 2.6-8.0 MPa. The uniaxial compression of unconfined brick masonry, under instantaneous and monotonic loading, combines a hardening and softening phase, described well by a parabolic function [Lourenço 1996]. Various equations exist, namely in Hognestad 1951, Ewing et al. 2004, Feenstra 1993, EN 1992-1-1 2004 and Thorenfeldt et al. 1987 (Figure 27). Most of them are based on experimental results on unconfined compression of concrete specimens, which can describe adequately the nonlinear behavior in masonry and are part of predefined material models in FE software (Figure 27) [Diana user's manual. 2020].

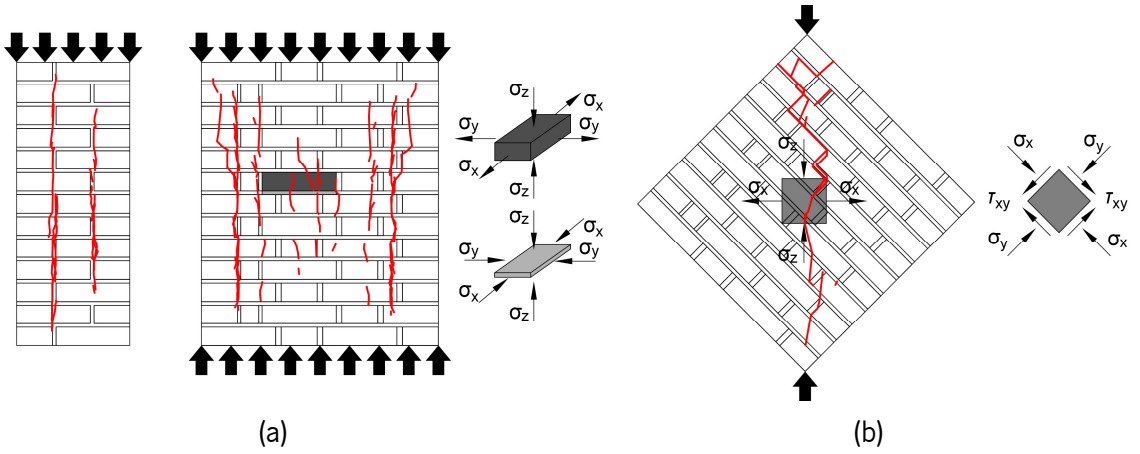


Figure 26. Masonry typical crack pattern and representation of stresses in a localized area of the specimen under: (a) uniaxial compression. Note the layer separation in section, following the alignment of head joints; (b) diagonal compression.

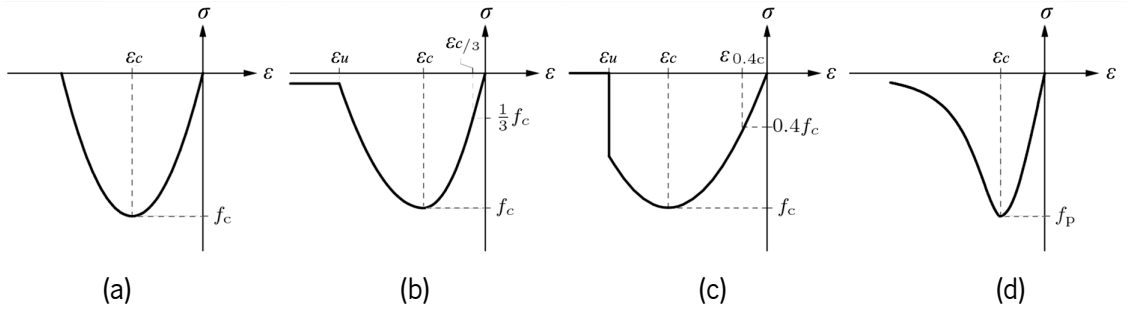


Figure 27. Material models of unconfined compression, based on concrete inelastic behavior: (a) Hognestad 1951 parabola; (b) parabolic curve according to Feenstra 1993; (c) inelastic curve of §3.1.5 EN 1992-1-1 2004; (d) the Thorenfeldt et al. 1987 curve [Diana user's manual. 2020].

Considering the best fitting process of experimental data to analytical models, according to Hognestad 1951, Ewing et al. 2004 and Kaushik et al. 2007, a 2nd order parabolic function can describe the stress-strain (f - ε) curve of masonry under monotonic uniaxial compression, while the descending part, which corresponds to a steady crack opening, may be described by a linear curve. Considering the vertex form of a parabolic equation with intercepts at (0,0) and ($2\varepsilon_c$,0), and a vertex at (ε_c, f_c), where ε_c and f_c are respectively the strain and stress of masonry at peak, a representative stress-strain (f_c, ε_c) parabolic equation is formed (Equation 28) from initial steps until a descending part of a stress equal to 0.9 f_c. For higher strains, the stress-strain curve can be simplified with a linear descending curve, until a residual compressive stress equal to 0.2 f_c [Ewing et al. 2004]. For lime-based mortars, which present high ductility, Kaushik et al. 2007 estimated an ultimate corresponding strain, equal to 2.75 ε_c. According to Hoshikuma et al 1997, for a quasi-brittle material under confinement, the ascending part of the stress-strain curve for uniaxial compression can be described better, in terms of boundary conditions, by Equation 29. For the descending part, in Facconi et al. 2018, a 2nd order parabolic curve is proposed,

considering also the ultimate strain ε_u, which can reach up to 1.5-2 ε_c (Equation 30). Additionally, in JCSS 2011 a 2nd order polynomial equation is proposed, similar to §3.1.5 of EN 1992-1-1 2004 (Equation 31). Finally, an alternative approach is given, in Alshebani et al. 1999, with the envelope curve described analytically by a 2nd order exponential growth function (Equation 32). In the respective expressions, E or E_o is the Young's tangent modulus of the ⅓f_c, while E_{SEC} is the corresponding stiffness at peak.

$$f = -f_c \cdot \left(2\frac{\varepsilon}{\varepsilon_c} - \left(\frac{\varepsilon}{\varepsilon_c}\right)^2\right), \quad \varepsilon_c = -\frac{2f_c}{E} \qquad \text{Equation 28}$$

$$f = -E\varepsilon\left[1 - \frac{1}{n}\cdot\left(\frac{\varepsilon}{\varepsilon_c}\right)^{n-1}\right], \quad n = \frac{E}{E - E_{SEC}}, \quad E_{SEC} = \frac{f_c}{\varepsilon_c} \qquad \text{Equation 29}$$

$$f = -f_c \cdot \left[1 - \left(\frac{\varepsilon - \varepsilon_c}{\varepsilon_u - \varepsilon_c}\right)^2\right] \qquad \text{Equation 30}$$

$$f = f_c\frac{k_o\eta - \eta^2}{1 + (k_o - 2)\eta}, \qquad \eta = \frac{\varepsilon}{\varepsilon_c}, \qquad k_o = \frac{E_o\varepsilon_c}{f_c} \qquad \text{Equation 31}$$

$$f = -E_{SEC}\varepsilon \cdot e^{(1-\frac{\varepsilon}{\varepsilon_c})\frac{\varepsilon}{\varepsilon_c}} \qquad \text{Equation 32}$$

As presented in Ewing et al. 2004, Feenstra 1993 and Kaushik et al. 2007, six transition states are identified in the stress-strain curve of masonry in compression: (1) for stresses below the ⅓ f_c of masonry, considering as linear-elastic; (2) at ¾ f_c masonry enters at the nonlinear phase, with the initiation of splitting cracks at bricks; (3) at $^9/_{10}$ f_c masonry is approaching the maximum stress with vertical continuous splitting cracks; (4) at peak stress f_c; (5) at ½ f_c after peak, masonry exhibits its maximum reliable compressive strain; and (6) at $^1/_5$ f_c after peak, masonry exhibits its ultimate compressive strain, before an uncontrolled collapse occurs.

The modulus of elasticity E of masonry is usually associated with the expected compressive strength f_c by the expression E = a·f_c, presenting a wide range of variation, given the numerous combinations of mechanical and geometrical properties of masonry constituents. According to Tomazevic 1999 E = (200:1000)· f_c, whereas in FEMA 306 1998, the recommended relationship for existing masonry is E = 550·f_c. Furthermore, in MSJC 2002 E = 700·f_c, in EN 1996-1-1 2005

$E = 833 \cdot f_c$[1], in CAN/CSA S304.1-04 2004 $E = 850 \cdot f_c$, in Paulay and Priestley 1992 $E = 750 \cdot f_c$ and in Drysdale et al. 1994 $E = 210\text{-}1670 \cdot f_c$. In Kaushik et al. 2007, from uniaxial compression tests on masonry prisms, with four different solid fired bricks and three mortar classes, a relation of $E = 550 \cdot f_c$ was found, with a COV of 30%. According to Feenstra 1993, TMS 402-11/ACI 530-11/ASCE 5-11 2011, Tomazevic 1999 and EN 1996-1-1 2005, the E is associated to the first linear branch of the stress strain curve of a quasi-brittle material under uniaxial compression and is the slope of the chord from $0.05 \cdot f_c$ to $\frac{1}{3} \cdot f_c$. According to §3.7.3 EN 1996-1-1 2005 the shear modulus G can be considered as 40% of E, thus assuming a Poisson ratio of 0.25.

The tensile strength of historic masonry is generally low and differs within one order of magnitude with the compressive strength, with a ratio in the range of 0.03-0.09 [Tomazevic 1999]. When the tensile failure is associated to out of plane flexure, along a plane parallel or vertical to a bed joint, the tensile strength is dependent on the adhesion between the mortar and bricks [Marques 2020]. When a crack is formed, and under the presence of friction, crack widths advance linearly, with no softening [Como 2016]. Usually, for considering the in-plane tensile failure of masonry, a diagonal compressive force is accounted, which simulates a direct shear load, i.e., a diagonal compression test on a square masonry wallet (Figure 26b). Cracks are either formed parallel to the compressive forces, by splitting bricks and mortar joints or progress through sliding within a single bed joint, in cases of poor adhesion between brick and mortar or a combination of the above, with partial sliding within a bed joint and progression from head joints, other bed joints and some bricks [Como 2016]. Associated material models, with predefined softening curves for tensile behavior, following a linear formation of tensile stresses until peak, are of linear, exponential or other convex form (Figure 28). In reality, masonry exhibits a linear-elastic behavior, for tensile stresses up to 90% of the tensile strength, followed by the formation of a localized macro-crack, which evolves rapidly until contact is lost [Rots 1988].

[1] According to EN 1996-1-1 2005 the Young's Modulus is determined according to $f_{c,k}$, the characteristic compressive strength of masonry. According to Table D1 of §D7.2 of EN 1990:2002, the $f_{c,k}$ can be assumed around $f_c / 1.2$, where f_c is the average compressive strength of masonry.

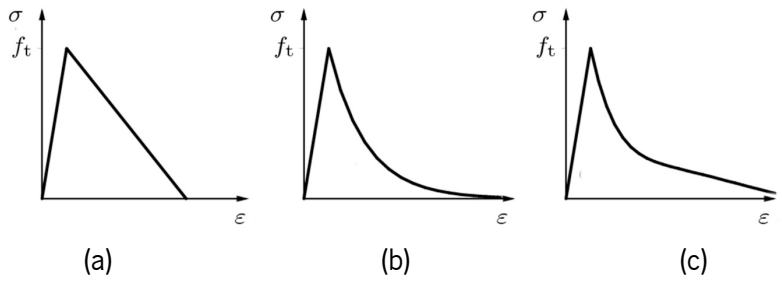


Figure 28. Material models of linear tension until tensile strength f_t and predefined softening for: (a) linear tension softening; (b) nonlinear exponential tension softening; (c) nonlinear tension softening according to Hordijk 1991 [Diana user's manual. 2020].

In physical terms, the progressive damage in quasi-brittle materials, occurs through the evolution from the state of diffused micro-cracks to localized macro-cracks, described by smeared crack models [Lourenço 1996]. The total strain rotating crack model is based on a macro-modelling approach and is able to replicate the expected quasi-brittle behavior of brick masonry in tension and compression, in a simplified way under the assumption of isotropic behavior. The basic concept is defined by incorporating fracture energy and stress-strain relations in the principal direction of the strain vector, thus following the crack formation [Lourenço 1998 and Diana user's manual. 2020]. For both compression and tension, in the post-peak of the stress-strain curve, fracture energy is the area under the σ-ε diagram, and represents the normalized energy released during crack formation and growth[2], i.e., G_c and G_f are the fracture energy values for compression and tension respectively, and are considered material properties related to ductility and cracking (Figure 29) [Angelillo et al. 2014 and Lourenço 1996]. According to experimental data from concrete specimen, often taken as a reference for masonry, as presented by Feenstra 1993, compressive fracture energy ranges between 10-25 $^{N}/_{mm}$, which is 50-100 times the tensile fracture energy. Yet, lower values can be also expected for brick masonry. As presented in Angelillo et al. 2014, CEB-FIP. Model Code 90 1993 and NTC 2018, and referencing mostly experimental

[2] In the σ-ε diagram, as shown in Figure 28, the integral of the area equal to the fracture energy normalized to the characteristic element length h. Here, h is the chosen reference size of the crack bandwidth. From experimental tests, h is associated to a referenced increment (brick or mortar joint) transversal to the crack or the default value for the crack bandwidth, which for a solid Finite Element (FE) may be considered equal to $\sqrt[3]{\Delta}$, where Δ is the volume of the FE [Lourenço 1996, Feenstra 1993, Diana user's manual 2020].

results from concrete, the determination of fracture energy is via recommended values of the average ductility index $\mathrm{d_u}$, which is the ratio between the fracture energy and the strength. Regarding compressive quasi-brittle behavior, for values of compressive strength lower than 12 MPa, a value of the ductility index $\mathrm{d_u}$ equal to 1.6 mm is suggested, and thus fracture energy $\mathrm{G_c}$ values, from the recommended range of fired clay brick masonry from the Italian building code NTC 2018, can vary within the range 4.2-12.8 $\mathrm{N/mm}$. Under a similar range, $\mathrm{G_c}$ can be calculated according to the formula in Equation 33 [Lourenco and Gaetani 2022].

Regarding the tensile fracture energy ($\mathrm{G_f}$), both the tensile failure of the brick, the mortar and the brick-mortar should be accounted. From §2.1.3.3.2 of CEB-FIP Model Code 90 1993, the tensile fracture energy of low strength concrete (maximum aggregate size of 8 mm), often taken as reference for masonry, is given by Equation 34. Considering the compressive strength range of brick masonry from the § C8.5.3.1 of NTC 2018, values of fracture energy $\mathrm{G_f}$ in tension are in the range of 0.010-0.021 $\mathrm{N/mm}$. Also considering the unit-mortar interface, a value of $\mathrm{G_f}$ equal to 0.012 $\mathrm{N/mm}$ is recommended [Angelillo et al. 2014].

$$\mathrm{G_c} = \frac{32 f_c}{10 + f_c} \qquad \text{Equation 33}$$

$$\mathrm{G_f} = 0.025 \cdot \left(\frac{\mathrm{f_c}}{10}\right)^{0.7} \qquad \text{Equation 34}$$

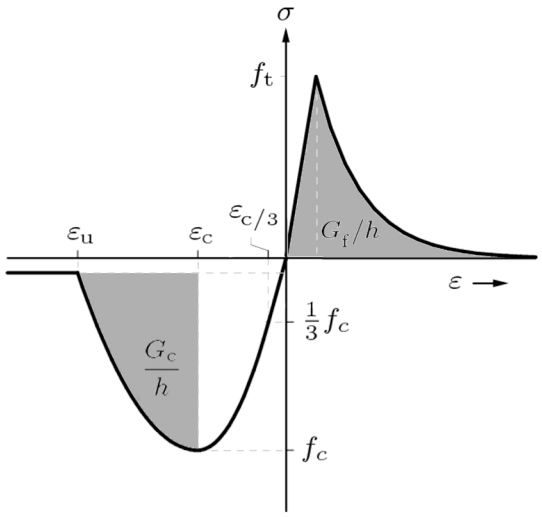


Figure 29. Indicative stress-strain curves, showing the tensile and compressive behavior and the area equal to the fracture energy. [Diana user's manual. 2020].

3.3.2. Capacity tests in uniaxial and diagonal compression, testing protocols and monitoring under cyclic loading

Is considered essential that testing techniques for a quasi-brittle material, such as brick masonry, are focused on the appropriate configuration of strain and stress rates. Importance is given on deformation-controlled test configurations, which are capable of capturing the entire load-displacement diagram [Lourenço 1996]. The concept of cyclic stress and cyclic load application in the mechanical characterization tests of masonry has certain advantages compared to monotonic load application, while the envelope results obtained are similar to the monotonic ones [Oliveira 2003]. Still, the cycling frequency usually is low enough that no dynamic effects are accounted, thus quasi-static loading conditions prevail.

Regarding uniaxial compression tests, in Oliveira 2003, it is stressed that cyclic tests offer a direct insight on the stiffness degradation characteristics and energy dissipation. Stress-strain diagrams obtained from capacity tests in quasi-brittle materials tend to be incomplete in the softening part, due to sudden early failures. Many of the difficulties encountered are related to testing equipment, testing control techniques, the specimen's size and the assigned boundary conditions [Vasconcelos 2005]. Cyclic loading is possible to be performed both in the pre-peak and post-peak region and a decrease in the stiffness properties is expected with the evolution of the loading cycles, due to the brittleness of masonry and the accumulation of damage. Besides, cyclic loading-unloading tests are mandatory for the determination of Young's modulus for concrete specimen, as defined in ASTM C469 2014 and ASTM E111-2017 and by extension to other quasi-brittle material, i.e., fired clay bricks and lime mortar.

Based on the theory of the damage plasticity model for quasi-brittle materials, under low confinement, nonlinearity and cumulative damage propagation in masonry may be quantified, under cyclic uniaxial loading, both in tension and compression [ABAQUS 2009]. During the load evolution and the progression of cycles, especially after 70-80% of the peak load, the evolution of stiffness is linked with the plastic strain $\tilde{\varepsilon}_{j,k}^{pl}$, which is the residual irrecoverable strain, after the unloading branch of each cycle k. Here is noted that j equals to t and c for compression and tension respectively. For each cycle, the subtracted part of the total strain is considered elastic and recoverable (Figure 30). The evolution of stiffness E_k and G_k, from the initial elastic stiffness E_o and shear modulus G_o respectively, can be described as a function of a scalar damage indicator

$d_{j,k}$ (Equation 35). Damage indicators $d_{j,k}$ or else stiffness degradation parameters range between 0-1, where zero represents the undamaged material, and one is for the total loss of stiffness.

$$E_k = (1 - d_{c,k}) \cdot E_o$$
$$G_k = (1 - d_{t,k}) \cdot G_o$$

Equation 35

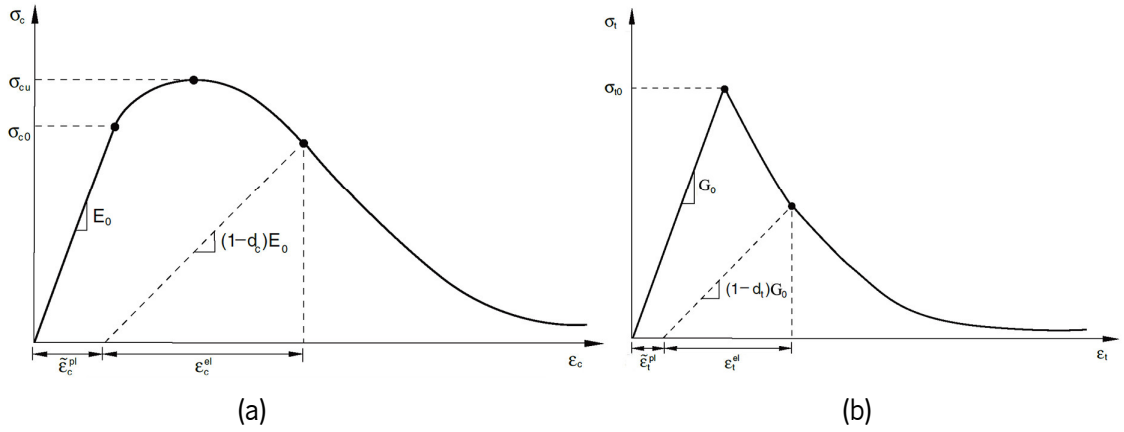


Figure 30. Monitoring of stiffness degradation, with the damage indicator $d_{j,k}$, under cyclic uniaxial loading in compression (a) and tension (b) [ABAQUS 2009].

Regarding loading application under displacement or force control or a combination of the above, low rates need to be set, in order to avoid instabilities at post-peak and early uncontrolled failure, i.e., a displacement rate of around 1.5-5 μm/s and an equivalent force control, according to the stiffness of the tested specimen. Such low rates of displacement control are applicable only by an externally attached Linear Variable Differential Transformer (LVDT) and an acquisition system which specifies a high measurement precision of 1 μm. A collection of testing protocols, size and data results of masonry specimen, for uniaxial and diagonal compression are presented in Table 5 and Table 6 respectively [Moreira 2015, Silveira et al. 2015, Ispir et al. 2013, Oliveira 2003, Vasconcelos 2005, Munoz et al. 2016, Almeida et al. 2015, Hoshikuma et al 1997, Bringola et al. 2008 and Bozzano et al. 2013].

Yet, setting cyclic loading protocols, of ascending loading cycles and of specific magnitude, are difficult to define accurately under displacement control, given the displacements of the testing frame and the early adjustments of the specimen within the testing platens. Instead, force control protocols are found better, since the loading application produces a direct reaction from the specimen, and unloading can safely reach low values, without losing contact with the specimen. In Oliveira 2003, the cyclic tests performed on masonry prisms and brick cylinders had the unloading

branch under force control, until a fixed load value, serving as a threshold limit of maintaining the contact between the actuator and the specimen. Yet, the cycles during the descending branch were not easily obtained [Oliveira 2003].

Considering the above, for uniaxial and cyclic capacity tests in brick masonry, a new, combined test protocol is proposed, with initial force-controlled loading cycles, until 70%-80% of the peak, and a last cycle with displacement control, in order to capture the entire post-peak. Initially, one specimen needs to be tested monotonically until failure, which will help adjusting the cycling loading protocols, according to the stiffness characteristics of the group of specimens. As demonstrated in Facconi et al. 2018, for the cyclic stress-strain curve for uniaxial compression of brick masonry, the equivalent monotonic stress-strain curve or else the envelope can be represented adequately by the Equation 29 and Equation 30 for the ascending and descending part respectively.

Table 5. Testing protocols in selected experimental campaigns of uniaxial compression of masonry specimens, with focus on loading or displacement control, monotonic or cyclic, and capacity range.

Author	Material	Length x Height x Width (mm^3)	(#) Type	Control	Capacity (MPa)
Moreira 2015	Rubble limestone masonry wallets with lime mortar	500x800x400	(1) Monotonic	Displacement rate of 10μm/s	1.84
			(4) Cyclic	2 cycles at 25% and 50% of peak load with loading rate of 0.5kN/s. After, displacement control with 5-10μm/s	1.53-1.96
Silveira et al. 2015	Adobe masonry wallets with render (adobe blocks with air-lime and mortar of hydrated lime and earth)	1260x1260x360	(5) Monotonic	Displacement rate of 10μm/s	0.26-0.41
Ispir et al. 2013	Extracted brick masonry prisms (solid bricks and hydrated lime mortar)	(165-278)x (237-289)x (143-244)	(10) Monotonic	Displacement rate of 5μm/s	1.14-2.48
			(5) Cyclic	Displacement rate of 15μm/s. 10 cycles in increments of strain (%)	1.26-2.20
Oliveira 2000	Brick masonry prisms (solid bricks and cement mortar)	285x280x130	(4) Cyclic	Displacement rate of 3μm/s for loading. Loading rate of 10 kN/s for the unloading (7 cycles)	28.2-28.9
Facconi et al. 2018	Brick masonry wallets (solid bricks and hydraulic lime-cement mortar)	780x510x245	(2) Cyclic	Displacement rate of 10μm/s for loading and 50μm/s for the unloading (7 cycles)	8.22 7.77
Vasconcelos 2005	Prisms of granite blocks with dry or clay or lime mortar joints	150x(450-490)x150	(12) Monotonic	Displacement rate of 3μm/s	18.4-73.0
			(26) Cyclic	Displacement rate of 3μm/s. 3 cycles at 25% 50% and 75%	
Munoz et al. 2016	Brick masonry wallets (solid bricks and hydraulic lime mortar)	400x500x400 400x400x200	(8) Monotonic	Displacement rate of 3μm/s	8.82 9.84

Table 6. Testing protocols in selected experimental campaigns of diagonal compression of masonry specimens, with focus on loading or displacement control, monotonic or cyclic, and capacity range.

Author	Material	Length x Height x Width (mm^3)	(#) Type	Control	Load (kN) Capacity (MPa)
Almeida et al. 2015	Clay brick masonry wallets (hollow ceramic bricks, cement mortar and rendering)	990x990x(140-190)	(2) Monotonic	Displacement rate of 10μm/s	97.3-409.5 kN
			(4) Cyclic	Displacement rate of 10μm/s, increments of 0.2ε_c (7 cycles)	50.89-315.35 kN 0.9-2.0 MPa
Moreira 2015	Rubble limestone masonry wallets with lime mortar	800x800x300	(3) Monotonic	Displacement rate of 150μm/s	58.2-80.8 kN 0.11-0.15 MPa
Silveira et al. 2015	Adobe masonry wallets with render (adobe blocks with air-lime and mortar of hydrated lime and earth)	1260x1260x360	(5) Monotonic	Displacement rate of 50μm/s and 25μm/s	0.022-0.032 MPa
Brignola et al. 2008	In situ diagonal compression test of 24 panels from 16 buildings of different materials and typologies	1200x1200x(25-67)	(24) Cyclic	Loading rate of 200N/s (4-5 cycles)	0.026-0.411 MPa
Bozzano et al. 2013	Clay brick masonry wallets (solid clay bricks, cement and hydraulic lime mortar)	1200x1200x(240-480)	(8) Cyclic	Loading rate of around 120N/s (6 cycles)	0.13-0.26 MPa
Munoz et al 2016	Brick masonry wallets (solid bricks and hydraulic lime mortar)	800x800x300	(3) Monotonic	Displacement rate of 3μm/s	0.10 MPa

3.4. Compressive and flexure tests on simulated historic masonry constituents, repair and retrofit material

The current research work carries a vast number of experimental laboratory tests on brick masonry with hydraulic lime mortar, which are meant to replicate historic brick masonry of the 19^{th}-20^{th} centuries. Several objectives are linked with the performed capacity tests on masonry wallets, both in uniaxial (UC) and diagonal (DC) compression. In specific, testing parameters, as defined through the EN 1052-1:1999 for uniaxial compression and ASTM E519/E519M-20 for diagonal compression are adjusted in order to obtain reference values of strength and the evolution of stiffness and energy dissipation at incremental steps, mainly through cyclic quasi-static loading. The abovementioned quasi-static properties will be compared in CHAPTER 5 with capacity tests on masonry wallets, having endured fatigue loading under a high stress state and various levels of stress reversals, characteristic of ground borne vibration amplitudes.

Testing on masonry constituents was performed in order to obtain the mechanical and physical characteristics of both fired bricks and mortar separately, as suggested in Binda et al. 2008. In specific, compressive and tensile tests on fired bricks and mortar were performed, aiming at statistical values for the compressive strength f_c, the Young's modulus E and the flexural strength f_f.

Besides determining the capacity of masonry and its constituents, the interest is also set on obtaining the stress-strain relationship and post-peak behavior, for which the force-displacement evolution is captured with external LVDT's under high sampling frequencies for static loading and low displacement control rates, i.e., 4 Hz and 1.5-3 μm/s respectively.

Regarding the mechanical tests for hydraulic lime mortar, specimens were tested at different ages, in order to check the strength evolution and to ensure the testing of masonry assemblies at full strength development. Yet, for associating the mechanical characteristics of hydraulic lime mortar and those of brick masonry, at the exact time of testing and ambient conditions in the laboratory, an extra batch of lime mortar prisms were tested. Those were sampled during construction and kept beside the assemblies. For the fired clay bricks, their orthotropic behavior was captured at the lengthwise and crosswise directions.

Finally, physical characterization tests were performed for repair and retrofit material, used during the laboratory tests of CHAPTER 6, i.e., high performance hydraulic lime-based render and fluid binder M15.

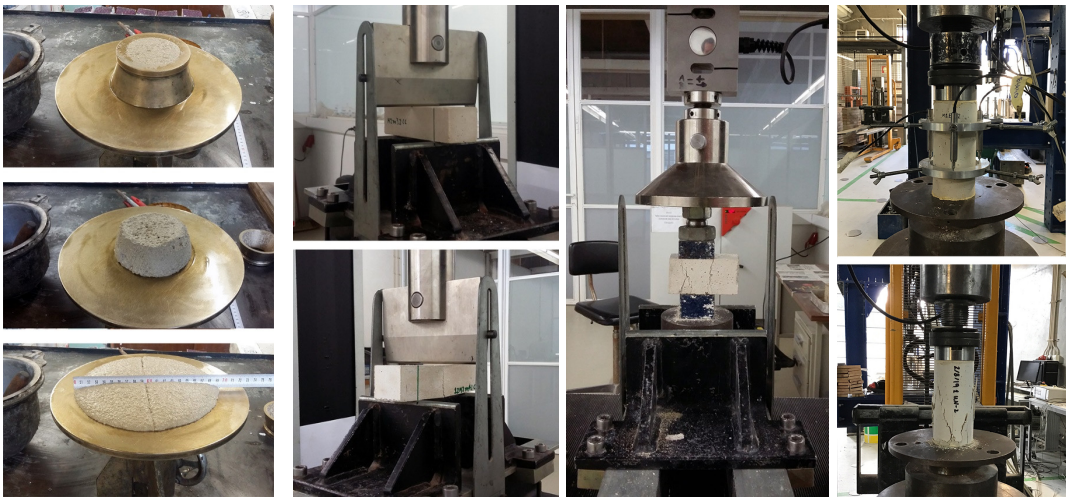
3.4.1. Hydraulic lime mortar

Part of the current experimental campaign of mechanical tests on simulated historic masonry assemblies, was the mechanical characterization of simulated weak historic lime mortar, used for the joints and rendering. Thus, a ready lime mortar premix was chosen, which fits the mortar classification of M4 and CS II, according to BS EN 998-2:2003 and EN 998-1:2016 respectively, i.e., the REABILITA Cal Consolidação hydraulic lime mortar for consolidation of historic masonry, from Secil, a Portuguese construction material company [REABILITA CAL CS 2019]. The exact composition of the used hydraulic lime mortar mix is not known, but it can be compared and identified as a NHL5 mortar mix with a weight ratio of 1:3:(0.5-0.6) for the lime, sand and water respectively [NHL 5 2014].

Hydraulic lime mortar specimens were prisms of 160x40x40 mm^3 in size, prepared in batches of three prisms. The processes of sampling, mold preparation, mixing and tampering were executed according to BS EN 1015-2:1998 and BS EN 1015-11:1999. Given the recommended water content range of 13-15%, compared to the mass of the dry ingredients, and as specified in REABILITA CAL CS 2019, the exact percentage was established through consistency and fluidity tests in fresh mortar samples, according to BS EN 1015-3:1999. In specific, two different test samples were tested in a manually operated flow table, out of different mortar mixes, with a water content range of 14-17%. All three mortars specimen for each group were casted on the same day, by preparing batches of 800 g, regarding the mass of the dry ingredients. After 15 vertical impacts in the flow table, the mean diameter of each test sample is measured in two directions (Figure 31a) and the results are presented in Table 7. According to the average measurements of flow rates and the specifications of BS EN 1015-2:1998, where the specified flow rate diameter is 175±10 mm, for a fresh mortar bulk density greater than 1200 kg/m^3, a water content percentage of 15% is selected for the hydraulic lime mortar mix.

Table 7. Flow rate test results for hydraulic lime mortar mixes with different water percentage.

	Dry mortar weight (gr)	Water (gr)	Water (%)	Flow rate (mm)		Mean flow rate (mm)
MIX1	799.9	112.1	14.01%	170	169	170
MIX2	800.0	120.2	15.03%	183	184	184
MIX3	800.3	122.1	15.26%	191	195	193
MIX4	800.3	124.1	15.51%	195	199	197
MIX5	800.1	128.1	16.01%	205	207	206
MIX6	800.0	136.1	17.01%	228	225	227



(a) (b) (c) (d)

Figure 31. Material characterization of hydraulic lime mortar M4: (a) flow table test; (b) three-point loading test for flexural capacity; (c) compression strength test; (d) test for Young's modulus and compressive strength.

For the mechanical characterization of mortar, prisms of 40x40x160 mm^3 are used [BS EN 1015-11:1999]. Curing is executed under controlled conditions in the laboratory, according to BS EN 1015-11:1999, i.e., first, for 48 h, the specimens in the molds, are kept in a sealed polyethylene bag (95%±5% RH) at a temperature of 20±2ºC; afterwards the molds are removed and the specimens are kept for another 120h in a sealed polyethylene bag; finally, the curing progresses in 65±5% RH and 20±2ºC. According to Lanas et al. 2004, NHL mortars experience three phases of hardening, starting with the reaction of hydraulic binders with water, i.e., the formation of hydrated calcium silicate compounds, namely C_3S and C_2S. The first phase covers the first 28 days and for a NHL mortar mix of a ratio 1:3 (lime:sand), the 85-90% increment of the compressive strength is activated [Lanas et al. 2004]. In a next stage (28-182 days) NHL mortars gain weight through the carbonation process and the compressive strength increases only slightly. The last phase is the long-term carbonation and hydration, covering from 182-365 days, but the effect is negligible for NHL mortars of a ratio 1:3 (lime:sand) [Lanas et al. 2004]. Thus, the lime mortar prisms are prepared for mechanical characterization tests on flexure, compression and Young's modulus, at 7, 14, 28, 56, 90 and 365 days. The mechanical tests on flexure and compression were performed in the EZ Series EZ50 50 kN Universal Materials Testing Machine, while the tests of Young's Modulus were performed with a 25 kN hydraulic actuator and external LVDTs.

For each curing period, a three-point loading test is performed in three specimens, in order to obtain the flexural strength (Figure 31b). According to the provisions of the BS EN 1015-11:1999

the loading rate is set at 15 N/s. Initially, a preload is applied, equal to 50 N for early age curing (7 and 14 days) and 150 N for later curing conditions, under a displacement control of $1\mu m/s$, in order to secure the contact with the upper metallic roller. The flexural strength f_f is given by Equation 36, where F is the maximum load applied to the specimen, L is the distance between the axes of the support rollers, b is the width of specimen and d is the depth of the specimen [BS EN 1015-11:1999]. At an early curing age (7 days) the flexural strength is 0.47 MPa, while at 365 days is 1.16 MPa (Table 8). From flexure tests at 28 days, the activated flexural strength is at 72% of the one at 365 days. The stress-strain curves for flexure, for each curing period, and its evolution in time, by means of a boxplot and a whisker chart, together with curves normalized to the flexural strength at 365 days, are presented in Figure 32, and Figure 34a and c respectively.

$$f_f = 1.5 \cdot \frac{FL}{bd^2} \qquad \text{Equation 36}$$

For the compressive strength test, the two half broken prisms provide six half prisms for each curing period (Figure 31c). According to BS EN 1015-11:1999, the load rate is set at 150 N/s, with the abovementioned preload, for ensuring contact between the specimen and the metallic platens. The compressive strength f_c is given by Equation 37, which for an early curing age (7 days) is 1.15 MPa, while at 365 days is equal to 4.13 MPa (Table 8). From compressive tests at 28 days, the activated compressive strength is at 77% of the one at 365 days, which denotes that the carbonation and hydration during the last curing phases is significant. Regarding the comparison with the flexural strength f_f and for the various curing ages, is found within the range of 0.03-0.04 times of f_c. The stress-strain curves for compression, for each curing period, and its evolution in time, by means of a boxplot and a whisker chart, together with curves normalized to the compressive strength at 365 days, are presented in Figure 33, and Figure 34b and d respectively.

$$f_c = \frac{F}{bd} \qquad \text{Equation 37}$$

Table 8. Physical and mechanical properties of M4 NHL mortar, i.e., mass density, compressive strength, flexural strength and Young's modulus.

Lime Mortar M4 Cubes/Prisms/ Cylinders	Mean Mass Density (kN/m^3) (Number of specimen)/(CoV) Prisms[1]: 40x40x160 (mm^3) Climatic chamber (60%RH, 20ºC)	Mean Compressive Strength (MPa) (Number of specimen)/(CoV) Cubes[1]: 40x40x40 (mm^3) Climatic chamber (60%RH, 20ºC)	Mean Flexural Strength (MPa) (Number of specimen)/(CoV) Prisms[1]: 40x40x160 (mm^3) Climatic chamber (60%RH, 20ºC)	Mean Young's Modulus (MPa) (Number of specimen)/(CoV) Cylinders[2]: Φ75x150 (mm^3) Climatic chamber (60%RH, 20ºC)
7 days	21.7 3/0.36%	1.15 4/3.28%	0.44 3/2.92%	948 3/15.38%
14 days	19.5 3/0.71%	2.53 4/2.8%	0.96 3/18.77%	2613 3/14.14%
28 days	19.4 3/0.53%	3.17 4/1.69%	0.84 3/8.78%	3757 3/10.07%
56 days	19.4 3/1.01%	3.04 4/6.23%	0.78 3/15.49%	4205 3/7.06%
90 days	19.7 3/0.78%	3.15 4/4.71%	0.95 3/3.67%	4147 3/2.00%
365 days	19.8 4/0.33%	4.12 8/2.22%	1.16 4/5.18%	4226 3/0.66%

1: BS EN 1015-11:1999 - Part 11: Determination of flexural and compressive strength of hardened mortar

2: ASTM C469/C469M-14 Standard Test Method for Static Modulus of Elasticity and Poisson's Ratio of Concrete in Compression

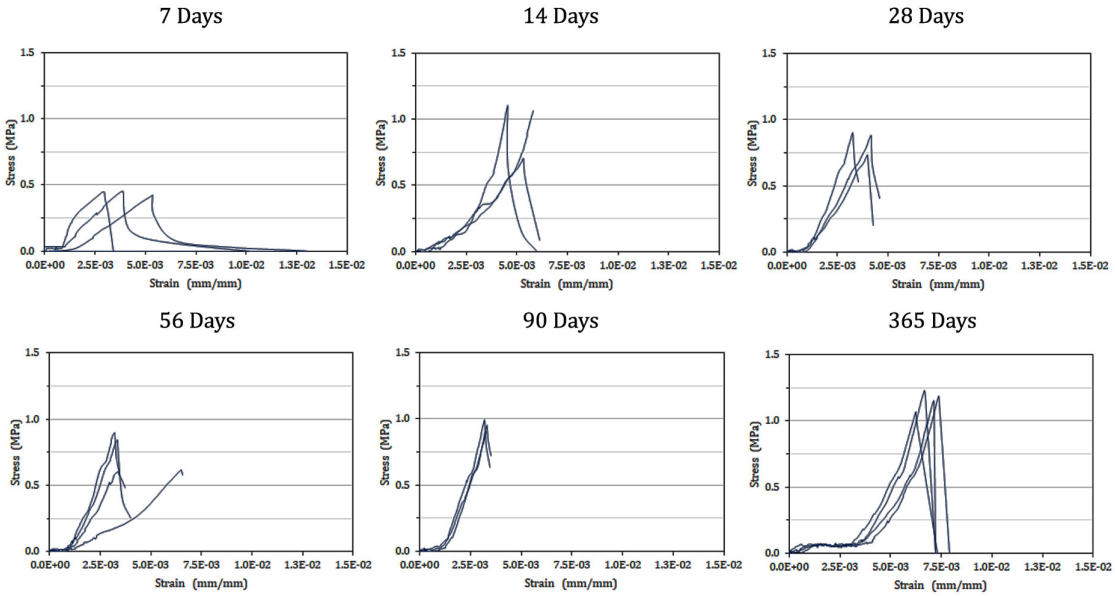


Figure 32. Stress-strain curves for flexure, of the M4 hydraulic lime mortar prisms, at different curing periods.

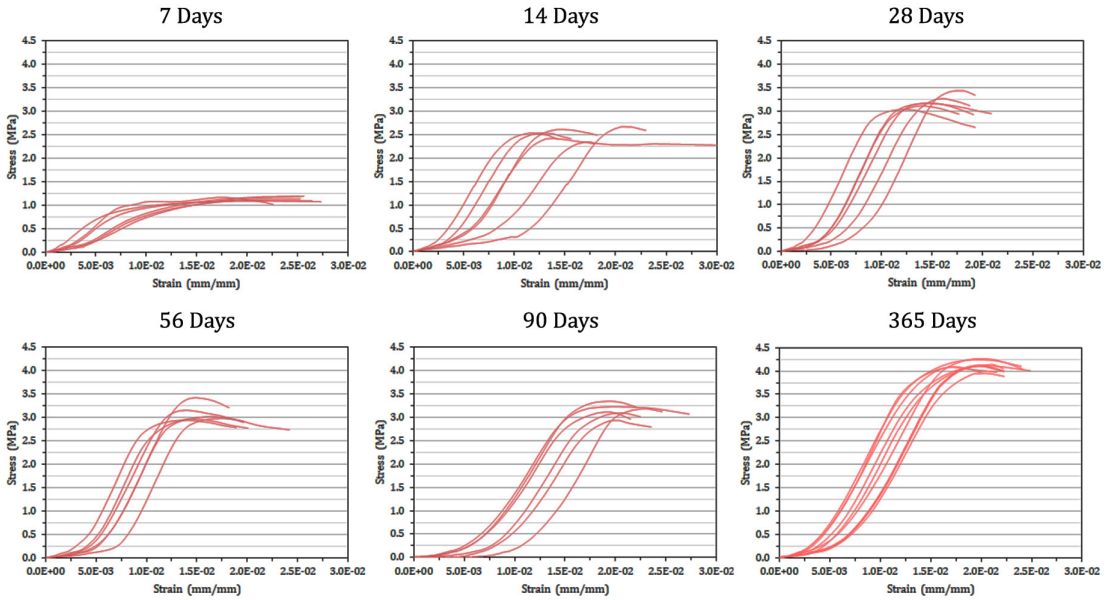


Figure 33. Stress-strain curves for compression, of the M4 hydraulic lime mortar prisms, at different curing periods.

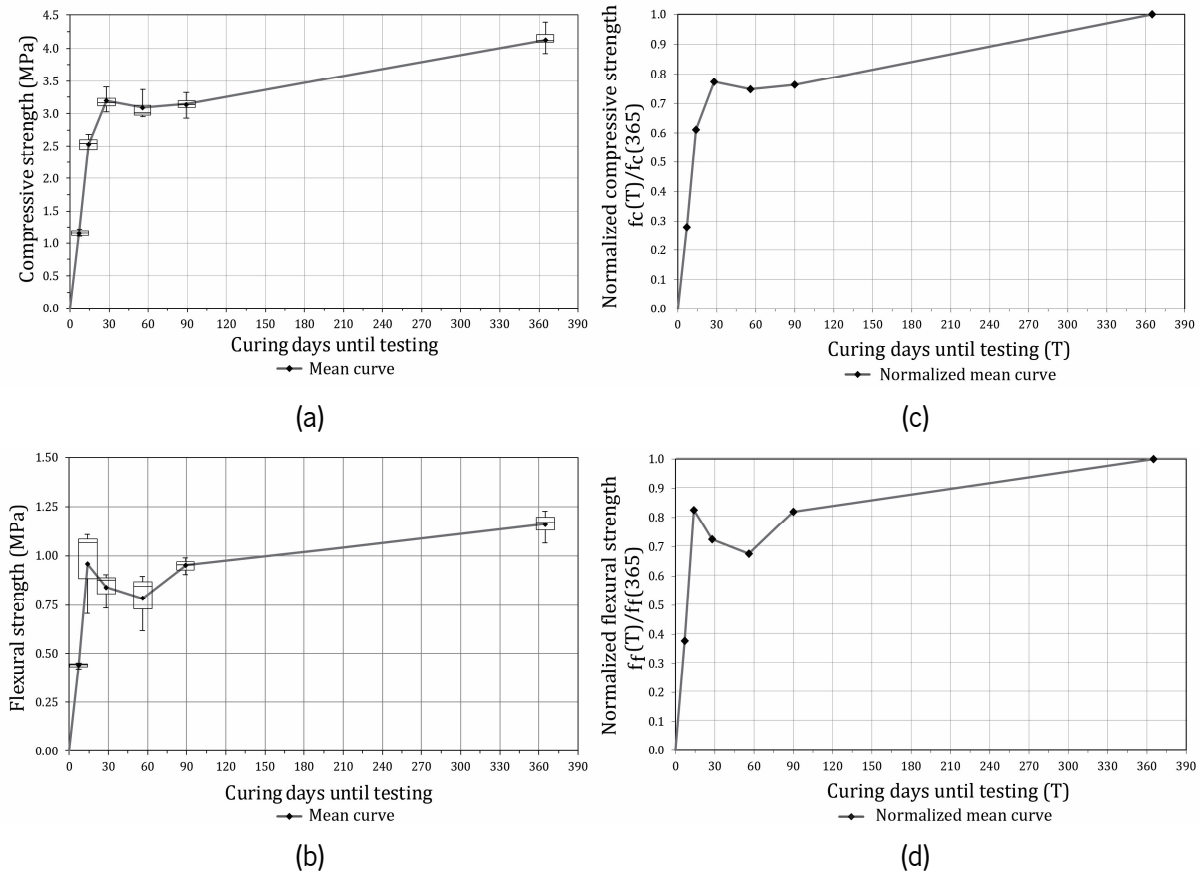


Figure 34. M4 hydraulic lime mortar prisms: (a) and (b) boxplot, whisker chart and mean curve of strength evolution in time, for the three-point loading flexure test and uniaxial compression test respectively; (c) and (d) respective normalized curves for the flexural and compressive strength at 365 days.

For determining the Young's Modulus and given the absence for standardization for hydraulic lime mortar specimen, the testing specifications are based on standards for concrete in

compression, namely ASTM C469 / C469M-14 2014. Specifically, three cylinders of size Φ75x150 are prepared for each curing period (7, 14, 28, 56, 90 and 365 days), and according to the same specifications, as described for hydraulic lime mortar prisms. In order to adjust the load rate and load pattern, an extra cylinder is tested in uniaxial compression, under displacement control of 2 μm/s, until failure. The calibrated compressive load consists of five loading-flat-unloading branches, until ⅓·f_c [ASTM E111-17 2017]. Loading is applied under force control and the rate is adjusted according to the expected capacity, so that each loading and unloading branch lasts for 60 s [ASTM C469 / C469M-14 2014, ASTM E111-17 2017 and CPC8 1975]. Three attached LVDTS, by means of cylindrical aluminum rings on the specimen, measure displacements for ⅔ of the specimen's height, as seen in Figure 31d [E111-17 2017]. The Young's modulus is calculated as the average chord modulus (5%-33% f_c) from the last three loading branches and all three LVDTs [ASTM C469/C469M-14 2014 and ASTM E111-17 2017]. As presented in Table 8 and Figure 35, the stiffness of the hydraulic lime mortar cylinders is fairly stabilized after 56 days, with a small increase of 0.5% at 365 days. Compared to the compressive strength f_c at 365 days, the ratio $E \simeq 1000 \cdot f_c$ is obtained. The evolution of the Young's Modulus in curing time is fitted in an exponential growth curve, under a similar formulation from Ramesh et al. 2019, of almost perfect correlation, given by Equation 38 and presented in Figure 35.

$$E(T) = 4283e^{\left(-43.65/T^{1.718}\right)}, \quad R^2 = 0.997 \qquad \text{Equation 38}$$

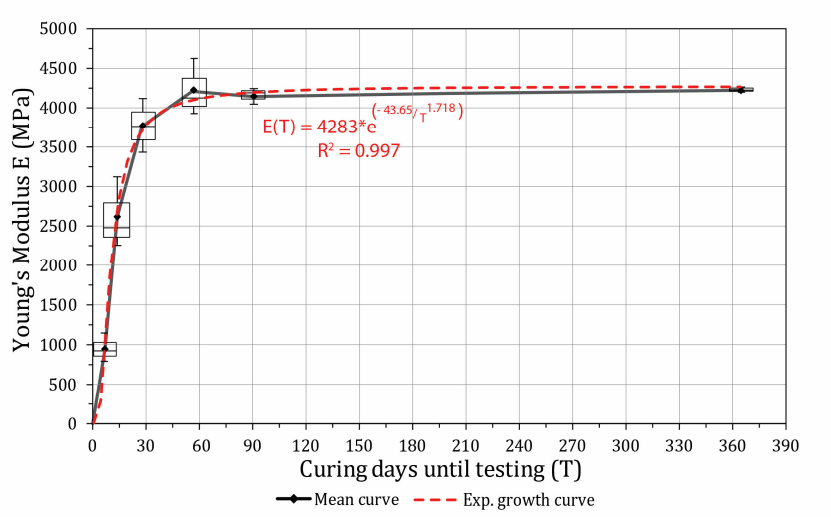


Figure 35. Young's modulus evolution in time, of the M4 hydraulic lime mortar cylinders, with a boxplot, a whisker chart and a mean curve.

3.4.2. Solid fired bricks

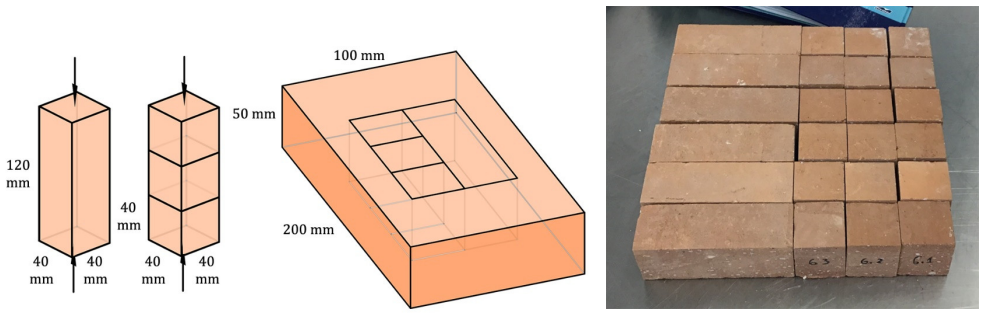
The mechanical and physical properties of fired clay bricks are closely linked to the manufacturing process and the raw materials used. Properties such as the compressive strength, the energy dissipation, the porosity and overall durability are closely related to the firing temperatures, the molding and the extrusion process [Fernandes et al. 2009]. From mechanical and physical characterization tests in 16 specimens from solid fired bricks of the 18th-19th centuries, from the Christ's Cloister in Tomar, Portugal, average values and CoV(%) of porosity, bulk mass, water absorption, and compressive strength were found equal to 27.5%(14.2%), 16.24 kN/m^3(3.0%), 15.0%(15.5%) and 21.8 MPa(31%) [Lourenço et al. 2010]. For the current experimental campaign, and with the aim of replicating low fired and low strength solid bricks of the 19th-20th centuries, solid fired bricks manufactured by Cenol were chosen, a brick manufacturing company in Amarante, Portugal. As customized and produced, the units were pressed or mildly extruded and their dimensions were 200x100x50 mm^3 (length x width x height). In order to achieve low-medium values of compressive strength and resemble a traditional brick production, the firing temperature was kept low. Here, it is noted that firing temperatures below 950ºC form partially molten clay particles, the consistency is grainier, with course voids, which translates to higher values of strength and stiffness in the extrusion direction, namely the lengthwise [Krakowiak et al. 2011]. First, the dried bricks were baked in a kiln for 9 h with the temperature linearly rising until 850ºC. Then, the baking process continues for 12 h, under a constant temperature. Right after, the bricks are left to cool down, until the temperature drops until 300ºC and as the last step, the kiln doors open, and the bricks are left to cool further at ambient temperature.

Following the specifications from BS EN 771-1:2011 a random sampling was performed from the acquired consignment of bricks, with any apparent damage being the only condition for the rejection of a sample. The locations for selection were evenly distributed and many sections from the stack were removed in order to gain access to lower ones. In total 12 bricks were selected, 6 for uniaxial compression and physical tests and 6 for 3-point load flexure tests [EN 772-1:2011 and ASTM C67/C67M-20 2020]. The former ones were cut into 3 cubes and a prism each, with a high precision water saw and later the contact areas were grinded and flattened, until reaching a size of 40x40x40 mm^3 and 40x40x120 mm^3 respectively (Figure 36) [EN 772-1:2011]. Prior to all the following testing, the specimens were dried in a ventilated oven at 105±5ºC for 24 h, and

after were let to cool for 4 h [ASTM C67/C67M-20 2020 and EN 772-1:2011]. According to the specifications of ASTM C67/C67M-20 2020 and considering only the cut and grinded cubes of 40x40x40 mm^3 size, the apparent dry density of the bricks is found 18.05 kN/m^3, with a CoV of 1.05% (Table 9). After a 24 h submersion in cold water, the average saturated density is found equal to 21.09 kN/m^3, with a CoV of 1.62% [EN 771-1:2011]. The average water absorption w_m, given by Equation 39, was found equal to 14.14%, with a CoV of 1.62%, while the average pore volume n, given by Equation 40, is found equal to 26.69% with a CoV of 3.64% (Table 9). Here m_w is the saturated mass, m_d is the dry mass, V is the volume of the specimen and p_w is the water density [BS EN 771-1:2011 and BS EN 772-3:1998].

$$w_m = \frac{m_w - m_d}{m_d} \cdot 100\% \qquad \text{Equation 39}$$

$$n = \frac{m_w - m_d}{p_w \cdot V} \cdot 100\% \qquad \text{Equation 40}$$



(a) (b)

Figure 36. Solid fired bricks: (a) schematic representation of a brick unit with cut cubes and prism specimen for uniaxial compression and Young's modulus tests; (b) stack of cubes and prisms from 6 bricks.

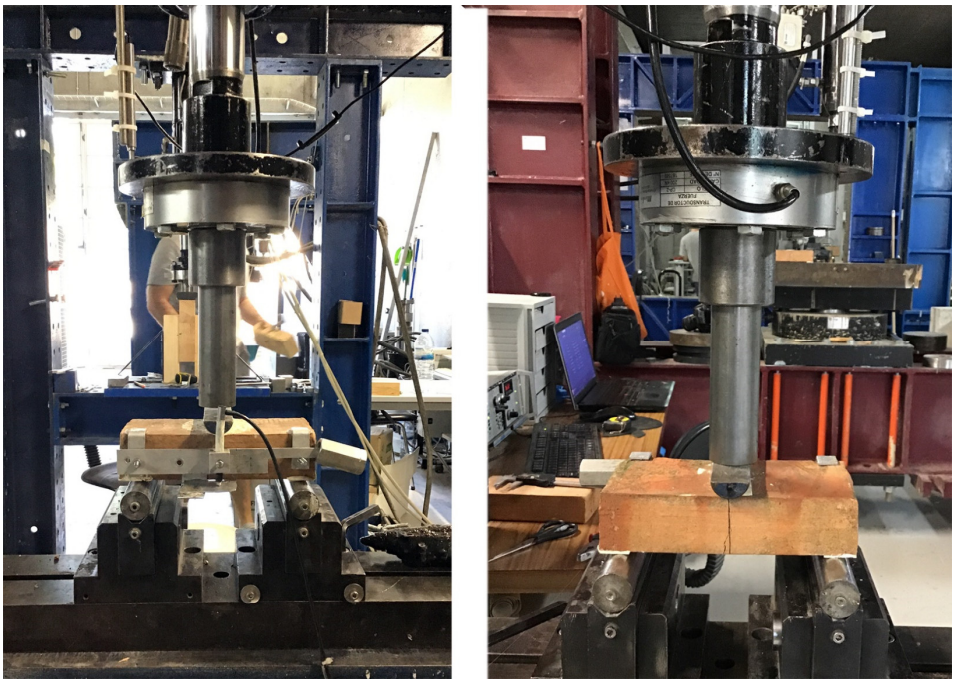
Table 9. Physical and mechanical properties of fired bricks, i.e., mass density, water absorption, mean porosity, compressive strength, flexural strength and Young's modulus.

Low Fired Clay Solid Bricks	Mean Mass Density (kN/m^3)	Mean Water Absorption (%)	Mean Porosity (%)	Compressive strength (MPa)		Flexural strength (MPa)	Young's Modulus (MPa)	
Cubes[1]/Prisms[2] b x d x h	40x40x40/ 40x40x120 mm^3	40x40x40/ 40x40x120 mm^3	40x40x40 mm^3	40x40 x(3x40) mm^3	40x40 x120 mm^3	200x100 x50 mm^3	40x40 x(3x40) mm^3	40x40 x120 mm^3
Load path direction	-	-	-	Vertical	Horizontal	Vertical	Vertical	Horizontal
Conditions[3]	Oven dried at 105oC ±5oC for 24h							
Mean value	18.1	14.1%	26.7%	17.17	29.69	3.62	1222	6028
#specimen/CoV	27/1.1%	5/5.0%	5/3.6%	6/6.9%	6/2.4%	6/34.1%	5/6.5%	5/2.8%

1: BS EN 772-1:2011 Methods of test for masonry units. Determination of compressive strength +A1:2015
2: ASTM C67/C67M-20 2020 Standard Test Methods for Sampling and Testing Brick and Structural Clay Tile
3: BS EN 772-1:2011 Methods of test for masonry units. Determination of compressive strength (+A1:2015) §7.3.3a)

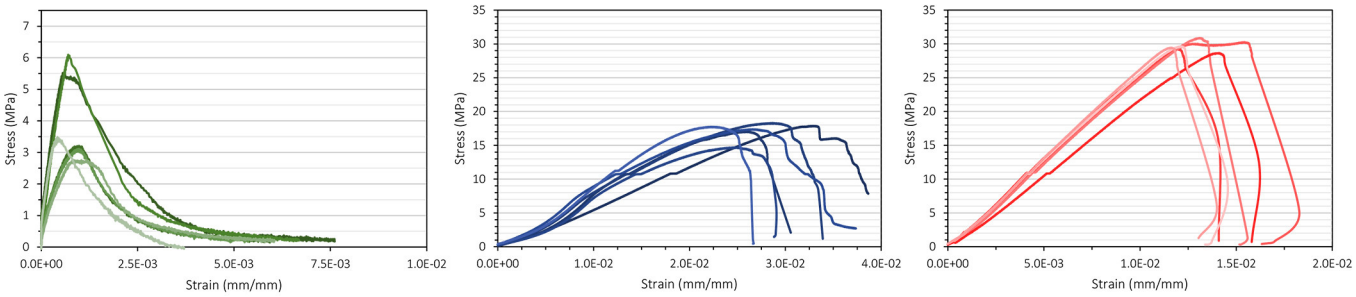
Regarding the flexural strength, which is associated to the tensile strength, 3-point loading tests were performed in 6 selected whole solid fired brick units, without the presence of a notch, and according to ASTM C67/C67M-20 2020 and RILEM TC 162-TDF 2002. The setup apparatus for the 3-point loading flexural tests consists of 3 rollers, whereas two act as supports, at a distance of 170 mm and one is placed at the mid span of the upper flat surface, for applying the load, from a hydraulic actuator of 100 kN capacity. All three contact areas of the brick are flattened by bitumen polyester mortar. The load is applied under displacement servo-control, from an external LVDT, at a rate of 3 μm/s, as specified by RILEM TC 162-TDF 2002, while the bending deformation at mid span, is measured by a vertically attached LVDT, at a sampling rate of 4 Hz (Figure 37). The flexural strength f_f is given by Equation 41, where F is the maximum load applied to the specimen, L is the distance between the axes of the support rollers, b is the width of specimen, d is the height of the specimen and x is the distance of the failure surface from the mid-span, averaged from both stretcher faces [ASTM C67/C67M-20 2020]. The average flexural strength, assumed equal to the tensile strength of the solid fired bricks is equal to 3.62 MPa, with a CoV of 34.07% (Table 9). The stress-strain curves of all six specimen are presented in Figure 38a.

$$f_f = \frac{3F\left(\frac{L}{2} - x\right)}{bd^2} \qquad \text{Equation 41}$$



(a) (b)

Figure 37. Three-point loading test for flexural capacity characterization of solid fired bricks: (a) front view; (b) back view. Note the flexural crack at mid-span.



(a) (b) (c)

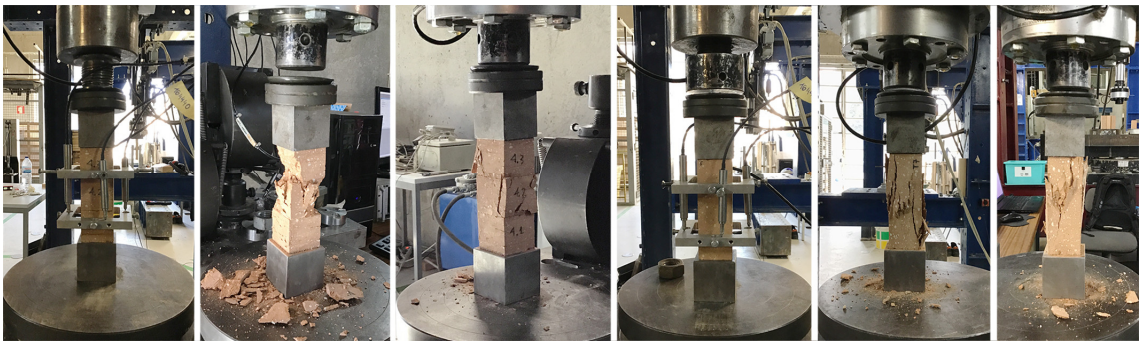
Figure 38. Stress-strain curves, of the tested solid fired bricks for flexural strength (a), and uniaxial compressive strength normal to the bed (b) and header face (c).

Regarding the strength and Young's modulus tests under uniaxial compression, they follow the specifications of BS EN 772-1:2011 and ASTM C469/C469M-14 2014. For the brick cubes of size 40x40x40 mm^3, composite specimens are built, by placing all three cubes from each brick, one over the other, without any binding material in between. In order to obtain mechanical properties under uniaxial compression, the cubes need to be placed in contact with their bed faces. As stated also in Oliveira 2000, prisms composed by aligned grinded cubes, with no bonding material, tend to behave as uniform prisms and the post-peak behavior in uniaxial compression is stable. Further on, the orthotropic behavior of the bricks is accessed with uniaxial compression tests along the direction of the header faces, thus with the prisms of size 40x40x120 mm^3.

Similar to the Young's modulus tests for hydraulic lime mortar cylinders, and based on the specifications of ASTM C469/C469M-14 2014, one monotonic uniaxial compression test is performed, until failure, in order to adjust the load rate and pattern, with five loading-flat-unloading branches, until ⅓· f_c, and a duration of 60 s and 20 s for the loading/unloading and flat branch respectively [ASTM E111-17 2017]. Since the prisms are square-shaped, four attached LVDTS, clamped to square-shaped aluminum rings and attached on the specimen, measure displacements for ⅔ of the specimen's height, as seen in Figure 39a and d [E111-17 2017]. The Young's modulus is calculated as the average chord modulus (5%-33%f_c) from the last three loading branches and from all four LVDTs [ASTM C469/C469M-14 2014 and ASTM E111-17 2017]. In order to increase the statistical validity and data resolution, the test was executed with a hydraulic actuator of 25 kN capacity, and several trials were performed, by adjusting the position of the prism, relatively to the actuator and hinge cap, in order to achieve an even stress distribution throughout the specimen. The latter translates to displacement recordings, with an acceptable condition of displacement differences less than 10%. As presented in Table 9, the average Young's modulus and CoV, normal to the bed faces is 1.22 GPa (6.50%), whereas in the direction normal to the header faces is 6.02 GPa (2.81%), thus approximately 5 times higher.

At a next testing phase, the same brick specimens are subjected to monotonic compression until failure, according to BS EN 772-1:2011 and the average strength and CoV are presented in Table 9. In order to obtain a stable post-peak behavior and fracture propagation, the test is performed under displacement control, with a load rate of 3μm/s, and a hydraulic actuator of 100 kN capacity. The chosen conditioning of the specimen prior to testing was to be dried in a ventilated oven at 105±5ºC for 24 h, and after let to cool for 4 h [§7.3.2 b) of BS EN 772-1:2011]. Thus, no conversion to the normalized compression strength is needed. The compressive strength f_c is given by Equation 36, and the average value and CoV for the bed and head face directions are 17.17 MPa (6.86%) and 29.69 MPa (2.37%) respectively, with the later higher at around 1.7 times. The comparison with the Young's modulus, is formed under the relations $E \simeq 71 \cdot f_c$ and $E \simeq 203 \cdot f_c$, for the bed and head face directions respectively. As seen in Figure 38b and c, and Figure 39, the fracture patterns normal to the bed face direction are more ductile with reasonably well formed cones of failure, mostly on the upper ⅔ of the prism's height. On the contrary, the compressive behavior normal to the header face direction is more brittle, with columnar vertical cracks through both ends and no well-formed cones.

Considering the documented differences in compressive strength, stiffness and failure patterns, in the directions normal to the bead and head joints, an orthotropic behavior is evident. As explained in Brooks 2015, the in-plane behavior of bricks is defined as orthotropic, with different strength and stiffness properties in the directions vertical to the bed and header faces. In microscopic and mechanical investigations in extruded clay bricks, by Krakowiak et al. 2011, the orthotropy in solid fired clay bricks is mostly the result of the manufacturing process, namely the level of firing temperatures and the type of pressure or extrusion.



(a) (b) (c) (d) (e) (f)

Figure 39. Material characterization of solid fired brick prisms: (a) Young's modulus and fracture patterns (b) and (c), under uniaxial compression normal to the bed face; (d) Young's modulus and fracture patterns (e) and (f), under uniaxial compression normal to the header face.

3.4.3. High performance hydraulic lime-based render and fluid binder

Part of the laboratory testing campaign was the mechanical and physical characterization of materials for the repair and retrofit of in-plane damage in brick masonry, i.e., a high performance hydraulic lime-based render M15, part of a Fabric Reinforced Cementitious Mortar (FRCM) system and a high performance hydraulic lime-based fluid binder M15, for crack filling, part of CHAPTER 6. For the hydraulic lime-based render, the GeoCalce® F Antisismico from KERAKOLL was chosen, a class M15 high performance mortar premix, for repair and retrofitting of masonry, from NHL3.5 and natural mineral binders, and siliceous, dolomitic and marble aggregates (0-1.4mm) [GeoCalce F Antisismico 2019]. Regarding the hydraulic lime-based fluid binder (grout), GeoCalce® FL Antisismico from KERAKOLL was chosen, a class M15 high performance grout premix, for consolidating injections in masonry structures, from NHL3.5 and natural mineral binders, and siliceous and marble aggregates (0-0.5mm) [GeoCalce FL Antisismico 2019].

Despite the extensive technical specifications and certified mechanical performance characteristics, mechanical laboratory tests were performed on prism (160x40x40 mm^3) and

cylinder (Φ75x150 mm^3) specimens, casted during construction, in order to conclude on the mechanical characteristics, at the time of testing of the retrofitting brick masonry assemblies, found in good agreement. Similar to the NHL mortar of 3.4.1, the curing conditions for the first 7 days were according to BS EN 1015-11:1999. Until then and the time of testing, at 28 days, the specimens were kept next to the retrofitted masonry assembly, under laboratory ambient conditions. Under the same standardized practice for the physical and material testing of 3.4.1, statistical data of density, uniaxial compression, 3-point flexure and Young's modulus for the repair and retrofit material are presented in Table 10, Figure 40 and Figure 41 [BS EN 1015-2:1998, BS EN 1015-11:1999, BS EN 1015-11:1999, ASTM C469/C469M-14 2014, ASTM E111-17 2017 and CPC8 1975].

Table 10. Physical and mechanical properties of M15 hydraulic lime-based render and fluid binder, i.e., mass density, compressive strength, flexural strength and Young's modulus.

	Mean Mass Density (kN/m^3) (Number of specimen)/(CoV)	Mean Compressive Strength (MPa) (Number of specimen)/(CoV)	Mean Flexural Strength (MPa) (Number of specimen)/(CoV)	Mean Young's Modulus (MPa) (Number of specimen)/(CoV)
Specimen Conditions	Prisms[1]: 40x40x160 (mm^3)	Cubes[1]: 40x40x40 (mm^3)	Prisms[1]: 40x40x160 (mm^3)	Cylinders[2]: Φ75x150 (mm^3)
Curing	Laboratory ambient conditions 28 days			
Hydraulic lime-based render M15	16.8	12.02	4.18	9802
	3/1.6%	6/4.9%	3/23.9%	3/1.0%
Hydraulic lime-based fluid binder M15	16.2	15.45	5.81	9159
	7/0.9%	12/4.0%	7/6.2%	3/1.6%

1: BS EN 1015-11:1999 - Part 11: Determination of flexural and compressive strength of hardened mortar

2: ASTM C469/C469M-14 Standard Test Method for Static Modulus of Elasticity and Poisson's Ratio of Concrete in Compression

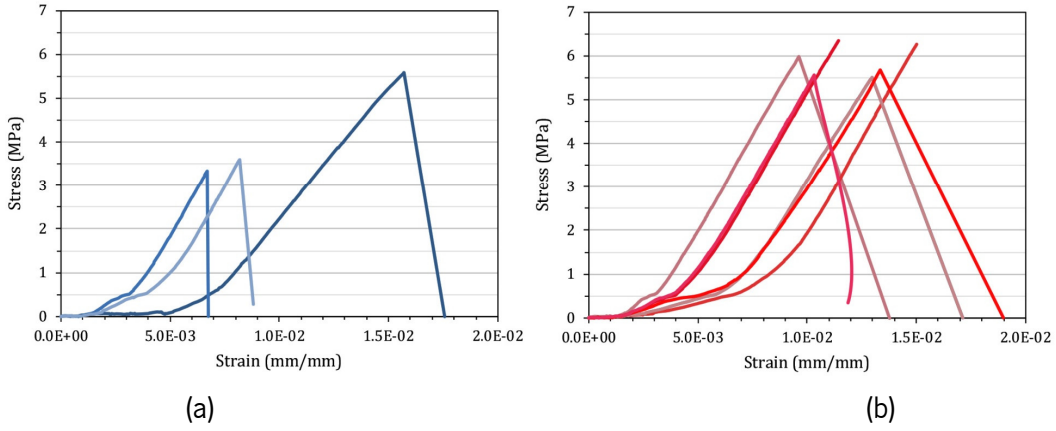
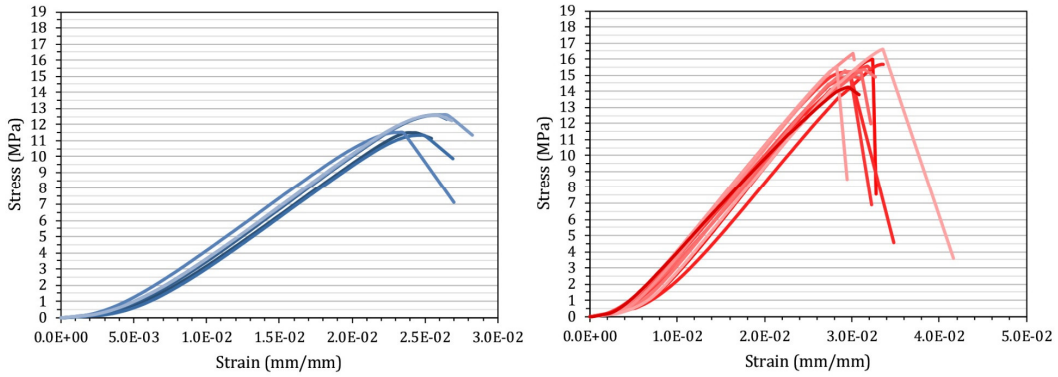


Figure 40. Stress-strain curves for flexure at 28 days of curing: (a) hydraulic lime-based render M15; (b) hydraulic lime-based fluid binder M15.



(a) (b)

Figure 41. Stress-strain curves for compression at 28 days of curing: (a) hydraulic lime-based render M15; (b) hydraulic lime-based fluid binder M15.

3.5. Mechanical tests on simulated historic masonry assemblies

Several objectives are linked with the performed strength tests, both in uniaxial (UC) and diagonal (DC) compression. In specific, testing parameters, as defined through the BS EN 1052-1-1999 for uniaxial compression and ASTM E519/E519M-20 for diagonal compression, are adjusted from monotonic to cyclic, in order to obtain reference values on strength and the evolution of stiffness at incremental steps. The crack development and strain distributions on the masonry wallets are continuously monitored with LVDTs, attached in various faces and orientations and with Digital Image Correlation (DIC) techniques. Contours of displacements, strains and cracks are obtained as an output.

In total, 4 wallets of size 625x310x800 mm^3 and 4 wallets of size 630x310x630 mm^3 (length x width x height) were built and tested for the UC and DC tests respectively. The bond pattern corresponds to a Flemish bond of 1 ½ brick thickness, as shown in Table 3 and Figure 42. The overall dimensions of the wallets for UC are within the specified range of the §7.1 of BS EN 1052-1-1999. Regarding the wallets for DC, their size is smaller than the nominal one recommended in ASTM E519/E519M-20, due to size restrictions of the testing frame. Yet, according to LUM B6 1991, the size of a wallet for a DC test should contain a sufficient amount of bricks, head and bed joints, representative of the bond pattern. For the hydraulic lime mortar, the mix specifications from 3.5.1 were used, with the thickness of the joints kept within the range 10-15 mm. In order to achieve a uniformity in workmanship all wallets were constructed by the same mason. For a high adhesion and bond strength at the mortar brick interface, each wallet was built within one day and following the recommendations of Binda et al. 2008 and Facconi et al. 2018, the bricks were soaked in water for 1 h, prior to construction, in order to minimize the absorption

of water from the mortar. Once constructed, each wallet was regularly sprayed with water, during 48 h, while for the first 7 days it was covered with a polyethylene sheet, so as to maintain RH conditions of around 90%. The total curing age, at ambient laboratory conditions, for all 8 wallets was within the period of 190-210 days. During construction, a total of 20 mortar sample prims were collected and cured under the same environmental conditions. The results from the mechanical and physical characterization tests are presented in Table 11. Here, the documented stiffness, compressive and flexural strength, under curing in ambient environmental conditions, and considering the inherit disperse, are very similar to the corresponding ones for 365 days (Table 8), cured under controlled conditions, as specified in 3.4.1. Considering also the density and actual volumetric ratio of bricks and mortar, in every UC and DC wallet, the expected density for the constructed wallets is 18.86 kN/m^3, with a CoV of 2.31%.

The tests were executed with a 2MN and a 200kN hydraulic actuator for the UC and DC respectively. First, one monotonic test in UC is carried out in order to obtain reference values for the compressive stress and strain at peak. For the DC test, and given the high expected variability of tensile strength, two wallets were tested under diagonal monotonic compression. According to Vasconcelos 2005, for capacity tests, a constant displacement control of 3μm/s dictates a low enough velocity to obtain a stable failure and long post-peak evolution, thus preventing any abrupt or explosive failure modes. Accounting also the total time duration of the test, the capacity and the resolution of the actuators, the UC and DC monotonic tests were performed under a constant displacement rate, of 5μm/s and 2μm/s respectively. Also, the post-peak behavior can be captured through the acquisition of lateral displacements, instead of the axial ones, since lateral displacements increase monotonically under compressive loads. Later, and with the monotonic tests as reference, cyclic capacity tests are performed [Vasconcelos 2005].

In total, 7 loading and unloading cycles are performed under force control, both in UC and DC, defined at around 10%, 20%, 30%, 40%, 50%, 60%, and 70% of the expected maximum load, obtained from the monotonic capacity tests. As explained in 3.3.2, in order for unrealistic displacements to be exempted, associated to the testing frame and the early adjustments of the specimen, within the testing platens, loading cycles under force control are chosen, as more explicit and accurate. In order to maintain permanent contact with the specimen, every unloading cycle reaches until a minimum load of 5 kN, both in UC and DC. The force control rate was adjusted from the acquisition data of the monotonic test, i.e., first the measured displacement and stiffness

defined the time duration of each loading-unloading cycle, with a displacement rate of 3μm/s and the force control rate was fitted for the exact time duration. Thus, 7 loading-unloading cycles for the UC and DC cyclic tests, were set to 1.1kN/s and 0.13kN/s respectively. Beyond the stress state of around 70% of f_c or f_t and until failure, the last loading branch is assigned a displacement rate of 5μm/s and 2μm/s respectively. The resulted testing time of the cyclic capacity tests in UC and DC, was around 4 h and 1 h respectively.



Figure 42. Building process of brick masonry wallets for UC and DC tests. Note the flemish bond pattern of 1½ brick thickness.

Table 11. Physical and mechanical properties of M4 hydraulic lime-based mortar prisms, collected during construction and cured at ambient environmental conditions in the laboratory, i.e., mass density, compressive strength, flexural strength and Young's modulus.

	Mean Mass Density (kN/m^3) (Number of specimen)/(CoV)	Mean Compressive Strength (MPa) (Number of specimen)/(CoV)	Mean Flexural Strength (MPa) (Number of specimen)/(CoV)	Mean Young's Modulus (MPa) (Number of specimen)/(CoV)
Specimen	Prisms[1]: 40x40x160 (mm^3)	Cubes[1]: 40x40x40 (mm^3)	Prisms[1]: 40x40x160 (mm^3)	Cylinders[2]: Φ75x150 (mm^3)
Conditions	Laboratory ambient conditions			
Curing	190-210 days			
Hydraulic lime mortar M4	19.5 17/1.2%	3.67 24/6.1%	1.22 20/15.0%	4248 6/12.4%

1: BS EN 1015-11:1999 - Part 11: Determination of flexural and compressive strength of hardened mortar
2: ASTM C469/C469M-14 Standard Test Method for Static Modulus of Elasticity and Poisson's Ratio of Concrete in Compression

3.5.1. Uniaxial cyclic compression tests

The acquisition of displacements for the uniaxial compression tests was performed with a total of eight LVDTs, attached on various directions and planes of the masonry wallets, and depicted in Figure 43. Specifically, three LVDTs measure axial deformations (z-z axis), namely LVDTs 1 and 2, while LVDT-4 measures deformations along the entire height, also containing adjustments of the specimen within the testing platens. LVDT-3 measures the lateral deformations for the in-plane expansion (x-x axis) and four LVDTs, attached along the thickness, on either side, measure the out-of-plane expansion (y-y axis), namely LVDTs 5-8. The front elevation was kept without LVDTs, in order to monitor strain and crack distributions, by means of DIC monitoring. The first wallet (UC1) was tested under monotonic uniaxial compression. The stress-strain curve of the axial and lateral deformations and maximum principal strain 2D plots from the DIC acquisitions, at five stress states, namely at 33%, 75%, 90%, 100% of f_c and at the last documented state before failure, as explained in Kaushik et al. 2007 and described in 3.3.2, are presented in Figure 44. The compressive strength f_c of the UC1 wallet is 9.75 MPa and the elastic stiffness (5%-33% f_c) is 831.65 MPa. As seen from the DIC 2D maximum principal strain distribution plots of Figure 44, vertical cracks start forming at 75% f_c, also along the thickness, and propagate extensively at 90% f_c. From the graphs of Figure 44 is evident that when the load is around 90% f_c, a destabilizing effect occurs, with the extension in axial displacements. In fact, at the last stages of the post-peak behavior, the in-plane vertical cracks in elevation form a conical failure mode, while the vertical cracks along the thickness appear to fragment the wall in discontinuous layers, which bend out-of-plane (note the reversal due

to this effect in LVDTs 1-2 after peak), with the lateral displacements (y-y axis) increasing monotonically. The post-peak evolves until a sudden explosive failure at 92%f_c.

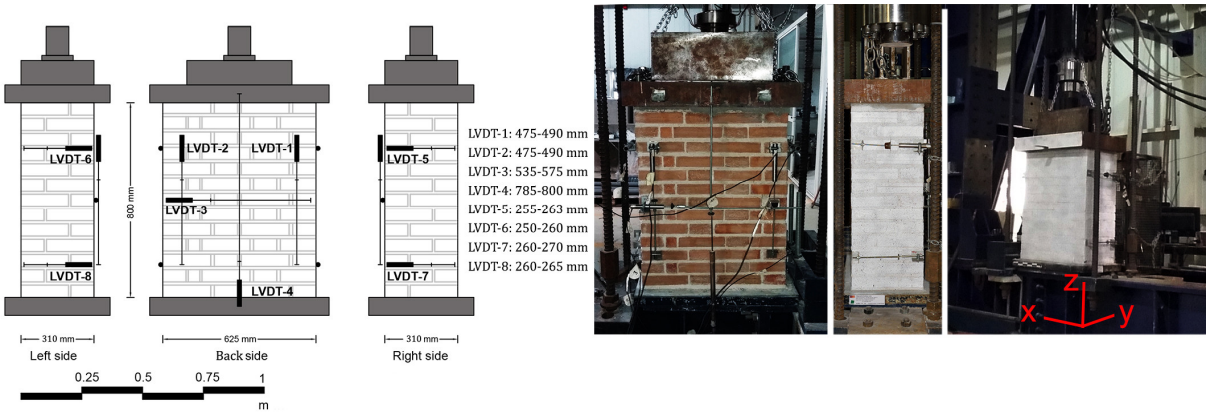


Figure 43. Geometry, instrumentation and setup of uniaxial compression tests on brick masonry wallets with lime mortar (UC_i). Note the range of the initial measuring lengths of the LVDTs, from all four UC_i wallets.

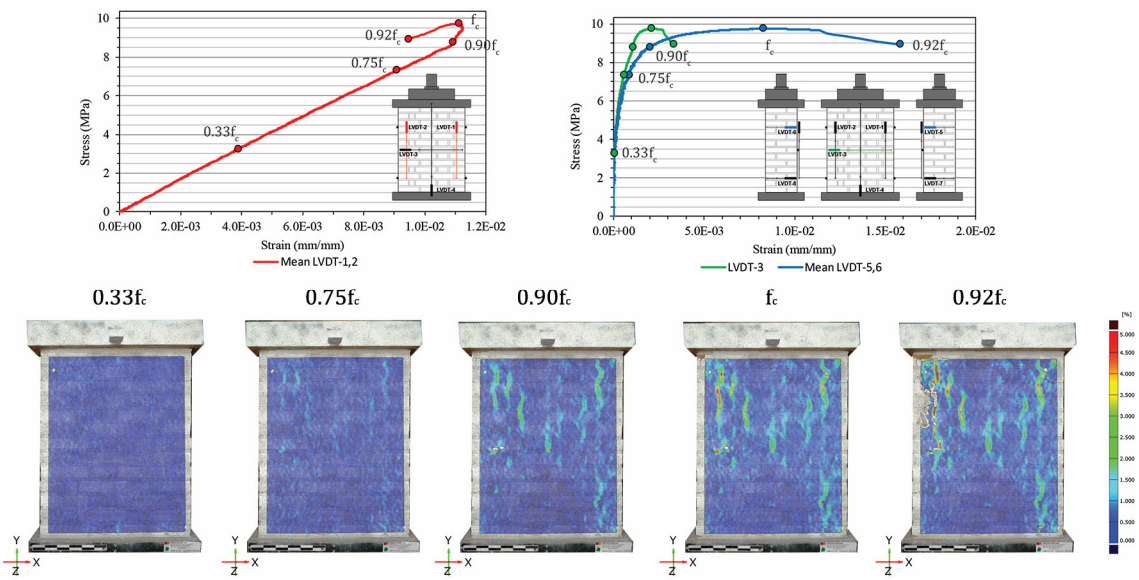


Figure 44. Stress-strain curves for axial and lateral strains of wallet UC1, tested monotonically under uniaxial compression. Here, the 2D maximum principal strain distribution plots are presented at five stress states, from DIC acquisitions.

Next, the wallets UC2, UC3 and UC4 are tested under cyclic uniaxial compression. The 7 loading-unloading cycles under force control, as adjusted from UC1, which correspond on average to 11%, 23%, 34%, 46%, 57%, 69% and 80% of the strength f_c. The last loading pattern, under displacement control increases monotonically until failure. The stress-strain curves of axial and lateral strains, for all three wallets, are presented in Figure 45. All three wallets present a similar stress-strain relation. The post-peak behavior under axial strains is highly brittle and cannot be captured, mainly governed by a complex combination of vertical in plane fragmentations and shear cracks in a conical formation. Yet, in-plane axial deformations around the peak stress and until

failure increase almost monotonically. The failure at the last stages of the post-peak is out-of-plane and explosive. As seen in the 2D principal strain distribution plots of the DIC acquisitions of Figure 46, vertical splitting cracks form around 75% f_c in the front and side elevations, while at peak stress several macro-cracks are found along the entire height. At the ultimate state, before failure, the relatively large thickness of the wallets is fragmented in three layers (through the entire thickness), following the divisions of the head joints. The UC4 wallet deviates from the classical compressive failure, with an in-plane flexural failure, which can be associated to internal stress distributions towards the one side of the wallet. Mechanical parameters of compressive strength, Young's modulus and maximum axial strain are presented in Table 12. The average compressive strength and Young's modulus are 8.80 MPa and 909 MPa respectively, in the same range as the experimental tests on brick masonry with NHL3.5 lime mortar in Costigan et al. 2015. Considering the value for compressive strength, is found in the same range compared to experimental tests on solid brick masonry and lime-based mortar specimens, as in Facconi et al. 2018 and Munoz et al. 2016. Yet, compared with the NTC 2018 recommendations for the specified type of masonry, the recommended range of 2.6-4.3 MPa and 1.2-1.8 GPa for the average compressive strength and Young's Modulus respectively, the experimental results differ significantly.

Considering the established relation for the Young's Modulus and the compressive strength, found equal to $E = 104 \cdot f_c$, with a CoV of 14.45%, is on the lower limit of those recommended for masonry, as shown in Figure 47a. Regarding the fracture energy in compression G_c, as described in 3.3.1, it can be defined as the product of the ductility index d_u, here equal to 1.6 mm, and the average compressive strength, thus equal to 14 $^{N}/_{mm}$ [Angelillo et al. 2014, CEB-FIP. Model Code 90 1993]. Lastly, considering the incremental plastic and elastic axial strains for each cycle, there is a steady increase of plastic strains, which can be directly associated to the accumulation of damage in the material (Figure 47b). In fact, for specimens UC2, UC3 and UC4, the evolution of the secant stiffness calculated from the envelope curves, and corresponding to the maximum stress-strain state of each cycle i, with the latter normalized with the strain at peak, reveals a constant stiffness loss with an R-squared value of 0.9, here presented in Figure 47c.

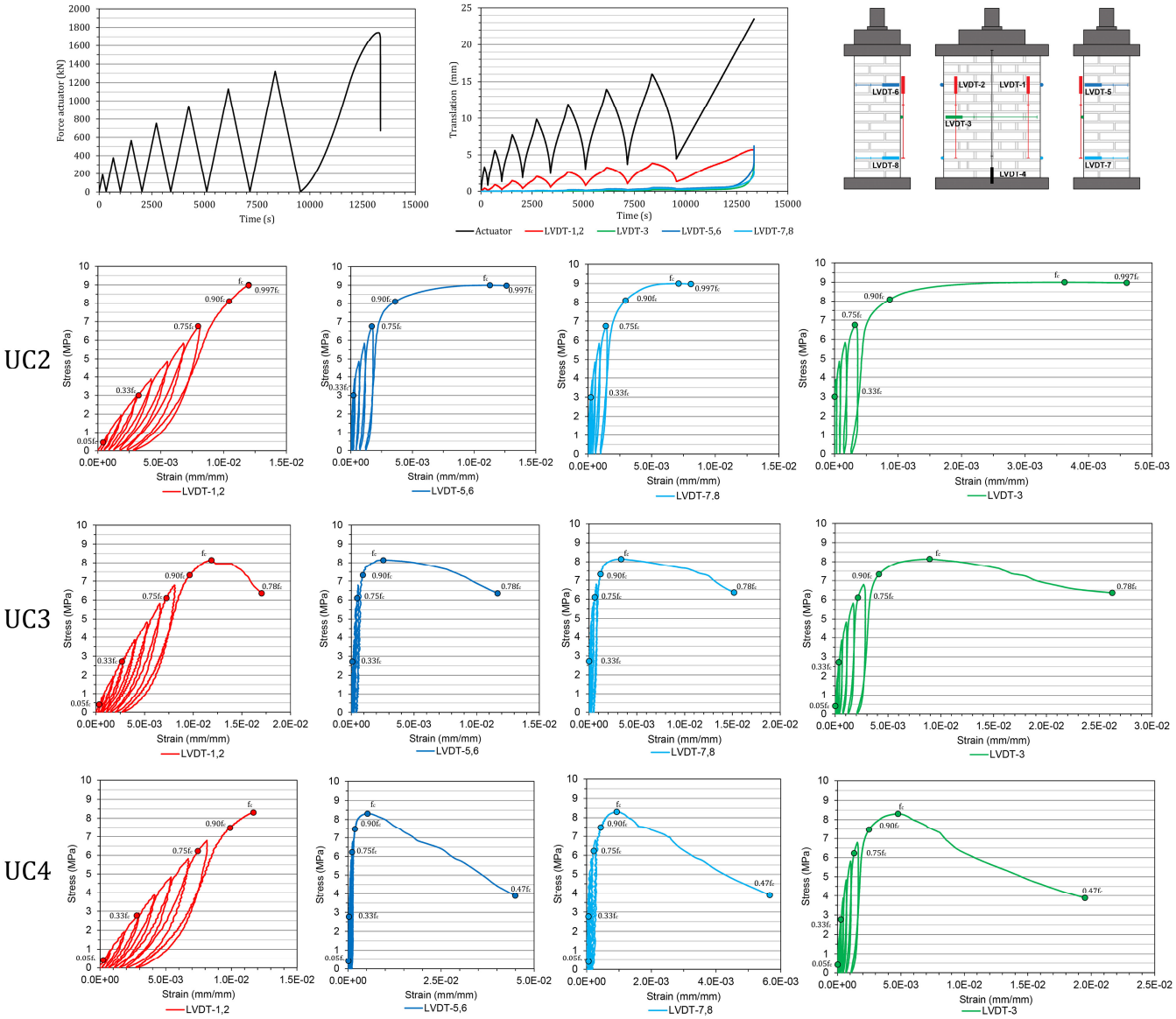


Figure 45. Stress-strain curves for axial and lateral strains of wallets UC2-4 tested under cyclic uniaxial compression. Note the force and displacement time-history pattern and the six stress states. Here, for display purposes, the absolute values of the compressive strains of LVDT-1 and LVDT-2 were chosen. Note the selected stress state points, for the corresponding DIC plots.

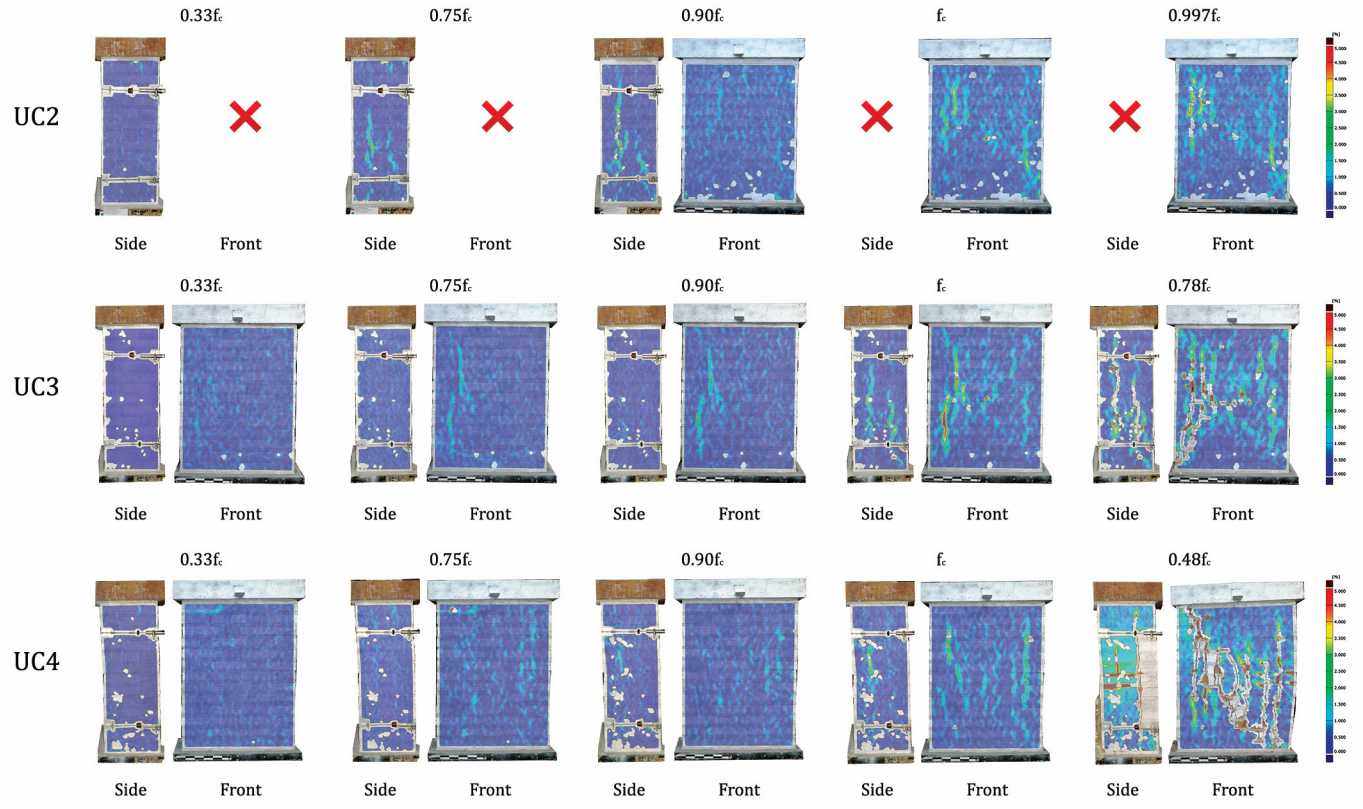


Figure 46. 2D maximum principal strain distribution plots at five stress states, from DIC acquisitions, of wallets UC2-4 tested under cyclic uniaxial compression. Note the ¨x¨ symbol for failed DIC acquisitions.

Table 12. Mechanical properties of UC1-4 brick masonry wallets with lime mortar M4 tested in uniaxial compression, i.e., compressive strength, Young's modulus, $^{E_{MOD}}/_{\sigma_{max}}$ ratio and maximum axial strain.

	Compressive Strength		Young's Modulus		$a = \frac{E_{MOD}}{\sigma_{max}}$		Ultimate axial strain	
	(MPa)	Mean (MPa)/(CoV)	(MPa)	Mean (MPa)/(CoV)	-	Mean -/(CoV)	(mm/mm)	Mean (mm/mm)/(CoV)
Specimen	Wallets: 625x310x800 (mm^3)							
Conditions	Laboratory ambient conditions							
Curing	190-210 days							
UC1	9.74	8.80 / 8.3%	831	909 / 6.7%	85	104.2 / 14.5%	1.13E-02	1.30E-02 / 21.2%
UC2	9.00		902		100		1.20E-02	
UC3	8.14		979		120		1.70E-02	
UC4	8.31		923		111		1.15E-02	

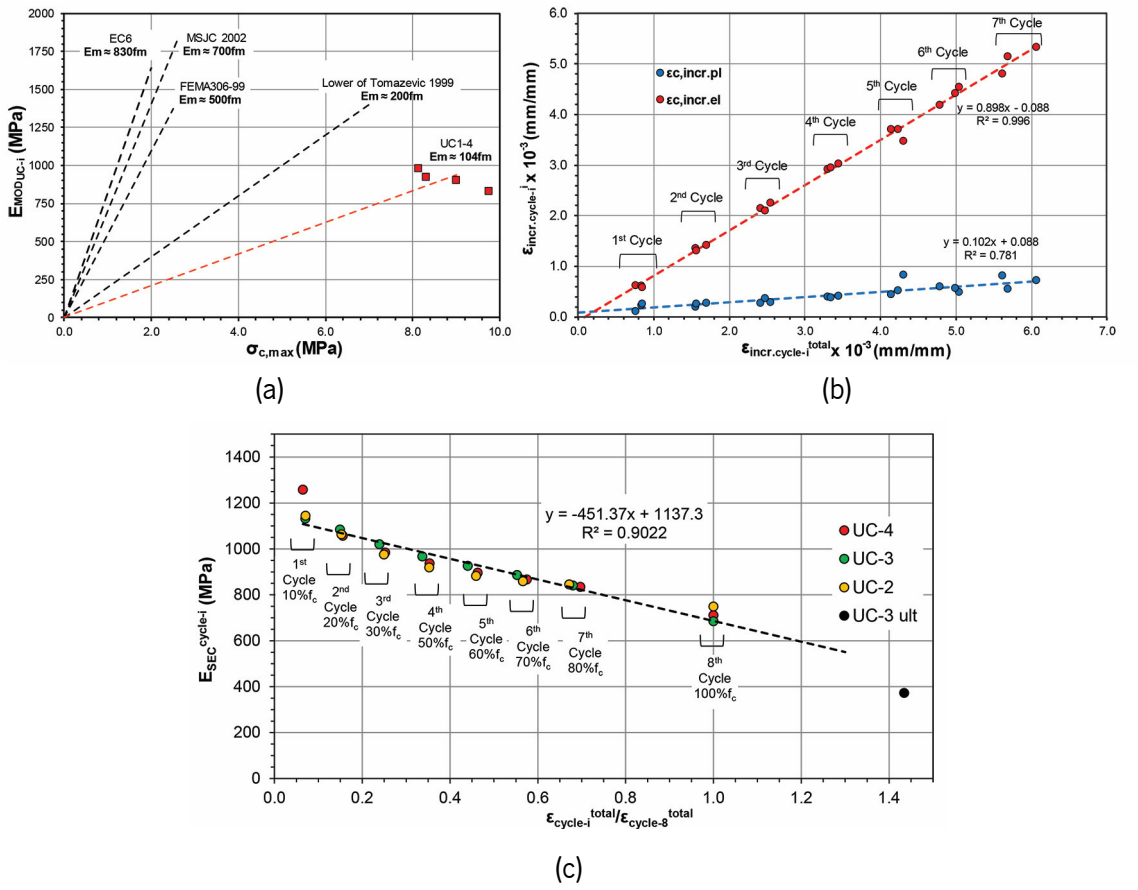


Figure 47. Graphic representations: (a) Young's modulus and compressive strength relation from uniaxial compressive tests in UC1-4 wallets and other sources; (b) propagation of elastic (el.) and plastic (pl.) axial strains for each cycle, of tested wallets UC2-4, under cyclic uniaxial compression; (c) linear regression analysis of the secant stiffness versus the vertical total strain at peak of each cycle i, normalized with the total strain at peak. Note the sole value for the ultimate secant stiffness and normalized strain for UC3, here not included in the regression analysis.

3.5.2. Diagonal monotonic compression tests

The diagonal compression tests, as explained in ASTM E519/E519M-20 and LUM B6 1991, reproduce the diagonal failure in masonry, under a 45º plane, with a principle stress state of pure shear. The capacity measured is the direct shear or tensile strength f_t, which for a wallet with solid bricks is given by Equation 42, while the shear strains γ are obtained as the sum of the absolute values of the axial and lateral strains of the diagonals, namely ε_v and ε_h respectively (Equation 43). Here is noted that P is the maximum compressive load, while w, h and t are the respective width, height and thickness of the square masonry wallet. The shear modulus G is associated to the shear stress and strain at peak (Equation 43). Here is noted that the shear modulus G is defined during the damaged state, namely the shear stress and strain at peak.

$$f_t = \frac{0.707 \cdot P}{\left(\frac{w+h}{2}\right) t} \qquad \text{Equation 42}$$

$$G = \frac{f_t}{\gamma}, \gamma = \varepsilon_v + \varepsilon_h \qquad \text{Equation 43}$$

In total, five LVDTS measured displacements during the diagonal compression tests, attached along the diagonals (LVDT-1 and LVDT-2), on the actuator and upper shoe (LVDT-3), and along the thickness (LVDT-4 and LVDT-5), as seen in Figure 48. Displacements along the thickness were found infinitesimal, present no clear trend and are not shown here, while LVDT-3 was used for imposing displacement control rates of 2 μm/s. Similarly to the UC tests, the front elevation was kept without LVDTs, for DIC monitoring (Figure 48).

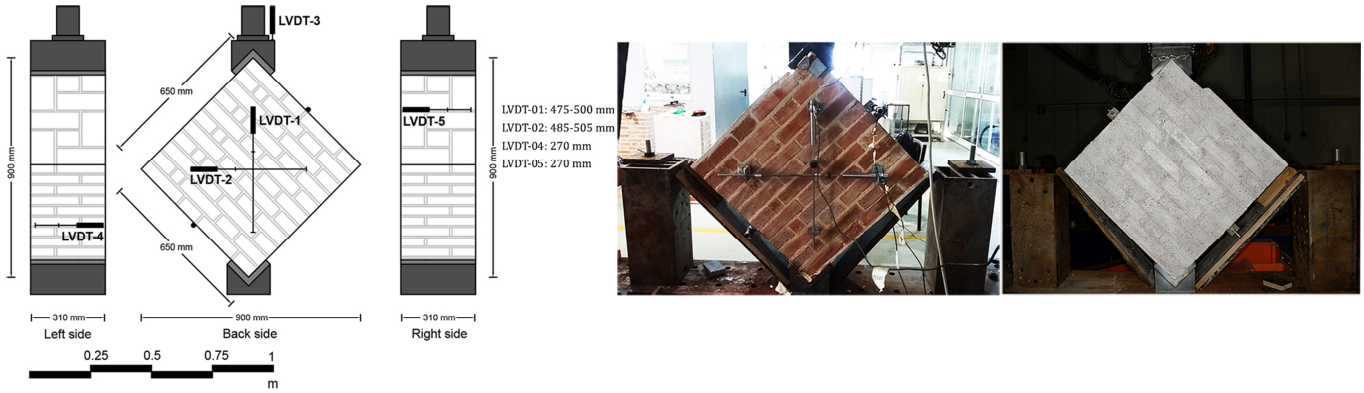


Figure 48. Geometry, instrumentation and setup of diagonal compression tests on brick masonry wallets with lime mortar. Note the range of the initial measuring lengths of the LVDTs, from all four DC_i wallets.

First, the wallets DC1 and DC2 were tested under monotonic diagonal compression. The load and displacement time-histories, the shear stress-strain curves and the failure modes are presented in Figure 49. The DC1 wallet fails under a splitting vertical crack, passing through the mortar joints and bricks. Despite the low displacement rate of 2μm/s, the failure is impetuous, and no post-peak is captured. The DC2 wallet fails early under sliding, along a bed joint plane, due to a weak bond strength at the mortar-brick interface, and thus, the resulting shear capacity is not accounted. The last stable plastic branch in the shear stress-strain curve if DC2 is associated solely to friction (Figure 49). The subsequent cyclic diagonal compression tests for the wallets DC3 and DC4 were configured based on the shear capacity of DC1. Yet, given the larger shear strength variation, both wallets were proven weaker and failed at an earlier stress state, with the peak shear stress and strain for each cycle presented in Table 13.

Table 13. Cyclic diagonal compression test variations in peak shear stress and strain, for wallets DC3 and DC4.

			DC3			DC4		
	Force		Shear stress (S)		Shear strain (γ)	Shear stress (S)		Shear strain (γ)
Cycle	kN	$\%f_t$ of DC1	MPa	$\%f_t$	mm/mm	MPa	$\%f_t$	mm/mm
1	17.97	10%	0.06	26%	1.48E-04	0.06	18%	5.16E-05
2	34.99	20%	0.12	50%	2.77E-04	0.12	35%	9.79E-05
3	53.01	30%	0.19	75%	4.39E-04	0.19	53%	1.83E-04
4	70.93	40%	0.25	100%	8.24E-04	0.25	71%	2.50E-04
5	87.94	50%	-	-	-	0.31	88%	4.05E-04
6	105.97	60%	-	-	-	0.36	100%	6.48E-04
7	123.54	70%	-	-	-	-	-	-

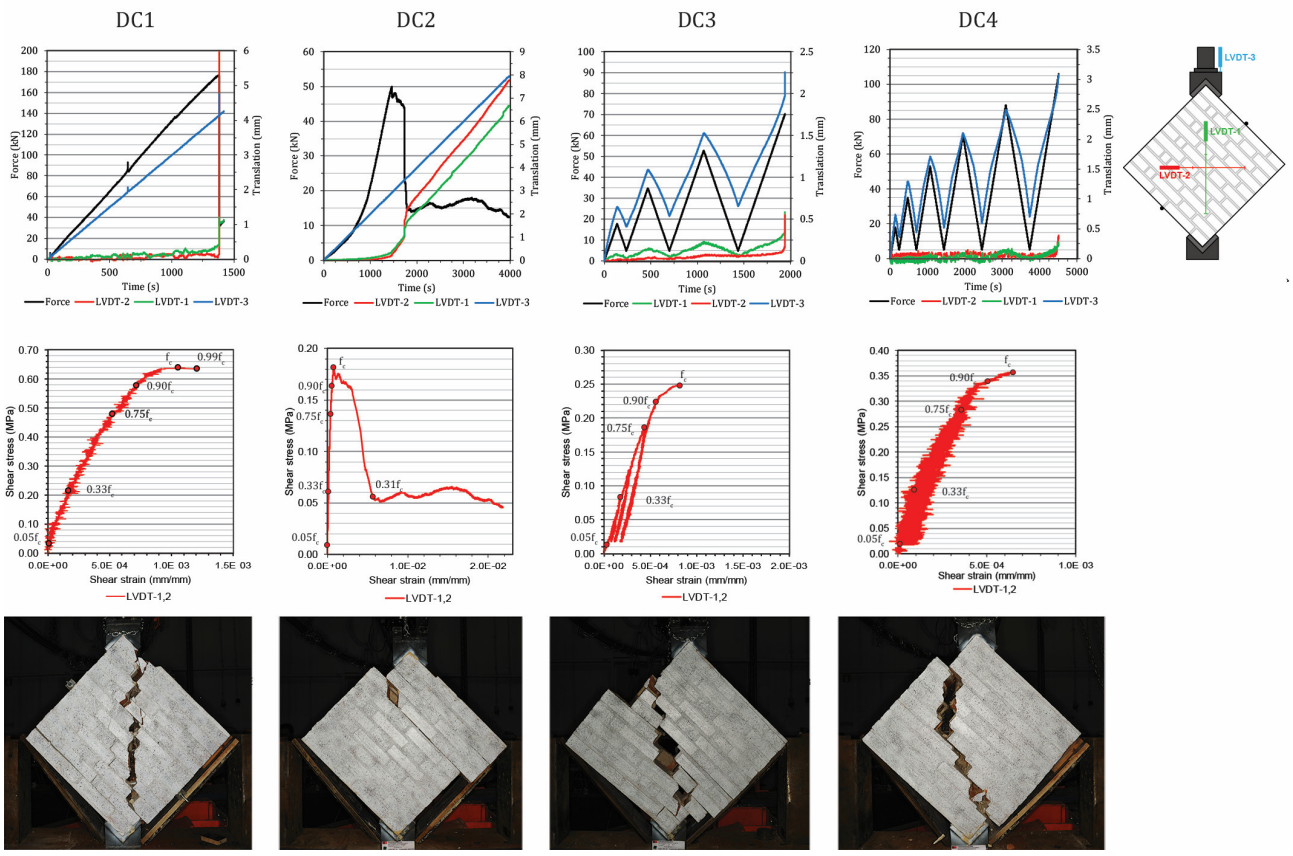


Figure 49. Force/translation time-histories, shear stress-strain curves and failure at last stage, of wallets tested under monotonic (DC1 and DC2) and cyclic (DC3 and DC4) diagonal compression. Note that the loading cycles for DC4 are not distinguishable, due to high noise.

The shear strain and stiffness values are presented in Table 14 and is evident that the tensile strength is highly dependent on the crack trajectory and therefore exhibits high variability, with an average value of 0.42 MPa and a CoV of 49%. Accounting for the uniaxial compressive tests of 3.5.1, the ratio of tensile and compressive strength for the studied simulated historic masonry is around 0.05. Cracks are a compilation of stepped and shear cracks, which propagate through the bed and head joints, with many cracked bricks. Yet, various aspects, such as the large thickness of the tested masonry wallets, the different brick-mortar ratio of crack sections and the

lack of control for consistent bonding within bricks and mortar are attributed to the high variability in shear material properties. The secant shear modulus G is equal to 485 MPa, with also a high CoV, of 33%. In addition, compared with the NTC 2018 recommendations for the specified type of masonry, the obtained average direct shear strength is found higher than the recommended range of 0.13-0.27 MPa, while the respective average shear modulus is within the recommended range of 400-600 MPa.

Table 14. Mechanical properties of DC1-4 brick masonry wallets with lime mortar M4, tested in diagonal compression, i.e., tensile strength, shear strain at peak, shear modulus and ratio with compressive strength.

	Tensile Strength		Shear strain at peak	Shear Modulus		$\frac{f_{t,mean}}{f_{c,mean}}$
	(MPa)	Mean (MPa)/(CoV)	γ (mm/mm)	(MPa)	Mean (MPa)/(CoV)	
Specimen	Wallets: 625x310x625 (mm^3)					
Conditions	Laboratory ambient conditions					
Curing	190-210 days					
DC1	0.64	0.42 / 48.7%	1.06E-03	605	485 / 33.4%	0.05
DC2*	0.18		8.26E-04	220		
DC3	0.25		8.24E-04	301		
DC4	0.36		6.48E-04	551		

* Excluded statistically due to sliding failure

From the shear stress-strain curves of Figure 49, no significant loss of shear stiffness occurs until 90% of the tensile strength f_t. As correlated with the DIC 2D maximum principal strain distribution plots of Figure 50, once the shear load reaches 90% of f_t, damage initiates, in form of shear cracks, with an increase in shear displacements. Cracks propagate as the shear stress reaches the peak. For the displacement control monotonic loading of wallet DC1 the failure was sudden, and no post-peak was recorded. For the cyclic loading with force control of the wallets DC3 and DC4, their failure at a lower tensile stress did not allow the transition to displacement control and the recording of the post-peak. For the fracture energy in tension G_f, as described in 3.3.1, it can be expressed with Equation 34 and is equal to 0.023 N/mm [Angelillo et al. 2014, CEB-FIP. Model Code 90 1993].

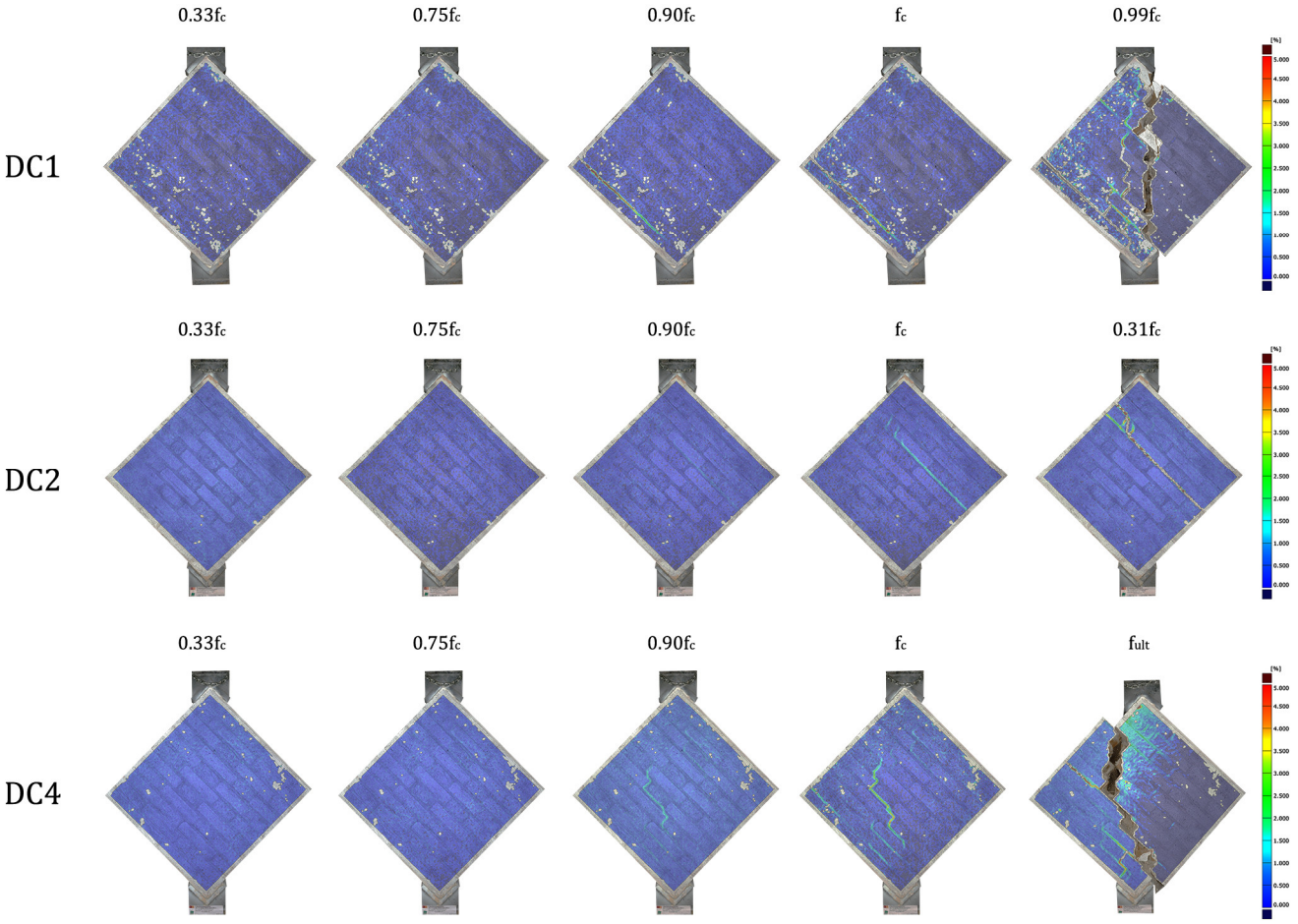


Figure 50. 2D maximum principal strain distribution plots at five stress states, from DIC acquisitions, of wallets DC1, DC2 and DC4 tested under uniaxial compression. Note the DIC acquisition for the DC3 the failure was sudden and was not captured.

3.6. Analytical stress-strain expressions from experimental data

As stated in JCSS 2011, the average compressive strength of masonry f_m is dependent on the average compressive strength of the bricks f_b and mortar f_{mo}, under the Equation 44. Here, the coefficients K, a and b are dependent on the relative height and compressive strength of the constituents, and therefore need to be updated under the actual statistical distribution of the test data. In EN 1996-1-1 2005 the abovementioned formula expresses the characteristic compressive strength of masonry $f_{m,k}$, which according to EN 1990:2002 corresponds to a nominal value (e.g. the minimum value of a sample) or the 5% quantile of the normal distribution of a test sample. By considering the known CoV of 8.34% from 4 tested wallets (Table 12) and Table D1 of §D7.2 of EN 1990:2002, the average compressive strength of masonry is given by Equation 45. According to table 3.3 of §3.6.1.2 of EN 1996-1-1 2005, for Group I of units and general purpose mortar the coefficients of K, a and b are equal to 0.55, 0.7 and 0.3 respectively. Thus, the average estimated compressive strength of masonry is equal to 7.02 MPa, which

compared to the average value from the uniaxial compression tests, is found lower by 20%. Such a difference can be attributed to the absence of the contribution of large relative ratios between the height of bricks and mortar joints, and the lack of experimental data for weak lime-based mortars. In Costigan et al. 2015 and Lumantarna et al. 2014 the expression in Equation 44 has been updated, by means of regression analysis of experimental data, accounting for tested masonry specimens with NHL mortar and weak bricks. Yet, compressive strength results of brick masonry might differ, especially when related brick to mortar height ratios are not included in the sample.

$$f_m = K \cdot f_b^a \cdot f_{mo}^b \qquad \text{Equation 44}$$

$$f_m = \frac{f_{m,k}}{1 - 1.83CoV} \qquad \text{Equation 45}$$

Regarding the stress-strain envelope curve relationship, both in uniaxial and diagonal compression, a correlation analysis and linear regression fit is performed by the least of squares method between the stress data from the tests and the stress response variables from Equation 28 to Equation 32. As described in 3.3.1, analytical expressions for the stress-strain nonlinear evolution of masonry are based on parabolic functions, 2nd order polynomials or even 2nd order exponential growth functions. Adjusting coefficients involve the peak stress and strain, the elastic and secant stiffness at peak and, for some, the ultimate strain ε_{ult}, which for the specific tests is assumed equal to 1.75 times the strain at peak.

First, a linear regression with a least of squares fit is attempted, between selected stress states as defined in Kaushik et al. 2007, corresponding to 5%, 33%, 75%, 90%, 100% of the strength and at ultimate stage, with the predicted stress values (Figure 51 and Figure 52). Criteria for selection are the coefficient of determination R^2 and the distribution of residuals SS_{resid}, in order to evaluate the goodness of fit and the extent of errors. The best fit among the analytical expressions for stress and strain in masonry is set mostly on the elastic and secant stiffness at peak, and the post-peak response, if captured from the tests. For the UC, the envelope curve of Equation 32, presented in Alshebani et al. 1999, exhibits the highest R^2 and the lowest sum of residuals, as seen in Table 15 (Figure 51). Focusing on the post-peak, captured only in UC3 wallet, curves of Equation 28 and Equation 32 present the best fit. Regarding the DC curves, all equations present an acceptable fit, until the peak shear strength, with Equation 31 presenting the lowest R^2 and SS_{resid} values (Table 15 and Figure 52).

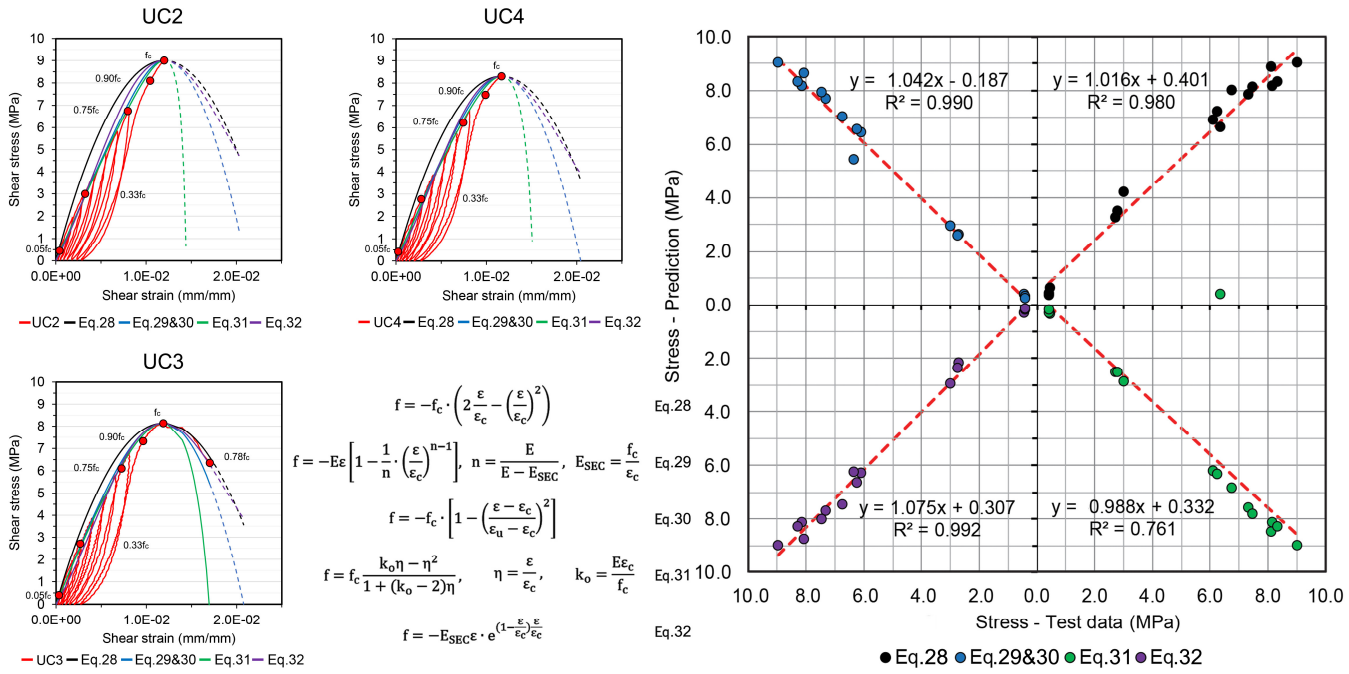


Figure 51. Envelope stress-strain curves from cyclic uniaxial compression tests of UC2, UC3 and UC4: (a) stress-strain curves versus envelope curves from Equation 28, Equation 29 and Equation 30, Equation 31 and Equation 32. Note the dashed curve, after the maximum obtained strain; (b) linear regression graph of test stress data for $0.05f_c$, $0.33f_c$, $0.75f_c$, $0.90f_c$, f_c and $f_{c,ult}$. Note the test and prediction data in x-x and y-y axis respectively.

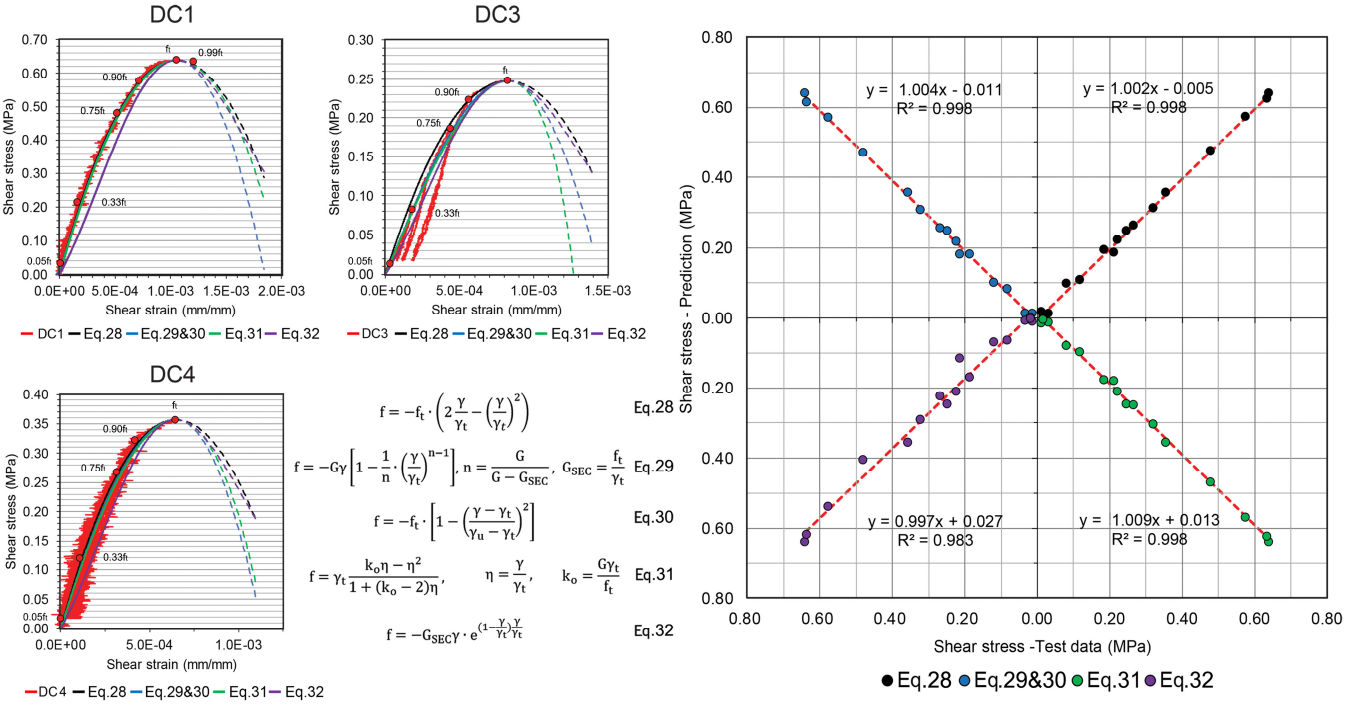


Figure 52. Envelope stress-strain curves from monotonic and cyclic diagonal compression tests of DC1, DC3 and DC4: (a) shear stress-strain curves versus envelope curves from Equation 28, Equation 29 and Equation 30, Equation 31 and Equation 32. Note the dashed curve, after the maximum obtained strain; (b) linear regression graph of test stress data for $0.05f_t$, $0.33f_t$, $0.75f_t$, $0.90f_t$, f_t and $f_{t,ult}$. Note the test and prediction data in x-x and y-y axis respectively.

Table 15. Goodness of fit from linear regression analysis, for selected stress values from tests of UC and DC, corresponding to 5%, 0.33%, 0.75%, 90%, 100% of the strength and at ultimate stage, with the predicted stress values from Equation 28, Equation 29 and Equation 30, Equation 31 and Equation 32.

		SS Residuals						*SS Residuals*			
UC	$\%f_c$	Eq.28	Eq.29&30	Eq.31	Eq.32	DC	$\%f_t$	Eq.28	Eq.29&30	Eq.31	Eq.32
UC2	5%	0.061	0.008	0.067	0.021	DC1	5%	7.36E-05	3.20E-05	1.79E-05	5.56E-05
UC3	5%	0.145	0.006	0.059	0.009	DC3	5%	2.39E-04	2.25E-04	2.71E-04	8.53E-04
UC4	5%	0.241	0.001	0.019	0.001	DC4	5%	2.04E-05	8.28E-07	3.65E-07	2.59E-04
UC2	33%	0.571	0.000	0.065	0.002	DC1	33%	2.88E-04	3.49E-04	3.76E-04	4.14E-03
UC3	33%	0.010	0.002	0.034	0.180	DC3	33%	5.96E-04	1.67E-04	1.45E-04	2.18E-04
UC4	33%	0.075	0.018	0.013	0.086	DC4	33%	2.59E-04	1.05E-04	7.22E-05	8.93E-04
UC2	75%	0.528	0.033	0.255	0.276	DC1	75%	1.86E-05	9.03E-06	1.85E-07	1.65E-03
UC3	75%	0.090	0.062	0.292	0.002	DC3	75%	3.01E-04	6.70E-05	1.55E-05	2.70E-04
UC4	75%	0.234	0.048	0.256	0.081	DC4	75%	6.31E-04	3.63E-04	2.95E-04	2.25E-03
UC2	90%	0.047	0.133	0.691	0.137	DC1	90%	2.78E-05	3.90E-05	1.09E-05	6.77E-06
UC3	90%	0.000	0.062	0.478	0.017	DC3	90%	7.83E-05	2.51E-05	2.32E-06	3.97E-04
UC4	90%	0.014	0.109	0.599	0.081	DC4	90%	7.71E-04	5.04E-04	4.43E-04	1.36E-03
UC2	100%	0.297	0.037	0.192	0.133	DC1	100%	5.61E-05	1.18E-04	8.85E-05	1.13E-03
UC3	100%	0.282	0.024	0.183	0.090	DC3	100%	8.13E-05	1.55E-04	1.65E-04	1.07E-03
UC4	100%	0.285	0.027	0.185	0.098	DC4	100%	7.38E-05	1.44E-04	1.41E-04	1.09E-03
UC4	78%	0.064	1.051	40.162	0.068						
Sum SS_{resid}		2.944	1.620	43.548	1.281	Sum SS_{resid}		3.51E-03	2.30E-03	2.04E-03	1.56E-02
R^2		0.980	0.990	0.761	0.992	R^2		0.995	0.997	0.997	0.977

3.7. Conclusions

The current laboratory testing campaign aimed at the mechanical characterization of thick brick masonry walls with NHL mortar, representative of brick masonry façades, from residential buildings, dating between the 19th-20th centuries in Europe and in particular the Iberian Peninsula. Out of the many historic masonry types, that of a Flemish bond and a 1½ brick thickness was chosen. The type of failure, the crack pattern, the strength and stress-strain evolution, under monotonic and cyclic uniaxial and diagonal compressive testing, mechanical parameters in brick masonry are dependent on the thickness of mortar joints, the brick size, the bond pattern, plus the strength and stiffness of bricks and mortar, and the present chapter provides data for this purpose.

Failure under uniaxial and unconfined compression is most of times brittle and follows a vertical cracking pattern, with a monotonic increase of in-plane and out-of-plane expansions. In the ultimate state, masonry is divided in discontinuous layers, as many as the bed joint planes in the side elevations. Axial displacements at face elevations tend to follow an inversed trend, around failure, mostly due to out-of-plane bending. Thus, the post-peak is difficult to be captured. During cycles of loading-unloading and until the peak stress, the elastic and plastic strains, and stiffness, follow a positive and negative linear trend respectively. Analytical expressions for the compressive

stress-strain evolution curves are parabolic functions, 2nd order polynomials and 2nd order exponential growth functions, with input parameters of the peak stress and strain, the elastic and secant stiffness at peak and for some, the ultimate strain. For the particular type of tested masonry, the envelope curve of Alshebani et al. 1999, exhibits the best fit among tested functions.

The behavior under diagonal compression exhibits high variability, given the different brick-mortar ratio of the diagonal crack sections and especially when there is lack of control for consistent bonding. Cracks are mostly a combination of splitting cracks in bricks and mortar joints, with stepped cracks from partial sliding within bed and head joints. Analytical expressions for the compressive stress-strain evolution curves can also serve for diagonal compression, at least until the peak shear stress.

The set of mechanical and physical properties characterizing the studied masonry with solid fired bricks and M4 NHL mortar, based on the performed laboratory tests and literature, are presented in Table 16.

Table 16. Average mechanical properties accounted for the characterization of simulated historic brick masonry with M4 NHL mortar, based on mechanical laboratory testing and literature.

Mechanical properties	Simulated historic brick masonry with M4 NHL mortar		Number of specimen / CoV
Compressive strength	f_c (MPa)	8.8	4 / 8.3%
Modulus of elasticity	E (MPa)	909	4 / 6.7%
Tensile strength	f_t (MPa)	0.42	3 / 48.7%
Fracture energy (tension)	G_f (N/mm)	14	-
Fracture energy (compression)	G_c (N/mm)	0.023	-
Specific weight	ρ (kN/m^3)	18.9	8 / 2.3%

CHAPTER 4. FIELD MONITORING OF INDUCED GROUND-BORNE VIBRATIONS

CHAPTER 4. Outline

4.1. Introduction

4.2. Criteria and aspects from international standards

4.2.1. General framework

4.2.2. Data acquisition planning

4.3. Field monitoring in the Church of the Angels

4.3.1. Historic perspective

4.3.2. Ambient vibration tests

4.3.3. Acquisitions of induced vibrations with geophones

4.3.4. Coupling acquisitions of induced vibrations with geophones and seismographers

4.4. Conclusions

4.1. Introduction

Cultural Heritage Buildings are irreplaceable and highly complex. These assets are becoming increasingly at risk due to unprecedented transformation processes in cities, due to tunneling. In general, heritage buildings, given their immense value, are highly susceptible to changes in their substrate. Besides original design and construction processes, operational use characteristics are among the challenges involved in the safety and risk assessment of monuments. Furthermore, the management of these assets is considered manifold and challenging, namely with respect to defining values for cultural heritage and acceptable damage levels. Under current demands, the concept of the structural performance assessment must address crack initiation and crack widths, not only defined at ultimate level, but also at intermediate serviceability levels. In case of valuable finishing, such as frescoes, tiles, timber marquetry or others, the definition of threshold damage values is particularly complex and differs from the values used for structural elements.

The effect of vibrations, induced by underground operating railways, in the performance of neighboring cultural heritage buildings, is an open challenge. General vibration threshold criteria

associated to non-structural damage are weakly applicable for historic structures, given their low mechanical material properties, quasi-brittle behavior, pre-existing damage and intrinsic architectural value. Special induced vibration criteria, present in international standards, minimize the possibility of immediate or fatigue damage from cumulative effects after continuous cycles of vibrations. In situ inspection and diagnosis, namely monitoring of structural and geotechnical properties, as well as wave propagation and amplitude, are popular trends and can offer a validation on the likelihood of fatigue damage, through long-term exposure to induced vibrations.

Railway induced vibrations are produced through quasi-static and dynamic axle loads. They exhibit an arbitrary time variation, duration and periodicity. In moving trains, the principal mechanism is the dynamic excitation due to unevenness of wheels and track lines, causing impact excitation in rail joints and wheel flats, but also from irregularities, i.e., switches and other mechanical elements. The vibration wave frequency is considered broad-band. The energy and frequency content are also highly dependent on the characteristics of the rail supporting system and those of the moving train, i.e., speed and weight [Thompson et al. 2009].

Vibrations induced from trains, running in tunnels, are transmitted through intermediate soil strata, in the 3D substrate space, with shear and compression waves or else defined as S-wave and P-waves respectively. Even though the highest amount of energy is transmitted downwards, the main interest is on the propagation of waves towards the surface and at the foundation level of the buildings of interest [Jones et al. 2002]. Vibrations travel first through the tunnel's lining and mostly propagate on the surface directly above. Next, at lower angles, the wave propagation adopts a cylindrical wave-front shape [Thompson et al. 2009 and Jones et al. 2002]. Yet, the maximum surface response depends on the depth and type of tunnel, and is expected within a range of 0º-50º from the tunnel's vertical axis.

The vibration signal that reaches a neighboring structure is then defined as ground-borne vibration. As explained in 2.4.2, the frequency content of a ground-borne vibration signal ranges from 30 to 250 Hz, for common supported rails, frequencies up to 100 Hz are considered as relevant for induced structural or aesthetic damage [ISO 4866:1990/Amd 2:1996 2010 and DIN 4150-3 2016].

The current chapter presents an example of short-term Structural Health Monitoring (SHM) employed in a building of cultural heritage, namely ambient vibration testing and ground-borne

vibration recordings, that can serve as diagnostic tools on the effects of long-term exposure to induced vibrations, from underground railways. Criteria from international standards provide empirical indexes of threshold values of kinetic quantities, and specify the framework for data acquisition, some with specific considerations for cultural heritage buildings. Yet, a large variability on acceptable levels of induced vibrations exists among different standards, whereas the level of exposure, and any cumulative effects in terms of fatigue can only be justified through oriented research. Part of the current work aims at the signal processing of ground-borne recordings and the effect of different primary measurements and corresponding inconsistencies that may arise, i.e., weak signal processing, low sampling frequencies, the type of integration in time or frequency domain and digital filtering with incorrect cut-off frequency bandwidths.

4.2. Criteria and aspects from international standards

In general, assessment criteria for ground-borne induced vibrations from international standards provide upper threshold values, mostly in terms of velocity, which are linearly related to stress and strain fields. Specific criteria are usually set for non-structural components, accounting among others, frequency bandwidths and levels of intermittency. Even if recommendations specify the velocity as a primary measurement, it is often needed to obtain velocity time histories from acceleration data, as accelerometers are more widely used in practice.

4.2.1. General framework

International standards cover several aspects and provide guidelines, regarding the measurement, instrumentation, processing and evaluation of induced vibrations, in structures of interest. A subway traffic induced vibration signal contains a broad frequency range from 1 to 100 Hz, it consists of small displacement amplitudes, of 1 to 200 μm, a particle velocity range of 0.2-50 mm/s and particle accelerations from 0.002g to 0.1g [ISO 4866:1990/Amd 2:1996 2010]. Here, is noted that earthquake signals have a lower frequency bandwidth, from 0.1 Hz to 30 Hz, displacement amplitudes of 10 to 10^5 μm, a particle velocity range of 0.2-400 mm/s and a range of particle accelerations 0.002-2g [ISO 4866:1990/Amd 2:1996 2010]. Regarding the effect on structures, traffic induced vibrations are considered permanent and intermittent effects, in which a sequence, sometimes regular, sometimes irregular, of transient vibrations occurs. Starting and finishing times, between successive events, are distinct, with intermediate periods of insignificant

vibration levels, and the duration is daily, with several events [ISO 4866:1990/Amd 2:1996 2010 and BS 7385-2:1993].

Parameters that influence the nature of generated underground railway vibrations are the stiffness of the vehicle suspension system, the rail support system, the mass and stiffness of the guideway structure and the stiffness, depth and layering of the soil layers that surround the metro tunnel [Andrews et al. 2013]. Parameters that influence a building's response to ground-borne vibrations are: (a) The type of building, i.e., the dimensions, the structural system and the material properties. Induced vibrations by traffic can be amplified within the building, according to its proportions and mass. Also, the distance from the source is of primary importance; (b) The building's dynamic properties, i.e., modes of vibration and damping. Dynamic magnification, under imposed vibrations, can occur if the resonant frequency of the structure or of individual components is in the band of excitation frequency [BS 7385-2:1993]. Resonant frequencies of individual structural components, such as columns, walls, floors, beams and ceilings, are usually higher than the dominant global frequency. Thus, specific parts of a building can be more susceptible to resonance, displacement amplification and potential damage, than the whole structure. Most residential structures have natural frequencies between 4 and 24 Hz [Siskind et al. 1980 and Konon 1985], but historic structures, with heavy walls, would typically tend to the lower bound of this range, often even lower, given pre-existing damage and deterioration. Considering code specifications, the fundamental frequency of the structure, as approximated in §4.3.3.2.2 EN 1998-1:2004, is inversely related to the height of the building and can reach as low as 1 Hz. In fact, low natural frequencies are associated with lower stiffness properties and typically large particle displacements; (c) The level of exposure, regarding the duration and the number of cycles. Cumulative effects in terms of fatigue are to be considered at high response levels and long exposure times [Konon 1985]. Yet, no specific guidelines are present in design codes, related to fatigue damage from induced vibrations, and such a justification can be validated only from additional references and oriented research. Especially for historic structures, in order to obtain references of potential fatigue damage from induced vibrations, research of long-term and low-level vibrations should be conducted, for a range of 10^5-10^{10} number of cycles [DIN 4150-3 2016 and Casas 2009]; (d) The soil type can affect the input frequency spectrum. Soft soils predominantly transmit vibrations with the greater energy content in low frequencies, whereas the opposite occurs in stiff soils or rocks [ISO 4866:1990/Amd 2:1996 2010].

Indicative vibration levels are assessed through different national standards and against criteria for damage on structural and non-structural components [Thompson et al. 2009]. Empirical indexes of kinetic quantities, based on numerous studies, have linked the vibration severity to each type of structure and its dynamic response (frequency and damping), as well as the duration and frequency content of the vibration input [ISO 4866:1990/Amd 2:1996 2010]. Buildings of cultural heritage are under special consideration and specific case-defined criteria are set. However, high variability is found, among criteria from different standards. Upper limits are set in values of peak particle velocities (ppv) in units of mm/s, that are meant to be compared with in situ measurements. In steady-state and transient vibrations, velocity is linearly linked with vibration energy, therefore with stresses and strains. Thus, when measuring vibrations in buildings, it is recommended that the velocity is to be taken as the primary measurement [DIN 45669-2:1995-06]. In addition, when recording the vibration velocity over time, information can also be gained concerning vibration displacements or acceleration time-histories. In case of recorded signals in terms of accelerations, an integration process would determine velocity and displacement signals, as explained in Andrews et al. 2013, but the process must be carried out carefully, since the acceleration amplitudes can be easily affected by digitizing and low noise contamination problems.

In many standards, acceptable vibration limits differ, according to the dominant vibration frequency range. Here is noted that vibrations with high energy content in low frequencies (below 30 Hz) are particularly problematic, since dominant natural frequencies of most residential buildings are below that limit [Siskind et al. 1980, Konon 1985 and EN 1998-1:2004]. Issues of importance and of increased complexity, are related to effects on the load-bearing capacity, mostly regarding fatigue. Also inflicted damage of cosmetic components is of importance.

Decibel levels (dB), which are commonly used for noise control measurements, can also be used for ground-borne vibration assessment in conjunction with peak particle velocities, i.e., vibration decibels (VdB) [Thompson et al. 2009, Peterson 1980 and Hanson et al. 2006]. The relation between vibration decibels VdB and vibration levels is expressed logarithmically by scaled ratios of vibration amplitudes, under a reference level, as presented in Equation 46 [Peterson 1980 and Saurenman et al. 1982]. Here, $\mathrm{L_{dB}}$ is the signal level in VdB, $\mathrm{L_1}$ is the vibration level in acceleration, velocity, or displacement units and $\mathrm{L_{ref}}$ is the chosen reference level. The reference value is then set equivalent to 0 VdB, i.e., in a level of 10^{-5} mm/s as specified in [Hanson et al. 2006], which is sufficiently small and all measurements will result in positive VdB numbers. Here

is noted that an increase in a level of 6 dB represents a doubling of the amplitude of a kinetic quantity, while a change of 20 dB represents a change in the vibration level by a factor of ten.

$$L_{dB} = 20 \log_{10} \frac{L_1}{L_{ref}} \quad \text{Equation 46}$$

4.2.2. Data acquisition planning

Prior to monitoring, a building inspection and diagnostic process should precede, namely a documentation of the observed damage, in terms of cracks. Crack long-term observations and monitoring can reveal trends of damage propagation, which can be further linked with induced vibrations. Yet, ambient variations shall be studied first. Criteria regarding measurements of vibrations in situ involve specific instrumentation and a setup planning methodology, i.e., vectorial components and location selection. Monitoring acquisitions require preferably the use of velocity transducers (geophones), at relative low frequency bandwidths, i.e., 1-200 Hz. According to the current evaluation process, a kinetic quantity, namely the peak particle velocity (ppv) is used as an empirical indicator, and monitoring data are compared with absolute peak limits for each kind of building, i.e., a peak-to-peak level analysis. Instead, in SN 640312A:1992, the determining factor for assessing the potential damage under induced vibrations is the maximum vector of velocity V_R, in mm/s. The norm of the three orthogonal velocity directions (v_x, v_y and v_z) is given by Equation 47. The dominant frequency is the one associated with the greatest amplitude.

$$|V_R| = \sqrt{v_x^2 + v_y^2 + v_z^2} \quad \text{Equation 47}$$

Permissible vibration bounds in terms of peak particle velocities, from various standards, with a focus on cultural heritage buildings, are presented in Table 17. Many of those damage indexes were obtained under a probabilistic process, with 5% probability of damage occurrence [ISO 4866:1990/Amd 2:1996 2010 and BS 7385-2:1993]. Thresholds refer mostly to the event of minor damage (serviceability limit state) and for the event of structural damage with continuous cracks, expected values of ppv should exceed several times the indicative ones [DIN 4150-3 2016 and National Research Council 1977]. In fact, as specified in Saurenman et al. 1982 and National Research Council 1977, a vibration limit beyond which a building is prone to adverse structural damage is set at around 25 mm/s. In steady-state vibrations associated with highly sensitive

buildings, i.e., damaged monuments and ruins, the abovementioned limit can be much lower, even reaching a limit of 1.3 mm/s [National Research Council 1977]. For higher exposure vibration rates, advanced structural analyses are advisable, focused on damage accumulation and 2nd order effects, in order to conclude on safety levels [National Research Council 1977]. Yet, ground-borne railway induced vibrations are generally low and levels associated to structural damage are rarely reached. In fact, high vibration levels would be practically intolerable to occupants, regarding annoyance and disturbance levels.

Table 17. Peak particle velocity limits for historic structures from various standards.

Type and condition of structure	Vibration source/type	Description	Dominant vibration frequency range (Hz)	Peak particle velocity (mm/s)	Indicator	Reference	Country
Structures of particular sensitivity to vibration and of great intrinsic value (e.g. listed buildings under preservation order)	Short-term	Vibrations at foundation level	1-10	3	$\lvert V_{max} \rvert$	DIN 4150-3 2016	Germany
			10-50	3-8			
			50-100	8-10			
		Vibration at a horizontal plane of highest floor	-	8	$\lvert V_{max} \rvert$		
	Long-term	Vibration in horizontal plane of highest floor	-	2.5	$\lvert V_{max} \rvert$		
Historical buildings or under protection	Occasional Frequent	Measures vibrations at foundation level	<30	1.5-3	$\lvert V_R \rvert$	SN 640312A 1992	Switzerland
			30-60	2-4			
			>60	3-6			
Historical buildings under state protection	-	Vibrations at highest level	Wave speed (m/s)			GB/T 50452 2008	China
			Brick <1600	0.15	$\lvert V_{max} \rvert$		
			Brick 1600-2100	0.15-0.2			
			Brick >2100	0.2			
			Stone <2300	0.20	$\lvert V_{max} \rvert$		
			Stone 2300-2900	0.20-0.25			
			Stone >2900	0.25			
			Timber <4600	0.18	$\lvert V_{max} \rvert$		
			Timber 4600-5600	0.18-0.22			
			Timber >5600	0.22			

$\lvert V_{max} \rvert$: Absolute peak particle velocity in any direction

$\lvert V_R \rvert$: Maximum amplitude of velocity vector

In BS 5228-2:2009+A1:2014 three mutual perpendicular components need to be measured simultaneously at each location, with the ppv, the maximum value of any of the three components, used as an indicator for the evaluation on potential damage levels. The orientation of the transducers should match the principal axes of the structure. Fixing of transducers on surfaces that have additional coverings can provide distorted results and should be avoided. Thus, coupling should be made in the actual rigid surface of the structural element. If more than one setup is to be used, one common reference point should be chosen, close to the foundation level and close to the source of vibration [DIN 4150-3 2016 and BS 5228-2:2009+A1:2014].

A representative number of cycles should be monitored, in order for the obtained ppv values to be representative of at least 16 h at daytime or 8 h of night-time operational period [BS 5228-2:2009+A1:2014]. The sampling frequency of the acquisition data needs to be high enough, in order to eliminate any aliasing effects, especially for post-processing purposes. According to the Shannon's theorem, the sampling frequency should be at least twice the highest frequency of interest for the acquired data, i.e., the Nyquist frequency [Rouphael 2009]. Still, when a signal is subjected to integration and/or differentiation, non-smooth transitions between sample points can highly reflect on aliasing and miscellaneous errors. Thus, the sampling frequency should be relatively high, i.e., at least 500 Hz. According to Worden 1990, a sampling frequency of ten times the highest frequency of the signal is advised.

The selection of monitoring points depends mainly on the size and complexity of the building. According to BS 5228-2:2009+A1:2014 and DIN 4150-3 2016, primary monitoring locations are on the lowest story of the building, close to the foundation level of the outer wall, to 0.5 m from the ground level, and on the side of the building facing the source of vibrations. Preferably, measurements are to be taken also on the exterior, near the vibration source. In buildings of large size, simultaneous measurements at several points within the building, can serve to establish transfer functions [ISO 4866:1990/Amd 2:1996 2010 and DIN 45669-2:1995-06].

The propagation of vibrations through buildings is complex, with attenuation or amplification functions, and depends on the direction of propagation, the relative stiffness between structural elements, and the frequency content of the vibration signal [Saurenman et al. 1982]. The horizontal components of vibrations might be amplified in elevation, especially in buildings with more than one story, whereas the vertical component can be amplified in horizontal planes, towards the mid-points of suspended floors [DIN 4150-3 2016 and BS 5228-2:2009+A1:2014].

For medium size masonry buildings on spread footings with 1-4 stories, empirical data have shown that vibration levels at the base of the building, compared to locations immediately outside, are about 5-10 VdB (≈ x2-x3) lower. Instead, for the case of large masonry buildings on spread footings, the abovementioned difference increases to about 15 VdB (≈ x5) lower. When vibration levels are compared solely within the building, e.g., floors (i.e. slabs on columns) are subjected to increased vibrations by up to 10 VdB (≈ x3). However, following vertical alignments in multi-story buildings, starting from the base and moving upwards, vibrations are generally attenuated by about 3 VdB from (≈ x0.7), between floors [Saurenman et al. 1982]. As stated in BS 5228-2:2009+A1:2014, if a building is higher than 12 m, measuring points should include points at the highest level. In buildings of large spans, measurements should be taken at horizontal intervals of about 10 m [BS 5228-2:2009+A1:2014].

In general, it is rather difficult to associate structural damage in buildings, solely to imposed vibrations. Crack formation may be initiated by shocks, but, additionally, would most probably further increase existing cracks or those that would most likely appear in the course of time (e.g. due to soil settlements). A potential effect of damage, arising from vibrations, can be considered solely if a building is in a very unstable and vulnerable state, e.g., buildings subjected to prior damage from large differential settlements or in ruins [DIN 4150-3 2016 and BS 7385-2:1993]. Yet, vibrations of high amplitude and intensity, can provoke damage, most likely linked with cosmetic and decorative elements, i.e., initiation or extension of cracks in plasterwork, and fall of plaster, roof tiles and chimney pots [BS 5228-2:2009+A1:2014]. Cracks are normally differentiated between superficial, affecting the aesthetic qualities of a building, and structural cracks [National Research Council 1977]. Regarding their width, they can be described as shown in Table 18. According to ISO 4866:1990/Amd 2:1996 2010, damages in buildings can be classified within three main categories; *cosmetic damage*, with hairline cracks in the plaster, drywall surfaces and mortar joints; *minor damage*, with large cracks or loosening and falling plaster or drywall surfaces, or cracks through bricks and blocks; *major damage* in structural elements, with loosening of joints and widespread masonry cracks.

Table 18. Distinction between cracks, regarding their width w [SN 604312A:1992].

Fine cracks	w ≤ 0.2mm
Medium cracks	0.2 mm ≤ w < 1 mm
Wide cracks	1 mm ≤ w < 3 mm
Open cracks	w ≥ 3mm

4.3. Field monitoring in the Church of the Angels

The current work discusses the structural performance of the Church of the Angels (Igreja dos Anjos), located on the Almirante Reis Avenue, in Lisbon. The Green line of the Lisbon Metro is aligned to this avenue, in close proximity to the church. In fact, vibrations from passing trains are easily perceivable when inside the church. Ambient and ground-borne vibration tests from the underlying metro lines were carried out in November 2016 and in November 2017, by the University of Minho. The main objective was to measure the amplitudes of kinetic quantities during the metro operation and compare them with limits from international standards. Obtained results from dynamic identification tests and measurements of induced vibrations are used for assessing the structure at current state.

4.3.1. Historic perspective

The Church of the Angels, in Lisbon, designed by architect José Luís Monteiro. The original church, located in close proximity, was demolished in 1908 due to the city's transportation network expansion. The proportions and general configuration respects those of the early church, with a neoclassical character, mostly characterized by its triangular pediment and a small oculus, as shown in Figure 53 [SIPA 2011].

The church is comprised of a single nave, covered by a barrel vault and rich baroque gilded carvings, characteristic of the baroque religious architecture in Portugal, of the 17th and 18th centuries. In specific, the interior barrel-vaulted ceiling is paneled with timber grid coffers and paintings with biblical motives [SIPA 2011]. The main façade is oriented to the west, with the main gate in the middle and with the presence of a timber choir-loft. In the rear east part of the church, a bell tower is situated, see Figure 53a.

As stated above, along the Almirante Reis Avenue and in close proximity with the building, the Green metro line passes. Signs of settlements are evident in the front part of the church, as

depicted in Figure 53b, together with perceivable vibrations during the metro operation. The metro line has been in operation since 1966 [Metro de Lisboa 2021]]. The church is constructed of stone masonry, with lime mortar, but the floor of the nave and the transept have been altered (1968-1971) in order to accommodate offices and teaching facilities. Thus, in the nave, the floor has been replaced with a reinforced concrete slab and columns, expanding the basement underneath, and an extra intermediate reinforced concrete slab and staircase were added in the transept, dividing the configuration in elevation in three floors. The plan and an image of the interior are given in Figure 53c and d.

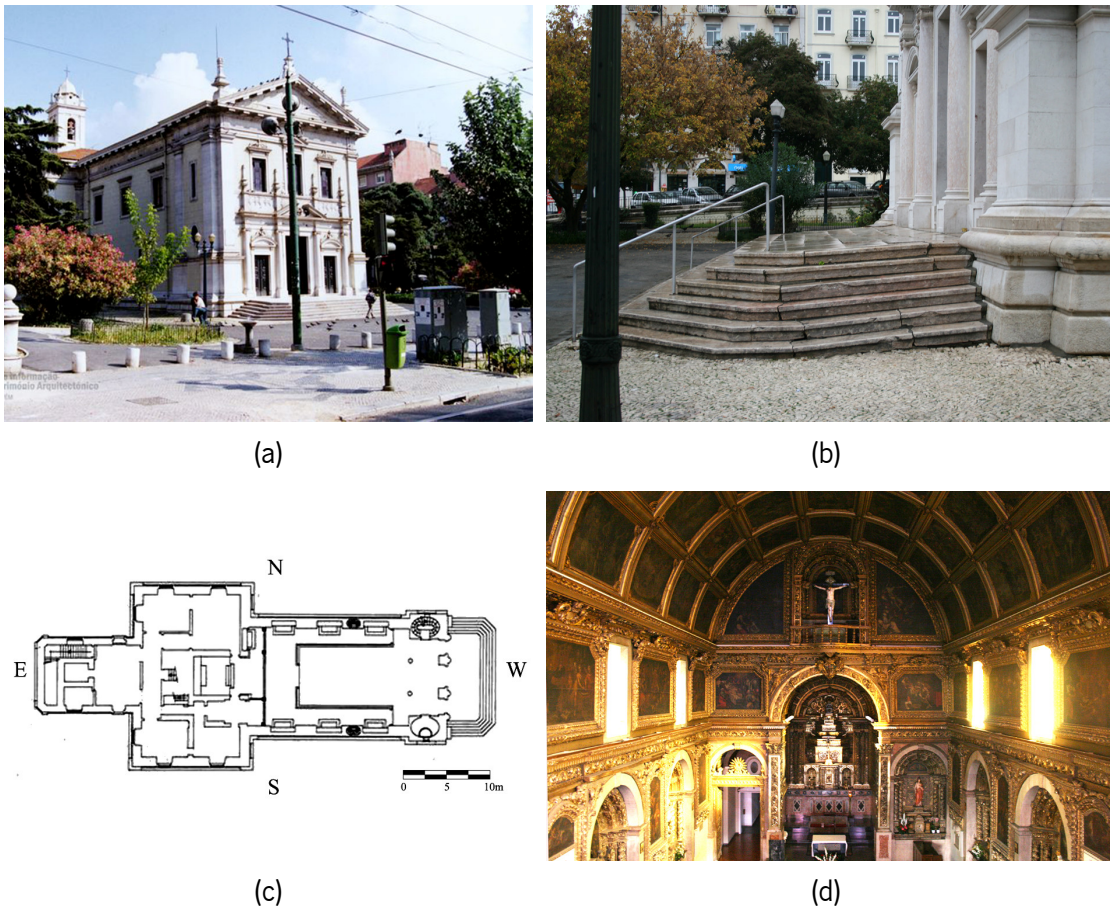


Figure 53. Church of the Angels: (a) view of the front façade [SIPA 2011]; (b) side view of the staircase, leading to the main entrance of the church, with evident signs of settlements; (c) plan view of the church [SIPA 2011]; (d) view of the nave and altar, looking east.

4.3.2. Ambient vibration tests

A monitoring strategy of long-term environmental effects, in buildings of cultural heritage, should allow to conclude on the current state and damage, and follow a combination of research and diagnosis tools as defined in the recommendations from ICOMOS/ISCARSAH Committee 2005. In specific, natural vibration modes of structures are directly linked with mechanical and

structural characteristics such as stiffness, mass, the connectivity between members and the boundary conditions [Ramos 2007]. For cultural heritage buildings, under a Structural Health Monitoring plan, ambient vibration tests, either continuous or intermittent, can be used to monitor the dynamic response of the structure, in conjunction with strong motion recordings, structural damage assessment, environmental parameters and anticipated changes within the service life, such as retrofitting techniques. Ambient vibration tests linked with structural assessment processes are presented in Pierdicca et al. 2019, Clementi et al. 2018, Saisi et al. 2015, Di Lorenzo et al. 2019, Clementi et al. 2017, Krstevska et al. 2010, Gentile et al. 2007, De Stefano et al. 2016, Rainieri et al. 2013, Cavalagli et al. 2018, Kita et al. 2019, Venanzi et al. 2019, Gentile et al. 2013, Gentile et al. 2016, Pierdicca et al. 2016, Tsogka et al. 2017 and García-Macías et al. 2019. Specifically, when the response of a structure is evaluated under the effect of induced vibrations, the definition of its dynamic properties is of relevance, i.e., vibration modes, frequencies, damping ratios and mode shapes.

Ambient vibration tests were carried out in November 2016 in the nave and transept of the Church of the Angels. For the ambient tests, monitoring acquisitions of triaxial electro-mechanical, force balanced recorders were used, i.e., three seismographers with GPS time base and relatively low frequency bandwidths, i.e., 1-200 Hz, with a dynamic measurement range of ± 1.0 g and a sampling rate range of 50-1000 Hz. Here, the frequency sampling was set to 200 Hz and the recording duration was equal to approximately 20-30 min. Many empirical rules exist on setting the data acquisition duration of ambient vibration testing (AVT). As a rule of thumb, a duration equal to 2000 cycles the longest period of the structure is sufficient, when using frequency domain techniques [Rodrigues 2004]. For historic masonry structures with heavy walls, the expected smallest natural frequency can reach values around 2 Hz. Thus, the calculated empirical duration for an AVT would be approximately around 17 min. Yet, in order to achieve a sufficient frequency resolution, especially for structures or modes not easily excited, and considering many practical aspects, such as the testing time limitations, the available number of sensors and the size of the building, an acquisition duration of at least 20-30 min is considered adequate for capturing the modes of vibration in cultural heritage masonry buildings.

The Operational Modal Analysis (OMA) was performed in the ARTeMIS software [SVS 2019], using the Stochastic Subspace Identification - Unweighted Principal (SSI-UPC) method. The SSI-UPC method aims to estimate the modal properties based on output only vibration tests, that

is dynamic identification tests in which only the vibration response is recorded during the service conditions of the structure. The SSI corresponds to a method with decomposition in the time domain, in which a parametric model is fitted directly to the raw time series data, and the SSI input matrix (compressed time series data) is weighted. In the UPC algorithm (Unweighted Principal Component algorithm), two different weight matrices, both of unit weight, are used [Ewins 2000 and Overschee et al. 1996]. Due to its simplicity, the SSI-UPC method, is found to perform better with modes of comparable energy levels [Shokravi et al. 2017]. The tests were carried out in three setups, with one seismographer, placed in the sill of the south-west window of the main façade in all setups for which the out-of-plane component of the first setup that presented the highest magnitude at the lowest identified frequency was used as a reference. The chosen monitoring points were in the main façade and on several other locations on the perimeter of the top floor of the transept (Figure 54). The geometrical model used - a representation of the structural configuration - contains the façade, the longitudinal and transversal walls of the nave and transept and the horizontal diaphragms, i.e., the choir floor, the barrel vault and floors at transept. In Figure 55, the position and direction of all the sensors in each setup are depicted. Given the complexity and large amplitude difference of the mode shapes from several preliminary trials, a few in-plane and all vertical components of recordings were discarded, in order to obtain sensible information regarding the mode shapes.



(a) (b)

Figure 54. Measuring equipment: (a) seismographers in the three windows of the main façade, in Setup 1; (b) close view of seismographer SO3 (Setup 1) placed in the south-west window of the main façade.

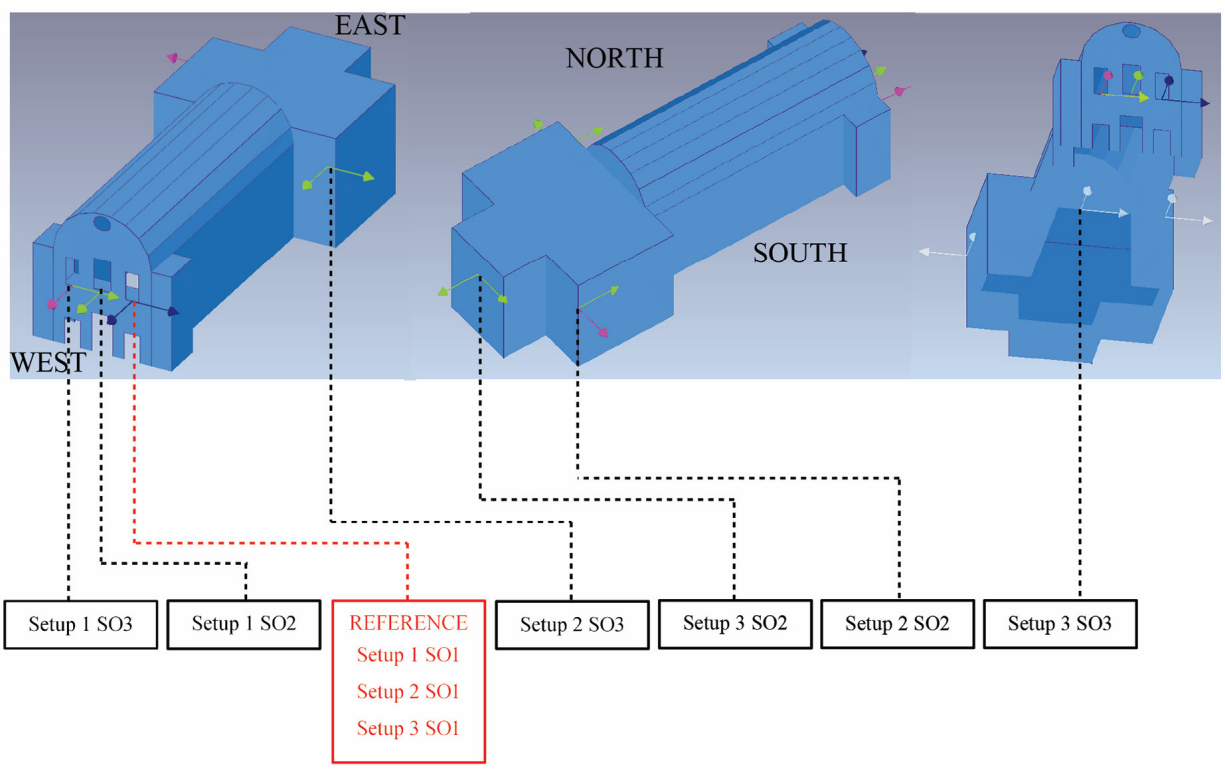


Figure 55. Disposition of seismographers in the performed setups, at the transept and chapels of the Church of the Angels.

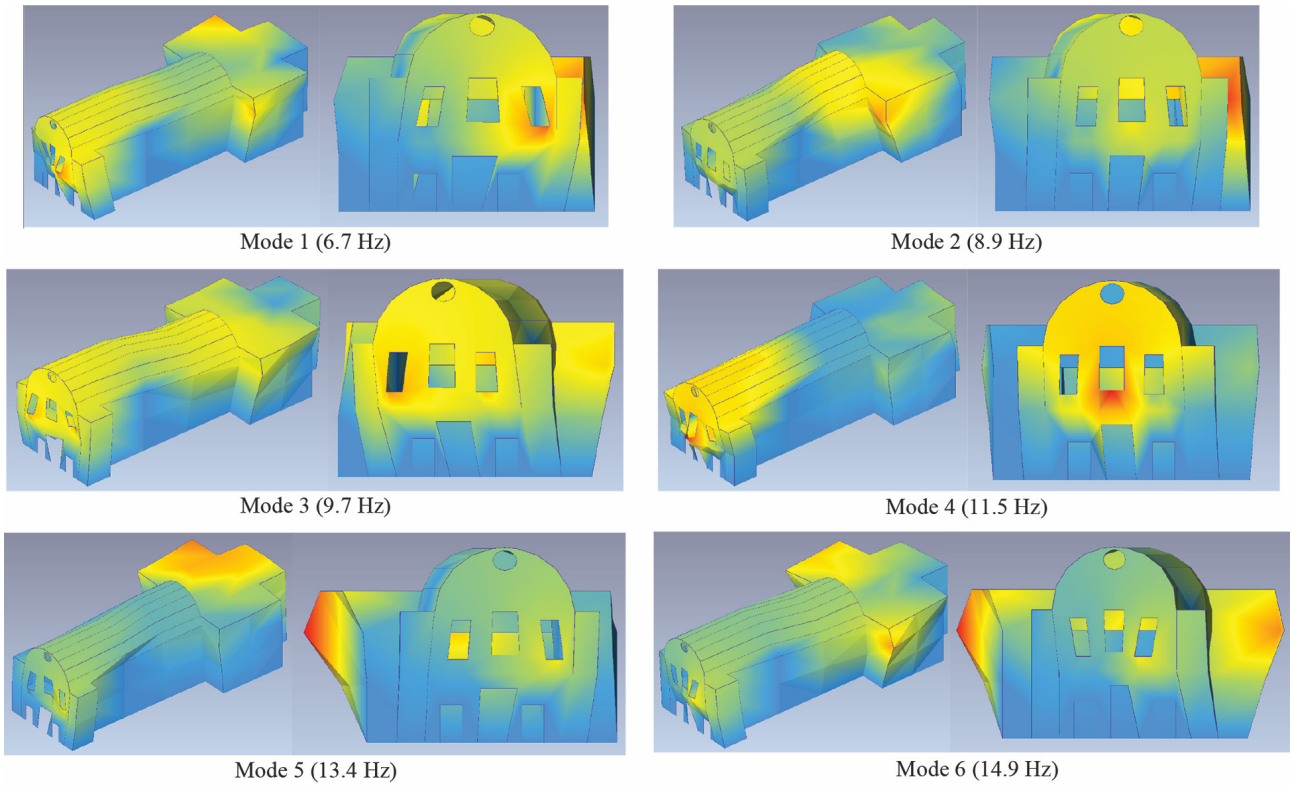


Figure 56. Mode shapes obtained from the SSI-UPC Method, of the first six modes, with interpolation [SVS 2019].

Table 19. Frequencies and damping ratios of the first six modal shapes with the SSI-UPC Method [SVS 2019].

Modes	Frequency [Hz]	Std. Dev. Freq. [Hz]	Damping Ratio [%]	Std. Dev. Damp. Ratio [%]
Mode 1	6.7	0.096	4.544	0.429
Mode 2	8.9	0.183	3.268	1.575
Mode 3	9.7	0.072	2.305	0.630
Mode 4	11.5	0.237	2.539	1.974
Mode 5	13.4	0.211	3.695	1.616
Mode 6	14.9	0.131	3.234	1.287

The first six modes were defined, and the frequencies and damping ratios are presented in Table 19. The frequencies and damping ratios of the modes range between 7 Hz and 15 Hz and between 2.3% and 4.5%, respectively. As can be seen from the configuration of the mode shapes in Figure 56, they are global, highly complex and exhibit large curvatures. Modes 1, 2, 3 and 5 are mainly transversal modes. In those modes the lateral walls of the nave and the entire transept engage in anti-symmetric out-of-plane deflections, along the north-south direction. For the lateral walls of the nave, the out-of-plane deflections are of 2nd and 3rd order of curvature. The main façade exhibits a combination of in-plane and out-of-plane excitation, with complex bending modes, of higher order. The only clear out-of-plane deflection mode, of single curvature, is Mode 4 (11.5 Hz) and involves only the main façade.

It is clear that even if the structure presents global modes, with several structural elements excited in similar frequencies, the response is non-uniform. This can be triggered by different stiffness characteristics, given also the extensive reconstruction process of the transept. According also to in-situ inspection, only few, minor micro-cracks were documented.

4.3.3. Acquisitions of induced vibrations with geophones

The monitoring campaign of ground-borne vibrations in the Church of the Angels was conducted in November 2017, with the use of a highly sensitive triaxial velocity meter (geophone), with a maximum measuring velocity range of +/-100 mm/s, a frequency range of 1-350 Hz, a sampling rate range of 50-2000 Hz, a dynamic measurement range of ±4.0g, with a resolution of 0.5 μg and noise levels within the range of around ±31-313 μg, depending on the frequency bandwidth (here under the maximum range of 10-1000 Hz). Acquisition points were chosen in vertical alignments and close to the main façade, which is in closer proximity to the metro line. In specific, data acquisitions were obtained from a location at the basement, three locations at the

floor level of the main entrance, two locations at the windowsills of the main façade and one location at the middle span of the timber choir floor. An additional external acquisition at the sidewalk level served as a reference point, in terms of assessing attenuating effects for amplitudes of velocities. All the above-mentioned acquisition points, uncorrelated in time, are presented in the schematic of Figure 57. Here, it is noted that only one geophone was available, meaning that independent recordings were planned in each location. According to BS 5228-2:2009+A1:2014, a peak-to-peak analysis will determine the maximum values and associated potential damage levels.

The choice of the sampling ratio highly reflects on the level of accuracy of the recorded digital signal, both in terms of amplitude and frequency content [Giron-Sierra 2018]. Sampling rate requirements should be defined both in time and frequency domain. First, the sampling rate should be high enough to cover the spatial frequency of the input wave. A sampling rate of $10 \cdot f_{sp}$ (Hz) is sufficient, where f_{sp} is the average measured spatial frequency of the vibration ground-borne signal. Here, the average measured spatial frequency of the recorded ground-borne vibrations is around 80 Hz (Table 20), thus a sampling rate of 800 Hz is considered sufficient. Second, and considering the Nyquist frequency, the minimum sampling rate should be at least twice the maximum frequency of the vibration wave with a significant energy content, in order to avoid aliasing. According to preliminary acquisitions, the frequency content of the vibration signal, was found within the range 30-200 Hz. For a noted upper frequency bound of 200 Hz (Table 20), a sampling rate of 400 Hz is considered sufficient. Further on, signals from single passing trains, as recorded in many locations and superposed under different sampling rates, presented in Figure 58, denote the loss of a smooth variation, as the sampling frequency decreases from 2000 Hz to 100 Hz. As a result, the corresponding captured maximum ppv was found to decrease by as much as 34%, solely as a result of the sampling rate. Thus, in order to capture accurately vibration profiles, accounting also the recommendations stated in section 4.2.2, the sampling rate for the uncorrelated recordings with the geophone was set at 1000 Hz. Vibration recordings were taken in frequent intervals, with time duration setups of half an hour. During the acquisitions, the church was not in operation, thus any internal noise was minimized. Time periods with no metro operating (01^{00}-06^{30} am) were also recorded, in order to obtain a base reference for comparison.

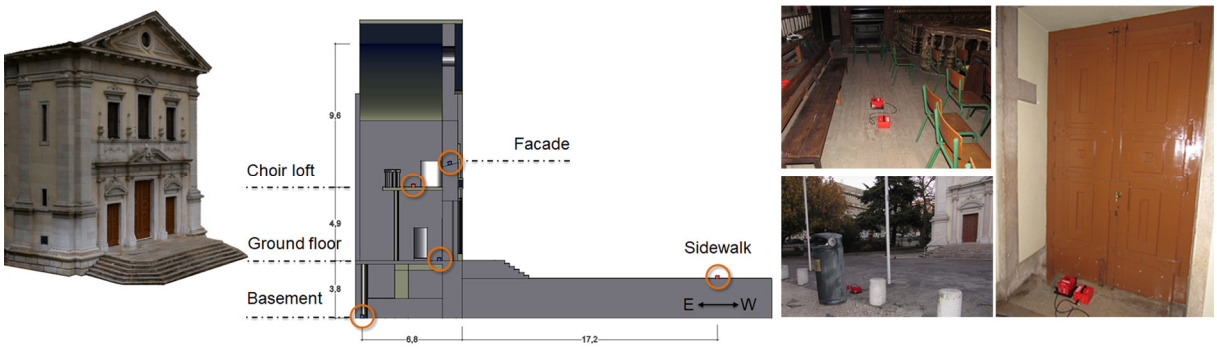
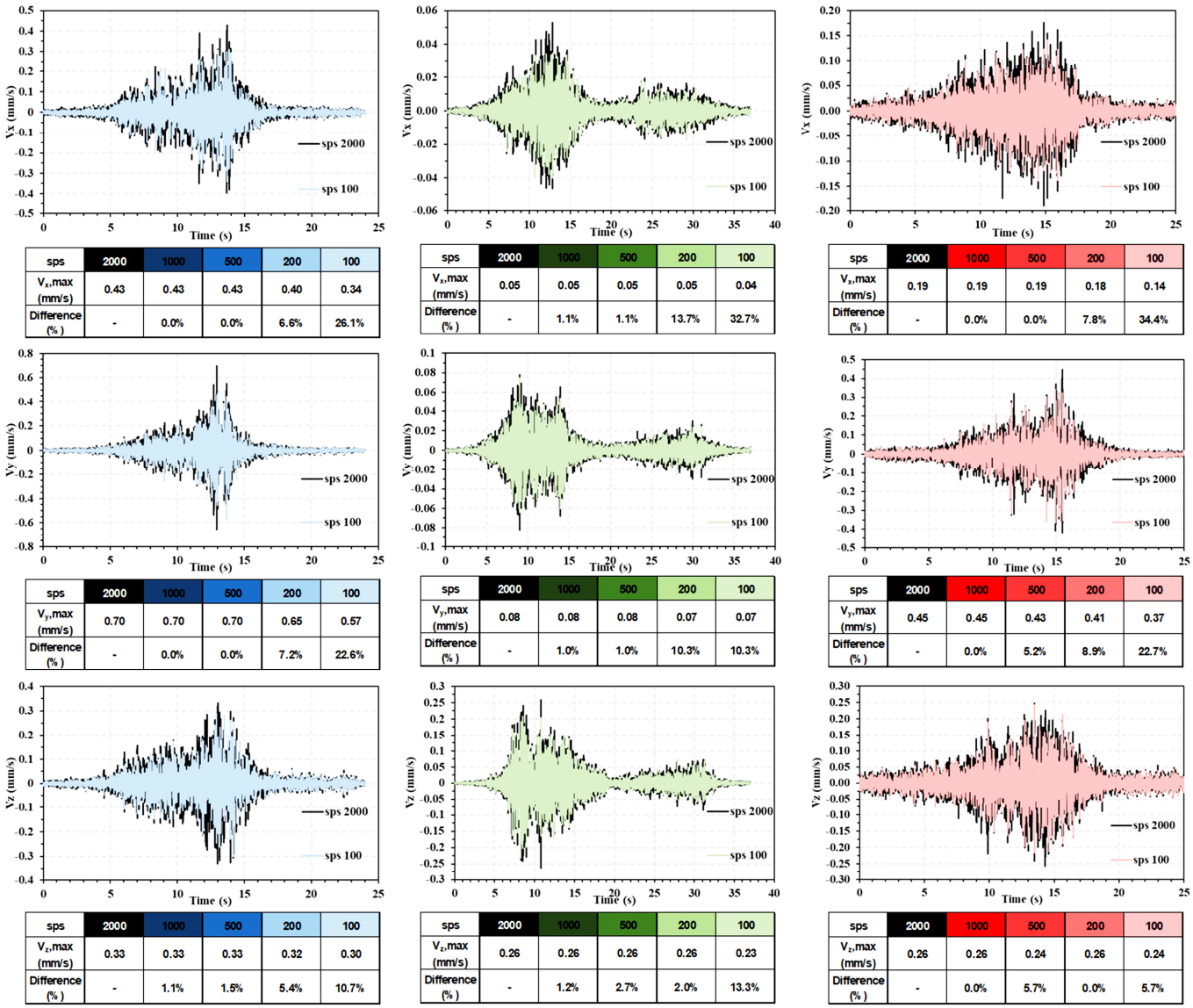


Figure 57. Different monitoring points, uncorrelated in time, at the basement and at intermediate heights in the front end of the Church of the Angels. Note the reference point near the source of vibration, at the level of the sidewalk.



sps	2000	1000	500	200	100
V_x,max (mm/s)	0.43	0.43	0.43	0.40	0.34
Difference (%)	-	0.0%	0.0%	6.6%	26.1%

sps	2000	1000	500	200	100
V_x,max (mm/s)	0.05	0.05	0.05	0.05	0.04
Difference (%)	-	1.1%	1.1%	13.7%	32.7%

sps	2000	1000	500	200	100
V_x,max (mm/s)	0.19	0.19	0.19	0.18	0.14
Difference (%)	-	0.0%	0.0%	7.8%	34.4%

sps	2000	1000	500	200	100
V_y,max (mm/s)	0.70	0.70	0.70	0.65	0.57
Difference (%)	-	0.0%	0.0%	7.2%	22.6%

sps	2000	1000	500	200	100
V_y,max (mm/s)	0.08	0.08	0.08	0.07	0.07
Difference (%)	-	1.0%	1.0%	10.3%	10.3%

sps	2000	1000	500	200	100
V_y,max (mm/s)	0.45	0.45	0.43	0.41	0.37
Difference (%)	-	0.0%	5.2%	8.9%	22.7%

sps	2000	1000	500	200	100
V_z,max (mm/s)	0.33	0.33	0.33	0.32	0.30
Difference (%)	-	1.1%	1.5%	5.4%	10.7%

sps	2000	1000	500	200	100
V_z,max (mm/s)	0.26	0.26	0.26	0.26	0.23
Difference (%)	-	1.2%	2.7%	2.0%	13.3%

sps	2000	1000	500	200	100
V_z,max (mm/s)	0.26	0.26	0.24	0.26	0.24
Difference (%)	-	0.0%	5.7%	0.0%	5.7%

(a) (b) (c)

Figure 58. Isolated, uncorrelated signals of passing underground trains, recorded in the level of the sidewalk (a), the basement (b) and the middle span of the choir loft floor (c). Note the vectorial components, the different sampling rates (sps) in color coding and the difference between maximum values.

Table 20. Ground-borne vibration levels and attenuation compared within the building. Note the reference of zero VdB at the level of the sidewalk.

Location	max PPV (mm/s)	max V_R (mm/s)	Frequency content[1] (Hz)	Spatial wave frequency[2] (Hz)	ΔVdB[5] attenuation
Choir loft Timber floor	0.42[3]	0.44[3]	x-x 30-200 y-y 30-200 z-z 30-200	76.9	4
Choir loft Facade windows	0.12[4]	0.13[4]	x-x 30-110 y-y 30-200 z-z 30-200	125	15
Ground floor	0.11[4]	0.12[4]	x-x 30-150 y-y 30-160 z-z 30-100	66.7	16
Basement	0.27[3]	0.27[3]	x-x 30-160 y-y 30-160 z-z 30-125	66.7	9
Sidewalk (Ref.)	0.65[3]	0.72[3]	x-x 30-100 y-y 30-100 z-z 30-100	71.4	0

[1] Refers to the maximum frequency range
[2] Refers to the number of cycles per second of the raw signal
[3] Refers to the confidence interval for 90% probability of exceedance for ppv≥0.05mm/s
[4] Refers to the confidence interval for 90% probability of exceedance for ppv≥0.025mm/s
[5] Refers to the maximum velocity vector V_R

Vibration signals converted to the frequency domain are complex and can be mathematically represented with a real and an imaginary part, highlighting aspects of magnitude and phase response. The main objective when discussing on the severity of induced vibrations is set on capturing the magnitude, in each vectorial component, i.e., in the N-S direction or x-x, the E-W direction or y-y and the vertical direction or z-z. Here, it is noted that the N-S and the E-W directions follow the alignment of the transversal and longitudinal walls of the church respectively (Figure 53c and Figure 57). Basic signal processing operations, both in time and frequency domain, involve cleaning, filtering and further processing. A raw signal can contain many disturbances, trends and unwanted frequency contents that need to be treated, while at the same time, preserving the information of interest. Many times, due to secondary sources of induced noise or vibration, certain parts of a signal, when identified, better to be cropped from the start. In the case where intermittent disturbances are present, distributed in the time domain, the only possible way to remove them is through digital filtering in the frequency domain, provided that they contain a distinct frequency bandwidth and different from the source of interest.

First, a recorded signal is often sensitive to disturbances from power line sources, which introduce systematic trends, i.e., mostly low-frequency drifts, approximated as a linear or quadratic

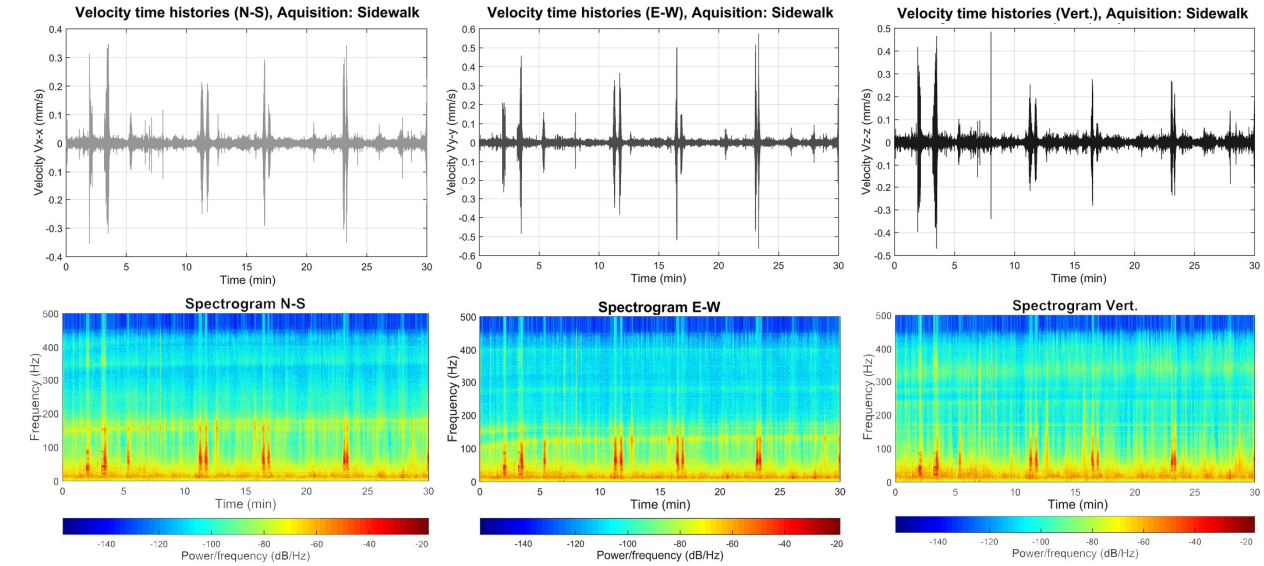
function in time [Brandt 2011]. Thus, initially, the recorded signals are processed through detrending, by means of a simple linear regression analysis, removing a mean value from the data. Alternatively, a high pass filter can be applied to the entire signal, under a low frequency passband, i.e., 1 Hz. Second, the recorded vibration intensity is identified both in the time and frequency domain, through spectrograms, i.e., a 2D or 3D color plot of short fast Fourier transforms (FFT) in time. Since ground-borne vibration related frequencies are under high energy content and vary in time, they are easily identified through a spectrogram, superposed with the velocity-time history plot, as shown in Figure 59a. Here, high color intensity dictates high power levels. Color profile distinct bands are quite clear during the passing instants, at which the vibrations from the passing trains occur. Though, in a vibration signal, many different frequency components coexist, i.e., natural frequencies, mechanical and electrical noise. The latter do not vary in time and are visualized as color bands of high intensity, constant in time, thus can be easily identified and removed.

In order to examine the signal solely in the frequency domain, under an FFT, the recorded signal is deconstructed in its individual sine wave components and the vibration amplitudes are expressed as a function of frequency, i.e., the power spectral density graph (PSD). Here, the real only spectrum of amplitudes is computed in dB^2, normalized to the half of the sampling frequency, i.e., 1000 Hz. The Welch's method for computing the PSD is used, which reduces variance of the spectral density, by breaking the signal into overlapping segments. A Hanning window is chosen, with long window segments of 2048 points, which results in greater resolution. Here, it is noted that the adopted Hanning window is an extended version, with higher peak sidelobes and thus deeper attenuation in the frequency range [Oppenheim et al. 2014].

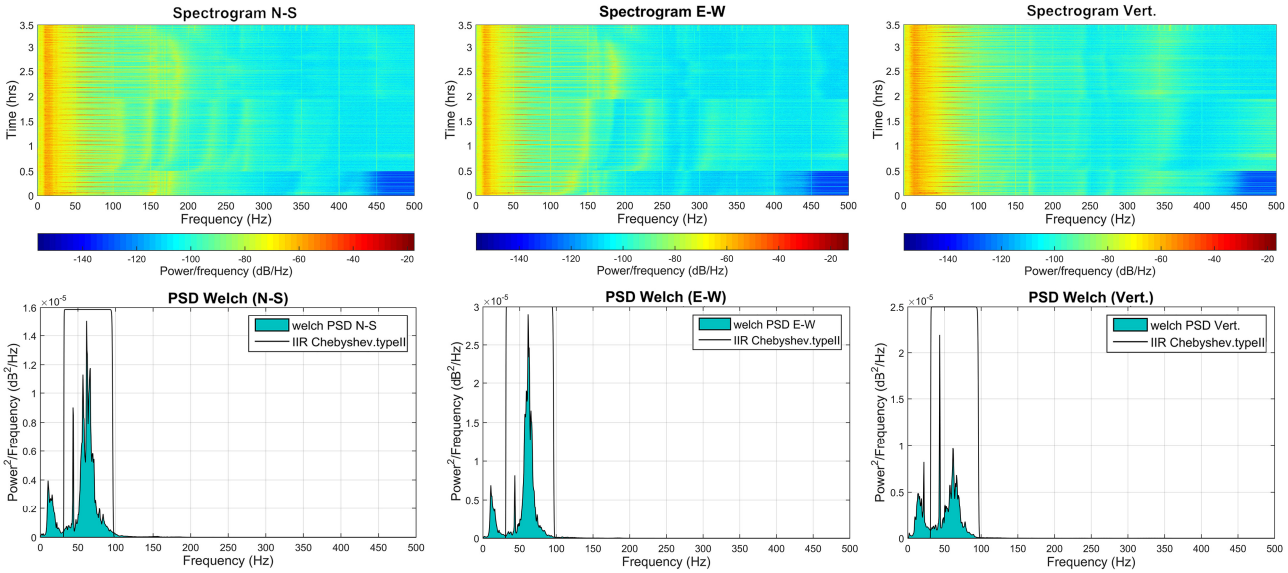
Any unwanted frequency components, which are not related to the ground-borne vibration source can be removed, through digital filtering. Since these vibrations normally exhibit a higher broadband frequency content than natural frequencies and low frequency noise, the latter can be cut-off by performing a band-pass digital filter. Yet, in cases of amplification due to resonance or a broader frequency content, no real method exists for choosing the actual range of the cut-off frequencies and distinguishing between actual data and other disturbances. Here, for each acquisition location and direction, and due to the closely located waveform and cut-off frequencies, a digital filter with the smallest transition width and equiripple stopbands is designed, namely a band-pass IIR Chebyshev Type II digital filter, of high order (i.e. 50^{th} order) [Oppenheim et al.

2014]. Each band-pass digital filter is applied, in order to produce a signal in the specified frequency bin, as defined in Table 20.

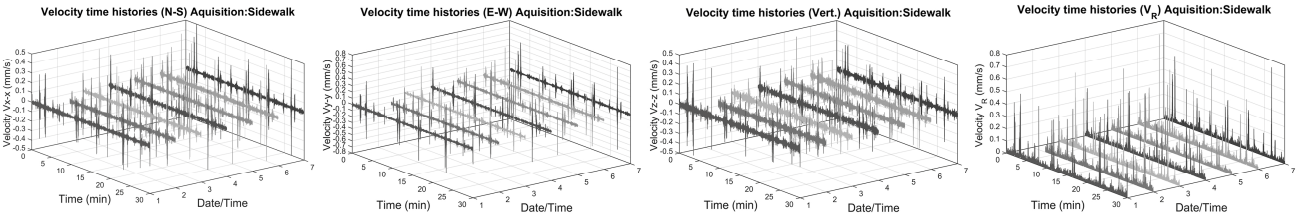
Regarding the obtained results from the acquisition at the sidewalk level, outside the Church of the Angels, clear peaks are detected, in time intervals of 3 to 5 min (Figure 59a), matching the time schedule of passing subway trains of the Green metro line [Metro de Lisboa 2021]. From the spectrogram of the detrended signals in all three directions, over an acquisition of 3.5 h, periodic peaks of high energy content are identified. These are clear signs from passing trains, versus constant frequencies below 30 Hz, which are associated mostly to natural frequencies. As presented in Figure 59b, by applying a band-pass IIR Chebyshev Type II digital filter, unwanted frequency bins are removed. From the filtered signals, a peak-to-peak analysis can be performed by examining the distribution of the signal data (Figure 59c). Under a statistical assessment of large data samples, the empirical cumulative probability plot (ECDF) is computed, and the absolute maximum value of velocity is delivered from a quantile associated to the complementary probability F(x) of 10^{-7}, i.e., 1-F(x), chosen considering the actual number of peaks, the sampling rate and the duration of the acquisition signal. Thus, the maximum velocity vector V_R is equal to 0.72 mm/s, with the highest component in the E-W direction, which indicates that the input signal, travelling through the soil continuum and measured in the ground surface, near to the metro line, is mainly through compression waves. This value can be used as a reference for monitoring of ground-borne vibrations within the building, which were found to attenuate.



(a)



(b)



$F(x) = 1\text{-}10^{-7}$, x = 0.42 mm/s $F(x) = 1\text{-}10^{-7}$, x = 0.65 mm/s $F(x) = 1\text{-}10^{-7}$, x = 0.44 mm/s $F(x) = 1\text{-}10^{-7}$, x = 0.72 mm/s

(c)

Date/Time 1: 13-Nov-2017 17:00, 2: 13-Nov-2017 17:55, 3: 13-Nov-2017 18:25, 4: 13-Nov-2017 18:55, 5: 14-Nov-2017 12:45, 6: 14-Nov-2017 13:15, 7: 14-Nov-2017 13:45

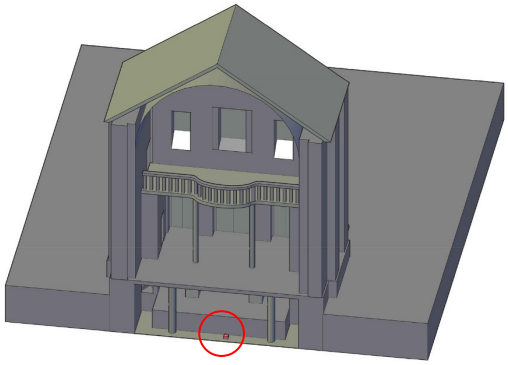
Figure 59. Data acquisition at the Church of the Angels, in the level of the sidewalk: (a) unfiltered triaxial velocity components of one acquisition (30min) and the corresponding spectrograms; (b) spectrograms of all unfiltered signals in three directions, during the entire acquisition (3.5 h), corresponding squared Welsh power spectral density graphs and band-pass Butterworth Chebyshev type II filter; (c) velocity-time history 3D plots, after filtering, for all three directions and velocity vectors V_R, for all setups. Note the absolute maximum ppv from the empirical cumulative distribution function and chosen quantile.

As an initial monitoring location inside the building of interest, a point in the basement was chosen, close the west wall of the front end, as shown in Figure 60a. Here, acquisitions with a total duration of 6.5 h were obtained. Part of the recordings were performed at early hours in the morning, without metro operation, which allowed to identify the constant frequency content cut-off of 0-30 Hz. Under the same filtering operations and statistical analysis, as described above, and a quantile from an ECDF plot, associated to the complementary probability F(x) of 10^{-6}, chosen according to the actual number of peaks, the sampling rate and the duration of the acquisition signal, for all acquisitions within the building, the maximum velocity values in the basement were found attenuated, equal to 0.27 mm/s. Here, the vertical component is prominent (Figure 60b).

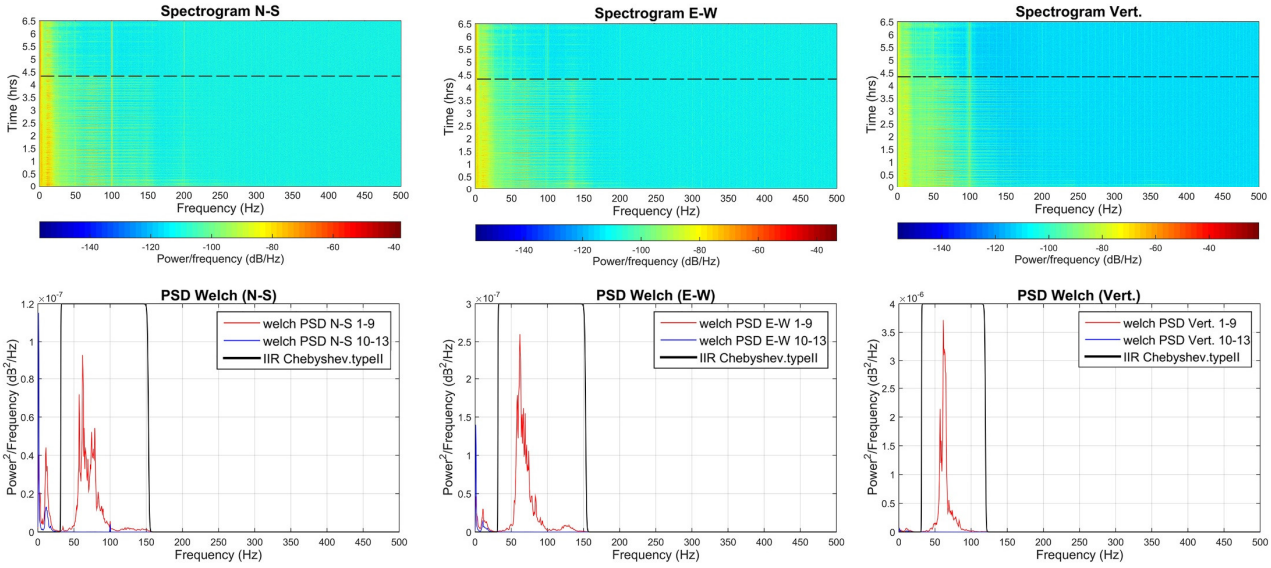
Moving to a higher position in the building, following a vertical alignment, various locations of the ground floor were preliminary assessed, near the front end of the church. As shown in Figure 61a, b and c, from the three selected locations at the front end, the one in the middle gate (Figure 61b), was found under higher amplitudes and was the one selected for monitoring. The frequency content of the input signal varies in each direction, mostly an indication of different stiffness properties and anisotropy, and covers a range of 30-160 Hz. The maximum recorded velocities are equal to 0.12 mm/s.

Further on, at the level of the 1st floor, two acquisition locations in the windowsills were chosen. Each sill surface was inclined, with an inclination angle of 36.8º and 16.6º, for the left and middle windowsill respectively (Figure 62). Thus, the signals obtained had to be rotated from the y-z plane of angle θ to the horizontal level. By identifying the frequency content of the ground-borne vibrations in each direction - within the range of 30-200 Hz -, the filtered signals present a maximum V_R velocity of 0.13 mm/s, similar to the one obtained in the ground floor (Figure 62).

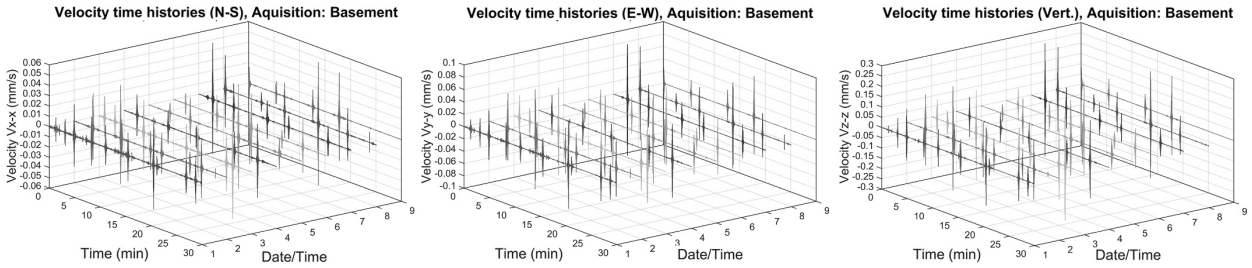
Finally, in the acquisition at the middle span of the choir loft timber floor, the frequency content of the ground-borne vibration signal is also within the range of 30-200 Hz (Figure 63a). As far as natural frequencies are concerned, those are below 30 Hz, and the vertical component presents a higher energy content, as expected, given the structural behavior and high deflection ratios of the floor (Figure 63a). After filtering, all three components are measured relatively amplified, with a documented maximum V_R velocity of 0.44 mm/s (Figure 63b).







(a)

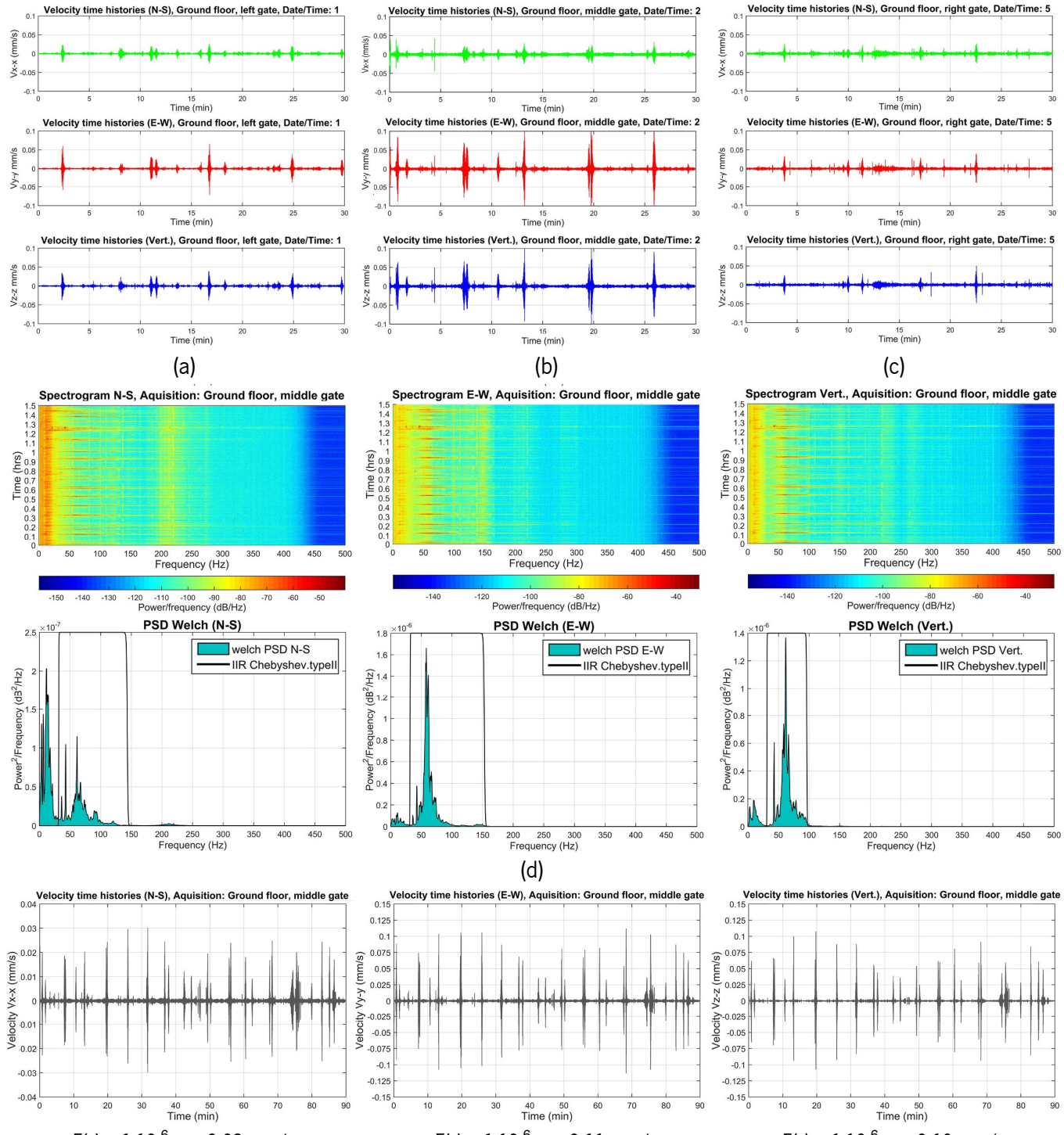


$F(x) = 1\text{-}10^{-6}$, x = 0.06 mm/s $F(x) = 1\text{-}10^{-6}$, x = 0.09 mm/s $F(x) = 1\text{-}10^{-6}$, x = 0.27 mm/s

(b)

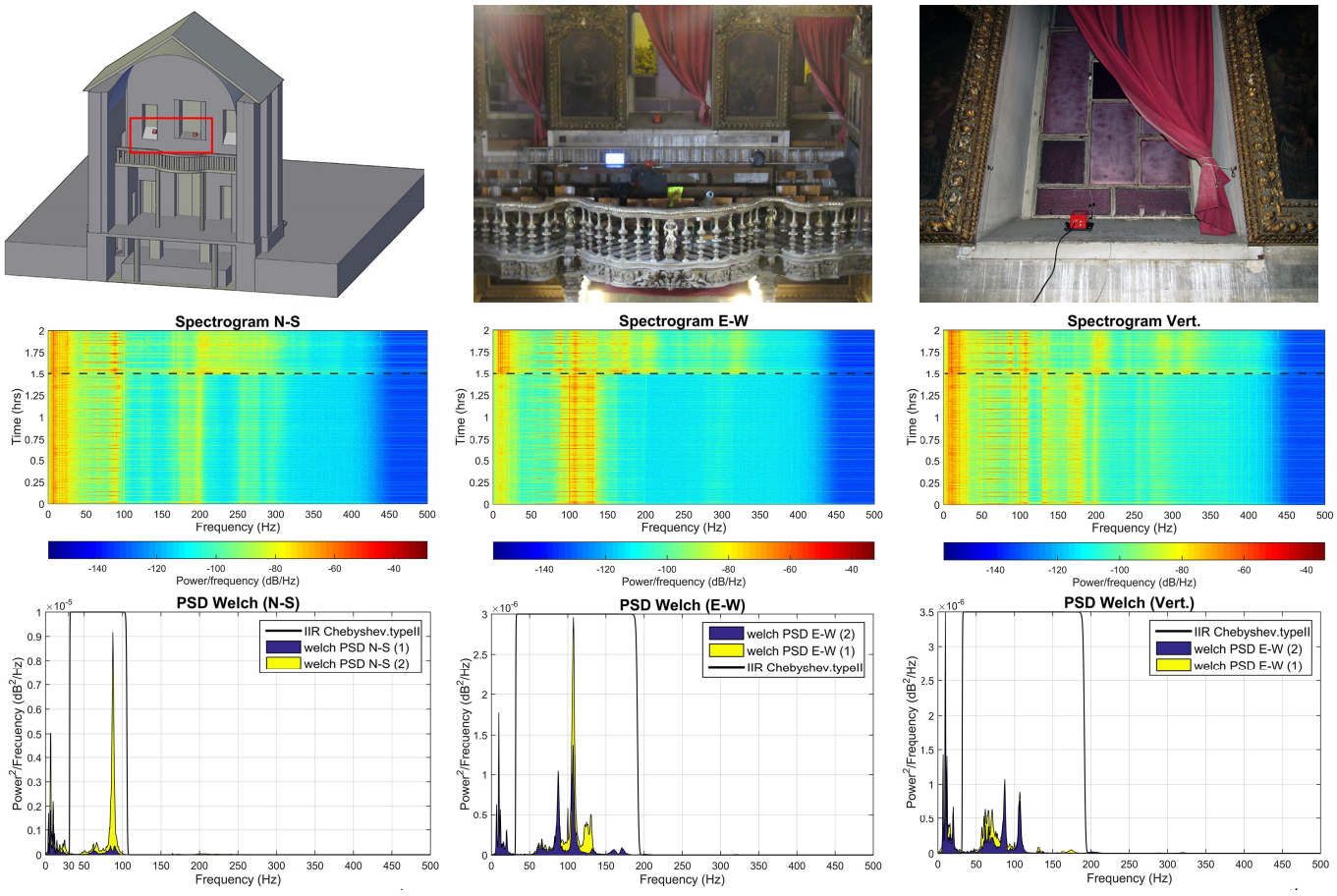
Acquisition date/time: 1: 13-Nov-2017 21:00, 2: 13-Nov-2017 21:30, 3: 13-Nov-2017 22:00, 4: 13-Nov-2017 22:30, 5: 13-Nov-2017 23:00, 6: 13-Nov-2017 23:30, 7: 14-Nov-2017 00:00, 8: 14-Nov-2017 00:30, 9: 14-Nov-2017 01:00, 10: 14-Nov-2017 01:30, 11: 14-Nov-2017 02:00, 12: 14-Nov-2017 02:30, 13: 14-Nov-2017 03:00

Figure 60. Data acquisition in the front end of the Church of the Angels, at the level of the basement: (a) spectrograms of all unfiltered signals in three directions, during the entire acquisition (6.5 h), corresponding squared Welsh power spectral density graphs and band-pass Butterworth Chebyshev type II filter. Note the division in 0.5 h increments, between acquisitions during operational passing trains (1-9) and during no operation (10-13), divided by a dashed line in PSD graphs; (b) velocity-time history 3D plots, after filtering, for all three directions, for all setups. Note the absolute maximum ppv from the empirical cumulative distribution function and chosen quantile.

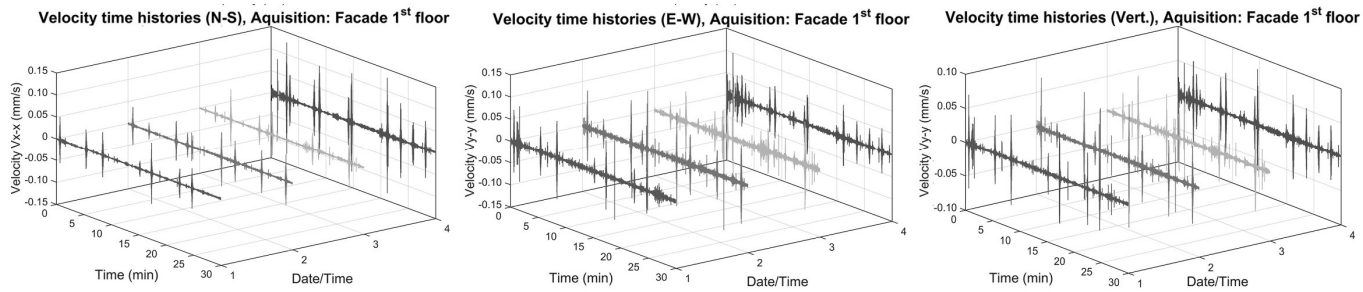


Acquisition date/time: 1: 13-Nov-2017 09:00, 2: (51)13-Nov-2017 14:35, 3: (52)13-Nov-2017 15:05, 4: (53)13-Nov-2017 15:35, 5: 12-Nov-2017 18:10

Figure 61. Data acquisition in the front end of the Church of the Angels, at the level of the ground floor. Comparative unfiltered velocity-time histories (30 min) plots in three locations of the ground floor; the left gate (a), the middle gate (b) and the right gate (c); (d) spectrograms of unfiltered signals (acquisitions 1-5), in the middle gate floor, in three directions, squared Welsh power spectral density graphs and band-pass Butterworth Chebyshev type II filter; (e) velocity-time history plots, after filtering, for all three directions, for all setups, in the middle gate floor. Note the absolute maximum ppv from the empirical cumulative distribution function and chosen quantile.



(a)

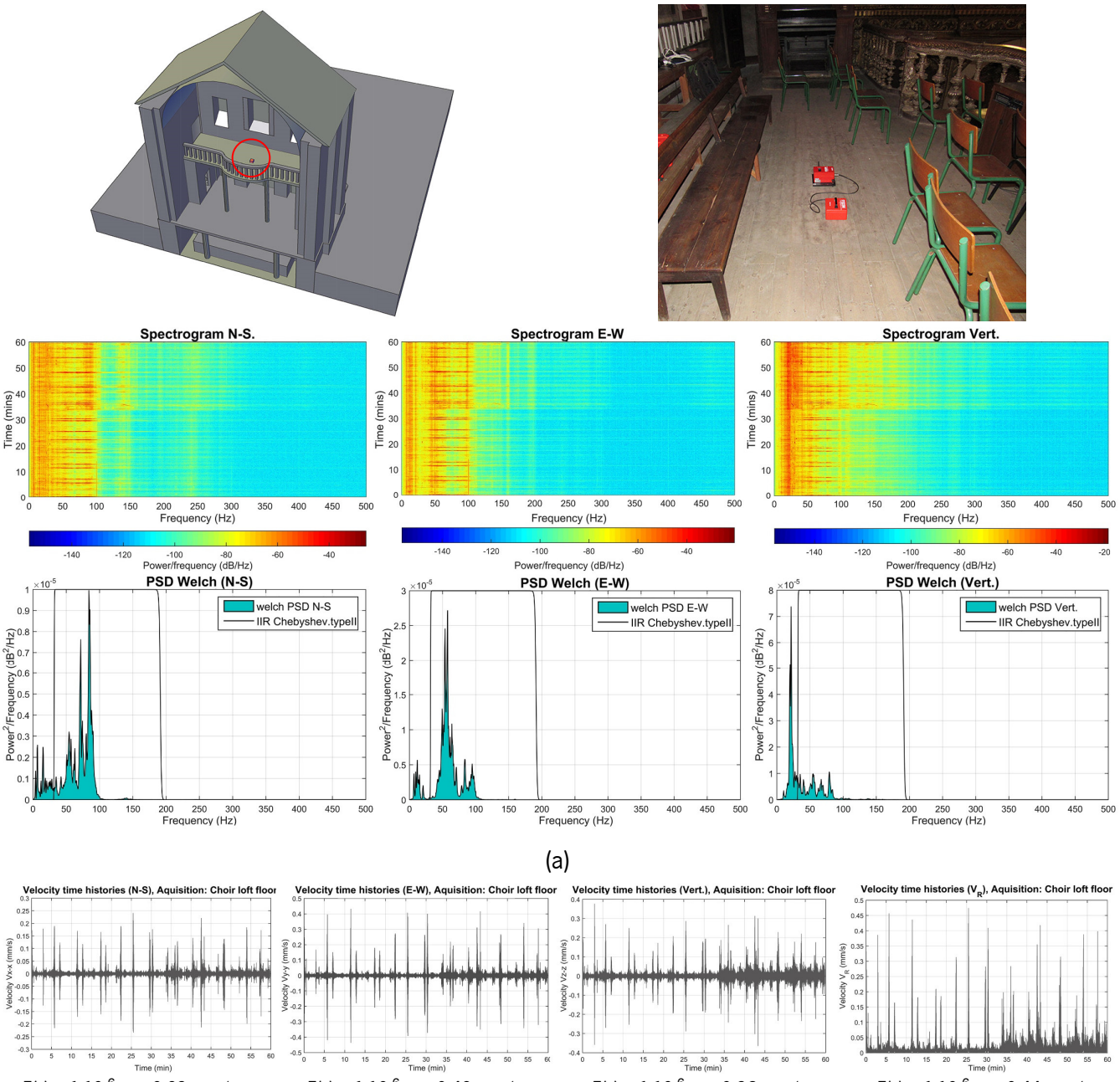


F(x) = 1-10^{-6}, x = 0.12 mm/s F(x) = 1-10^{-6}, x = 0.12 mm/s F(x) = 1-10^{-6}, x = 0.09 mm/s

(b)

Acquisition date/time: 1: 12-Nov-2017 15:50, 2: 12-Nov-2017 16:20, 3: 12-Nov-2017 16:50, 4: 13-Nov-2017 13:15

Figure 62. Data acquisition, in the facade of the Church of the Angels, at the level of the first floor and after vectorial rotation; (a) spectrograms of all unfiltered signals in three directions, corresponding squared Welsh power spectral density graphs and band-pass Butterworth Chebyshev type II filter. Note the division between different acquisition locations, i.e., the middle windowsill (1) (Date/Time 1-3) and the left windowsill (2) (Date/Time 4), divided by a dashed line in PSD graphs; (b) velocity-time history 3D plots, after filtering, for all three directions, of all setups. Note the absolute maximum ppv from the empirical cumulative distribution function and chosen quantile.



Acquisition date/time: 1: 14-Nov-2017 14:50

Figure 63. Data acquisition in the front end of the Church of the Angles, at the mid-span of the choir loft floor; (a) unfiltered velocity-time histories plots of an hourly signal in three directions, corresponding spectrograms, squared Welsh power spectral density graphs and band-pass Butterworth Chebyshev type II filter; (b) velocity-time history 3D plots, after filtering, for all three directions and velocity vectors V_R. Note the absolute maximum ppv from the empirical cumulative distribution function and chosen quantile.

As shown in Table 20, the relative vibration decibel levels (ΔVdB) for each interior location, as computed by Equation 46, with the reference value of the sidewalk location set to 0 VdB, depicts an attenuation, which is not uniform in elevation, but it is consistent with findings from other studies [Saurenman et al. 1982]. In fact, vibration levels at the basement are found 9 ΔVdB lower than immediate exterior levels. Vertical elements, in the level of the 1st floor, are subjected to vibrations,

further attenuated, at around 15 ΔVdB. In the mid-span of the choir loft floor, a relative amplification is present, with vibration levels attenuated at 4 ΔVdB, compared to the exterior location. Yet, the amplitudes of recorded velocity in all locations are lower than the limit thresholds from international standards (Table 17), posing no actual case of cosmetic or structural damage, related to ground-borne vibrations.

4.3.4. Coupling acquisitions of induced vibrations with geophones and seismographers

In order to compare the use of different type of instrumentation, with different outputs of kinetic quantities, i.e., velocities and accelerations, from geophones and seismographers respectively (see section 4.3.2 and 4.3.3 for technical specifications), coupled simultaneous acquisitions were performed, in various locations in the Church of the Angels, as shown in Figure 64a. Mostly, the comparison accounted locations in a vertical alignment, thus accounting for different vibration amplitudes and frequency broadbands. The sampling rate in all acquisitions was set at 1000 Hz.

In many international standards oriented to monitoring of induced vibrations, the velocities are considered as the primary measurement, mostly due to the linear relationship between velocities and stresses, whereas accelerations are mostly frequency dependent, especially at higher frequencies [DIN 45669-2:1995-06].

Examining the obtained acceleration signals in the frequency domain, through a Welch PSD function (Figure 65a, Figure 66a and Figure 67b), the DC component involves a high power density peak at 0 Hz and is considered responsible of an initial asymmetrical response of the signal, associated to the electrical circuits [Giron-Sierra 2018]. Here, it is also noted that, similar to earthquake signals, ground-borne acceleration signals can contain low signal to noise ratios (SNR) and real data can be masked by traffic, stationary or instrumental noise of high intensity, which can occupy a frequency bin of 1-10 Hz [Bormann and Wielandt 2013]. In fact, the current acquisition acceleration recordings are considered noisy at low frequencies (0-5 Hz) due to a combination of secondary induced vibrations (i.e. traffic), from gravitational disturbances (i.e. horizontal accelerations from surface tilt), as described in Boroschek and Legrand 2006, and from poor coupling to the ground. A linear detrending of the acceleration signals in the time domain, is able to reduce the amplitudes of low energy peaks, but is not able to eliminate them. In order to

compensate further the DC component, a baseline correction is performed, among others, by subtracting the mean amplitude of the signal in real-time. The estimation is performed through a low pass IIR elliptic filter of 6^{th} order, of a 0.001 Hz bandwidth. Further on, the remaining noise component was reduced by applying a band-pass digital filter, i.e., a 50^{th} order band pass IIR Chebyshev Type II digital filter, according to the broadband frequency content in each direction. Alternatively, two different high-pass digital filters were applied, i.e., a 50^{th} order high pass IIR Chebyshev Type II digital filter at 5 Hz and at the lower bound of the broadband frequency range of the recorded vibrations. The processed acceleration-time histories present amplitudes, very similar to the original data, that range from 5-45 mm/s^2, depending on the location and vectorial direction, whereas in no passing train laps, maximum values of around 2 mm/s^2 are recorded, reduced further by filtering until around 1 mm/s^2. Though, one should keep in mind, even in cases of precise filtering for suppressing noise, the cut-off frequency bins that do not belong to the source of studied vibration, will in any case reduce the amplitudes and alter somewhat the phases of the signal of interest. Thus, the concept of filtering should be limited, whereas instrumentation and acquisition specifics (i.e. location, operational time and coupling) should be chosen carefully, in order to ensure a good SNR [Bormann and Wielandt 2013].

The acquisition process provides discrete signals, as recorded increments of an analog signal, sampled under the sampling frequency f_s [Brandt 2011]. The transition from acceleration to velocity time histories is performed through numerical integration, under different cumulative integration schemes. Yet, any errors reflect highly on the integration process and is preferable to be avoided [ISO 4866:1990/Amd 2:1996 2010]. In specific, low sampling rates in the acquisition of a discrete signal can reduce the accuracy of the integration process, since they are responsible for aliasing and the loss of real amplitudes. Up-sampling of the discrete signal in the time domain is often considered and done by increasing the sampling frequency, by means of linear or of higher order interpolation functions, i.e., a low-pass filter. Yet, no compensation on the amplitude profiles or the frequency content is possible and cannot present any effect on increasing the accuracy of the integration scheme.

In general, integration methods for discrete acceleration signals can be divided in two categories, i.e., integration methods in the time and the frequency domain [Worden 1990]. The trapezoidal rule of integration is considered a common method of integration of discrete signals in the time domain. The accuracy depends mostly on the quality of the acquisitions, i.e., the sampling

ratio. Here is noted that the Simpson rule of integration is more appropriate for analogue signals since linear interpolation is applied unavoidably in discrete signals. Still, low frequency contents can affect the integrated signal and add linear or higher order trends. Thus, a detrending, a baseline correction and/or high pass or band pass filtering should precede the integration process [Brandt et al. 2014]. Similarly to the trapezoidal rule of integration in the time domain, a Z-transfer function of $1/(1\text{-}Z^{-1})$ can act as an integrator, applied as a filter in the vibration amplitudes and divided by the sampling ratio f_s. The operation follows the finite difference between infinitesimal discrete values in time, an approximation of differentiation, here inversed. The output is accumulated in time, thus providing the integral of the acceleration input [Saisi et al. 2015 and Gentile et al. 2007]. Here is noted that the trapezoidal rule of integration is chosen for the coupling and correlation of the acceleration and raw velocity signals, in the time domain.

A discrete signal is converted to the frequency domain with a discrete Fourier transform (DFT). The signal $x(n\Delta t)$, as a discrete block sample of N equally spaced time increments of Δt size (for a time index n = 0, 1, ..., N-1), is transformed to the equivalent function in the frequency domain, here as $X(k\Delta f)$, with Δf the frequency bin (for a frequency index k = 0, 1, ..., N-1) (Equation 48) [Brandt 2011]. The concept of integration of an acceleration signal in the frequency domain can be achieved by dividing the DFT with the factor of frequency $j\omega$ (or else $2j\pi f$). Here, j is the imaginary number and ω is the radial frequency [Brandt and Brincker 2014]. Under the inverse Fourier transform, the signal is being transformed from the frequency to the time domain and velocities are obtained (Equation 49).

$$F\big(x(n\Delta t)\big) = X(k\Delta f) = \sum_{n=0}^{N-1} x(n\Delta t) e^{-j\omega kn} \qquad \text{Equation 48}$$

$$F^{-1}\left(\frac{X(k\Delta f)}{j\omega}\right) = \frac{1}{N}\sum_{k=0}^{N-1} \frac{X(k\Delta f)}{j\omega} e^{j\omega kn} \qquad \text{Equation 49}$$

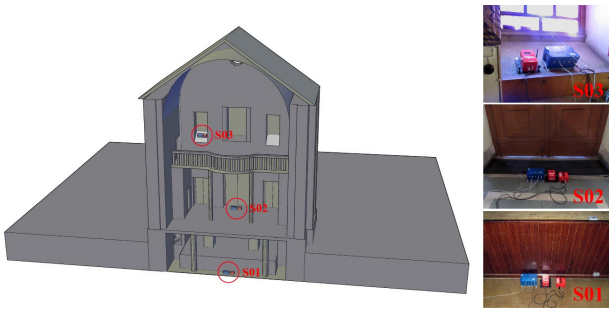
Integration schemes of acceleration signals, both in the time and frequency domain, in all three acquisition locations of Figure 64a, present almost identical amplitudes and profiles (Figure 64b).

The results of the coupling setup S01, at the location of the basement (Figure 64a), are presented in Figure 65. From the squared Welsh PSD graph, the frequency content of the vibration signal, in all three orthogonal components is within the range of 45-115 Hz (Figure 65a). Acceleration-time histories, under different filtering strategies, present varying SNR, while the vibration amplitudes decrease by as maximum at 2 mm/s^2 (Figure 65a). Through the trapezoidal rule of integration in the time domain, derived velocity-time histories are superposed with raw velocity data and empirical cumulative probability plots (ECDF) are computed (Figure 65b). As seen clearly from the related graphs and the absolute maximum values of velocity of each case, derived as a quantile (i.e. probability of 10^{-6}), the amplitudes of velocities, as the product of integration in the time domain, compared to the raw velocity data, are significantly lower by 86-133%, according to the direction and type of digital filtering.

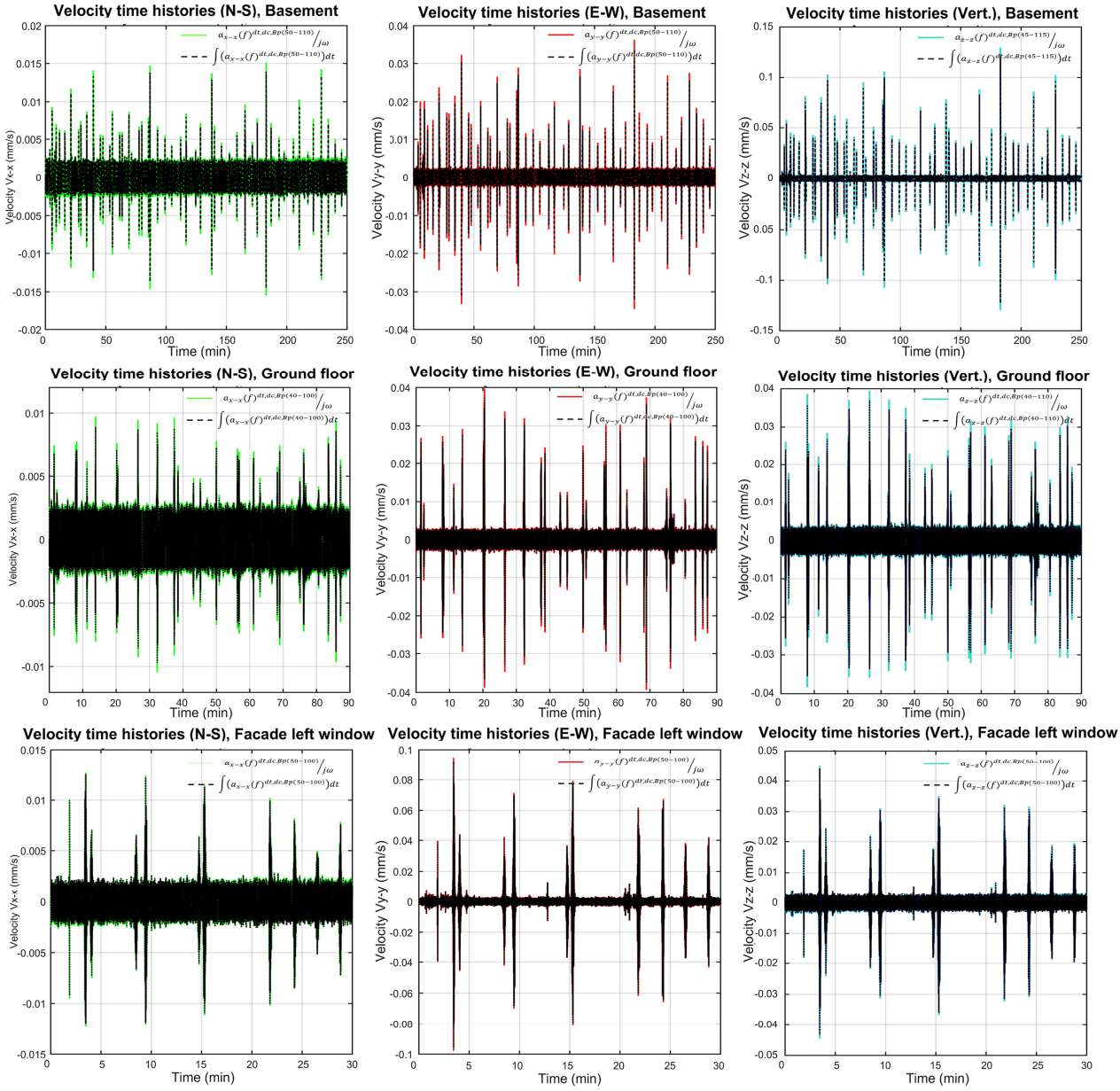
From the data acquisition setup S02, regarding the acceleration and velocity-time histories, at the ground floor of the Church of the Angels, a significant difference is documented between the raw velocity data and the integrated accelerations (Figure 66c). The absolute amplitudes of integrated accelerations in the time domain are also significantly lower, compared to the raw velocity data, with a difference at the range of 40-100%. Thus, the acceleration signals, as acquired from the seismographers and later processed, are not able to capture the same vibration profiles as the geophone. The comparison between the squared Welsh PSD graphs, from the different instrumentation, is only performed qualitatively and not in absolute terms, since the function between the velocity and acceleration is unknown. From the two PSD graphs of Figure 66a is evident that the recorded signals have a different energy content, translated to large differences in the vibration profiles in the time domain.

Finally, the results from the coupling acquisition S03 (left façade window) are presented in Figure 67. Under the inclined surface of acquisition (36.8º), the acquired signals (Figure 67a) are transformed with the rotation matrix, as described in section 3.3.1. Under different filtering strategies, detrending and DC offset, on the rotated signals, noise levels are reduced (Figure 67b). As seen from the squared Welsh PSD graph (Figure 67d) the highest amplitude is recorded at 84 Hz, in the out-of-plane direction of the façade (y-y). Yet, very low amplitudes are recorded in the in-plane direction (x-x), in contrast with the high peak at 84 Hz in the squared Welsh PSD graph of the raw velocity signal (Figure 62a). Under the trapezoidal integration in the time domain, the derived velocity profile in the out-of-plane direction (y-y) achieved a high correlation with the raw

velocity data. Instead, in the vertical (z-z) and in-plane direction (x-x), as shown in Figure 67b, the absolute maximum values of velocities, derived as a quantile (i.e. probability of 10^{-6}) from the empirical cumulative probability plots (ECDF) of each case, are significantly lower, compared to the respective raw velocity data, by 50-170%, according to the direction and type of digital filtering. This large difference adds on the inconsistency and blind processing of integrated acceleration data, in order to compare with values from international standards. As probable causes for the abovementioned inconsistency, between the acquisitions of coupled instrumentation, are the weak coupling to the ground, the high SNR, and the relatively low sensitivity of the seismographer, at high frequencies. Thus, acquisitions of velocity, as the primary measurement, are preferable.



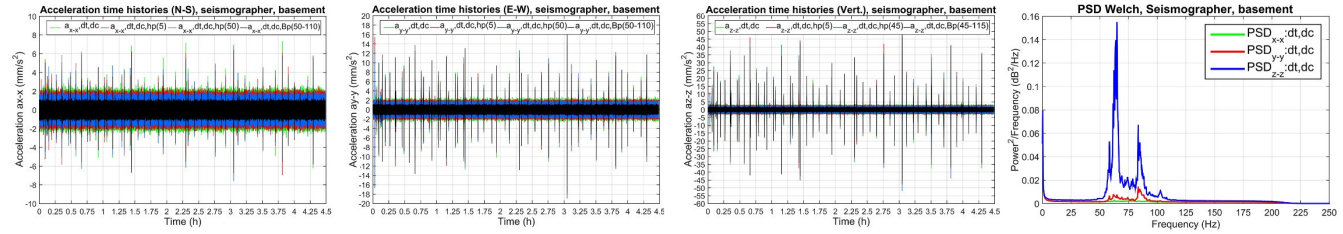
(a)



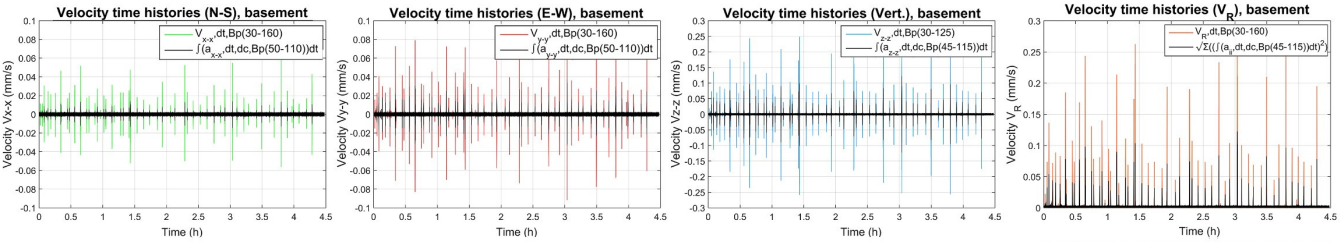
(b)

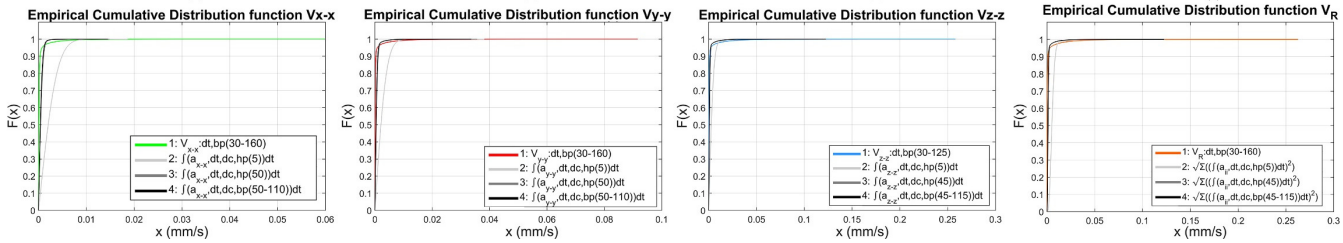
Abbreviations: dt: detrending of mean values, dc: base line correction for by a DC offset algorithm, i.e., a 6th order IIR lowpass elliptic filter, Bp(_Hz): bandpass digital filter with a specified frequency bandpass, i.e., a 50th order IIR Chebyshev Type II digital filter, integration in time domain, i.e., ∫x(t)dt, integration in frequency domain, i.e., X(f)/jω.

Figure 64. Coupled, synchronized recordings with geophones and seismographers at the Church of the Angels: (a) acquisition points in elevation, at the basement, the middle gate at ground floor and at the level of the 1st floor (left façade window); (b) correlation between integration schemes of accelerations in the time and frequency domain.



(a)





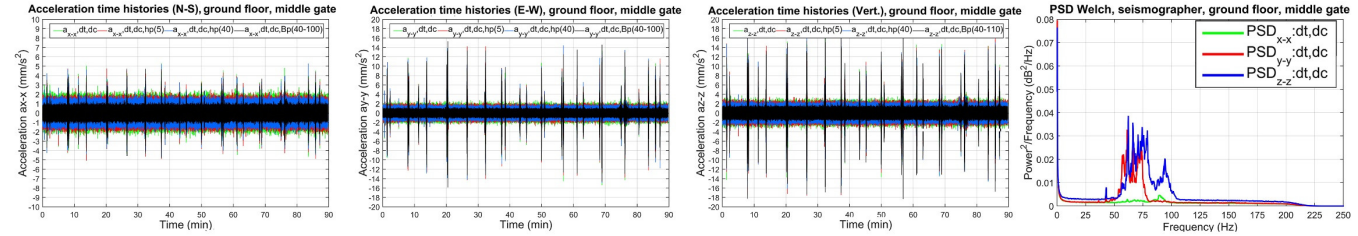
F(x) = 1-10^{-6}	1:x = 0.05 mm/s 2:x = 0.02 mm/s 3:x = 0.01 mm/s 4:x = 0.01 mm/s	F(x) = 1-10^{-6}	1:x = 0.08 mm/s 2:x = 0.03 mm/s 3:x = 0.03 mm/s 4:x = 0.03 mm/s
F(x) = 1-10^{-6}	1:x = 0.25 mm/s 2:x = 0.10 mm/s 3:x = 0.10 mm/s 4:x = 0.10 mm/s	F(x) = 1-10^{-6}	1:x = 0.25 mm/s 2:x = 0.11 mm/s 3:x = 0.10 mm/s 4:x = 0.10 mm/s

(b)

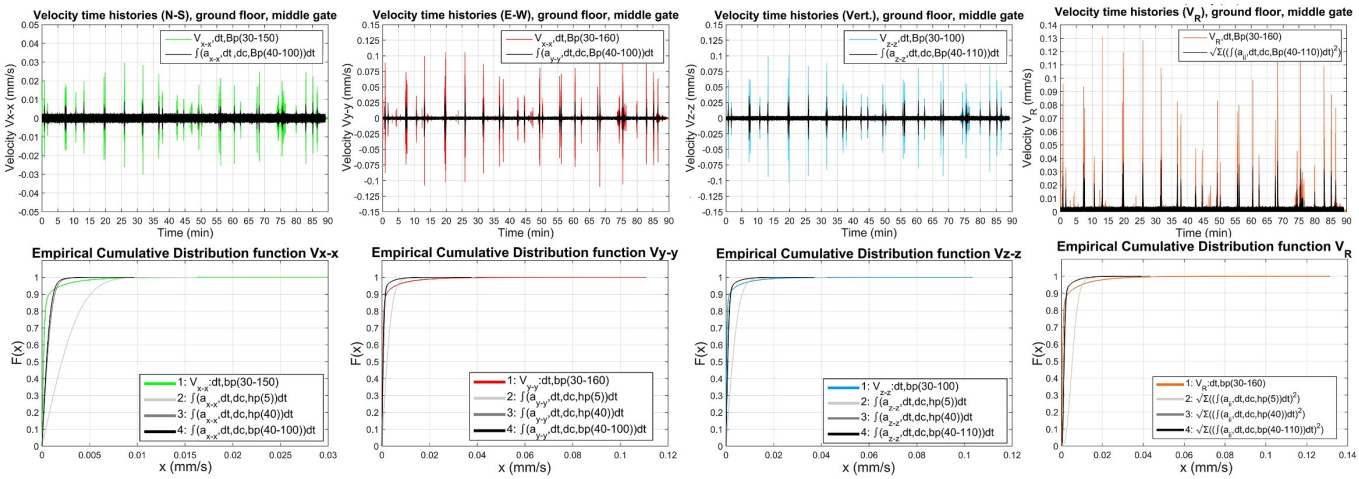
Acquisition date/time: 1: 13-Nov-2017 21:00, 2: 13-Nov-2017 21:30, 3: 13-Nov-2017 22:00, 4: 13-Nov-2017 22:30, 5: 13-Nov-2017 23:00, 6: 13-Nov-2017 23:30, 7: 14-Nov-2017 00:00, 8: 14-Nov-2017 00:30, 9: 14-Nov-2017 01:00

Abbreviations: dt: detrending of mean values, dc: base line correction for by a DC offset algorithm, i.e., a 6th order IIR lowpass elliptic filter, hp(_Hz): highpass digital filter with a specified frequency pass, i.e., a 50th order IIR Chebyshev Type II digital filter, Bp(_Hz): bandpass digital filter with a specified frequency bandpass, i.e., a 50th order IIR Chebyshev Type II digital filter

Figure 65. Data acquisition at the basement of the Church of the Angels, from coupled velocity and acceleration recordings of setup S01; (a) acceleration-time history plots of a 4.5 h signal in three directions, under different filtering and an initial squared Welsh PSD graph; (b) synchronized velocity-time history 3D plots, after filtering, for all three directions, from non-spurious velocity signals and integrated accelerations. Note the empirical cumulative distribution function plot and chosen quantiles for each case.



(a)



F(x) = 1-10^{-6}
1:x = 0.03 mm/s
2:x = 0.02 mm/s
3:x = 0.01 mm/s
4:x = 0.01 mm/s

F(x) = 1-10^{-6}
1:x = 0.11 mm/s
2:x = 0.04 mm/s
3:x = 0.04 mm/s
4:x = 0.04 mm/s

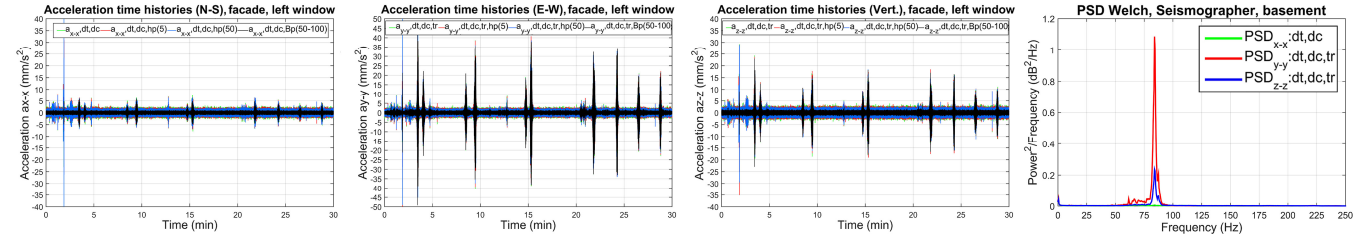
F(x) = 1-10^{-6}
1:x = 0.10 mm/s
2:x = 0.04 mm/s
3:x = 0.04 mm/s
4:x = 0.04 mm/s

F(x) = 1-10^{-6}
1:x = 0.10 mm/s
2:x = 0.04 mm/s
3:x = 0.04 mm/s
4:x = 0.04 mm/s

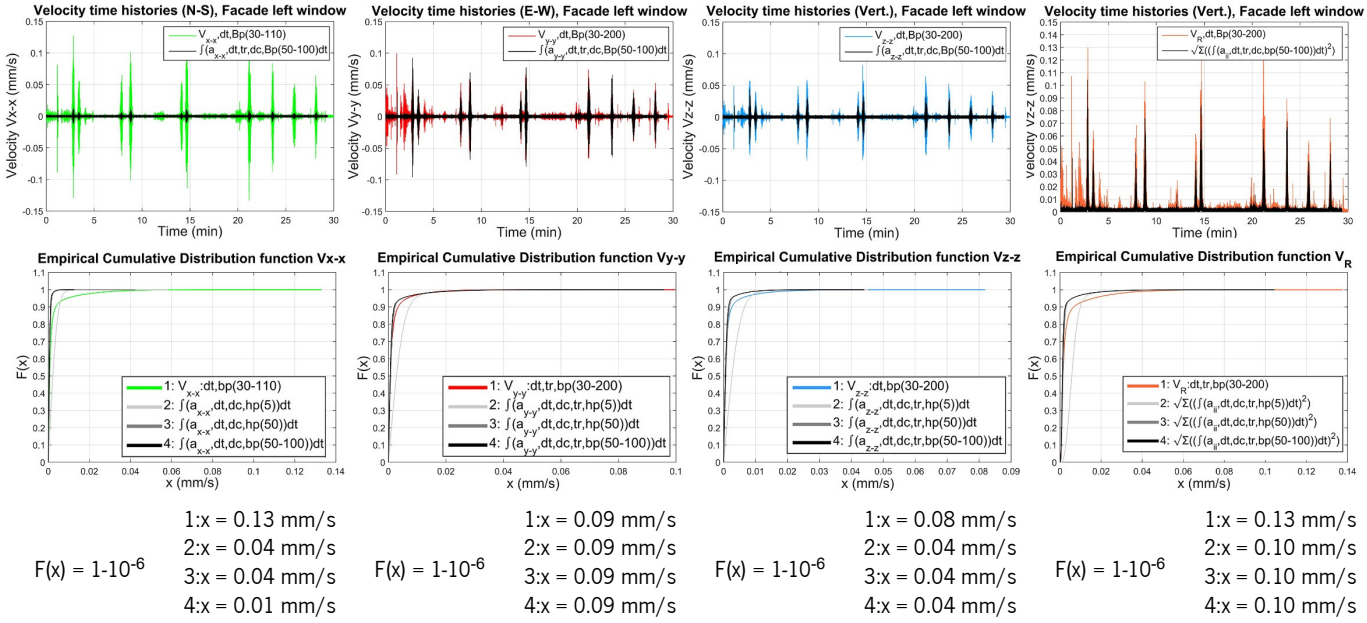
(b)

Acquisition date/time: 13-Nov-2017 14:35, 13-Nov-2017 15:05, 13-Nov-2017 15:35
Abbreviations: dt: detrending of mean values, dc: base line correction for by a DC offset algorithm, i.e., a 6th order IIR lowpass elliptic filter, hp(_Hz): highpass digital filter with a specified frequency pass, i.e., a 50th order IIR Chebyshev Type II digital filter, Bp(_Hz): bandpass digital filter with a specified frequency bandpass, i.e., a 50th order IIR Chebyshev Type II digital filter

Figure 66. Data acquisition at the ground floor of the Church of the Angels, from coupled velocity and acceleration recordings of setup S02; (a) acceleration-time history plots of a 1.5 h duration signal in three directions, under different filtering and an initial squared Welsh PSD graph; (b) synchronized velocity-time history 3D plots, after filtering, for all three directions, from non-spurious velocity signals and integrated accelerations. Note the empirical cumulative distribution function plot and chosen quantiles for each case.



(a)



$F(x) = 1\text{-}10^{-6}$	1:x = 0.13 mm/s 2:x = 0.04 mm/s 3:x = 0.04 mm/s 4:x = 0.01 mm/s	$F(x) = 1\text{-}10^{-6}$	1:x = 0.09 mm/s 2:x = 0.09 mm/s 3:x = 0.09 mm/s 4:x = 0.09 mm/s
$F(x) = 1\text{-}10^{-6}$	1:x = 0.08 mm/s 2:x = 0.04 mm/s 3:x = 0.04 mm/s 4:x = 0.04 mm/s	$F(x) = 1\text{-}10^{-6}$	1:x = 0.13 mm/s 2:x = 0.10 mm/s 3:x = 0.10 mm/s 4:x = 0.10 mm/s

(b)

Acquisition date/time: 13-Nov-2017 13:15
Abbreviations: dt: detrending of mean values, tr: vectorial transformation by means of a rotational matrix, dc: base line correction for by a DC offset algorithm, i.e., a 6th order IIR lowpass elliptic filter, hp(_Hz): highpass digital filter with a specified frequency pass, i.e., a 50th order IIR Chebyshev Type II digital filter, Bp(_Hz): bandpass digital filter with a specified frequency bandpass, i.e., a 50th order IIR Chebyshev Type II digital filter

Figure 67. Data acquisition at the 1st floor façade of the Church of the Angels, from coupled velocity and acceleration recordings of setup S03; (a) acceleration-time history plots of a 0.5 h duration signal in three directions, under different filtering and an initial squared Welsh PSD graph; (b) synchronized velocity-time history 3D plots, after filtering, for all three directions, from non-spurious velocity signals and integrated accelerations. Note the empirical cumulative distribution function plot and chosen quantiles for each case.

4.4. Conclusions

The current work provides a collection of references and practical application, regarding the instrumentation and processing of induced ground-borne vibrations, part of a Structural Health Monitoring plan. Induced ground-borne vibrations from underground railways are assessed, under current standards and in velocity terms. These vibrations are compared with values stipulated as upper bounds for minor damage (serviceability limit state). When accelerations are obtained, different integration schemes are applied, in order to obtain velocities. Though, discrete data acquisitions and post-processing in assessing ground-borne vibrations, especially in historic buildings, has proven rather challenging. The poor choice of a sampling frequency can be the source of aliasing and loss of maximum amplitudes. Thus, a sampling frequency of at least ten

times the average measured spatial frequency of the signal is advised. Also, errors during acquisitions, i.e. poor coupling to the ground, bad choice of monitoring points and inappropriate instrumentation in terms of sensitivity and SNR, can highly reflect on the integration process and data can be masked. Post-processing strategies are employed, i.e., removing non-zero components, linear or polynomial trends, high-pass or band-pass filters. Many are the cases where additional disturbances of high intensity produce a wide range frequency spectrum and mask real data profiles. Thus, additional acquisitions, under no ground-borne vibrations should establish the initial conditions and cut-off frequencies. Thus, low-frequency noise can be removed through more precise filtering.

Integration schemes of acceleration signals can be performed both in the time and frequency domain, while prior to integration, any low frequency variations due to noise can be removed with high-pass filters and a cut-off frequency of around 5 Hz, in the current case. Though, through integration, a perturbation in the actual amplitudes is expected. Thus, appropriate instrumentation with high sensitivity at the expected frequency range is essential. In addition, the use of instrumentation that measures directly the kinetic quantity of interest is preferable.

CHAPTER 5. FATIGUE TESTS ON MASONRY WALLETS UNDER DIAGONAL COMPRESSION

CHAPTER 5. Outline

5.1. Introduction

5.2. Experimental research for fatigue loading on masonry

5.3. Experimental fatigue tests on masonry specimen, under high static diagonal compression loading and medium-low stress ratios

5.3.1. Introduction

5.3.2. Test specimen configuration and initial material properties under a monotonic diagonal compression loading test

5.3.3. Static shear cyclic preload, initial stiffness monitoring and estimated initial material properties from analytical curve fitting

5.3.4. Diagonal compression fatigue test setup, preparation, instrumentation and data acquisition

5.3.4.1. Equivalent oscillating motion characteristics of a fatigue loading regime

5.3.4.2. Selection of fatigue equivalent sinusoidal load for assigned levels of ground-borne vibrations

5.3.4.3. Fatigue testing protocols

5.3.4.4. Instrumentation and data acquisition

5.3.4.5. Temperature effect and displacement compensation

5.3.4.6. Fatigue shear cyclic loading and stiffness monitoring

5.3.4.7. Analytical stress-strain interpretations and correlations in fatigue loading

5.4. Conclusions

5.1. Introduction

Fatigue, based on FIB Model Code 2013, can be defined as the process of initiation and propagation of damage in structural parts, due to frequently repeated actions. The fatigue assessment of a structural part is a manifold and complex process, relative to the ultimate tensile or compressive strength, the fracture parameters and the stiffness properties of the material present, but also to the natural frequencies, the static loading conditions and the characteristics of the fatigue load, i.e., the stress range and the frequency of the loading cycles. According to the EN 1992.1.1:2004, the presence of fatigue loading should be considered for the ULS verification. For the design of transient or persistent fatigue assessment in concrete structures, and only for the ultimate limit state (ULS), the recommended partial factor $\gamma_{c,fat}$ that reduces the compressive strength is equal to 1.8, when the nominal strength is considered, whereas fatigue loads are considered without factorization. For the process of fatigue assessment, as defined in EN 1990:2002, the design working life category for monuments is 5 (100 years).

Nevertheless, long-term effects on durability have not been fully evaluated and many times are not accounted for the assessment process of historical masonry buildings. Structural assessment strategies mostly involve independent loading regimes, under average static loading envelopes, with stress variations in time often disregarded. Still, time-based variations of stress and strain are characteristic for many historic structures, in the course time, mainly from environmental and anthropogenic influence [Binda 2008].

Fatigue can be linked with creep, since both are time dependent phenomena, during which diffused micro-cracks occur in quasi-brittle materials, that can evolve into macro-cracks, leading to potential failure and collapse. However, under accelerated fatigue laboratory tests, fatigue can be examined separately from creep. Additional environmental effects and material deterioration may also interact with the creep and fatigue process and reduce further the available mechanical properties over time. In brick masonry, fatigue related strength reductions may be attributed to inelastic strain accumulation between mortar and brick. Also, it is possible that the splitting strength (tensile strength) of brick units deteriorates with repeated lateral tensile stresses under compression [Abrams et al. 1985]. Historic masonry structures, in particular, are highly susceptible to mechanical damage from creep and fatigue, given their low mechanical properties, pre-existing damage and areas of high-sustained loading. Fatigue effects under long-term cyclic loading are attributed to traffic loads, wind, ringing bells, temperature and humidity [Binda 2008].

The current experimental work is focused on fatigue quasi-static cyclic tests on brick masonry wallets with single face rendering, composed by solid bricks and lime mortar, and simulating historic brick masonry. Given the damaging effects of tension and shear for masonry, fatigue loading protocols are designed under diagonal compression fatigue tests. The main objectives and expected results of the present work are:

(a) Document and assess the current knowledge on the fatigue studies in brick masonry.

(b) Generate acquisition data on the response of a specific brick masonry typology, under quasi-static fatigue diagonal compression loading, under high static shear stress and low to medium stress reversals.

(c) Monitor changes on the material properties of brick masonry, regarding load capacity, softening and energy dissipation.

(d) Formulate analytical models for fatigue deterioration in masonry structures, in the form $S - N_i$ (Stress vs. Number of cycles up to failure) and $\varepsilon - N_i$ (Strain vs. Number of cycles up to failure).

(e) Assess the safety factors and residual life in stress and number of cycles combinations that do not result to failure.

(f) Propose a mathematical model for the evolution of shear strain and shear modulus, under high static shear stress and low to medium stress reversals fatigue loading.

5.2. Experimental research for fatigue loading on masonry

Fatigue damage in masonry structures, under dynamic or quasi-static cyclic stress-strain reversals, is mostly related to cracking, under tensile or compressive stresses. The nature of fatigue damage is linked with long-term performance and is somewhat different than the quasi-static load application, with failure occurring at a level lower than the ultimate quasi-static loads. Thus, the knowledge of fatigue properties of masonry is vital for understanding the rate of deterioration due to various levels of fatigue loading, and estimating the ultimate capacity, the remaining service life and the efficient planning of maintenance works [Melbourne et al. 2007].

Basic fatigue properties are mostly defined through standards and studies of steel specimens. According to BS EN 10080:2005, the fatigue strength $\Delta\sigma$ or else $2\sigma_a$ is the stress range of a sinusoidal cyclic load, linked to a specific static stress state σ_{max} and a specified

number of cycles N_f. For the ULS, and according to EN 1992.1.1:2004, the fatigue strength, under a specified σ_{max} and N_f is taken equal to $2\sigma_a/\gamma_{c,fat}$. Given the high variability of fatigue strength, a higher number of test specimens is needed for a statistical average, e.g., five samples, regarding fatigue testing in reinforcement bars, girders, welded wire mesh etc. [BS EN 10080:2005]. Fatigue loading in masonry structural parts, in correlation with stiffness degradation, resulting damage and potential failure involves a large number of cycles, which according to DIN 4150-3 2016, Nicholas 2006 and Casas 2009 can range from 10^5-10^{10}.

Experimental studies on fatigue have been conducted for masonry arch bridges and on masonry prisms, regarding mostly fatigue under compressive stresses, aiming on detecting changes on the material properties, i.e., the load capacity and softening properties [Melbourne et al. 2007]. Many recent fatigue experimental campaigns employ non-destructive testing (NDTs) strategies, for detecting mechanical and microstructural changes, such as the use of acoustic emission tests in Carpinteri et al. 2014 and Tomor and Verstrynge 2013, and ultrasonic measurements in Breitenbucher and Ibuk 2006. Stress-strain curves during the evolution of a fatigue-cyclic load are similar to a hysteresis curve, showing the effects of stiffness degradation and changes in deformability, during loading-unloading cycles. Analytical prediction models for fatigue deterioration in masonry structures usually provide functions of the stress state with the number of cycles leading to failure, thus applicable to the ULS.

For the objectives of assessing fatigue in laboratory conditions, the random nature of the vibration signals, is usually transformed into a regular sinusoidal signal, easily applicable, as a cyclic load, from an actuator. Under force controlled fatigue testing, basic symbols are the loading frequency f and period T, the stress range $\Delta\sigma$, the mean static stress σ_m, the stress amplitude σ_a, the maximum σ_{max} and minimum σ_{min} stress, the stress ratio R and the amplitude ratios A_σ and S, as presented in Figure 68 and in Equation 50, Equation 51 and Equation 52. Here is noted that under displacement control fatigue, the basic fatigue symbols are defined in terms of strain.

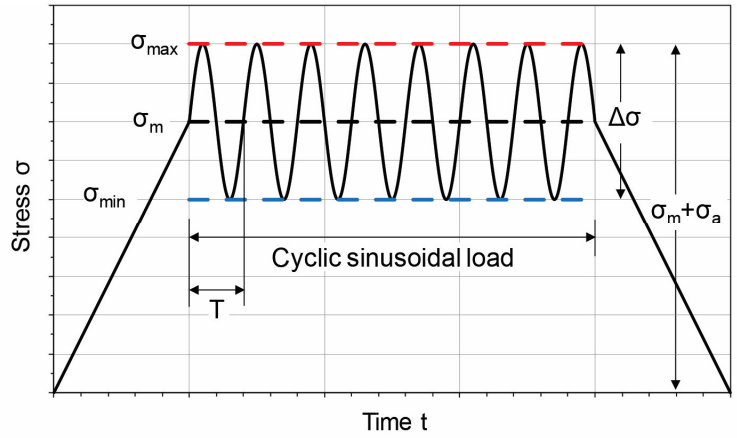


Figure 68. Equivalent fatigue loading under a constant amplitude, cyclic sinusoidal pattern, with the associated abbreviations. Note the higher mean stress σ_m, compared to the stress range $\Delta\sigma$, for testing masonry specimens under compressive or tensile stresses.

$$\sigma_a = \frac{\Delta\sigma}{2} = \frac{\sigma_{max} - \sigma_{min}}{2}, \sigma_m = \frac{\sigma_{max} + \sigma_{min}}{2} \quad \text{Equation 50}$$

$$\sigma_{max} = \sigma_m + \sigma_a, \sigma_{min} = \sigma_m - \sigma_a \quad \text{Equation 51}$$

$$R = \frac{\sigma_{min}}{\sigma_{max}}, A_\sigma = \frac{\sigma_a}{\sigma_m}, S = \frac{\sigma_{max}}{f_m} \quad \text{Equation 52}$$

Fatigue damage assessment is mostly based on semi-logarithmic $S - N_f$ ($\Delta\sigma$ or $\sigma_a - \log N_f$) and $\varepsilon - N_f$ ($\Delta\varepsilon$ or $\varepsilon_a - \log N_f$) curves for the material, providing threshold values, under the correlation of the nominal stress S and strains ε respectively, either compressive or tensile, and the number of cycles N_f that lead to failure. The $S - N_f$ curve, according to the varying amplitude of the terms, can be approximated either with the relation of Equation 53 or Equation 54, and a linear curve under a log-linear and log-log plot respectively [Dowling 2007]. Here, A, B, C and D are numeric constants, obtained from the least squares regression method. Incorporating the static failure f_c, the first point of the $S - N_f$ curve is at $\Delta\sigma_u = f_c - \sigma_{min}$, while N is equal to 1.

$$\sigma_a = A - B \cdot \log(N_f) \quad \text{Equation 53}$$

$$\sigma_a = C \cdot {N_f}^D \quad \text{Equation 54}$$

Typically, if for a significant number of cycles ($\simeq 10^7$) and at a certain value of $\Delta\sigma$ and below (defined as endurance limit $\Delta\sigma_e$), no fatigue failure occurs, the $S - N_f$ curve is represented with a constant branch [Carpinteri and Paggi 2009]. According to serviceability assessment criteria for unreinforced masonry bridges, the limit for S is set at $0.5f_c$, as far as compressive stresses are

concerned [BD 91/04-14]. Yet, according to experimental fatigue tests in scaled masonry arches, in Melbourne et al. 2004, a lower endurance fatigue limit was established, around $0.4f_c$. Similar limits could be established for shear or tensile fatigue stresses.

For a known stress level $\hat{\sigma}_a$ and number of cycles $\hat{N}_f$, associated to actual service life conditions and no failure, safety factors γ_S and γ_N can be associated to a known $S-N_f$ curve, and according to a critical stress level σ_{a1} and a critical number of cycles N_{f2} respectively, as shown in Equation 55 and Figure 70a [Dowling 2007]. As explained in Dowling 2007, typical stress-based γ_S safety factors are within the range of 1.5-3, whereas fatigue-life γ_N safety factors, having greater variability, are within the range of 5-20. The relation between the two safety factors is established from the slope of the $S-N_f$ curve and, according to the log-linear and log-log equations, it is formed respectively in Equation 56 and Equation 57.

$$\gamma_S = \frac{\sigma_{a1}}{\hat{\sigma}_a}, \gamma_N = \frac{N_{f2}}{\hat{N}} \quad \text{Equation 55}$$

$$\gamma_S = \frac{\hat{\sigma}_a - \sigma_{a1}}{\log(N_{f2}) - \log(\hat{N})}\gamma_N \quad \text{Equation 56}$$

$$\gamma_S = \frac{\log(\hat{\sigma}_a) - \log(\sigma_{a1})}{\log(N_{f2}) - \log(\hat{N})}\gamma_N \quad \text{Equation 57}$$

A basic formulation of a fatigue damage model and resulting life expectancy, according to the loading regime, is performed with the Miner's rule, where the expected remaining life, is expressed by the limit state function G, as the sum of the number of cycles for different stress levels, with a simple linear relation between the number of cycles $n_{i,j}$, the total number of cycles $N_{f(i,j)}$ leading to failure under a designated stress range $\Delta\sigma_i$, and a static stress level $\sigma_{m,j}$ (Equation 58 and Figure 69b) [Miner 1945]. Here, for summing the different load cycles and assessing the remaining service life, the same failure mechanism should occur, under different j stress levels.

$$G = 1 - \sum_{\substack{\Delta\sigma_i \\ \sigma_{m,j}}}^{k} \frac{n_{i,j}}{N_{f(i,j)}} \quad \text{Equation 58}$$

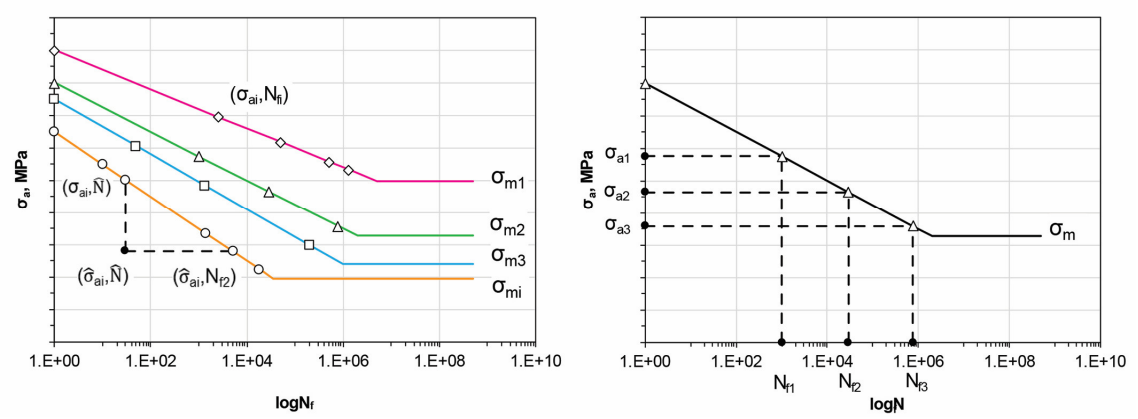


Figure 69. Stages of fatigue life: (a) indicative load patterns of fatigue tests, under different static stress levels σ_{mi}, in MPa, vs. cycles, and safety factor relation of a known fatigue stress combination; (b) cumulative life expectancy of a fatigue regime, linked to the different cyclic stress amplitudes σ_{ai} and number of cycles N_{fi}, based on the Miner´s rule.

Fatigue damage in masonry structural parts, under permanent or intermittent dynamic or quasi-static cyclic loads, is performed through a reliability-based assessment, accounting for the distribution of the data in the $S - N_f$ and $\varepsilon - N_f$ curves. A deterministic approach can also be followed, with expected values and without considering any variation. In fact, in cases of limited experimental data, probabilistic functions of fatigue assessment are of low or even unknown correlation. When reliability functions for fatigue are present, formulated by experimental tests, a deterministic approach can be followed, by choosing a confidence level of remaining fatigue life. The formulation of $S - N_f$ and $\varepsilon - N_f$ curves from experimental tests on masonry specimens can be found in Casas 2009, Casas 2010, Koltsida et al.2018A, Koltsida et al.2018B, Carpinteri et al. 2014, Melbourne et al. 2004, Roberts et al. 2006 and Ronca et al. 2005.

In Casas 2009 and Casas 2010, fatigue probabilistic functions, between the ratio S of the maximum compressive stress σ_{max} to the strength f_c, the ratio R and the equivalent fatigue life EN, are in form of Equation 59, Equation 60 and Equation 61. Here A, B, C and D are numeric coefficients, derived from experimental data and a specific confidence level, e.g., a survival probability of 95%.

$$S = C \cdot N_f^{-D(1-R)} \qquad \text{Equation 59}$$

$$EN = N_f^{(1-R)} \qquad \text{Equation 60}$$

$$\log(S) = A - B \cdot \log(EN) \qquad \text{Equation 61}$$

According to Roberts et al. 2006, the deterministic fatigue strength function F(S), was derived from the linear lower bound of high stress rate fatigue tests on masonry prisms in compression, and under submerged, wet and dry conditions, with the frequency of the applied sinusoidal fatigue load equal to 5 cycles/sec. The F(S) function is related to the induced stress range $\Delta\sigma$, the maximum stress σ_{max}, the ultimate compressive strength f_c, under quasi-static loading and the number of cycles N_f until failure, under Equation 62. Here, the numeric constants, defined for the specific fatigue tests, are substituted with A and B.

$$F(S) = \sqrt{\frac{\Delta\sigma \cdot \sigma_{max}}{{f_c}^2}} = A - B \cdot \log(N_f) \qquad \text{Equation 62}$$

In Koltsida et al. 2018A, uniaxial compression high stress rate cyclic tests in brick masonry prisms with cement and lime mortar, with a sinusoidal pattern and a frequency of 2 cycles/sec, were used to evaluate the long-term performance and the stages of fatigue deterioration. The correlation between stress levels, number of cycles and stress-strain evolution, revealed a strain rate evolution in three stages, according to a percentage of the total number of cycles N_f, also evident from fatigue studies in concrete, i.e., a rapid increase until 10% of the normalized fatigue life N/N_f (Stage I), a steady increase until 80-90% of N/N_f (Stage II), and a final rapid increase, until failure (Stage III) (Figure 70). In Koltsida et al. 2018A, the strain rate of Stage II, increases with the maximum stress level, as a result of fatigue tests performed with σ_{min} equal to $0.1f_c$ and σ_{max} varying from 0.55 to 0.80 of f_c. Considering that the strain rate $\dot{\varepsilon}$ gradient as the strain derivative to the number of cycles N, the comparison between different fatigue tests is achieved by normalizing the strain with the one at the total number of cycles N_f, until failure (Equation 63). As a result, indications of higher strain rates for fatigue Stage II were achieved, under higher maximum fatigue stresses σ_{max}, yet subjected to high scatter, which can be also explained by the relative difference in the stiffness within the tested specimens. In Carpinteri et al. 2014 the linear regression of Stage II of fatigue, for the semi-log plot, can be obtained through the empiric analytical Equation 64, where A and B are parametric constants, to be fitted from experimental results.

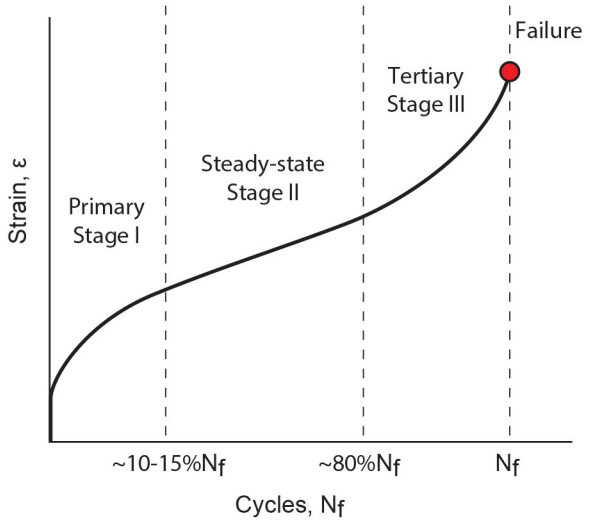


Figure 70. Three stages of fatigue strain, under constant fatigue stress: a rapid increase of Stage I, steady Stage II and a tertiary Stage III, until failure. Note the indicative percentage of each stage, with respect to the fatigue life N_f, as established from fatigue studies.

$$\dot{\varepsilon} = \frac{\partial \varepsilon}{\partial N} = \left(\delta/L\right) \Big/ N_i/N_f \qquad \text{Equation 63}$$

$$N_f = A\left(\frac{\partial \varepsilon}{\partial N}\right)^B \qquad \text{Equation 64}$$

Through intermediate loading and unloading, within fatigue loading branches, the accumulation of compressive plastic strains is evident, under a combination of fatigue and creep. In Koltsida et al. 2018B, accounting for a sample of specimens, varying within 4-21 and tested under a specific stress range, fatigue data were fitted under a logarithmic normal distribution, and the probability density function (PDF) and cumulative density function (CDF) were calculated. In the semi-log $S - N_f$ plot, a logarithmic mathematical model was fitted, for various probabilities of survival.

In Carpinteri et al. 2014 the different stages of fatigue damage were performed under direct cyclic shear tests in masonry specimens. The load ratio S was 0.30, 0.50 and 0.70 of f_c, at a total of 10^5 cycles and a cyclic frequency of 1-2 Hz. The fatigue strength was assessed with respect to the number of cycles N_f, together with monitoring of damage evolution and crack localization with NDT methods, i.e., the acoustic emission (AE) technique.

Besides the fatigue assessment in terms of the ULS and failure, quantitative fatigue crack and damage propagation, in terms of strength, fracture energy G_c and G_f, and stiffness, is

considered significant for historic brick masonry. In Breitenbucher and Ibuk 2006 several concrete cylinders were subjected to uniaxial compressive cyclic loading, at a stress range S from 0.65-0.55f_c to 0.10-0.05f_c, with a frequency of 7 Hz and for 10^6-10^7 cycles. From intermediate ultrasonic measurement acquisitions, until the completion of the fatigue tests, the dynamic Young's modulus exhibited a gradual decrease, which accelerated at the last steps. At maximum, the residual dynamic Young's modulus was lower by 55-77% from the initial state. Besides, from quasi-static cyclic tests on cylinders, after being subjected to fatigue loading of 350000 cycles, the fracture energy in compression G_c was found decreased by 20%, compared to specimen with no fatigue loading.

In Melbourne et al. 2004 cyclic fatigue tests were performed on multi-ring brick masonry segmental arches with cement-lime mortar, in conjunction with static tests. The loading was applied as point loads at ¼ and ¾ of the arch's span. The cyclic fatigue loading, was executed progressively for all the arches, in a range of $2 \cdot 10^4$ to $2 \cdot 10^6$ cycles, with maximum fatigue stress within the range of 0.28-0.6f_c, and a cyclic frequency of 2Hz, together with a static preload, representing dead and live loads. Instead of the prevalent four-hinge static failure, the failure under cyclic fatigue tests was the ring separation or slippage, under shear stresses.

Here is noted that any fatigue assessment study should be associated with real-time conditions in a structure, regarding the number of cycles, the static stress state, the fatigue stress rate and the expected service life [Ronca et al. 2005, Binda 2008 and Binda et al. 2007]. Focusing on historic masonry structures and the process of admissible loading conditions, realistic static load paths should be accounted, many of which result to high stresses in areas and at specific directions. Yet, many of the current experimental studies, on fatigue loading in masonry, focus on high stress ratios of fatigue, under very low static stresses, which are not always representative of loading regimes in historic masonry. On the contrary, the presence of high static loads is common in many historic buildings and thus, fatigue assessment under high compressive loads, with stress cyclic loading under low-medium stress ratios is a realistic scenario. Normally the first cracks in masonry appear at 70% of the maximum compressive load, in the form of small vertical cracks, in the bricks and in the brick-mortar interface [Binda 2008]. In contrast, modern masonry, under current design regulations, is designed around 30-40% of the nominal compressive strength, thus almost in the elastic range [EN 1052-1:1999]. That contributes to the fact that the safety level of vertical capacity, especially in multi-story historic masonry buildings is moderate. Still, the

probability of failure in tension and shear seems higher. Additionally, pre-existing damage, from more extreme and sudden events, such as earthquakes and settlements, can introduce additional discontinuities, changes in load paths and result locally to stress intensities close to the ultimate capacity.

In Binda et al. 2007, under the assessment of several historic masonry buildings, a comparison was attempted between the local state of stress, from single flat jack tests, with the state of stress corresponding to the appearance of the first cracks, measured with double flat jack tests (Figure 71). Under the assumption that the latter limit corresponds at around 0.70-0.80f_c, the capacity margin is rather small, while in some cases is surpassed.

In Ronca et al. 2005, experimental tests on fatigue loading in masonry prisms, perpendicular to the bed joints were conducted under medium to high static compression (0.55-0.80f_c), with fatigue stress ratios varying from 0.05-0.1f_c and cyclic frequencies of 1, 5 and 10 Hz. Here, axial deformations were found increasing with the increase of cyclic frequencies. The strain rate in all tested frequencies is exhibiting a linear trend for static loads up to 0.65f_c. For samples tested under fatigue a stress ratio of 0.05f_c and a static stress of 0.8f_c, a sudden explosive failure occurred after a relatively small number of cycles, which contributes to the fact that there is a higher sensitivity for fatigue failure at high static stresses.

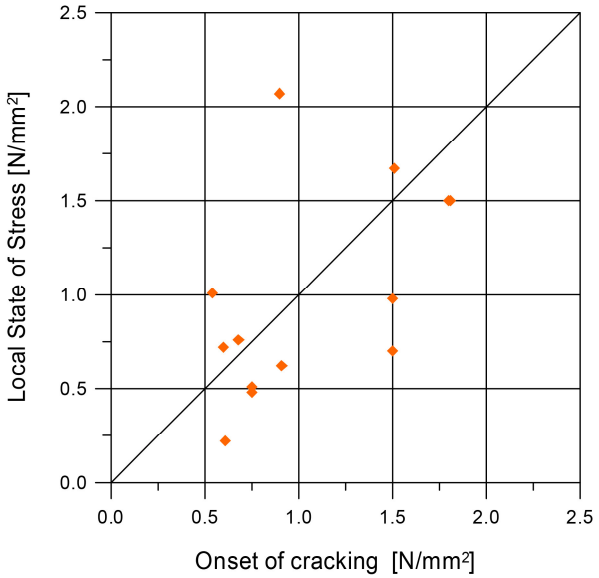


Figure 71. Correlation between the local state of stress and the initiation of cracking, from single and double flat jack tests in historic brick masonry buildings. Note that stress data over the correlation line exceed the state of the first crack, while the rest are below the onset of cracking. Adapted from Binda et al. 2007.

5.3. Experimental fatigue tests on masonry specimen, under high static diagonal compression and medium-low stress ratios

5.3.1. Introduction

An accelerated fatigue experimental test is designed under the concept of a continuous imposed vibration, i.e., a cyclic applied load, namely a sinusoidal function, of a constant angular frequency and amplitude. In fact, under real conditions, continuous vibrations are less common, whereas instead, varying time periods of vibration occurrence, and either in decay or overlap, define transient, intermittent and pseudo-steady state vibrations, which can better describe induced ground-borne vibrations from passing trains (Figure 72). Yet, under the same concept, the time duration of an accelerated fatigue experimental test should cover a sufficient number of vibration amplitudes or passing trains, e.g., 10^5-10^{10} cycles [DIN 4150-3 2016, Nicholas 2006 and Casas 2009].

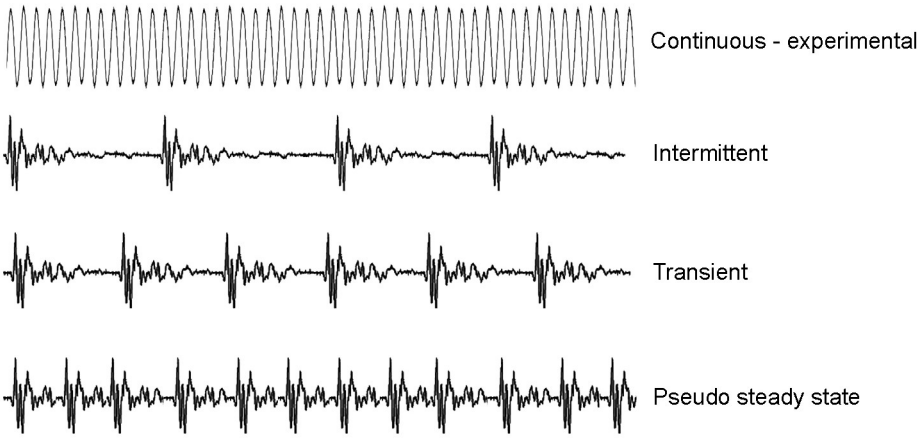


Figure 72. Accelerated fatigue experimental tests, under continuous cyclic vibrations, versus an intermittent, transient and pseudo steady state vibration regime.

Fatigue can be distinguished under compressive and/or shear stresses. Fatigue damage from induced ground-borne vibrations, given the amplitude range and level of intermittency, is not directly associated to structural failure. Yet, in masonry structures, long-term effects on ductility, durability, stiffness and strain increase due to operational fatigue conditions have not been fully investigated.

In general, fatigue loading data for brick masonry, accounting for medium to large scale specimen are scarce, given the long testing durations, the overheating of actuators and their potential failure during testing, the high variability of results, the inability of controlled environmental testing conditions and the demanding data processing of the large time series. Also, accounting

for the construction costs, a deterministic fatigue approach is a more probable scenario than a probabilistic one.

As far as the initial static stress (σ_m) is concerned, for a fatigue experimental test in brick masonry, is essential to be representative of a real stress state. Besides an average expected compressive stress state of 0.2-0.25 MPa, at the base of masonry structures of several stories, the presence of discontinuities, excessive dead loads, pre-existing damage, separation of masonry walls into layers etc., may alter the load path trajectories, and in extreme cases, compressive stresses are even considered higher than 70% of the maximum capacity, with a relatively low margin [Binda et al. 2007]. Tensile stresses in a confined stress state (restrained conditions) are a portion of the compressive stresses, according to the Poisson ratio (v=0.2-0.25). Thus, high tensile stresses are also expected in areas of compressive stress concentration.

Under the current experimental work, long term diagonal compression fatigue tests were conducted in brick masonry wallets, under high static diagonal compression loading and medium-low level of strain reversals, replicating the strain levels and displacement amplitudes from ground-borne vibrations, as imposed by neighboring underground railways. The main objective of the experimental fatigue study in simulated historic brick masonry wallets with lime mortar joints and plaster, under diagonal compression loading regimes, is defined by pairing the loading stress levels (σ_m), the stress range levels ($\pm\sigma_a$) and the number of cycles (N_i) to certain quantifiable levels of damage, stiffness degradation and failure. Monitoring parameters during the initiation, propagation and ultimate failure of accelerated fatigue loading are the shear modulus G_{mod}, the secant stiffness G_{sec} and the plastic strain.

5.3.2. Test specimen configuration and initial material properties under a monotonic diagonal compression loading test

In total, four masonry wallets, built at the same time and cured for 200 days, designated as DCfi-j, being of the same size, as those used for the mechanical characterization tests of CHAPTER 3, Section 3.5.2, and plastered only in one side, were used for the experimental diagonal compression fatigue tests (Figure 73). Here is noted that i is the wallet's assigned number and j is the sequential part of the fatigue test, also accounting for the static loading and unloading conbinations. In specific, time accelerated fatigue tests were performed in three of the masonry wallets in diagonal compression, under different static diagonal compression loading conditions

and three different diagonal compression stress fluctuations, according to vibration limits from standards [DIN 4150-3 2016, SN 640312A 1992]. The fourth wall specimen (DCf1) was primarily tested under a monotonic diagonal compression load, until failure, in order to obtain a reference diagonal compression capacity curve.

Regarding the collection and interpretation of acquisition data, those are performed by means of LVDTs and strain gauges, attached to the surface of the masonry and plaster. Regarding the strain gauges, the PL-120-11 single element strain gauges were used, with a length of 120 mm, a gauge factor of 2.10 (±1%) and attached to the masonry by means of an adhesive resin [Concrete Material Use Strain Gauge 2021]. Given the unknown exact location of the diagonal shear crack, two strain gauges were attached in masonry, in vertical or horizontal alignment, in order to increase the chances of covering the shear crack formation, while for a more accurate representation of the strain in masonry, the gauge length was aligned to three bricks and the two corresponding bed joints (Figure 73).

Here is noted that most of the historic masonry walls carry rendering, mostly lime-based, with a thickness of 10-30 mm. Exterior lime-based renders are mostly accounted for environmental protection, and as finishes for rubble masonry bonds. Instead, many unrendered stone masonry walls are composed by perfectly cut stone blocks with thin mortar joints, while many of the unrendered brick facades have an external layer of water resistant, less porous and frogged bricks, with the joints being regularly thin [Corradi et al. 2018, Camino Olea 2001]. For the current experimental work, a lime-based render of 30 mm thickness was chosen.

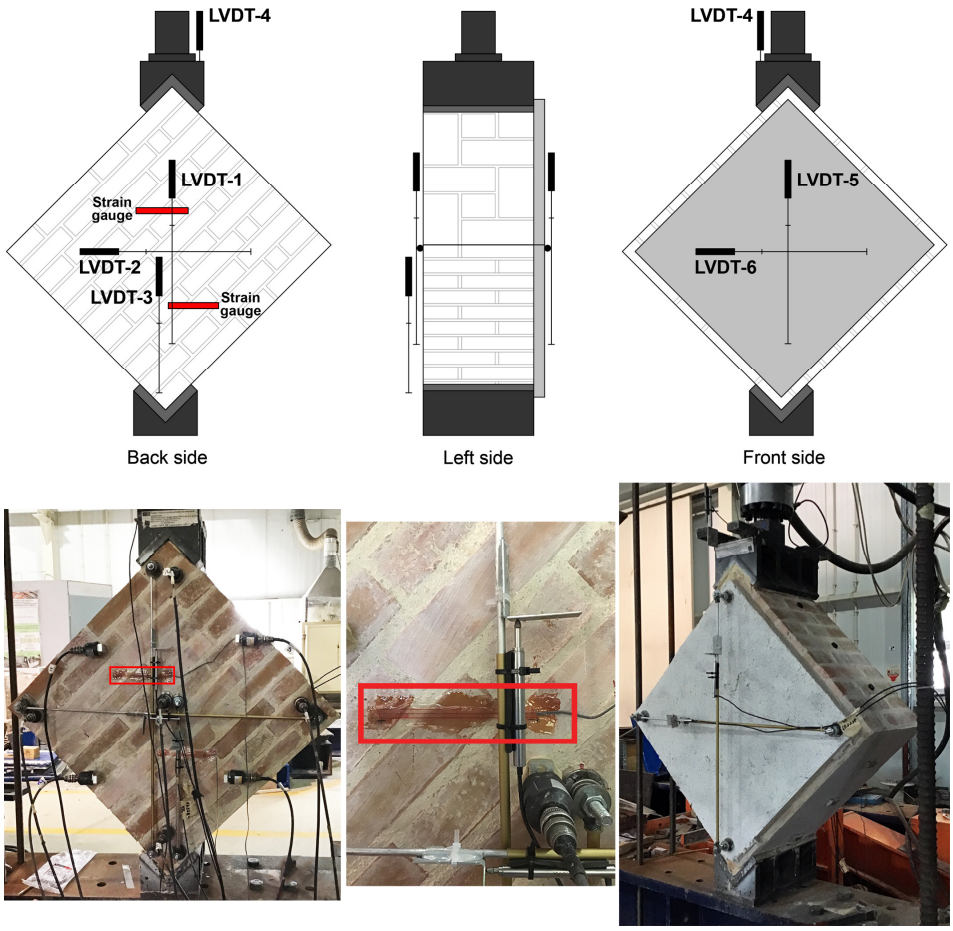


Figure 73. Geometry and instrumentation setup of the diagonal compression cyclic fatigue tests on brick masonry wallets, with lime mortar joints and plaster (DCfi-j).

Regarding the mechanical properties of masonry in shear (strength and stiffness), the effect of the plaster, depending on its relative thickness, stiffness and strength, can be significant, though often disregarded. As presented in Corradi et al. 2018, diagonal shear in-situ tests in rendered masonry wallets exhibited an increase in shear strength and stiffness by a factor of 5 and 8 respectively, compared to unrendered masonry wallets, while the render follows the shear crack in masonry and splits, without any detachment. This certainly applies in the case that the render is not highly deteriorated or partly missing. A diagonal compression test on a rendered wall, under a logic simplification, will include the thickness of the render into the net cross section shear area. Despite the asymmetry in sectional stiffness for one-sided rendered walls, it can be assumed that only the diagonal elongations from the unrendered side are accounted for the shear strains in masonry, and that the direct shear failure pattern will not change, as indeed verified during the capacity and fatigue diagonal compression test of the wallet DCf1. The shear strength of a rendered wall f_t, given the same lime-based mortar for joints and render and a hypothesis of simultaneous shear failure, can be considered as the sum of the shear strength of the masonry wall f_t^w and that

of the render f_t^r, according to the shear stress equations in ASTM E519/E519M-20 (Equation 65). Here, P_{max}^i, w_i, h_i and t_i are the respective maximum direct shear force, width, height and thickness of the masonry wallet (i=w) and render (i=r).

$$P_{max} = P_{max}^w + P_{max}^r = \sqrt{2} f_t^w \left(\frac{w_w + h_w}{2}\right) t_w + \sqrt{2} f_t^r \left(\frac{w_r + h_r}{2}\right) t_r \qquad \text{Equation 65}$$

Regarding the monotonic diagonal compression tests of the wallet DCf1, the shear stress-strain curve, and lateral strains from the attached LVDTs and strain gauges, both in masonry and in render are presented in Figure 74a and b. The diagonal compression test is performed with a displacement control rate of 2μm/s and the sampling rate is set at 4 Hz. As seen in Figure 74c, d and e, the wallet DCf1 fails under a diagonal splitting crack pattern, passing through the mortar joints and bricks, while the plaster follows the same splitting pattern, without a detachment at the interface with the masonry. Despite the low displacement control rate, the failure is abrupt, and no post-peak response is captured. Here is noted that considering the two strain gauges and their relative location, one is located directly over the shear crack (SG1), while the other is directly beside it (SG2), as seen in Figure 74e. Regarding the lateral strains in masonry and in the render, as recorded from the LVDTs and the strain gauges, those increase exponentially close to the point of failure, while the recorded strains from the strain gauges are much larger than the LVDTs, given the non-uniform strain conditions and the different measurement lengths. In fact, comparing the strain evolution from the two strain gauges, in SG1 is evident that the strains tend to localize and evolve exponentially in the area of the crack, while for SG2, in the masonry next to the crack, and right before failure, the tensile strain is reversed, with potential microcracks closing (Figure 74 b). Such an observation appears consistent with the smeared crack model, describing the transition from diffused microcracks to a macrocrack, and the post failure strain localization in the fracture process of brittle materials [Dvorkin et al. 1989 and Lourenco 1996]. The peak shear stress and shear modulus are equal to 1.1 MPa and 1.1 GPa respectively, found 3 and 1.3 times higher, compared to the average tensile strength and shear modulus of the unrendered wallets respectively, from the mechanical characterization tests of CHAPTER 3, Section 3.5.2 (Table 14). Regarding the secant shear stiffness evolution, a progressive decrease is evident after $0.5f_t$, while from 0.9-1.0f_t it drops immensely by 21%, as presented in Table 21.

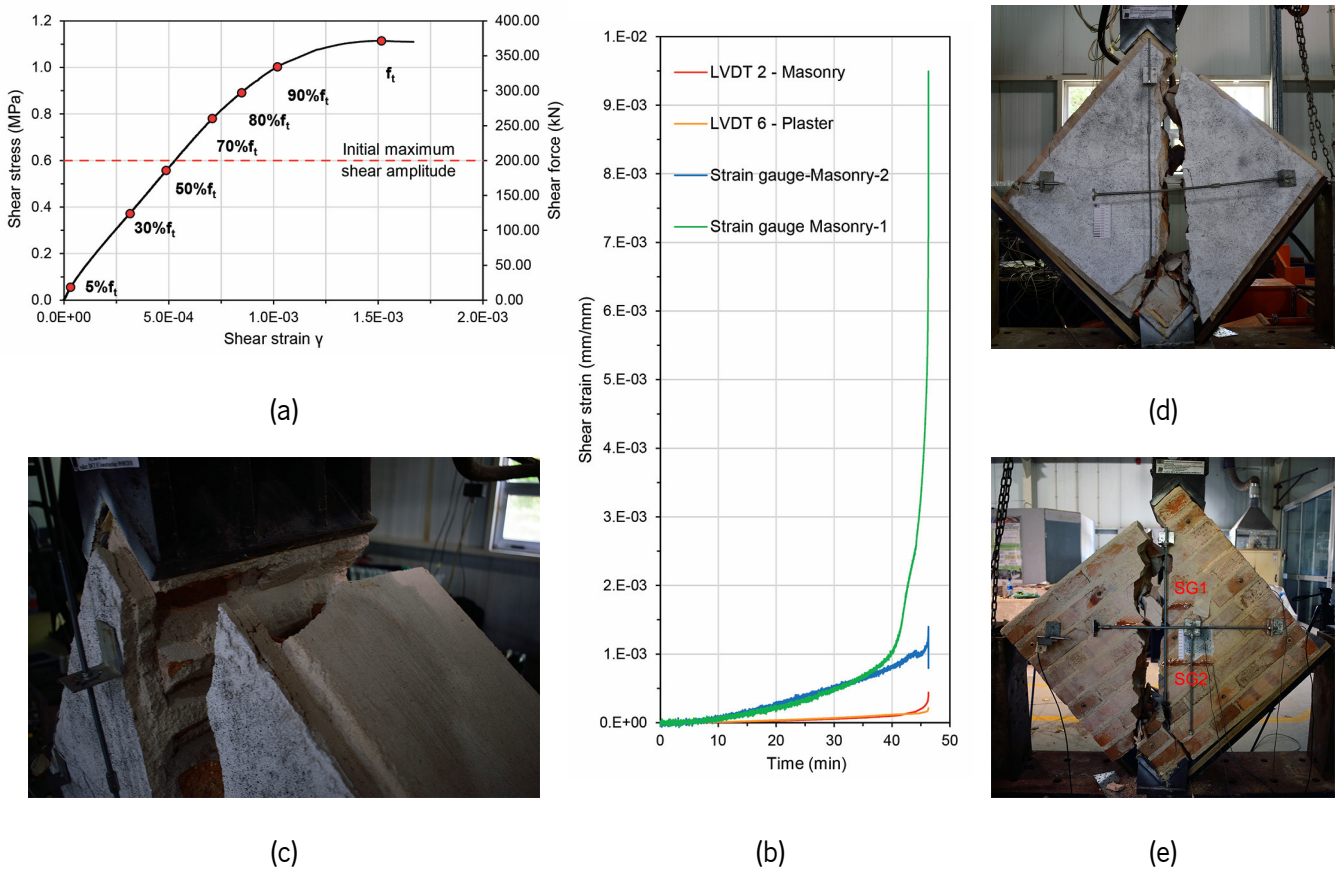


Figure 74. Monotonic diagonal compression test of wallet DCf1: (a) shear stress-strain curve until ultimate step. Note the chosen initial maximum shear amplitude of 200 kN for the fatigue tests of wallets DCfi-j; (b) lateral strains in time, from horizontal LVDTs and strain gauges attached in masonry and in plaster; (c) closeup on shear diagonal crack, with the splitting of plaster and without detachment from the substrate; failure of at last stage, as shown from the front (d) and the back side (e). Note the relative location of strain gauges SG1 and SG2.

In an attempt of curve fitting the shear stress strain behavior of a one-sided rendered brick masonry wallet, Equation 29 was used, found in Hoshikuma et al 1997, which as seen is Section 3.6, can even capture well the stress-strain envelope curve from the cyclic diagonal compression tests, until the peak (Figure 52). Still, at an intermediate step, a link should be established between the diagonal compression stiffness of rendered masonry and that of its individual components, i.e., the masonry wallet and the render. Here the combined shear modulus of plastered masonry $G_{mod,comb.}$ can be derived from Equation 66 as a function of the shear moduli $G_{mod,w}$ and $G_{mod,r}$ of the wallet and render respectively, under the concept of an equal shear strain hypothesis, as presented in Equation 65. Here, L and H are the respective length and height of the masonry wallet. Thus, considering for the shear modulus of masonry the average value from the characterization tests of CHAPTER 3, Section 3.5.2 (Table 14), equal to 868 MPa, while for the lime mortar render, the shear modulus can be associated to the bending modulus, which for rectangular sections is equal to the Young's modulus. Here, as a value for the Young's modulus of

lime mortar for 200 days of curing, a linear interpolation is performed from values of Table 8 with the value of 4.2 GPa assigned. Thus, under the analytical expression of Equation 66, a value for the shear modulus of the rendered masonry wallet DCf1 is calculated equal to 1.1 GPa, almost identical to the one derived from the diagonal compression test. Considering also the material properties of G_{mod}, G_{sec}, $\gamma_{33\%ft}$, γ_{ft} of DCf1, as presented in Table 21, the shear strength calculated from Equation 29 is equal to 1.1 MPa, identical to the actual shear strength of the diagonal compression test.

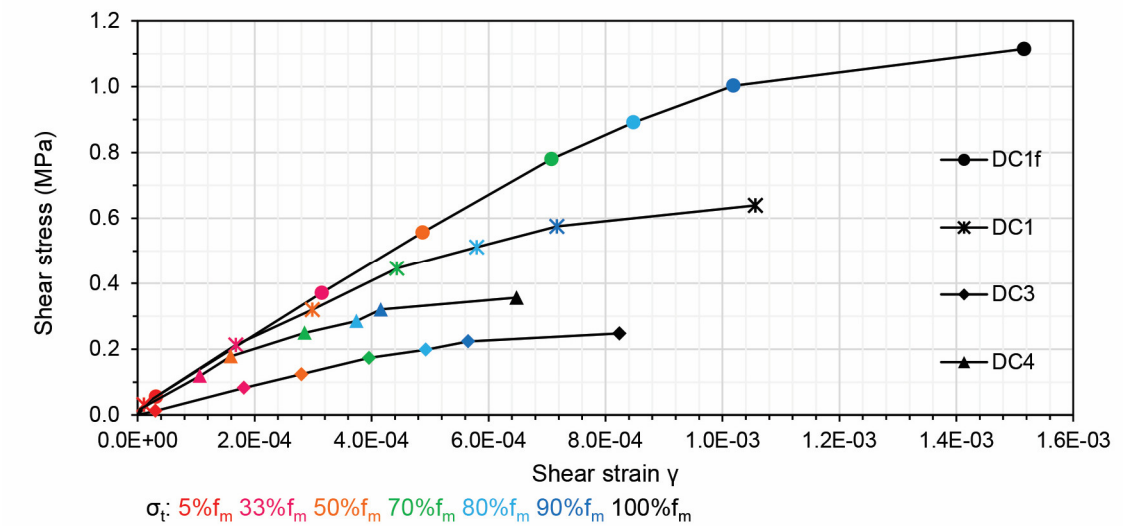
$$G_{mod,comb.} = \frac{L}{H} \cdot \frac{t_r G_{mod,r} + t_w G_{mod,w}}{t_w + t_r} \qquad \text{Equation 66}$$

In order to compare further the shear stress-strain response of the rendered wallet DCf1 and those from the mechanical characterization tests of CHAPTER 3 (DC1, DC3 and DC4), as seen initially from the graph of Figure 75a, no correlation is evident, except when values of stress and strain, corresponding to 5%, 33%, 50%, 70%, 80%, 90% and 100% of the shear strength, are normalized and superposed in the graph of Figure 75b and presented in Table 21. Is evident that the rendered wallet DCf1 presents a very similar normalized shear stress-strain response, and thus the same statistical normalized average can be used for both rendered and unrendered wallets. Similarly, the envelope curve of the Equation 29 can be used for rendered wallets, in order to fit the complete envelope and calculate the shear strength. Here, the relation between the shear modulus and secant shear modulus at peak, for the wallet DCf1 are used to define the constant n of Equation 29, which equals 2.36.

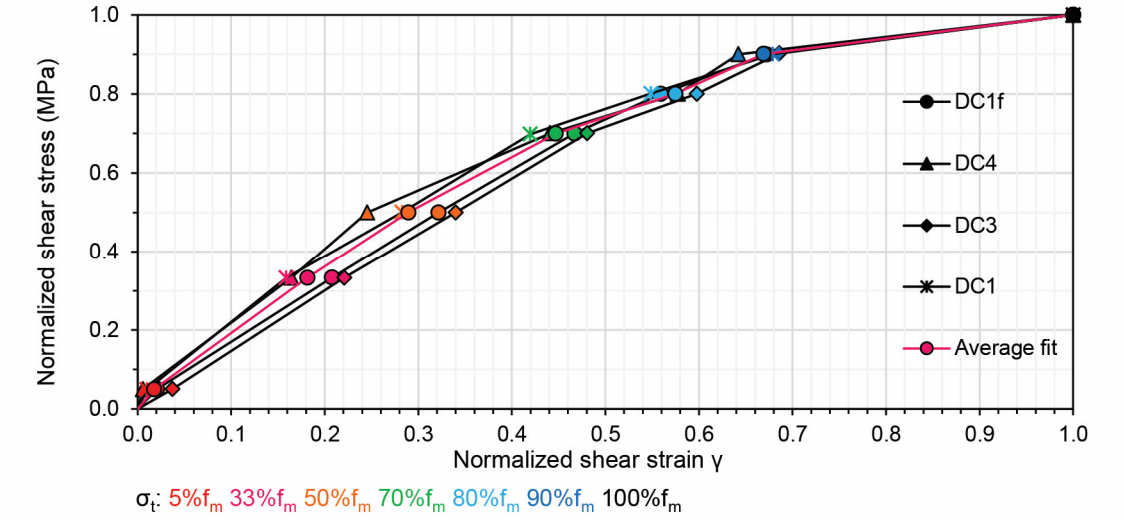
Table 21. Evolution of shear stress, shear strain and shear stiffness, during the monotonic diagonal compression test of wallets DCf1, DC1, DC2, DC3, DC4.

	%f_t	F (kN)	σ_t (Mpa)	$\sigma_{t,norm}$	γ (mm/mm)	γ_{norm}	G_{sec} (MPa)	$G_{sec,norm}$	G_{mod} (MPa)
DCf1	5%f_t	17	0.06	0.05	3.15E-05	0.02	1770	-	1114
	33%f_t	116	0.37	0.33	3.15E-04	0.21	1180	1.00	
	50%f_t	173	0.56	0.50	4.88E-04	0.32	1143	0.97	
	70%f_t	243	0.78	0.70	7.08E-04	0.47	1102	0.93	
	80%f_t	278	0.89	0.80	8.48E-04	0.56	1051	0.89	
	90%f_t	312	1.00	0.90	1.02E-03	0.67	984	0.83	
	100%f_t	347	1.11	1.00	1.52E-03	1.00	735	0.62	
DC1	5%f_t	9	0.03	0.05	1.07E-05	0.01	2908	-	1157
	33%f_t	59	0.21	0.33	1.68E-04	0.16	1269	1.00	
	50%f_t	88	0.32	0.50	2.99E-04	0.28	1071	0.84	
	70%f_t	123	0.45	0.70	4.43E-04	0.42	1007	0.79	
	80%f_t	141	0.51	0.80	5.80E-04	0.55	883	0.70	
	90%f_t	159	0.58	0.90	7.17E-04	0.68	802	0.63	
	100%f_t	179	0.64	1.00	1.06E-03	1.00	605	0.48	
DC2*	5%f_t	2	0.01	0.05	1.30E-05	0.02	654	-	422
	33%f_t	17	0.06	0.33	1.36E-04	0.16	444	1.00	
	50%f_t	25	0.09	0.50	2.19E-04	0.26	413	0.93	
	70%f_t	35	0.13	0.70	3.65E-04	0.44	345	0.78	
	80%f_t	40	0.14	0.80	4.56E-04	0.55	315	0.71	
	90%f_t	45	0.16	0.90	5.94E-04	0.72	274	0.62	
	100%f_t	50	0.18	1.00	8.26E-04	1.00	219	0.49	
DC3	5%f_t	4	0.01	0.05	3.06E-05	0.04	405	-	463
	33%f_t	23	0.08	0.33	1.82E-04	0.22	453	1.00	
	50%f_t	35	0.12	0.50	2.80E-04	0.34	442	0.98	
	70%f_t	49	0.17	0.70	3.96E-04	0.48	438	0.97	
	80%f_t	56	0.20	0.80	4.93E-04	0.60	402	0.89	
	90%f_t	63	0.22	0.90	5.65E-04	0.69	395	0.87	
	100%f_t	70	0.25	1.00	8.24E-04	1.00	301	0.66	
DC4	5%f_t	5	0.02	0.05	3.71E-05	0.01	4778	-	984
	33%f_t	33	0.12	0.33	1.06E-04	0.16	1117	1.00	
	50%f_t	50	0.18	0.50	1.59E-04	0.25	1121	1.00	
	70%f_t	70	0.25	0.70	2.86E-04	0.44	874	0.78	
	80%f_t	80	0.29	0.80	3.74E-04	0.58	763	0.68	
	90%f_t	90	0.32	0.90	4.16E-04	0.64	772	0.69	
	100%f_t	100	0.36	1.00	6.48E-03	1.00	550	0.49	

* DC2 Excluded due to sliding failure



(a)



(b)

Figure 75. Diagonal compression tests of DCf1, DC1, DC3 and DC4: (a) linearized piecewise functions of shear stress-strain curves until peak; (b) normalized shear stress-strain curves until peak and average fit at each designated point.

5.3.3. Static diagonal compression cyclic preload, initial stiffness monitoring and estimated initial material properties from analytical curve fitting

Prior to the fatigue tests, under diagonal compression cyclic loading, the rendered wallets DCf2, DCf3 and DCf4 were subjected to a preliminary cyclic diagonal compression test, with the primary objective to acquire the shear stiffness and obtain a diagonal compression capacity envelope fit. The preliminary cyclic diagonal compression tests were performed until a direct shear force of 200 kN, which according to the monotonic diagonal test of the wallet DCf1 corresponds to a tensile stress greater than 50% of the tensile strength. The diagonal compression cyclic load was applied gradually in 5-7 cycles, under a displacement control rate of 2μm/s and a sampling rate of 4 Hz, in order to acquire initial stiffness characteristics and to design the fatigue shear loading

protocols. Thus, considering the evolution of the shear stress-strain curve, the peak shear stress-strain values for each cycle were used as input data for finding the best envelop fit from Equation 29, and according to the variables of G_{mod}, f_t and γ_{ft}, for each of the rendered wallets DCfi. Here, the n parameter and the corresponding ratio of the shear modulus to the secant one, was fixed to 2.63 and 1.73 respectively, according to the testing results of DCf1. As presented in Figure 76a, b and c and in Table 22, through the fitting process, and before the actual diagonal compression fatigue tests, the initial shear modulus and tensile strength for the wallets DCf2, DCf3 and DCf4, were statistically verified. As seen also in the graphs of Figure 76d and e, the initial shear stiffness is similar to the fully tested masonry wallets (DCf1, DC1, DC3 and DC4) and the normalized shear stress-strain evolution follows the same curvature.

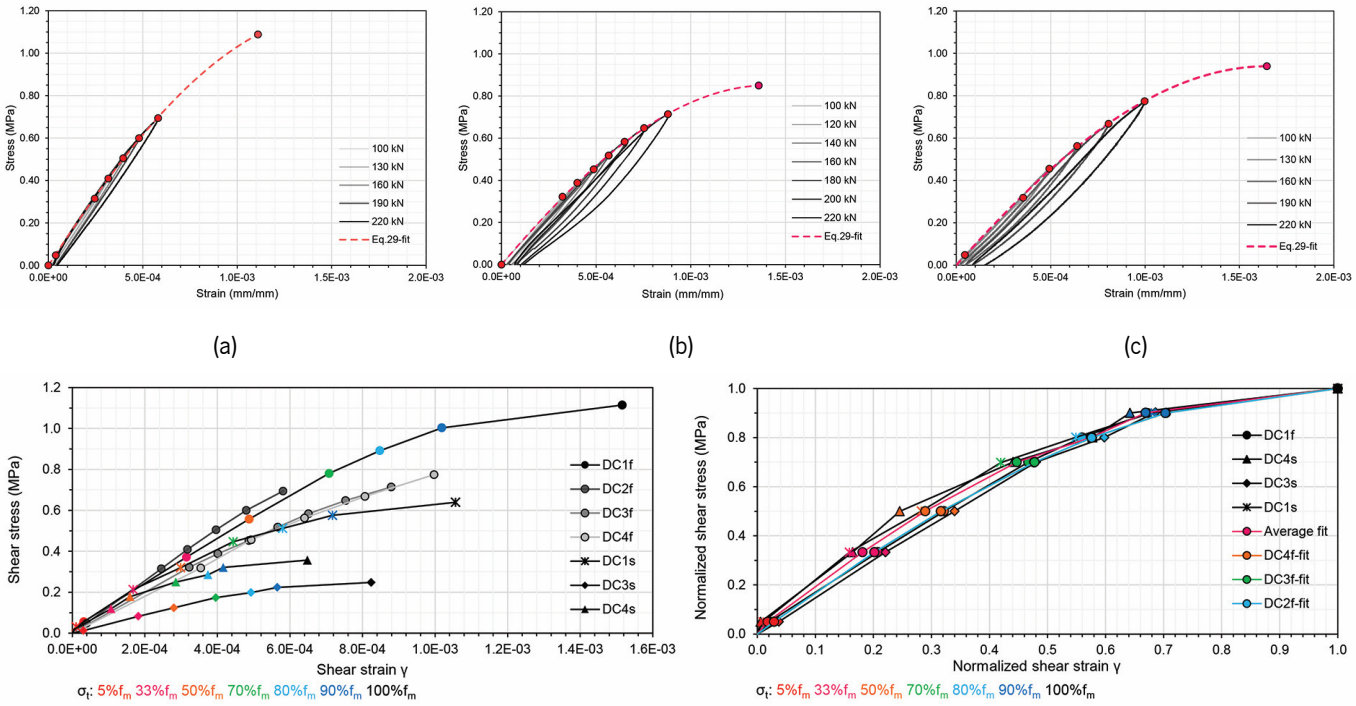


Figure 76. Preliminary cyclic diagonal compression tests for wallets DCf2 (a), DCf3 (b) and DCf4 (c), with fit envelope curves until peak; (d) linearized shear stress-strain curves of wallets DCf1, DC1, DC3, DC4, DCf2, DCf3 and DCf4; (e) normalized shear stress-strain curves until peak, of wallets DCf1, DC1, DC3, DC4, DCf2, DCf3 and DCf4 and average fit at each designated point.

Table 22. Evolution of shear stress, shear strain and shear stiffness, for rendered wallets DCf2, DCf3 and DCf4, retrieved from the envelope curve of the preliminary cyclic diagonal compression tests and the envelope curve fit of Equation 29, until the peak. Note the predicted tensile strength, peak shear strain and shear modulus, according to the curve fitting process.

	%f_t	F (kN)	σ_t (MPa)	$\sigma_{t,norm}$	γ (mm/mm)	γ_{norm}	G_{sec} (MPa)	$G_{sec,norm}$	G_{mod} (MPa)	Goodness of fit
DCf2	5%f_t	19	0.06	0.05	4.36E-05	0.03	1353	-	**1358**	SSE 1.1E-04 R-square / Adj. R-square 0.999 / 0.998 RMSE 6.0E-3
	33%f_t	124	0.39	0.33	3.05E-04	0.20	1293	1.00		
	50%f_t	186	0.59	0.50	4.77E-04	0.32	1238	0.96		
	70%f_t	261	0.83	0.70	7.21E-04	0.48	1148	0.89		
	80%f_t	298	0.95	0.80	8.69E-04	0.58	1087	0.84		
	90%f_t	335	1.06	0.90	1.06E-04	0.70	1003	0.78		
	100%f_t	372	**1.18**	1.00	**1.51E-03**	1.00	**784**	0.61		
DCf3	5%f_t	13	0.04	0.05	4.09E-05	0.03	1041	-	**1045**	SSE 7.5E-05 R-square / Adj. R-square 0.999 / 0.999 RMSE 3.9E-3
	33%f_t	87	0.28	0.33	2.85E-04	0.20	995	1.00		
	50%f_t	131	0.43	0.50	4.47E-04	0.32	953	0.96		
	70%f_t	183	0.60	0.70	6.73E-04	0.48	884	0.89		
	80%f_t	209	0.68	0.80	8.15E-04	0.58	836	0.84		
	90%f_t	235	0.77	0.90	9.94E-04	0.70	771	0.77		
	100%f_t	261	**0.85**	1.00	**1.41E-03**	1.00	**603**	0.61		
DCf4	5%f_t	15	0.05	0.05	4.77E-05	0.03	984	-	**987**	SSE 2.7E-04 R-square / Adj. R-square 0.998 / 0.997 RMSE 9.5E-3
	33%f_t	97	0.31	0.33	3.33E-04	0.20	940	1.00		
	50%f_t	146	0.47	0.50	5.22E-04	0.32	900	0.96		
	70%f_t	204	0.66	0.70	7.86E-04	0.48	835	0.89		
	80%f_t	233	0.75	0.80	9.51E-04	0.58	790	0.84		
	90%f_t	262	0.85	0.90	1.16E-04	0.70	729	0.77		
	100%f_t	291	**0.94**	1.00	**1.65E-03**	1.00	**570**	0.61		

5.3.4. Diagonal compression fatigue test setup, preparation, instrumentation and data acquisition

5.3.4.1. Equivalent oscillating motion characteristics of a fatigue loading regime

In order to design an accelerated fatigue experimental test, and according to the exact intermittent, transient or pseudo-steady vibration regime, an equivalent, continuous oscillation is designed. In oscillatory signals under a constant excitation frequency f, the acceleration is the second time derivative of displacement or the first time derivative of velocity. Since in oscillatory motion, the peak particle velocity (ppv) v is directly linked to the peak particle displacement (ppd) d, the peak particle acceleration (ppa) a, and the vibration frequency f or the radial frequency ω, under the Equation 67, found in BS 5228-2:2009+A1:2014.

$$a = 2\pi f v = (2\pi f)^2 d \, , \omega = 2\pi f \qquad \text{Equation 67}$$

In general, vibration induced loading stresses are expressed as a function of velocity. The equation of motion, under the equilibrium of gravitational forces and those of a dynamically induced displacement field, with time-histories of velocities $\dot{u}(x,t)$, accelerations $\ddot{u}(x,t)$ and displacements $u(x,t)$ is given by Equation 68. All forces are acting in the direction of the

displacement, here noted as x. By differentiating in time, the equilibrium equation contains only the dynamic quantities (Equation 69). Total deflections and stresses can be obtained by the corresponding static quantities and the dynamic ones [Bai and Xu 2019]. Here, M is mass of the dynamic system, C is the damping, W is the weight of the dynamic system, p(t) is the dynamic external force, Δ_{st} is the static displacement, p_{st} is the static external force and K is the stiffness of the dynamic system.

$$M\ddot{u}(x,t) + C\dot{u}(x,t) + K\big(\Delta_{st}(x) + u(x,t)\big) = p(t) + p_{st} + W \qquad \text{Equation 68}$$

$$M\ddot{\bar{u}}(x,t) + C\dot{\bar{u}}(x,t) + K\bar{u}(x,t) = p(t) \qquad \text{Equation 69}$$

The external real motion expression, of the displacement $u(t)$ under an elastic sinusoidal waveform of angular frequency ω is expressed by Equation 70. Here the phase is adjusted so as the peak displacement occurs at time zero.

$$u(t) = u_o \sin(-\omega t + \frac{\pi}{2}) \qquad \text{Equation 70}$$

The internal real motion expression of the displacement $u(x,t)$, under an elastic sinusoidal waveform, with the peak displacement at time zero, equal to the static one, is given by Equation 71. Here, k is the angular wavenumber of the wave. The first and second derivative of displacement, per length and in time are given by Equation 72, Equation 73, Equation 74 and Equation 75. By equalizing Equation 73 and Equation 75, the strain is inversely proportional to the speed of propagation c and proportional to the velocity, as shown in Equation 77. Regarding the propagating wave medium and accounting for fixed boundaries at both ends in elevation, mostly due to compression, and similar to an infinitely long longitudinal rod, the dynamic axial stress is proportional to the velocity (Equation 78) [Gazonas et al. 2015]. Here, uniform elastic conditions are assumed through the height of the specimen, which under longitudinal stress waves, the wave velocity is given by Equation 79, with v the Poisson ratio, E the modulus of elasticity and p the density of the elastic medium [C 597-02 2003].

$$u(x,t) = u_o \cos(kx - \omega t + \frac{\pi}{2}) \qquad \text{Equation 71}$$

$$\frac{\partial u}{\partial x} = -k u_o \sin(kx - \omega t + \frac{\pi}{2}) \qquad \text{Equation 72}$$

$$\frac{\partial^2 u}{\partial x^2} = -k^2 u_o \cos(kx - \omega t + \frac{\pi}{2}) \quad \text{Equation 73}$$

$$\frac{\partial u}{\partial t} = \omega u_o \sin(kx - \omega t + \frac{\pi}{2}) \quad \text{Equation 74}$$

$$\frac{\partial^2 u}{\partial t^2} = -\omega^2 u_o \cos(kx - \omega t + \frac{\pi}{2}) \quad \text{Equation 75}$$

$$\frac{\partial^2 u}{\partial x^2} = \frac{1}{c^2}\frac{\partial^2 u}{\partial t^2}, k = \frac{\omega}{c} \quad \text{Equation 76}$$

$$\frac{\partial}{\partial x} u(x,t) = -\frac{1}{c}\frac{\partial}{\partial t} u(x,t) \quad \text{Equation 77}$$

$$\sigma_c(x,t) = E\frac{\partial}{\partial x} u(x,t) = -\frac{E}{c}\frac{\partial}{\partial t} u(x,t) = \frac{E\omega u_o}{c} \sin\left(kx - \omega t + \frac{\pi}{2}\right) \quad \text{Equation 78}$$

$$c = V_S = \sqrt{\frac{E}{p}\frac{1-v}{(1+v)(1-2v)}} \quad \text{Equation 79}$$

5.3.4.2. Selection of fatigue equivalent sinusoidal load for assigned levels of ground-borne vibrations

After obtaining the link between shear stiffness and displacement for each wallet (Table 22 in Section 5.3.3), shear fatigue cyclic amplitudes were established, in terms of targeting displacements, and according to the measured stiffness of each wallet. Here is noted that for the tested specimens, acquisition data from LVDTs and strain gauges were used, as described in 5.3.2.

Regarding the in-situ statistical amplitudes of velocity and acceleration time histories from the Church of the Angels in Lisbon (see CHAPTER 4), they were found quite low, and thus were not used as a reference for the diagonal compression fatigue tests. Instead, three amplitude thresholds of ppv were chosen, one for each of the three tested wallets, according to DIN 4150-3 2016. Thus, considering a reference location at the basement of a building and counting for the average dominant frequency of the induced ground-borne vibration signals, as measured in the Church of the Angels, namely 65 Hz (408 rad/s) (Table 20), the ppv values of 8, 10 and 16 mm/s were chosen, which correspond to a lower bound, an upper bound and a chosen extreme value respectively, for the category of monumental structures and a dominant frequency vibration range of 50-100 Hz (Table 17) [DIN 4150-3 2016].

Moving on to the actual specimens, the targeted displacement amplitudes to be applied during the diagonal compression fatigue tests, were adjusted according to chosen ppv values and the averaged dominant frequency of the induced ground-borne vibration signals, according to Equation 67. In order to match the ppd target values for the fatigue tests, direct measurements were used from a vertical LVDT, attached in masonry and measuring from the center of the diagonal until the lower corner, here the LVDT 3 in Figure 73. According to the average chord stiffness in each wallet, corresponding to a shear force range of 100-200 kN, from the loading and unloading branches of a cyclic static preload diagonal compression test, the shear force amplitude P_a, of the sinusoidal fatigue load, was defined, as shown in Table 23.

Table 23. Fatigue ppv, ppd target amplitudes, with the corresponding shear force amplitudes for each wallet.

Specimen DCfi	Target ppv (mm/s)	Reference dominant radial frequency ω (rad/s)	Reference dominant frequency f (Hz)	Target ppd $\delta_o = \frac{u_o}{\omega}$ (mm)	$K_{chord}^{(100-200)kN*}$ (kN/mm)	Target shear force amplitude P_a (kN)
DCf4	8	408	65	0.018	758.41	14
DCf2	10			0.025	1113.92	28
DCf3	16			0.040	771.64	31

* Average chord stiffness from loading and unloading branch.

5.3.4.3. Fatigue testing protocols

Once the fatigue loading amplitudes were calibrated, the fatigue loading history for each specimen contained a constant shear stress amplitude σ_a, applied under a cyclic sinusoidal pattern, and at a relatively low frequency, that of 2 Hz, a decision based, considering also to safety performance criteria during the long-term duration of the tests. Here is noted that under regular hydraulic actuators, fatigue loading in the laboratory can only be applied as a cyclic quasi-static load, thus, with no dynamic effects. The static shear stress σ_m was considered also a parameter of influence. Thus, fatigue tests were divided into static loading (A_j), cyclic fatigue loading (B_j) and static unloading (C_j) branches, all under force control, in order to maintain the same stress amplitudes, under cumulative shear strains and progressive stiffness degradation. Here, the load rate and sampling frequency for each branch are presented in Figure 77 and Table 24. For a realistic, accelerated, fatigue testing duration (B_j), considering an average passing train time interval of 4 min and a period of 1.5 years, with high vibration amplitudes, it returns a total number of around 150000 cycles. According to the assigned cyclic frequency of 2Hz, the duration of a single fatigue branch was around 21h. Initially, an upper bound for the fatigue shear stress (σ_{max})

is set, that of 200 kN, as selected in 5.3.2. Once a fatigue test j is complete, and without failure ($A_j - B_j - C_j$), the wallet is loaded at a higher average static shear stress, with an additional increment of 15 kN ($\simeq 5\% f_t$) and the fatigue test is repeated, until failure is reached. Such a logic can reflect on constant fatigue loading conditions and a static service load increase, i.e., a dead load increase from structural interventions (floor additions, strengthening etc.) and a change of load paths from non-fatigue related damage, namely settlements, earthquakes etc. Here the sequential process of diagonal compression fatigue testing for all three brick masonry wallets, with lime mortar joints and a one-sided render, together with shear stiffness acquired data at the beginning and end of the fatigue test, are presented in Table 25. Note that stiffness properties at the end of each fatigue branch were acquired after the temperature compensation of the following Section 5.3.4.5.

According to the fatigue loading regimes, the DCf2 wallet was subjected to 11 fatigue tests (σ_a = 0.09 MPa and σ_m = 0.59-0.94 MPa), the wallet DCf3 to 3 fatigue tests (σ_a = 0.1 MPa and σ_m = 0.54-0.64 MPa), and the wallet DCf4 to 6 fatigue tests (σ_a = 0.04 MPa and σ_m = 0.60-0.84 MPa), presented in Table 25. As can be seen in overall from Table 25, for all testing wallets, the elastic and secant shear modulus of each loading branch A_j, progressively diminishes, after each fatigue branch (B_j), a clear indication of fatigue damage and progressive softening, discussed in the following chapters. Regarding the shear modulus of the first loading branch (A_1), that is found lower compared to the one from the cyclic static preload of Table 22, by 12%, 17% and 33% for DCf2, DCf3 and DCf4 respectively, and is attributed to the accumulated damage during those cycles.

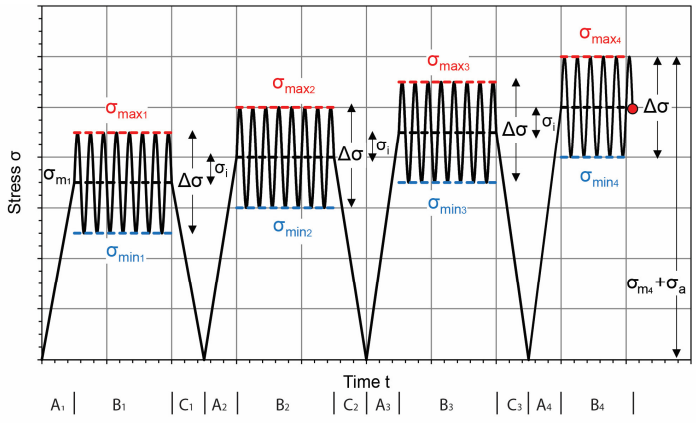


Figure 77. Load rate scheme on loading-fatigue-unloading branches of performed diagonal compression fatigue tests. Note the constant stress range $\Delta\sigma$ and the steady increase of static stress increment σ_i, for each consecutive fatigue test, until the failure of the wall specimen.

Table 24. Fatigue testing protocols for the three consecutive loading branches.

Loading branch	A_j	B_j	C_j
Load Pattern	Monotonic	Sinusoidal	Monotonic
Control type	Force	Force	Force
Loading rate	0.12 kN/s	2Hz	0.12 kN/s
Sampling rate	4 Hz	25 Hz	2 Hz
Recording	Continuous	5 Cycles/100s	Continuous
Safety condition	Relative displacement of 25 mm	Relative displacement of 25 mm	Relative displacement of 25 mm
Cycles	1	150000	1

Table 25. Fatigue sign variables for diagonal compression, for each of the testing wallets (DCfi) and fatigue parts (j).

	A_i				**B_i**							**C_i**		**A_{i+1}**	
DCfi,j	Peak shear load P_m kN	Peak shear load σ_m mPa/%ft*	G_{MOD}** MPa	G_{SEC} MPa	Shear load range P_a (P_{max}-P_m) kN	Shear stress range σ_a (σ_{max}-σ_m) MPa/%ft*	R $\left(\frac{\sigma_{min}}{\sigma_{max}}\right)$	A $\left(\frac{\sigma_a}{\sigma_m}\right)$	S $\left(\frac{\sigma_{max}}{\sigma_m}\right)$	Cycles	G_{SEC} MPa	Peak shear load P_m kN	Peak shear stress σ_m MPa/%ft*	Shear force incr. P_i kN	Shear stress incr. σ_i MPa/%ft*
DCf2,1	200	0.59/50%	1188.8	1180.9	28	0.09/8%	0.74	0.15	1.15	$1.5{\cdot}10^5$	1073.3	200	0.59/50%	-	-
DCf2,2	200	0.59/50%	1131.7	1122.5	28	0.09/8%	0.74	0.15	1.15	$1.5{\cdot}10^5$	1047.6	200	0.59/50%	-	-
DCf2,3	200	0.59/50%	1076.7	1098.7	28	0.09/8%	0.74	0.15	1.15	$1.5{\cdot}10^5$	1059.7	200	0.59/50%	-	-
DCf2,4	200	0.59/50%	1091.7	1089.6	28	0.09/8%	0.74	0.15	1.15	$1.5{\cdot}10^5$	1034.0	200	0.59/50%	-	-
DCf2,5	215	0.64/54%	1068.5	1065.6	28	0.09/8%	0.75	0.14	1.14	$1.5{\cdot}10^5$	962.6	215	0.64/54%	15	0.05/4%
DCf2,6	220	0.69/58%	1051.4	1060.2	28	0.09/8%	0.77	0.13	1.13	$1.5{\cdot}10^5$	977.9	220	0.69/58%	15	0.05/4%
DCf2,7	235	0.74/63%	993.7	1028.7	28	0.09/8%	0.78	0.12	1.12	$1.5{\cdot}10^5$	953.9	235	0.74/63%	15	0.05/4%
DCf2,8	250	0.79/67%	979.5	1004.6	28	0.09/8%	0.80	0.11	1.11	$1.5{\cdot}10^5$	913.9	250	0.79/67%	15	0.05/4%
DCf2,9	265	0.84/71%	959.4	976.4	28	0.09/8%	0.81	0.11	1.11	$1.5{\cdot}10^5$	879.6	265	0.84/71%	15	0.05/4%
DCf2,10	280	0.89/75%	922.0	946.5	28	0.09/8%	0.82	0.10	1.10	$1.5{\cdot}10^5$	817.0	280	0.89/75%	15	0.05/4%
DCf2,11	295	0.94/79%	856.1	891.1	28	0.09/8%	0.83	0.10	1.10	4	-	295	0.94/79%	15	0.05/4%
DCf3,1	165	0.54/63%	867.4	886.8	31	0.10/12%	0.64	0.22	1.22	$1.5{\cdot}10^5$	743.5	165	0.54/63%	-	-
DCf3,2	180	0.59/69%	851.7	877.6	31	0.10/12%	0.66	0.20	1.20	$1.5{\cdot}10^5$	726.2	180	0.59/69%	15	0.05/6%
DCf3,3	195	0.64/75%	750.0	779.5	31	0.10/12%	0.68	0.19	1.19	$7.0{\cdot}10^5$	323.4	195	0.64/75%	15	0.05/6%
DCf4,1	185	0.60/64%	662.5	716.0	14	0.04/4%	0.88	0.07	1.07	$1.5{\cdot}10^5$	740.3	185	0.60/64%	-	-
DCf4,2	200	0.65/69%	627.6	704.8	14	0.04/4%	0.88	0.06	1.06	$1.5{\cdot}10^5$	666.5	200	0.65/69%	15	0.05/5%
DCf4,3	215	0.69/73%	607.0	703.8	14	0.04/4%	0.89	0.06	1.06	$1.5{\cdot}10^5$	657.3	215	0.69/73%	15	0.05/5%
DCf4,4	230	0.74/79%	581.4	685.7	14	0.04/4%	0.90	0.05	1.05	$1.5{\cdot}10^5$	641.5	230	0.74/79%	15	0.05/5%
DCf5,5	245	0.79/84%	562.7	678.8	14	0.04/4%	0.90	0.05	1.05	$1.5{\cdot}10^5$	638.2	245	0.79/84%	15	0.05/5%
DCf4,6	260	0.84/89%	507.2	632.9	14	0.04/4%	0.91	0.05	1.05	$6.3{\cdot}10^5$	461.1	260	0.84/89%	15	0.05/5%

* Estimated diagonal compression monotonic capacity, from fitting cyclic preload tests with Equation 29

** Estimated from 5-100 kN shear load range

5.3.4.4. Instrumentation and data acquisition

By enforcing the specifications of Section 5.3.4.3, the accelerated diagonal compression fatigue tests were performed for wallets DCf2, DCf3 and DCf4. In total, continuous regular acquisitions of diagonal compression fatigue tests until failure, for each masonry wallet, lasted from 3-11 days. Here, the diagonal compression load-time histories and the failure modes for all three specimens are presented in Figure 78. From Figure 78d, e and f is evident that the resulting failure from the diagonal compression fatigue tests is the same as the one from the monotonic diagonal compression load application, namely the vertical shear crack at the diagonal, with cracks compiled by sliding of bed and head joints, and with the splitting of brick units. From the upper corner, the shear crack initiates from the first or second bed joint, after the steel cap. Regarding the render, it detaches only at the corners, while for the rest of the wall, it follows the same split throughout. For wallet DCf3, a double vertical fragmentation occurs, from both sides of the steel caps, forming a somewhat diagonal pole (Figure 78f).

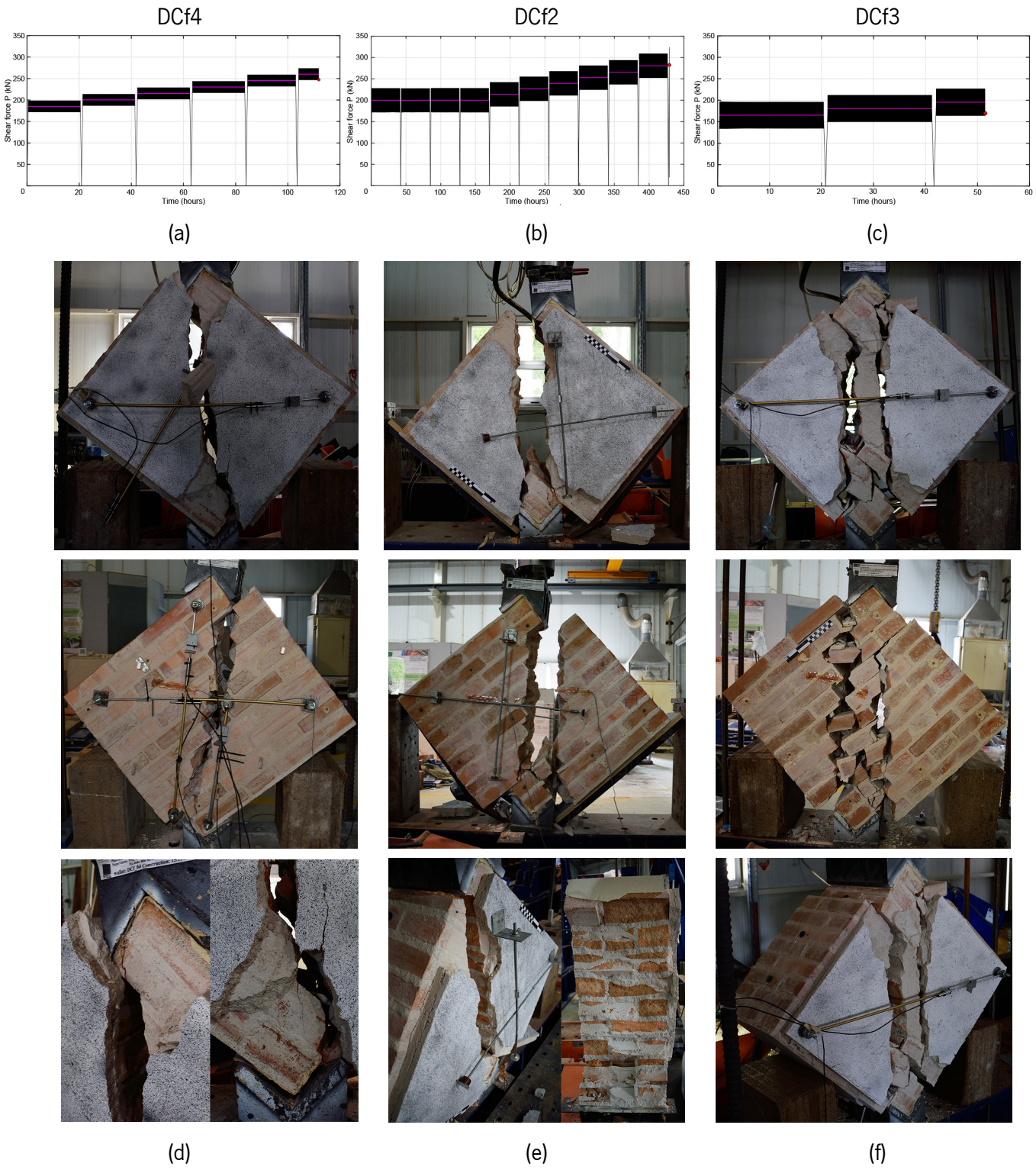


Figure 78. Diagonal compression fatigue load-time histories for wallets DCf4 (a) DCf2 (b) and DCf3 (c), and respective failure modes (d), (e) and (f). Note the presented order of the tested specimens, according to the chosen progressive amplitude of the fatigue diagonal compression loading.

5.3.4.5. Temperature effect and displacement compensation

Given the size of the wallets, the fatigue tests were performed in a conventional steel testing frame, under interior, but not controlled environmental conditions. Thus, displacement data were temperature dependent, following complex contractions and dilations, part from the masonry wallets and part from the metallic bearing rods of the LVDTs, which for detecting infinitesimal strain variations from fatigue, were found significant. In fact, a 48 h acquisition was performed with one of the specimens at zero load application and the displacement-time histories, superposed with the temperature variations are presented in Figure 79. Is clearly evident that the measured dilations and contractions follow the temperature evolution in a somewhat linear trend (Figure 79). In fact, the masonry wallet, with the increase of temperature, appears to dilate, both in the vertical and horizontal diagonal, judging from the relative positive (for tension) and negative (for compression) recorded translations of the LVDTs.

Thus, temperature and humidity sensors provided continuous readings throughout the fatigue tests, and the linear temperature effects were compensated, up to an extent, while for the loading and unloading branches, those were found to be insignificant (given the relatively short time). Such a temperature perturbation could be avoided by performing the fatigue tests in a controlled environment, that of a climatic chamber. Yet, given the size of the tested specimens, no such space was available.

The process of temperature compensation, for the resulted shear strains from the LVDTs and the lateral strains from the strain gauges, for every fatigue branch, had to follow an initial stage of resampling, through linear interpolant functions, in order to match the sampling rates for both measured quantities. The entire process of temperature compensation is visualized in the process diagram of Figure 80.

In Figure 81a, c and e, Figure 82a, c, e and g, and Figure 83a, c and e, the resulted raw data of shear strain-time histories from the LVDTs in masonry and render, and the lateral strain-time histories of the strain gauges in masonry are superposed with the recording temperatures, during the fatigue branches. The trend lines for each fatigue branch j, of each wallet DCfi, together with the resulting crack-line in masonry are presented in Table 42, Table 43 and Table 44 in ANNEX A. Here is noted that temperature correlation was performed with the average direct displacements of the fatigue loading branch, as obtained from the upper and lower envelops. The translation-

temperature correlation differs between each fatigue branch, which can be attributed to the compilation of the many dilating and contracting elements. A limit though was established, for accounting the temperature effects, namely an R-square value of the linear trendline higher than 0.7. In fact, in acquisitions with low temperature variations, a linear trend with translations was not possible to be established, also given the low resolution of the temperature and humidity sensors ($\pm 0.5C^{o}$). Such a task was proven more cumbersome for the translations from the LVDTs attached in the render, given their much lower amplitude. As fatigue cycles progressed, and moving closer to failure, where strains increased in order of magnitude, the temperature effect was also found less significant (Table 42, Table 43and Table 44 in ANNEX A). Resulting strain-time histories with temperature compensation are presented in Figure 81b, d and f, Figure 82b, d, f and h, and Figure 83b, d and f.

Considering the shear and lateral strain-time histories, in each fatigue branch, and after the temperature detrending, the direct average shear strain in masonry exhibits a small but positive trend (Figure 81b, Figure 82b, and Figure 83b). Direct fatigue shear strains in the render surface are also found with a small positive trend, but less in absolute amplitudes, compared to those in masonry, which is attributed to the uneven sectional stiffness of the one-sided rendered wallet (Figure 81d, Figure 82d, and Figure 83d). Yet at the last fatigue branch, and right before failure, for wallets DCf3 and DCf4, the diagonal compression strains in the render, instead of increasing exponentially, as documented in the masonry surface, they diminish, which indicates that the render is in fact under a reversed mostly vertical deformation, due to out-of-plane bending and bulging (Figure 83b and d and Figure 81b and d).

Regarding the strain gauges attached in masonry, their use appears particularly beneficial, as they can capture fatigue strain reversals, with either positive or negative trends. As seen in Figure 81f and in Figure 82h and considering their relative location, with respect to the vertical shear crack (ANNEX A), for wallets DCf4 and DCf2 respectively, the final macro crack forming out of the range of the strain gauge, is documented with the acquired lateral strain diminishing, that for the entire last fatigue branch for wallet DCf4 (DCf4-6) (Figure 81f) and most of the fatigue branches for wallet DCf2 (Figure 82h). Instead, if the strain gauge covers the crack area, as in the case of wallet DCf3 (Figure 83f) and the second one for wallet DCf2 (Figure 82f), the acquired lateral fatigue strains, increase exponentially, until failure.

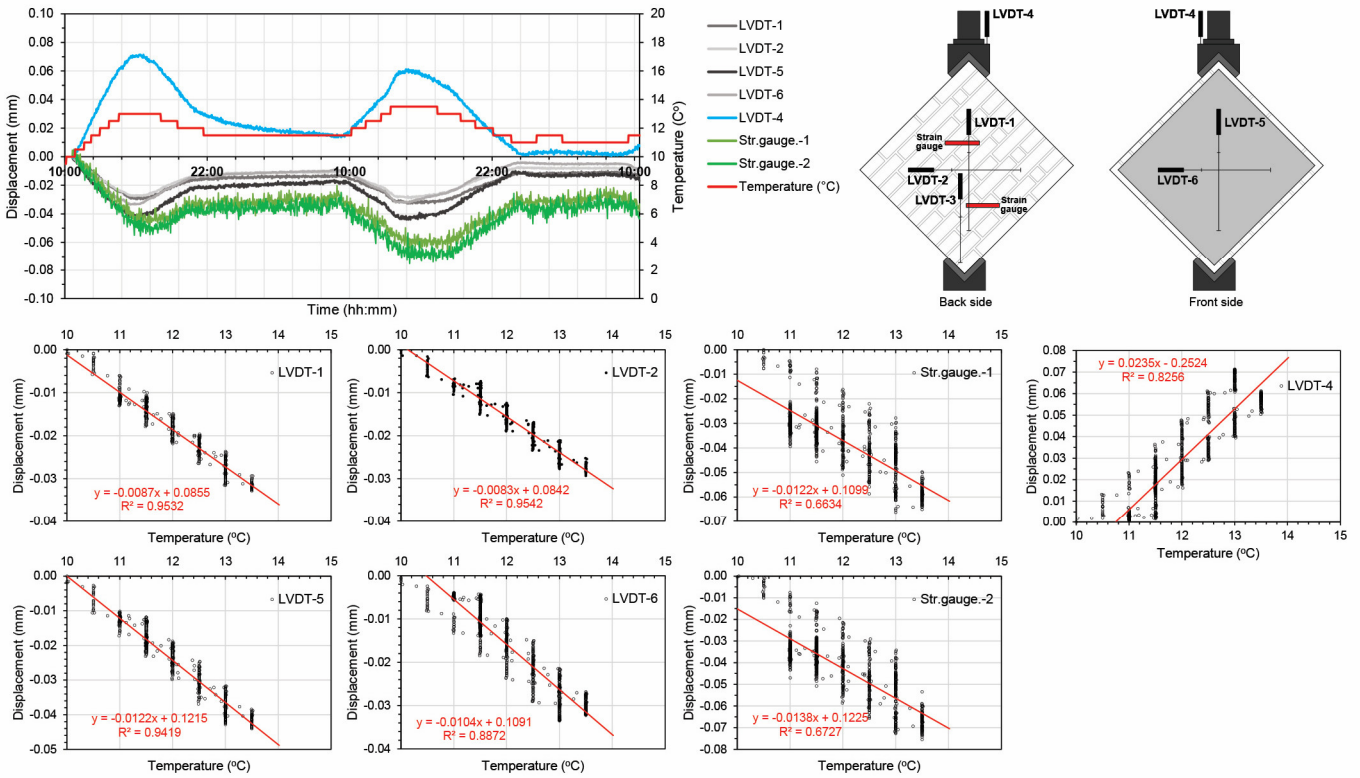


Figure 79. Temperature variation in displacement acquisition data for testing conditions of DCfi wallets. Displacement and temperature time histories from respective LVDTs, strain gauges and temperature sensors, for a 48h recording period, and without external loading. Correlation graphs of displacement and temperature data and linear trends.

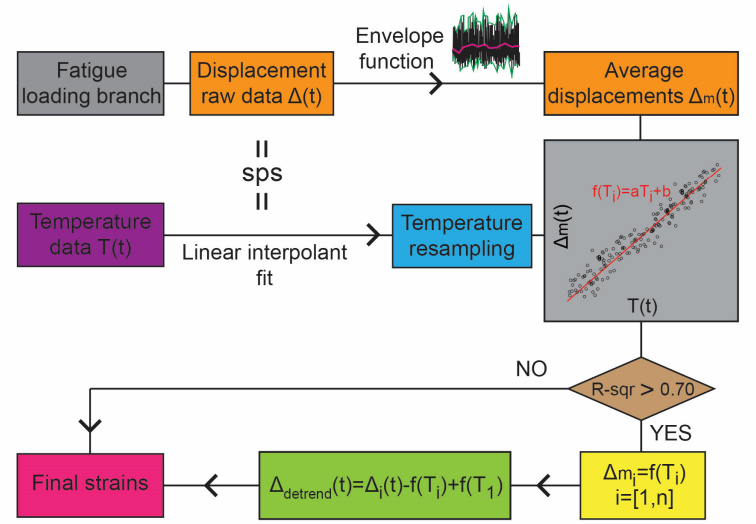


Figure 80. Process diagram for temperature compensation of large time series fatigue displacement raw data, from LVDTs and strain gauges. Note the equal condition for the samples per sec (sps) of temperature and displacement data.

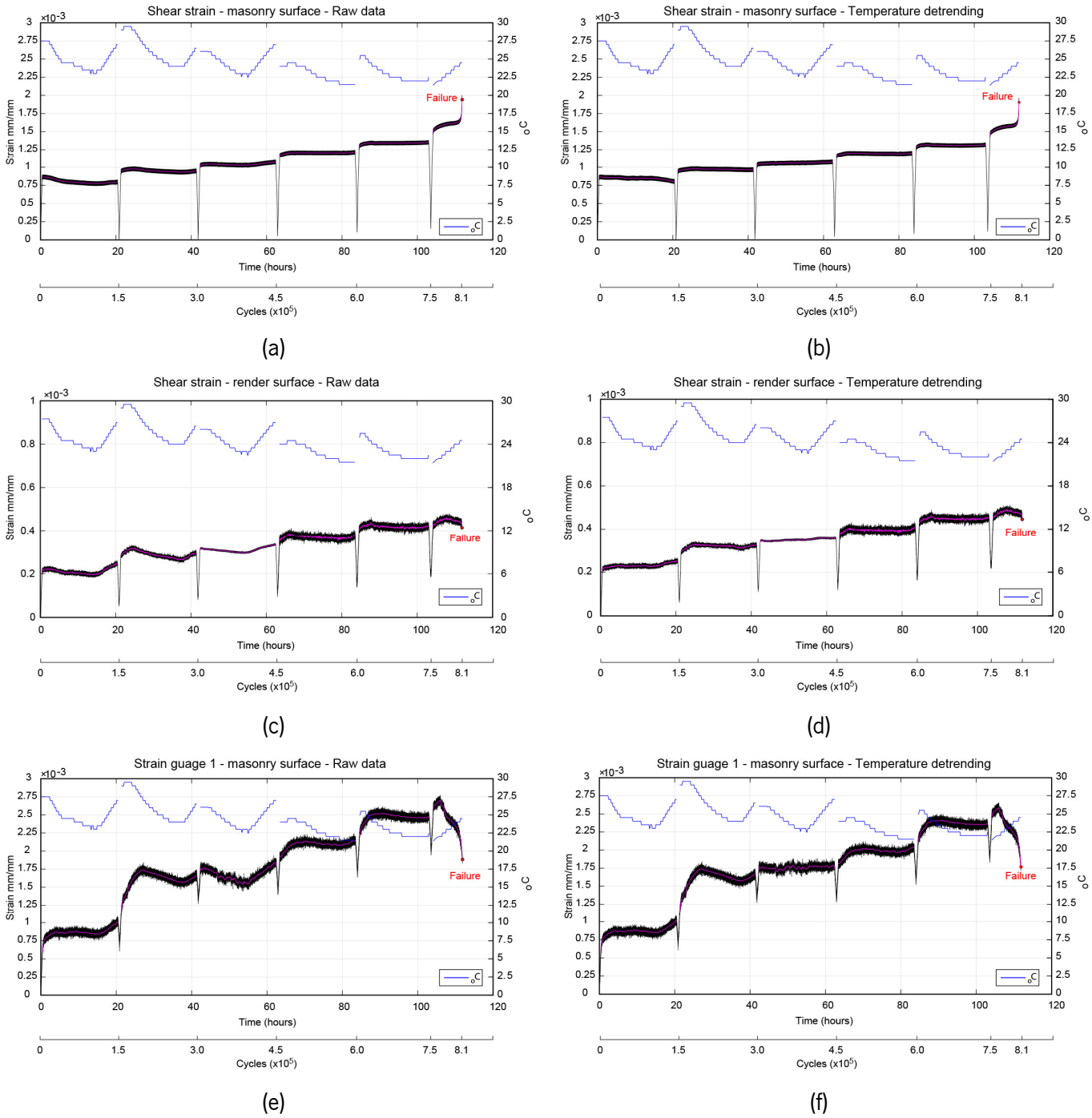


Figure 81. Raw data and temperature detrending of fatigue cyclic shear tests in diagonal compression for wallet DCf4: (a) and (b) shear strain in masonry; (c) and (d) shear strain in render; (e) and (f) lateral strain from strain gauge, attached in masonry. Note the temperature evolution in the secondary vertical axis, the failure point and the average fatigue strain in magenta.

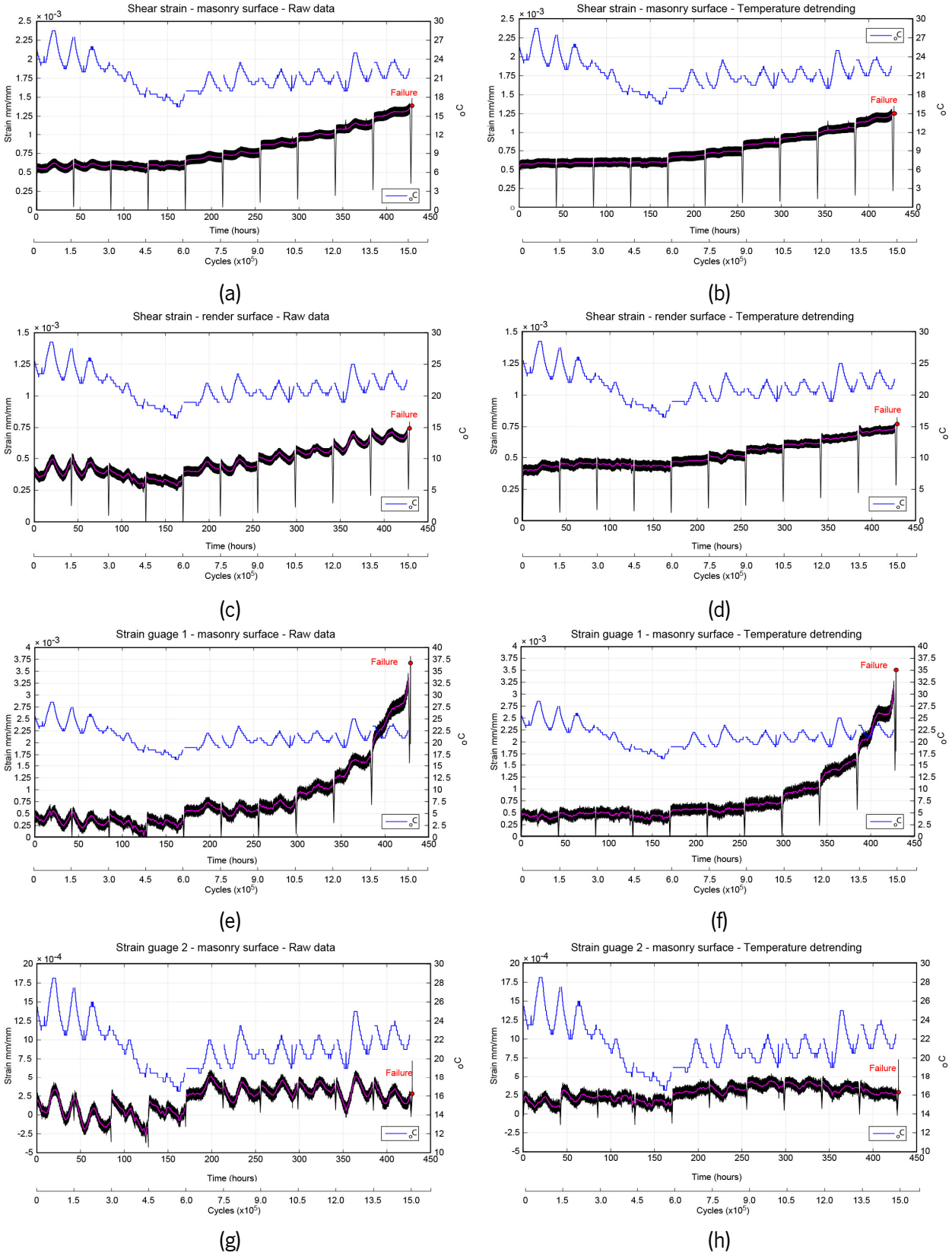


Figure 82. Raw data and temperature detrending of fatigue cyclic shear tests in diagonal compression for wallet DCf2: (a) and (b) shear strain in masonry; (c) and (d) shear strain in render; (e) and (f) lateral strain from strain gauge-1, attached in masonry; (g) and (h) lateral strain from strain gauge-2, attached in masonry. Note the temperature evolution in the secondary vertical axis, the failure point and the average fatigue strain in magenta.

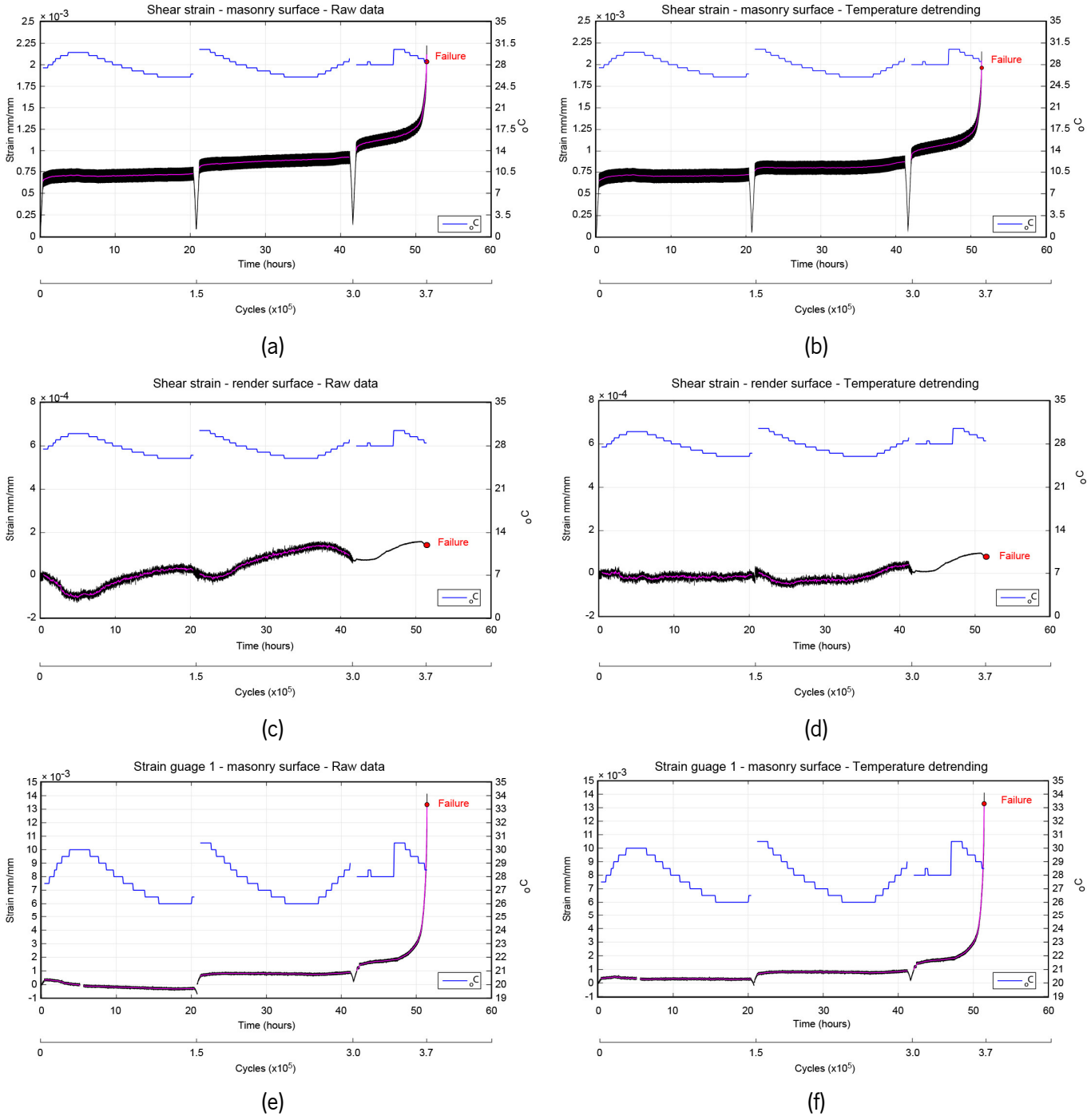


Figure 83. Raw data and temperature detrending of fatigue cyclic shear tests in diagonal compression for wallet DCf3: (a) and (b) shear strain in masonry; (c) and (d) shear strain in render; (e) and (f) lateral strain from strain gauge, attached in masonry. Note the temperature evolution in the secondary vertical axis, the failure point and the average fatigue strain in magenta.

5.3.4.6. Fatigue shear cyclic loading and stiffness monitoring

Materials subjected to fatigue tests under a constant stress state, exhibit a cyclic softening response, or else a strain relaxation. Thus, a strain-based approach to fatigue, namely with $\varepsilon - N_f$ curves can be often beneficial for monitoring plastic deformations, crack evolution, strain

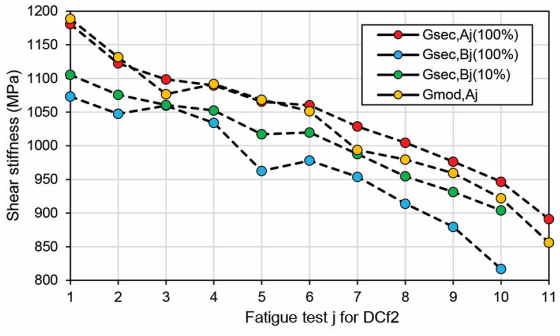
localization, and associate fatigue life estimates [Dowling 2007]. As described by the Ramberg-Osgood relationship of non-linear fatigue strain in materials with yielding and hardening phases, both the elastic and plastic components of fatigue strain exhibit positive linear trends, in a $\log(\varepsilon) - \log(N_f)$ plot [Dowling 2007]. In addition, a direct indication of concurring fatigue damage in the material, caused by strain softening, is directly translated in the decline of the elastic and secant moduli, during the fatigue cycles. Finally, fatigue monitoring quantities, normalized according to initial values can determine on how detrimental certain fatigue combinations are.

Considering the cyclic nature of the diagonal compression fatigue tests in wallets DCfi, under different static diagonal compression stresses and fatigue amplitudes, and in order to have a direct comparison with static shear strain and stiffness properties, average shear strains and stiffness time-histories were obtained, from the upper and lower bound fatigue envelopes. Similarly to creep monitoring, fatigue acquired data are processed in order to determine on cumulative damage and potential failure scenarios [Dowling 2007].

Initially, the secant shear stiffness at the end of each loading (A_j) and fatigue branch (B_j) are compared, and the respective values for each branch j and wallet DCfi-j are presented in Table 26, Table 27 and Table 28. Values of the secant shear stiffness pose an evident decrease after each fatigue branch, which for fatigue loads not leading to failure ranges between 3-17%, with higher differences involving higher fatigue stress rates, i.e. fatigue branches 1 and 2 of wallet DCf3 (Table 27). Yet no indication is established on higher shear stiffness decrease with higher static shear stresses, except for the last fatigue branches, leading to failure. In fact, for the DCf3-3 and DCf4-6 branches, where fatigue failure occurs, the relative decrease in the secant shear stiffness reaches 59% and 27% respectively (Table 27 and Table 28). By considering the distinctive fatigue stages, for DCf3-3 the shear stiffness decrease concurs to 22% for Stage I(0-10%N_f), 20% for Stage II(10-80%N_f) and 58% for Stage III(80-100%N_f). Similarly, for DCf4-6 the shear stiffness decrease corresponds to 18% for Stage I(0-10%N_f), 19% for Stage II(10-80%N_f) and 63% for Stage III(80-100%N_f). Considering the maximum shear stress σ_{max} of the last fatigue branch, both specimens DCf3 and DCf4 appear to have crossed the static stress limit for macrocracks, which according to Brooks 2015 is set at $0.7f_t$, while for DCf4-6 σ_{max} is in fact placed in the last stress area of unstable crack-growth (>$0.9f_t$). The elastic behavior of the masonry wallets in diagonal compression is also affected by fatigue, with the elastic shear modulus diminishing gradually, after

each fatigue branch, with the highest difference at the last loading branch before failure (Table 26, Table 27 and Table 28).

Table 26. Shear stiffness evolution during static (A_j) and fatigue (B_j) loading branches, for wallet DCf2.

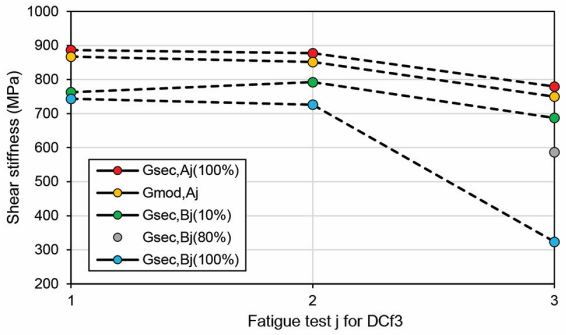


DCf2-j(σ_m*,$\pm\sigma_a$*)	Cycles**	ΔG_{sec} ($B_{j,10\%}$-A_j)	ΔG_{sec} ($B_{j,100\%}$-A_j)	ΔG_{mod} (A_j-A_1)
DCf2-1(0.50f_t,±0.08f_t)	1.50E+05	-6%	-9%	0%
DCf2-2(0.50f_t,±0.08f_t)	3.00E+05	-4%	-7%	-5%
DCf2-3(0.50f_t,±0.08f_t)	4.50E+05	-3%	-4%	-9%
DCf2-4(0.50f_t,±0.08f_t)	6.00E+05	-3%	-5%	-8%
DCf2-5(0.54f_t,±0.08f_t)	7.50E+05	-5%	-10%	-10%
DCf2-6(0.58f_t,±0.08f_t)	9.00E+05	-4%	-8%	-12%
DCf2-7(0.63f_t,±0.08f_t)	1.05E+06	-4%	-7%	-16%
DCf2-8(0.67f_t,±0.08f_t)	1.20E+06	-5%	-9%	-18%
DCf2-9(0.71f_t,±0.08f_t)	1.35E+06	-5%	-10%	-19%
DCf2-10(0.75f_t,±0.08f_t)	1.50E+06	-4%	-14%	-22%
DCf2-11(0.79f_t,±0.08f_t)	1.50E+06	-	-	-28%

* Stated as a ratio of f_t, with f_t estimated according to 5.3.3.

** Counting from the beginning of the fatigue tests, presented as a sum.

Table 27. Shear stiffness evolution during static (A_j) and fatigue (B_j) loading branches, for wallet DCf3.

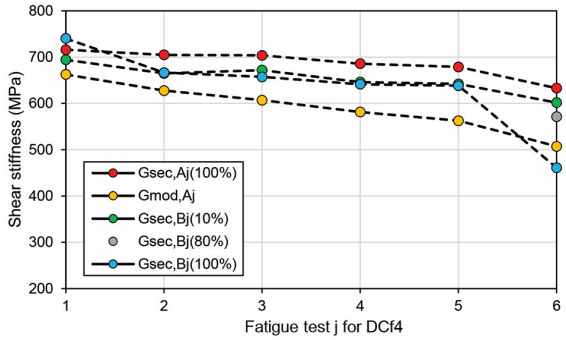


DCf3-j(σ_m*,$\pm\sigma_a$*)	Cycles**	ΔG_{sec} ($B_{j,10\%}$-A_j)	ΔG_{sec} (A_j-$B_{j,80\%}$)	ΔG_{sec} ($B_{j,100\%}$-A_j)	ΔG_{mod} (A_j-A_1)
DCf3-1(0.54f_t,±0.12f_t)	1.50E+05	-14%	-	-16%	0%
DCf3-2(0.59f_t,±0.12f_t)	3.00E+05	-11%	-	-17%	-2%
DCf3-3(0.64f_t,±0.12f_t)	3.70E+05	-13%	-25%	-59%	-14%

* Stated as a ratio of f_t, with f_t estimated according to 5.3.3.

** Counting from the beginning of the fatigue tests, presented as a sum.

Table 28. Shear stiffness evolution during static (A_j) and fatigue (B_j) loading branches, for wallet DCf4.



DCf4-j(σ_m*,$\pm\sigma_a$*)	Cycles**	ΔG_{sec} ($B_{j,10\%}$-A_j)	ΔG_{sec} (A_r-$B_{j,80\%}$)	ΔG_{sec} ($B_{j,100\%}$-A_j)	ΔG_{mod} (A_j-A_1)
DCf4-1(0.64f_t,±0.04f_t)	1.50E+05	-3%	-	3%	0%
DCf4-2(0.69f_t,±0.04f_t)	3.00E+05	-6%	-	-5%	-5%
DCf4-3(0.73f_t,±0.04f_t)	4.50E+05	-5%	-	-7%	-8%
DCf4-4(0.79f_t,±0.04f_t)	6.00E+05	-6%	-	-6%	-12%
DCf4-5(0.84f_t,±0.04f_t)	7.50E+05	-5%	-	-6%	-15%
DCf4-6(0.89f_t,±0.04f_t)	8.13E+05	-5%	-10%	-27%	-23%

* Stated as a ratio of f_t, with f_t estimated according to 5.3.3.

** Counting from the beginning of the fatigue tests, presented as a sum.

A basic damage and failure identification criterion, used widely for monitoring crack formation at notched components, is the time evolution (first derivative in time) of the average fatigue strains, here the direct shear strains $\gamma_m(N_i)$, from the initiation of the fatigue test, until the last fatigue cycle (Equation 80) [Glinka 1985]. Similarly, the evolution of the average secant shear modulus $G_{sec}(N_i)$, during the fatigue branches B_j can be used (Equation 81). By comparing both quantities and their trends with the ones from preceding static and fatigue loading branches

respectively, the possibility of fatigue inflicted damage can be verified, i.e., under constant loading conditions, fatigue damage is determined under positive and negative rates in shear strains and secant shear stiffness respectively. Eventually, the average fatigue shear strain and shear stiffness evolve exponentially to a critical value and the material fractures and collapses disproportionally [Hu et al. 2021 and Glinka 1985]. In order to associate the strain and stiffness rate with the number of cycles N_i, instead of the time, those are transformed in an equivalent numeric array, with 12 increments per cycle, following the sampling frequency of the fatigue tests. However, for time increments with no data, according to recording sampling protocols (Table 24) and only for the averaged fatigue quantities, those were filled out with a linear interpolation function, in order to obtain continuous average shear strain and stiffness time series.

$$\frac{d(\gamma_{t,m})}{d(N_i)} \qquad \text{Equation 80}$$

$$\frac{d(G_{sec,m})}{d(N_i)} \qquad \text{Equation 81}$$

For each tested wallet DCfi, since fatigue was assessed under various static shear stress levels $\sigma_{m,j}$, constant shear stress rates $\sigma_{a,ij}$, and under a constant number of cycles, i.e., $1.5x10^5$ cycles, shear strain quantities from each fatigue branch were assessed individually. Thus, average shear strain and secant shear stiffness evolution graphs, for each fatigue cycle B_j, and each masonry wallet DCfi, together with superposed shear stress and strain curves are presented in Figure 84, Figure 85 and Figure 86. Yet, considering only stiffness properties, which are directly associated with concurring damage, each part of loading-fatigue-unloading branches ($A_j - B_j - C_j$) can also be considered as independent, with the ones leading to failure considered as a complete fatigue test. Here is noted that for real time-history data, often being abrupt and noisy, their first derivative in time can be highly unreliable, with extreme peaks and offsets. Thus, in order to obtain smooth time rates (Figure 84c and e, Figure 85c and e, and Figure 86c and e), average fatigue strains and stiffness were fitted into a 9^{th} order Polynomial, and subsequently differentiated.

From Figure 85a, Figure 86a and Figure 87a, it is evident that for all wallets DCfi during the progression of fatigue tests B_j, strain relaxation increases, under constant fatigue shear loading and increasing static shear stress conditions. Elastic and secant stiffness quantities, at the initiation of fatigue branches, and normalized to initial values from the first loading branch, are found diminishing exponentially, as fatigue tests progress.

Considering the two complete fatigue tests, resulting to failure, namely DCf3-3 and DCf4-6, the exponential decay of the secant shear stiffness versus the shear strain was fitted to an exponential equation under a reverse power law curve, presented in Equation 82, where b is the order of scaling and a is a numeric constant. In order to compare both curves, from the selective fatigue branches of each specimen, the secant shear stiffness and shear strain values were normalized with respect to the secant shear stiffness of the preceding loading branch and the shear strain at failure, with the results visualized graphically in Figure 87. For both tests, an identical order of scaling is fitted, with the b exponent equal to 1.08. Since b is very close to -1, the normalized shear strain and stiffness present an almost linear, but reverse correlation, throughout the evolution of the fatigue tests, with the secant shear stiffness exhibiting slightly larger values than the shear strain. Instead, the a constant can be hypothesized to be a function of the fatigue stress rates (R, A_σ or S in Table 25), but additional curves should be obtained from other fatigue tests, in order to establish a valid correlation.

$$G_{sec,m,Ni} = a\gamma_{t,m,Ni}{}^{b}\,,\ a > 0 \text{ and } b < 0 \qquad \text{Equation 82}$$

Next, accounting for the shear strain and secant shear stiffness, during each fatigue loading branch (B_j) for all three wallets DCfi, their evolution with respect to the number of cycles is presented in Figure 84b and d, Figure 85b and d, and Figure 86b and d. After each consecutive series of loading-fatigue-unloading branches ($A_j - B_j - C_j$), initial fatigue shear strains increase in amplitude and progress under a small but positive slope. Thus, at the end of each fatigue test, the residual-irrecoverable or else plastic strains, are partly the result of fatigue, and partly from the cyclic progression of the static shear stresses.

Considering the evolution of the fatigue shear strains and by extension the fatigue secant shear stiffness in accordance to the fatigue cycles, as presented in the first derivative graphs in Figure 84c and e, Figure 85c and e, and Figure 86c and e, and after the initial large rates (Stage I), they do not present a stable linear slope, instead they vary fluctuating, with resulting high standard deviation values, which can be explained by the diversion of load paths as cracks progress. Here is noted that for fatigue branches with no failure, the average shear strain and secant stiffness rates, corresponding to fatigue Stage II were considered for 30-100% of the applied cycles, while for the last fatigue branch resulting to failure the respective rates correspond to the range of 10-80% of the cycles (Table 29). In general, consecutive cyclic fatigue branches under increasing static shear levels, exhibit growing and decaying rates, regarding the mean shear strains

and mean shear secant stiffness respectively, which are indicative of cumulative fatigue damage, through the formation of diffused microcracks, the transition to macrocracks and concluding to failure. In wallet DCf2, shear strain rates for fatigue branches DCf2-1 until DCf2-5 (S=1.15-1.14) are found somewhat stable, while the rest keep increasing until the last fatigue branch of DCf2-10, reaching the highest shear strain rate of 4.5E-11. Further on, in wallet DCf3, and given the higher fatigue rates (S=1.22-1.19), shear strain rates are found increasing for each consecutive fatigue branch, reaching the highest values of 2.8E-10. The wallet DCf3, being subjected to the lower shear stress rates of fatigue (S=1.07-1.05), exhibits positive shear strain rates from the fatigue branch DCf4-3, which keep increasing until the value of 1.5E-10, measured during the Stage II fatigue branch of DCf4-6. Thus, higher shear strain rates of fatigue Stage II, under the several examined fatigue shear stress rates, are found for higher static shear stresses, which under the conducted fatigue tests range between 75-89% of the shear static strength f_t. As far as the cyclic rates of the secant shear stiffness are concerned, which are diminishing during each fatigue branch, exhibit the highest decay within the range of 4.0E-05 to 1.9E-04.

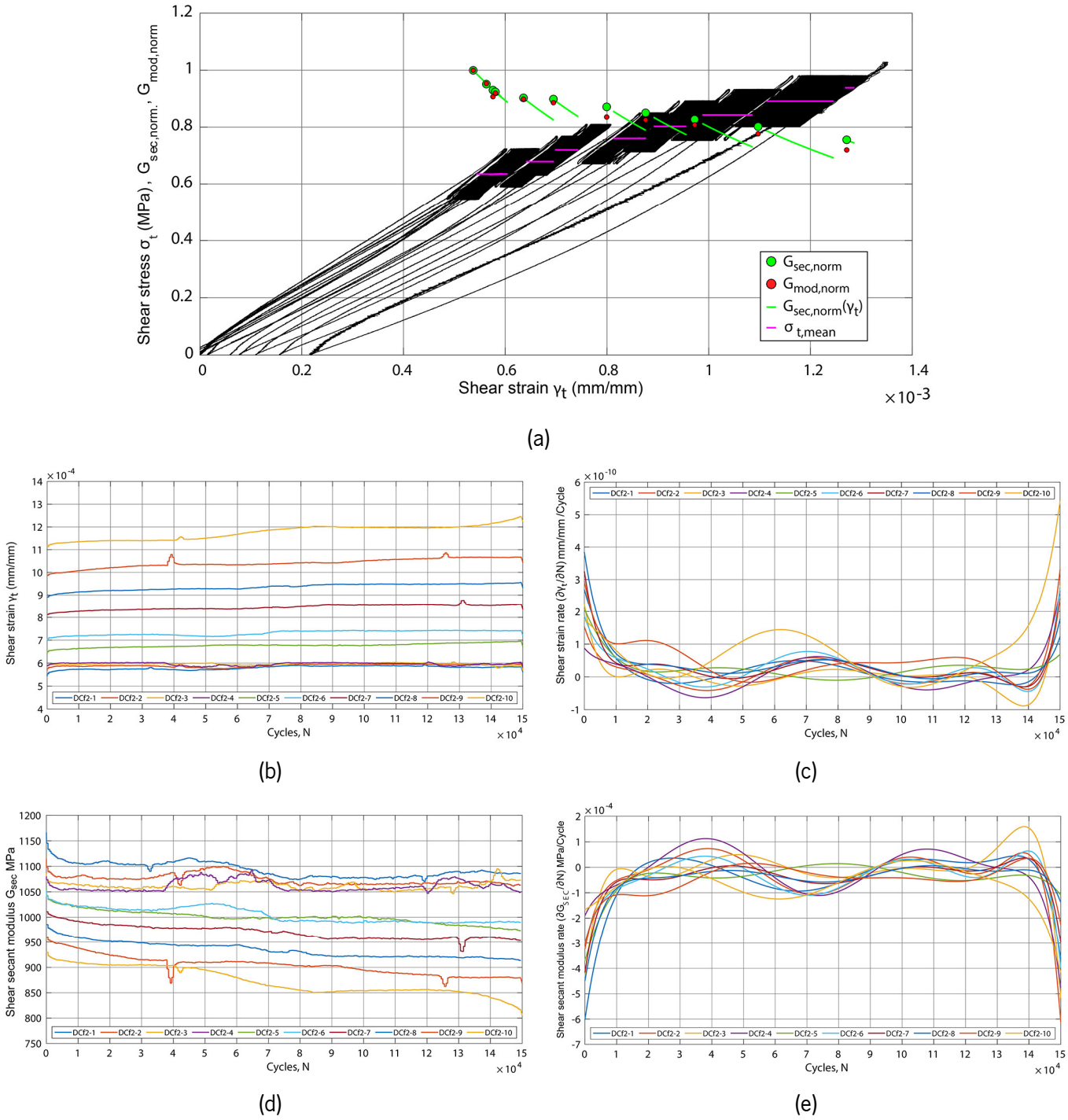


Figure 84. Fatigue acquisition data after temperature detrending, for wallet DCf2 in diagonal compression: (a) diagonal compression stress-strain curve in masonry surface, superposed with the shear elastic and secant modulus, normalized to the initial respective values from the first static loading branch; (b) and (c) average shear strain evolution and first derivative, with respect to fatigue cycles N; (d) and (e) average shear secant stiffness and first derivative, with respect to fatigue cycles N. Note the positive and negative trends for shear strain and stiffness respectively, indicative of fatigue softening.

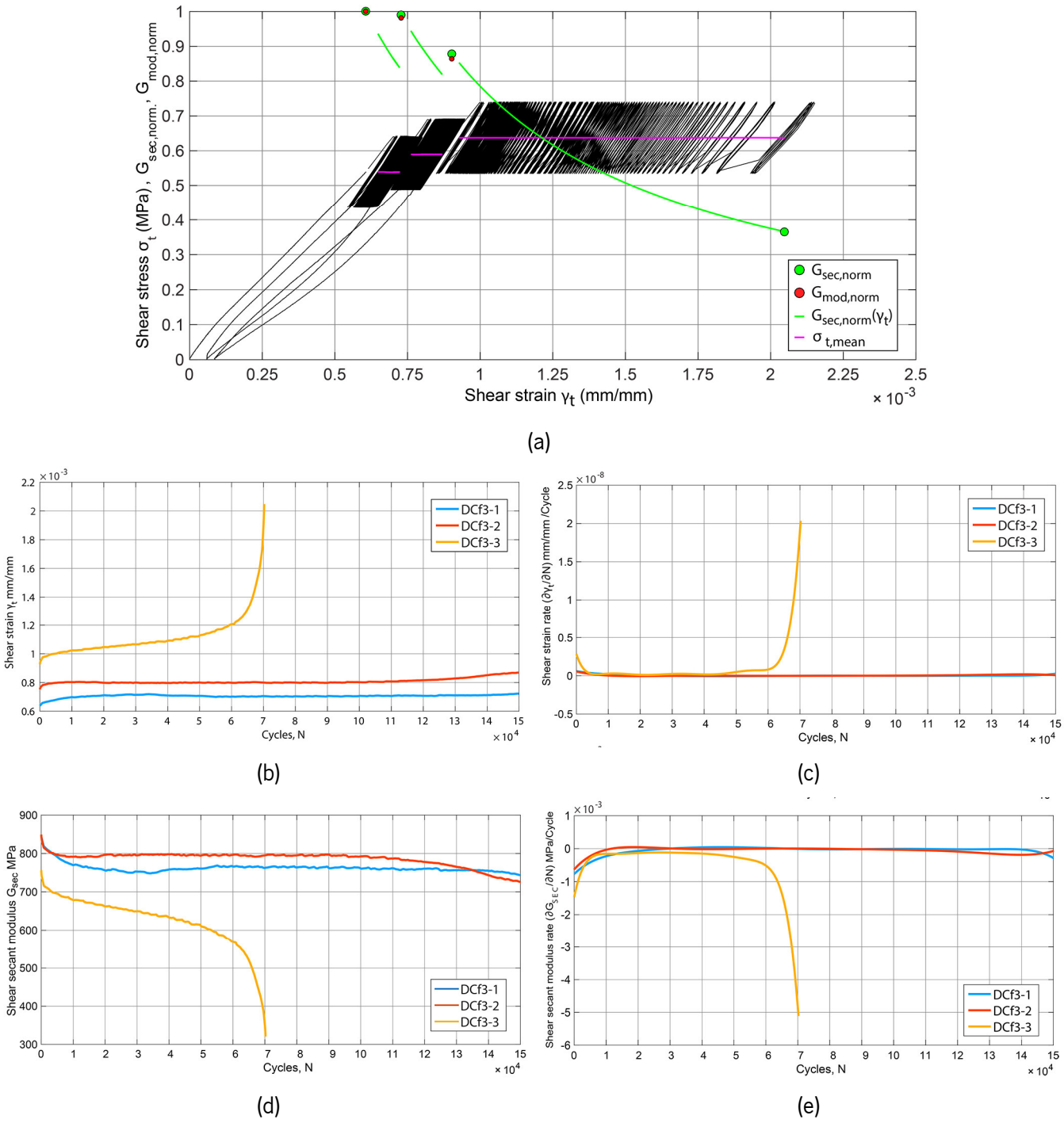


Figure 85. Fatigue acquisition data after temperature detrending, for wallet DCf3 in diagonal compression: (a) diagonal compression stress-strain curve in masonry surface, superposed with the shear elastic and secant modulus, normalized to the initial respective values from the first static loading branch; (b) and (c) average shear strain evolution and first derivative, with respect to fatigue cycles N; (d) and (e) average shear secant stiffness and first derivative, with respect to fatigue cycles N. Note the positive and negative trends for shear strain and stiffness respectively, indicative of fatigue softening.

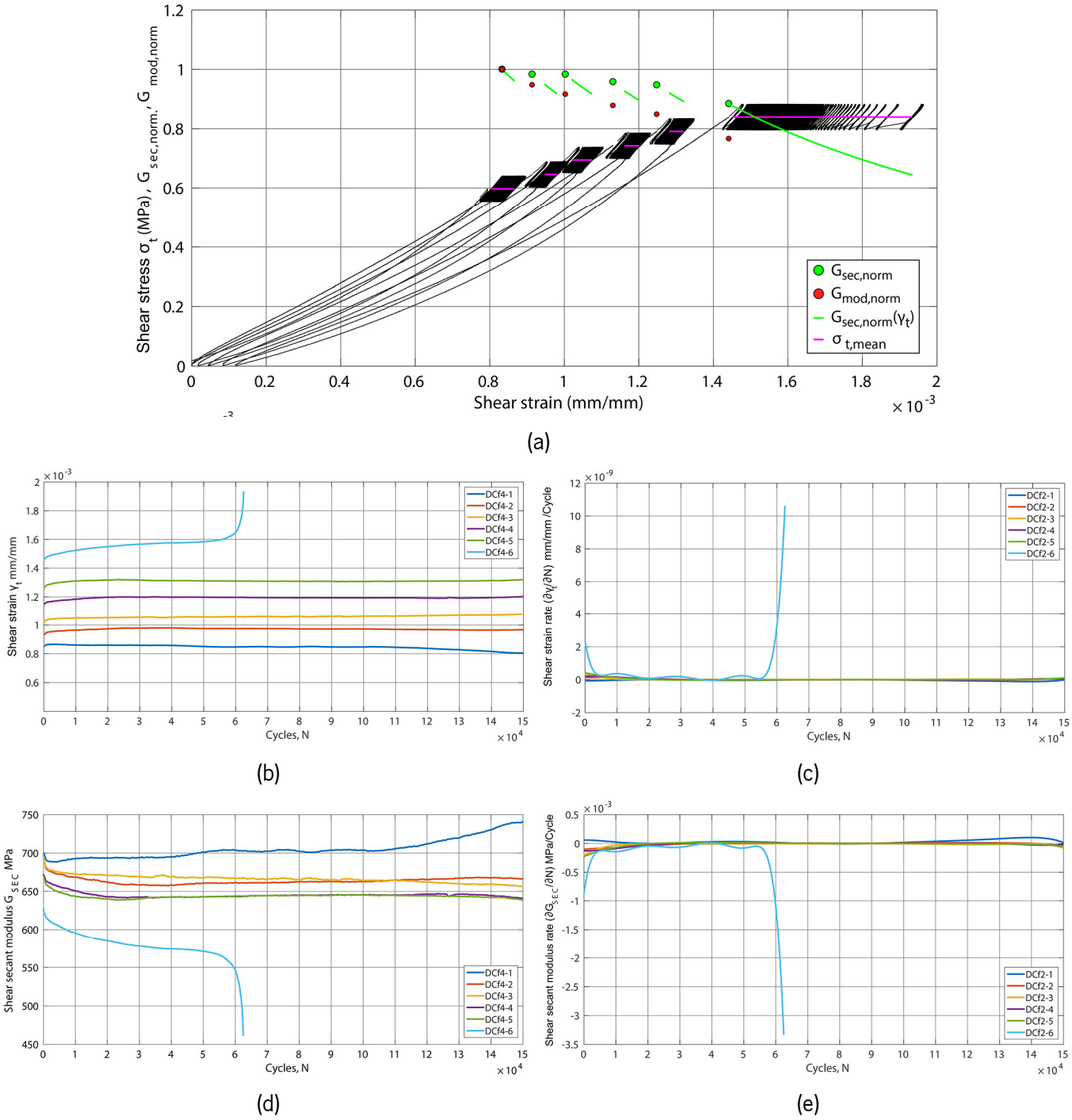


Figure 86. Fatigue acquisition data after temperature detrending, for wallet DCf4 in diagonal compression: (a) diagonal compression stress-strain curve in masonry surface, superposed with the shear elastic and secant modulus, normalized to the initial respective values from the first static loading branch; (b) and (c) average shear strain evolution and first derivative, with respect to fatigue cycles N; (d) and (e) average shear secant stiffness and first derivative, with respect to fatigue cycles N. Note the positive and negative trends for shear strain and stiffness respectively, indicative of fatigue softening.

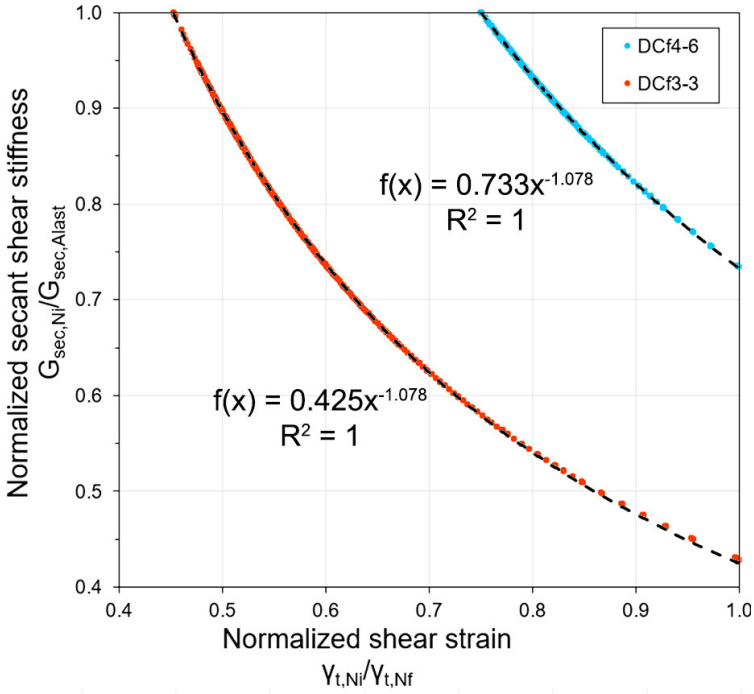


Figure 87. Exponential decay curve fitting of the normalized secant shear stiffness versus the normalized shear strain of the last fatigue loading branch, leading to failure, for wallets DCf3 and DCf4.

Table 29. Mean and standard deviation of shear strain secant stiffness rate of Stage II fatigue, in B_j loading branches, for wallets DCf2, DCf3 and DCf4. Note the fatigue branches resulting to failure in red. Note the computation of the first derivative from the 9th order polynomial fit for the average shear strains and secant shear stiffness of the fatigue cycles.

		$d(\gamma_{t,m})/d(N_i)$		$d(G_{sec,m})/d(N_i)$	
Wallet DCfi-j	Fatigue Bj Stage II	mean	Std	mean	Std
DCf2-1	$N_{30\%}$- $N_{100\%}$	1.30e-11	3.22e-11	-2.48e-05	6.26e-05
DCf2-2	$N_{30\%}$- $N_{100\%}$	1.65e-11	4.66e-11	-2.99e-05	8.55e-05
DCf2-3	$N_{30\%}$- $N_{100\%}$	-3.15e-12	4.31e-11	5.44e-06	7.82e-05
DCf2-4	$N_{30\%}$- $N_{100\%}$	1.35e-11	4.83e-11	-2.42e-05	8.64e-05
DCf2-5	$N_{30\%}$- $N_{100\%}$	1.69e-11	1.69e-11	-2.44e-05	2.49e-05
DCf2-6	$N_{30\%}$- $N_{100\%}$	2.17e-11	4.35e-11	-3.08e-05	6.24e-05
DCf2-7	$N_{30\%}$- $N_{100\%}$	1.85e-11	3.34e-11	-2.28e-05	4.10e-05
DCf2-8	$N_{30\%}$- $N_{100\%}$	2.32e-11	2.14e-11	-2.51e-05	2.35e-05
DCf2-9	$N_{30\%}$- $N_{100\%}$	2.69e-11	3.64e-11	-2.56e-05	3.41e-05
DCf2-10	$N_{30\%}$- $N_{100\%}$	4.54e-11	5.89e-11	-3.96e-05	5.06e-05
DCf3-1	$N_{30\%}$- $N_{100\%}$	1.29E-11	4.15E-11	-1.34E-05	4.30E-05
DCf3-2	$N_{30\%}$- $N_{100\%}$	5.60E-11	6.61E-11	-5.51E-05	6.31E-05
DCf3-3	$N_{10\%}$- $N_{80\%}$	2.76E-10	1.54e-10	-1.68e-04	5.86e-05
DCf4-1	$N_{30\%}$- $N_{100\%}$	-3.87e-11	3.92e-11	3.37e-05	3.46e-05
DCf4-2	$N_{30\%}$- $N_{100\%}$	-7.71e-12	1.40e-11	5.22e-06	9.70e-06
DCf4-3	$N_{30\%}$- $N_{100\%}$	1.57e-11	1.57e-11	-9.96e-06	1.00e-05
DCf4-4	$N_{30\%}$- $N_{100\%}$	2.05e-12	1.85e-11	-1.13e-06	1.03e-05
DCf4-5	$N_{30\%}$- $N_{100\%}$	6.03e-12	2.09e-11	-3.17e-06	1.10e-05
DCf4-6	$N_{10\%}$- $N_{80\%}$	1.52e-10	1.13e-10	-6.09e-05	4.24e-05

5.3.4.7. Analytical stress-strain interpretations and correlations in fatigue loading

Regarding the three stages of a complete fatigue test, resulting to failure, the fatigue shear strain and secant shear stiffness evolution, with respect to the number of cycles, resembles a reverse, non-symmetric S-shaped curve, with a zero and a maximum asymptote, and a known cycle size N_f. Thus, a non-linear least-squares regression analysis is attempted, by data fitting with the Gompertz curve, given by Equation 83 [Jukic et al. 2004]. Here a, b and c are positive coefficients. Transforming the Equation 83 into a reverse form, with the y and x variables representing the fatigue cycles N_i and the average shear strain γ_t or secant shear stiffness G_{sec} respectively, the reversed non-symmetrical sigmoid functions of the Gompertz equation are presented in Equation 84 and Equation 85.

For the shear secant stiffness sigmoid fit, a negative sign and a fourth coefficient d are considered in the Gompertz equation, in order to accommodate the inverted N_i axis and the offset from zero respectively. In physical terms, the a coefficient is equal to the number of fatigue cycles leading to failure N_f, the b coefficient controls the deflection point of the curve, and the c coefficient represents the scale of the shear strains and secant shear stiffness. By means of minimizing the sum of square errors, between the real and fitted data, the resulted analytical coefficients and analytical curves for the average shear strain and secant shear stiffness of the fatigue branches DCf3-3 and DCf4-6 are presented in Figure 88. For both fitted curves, R-squared values higher than 0.90 were achieved. Yet, a larger number of fatigue tests is needed, in order to establish relative correlations with static shear properties and fatigue shear rates.

$$Y(x) = e^{a-be^{-cx}} \qquad \text{Equation 83}$$

$$\gamma_t(N_i) = \frac{b - \ln\left(\ln\left({}^{a}/_{N_i}\right)\right)}{c} \qquad \text{Equation 84}$$

$$G_{sec}(N_i) = d - \frac{b - \ln\left(\ln\left({}^{a}/_{N_i}\right)\right)}{c} \qquad \text{Equation 85}$$

In order to conduct a fatigue life-estimate assessment, under a specific static and fatigue stress regime, and before failure is reached, the hypothesis of Holmen 1982 of equal fatigue failure properties is used, namely the maximum shear strain $\gamma_{t,max}(N_f)$. Considering an end-to-end linear piecewise function for the normalized secant shear stiffness curve, with respect to the x-axis of normalized fatigue cycles, the decaying linear curve, unique for each of the wallets DCf3 and DCf4

is given by Equation 86. Here, the λ slope and end-to-end piecewise linear functions for the normalized secant shear stiffness, as found from the fatigue branches DCf3-3 and DCf4-6 are presented in Figure 89. Under the hypothesis of constant fatigue failure properties, the estimated fatigue life of the various, preceding fatigue stress states, without reaching failure is presented in Table 30. As seen in Table 30, estimated fatigue lives for the same shear stress rate and under lower static direct shear stresses for DCf3-(1-5) and DCf4-(1-2), are higher by one and two orders of magnitude respectively, compared to the actual fatigue branches resulting in failure.

$$\frac{G_{sec,N_i}}{G_{sec,N=1}} = 1 - \lambda \frac{N_i}{N_f} \qquad \text{Equation 86}$$

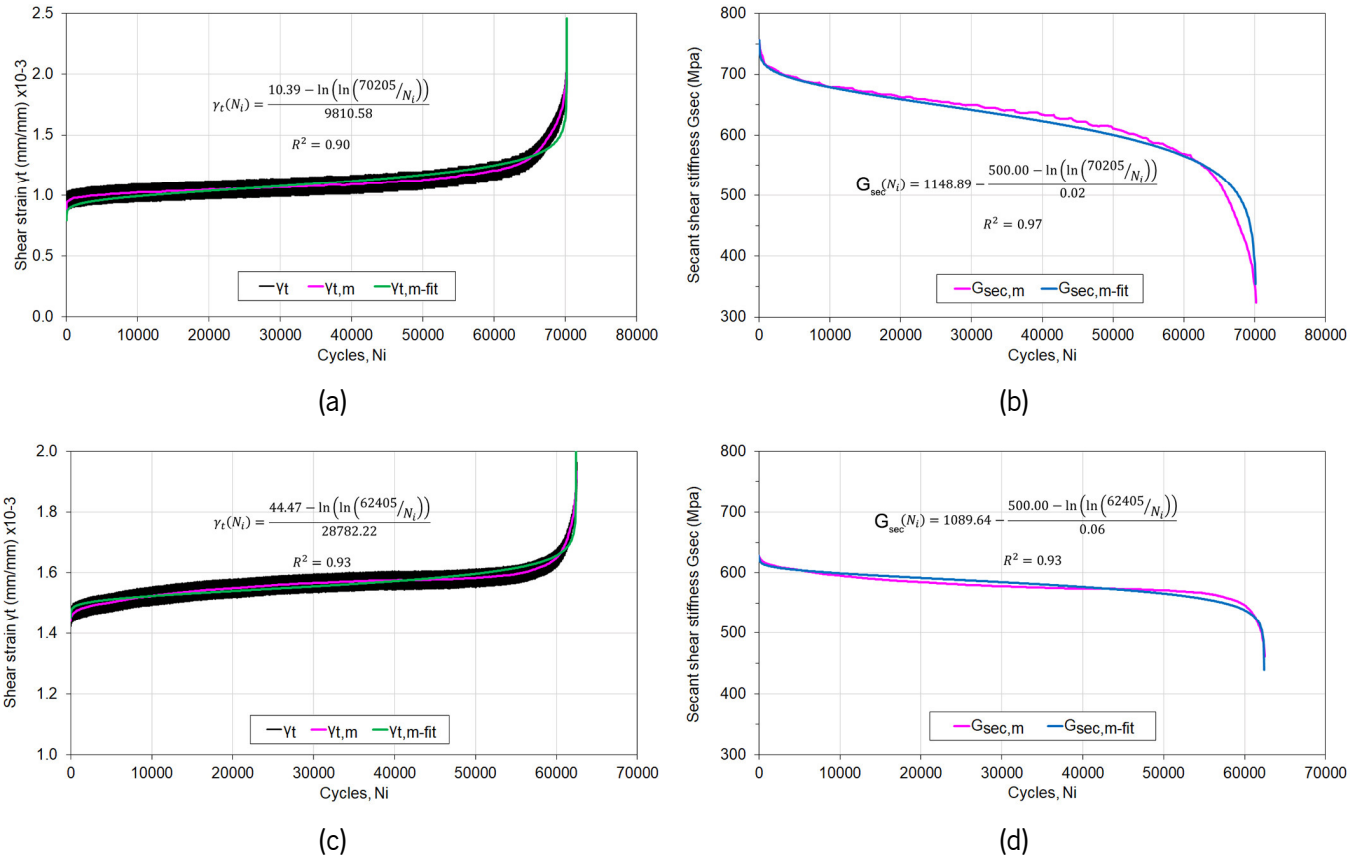


Figure 88. Fatigue loading data fitting with a reverse Gompertz curve for: (a) and (b) the fatigue average shear strain and average secant shear stiffness for DCf3-3 respectively; (c) and (d) the fatigue average shear strain and average secant shear stiffness for DCf4-6 respectively.

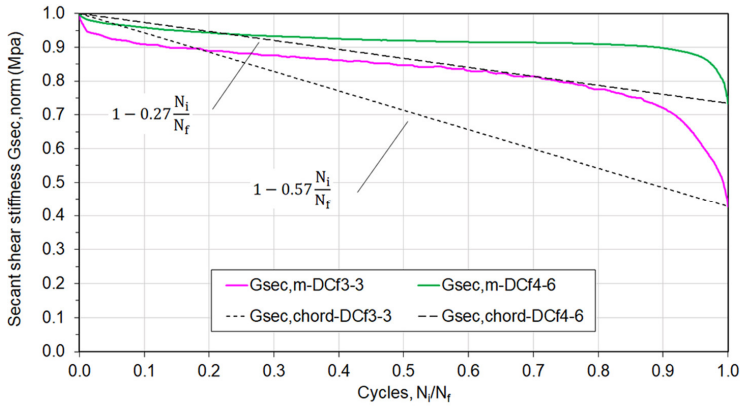


Figure 89. End to end linear piecewise function for normalized secant shear stiffness evolution and normalized cycles, for fatigue branches DCf3-3 and DCf4-6.

Table 30. Estimated fatigue cycles to failure for incomplete fatigue branches, according to the obtained end to end linear piecewise functions for fatigue, and under the hypothesis of constant fatigue failure properties, for each of the tested wallets DCf3 and DCf4. Note the deterministic fatigue cycles until failure for fatigue branches DCf3-3 and DCf4-6, in red.

Wallet DCfi-j	Fatigue Bj Cycles	$G_{sec,N=1}$	$G_{sec,N_{Bj}}$	λ	$N_{f,est} = \frac{\lambda N_{Bj}}{1 - \frac{G_{sec,N_{Bj}}}{G_{sec,N=1}}}$
DCf3-1(0.63ft,±0.12ft)	1-1.5E+05	830.4	743.5		8.21E+05
DCf3-2(0.69ft,±0.12ft)	1-1.5E+05	837.6	726.2	0.57	6.46E+05
DCf3-3(0.75ft,±0.12ft)	7.02E+04	756.5	323.4		7.02E+04
DCf4-1(0.64ft,±0.04ft)	1-1.5E+05	691.1	740.3		-
DCf4-2(0.69ft,±0.04ft)	1-1.5E+05	680.0	666.5		2.01E+06
DCf4-3(0.73ft,±0.04ft)	1-1.5E+05	692.0	657.3	0.27	7.94E+05
DCf4-4(0.79ft,±0.04ft)	1-1.5E+05	663.6	641.5		1.20E+06
DCf4-5(0.84ft,±0.04ft)	1-1.5E+05	659.3	638.2		1.24E+06
DCf4-6(0.89ft,±0.04ft)	6.25E+04	628.0	461.1		6.25E+04

5.4. Conclusions

In general, cyclic softening in masonry is a significant, catalytic factor for the shear stress-strain relationship, with bricks, mortar and brick-mortar interfaces contributing on the volume growth of microcracks, and by extension to the decay of the elastic and secant shear stiffness, up to ultimate failure. In terms of material constitutive models for masonry, the effect of fatigue or quasi-static loading can follow either an updated yield surface limit of the 3D material space or through the assignment of damage tensors, allowing to account the inelastic cumulative strains and damage under each cycle [Alliche 2004].

Real transient or intermittent fatigue loading from induced ground-borne vibrations in masonry structures is usually assessed and replicated as an accelerated fatigue experimental test of a continuous imposed vibration, i.e., a cyclic applied load, namely a sinusoidal function, of a constant spatial frequency and amplitude. Under the current experimental work, time accelerated

fatigue tests were performed in three solid brick masonry wallets DCfi with lime mortar joints and lime mortar one-sided render, in diagonal compression, under different static diagonal compression loading conditions and three different diagonal compression stress fluctuations, according to vibration limits from the DIN 4150-3 2016 standard. The long-term fatigue tests, were conducted under a constant shear stress rate $\Delta\sigma$, of a medium to low level, and high static shear loading σ_m, designed according to force amplitudes, converted from displacement amplitudes of ground-borne vibrations. Considering a certain number of cycles (N_i), the main objective was set on quantifying levels of damage, stiffness degradation and failure.

The process of designing experimental fatigue protocols was initiated with stress-strain static preloads used as input data for envelop fits and initial reference variables of G_{mod}, f_t and γ_t, for each of the tested, rendered wallets DCfi. The normalized shear stress-strain response, as correlated from several tested brick masonry wallets, both with and without render, presents an optimized response, regarding relative stress and strain curvatures, until the peak. Also considering crack growth at microlevel and the transition to macrocracking, at high diagonal compression static stress levels (70% of the shear strength), the transition to macrocracking is already established, while moving closer to failure (stresses larger than 90% of the shear strength), crack growth is considered highly unstable [Brooks 2015].

Experimental fatigue shear loading protocols, configured as cyclic quasi-static sinusoidal loading, were designed according to the shear stiffness of each masonry wallet and fatigue diagonal compression stresses were expressed as a function of displacement and velocity amplitudes, with the latter specified in DIN 4150-3 2016. Under the configuration of three distinct vibration amplitudes, customized in fatigue loading amplitudes for each specific masonry wallet DCfi, a fatigue experimental campaign accounted for progressively increased static shear stress levels, until failure was reached, resembling time-varying loading conditions, e.g., a dead load increase from structural interventions and a change of load paths from settlements, earthquakes etc.

By summarizing the outcomes of the fatigue diagonal compression experimental campaign, the fatigue shear loading under a high static shear stress regime ($\geq 0.7 f_t$) and along the entire permissible range of peak particle velocities, i.e., higher than 8 mm/s for a 50-100 Hz dominant frequency range, can result to cracking and local shear failure at relatively low number of cycles, namely 7-9 months (Table 25), accounting for ground-borne vibrations from train passing

intervals (Section 5.3.4.3). Even if fatigue shear cracking will not result to global structural failures or instabilities, local discontinuities are bound to arise, and pre-existing cracks may evolve, with focus on areas of shear stress concentrations, e.g., windowsills, arches, shear connectors, walls under in-plane actions etc.

The philosophy of design building codes, accounts for the nature of the loading regime, namely static, dynamic, creep, fatigue etc., which can potentially decay stiffness and capacity, and thus, reduction coefficients are assigned for the material properties. In fact, for the presence of fatigue in concrete structures, and only for the ULS, the recommended partial factor for the design fatigue strength under compression, namely $\gamma_{c,fat}$, is considered equal to 1.8 - a reduction to 56% -, when nominal values are considered [EN 1992.1.1:2004]. In addition, a fatigue design in monuments, as defined in EN 1990:2002, should cover the design working life category of 100 years (category 5). Considering the outcomes of the conducted fatigue diagonal compression tests, namely the fatigue failure of DCf4-6, at a cyclic loading, equivalent to vibrations of 8 mm/s, fatigue failure occurred at σ_m = 0.89f_t and σ_{max} = 0.93f_t, (mean static stress and maximum stress amplitude respectively). For fatigue loads at the higher limit of permissible vibrations, e.g., higher than 10 mm/s for a vibration frequency range of 50-100 Hz, according to DIN 4150-3 2016, namely the fatigue failure of DCf3-3, of an equivalent estimation of applied ppv of 16 mm/s, resulted to diagonal compression failure for similar levels of direct shear stresses, a σ_m = 0.75f_t and a σ_{max} = 0.87f_t. Thus, for fatigue shear loading combinations, close to the highly unstable zone of 0.9f_t, fatigue failure occurs, at relatively low number of cycles, i.e., around 10^5.

Furthermore, the concurring strain softening and stiffness degradation during a fatigue load should be also accounted during the assessment and design analyses. Based on the creep design approach for masonry structures in EN 1996:2005 (§3.7.2), where long-term Young's modulus is reduced by a creep coefficient φ_∞, a similar stiffness reduction can be accounted for the elastic shear stiffness during fatigue loading (Equation 87). Thus, considering the maximum decay in the values of shear modulus found in this work, a fatigue reduction coefficient in the range of 0.5 applies.

$$G_{mod,longterm} = \frac{G_{mod}}{1 + \varphi_\infty} \qquad \text{Equation 87}$$

Lastly, accounting for field monitoring aspects, within the process of fatigue assessment in masonry historic structures, first, a long-term monitoring process should conclude on the

amplitude, frequency and spatial distribution of ground-borne induced vibrations, according to processes explained in CHAPTER 4. Second, material properties for the structural elements, under a fatigue assessment process, should be established, namely the local stress state, stiffness evolution, compressive and shear capacity, with the use of minor destructive testing - single and double compressive and shear flat jack tests, mortar bed joint shear resistance tests etc. -. Third, a stress-strain investigation should be conducted with nonlinear static numerical analyses, using partial FE models, in order to identify shear stress concentration areas, in correlation with areas under high induced vibration amplitudes. Fourth, and once the identification of potential areas for fatigue damage is established, a field fatigue monitoring process should be implemented, with the installation of strain gauges, attached in masonry, covering high shear stress zones and existing crack patterns, for long-term monitoring of fatigue strain reversals, and potential positive trends. Together with the monitoring of temperature variations, in order to remove temperature linear trends, this procedure allows to verify the possibility of fatigue strain softening, in situ.

CHAPTER 6. TESTS OF DIFFERENTIAL SETTLEMENTS ON PIERS AND SPANDREL SPECIMENS, REPAIR AND RETROFIT APPLICATIONS

CHAPTER 6. Outline

6.1. Introduction

6.2. Theoretical background on structural interaction of piers and spandrels and abacus of kinematic-static in-plane mechanisms under differential settlements

6.3. Experimental investigation for capacity tests on masonry assemblies, composed by piers and spandrels

6.4. Building codes mechanical strength models on dominant failure modes for piers and spandrels

6.5. Experimental works on masonry piers and spandrel assemblies under a vertical displacement field

6.5.1. Masonry assemblies, setup implementation and testing protocols

6.5.2. Experimental results

6.5.2.1. Testing of piers and spandrel masonry assemblies at the undamaged state

6.5.2.2. Testing of piers and spandrel masonry assemblies at the damaged state, under structural repair and retrofit measures

6.5.2.3. Ambient vibration testing and correlation with damage, repair and retrofit schemes

6.5.3. Application of mechanical strength models for masonry spandrels UN1 and UN2

6.6. Conclusions

6.1. Introduction

For masonry perforated walls, under in-plane earthquake forces or differential vertical settlements, load trajectories present in spandrels are guided through diagonal compression and tension, with subsequent formation of diagonal and, usually, vertical cracks. The ductility of the structural system relies on the level of coupling between piers, the relative spacing and height of spandrels and the presence of strengthening in the spandrels, e.g., timber lintels, horizontal prestressed rods or angled profiles [Paulay and Priestley 1992, Tomazevic 1999]. It is known that there is a significant contribution of the spandrels in the overall in-plane capacity of masonry perforated walls, as they offer some level of coupling between the adjacent piers. In the presence of timber lintels, as shown in Gattesco et al. 2015

and Beyer and Dazio 2012, the in-plane capacity of the spandrel is improved, also attaining reasonable ductility after the post-peak and until failure.

In general, the shear and flexural capacity of a spandrel depends on several interrelated factors, among which are the axial and flexural stiffness of masonry, the horizontal boundary conditions from the adjacent piers, the presence of steel ties, the shear bond strength in the bed and collar joints, the configuration of interlocking bricks at the spandrel's interface and at the main body, and the presence of timber lintels or arches, at the intrados of the spandrel [FEMA 306 1998, NTC 2018 and Beyer 2012]. According to EN 1998-1 2004 masonry spandrels can be accounted in the overall in-plane capacity of the wall, provided that they present a regular bond with the adjoining walls and that they are connected to the floor beams and the lintel below. In case of high performance from adequately reinforced spandrels, damage is distributed both in the piers and spandrels, and the structural system of the façade exhibits an improved in-plane resistance and dissipation capacity [Tomazevic 1999].

The primary objectives of the conducted testing campaign on full scale masonry spandrel and piers structural systems, subjected to in-plane, monotonic, vertical and asymmetrical, large displacements are summarized as follows:

- Investigate the in-plane damage mechanisms and structural interaction of piers and spandrels;
- document and interpret the contribution on shear strength, flexural strength and cracking of the brick interlocking and shear bond mechanisms at spandrel-pier intersections, as well as the thrust trajectories of hinged masonry arches and the coupling effect of timber lintels (and their complex interaction);
- quantify the nonlinear in-plane response and its evolution in both piers and spandrels, and
- assess the effectiveness and performance of up-to-date structural repair and retrofit techniques on pier and spandrel systems that have suffered extensive cracking.

In terms of analytical processes implemented, the main objective set is to correlate testing results with analytical formulations of macro-element capacity models, present in building codes, also accounting for boundary conditions, repair, and retrofitting.

6.2. Theoretical background on structural interaction of piers and spandrels and abacus of kinematic-static in-plane mechanisms under differential settlements

In the case of weak and arched spandrels, as it is often the case with unreinforced masonry, in-plane damage, is mostly concentrated in the spandrels, in terms of hinging at both ends, shear cracking or sliding under diagonal compression and compressive crushing at the hinges, which is distributed in the spandrels along the elevation [Tomazevic 1999, FEMA 306 1998]. Once the damage in the spandrels has progressed, the piers can also exhibit shear failure, under diagonal compression and hinging, the latter, at the base of the structure, with progressive crushing at compressive zones [Tomazevic 1999]. Instead, in spandrels composed either fully or partially in thickness with timber lintels, and depending on their coupling, dimensions and spacing, along with the presence of timber wall plates and the connection with timber floors, all of which can offer a sufficient in-plane stiffness, a story mechanism can occur, with in-plane diagonal shear failure concentrated in the piers [Tomazevic 1999, Paulay and Priestley 1992]. Under adequate coupling and reinforcement in piers, spandrels, and foundations (if applicable), damage is widely distributed over the façade, while the energy dissipation and the overall in-plane capacity increase [Tomazevic 1999].

According to FEMA 306 1998 in-plane structural damage in coupled masonry walls, composed by piers and spandrels, provides mostly moderate ductility modes, and the localization of damage depends on the relative stiffness and strength of the subsidiary systems. Here, it is noted that the bending moment and shear force distribution in a coupled masonry wall, under the presence of differential subsidence, is similar to a unidirectional lateral seismic load, and hence the respective crack patterns are also similar [Vinci 2019]. Under the defined context, probable in-plane failure modes, under different likelihoods of occurrence, and according to the relative stiffness between piers and spandrel, are clearly identified in FEMA 306 1998 and presented as follows:

- Pier rocking and toe crushing. Considered likely for slender piers, piers at low compressive stresses and under the presence of strong spandrels. Toe crushing may occur at relatively high drifts, and defines the ultimate state of structural damage;
- flexural cracking (at the heel of the pier) and toe crushing. The failure mode is mostly associated to stocky piers, hence under low aspect ratios and piers working in diagonal tension. Cracking occurs in a series of horizontal cracks over the heel, diagonal cracks and toe crushing before the pier is

structurally compromised. Also, considering more localized vertical settlements, horizontal flexural cracking can localize in piers, at intermediate levels;

- bed joint sliding, at the base of piers or at intermediate floor levels. Considering the evolution of counteracting forces from compression structs in spandrels and the presence of vertical and horizontal differential settlements, the configuration of sliding cracks in piers can be either horizontal or stepped, with bed joint sliding and head joint opening;
- flexural cracking in spandrels. Here, bed joint sliding and head joint opening occurs at spandrel ends, once the in-plane moment and shear capacity of the spandrel are reached. Bed joint sliding is often stepped, while head joint opening is almost vertical, with some bricks fractured in flexure. The failure mode is considered ductile, as long as lintels are present;
- diagonal shear cracking in spandrels, under diagonal tension, transversally to the formed compression strut, between the formed toes of the spandrel. Such a failure can likely succeed flexural cracking and can even lead to toe crushing in the spandrel, and
- corner damage at top corners. Those areas are considered of low ductility, given the lower compressive stresses. Cracking mostly evolves diagonally, under a stepped crack of sliding bed joints.

Lastly, it can be also noted that under little or no ductility, all the above-mentioned failure modes are bound to occur, with no clearly defined likelihood. In addition, an out-of-plane flexural response is more likely to be merged with an in-plane one [FEMA 306 1998].

6.3. Experimental investigation for capacity tests on masonry assemblies, composed by piers and spandrels

Many are the experimental works in the structural in-plane behavior of full-scale unreinforced masonry specimens, replicating parts of perforated walls, and composed by two piers and a spandrel [Augenti et al. 2016, Gattesco et al. 2015, Gattesco et al. 2008, Parisi et al. 2014 and Beyer and Dazio 2012]. Considering the structural sub-systems as parts of a façade in multistory masonry buildings, with weak horizontal diaphragms of timber floors, and sufficient connections with the transversal walls, the in-plane failure is prominent, with a combination of in-plane and out-of-plane damage also likely to occur [FEMA 306 1998]. Testing regimes are configured under a quasi-static load application, with displacement control, while different types of spandrels, coupling with piers and horizontal compressive stresses at the spandrel level, appear to control the in-plane response. With respect to the hazard under

study, experimental loading protocols can replicate the seismic response, under a cyclic pattern, of horizontal or vertical applied loading. Regarding the testing of piers and spandrels for differential settlements, the loading application is monotonic, under a vertical direction, applied in one of the piers.

The response of the structural system is analyzed according to resistance mechanisms, cracking, force-displacement, shear strain or drift curves, ultimate and residual capacity, drifts for spandrels and piers, degradation of stiffness and strength, relative in-plane deformations, non-dilatational strain angles and energy dissipation capacity.

Additional testing on damaged spandrel and piers, as in Augenti et al.2016 and Gattesco et al. 2015, focused on the effect of strengthening techniques, such as grouting, the application of near surface inorganic matrix-grid systems, with mortar coatings, the drilling and placement of externally bonded steel fiber-reinforced polymer (SFRP) ties, along the thickness, the placement of longitudinal steel ties and steel angles, at the mid-height of the spandrel, all aiming at improving the overall in-plane displacement ductility, shear and flexural strength.

Considering experimental results, in Gattesco et al. 2015 and Gattesco et al. 2008, for a piers and spandrel masonry assembly, with a continuous timber lintel in the spandrel, the crack sequence under a vertical cyclic load, applied to one of the piers, and representing in-plane seismic loading, is configured with vertical flexural cracks at both ends of the spandrel, shear diagonal cracking in the spandrel, which at an ultimate stage results to the loss of the support of the timber lintel and the free rocking of the spandrel. When the spandrel is configured by ⅔ with a flat arch, the crack pattern involves mostly diagonal shear cracks at the spandrel. Here, the ultimate drift at the spandrel, in both tested assemblies, reached 1.0% (Table 31).

Further on, in Parisi et al. 2014, a pier and spandrel, tuff masonry assembly, of a full story height at real scale, with an arched spandrel, and an initial vertical prestress, was tested under quasi-static horizontal, in-plane loading. The increasing evolution of the lateral in-plane cyclic displacement resulted to x-shaped diagonal shear and vertical flexural cracks in the spandrel, with the piers experiencing horizontal tensile cracks at the base, due to the rocking response. The ultimate state was set with diagonal shear cracks covering the entire height of the spandrel, at an inter-story drift of 1.1% (Table 31).

Following, in Graziotti et al. 2016, piers and spandrel, double-leaf, stone masonry assemblies, coupled with a timber lintel, under a constant vertical prestress and different horizontal precompression

states at the spandrel zone, have been tested under cyclic vertical loading, and until failure is reached. Under zero precompression at the spandrel, cracking is configured by a flexural vertical crack at the intersections, sliding of the lintel and the rocking of the entire spandrel, as the ultimate cyclic response, with a maximum spandrel drift of 1.5%. Under a shorter spandrel with horizontal precompression from prestressed tie rods, the crack pattern consists of diagonal shear cracks in the spandrel and horizontal sliding in the proximity of the lintel, with the ultimate spandrel drift reaching 2.5%, under a post-hardening phase. Here is also noted that for both tested assemblies, the uplifting pier is allowed to rotate freely, which results to a partial rotation at both piers (Table 31).

Lastly, in Beyer and Dazio 2012, two types of masonry piers and spandrel, one with a timber lintel spandrel and one with an arched spandrel, were tested under vertical quasi-static loading, with hinged supports at the piers and a constant axial prestress for the spandrels and piers. The failure mechanism, under the presence of the timber lintel is compiled by flexural vertical cracks in the intersection and a shear stepped crack at the middle of the spandrel, with an ultimate pier drift of 3.0%. Under the presence of an arched spandrel, the failure is governed by the diagonal shear cracks in the spandrel, with the ultimate softening and loss of the spandrel, at a pier drift of 3.5% (Table 31).

An important aspect, proven rather cumbersome to implement in laboratory conditions, is the realistic replication of the boundary conditions, both in the horizontal and vertical direction, in the piers and spandrel system. As explained in Beyer and Dazio 2012 and Gattesco et al. 2015, the level of axial and horizontal prestress in a pier and spandrel specimen is implemented experimentally through hydraulic jacks and circumferential horizontal rods respectively, connected at both ends, and acting independently from the application of the lateral or vertical in-plane loading. In terms of the axial loading, in piers of intermediate floors, and in order to replicate the gravity loading from overlying masonry parts and connected floors, the decision to maintain a constant prestress throughout the testing and by extent, allowing the piers to rotate, accounts for a more realistic scenario [Gattesco et al. 2015]. Instead, the concept of axial prestress in the spandrel is much more complex, as is expected to variate throughout the evolution of the in-plane loading, and no sufficient field data exist. As seen also in Beyer and Dazio 2012 and Graziotti et al. 2016, the performance of spandrels, with respect to the shear capacity and ductility, under the presence of axial prestress is further improved. Yet, under the condition of a perforated wall with a uniform spacing for piers and spandrels, hence a uniform in-plane stiffness distribution and with the absence of additional in-plane restrains from stiff diaphragms and adjacent buildings, a null or low, constant, axial prestress can be also considered.

Table 31. Experimental data collection of unreinforced masonry piers and spandrels from literature, considering aspects of shear capacity and drift ratio thresholds [Gattesco et al. 2015, Parisi et al. 2014, Graziotti et al. 2016 and Beyer and Dazio 2012].

				Piers		Spandrel						
	Block size L:W:H	Block Mortar	$f_{c,b}$ $f_{c,m}$	Brick pattern	L_P:W_P:H_P	Aspect ratio	L_S:W_S:H_S	Aspect ratio	Type	Loading regime	Shear capacity	Maximum/ Residual drift	Prestress in piers	Prestress in spandrel
	[mm^3]	[MPa]			[mm^3]	$L_P/H_{P,eff}$[4]	[mm^3]	H_S/L_S			[kN]	[%]	[MPa]	MPa
Gattesco et al. 2015	250:120:55[1]	44.0 2.17-2.48		English	1500:380:2600 1420:380:2600	0.58[5] 0.55[5]	1200:380:1080 1050:380:1235	1.20 1.18	T.L. F.A.+T.L.	V.C. V.C.	70 50	0.30/1.0[6] 0.15/1.0[6]	0.50	-
Parisi et al. 2014	300:150:100[2]	4.13 2.50		English	1700:310:3620	0.47[7]	1700:310:1000	0.59	M.A.	H.C.	153	0.38/1.1 [8]	0.40	-
Graziotti et al. 2016	-[3]	165-172 2.00		Irregular	1400:320:2400 1400:320:2400	1.17[5]	1200:320:1080 1200:320:900	1.00 0.75	T.L. T.L.	V.C. V.C.	32 38	0.15/1.5[6] 2.5/-[6]	0.17	- 0.11
Beyer and Dazio 2012	250:120:60[1]	30.2-36.2 11.2-20.3		English	2070:380:2283	0.91[5]	1180:380:1260	1.07	T.L. M.A.	V.C.	90 80	0.20/3.0[9] 0.20/3.5[9]	0.33 0.43	0.16,0.08 0.16

[1] Solid fired brick
[2] Tuff block
[3] Irregular sandstone blocks
[4] $H_{P,eff}$: effective height of pier, which according to FEMA 306 1998 must respect crack locations and the lateral seismic load application
[5] L_P: length of one pier, $H_{P,eff}$: height from the base line to the upper surface of the pier, with the spandrel placed at mid height, considering the free rocking of piers
[6] Spandrel drift: Vertical displacement divided to spandrel length
[7] L_P: length of one pier, $H_{p,\,eff}$: height from the base line to the plane of the lateral load application
[8] Horizontal displacement to the height of lateral loading line from the base of the piers
[9] Rotation of piers at the base
Abbreviations: Vertical cyclic (V.C.), Horizontal cyclic (H.C.), Timber lintel (T.L.), Segmental masonry arch (M.A.) and Flat masonry arch (F.A.)

6.4. Building codes mechanical strength models on dominant failure modes for piers and spandrels

Under a popular trend, mechanical capacity models are also used to predict the in-plane resistance of coupled masonry walls, which are calibrated against experimental results on material characterization, and geometric attributes of piers and spandrels. Such capacity models can be found in the manual of FEMA 306 1998 and the Italian technical construction norm of NTC 2018. FEMA 306 1998 provides two sets of verification mechanisms for the flexural and shear strength of a masonry spandrel, related to uncracked and cracked conditions, while NTC 2018 considers the effect of horizontal axial stresses in the spandrel, under diagonal compression. In general, and considering the force-moment diagram of a deformed pier and spandrel system, as shown in Figure 90a, the flexural mechanism in the mesoscale of the spandrel is generated through shear deformations at the bed, head, collar joints and splitting of interlocking bricks at the spandrel's interfaces, while the shear mechanism, within the central part of the spandrel, is established by means of diagonal compressive stresses, and is associated with the tensile strength of masonry (Figure 90). As described in Beyer 2012, flexural cracking, progressing in vertical shear cracks at the spandrel's intersections, mostly precedes in slender spandrels (Figure 90b). Once flexural cracks and global deformations progress, the axial force in the spandrel increases and defines a diagonal trajectory. Hence, shear cracking is likely to succeed the flexural one, under a mixed failure (Figure 90c). Evidently, under larger deformations and increasing axial stresses in the spandrel, the piers might exhibit a third failure mode, under sliding in a horizontal or stepped crack, initiating in the compression zone of the spandrel (Figure 90d).

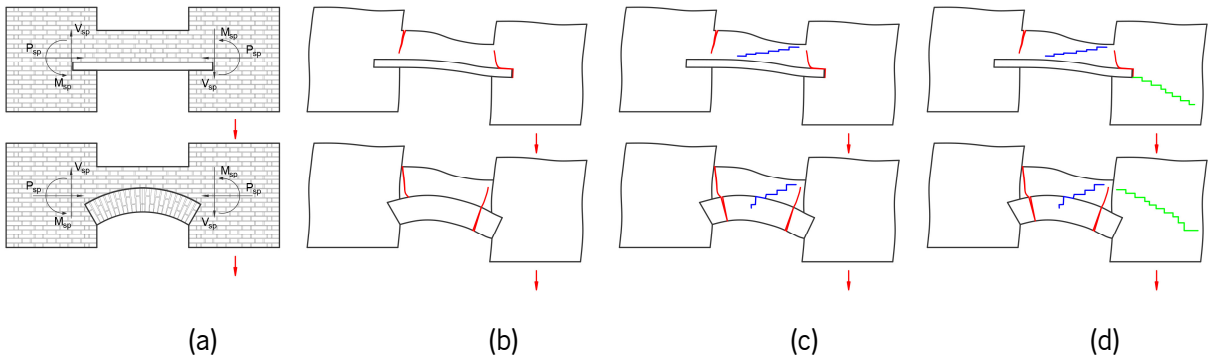


Figure 90. Abaqus of probable in-plane failure modes in a system of masonry piers and spandrels, subjected to an asymmetric vertical deformation; (a) configuration of spandrels with a timber lintel and a masonry arch at the intrados, and representation of in-plane failure modes in the spandrel, with a potential prioritization of bending failure (b), diagonal shear failure (c), and sliding shear failure in one of the piers (d).

Regarding the behavior of masonry piers under lateral deformation, in coupled wall systems, their nonlinear in-plane behavior appears to be defined by their aspect ratio (length to height, L/h), the level of precompression, their tensile strength, and the shear bond strength, at the bed joint level [FEMA 274 1997]. As grouped in FEMA 274 1997, stocky masonry piers with an aspect ratio greater than 1.5, exhibit an in-plane failure, governed by diagonal shear and/or bed joint sliding shear, with diagonal shear cracks forming either in a stepped joint pattern, a straight diagonal crack covering split bricks or a combination of both. Following, moderate size masonry piers (1.5>L/h≥1.0) exhibit primarily flexural shear cracks over their heel. As the lateral deformation progresses and depending on the level of compressive stresses at the toe, failure can either form in diagonal shear or toe crushing. Lastly, relatively slender masonry piers (L/h<1) fail in-plane, under a horizontal hinge line, at a bed joint level close to the base, followed by a progressive in plane rotation around the toe, under large drifts. Also considering the level of coupling with spandrels and the in-plane floor stiffness, the effective height of each pier can be confined within each floor or cover the entire height of the building, often defined by continuous crack-line boundaries, as described in FEMA 356 2000.

Regarding an in-plane strength verification of a masonry pier, in a weak pier-strong spandrel scenario, here denoted as $\mathrm{Q_{CE}}$, according to FEMA 356 2000 and FEMA 306 1998, the expected lateral strength is the lesser of the expected lateral shear strength at the uncracked bed joint level $\mathrm{V_{bjs1}}$ and the expected rocking strength $\mathrm{V_r}$, given in Equation 88 and Equation 89 respectively. Here, $\mathrm{A_n}$ is the net area at the bed joint section, $\mathrm{h_{eff}}$ can be either the full height of the pier, a portion corresponding to crack locations or the one corresponding to a rocking mechanism, L is the length of the pier, $\mathrm{P_{CE}}$ is the axial compressive force due to gravity loads, $\mathrm{v_{me}}$ is the expected bed-joint bond shear strength, given by Equation 90, α is a reduction factor equal to 0.5 and 1.0 for a cantilever and fixed pier respectively, and $\mathrm{v_{te}}$ is the average bed-joint shear strength, for zero axial stress.

Where instead, and for relatively slender masonry piers, with an aspect ratio $\mathrm{L/h_{eff}}$ between 0.67 and 1.00, in-plane rocking is not expected and the diagonal tensile strength $\mathrm{f'_{dt}}$ of masonry is used. The in-plane shear strength, designated as $\mathrm{Q_{CL}}$, is accounted as a lower bound, the lesser of the lateral shear strength $\mathrm{V_{dt}}$ and the toe compressive strength $\mathrm{V_{tc}}$, given in Equation 91 and Equation 92 respectively [FEMA 306 1998 and FEMA 274 1997]. Here, $\mathrm{f_{ae}}$ is the axial compressive stress due to gravity loads, $\mathrm{f'_{dt}}$ is the lower masonry strength in diagonal tension,

which can be also assumed equal to v_{me}, f'_m is the lower bound masonry compressive strength, taken as a fraction of the expected compressive strength fme, equal to $f_{me}/1.6$, and P_{CL} is the lower bound axial compressive force due to gravity loads. In order to determine the expected failure mode of a weak pier, from the prioritized strengths, a relative comparison sequence is defined in FEMA 306 1998, according to the aspect ratio of the pier and correlated with the observed damage.

$$Q_{CE} = V_{bjs1} = v_{me} A_n \quad \text{Equation 88}$$

$$Q_{CE} = V_r = 0.9\alpha P_{CE}\left(\frac{L}{h_{eff}}\right) \quad \text{Equation 89}$$

$$v_{me} = \frac{0.75\left(0.75v_{te} + \frac{P_{CE}}{A_n}\right)}{1.5} \quad \text{Equation 90}$$

$$Q_{CL} = V_{dt} = f'_{dt} A_n \beta \sqrt{1 + \frac{f_{ae}}{f'_{dt}}}, \begin{matrix} \beta = 0.67 \text{ for } L/h_{eff} < 0.67 \\ \beta = L/h_{eff} \text{ for } 0.67 \le L/h_{eff} \le 1 \\ \beta = 1 \text{ for } L/h_{eff} > 1 \end{matrix} \quad \text{Equation 91}$$

$$Q_{CL} = V_{tc} = \alpha P_{CL}\left(\frac{L}{h_{eff}}\right)\left(1 - \frac{f_{ae}}{0.7f'_m}\right) \quad \text{Equation 92}$$

Moving to the coupling elements, the spandrels are subjected to a much lower level of vertical stresses, compared to those of the piers. In fact, vertical stresses in the midspan of the spandrel are only due to the self-weight, while in the spandrel-pier interface are under a portion of the vertical stress field of the piers, which in FEMA 306 1998 is reduced to 50%. As explained in Beyer 2012, the percentage of the vertical stress in the piers, present at the spandrel's interface is according to its aspect ratio and varies within the range of 55-60%. From the onset of flexural cracking at the interfaces, the vertical compressive stresses become diagonal, along the compression toes of the spandrel, and the spandrel can be modeled as a compression strut [Beyer 2012].

In order to determine the flexural and shear strength of a masonry spandrel, both in uncracked and cracked conditions, a set of formulations exist in FEMA 306 1998, similar to those for piers, and for the flexural strength, graphically represented in Figure 91. For the flexural strength at the elastic limit, according to FEMA 306 1998, only the shear strength of the corresponding bed

and collar joints of the spandrel interface are considered, with an effective length b_{effun}, taken equal to the half of the masonry unit. Hence, a linear stress-distribution along the spandrel's centerline is assumed to be taken by means of shear, by the corresponding bed and collar joints at the interface, while the splitting strength of brick is disregarded. Here, the shear stress at the bed joint plane v_{bjun} is given by Equation 93, where v_{te} is the bond strength, γ is equal to 0.5, which accounts for a reduced level of vertical stresses, compared to the ones at the base of the piers, here denoted as the axial force P_{CE}, and A_n corresponds to the area of the participating joints of the pier. In accordance, the elastic collar joint shear stress v_{cun} is also given by Equation 93, where the axial force is exempted, hence γ is equal to zero.

Here, the collar joints are accounted for multi-layered masonry, but the same concept exists for the collar joints of uniform masonry. The horizontal shear force of the elastic limit at the spandrel denoted as T and presented in Figure 91, is given by Equation 94. Here, b_w and b_h are the width and height of the brick unit respectively, NB can be interpreted as the number of the collar joints of each horizontal course and NR is the number of the bed joints in half of the spandrel's height, given by Equation 95, where for the latter, the brick unit height includes the thickness of the bed joint. The η coefficient is given by Equation 96. The elastic flexural strength of the spandrel M_{spun} is given by Equation 97, where d_{sp} is the depth of the spandrel.

Also, instead of the use of Equation 93 and Equation 94, the Mohr-Coulomb relationship can be used, as described in Beyer 2012. In addition, in FEMA 306 1998, the contribution of the normal tensile strength of the head joints is exempted in the formulations for the flexural strength of spandrels. In fact, the tensile strength is only a portion of the in-plane shear, which according to Lourenco et al. 1995 is around to 70% and accounting for both contributing to the last stages of the elastic response appears nonrealistic.

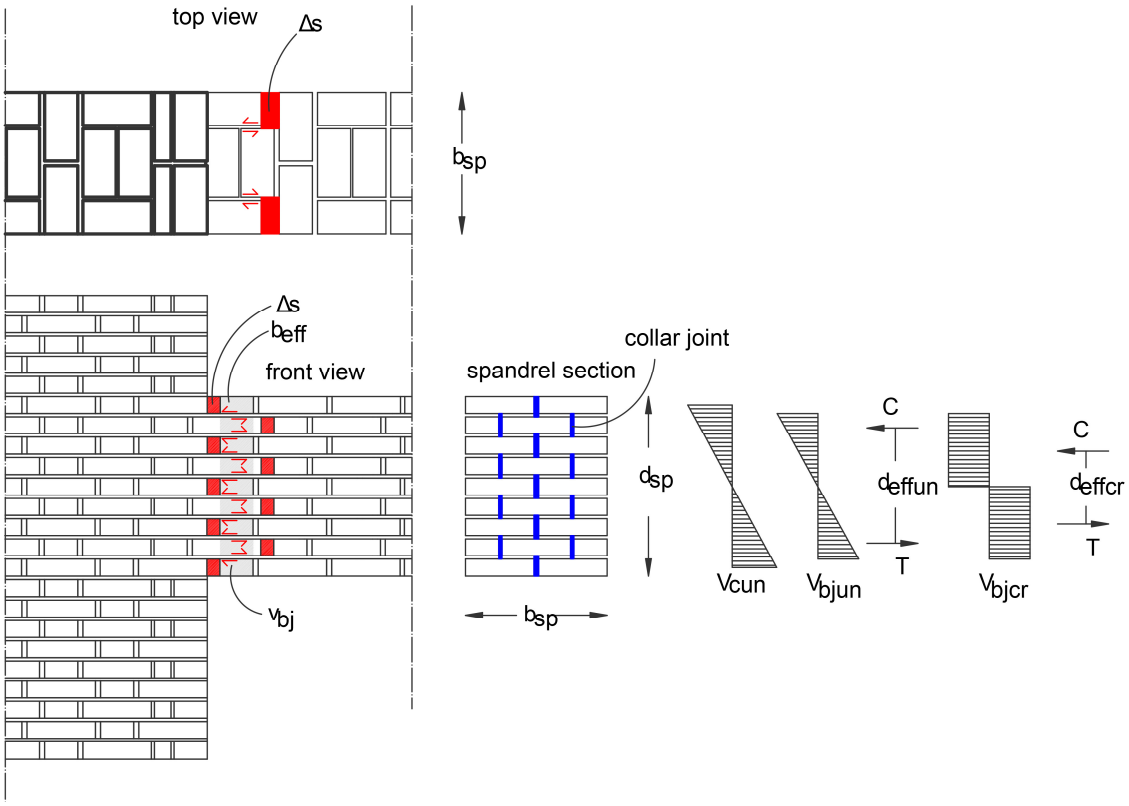


Figure 91. Flexural strength verification, through shear interaction of interlocking bricks, bead and collar joints, at the interface of spandrels with piers. Adapted from FEMA 306 1998.

$$v_{bjun} = \frac{0.75\left(0.75v_{te} + \frac{\gamma P_{CE}}{A_n}\right)}{1.5}, v_{cun} = 0.375v_{te} \quad \text{Equation 93}$$

$$T = \left[v_{bjun} b_w b_{effun} + v_{cun} b_h b_{effun}(NB - 1)\right]\eta \quad \text{Equation 94}$$

$$NR = 0.5\frac{d_{sp}}{b_h} \quad \text{Equation 95}$$

$$\eta = \frac{NR}{2} \text{ OR } \sum_{i=1,NR}\left[\frac{d_{sp}}{2} - b_h(i) \Big/ \frac{d_{sp}}{2} - b_h\right] \quad \text{Equation 96}$$

$$M_{spun} = \frac{2d_{sp}}{3}T \quad \text{Equation 97}$$

In accordance with the formulations for the shear strength of the bed and collar joints in uncracked conditions, when accounting for cracked conditions, only the shear strength of the bed joints v_{bjcr} is considered, accounting that the bond strength v_{te} is lost, and solely the frictional

component from the axial force is accounted (Equation 93) [FEMA 306 1998]. Also considering the opening of the head joints at the interface, the effective interface length for cracked conditions b_{effcr} is actually the effective length b_{effun}, reduced by the average slip, here denoted as Δs (Figure 91). The updated shear horizontal cracked force T_{cr} and cracked moment M_{spcr} are given in Equation 98 and Equation 99 respectively. In order to account for the cracking of the brick units at the interfaces of the spandrel, in FEMA 306 1998, the effective depth of the spandrel is further reduced, here denoted as d_{spcr}, including only the portion of uncracked bricks, a condition that is further confirmed in Roca et al. 2005.

$$T_{cr} = v_{bjcr} b_w b_{effcr} NR \qquad \text{Equation 98}$$

$$M_{spcr} = \frac{d_{spcr}}{2} T_{cr} \qquad \text{Equation 99}$$

Following, the alternate strength mechanism of the spandrel under diagonal tension, considering uncracked conditions, denoted as V_{spun}, and similarly to the shear strength at piers is formed in Equation 100. Here, f_{ae} corresponds to the expected axial compressive stress in the spandrel, if any, and b_{sp} is the width of the spandrel. For cracked conditions the shear capacity of the spandrel is considered unreduced, accounting for the bearing resistance of the bed joints and interlocking bricks at the diagonal. Here, the aspect ratio of the spandrel β is defined according to the formation of the compressive struct and the in-plane rotation.

$$V_{spun} = f'_{dt} d_{sp} b_{sp} \beta \sqrt{1 + \frac{f_{ae}}{f'_{dt}}}, \beta = \begin{cases} \beta = 0.67 \text{ for } {L_{sp}}/{h_{sp}} < 0.67 \\ {L_{sp}}/{d_{sp}} \text{ for } 0.67 \le {L_{sp}}/{h_{sp}} \le 1 \\ \beta = 1 \text{ for } {L_{sp}}/{h_{sp}} > 1 \end{cases} \qquad \text{Equation 100}$$

In conclusion, the relative comparison of the different strength types between spandrels and piers, will form the prioritization of in-plane failure modes, within a masonry façade.

Yet considering the presence of many interacting structural elements in coupled and composite masonry walls, such as arches, lintels and floor diaphragms, the accurate analytical computation of stiffness and strength properties is not an easy task. In FEMA 306 1998, for the overall in-plane flexural and shear resistance in a masonry spandrel, the contribution of a timber

lintel or an arch, as parts in the structural configuration of the spandrel, is not accounted, which according to Beyer 2012 can have a significant influence for the residual strength, during cracked conditions.

The presence of a timber lintel contributes significantly to the overall ductility of the masonry spandrel, as shown in Gattesco et al. 2015 and Beyer and Dazio 2012. In addition, considering the contribution in the flexural peak and residual strength, at the bearing plane of a timber lintel, with a bearing length $\mathrm{l_b}$, a thickness $\mathrm{t_b}$, and a mortar interface, the additional joint shear stress $\mathrm{T_b}$ and $\mathrm{T_{bcr}}$ for uncracked and cracked conditions respectively is calculated from the Equation 101 and Equation 102 and can be added in the force resultant T and $\mathrm{T_{cr}}$ respectively.

$$\mathrm{T}_b = \mathrm{v_{bjun}} \mathrm{l}_b \mathrm{t}_b \qquad \text{Equation 101}$$

$$\mathrm{T_{bcr}} = \mathrm{v_{bjcr}} (\mathrm{l_b} - \Delta \mathrm{s}) \mathrm{t_b} \qquad \text{Equation 102}$$

Following the same reasoning, the shear action under diagonal compression in the spandrel, under the presence of a timber lintel, and considering its high stiffness in comparison to the one of masonry, it can be assumed that is shortening the height of the compressive strut. Thus, in Equation 100, the diagonal tension capacity is found decreased, considering that the spandrel's depth $\mathrm{d_{sp}}$ is configured by subtracting the height of the timber lintel, denoted here as $\mathrm{h_b}$.

When instead an arch is present, and given the low level of vertical stresses, the arch tends to crack early in tension, under flexural loading. Thus, under a conservative approach and given the uncorrelated tensile and shear failure at the joint level, the contribution of the arch in the flexural response of the spandrel can be exempted. Considering the spandrel's response under diagonal compression, the arch is believed to contribute greatly, mostly depending on its geometric configuration. In fact, semicircular or segmental masonry arches can even have the joint planes at the springings transversally oriented to the compression strut of spandrel, and thus working in compression. Here, and considering an uncracked arch, for the calculation of the shear strength of the spandrel, the full spandrel height at the intersections $\mathrm{d_{sp}}$ is advised. Yet, given the activation of the arch in compression, together with the formation of hinges, as is mostly the case in sequential flexural and shear failure in an arched spandrel, diagonal shear cracks might involve only over the arch, with shear sliding of even plain opening at the interface with the arch. Such a discontinuity at the arche's extrados can move the compressive strut over the arch springings.

Hence, the consideration of the full spandrel height at the intersections, including the arch, for the diagonal shear failure at the spandrel, has to be verified with experimental or numerical data.

According to NTC 2018, there is a distinction between in-plane capacity models for vertical and horizontal masonry elements, for which the lower bound, under the specified deformation and angular fields, defines the response. Regarding the horizontal coupling elements in masonry, two in-plane capacity verifications are identified; the failure due to bending and diagonal tension.

For the bending capacity in the spandrel, a critical aspect is the presence of axial stresses, which is influenced by the interaction of rotation and axial deformations, within the system of coupled walls, but also by the activation of ties, serving as strengthening elements. The bending failure mechanism, located at the ends of the spandrel, is associated to the horizontal tensile strength f_{ftd}, taken as the minimum between the half of the tensile splitting strength of unit blocks f_{btd} and the shear bond strength of the horizontal joints, under a normal stress field (Equation 103). For regular shaped blocks a limit for the tensile splitting strength is obtained from values in literature, mechanical characterization tests or given as a portion of the normalized compressive strength f_b, with an estimate of $0.1f_b$, σ_y is the normal stress acting on the bed joints of the spandrel, f_{vod} is the shear strength for zero axial stress, μ is the coefficient of friction, with 0.577 taken as a recommended value (corresponding to a friction angle of 30°), and Φ is the ratio between the height of a block h_b and the overlap length of two consecutive blocks, from two successive courses, which in fact defines the slope of the stepped shear crack. In the absence of knowledge for the vertical stress field at the intersections of the spandrel, the 50% of the average vertical stress in the adjoining pier can be considered [NTC 2018]. Considering the shear sliding resistance limit, in locations where the bending moment is maximum, is related to the breaking of blocks, given in Equation 104.

$$f_{ftd} = \min\left(\frac{f_{btd}}{2}, f_{v0d} + \frac{\mu\sigma_y}{\Phi}\right) \qquad \text{Equation 103}$$

$$f_{V,lim} = \frac{0.065 f_b}{0.7} \qquad \text{Equation 104}$$

The bending strength can be calculated by assuming a planar section of elasto-plastic compression and elasto-fragile tension, in the case of breakage of the blocks, elastoplastic, possibly with controlled ductility, in the case of breakage by joint sliding.

Considering the expression in NTC 2018, for quantifying the frictional resistance of connections with transversal walls, the resultant force of the frictional resistance can be defined, due to the coupling with the piers, which for one of the coupled shear components corresponds to the half-height of the spandrel, given by Equation 105. Here, n is the number of units, consecutive in rows, which are involved in a vertical crack, hence the height of involved courses with good interlocking, equal here to the total height h_{sp} of the spandrel, divided with the unit's height h_b, l_b is the length of the frictional joints, t_s is the thickness of the adjoining pier, μ is the coefficient of friction, Φ is the ratio between the height of a block h_b over l_b, and W is the specific weight of masonry. Considering a triangular stress configuration, the point of application for the resultant frictional force is located at the $1/3$ of the accounted height, from the extrados of the spandrel.

$$T = 0.4n(n+1)\Phi\mu {l_b}^2 t_s W \qquad \text{Equation 105}$$

Continuing, the capacity in diagonal compression V_t in the spandrel, under a regular masonry pattern, is given by Equation 106 and can be evaluated if the axial force in the spandrel is known [NTC 2018]. The formation of the diagonal crack is configured either through a stepped crack in the bed and head joints and governed by the normal tensile strength f_{vod} or the diagonal failure of the blocks, by surpassing the splitting tensile strength f_{btd}. Following, σ_0 is the axial stress over the total area of the spandrel, and considered positive if is compressive, while l, t and b are respectively the length, the thickness and the slenderness ratio of the spandrel, within the range of 1.5>b≥1.0. The capacity V_t cannot exceed a function of $V_{t,lim}$, derived from the tensile failure of blocks, given in Equation 107. Instead, a more simplified expression exists, applied to spandrels with more irregular masonry (Equation 108) [NTC 2018]. Here, f_{td} is the diagonal shear strength in masonry, taken equal to 1.5 times the direct tensile strength [NTC 2018]. Considering the presence of timber lintels and masonry arches in the spandrel, their influence in the overall ductility of the spandrel is favorable, with a residual provided resistance of 40% and 10% of the peak diagonal shear strength respectively [NTC 2018].

$$V_t = \frac{lt}{b}\left(\frac{f_{vod}}{1+\mu\Phi} + \frac{\mu}{1+\mu\Phi}\sigma_0\right) \le V_{t,lim} \qquad \text{Equation 106}$$

$$V_{t,lim} = \frac{lt}{b}\frac{f_{btd}}{2.3}\sqrt{1+\frac{\sigma_0}{f_{btd}}} \qquad \text{Equation 107}$$

$$V_t = \frac{lt}{b} f_{btd} \sqrt{1 + \frac{\sigma_0}{f_{td}}} \qquad \text{Equation 108}$$

6.5. Experimental works on masonry piers and spandrel assemblies under a vertical displacement field

6.5.1. Masonry assemblies, setup implementation and testing protocols

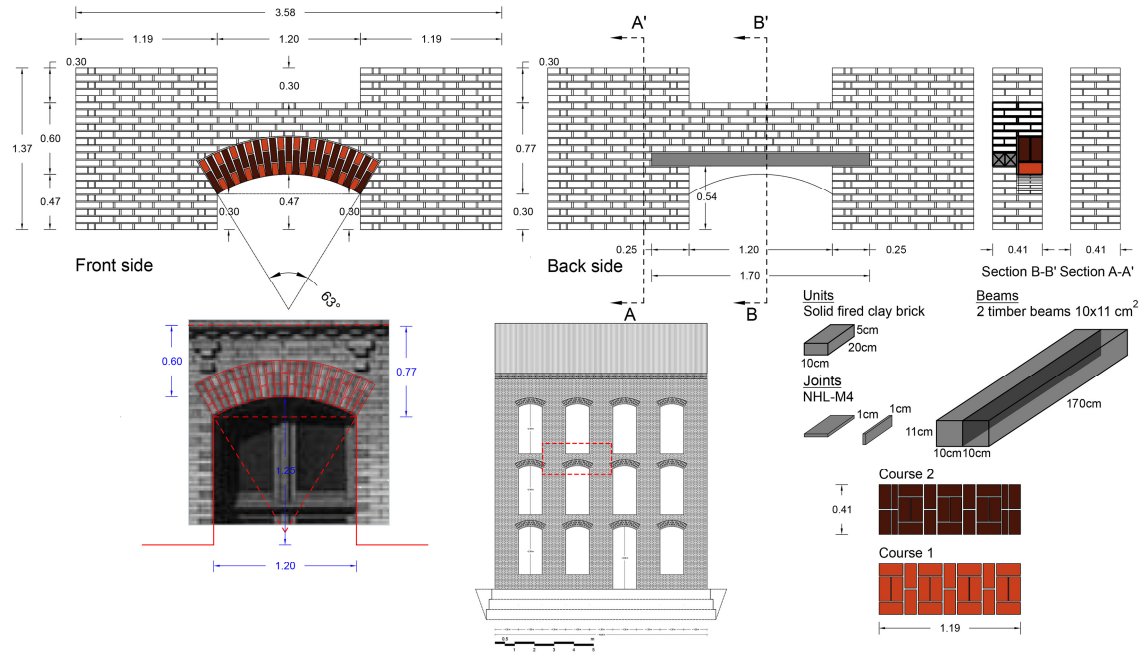
The current experimental campaign investigates the in-plane structural behavior and damage due to subsidence, in historic solid brick and lime mortar masonry buildings, with flexible timber diaphragms. Thus, partial masonry assemblies are subjected to monotonic, differential displacements in the laboratory. Under the focus of coupled masonry components, a set of twin, real-scale masonry assemblies, designated as UN1-US and UN2-US, were constructed in the ISISE Laboratory of the Civil Engineering Department of the University of Minho (Portugal), and are composed by a pair of piers and a spandrel, as shown in Figure 92. By adjusting boundary conditions and axial loading, the tested masonry assemblies can be considered as part of a load bearing, single leaf, masonry facade, of more than one stories, with weak horizontal diaphragms of timber floors. First, two tests of an asymmetrical monotonic vertical uplift were conducted, divided in sub-setups, for adequate control and documentation, under different lateral restrain conditions, and until significant in-plane damage levels were reached. In addition, the effectiveness of two strengthening techniques was investigated in the already damaged assemblies. These include namely a simple reintegration of the internal crumbling and fragmentations, by means of lime-based grouting (UN1-DS-GR), and a more comprehensive strengthening strategy with grouting and a structural render with a Fiber Reinforced Cementitious Matrix system (FRCM), and additional in-plane FRCM anchors (UN2-DS-GR-SS). The four different tests of asymmetrical monotonic vertical uplift in masonry piers and spandrels, under various boundary conditions and structural interventions, are presented in Table 32.

Table 32. Experimental testing on asymmetrical monotonic vertical uplift in masonry piers and spandrels: tested assemblies, types of boundary conditions and strengthening specifications.

Testing assembly of piers and spandrel	Vertical prestressed rods	Lateral support at uplifting pier with rollers	Crack filling with grout	FRCM structural render, with in-plane (in thickness) adhesive anchors
UN1-US	✓			
UN1-DS-GR	✓	✓	✓	
UN2-US	✓	✓		
UN2-DS-GR-FRCM	✓	✓	✓	✓

US: Undamaged state, DS: Damaged state, GR: Grouting, FRCM: Fiber Reinforced Cementitious Matrix system

In order to select the geometrical characteristics for the assemblies, the masonry pattern and constituents, the coupling state of the spandrels and the axial loading in the piers, the masonry façade of the reference building of Table 4 and Figure 24 (CHAPTER 3) was chosen, configured as a typical residential building of the 19th and 20th centuries in Europe and in particular the Iberia peninsula, with three stories and an attic [Camino Olea 2001]. Here, the selected masonry pattern is of a Flemish bond with a thickness of 0.41 m, the equivalent length of two bricks and a head joint (Table 3), typical for the façade of the upper stories, while the length of the piers and spandrel is equal to 1.2 m (Table 4). In order to simulate historic masonry, low temperature fired solid clay bricks were used, with weak lime mortar joints of 1 cm, as characterized mechanically, under specific curing (approximately 200 days) and laboratory conditions, which are presented in Section 3.4 and Section 3.5 (Table 8, Table 9 and Table 11). The mechanical characterization of masonry wallets of a thickness of 1.5 brick-size, both in uniaxial and diagonal compression are presented in Section 3.5.1 (Table 12) and in Section 3.5.2 (Table 14) respectively.



(a)



(b) (c)

Figure 92. Experimental tests: (a) details of UN1 and UN2 twin assemblies, side by side, as a portion of the reference façade of Figure 24, and phases during construction (b) and (c). Note the segmental masonry arch and timber lintel, configured each, at a half of the spandrel's thickness, the material constituents and the Flemish bond, with a thickness of two bricks.

Following the technical and architectural details of Chabat 1886, the spandrels were typically configured by a relieving segmental arch, in the half outer thickness and a set of timber lintels in the half inner one, the later configured with a bearing length of 0.25 m (Figure 92). In the outer circumference of the segmental arch, bricks, cut with a water chain saw, were used to accommodate the space of the axially arranged bricks.

The boundary conditions, imposed at the piers were established, according to the level of confinement, both in the vertical and lateral directions. First, the axial loading, at a certain level of

the façade, is the result of the gravitational loads from the upper stories, mostly under a vertical stress field in the piers. Here, the selected level of pre-compression was equivalent to that of the 2nd story of the reference facade (Figure 92). Hence, in order to validate a realistic vertical stress state for the piers, a preliminary static nonlinear phased analysis was conducted for the reference façade, presented in Figure 93, which at the corresponding plane of the masonry piers of the 2nd story is in the range of 0.1-0.2 MPa. A set of preliminary material properties for masonry and timber, together with a basic configuration of historic soft timber floor and roof diaphragms, according to Apolo and Martínez-Luengas 1995 and NBE-AE/88 are presented in Table 33.

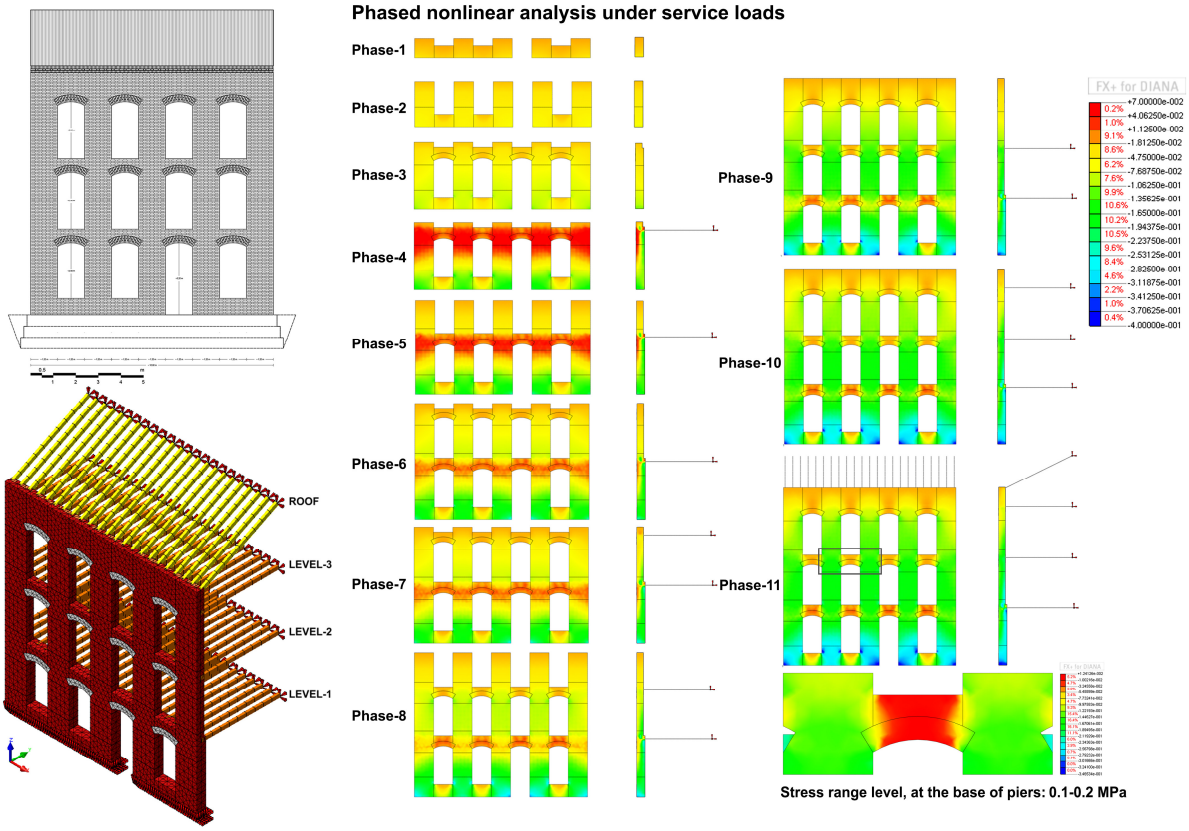


Figure 93. Preliminary FEM static nonlinear phased analysis of the reference façade, under service loads. Plots of vertical stresses in MPa. For the boundary conditions, note the simply supported beams of the roof and floors and the pinned supports at the base of the masonry façade.

Table 33. Preliminary material properties, cross-sections and spacing of floor and roof diaphragms.

		h (m)	b (m)	A (m^2)	L (m)	ρ (kg/m^3)	ρ (kg/m^2)	W (kg)	$\rho_{eq.}$[1] (kg/m^3)	E (MPa)	v	f_c (MPa)	f_t (MPa)	G_c (N/mm)	G_f (N/mm)
Roof	Principal rafter[2]	0.12	0.20	0.024	5	800[2]	-	96.0	2458.3	11000[4]	0.2	-	-	-	-
	Secondary rafter[2]	0.10	0.10	0.01	0.5[3]	800[2]	-	4.0	-	-	-	-	-	-	-
	Blanks[2]	0.03	5.0	0.15	0.5[3]	600[2]	-	45.0	-	-	-	-	-	-	-
	Tiles[2]	-	5.0	2.5	0.5[3]	-	60[2]	150.0	-	-	-	-	-	-	-
Floor	Principal beam[3]	0.12	0.2	0.024	4.195	800[2]	-	80.5	5341.7	11000[4]	0.2	-	-	-	-
	Overload	-	0.5	2.1	4.195	-	200[2]	420.0	-	-	-	-	-	-	-
	Planks[3]	0.03	0.5	0.015	4.195	600[2]	-	37.8	-	-	-	-	-	-	-
	Brick masonry with lime mortar	-	-	-	-	1923.2[5]	-	-	-	908.7[5]	0.2	8.8[5]	0.42[5]	14[5]	0.023[5]

[1] Equivalent density for roof rafters and floor beams, considering additional layers and overloads
[2] From NBE-AE/88
[3] Effective width
[4] Timber class C24 EN 338:2009
[5] Table 16

The implemented setup for the testing under monotonic, asymmetric, vertical displacements is presented in Figure 94, Figure 95 and Figure 96. Here is noted that instead of a vertical down-lift, the reversed action was chosen, which provided a higher level of control for the setup arrangement, together with higher safety conditions during testing. Hence, the resulted damage and deformation can be considered identical to that of a vertical down-lift, in horizontal symmetry. Hence, the reported damage in the non-moving pier corresponds to the one subjected to the downward settlement in reality. The masonry assemblies were built on top of two tapered steel beams, with one free to be lifted upwards and the other end mounted to the strong floor. The vertical uplift for one of the piers was applied by means of two electro-mechanic actuators with loading cells, connected in a series, each with a 300 kN maximum capacity, placed on either side of the movable pier, and mounted in the strong floor. The uplifting mechanism is configured by a peripheral steel frame of HEB200 beams, columns and steel angles, connected to the free beam at the base. Here is noted, that all the connections, between steel parts of the frame, are bolted, while no welding was used. The absence of outward rotations was verified with preliminary testing on assemblies constructed with modern bricks and, thus, no out-of-plane supports were needed.

Considering the application of boundary conditions, first, the axial stresses in the piers of UN1 and UN2, were replicated by means of prestress, through the vertical elongation of eight steel tie rods, with a diameter of 30 mm, placed at each pier. The prestress action is applied through a

total of four hydraulic jacks, placed at the top steel caps of both piers, which were clamped by means of the vertical steel tie rods, a steel plate on top, and steel angles, attached in the beams of the base (Figure 94 and Figure 96a). Thus, by applying an axial force of 34 kN, measured in each of the four hydraulic jacks and considering also the self-weight of the parts of the setup, laid over the piers, i.e., the tapered top beams, the hydraulic jacks, the steel plates and the steel tie rods, the axial prestresses at the base of both piers is estimated at 0.21 MPa. The axial prestress system, similar to Gattesco et al. 2015, Parisi et al. 2014, Graziotti et al. 2016 and Beyer and Dazio 2012, is applied first and is kept constant throughout the application of the vertical displacement.

Next, the concept of lateral boundary conditions for the piers proved to be rather complex. As explained in Gattesco et al. 2015 piers subjected to in-plane seismic loads generally tend to rotate. In addition, monotonic asymmetrical settlements, often with vertical and horizontal components can impose non-uniform rotations in piers, especially in those located at the ends of a façade, and with no interaction with adjacent buildings. Thus, two different lateral restrain conditions were chosen for the uplifting testing frame and pier. First, for the undamaged assembly of UN1-US, the supporting frame and pier were allowed to rotate freely, which led to high rotation angles of at maximum 1º. Second, for UN2-US, in order to simulate an intermediate lateral restrain condition and reduce the in-plane rotations of the uplifting pier, lateral supports were placed, at both sides of the uplifting frame, by means of eight axial roller bearings and two diagonal prestressed rods, tying the lateral supporting frame with the reaction wall (Figure 94 and Figure 95). The resulted structural interaction of the spandrel, under lower maximum rotation angles in the uplifting pier of 0.8º, was configured with a combined bending and shear failure, and considered as more ductile. Hence, the abovementioned lateral restrain system was kept as is, throughout the duration of the setups for the UN1-DS-GR, UN2-US and UN2-DS-GR-SS assemblies (Table 43).

Regarding the horizontal axial restrain in the spandrels, as documented in Beyer and Dazio 2012 and Graziotti et al. 2016, throughout the evolution of in-plane loading and elongation, in the spandrel, compressive forces in counteraction with the piers tend to increase. Yet, given the lack of field data on the exact level of axial prestress in masonry spandrels, the absence of active strengthening in-plane systems and the study of spandrels and piers under uniform spans and spacing, no axial prestress was applied, along the spandrel's main axis.

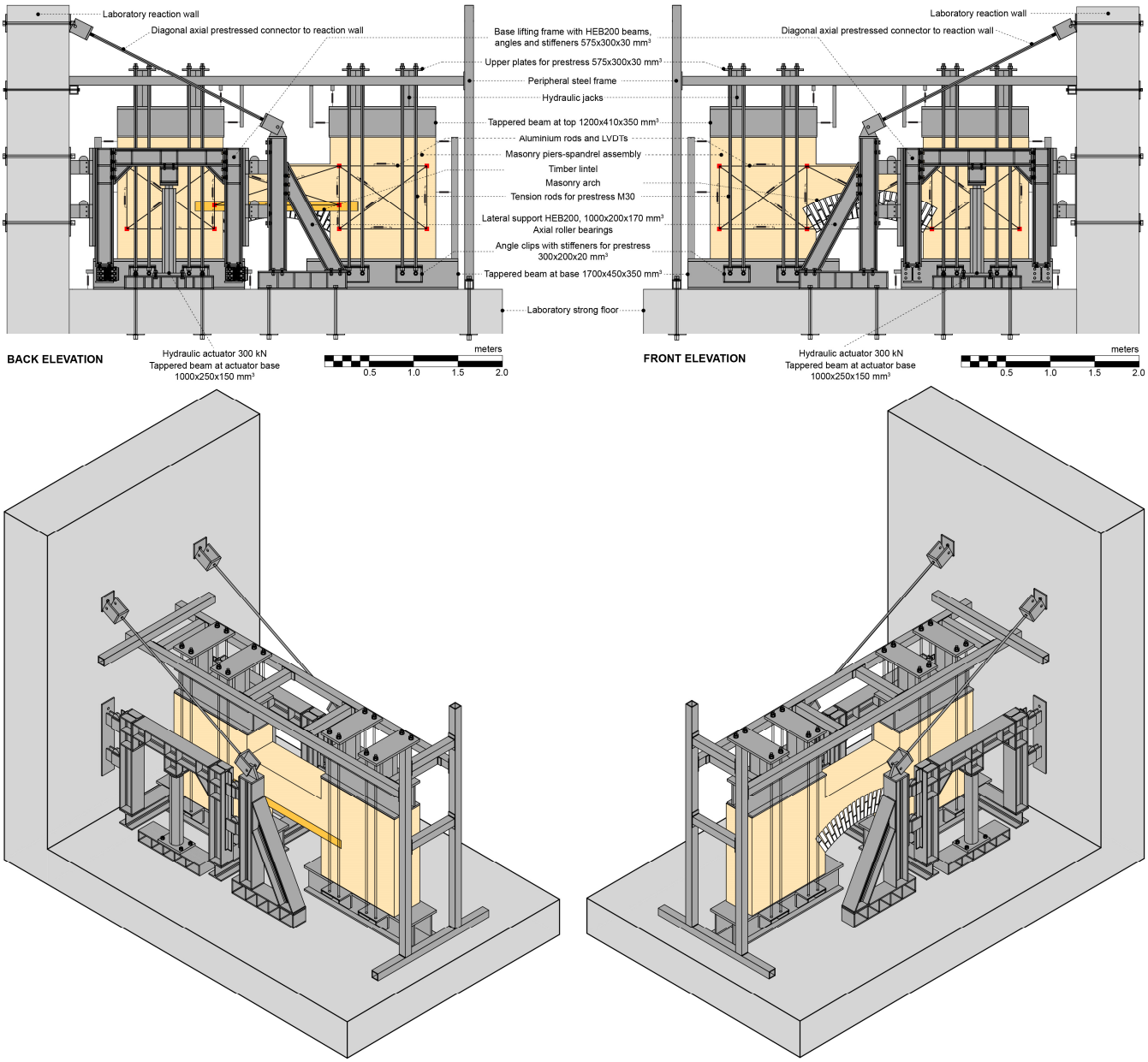


Figure 94. Schematic representation in elevations and perspective views, of the experimental setup arrangement for UN1 and UN2 piers and spandrel masonry assemblies.

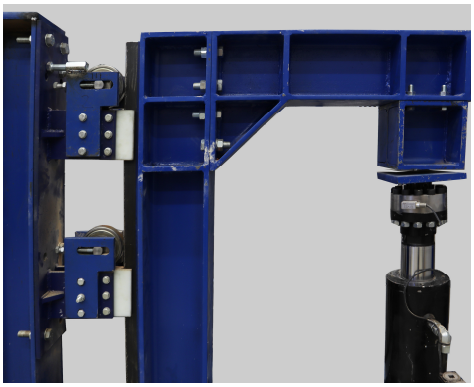


Figure 95. View of the axial roller bearings, part of the lateral, in-plane restrain system for the uplifting frame and pier.

Following, for the documentation of the tests, a total number of 44 linear variable differential transformers (LVDTs) were used, which given their large number, were divided in two different acquisition boards. Their relative measuring range varied from ±10 to ±150 mm, and were distributed accordingly in locations, accounting for preliminary testing and numerical simulations. In particular, 10 LVDTs were attached to an external, peripheral, steel frame, supported in the reaction wall and the strong floor, which measured the global in-plane deformations and rotations in the piers (Figure 96). The additional 34 LVDTs were distributed in a grid of vertical and diagonal aluminum extension rods, in order to acquire axial, lateral and shear deformations in the in-plane surfaces of the piers and spandrel, at both sides, as shown in Figure 96b. The extension rods were allowed to rotate freely, attached at both ends to metallic nodes, with the latter being firmly mounted in the surface of the masonry, with polyester mortar.

Considering the loading protocols, a sampling rate of 4 Hz was selected, and the applied load was under a displacement control, at a rate of 10 μm/s. In addition, the imposed global vertical displacements were applied monotonically, in increments of 1 or 2 cm, and afterwards were kept constant, while the assembly was secured in position with movable supports, until the next increment was applied. Hence, the crack progression could be documented for each displacement increment. In total, vertical displacements of 6-10 cm were applied, which resulted to fully progressed cracks along the entire spandrel or pier. Considering the deformations of the frame, being in the order of millimeters, and mostly attributed to the deformations of the bolted connections between steel parts, each displacement input had to be compensated, according to estimations from previous setups. Yet, given the varying negative deformations at the end of the stable displacement branch, when the movable supports were placed and the actuators were retracted, vertical displacement inputs in some setups varied slightly from the designed ones.

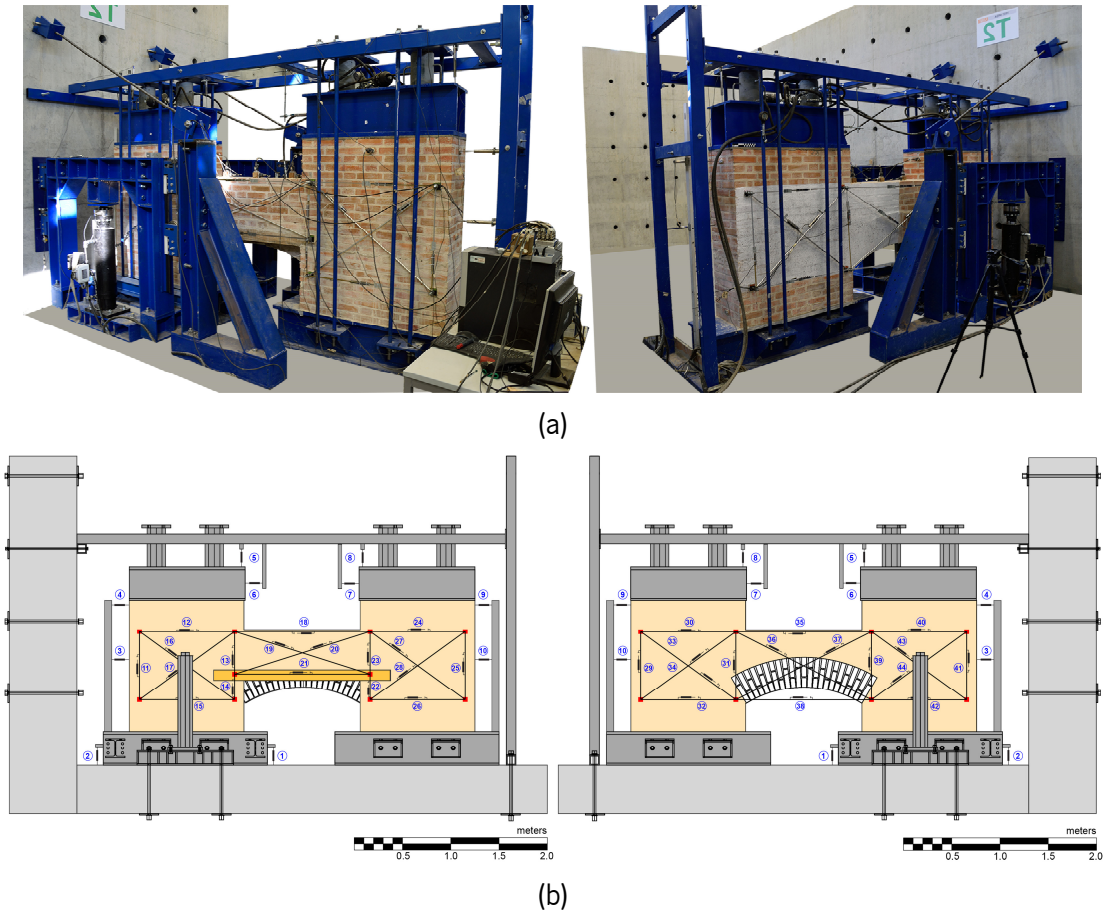


Figure 96. Front and back views of the experimental setup for UN1 and UN2 masonry assemblies (a) and configuration of the grid of extension rods and LVDTs with numbering (b).

6.5.2. Experimental results

6.5.2.1. Testing of piers and spandrel masonry assemblies at the undamaged state

As described in Section 6.5.1 the vertical upward displacements in one of the piers, increases monotonically in increments, and until the development of fully formed cracks in the spandrel and piers, while the movable frame is secured in position for conducting the damage assessment. In total, for UN1-US and UN2-US masonry assemblies, the maximum imposed vertical displacement, in the movable frame and pier, reached 6 cm (Figure 97). Accounting for the relative deformation of the moving setup and the in-plane rotation of the piers, the resulted average uplift in the moving masonry pier, as measured from the two vertical LVDTs at the top steel cap, is also presented in Figure 97. Considering the resulted in-plane rotation for the piers with the non-moving base, it was found under a steady increase, along the duration of the setup, yet rather small for both assemblies, reaching by maximum 0.05º and 0.30º, for UN1-US and UN2-US respectively. As for the in-plane rotation of the movable piers, and despite the difference in lateral restrain, they were found relatively similar, with those of UN1-US -no lateral restraint- and UN2-US -lateral

restraint with axial roller bearings and prestressed rods- being equal to 1.03º and 0.75º respectively. Such values of in-plane rotations are attributed mostly to the in-plane bending and shear stiffness of the timber lintels in half of the spandrel's thickness. Here, the evolution of the average displacement control from the two actuators, in both masonry assemblies, is superposed with the average uplift of the moving pier and the in-plane rotation of the piers -non-moving and moving-, as configured from the LVDTs placed vertically to the upper beam caps, as shown in Figure 97. It is noted that drift values were not of interest, since the full height of piers confined within a story, was not represented in the tests. Considering the evolution of the in-plane rotations of the moving piers, they follow the advancement of the absolute vertical displacements, except from parts with a negative slope, during a range of absolute vertical displacements of 2-3 cm for UN1-DS and 3.5-4 cm for UN2-DS. Such a negative slope is indicative of extensive cracking in the spandrel area, with a considerable decrease in the bending stiffness.

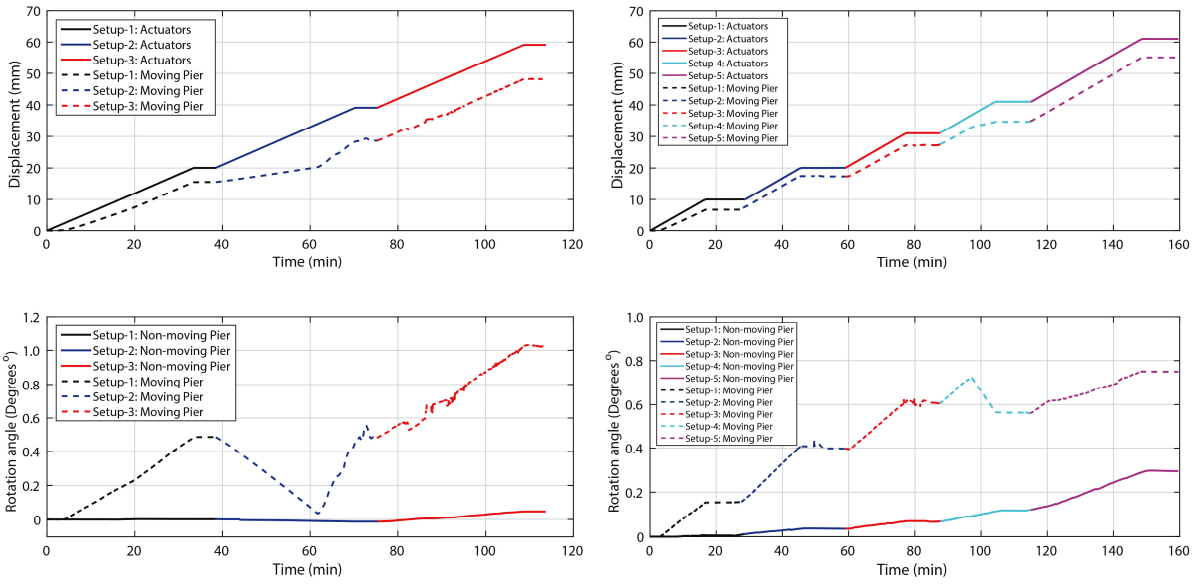


Figure 97. Masonry assemblies UN1-US (a) and UN2-US (b): time histories of the averaged monotonic vertical displacements from the actuators, the top LVDTs and the in-plane rotation of the non-moving and moving piers.

In Figure 98, for the UN1-US and UN2-US masonry assemblies, the variation for the average vertical uplift of the spandrel is presented, here computed as the relative displacement, measured from the vertical LVDTs placed in the inner ends of the upper beam caps of the piers, versus the shear force in the spandrel, denoted as V_{sp}. The corresponding shear force for the spandrel is computed from the sum of the total force from the actuators by subtracting the gravitational loads of the moving pier and participating setup, here found equal to 20.38 kN.

For the UN1-US and UN2-US a maximum shear force $V_{sp,max}$ of 39.95 kN and 58.22 kN was reached respectively. The response is assessed as highly ductile, nonlinear, with moderate hardening after yield and almost flattened at the last steps. In particular, after a vertical displacement of around 4.5 mm, which for UN1-US and UN2-US corresponds to a shear force in the spandrel of around $0.8V_{sp,max}$ and $0.6V_{sp,max}$ respectively, and given the abrupt change of curvature, is considered the yielding point for the spandrels. Such a difference in the yielding point between the two assemblies is attributed to the difference in boundary conditions and resulting difference in failure modes. Thus, the corresponding yielding shear stiffness $V_{sp,y}$ for the spandrel is equal to 6731 N/mm and 6995 N/mm, for the UN1-US and UN2-US respectively. Accounting for the ductility μ, at the point of the maximum shear force at the spandrel, given as the ratio $d_{Vsmax,UNi-DS}/d_{y,UNi-DS}$, is equal to 6.91 and 8.47 for UN1-US and UN2-US respectively.

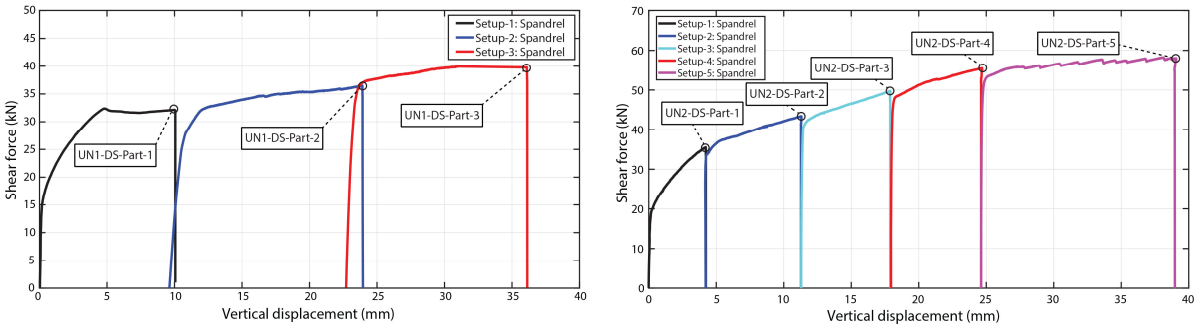


Figure 98. Experimental shear-displacement curves for the spandrels of the masonry assemblies UN1-US (a) and UN2-US (b). Note the relative vertical displacement of the spandrel at x-axis, and the corresponding parts (UNi-DS-Part-j) of documented damage assessment, in Figure 100 and Figure 101.

Accounting for the spandrel's flexural and shear response, in the UN1-US and UN2-US (Figure 98), and the respective damage progression at each damage state, as shown in Figure 99, Figure 100, Figure 101 and Figure 102, it can be observed that the yielding point of around 4.5 mm, for the relative vertical displacement of the spandrel, is associated to the initiation of flexural cracking at one end of the spandrel (UNi-DS-Part-1). Cracking initiates with a hinge of the arch, at the intrados and near the springing of the fixed pier. For UN1-DS, flexural cracking is progressing vertically, under the failure in horizontal tension at the plane of bed and collar joints, and through the splitting of interlocking bricks at the spandrel interface (Figure 99 and Figure 100), whereas for UN2-DS, the flexural crack is shifted more within the pier (Figure 101 and Figure 102). Considering the lack of lateral restrain in UN1-US, the spandrel is experiencing early rocking, immediately after yielding, as represented with an almost flattened post-yield response in Figure

98a, with solely flexural cracks that intensify in width, and cover the entire thickness of the spandrel. At the end of UN1-DS-Part-2 in Figure 98 and Figure 100, and under increasing axial stresses in the compression zone of the spandrel, the fixed pier experiences a sliding shear failure, under a stepped joint crack, which progresses, at the last steps, to a vertical shear crack, with the splitting of bricks.

Instead, the post-yield response of UN2-DS, is influenced by the increased axial stresses in the spandrel, provided by the lateral restrain in the moving frame and pier, from the use of axial roller bearings and diagonal prestressed rods. Hence, the response is more ductile, it exhibits hardening, and the flexural failure is followed by a combined shear action, along the compressive struts of the spandrel and fixed pier, with sliding, stepped, shear cracks (Figure 102). At the last steps (UN2-DS-Part-5), the shear crack at the spandrel propagates along the joints and the voussoirs of the arch, thus resulting to the rocking of a large portion of the spandrel.

Considering the presence of the timber lintel, and besides the extensive cracking in both masonry assemblies UN1-DS and UN2-DS, the spandrels sustained a certain level of embedment, which allowed the gradual loss of strength and prevented their collapse. Here is also noted that during the evolution of the vertical uplift, axial stresses in the piers tend to increase, given the reversed interaction between the rocking of piers, the confined system of beam caps with the prestressed rods and the compressive interaction with the spandrel. Hence, hydraulic pressure was gradually released in order to maintain a constant the level of axial prestress in both piers.

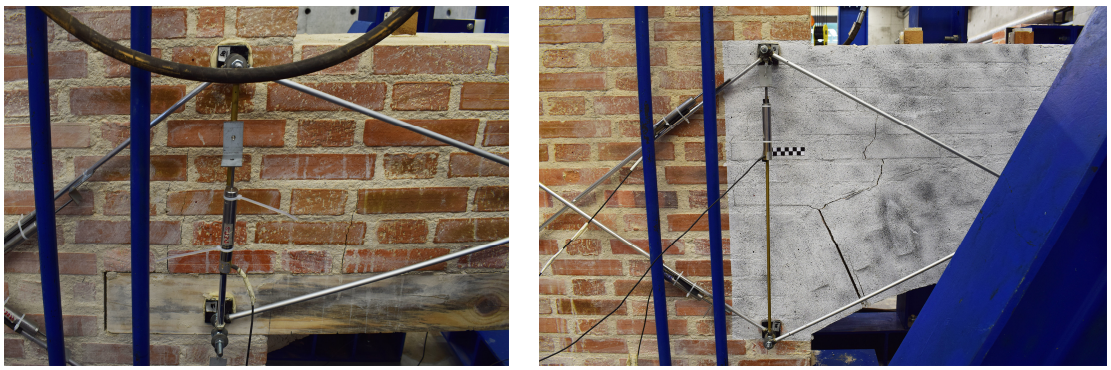


Figure 99. Cracked spandrel from the part of the timber lintel (left) and arch (right) for UN1-US.

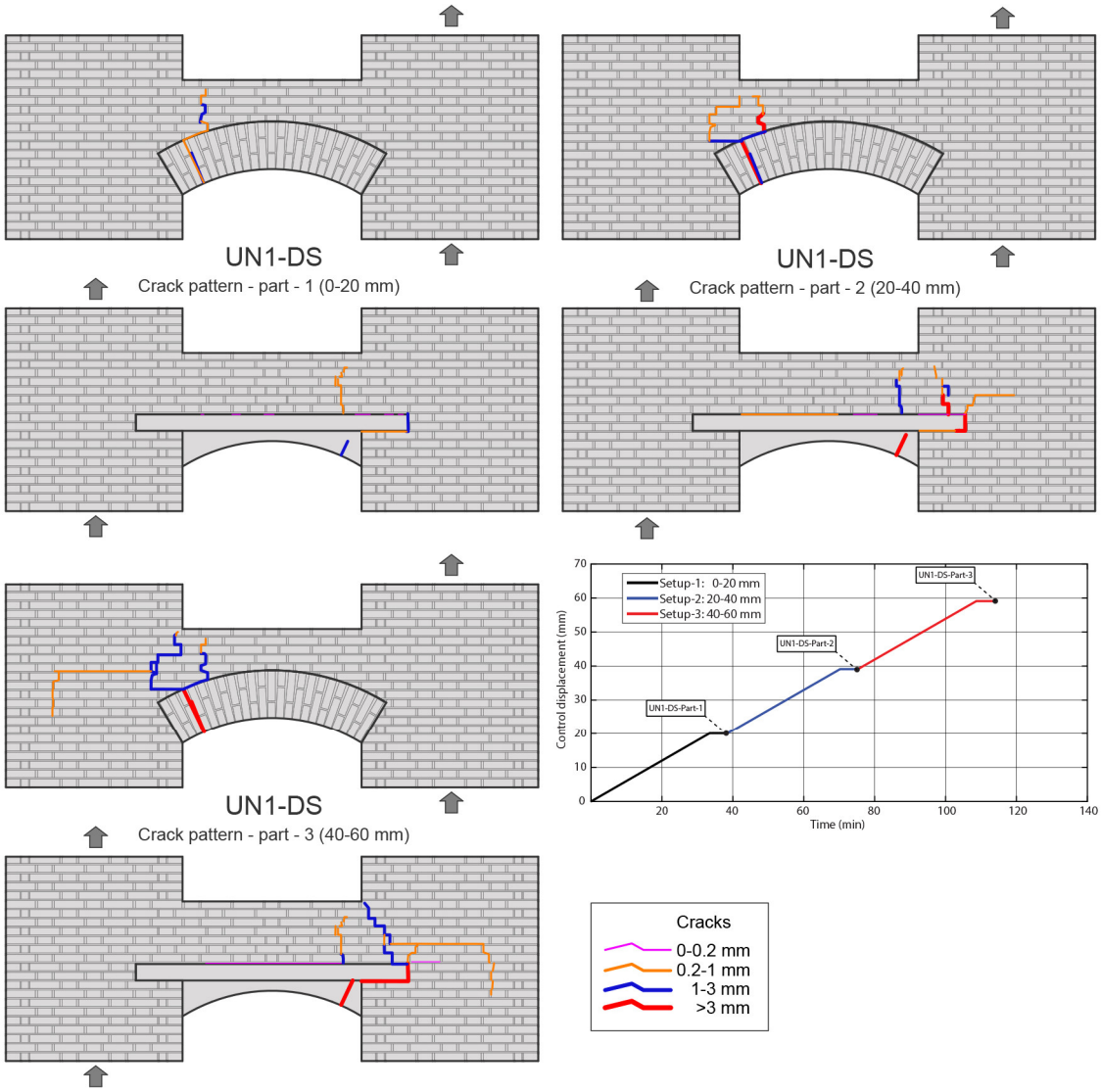


Figure 100. Masonry assembly UN1-US: Damage State (DS) assessment at the end of each partial testing setup, of the monotonic, differential uplift. Note the arrows corresponding to the direction of the monotonic differential uplift, from each elevation side of the assembly, the differentiation of structural cracks in terms of width and color.



Figure 101. Cracked spandrel from the part of the timber lintel (left) and arch (right) for UN2-US.

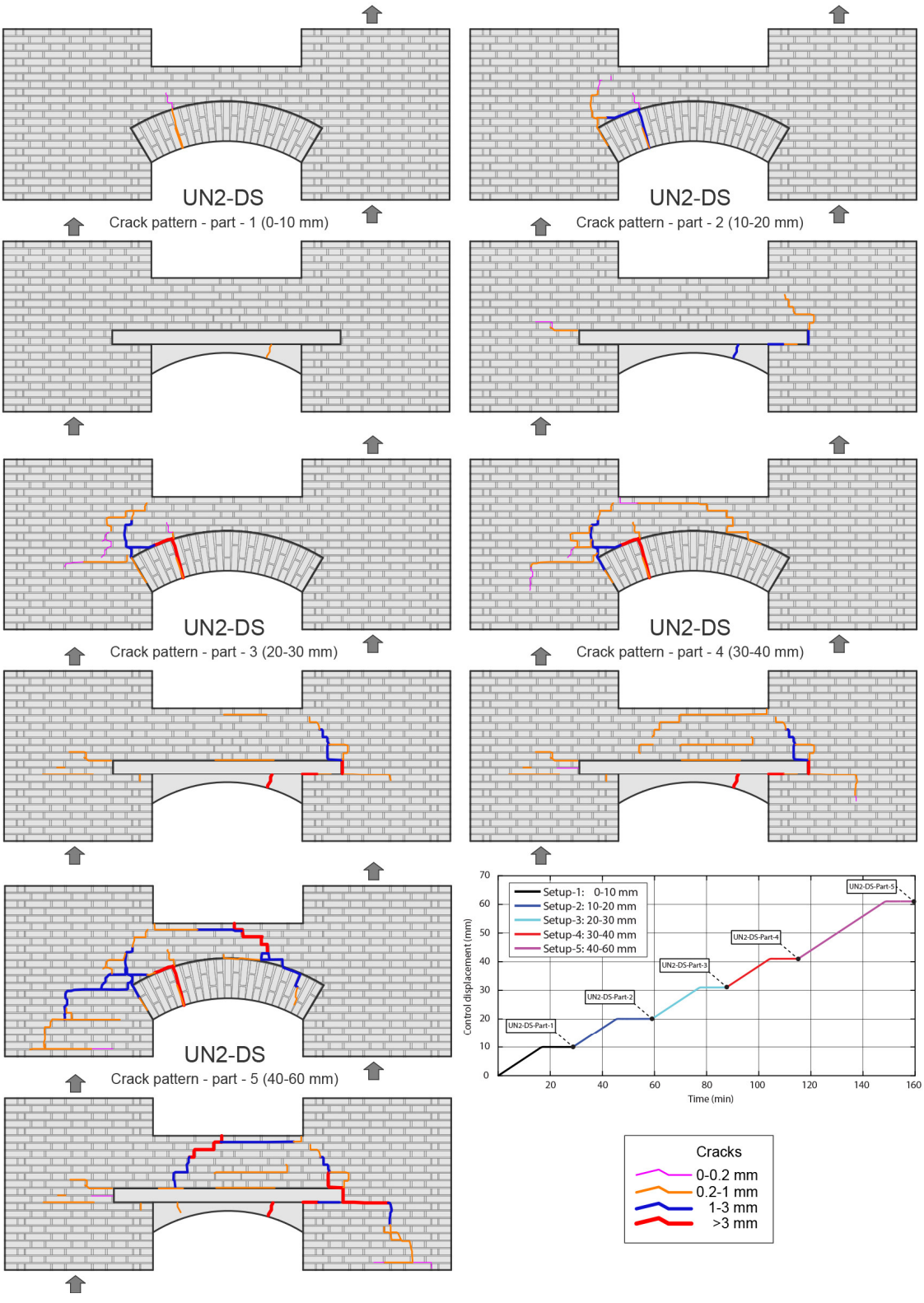


Figure 102. Masonry assembly UN2-US: Damage State (DS) assessment at the end of each partial testing setup, of the monotonic, differential uplift. Note the arrows corresponding to the direction of the monotonic differential uplift, from each elevation side of the assembly, the differentiation of structural cracks in terms width and color.

6.5.2.2. Testing of piers and spandrel masonry assemblies at the damaged state, under structural repair and retrofit measures

The use of structural injection grouts, by means of high-performance lime-based fluid mortars, is considered a simple and efficient repair technique for damaged masonry. Besides the many attributes on material and physical properties of masonry and fluid mortars, that influence the response of repaired walls, and mostly the shear bond strength to the substrate, it can be well recognized that grouting injections may be able to increase the in-plane capacity of masonry -compressive and tensile strengths-, up to 1.6-5 times, while the stiffness can be either fully reintegrated or increased [Luso and Lourenco 2017, Luso and Lourenco 2019 and Vintzileou and Miltiadou-Fezans 2008]. In accordance, the structural reintegration of masonry by means of grout injections is acknowledged by the NTC 2018, assigning multiplicative coefficients on the recommended material properties, ranging from 1.2-2, according to the type of masonry.

Following, the use of structural renders, reinforced with textile fiber grids, or else Fiber Reinforced Cementitious Matrix systems (FRCM) is considered an efficient retrofitting solution for unreinforced and damaged masonry walls. In particular, when applied at both sides, they offer the advantage of high compatibility in physical and mechanical properties, a high in-plane shear performance, a small additional weight and an efficient speed of execution [Prota et al. 2006 and Carozzi et al. 2018]. In addition, the use of mechanical anchors, along the thickness of masonry walls, can ensure the activation of the FRCM system, in cases where a sufficient bearing length cannot be accomplished, and also counteracts leaf separations and bulging, in multi-leaf masonry [CNR-DT 215 2018 and Gattesco and Boem 2015].

Implementation of FRCM systems in unreinforced masonry, can be found in Carozzi et al. 2018, Prota et al. 2006 and Wang et al. 2019. Here, capacity mechanical tests were mostly performed in masonry wallets, under diagonal compression schemes, and the updated direct shear strength was obtained (Table 34). Failure observed modes are the slippage and rupture of the mesh filaments, at transversal directions to shear cracks, while the bond detachment of the structural render is considered less probable. Compared to unreinforced reference wallets, the direct shear capacity of the reinforced wall is increased by 2-4 times, with higher displacement ductility [Carozzi et al. 2018, Prota et al. 2006 and Wang et al. 2019].

Considering large masonry assemblies, with a more complex in-plane stress and stiffness distribution, in Augenti et al. 2011, a damaged URM specimen, built of tuff stone blocks and lime-based mortar, and composed of piers and a spandrel, was repaired and retrofitted with an FRCM system, of a biaxial glass fiber grid and a lime-based render, placed at the level of the spandrel, and at both sides. The observed performance under a quasi-static, in-plane, cyclic lateral loading, revealed a complete reintegration for the in-plane initial stiffness and capacity, with the ductility, in terms of maximum inter-story drift ratio, increasing by almost 3 times. Here, the same level of achieved lateral capacity, before and after the retrofit, can be partly attributed to the localized strengthening, at the level of the spandrel.

Hence, considering the in-plane capacity tests of unreinforced masonry perforated walls, under the effect of differential vertical displacements, an additional set of mechanical testing aimed on the assessment of repair and retrofitting techniques, namely through basic grouting injections and a comprehensive FRCM system, with in-plane adhesive anchors. For the repair of the damaged masonry assembly UN1-DS, from now on denoted as UN1-DS-GR (Table 32), a reintegration of the ductility and strength, for the damaged spandrel and piers, was attempted, through crack filling with a fluid, lime-based, hydraulic geo-binder. Considering the repair and retrofitting of the damaged masonry assembly UN2-DS, from now on denoted as UN2-DS-GR-FRCM (Table 32), and aiming for a higher ductility and strength, after the crack filling with injection grouting, a strengthening system with the FRSM structural render and adhesive anchors was implemented. Prior to any implementation, both damaged masonry assemblies reentered at their initial position, allowing for the partial closure of some cracks, but also for the propagation of others, given mostly in-plane tractions between the cracked interfaces of the macro-elements.

Table 34. Experimental data collection of unreinforced and reinforced masonry wallets, with FRCM systems, tested under uniaxial compression [Carozzi et al. 2018, Prota et al. 2006 and Wang et al. 2019].

Reference	Description of testing	Type of masonry Type of Reinforcement grid Material characterization		f_t (MPa) (Num. samples)	Specimen
Carozzi et al. 2018	Mechanical performance of cut brick masonry wallets, tested in-situ, under diagonal compression	2 leaf masonry with a running bond, a vertical separation joint of 1 cm and several brick connectors Solid bricks Lime mortar	 f_c = 40MPa -	0.07 MPa (1 sample)	*Reference* Undamaged masonry wallet (100x100x30 cm^3)
		G-TRM (20x20 mm^2) with lime mortar Helical steel connectors at diagonals	f_t = 1.4 GPa E_{mod} = 75.4 GPa -	0.26 MPa (1 sample)	Undamaged masonry wallet (100x100x30 cm^3) Thickness of FRCM: 10mm
		cG-TRM (20x20 mm^2) with lime mortar Helical steel connectors at diagonals	f_t = 1.2 GPa E_{mod} = 55.6 GPa -	0.30 MPa (1 sample)	Undamaged masonry wallet (100x100x30 cm^3) Thickness of FRCM: 10mm
		G-TRM (20x20 mm^2) NSM Helical steel connectors at diagonals	f_t = 1.1 GPa E_{mod} = 60.5 GPa f_t = 1.1 GPa E_{mod} = 195 GPa -	0.13 MPa (1 sample)	Undamaged masonry wallet (100x100x30 cm^3) Thickness of FRCM: 10mm
Prota et al. 2006	Mechanical performance of tuff masonry wallets, tested in the laboratory, under diagonal compression	Single leaf tuff masonry with a running bond. Tuff bricks Lime mortar	 f_c = 2 MPa E_{mod} = 1.8-2 GPa f_t = 1.57 MPa f_c = 5 MPa	0.24 MPa (4 samples)	*Reference* Undamaged masonry wallet (120x120x9 cm^3)
		G-TRM (25x25 mm^2)	f_t = 1.3 GPa E_{mod} = 72 GPa	0.54 MPa (4 samples)	Undamaged masonry wallet (120x120x9 cm^3) Thickness of FRCM: 10mm
Wang et al. 2019	Mechanical performance of brick masonry wallets, tested in the laboratory, under diagonal compression	Single leaf tuff masonry with a running bond. Solid bricks Cement mortar	 f_c = 10.3 MPa f_t = 2.9 MPa f_c = 31.8 MPa	0.85 MPa (2 samples)	*Reference* Undamaged masonry wallet (91x90x11 cm^3)
		S-TRM (10x10 mm^2)	f_t = 2.8 GPa E_{mod} = 160 GPa	1.5 MPa (1 sample)	Undamaged masonry wallet (91x90x11 cm^3) Thickness of FRCM: 10mm
		C-TRM (10x10 mm^2)	f_t = 3.1 GPa E_{mod} = 230 GPa	1.8 MPa (1 sample)	Undamaged masonry wallet (91x90x11 cm^3) Thickness of FRCM: 15mm
		B-TRM (10x10 mm^2)	f_t = 1.0 GPa E_{mod} = 89 GPa	1.67 MPa (1 sample)	Undamaged masonry wallet (91x90x11 cm^3) Thickness of FRCM: 15mm

TRM: Textile Reinforced Mortar, NSM: Near Surface Mounted system, G: Glass fiber grid, cG: Coating Glass fiber grid, S: Steel fiber grid, C: Carbon fiber grid, B: Basalt fiber grid

For the consolidation of cracked masonry areas with injection grouting, the GeoCalce® FL Antisismico from KERAKOLL was chosen, a class M15 (28 days), high performance grout premix, from NHL3.5, with natural mineral binders, of siliceous and marble aggregates (0-0.5mm) [GeoCalce FL Antisismico 2019]. Considering the results of mechanical testing on prisms and cylinders, after curing at ambient environmental conditions for 28 days, the mean strength for compression, flexure, and the value for Young's modulus, were found equal to 12 MPa, 4.2 MPa and 9.8 GPa respectively (Table 8). The acquired mechanical properties of the fluid mortar appear in good agreement with the certified ones provided by the manufacturer (Table 35).

The positioning of the injection points for grouting followed the crack formation, at regular intervals of 30-50 cm, with drilled, slightly downward-inclined perforations, of 10-15 cm in length, and from both sides. After cleaning the holes with compressed air, flexible plastic injection nozzles of Ø8 mm were placed, while the external crack patterns were sealed with mortar. Following, 24 hours before grouting, the injection of water proceeded through the nozzles, by means of syringes, and from top to bottom, to eliminate dust, and saturate the masonry crack interfaces, thus, slowing the rapid dehydration of the injection mortar. Finally, by means of syringes and under low-pressure, the fluid mortar was injected manually, starting from the lowest positions, simultaneously from both sides, and progressing in elevation. The consecutive execution steps of grouting for the masonry assemblies UN1-DS-GR and UN2-DS-GR-FRCM are presented in Figure 103, Figure 104 and Figure 105a respectively.

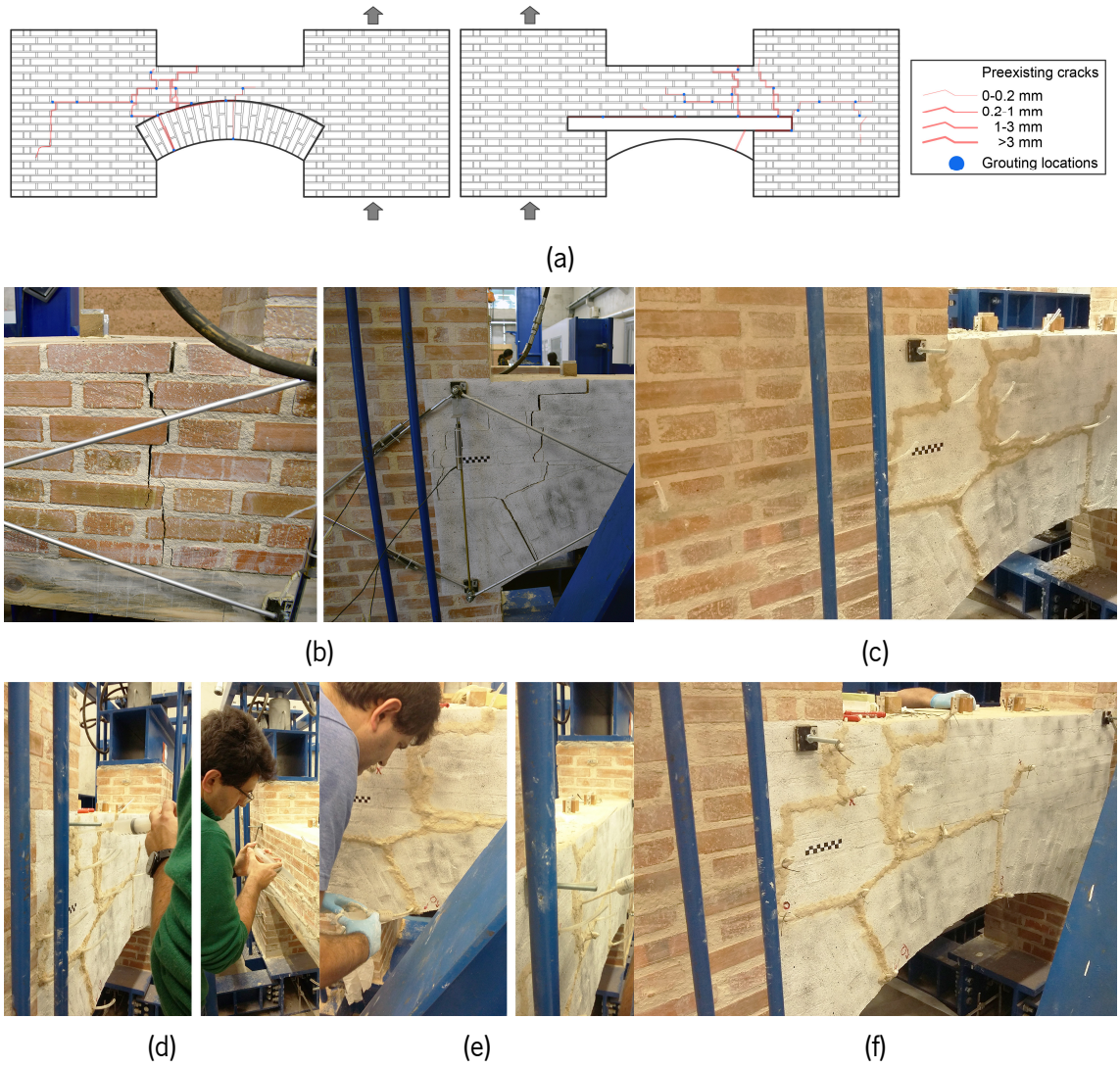


Figure 103. UN1-DS-GR: (a) scheme of damaged state and crack filling locations; (b) cracked spandrel from the part of the timber lintel (left) and arch (right); (c) perforations at crack interfaces, insertion of tubes and sealing with mortar; (d) influx of water; (e) grout injection; (f) sealing of tubes.

For the application of the FRCM system, with in-plane adhesive anchors, in the damaged masonry assembly UN2-DS-GR-FRCM, and following the grout injections at crack interfaces, a careful execution of steps was followed, according to the instructions of the installation manual of the manufacturer, presented in Figure 104 and Figure 105 [27A 2020]. The FRCM reinforcement was arranged symmetrically on both sides and was extended along the entire surface. Considering the effectiveness of the reinforcement and aiming for an increased shear bearing capacity, the use of a biaxial fiber mesh ensured both a parallel and transversal alignment of fibers to shear and bending actions respectively, under the diverse cracking of the spandrel and piers. Additionally, in order to ensure the connection between the two sides of the FRCM and avoid the out-of-plane bulging and leaf separation, the in-plane anchoring of the fiber mesh is configured, by means of adhesive anchors that pass along the entire thickness of the walls. According to §6 of CNR-DT 215

2018, in the case of walls around 40 cm of thickness, strengthened with FRCM systems, an inter-axis distance i of in-plane anchors is suggested, equal to i≥3t, and not more than 1600 mm, where t is the thickness of the wall. Hence, prior to any repair, and considering the configuration of the masonry assembly, 20 perforations of Φ25-30mm were drilled along the thickness of masonry, at the intersection of head and bed joints, and at relative distances ranging between 0.24-0.80 m, two of which crossing through the damaged arch and timber lintel, as seen in Figure 104 and Figure 105. Soon after the cleaning of dust with compressed air, plastic tubes were inserted, to isolate the voids from the injection grouting paths, later removed, before the application of the first layer of the structural render.

As described in Section 3.4.3, for the hydraulic lime-based render, the GeoCalce® F Antisismico from KERAKOLL was chosen, a class M15 high performance mortar premix, from NHL3.5 and natural mineral binders, of siliceous, dolomitic and marble aggregates (0-1.4mm) [GeoCalce F Antisismico 2019]. From the mechanical characterization tests on prisms and cylinders, and ambient laboratory conditions of curing for 28 days, the mean strength for compression, flexure, and the value for Young's modulus, were found equal to 15.5 MPa, 5.8 MPa and 9.2 GPa respectively, in good agreement with the certified ones provide by the manufacturer (Table 10 and Table 35). After the substrate was cleaned and sprayed with water, the first layer of the structural render was applied, with an average thickness of 5 mm. Then, and while the mortar was fresh, a biaxial basalt-fiber mesh, of a 17x17 mm^2 grid, with stainless steel micro-filaments, the GEOSTEEL GRID 200 from KERAKOLL, was laid, by means of a flat-toothed spatula, and pressed within the layer of render, ensuring full contact [GeoSteel Grid 200 2019]. Considering the length of the biaxial basalt-fiber mesh roll, of 1.0 m wide, several sub-parts were cut and placed on each side, with 0.3 m of overlap, following the instructions of the installation manual (Figure 105) [27A 2020].

Following, at the locations of the drilled holes for the adhesive anchors, and after the overlapping part of the biaxial basalt fiber mesh was cut, cylinders of unidirectional galvanized steel micro-cords, of the GEOSTEEL G600 fabric from KERAKOLL, were inserted. Their ends were extended beyond the thickness of the masonry, arranged in threads, and bend in 90º, with a certified bending machine. The threads are then distributed evenly along the masonry surface, thus, creating a circular pattern of 20-25 cm, of diameter, and were attached to the first layer of the structural render, so as for the anchors to work under the designed tensile strength (Figure 105b) [GeoSteel 600 2019 and GeoSteel Injector&Connector 2019]. Later, glass fiber-reinforced polypropylene

connectors are inserted at both sides and the fluid grout GeoCalce® FL Antisismico is poured (Figure 105b). At the last step, the 2nd layer of the hydraulic lime-based render, of 5 mm in thickness, is laid. The FRCM system was then covered with plastic sheets and was regularly sprayed with water for the next 48 hours, while attaining a curing period of 28 days, prior to testing. Certified material properties of all the components of the FRCM system with adhesive anchors are presented in Table 35.

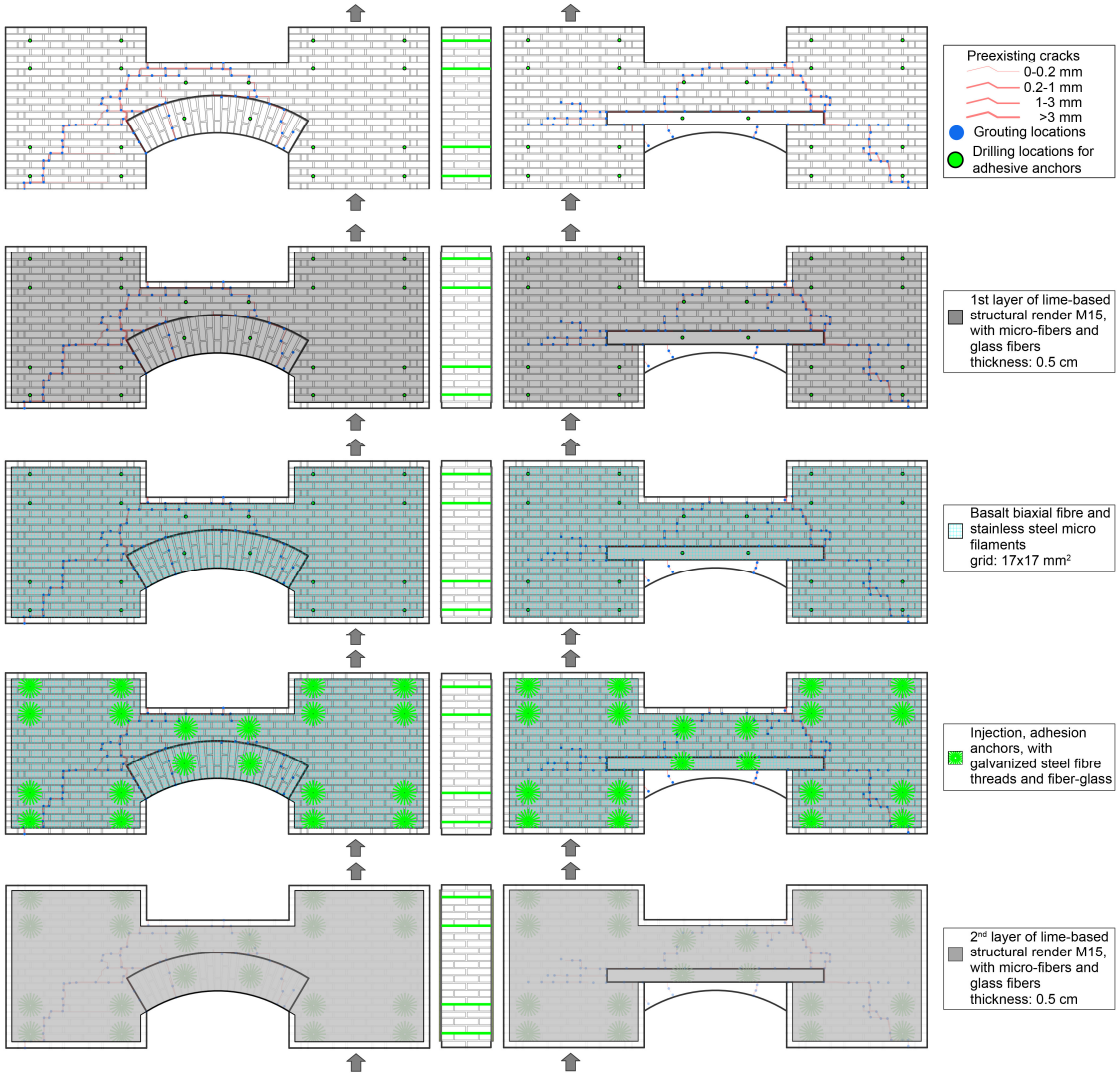
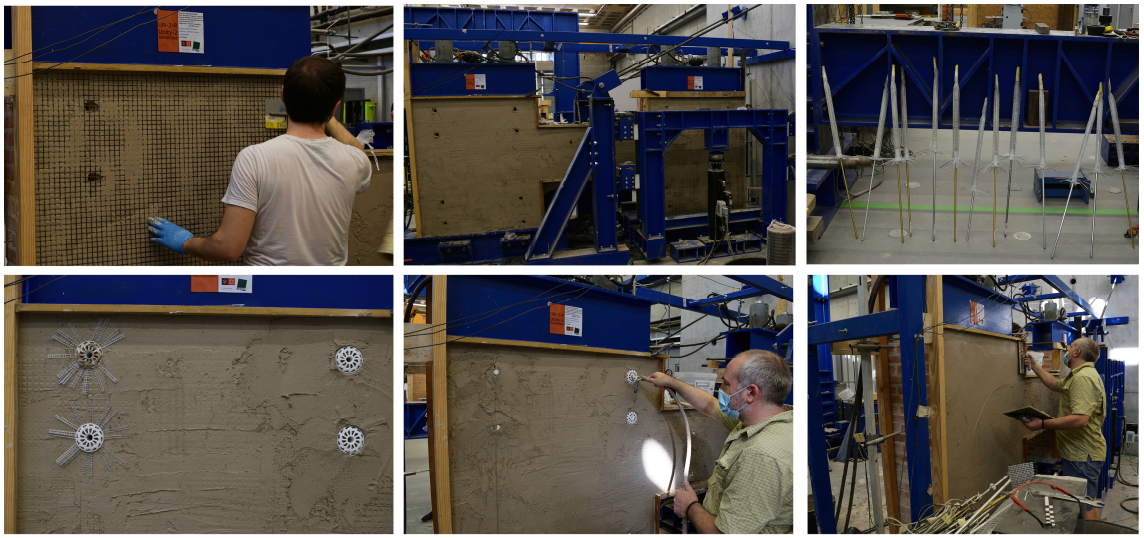


Figure 104. Masonry assembly UN2-DS-GR-FRCM and schematic representation of the damaged state, crack filling locations, and implementation stages of the FRCM retrofitting system.



(a)



(b)



(c)

Figure 105. Masonry assembly UN2-DS-GR-FRCM (a) grouting injections of cracked masonry. Note the drilling holes for the adhesive in-plane anchors; (b) implementation stages of the FRCM system, involving the laying of the first layer of render, the placement of the fiber mesh, the insertion of the fiber mesh grid for the in-plane anchors, together with grouting, and the final layer of render; (c) retrofitted masonry assembly with a FRCM system after curing of 28 days.

Table 35. Certified material properties of sub-components of the FRCM system with adhesive anchors [GeoCalce FL Antisismico 2019, GeoCalce F Antisismico 2019, GeoSteel 600 2019 and GeoSteel Injector&Connector 2019].

Material	Characteristics	Density	f_c (MPa)	E_{mod} (GPa)	f_t (MPa)	F_t (kN)	f_s (MPa)
GeoCalce® FL Antisismico	Class M15 - 28 days	1500[1]	≥15	9.5	-	-	-
GeoCalce® F Antisismico	Class M15 - 28 days	1580[1]	≥15	9.0	≥5	-	≥1[3]
GeoSteel Grid 200	17x17 mm^2 [4]	0.2[2]	-	≥70	≥1700	-	-
GeoSteel G600	1.57 Cords/cm [5] 0.538 mm^2 [6]	0.67[2]	-	≥190	≥3000	-	-
GeoSteel G600 Connector for adhesive anchors	Width of band: 10 cm Number of cords: 16	-	-	-	-	≥24	-

[1] kg/m^3
[2] kg/m^2
[3] Shear bond strength on clay brick
[4] Biaxial grid
[5] Uniaxial mesh
[6] Area of 5 chords

The repaired and retrofitted masonry assemblies UN1-DS-GR and UN2-DS-GR-FRCM, after the conclusion of the 28-day curing period, were tested under differential vertical displacements, following the protocols described in Section 6.5.2.1. The progression of vertical uplift, in the moving frame and pier, was applied in increments, and until the maximum shear capacity or post-peak in the spandrel was reached. Here, is noted that for both tested assemblies, lateral restrain conditions, for reducing the in-plane rotations of the uplifting pier, were applied, by means of axial roller bearings and diagonal prestressed rods. In addition, axial stresses in the piers were kept constant, throughout the duration of the tests, under the decided prestress level of 0.21 MPa, at the base of each pier (Table 32 and Figure 96).

For UN1-DS-GR, as presented in Figure 106a, the imposed vertical upward displacements in the moving pier, were applied monotonically, in four increments of around 2 cm, while as for the average relative uplift of the moving pier, it reached at maximum 7.5 cm. Considering the resulted in-plane rotation for the piers, it follows in linear correlation the vertical displacements, reaching by as maximum 0.60º and 1.68º, in the non-moving and moving pier respectively (Figure 106a). Focusing on the rotation of the moving pier, and besides the similar rotation increments of the first three setups, which indicate a bending response in the spandrel, under a steady bending stiffness, the evolution of rotation at the last setup appears flattened, which is indicative of extensive damage and decrease in the bending stiffness of the spandrel.

Following, the acquisition for UN2-DS-GR-FRCM, the imposed vertical upward uplift in the moving pier, reaches by maximum 10.0 cm and is applied in six initial increments of around 1 cm and two final ones of 2 cm. Considering the in-plane rotation for the fixed and movable piers, they are found increased, compared to UN2-DS, and reaching by as maximum 0.81º and 1.98º, in the

non-moving and moving pier respectively (Figure 106b). Is worth mentioning that in plane rotations in piers are attained by larger instances, of what seems a steady in-plane bending stiffness, throughout the entire duration of the test (Figure 106b).

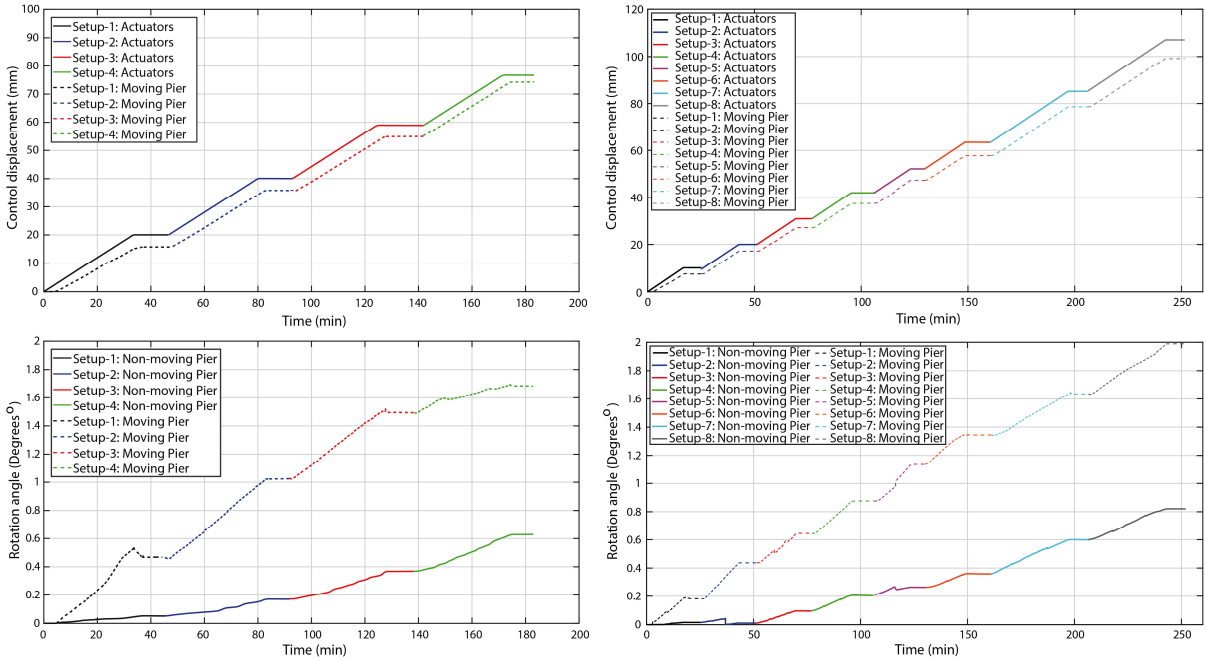


Figure 106. Masonry assemblies UN1-DS-GR (a) and UN2-DS-GR-FRSM (b): time histories of the averaged monotonic vertical displacements from the actuators, the top LVDTs and the in-plane rotation of the fixed and moving piers.

Under a similar approach, as described in Section 6.5.2.1, capacity curves are compiled for UN1-DS-GR and UN2-DS-GR-FRCM, in terms of the shear force V_{sp} versus the relative vertical displacement in the spandrel, and presented in Figure 107 a and b. For UN2-DS-GR-FRCM, the sum for gravitational loads of the moving pier and participating setup was updated, in order to include the self-weight of the FRCM render, found equal to 21.28 kN. Here is noted that for UN2-DS-GR-FRCM, during the acquisition of Setup-5, one of the bearing axial rollers failed, which caused an abrupt adjustment of the moving frame, under a slight vertical subduct, as can be observed in Figure 107b. Subsequently, the abovementioned sub-test was forced to terminate, and the Setup-6 was initiated, which was adjusted in order to include the previous, lost, vertical uplift increment. Hence, no damage assessment was performed during Setup-5.

Here, the documented values of shear force, yield displacement, peak displacement and ductility for UN1-DS, UN1-DS-GR, UN2-DS and UN2-DS-GR-FRCM and their relative differences are reported in Table 36.

Hence, for UN1-DS-GR, the maximum reached shear force is equal to 55.61 kN, higher than 40% from the UN1-US, evidencing the efficiency of grouting injections for the structural reintegration and retrofitting of damaged brick masonry (Figure 107a). Yet, the change in boundary conditions, as stated in Table 32, should also be pointed out, which can be attributed to the vast transition towards a shear mode of failure in the spandrel. In fact, the shear capacity of the repaired assembly is almost identical to that of UN2-US, considering the same boundary conditions of lateral restrain, with the former under a maximum vertical spandrel displacement, higher by 89% (Table 36). Considering the initial stiffness at the accounted displacement $d_{y,UN1-US}$, prior to the structural repair, no significant change is documented. Yet, right after the yield displacement, the shear response of the spandrel follows a steeper hardening phase, which is where the actual stiffness upgrade is present. In fact, as shown in Table 36, the increase in the stiffness of the hardening branch is 29%, compared to the one of UN1-US. Considering also the maximum relative vertical uplift of the spandrel for UN1-DS-GR, equal to 72.13 mm, thus, the reported upgraded ductility $\mu_{UN1-DS-GR}$, as a direct result of the grouting injection, taken here as the ratio $d_{Vsmax,UN1-DS-GR}/d_{y,UN1-US}$ is equal to 16.03, larger by 132% and 89% from the one reported for UN1-US and UN2-US respectively.

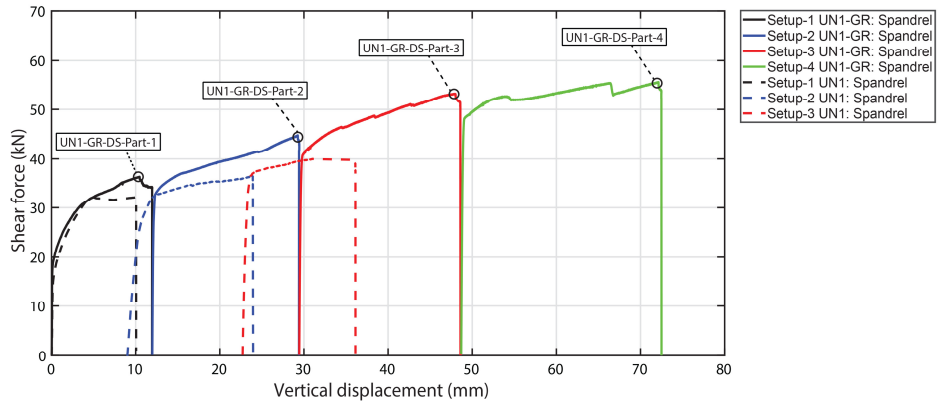
Subsequently, for UN2-DS-GR-FRCM, the maximum reached shear load in the spandrel reaches 88.45 kN, higher by 52% than the one for UN2-US, which denotes that the retrofit scheme with grouting injections and the FRCM system, with adhesive anchors, had significantly upgraded the shear capacity of the damaged spandrel and piers. The initial shear stiffness, at the prior point of yield displacement $d_{y,UN2-US}$ is also improved, reported equal to 8544 N/mm, higher than 22%, compared to UN2-US. Here, and despite the higher average vertical uplift in the moving pier, the maximum, relative vertical uplift of the spandrel reports equal to 59.43 mm, being lower than the one reached in UN1-DS-GR, even if the total displacement in the actuators is higher. Accounting for the significant upgrade in the in-plane stiffness, and the constant level of axial prestress in the piers, of 0.21 MPa, the non-moving pier is therefore experiencing rocking, under increased rotations, which decrease the maximum relative uplift accounted for the spandrel. Yet, considering the large magnitude of applied vertical uplift in the moving frame and the level of resulted damage, the test was terminated, but the shear capacity could have been higher. The resulted upgraded ductility $\mu_{UN2-DS-GR-FRCM}$, taken as the ratio $d_{Vsmax,UN2-DS-GR-FRCM}/d_{y,UN2-US}$ is equal

to 13.21, larger by 56% from the one reported for UN2-US. Considering the stiffness at the hardening phase is found lower by 10%, compared to the one of UN2-US.

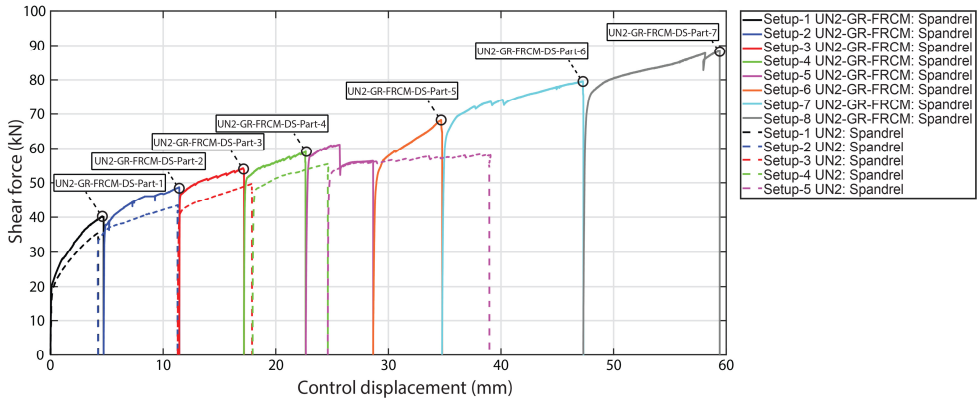
Table 36. Test results: spandrel maximum shear force and peak displacement, yield displacement and shear force ordinate, displacement ductility and hardening stiffness for UN1-US, UN1-DS-GR, UN2-US and UN2-DS-GR-FRCM.

Masonry assembly	d_y (mm)	$Ps(d_y)$ (kN)	d_{max} (mm)	$Ps_{,max}$ (kN)	μ (-)	Hardening branch [1] (N/mm)/R^2
UN1-US	4.50	31.97	31.08	39.95	6.91	370.8/0.99
UN1-DS-GR	-	-	72.13	55.61	16.03	477.3/0.99
UN2-US	4.50	34.65	38.12	58.22	8.47	942.5/1.0
UN2-DS-GR-FRCM	-	-	59.43	88.45	13.21	844.5/1.0

[1] Hardening stiffness, excluding the first and last test sub-parts.



(a)



(b)

Figure 107. Experimental shear-displacement curves for the spandrels of the masonry assemblies UN1-DS-GR (a) and UN2-DS-GR-FRSM (b), superposed with UN1-US and UN2-US respectively. Note the relative vertical displacement of the spandrel at the plot's x-axis, and the corresponding parts (UN1-DS-GR-Part-j and UN2-DS-GR-FRSM-Part-j) of documented damage assessment, corresponding to Figure 107, Figure 108 and Figure 109.

In addition, the documentation of damage progression during the testing of the repaired and retrofitted masonry assemblies, also a correlation with the prior crack pattern, can provide significant information on the type of failure and the effectiveness of the intervention.

First, for UN1-DS-GR, the respective damage progression at each damage state is presented in Figure 108. Cracking appears to progress under the same paths, as in UN1-US, under an initial flexural failure in the intrados of the arch and near the springing of the fixed pier, moving upwards, along the elevation of the spandrel. Yet, it appears to deviate slightly in paths, of neighboring joints and splitting of new bricks. Thus, the crack filling with grout injections, appears to have sealed and strengthened the crack interfaces, with the flexural cracking forming in weaker masonry parts. With the advancement of vertical displacements and the activation of compressive struts in the spandrel, the transition towards a shear failure is now formed, through a new shear stepped crack in the extrados, towards the moving pier (Part-3 in Figure 108). Already from Part-2 of the testing branch, and while the moving pier undergoes around 35 mm of relative vertical uplift, the sliding of the fixed pier has progressed, following the prior crack pattern of UN1-US, and finalizing almost vertical, at the outer side of the non-moving pier (Part-4 in Figure 108).

For the crack evolution of the UN2-DS-GR-FRCM, a graphic crack correlation is performed with the documented crack pattern at the surface of the FRCM and that of the UN2-US, as shown in Figure 109 and Figure 110. Considering the interaction of the FRCM system with the substrate, no detachment was witnessed, for the duration the test, besides small areas in the proximity of cracks, while none of the inserted adhesive anchors failed in tension. Right after the imposition of a vertical displacement of 10 mm from the actuators, which corresponds to vertical deformation of around 4.5 mm in the spandrel, the render of the FRCM is cracked under flexure, starting from the intrados of the arch, at approximately ¼ of the arc's length from the springing, with the non-moving pier, and leading diagonally, towards the inner corner of the spandrel's extrados (Part-1 Figure 109). From the crack initiation and forward it can be assumed that the biaxial fiber mesh in the cracked areas is activated in tension. Following the advancement of the vertical uplift and until Part-4, of almost 40 mm, two main flexure cracks are already fully progressed in the springing of the arch with the non-moving pier, both converging in the upper corner of the spandrel, thus creating an in-plane cone. From the side of the timber lintel, cracks are more distributed, and oriented vertically. In addition, the horizontal slip in the non-moving pier has been already formed. Considering the next steps, a second flexure crack is formed, in the extrados of the spandrel, near

the moving pier, which under a diffused crack pattern, progresses diagonally in the intrados of the spandrel's interface with the moving pier, and from both sides. At the last documented step, a widespread crack pattern is defined by a clear flexural failure of the spandrel, plus the shear diagonal failure of the fixed pier. No diagonal shear cracks in the spandrel are detected, compared to the cracks of UN2-US, which contributes to the fact that the application of the FRCM system is able to increase significantly the in-plane tensile and flexural strength, which until the last step of the test, appears not to have been fully exhausted, with none of the visible fiber mesh appearing ruptured (Figure 111), while diagonal shear struts appear to be operating. In fact, since the peak shear strength was not reached, given the rocking of the non-moving pier, the actual shear capacity of the spandrel is expected higher than the one documented.

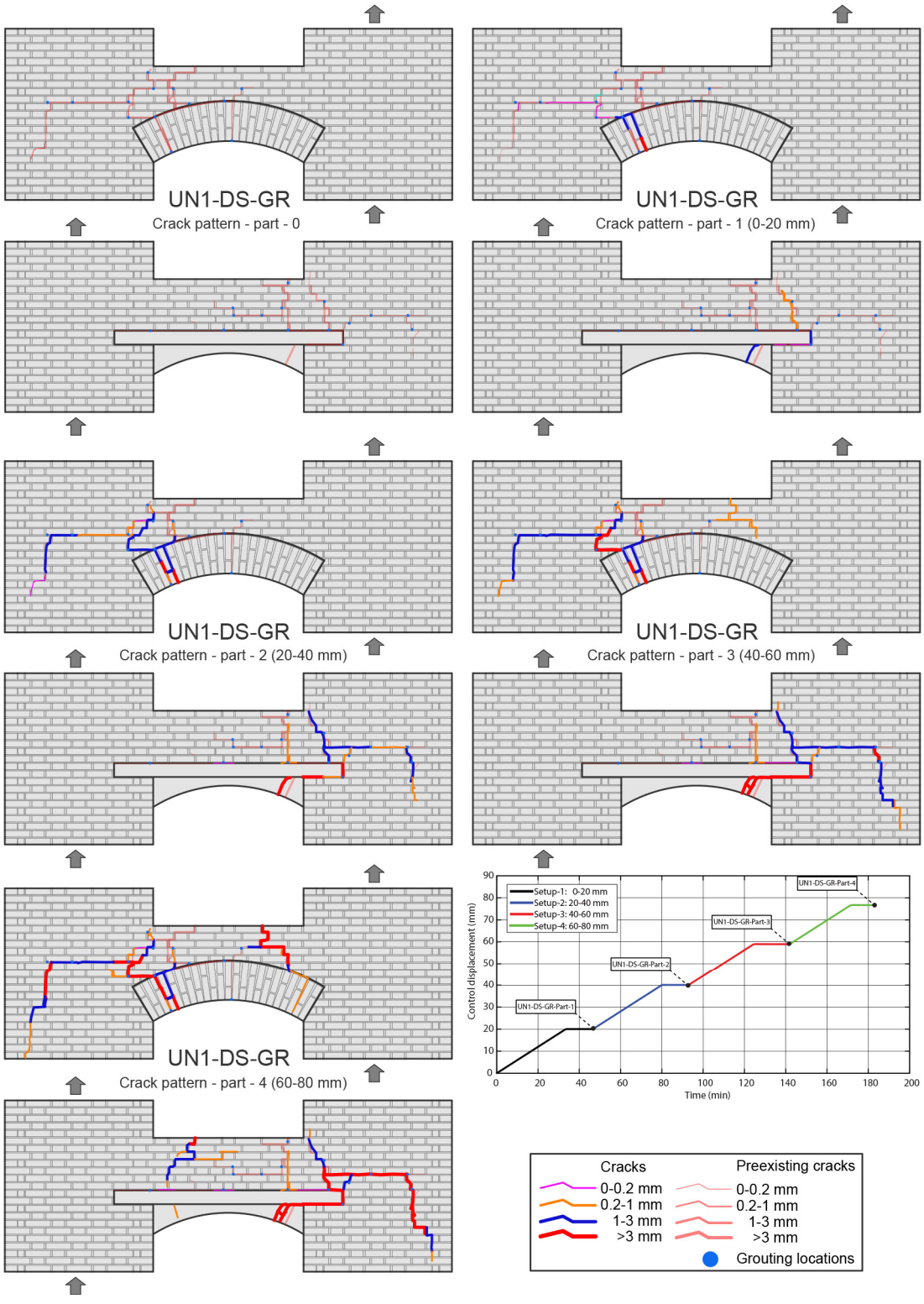


Figure 108. Masonry assembly UN1-DS-GR: Damage State (DS) assessment at the end of each partial testing setup, of the monotonic, differential uplift. Note the arrows corresponding to the direction of the monotonic differential uplift, from each elevation side of the assembly, the differentiation of structural cracks in terms width, and under different contours.

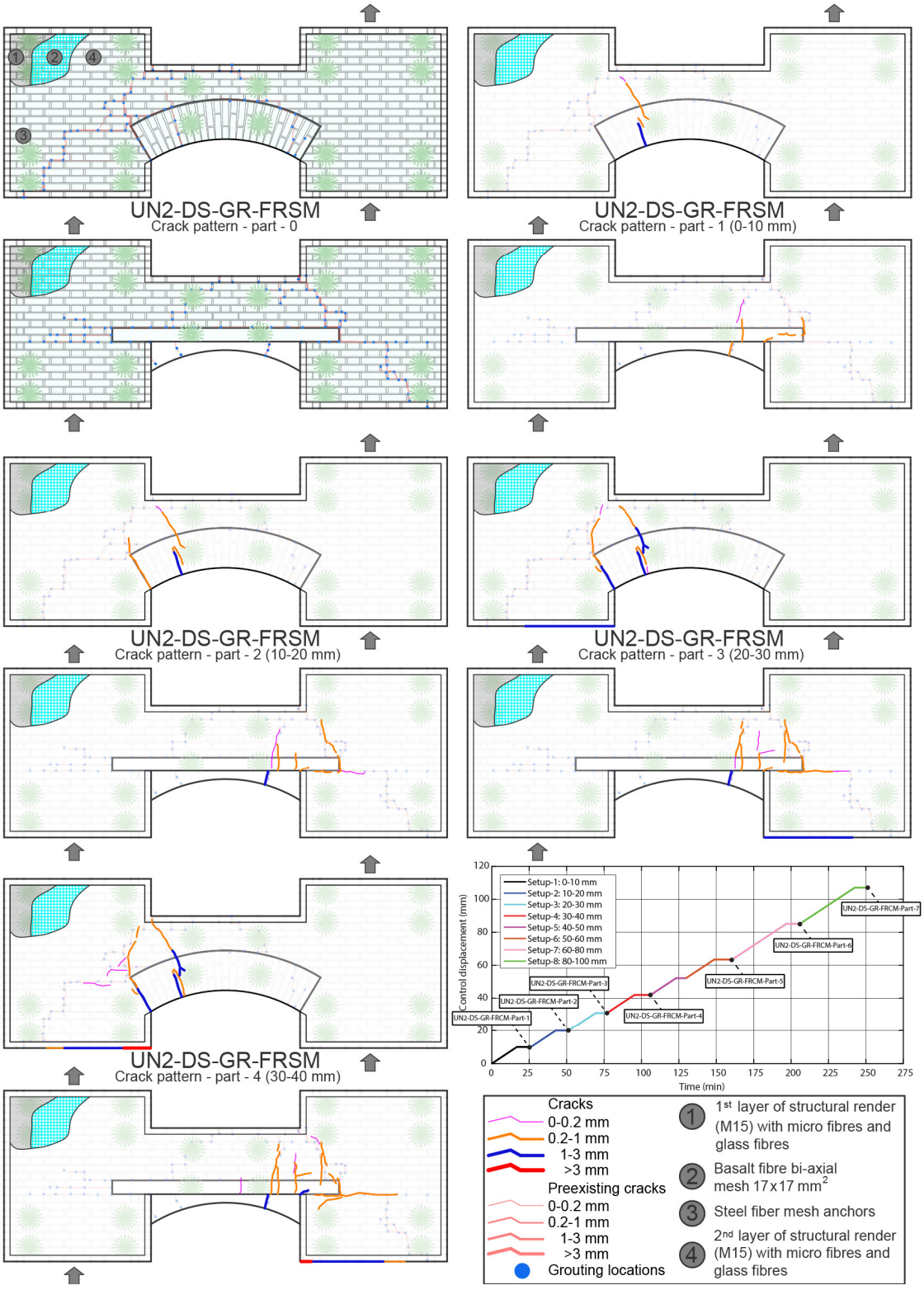


Figure 109. Masonry assembly UN2-DS-GR-FRSM (Setups 1-4): Damage State (DS) assessment at the end of each partial testing setup, of the monotonic, differential uplift. Note the arrows corresponding to the direction of the monotonic differential uplift, from each elevation side of the assembly, the differentiation of structural cracks in terms width, and under different contours.

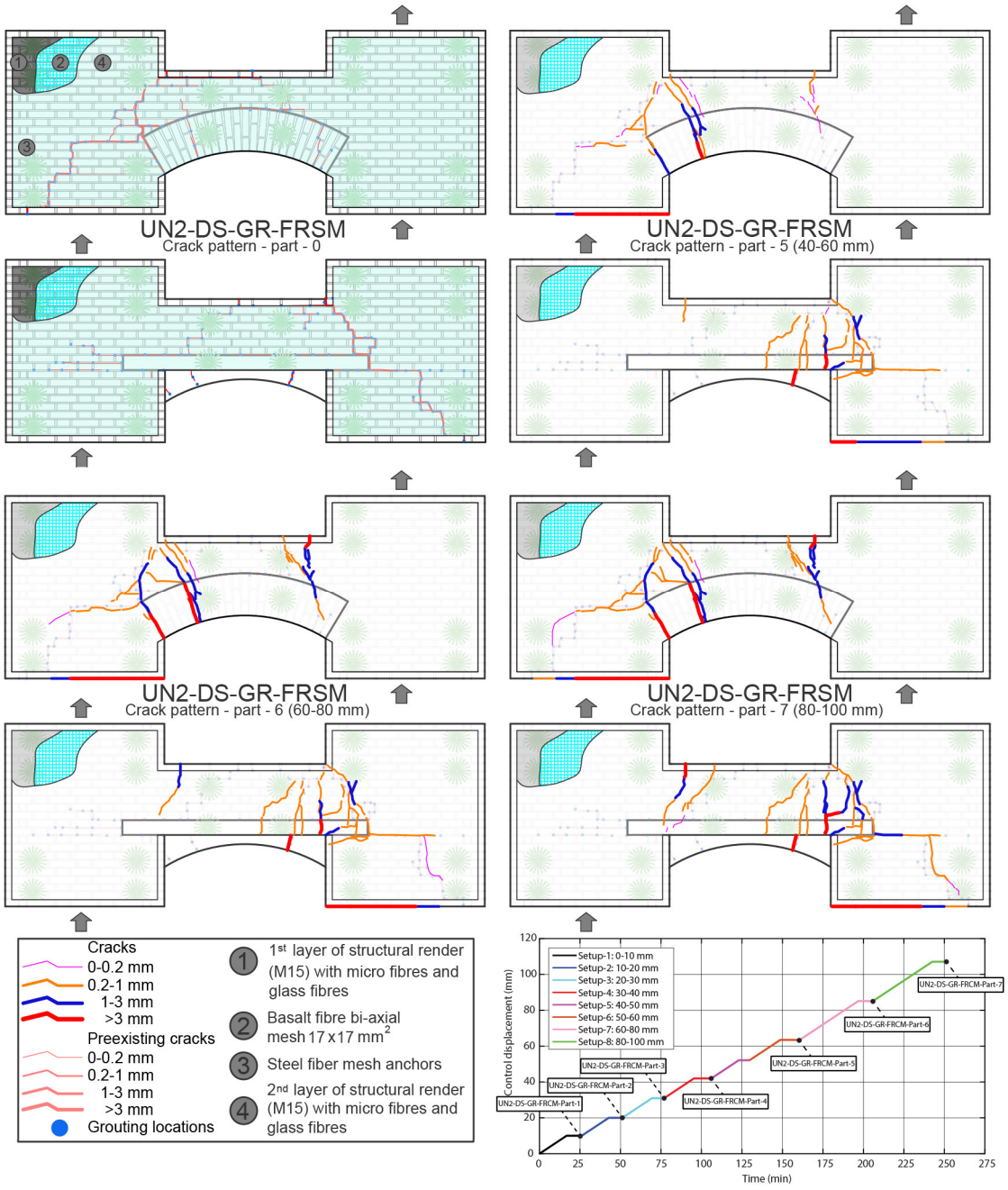
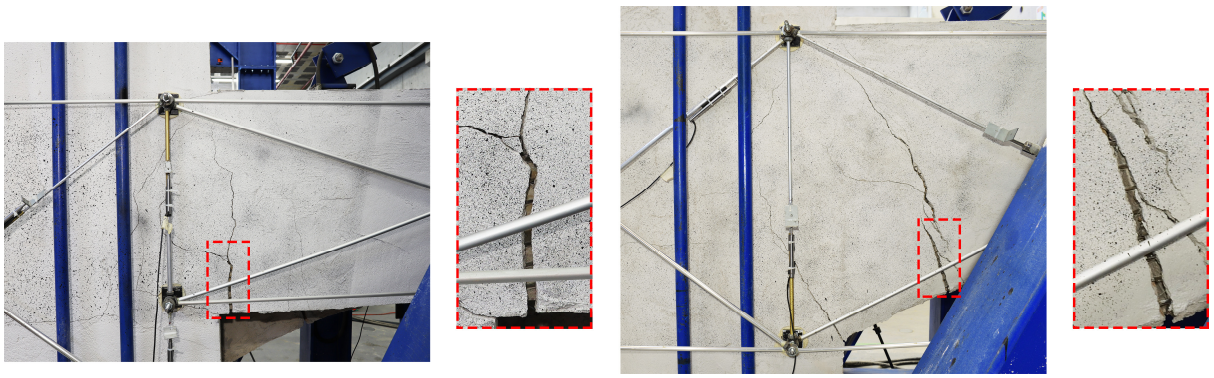


Figure 110. Masonry assembly UN2-DS-GR-FRSM (Setups 5-8): Damage State (DS) assessment at the end of each partial testing setup, of the monotonic, differential uplift. Note the arrows corresponding to the direction of the monotonic differential uplift, from each elevation side of the assembly, the differentiation of structural cracks in terms width, and under different contours.



(a) (b)

Figure 111. Testing of UN2-DS-GR-FRCM: close view of crack patterns at the intrados of the spandrel close to the fixed pier, from the side of the timber lintel (a) and of the arch (b).

6.5.2.3. Ambient vibration testing and correlation with damage, repair and retrofit schemes

In addition to the testing acquisition data for the piers and spandrel masonry assemblies, ambient vibration testing (AVT), conducted prior to each test, was used as a tool for structural and damage assessment. Here, an output only type of AVT was performed, with the vibration response acquired, during service conditions, thus, under the axial prestress at the piers, replicating gravitational loading. Vibration recorded signatures were later used as base reference for the structural assessment of the tested assemblies.

As stated in Ramos 2008 and Mendes 2012, the modes of vibration and damping ratios for masonry structures, of often high complexity, are direct indicators to the change of mechanical and structural characteristics -stiffness, mass, connectivity between members, boundary conditions-, and can serve to interpret their structural behavior. Especially, the presence of damage, as well as the application of repair and retrofit schemes can modify the dynamic properties of a structure, and hence, AVT are also considered as a vital calibration tool for numerical models [Ramos 2007].

As also stated in Siskind et al. 1980 and Konon 1985, natural frequencies in residential structures range between 4 and 24 Hz, with damping values from 2-10%. Yet considering historic masonry structures and the level of damage and deterioration, natural frequencies, especially corresponding to out-of-plane modes, converge towards the lower bound of the above-mentioned range, since they are associated to lower stiffness properties [Konon 1985], even in cases as low as 1 Hz [§4.3.3.2.2 EN 1998-1:2004]. For the tested masonry assemblies, and considering the

in-plane loading, the interest for determining their dynamic properties is concentrated mostly in the in-plane directions.

Considering the comparison between undamaged and damaged state, as well as repair or retrofitted stage, identified shape vectors, of natural vibration modes, can be numerically correlated by means of the Modal Assurance Criteria (MAC), given by the Equation 109 [Ramos 2007]. Here, φ^{u} and φ^{d} are a set of mode vectors, tested for correlation, under the defined n degrees of freedom, corresponding to the sensor locations. Here is noted that MAC values close to zero indicate uncorrelated (orthogonal) vectors, whereas a MAC value close to one is considered as a perfect match. As shown in Mendes 2012, damage propagation can reduce significantly the frequency of the first mode, while in general, as stated in Ramos 2007, the damping ratios are bound to increase. Nevertheless, as also stated in Mendes 2012, and verified during the performed AVT in the current masonry assemblies, due to the high differences in stiffness and the complexity of damage and strengthening schemes, the correlation with natural modes of vibration, at different stages, especially under a global dynamic response, was proven difficult, since dynamic properties alter significantly, in terms of mode shapes, frequency shifts and damping participation. Besides, many primary modes were subdivided, totally altered, while others became undetectable. Hence, associating numerically obtained modes of vibration, under the evolution of damage or retrofit, is proven a cumbersome task, especially when large differences in stiffness occur among each compared stage.

$$\mathrm{MAC}_{u,d} = \frac{\left|\sum_{i=1}^{n} \varphi_i^{u} \varphi_i^{d}\right|^2}{\sum_{i=1}^{n} (\varphi_i^{u})^2 \sum_{i=1}^{n} \left(\varphi_i^{d}\right)^2} \qquad \text{Equation 109}$$

Following, for the initial state of the masonry assemblies UN1-US, UN1-DS, UN1-DS-GR, UN2-US, UN2-DS and UN2-DS-GR-FRCM, and prior to the application of the differential displacement field, AVT were conducted, as shown in Figure 112, soon after the application of the vertical axial prestress at the piers, replicating axial stresses of 0.21 MPa at the base of the piers. A total of 12-16 monitoring points were chosen and referenced as $\mathrm{ACC}_{i,j}$, where i signifies the Setup number and j is the numbered accelerometer sensor, as depicted in Figure 113 and Figure 114. Monitoring points in the piers, cover degrees of freedom, of in-plane, horizontal directions, and in elevation, while for the UN2 assemblies, two out-of-plane directions were added at the top of the piers. For the spandrel, in-plane degrees of freedom were selected, both in the horizontal

and vertical directions. In the case of two Setups, two reference accelerometers were chosen in each Setup, as seen in Figure 113 and Figure 114.

The sensors were piezoelectric mono-axial accelerometers with a frequency range of 0.15 to 1000 Hz, a measurement range of ±0.5 g and of a high sensitivity of 10000 mV/g. The signals were recorded by an acquisition system of 24-bit resolution, with a frequency sampling equal to 200 Hz and under acquisitions of 30-40 min for each setup. The results were processed by the ARTEMIS software, in which the Stochastic Subspace Identification Method (SSI) was used, for which, the modal decomposition is performed in the frequency domain, under a mathematical linear fitting with state space formulations [SVS 2019]. In detail, the Extended Unweighted Principal Component (SSI-UPCX) algorithm was used, which allows for a more accurate selection, either automatic or manual, of stable modes, on the basis of the statistical confidence of mean values, for the natural frequencies and damping ratios (Figure 115) [SVS 2019]. For all the tested assemblies, the identified modes, by means of frequencies, damping ratios and deformed shapes are presented in Table 37, Figure 113 and Figure 114.

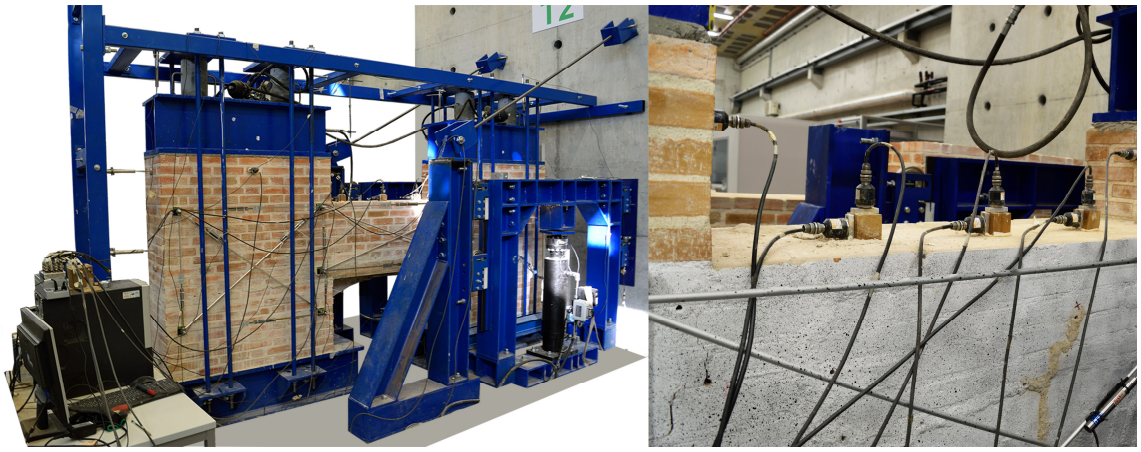
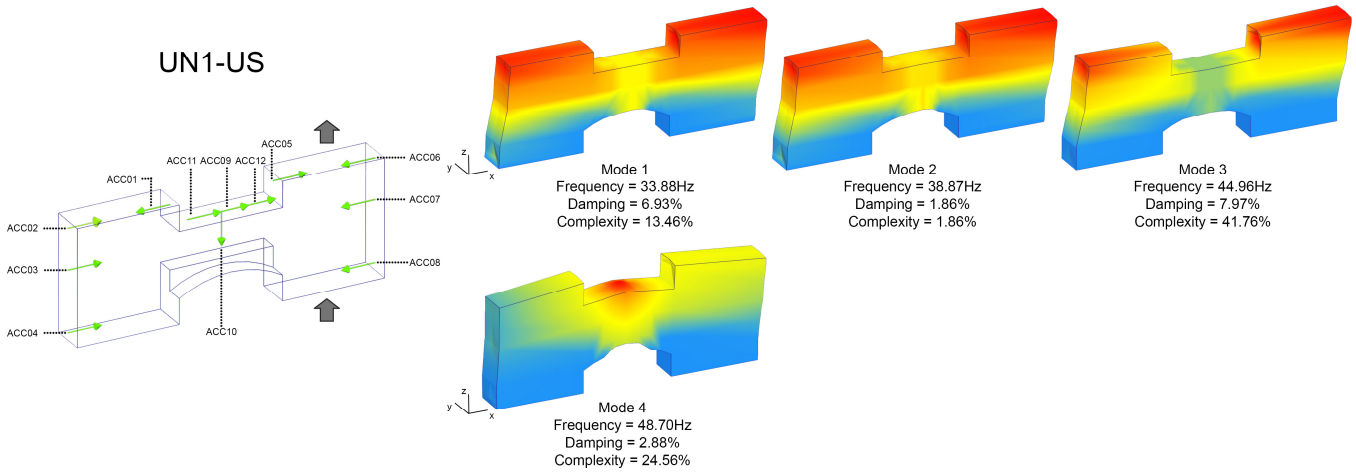
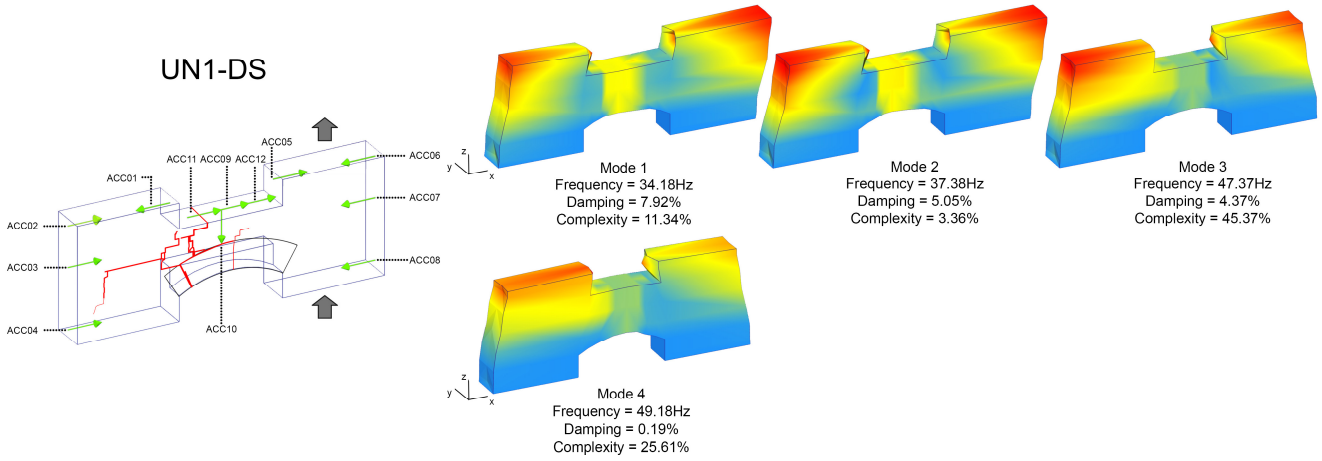


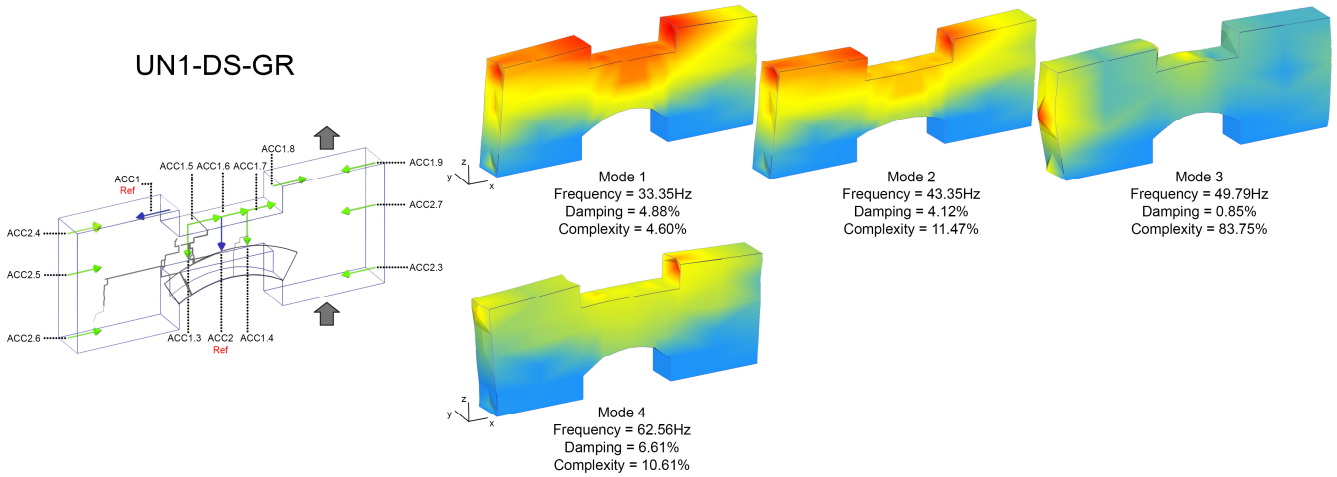
Figure 112. View of testing masonry assembly of UN1-DS-GR, during an AVT Setup.



(a)



(b)



(c)

Figure 113. Disposition of accelerometers in the performed Setups for: (a) UN1-US; (b) UN1-DS, and (c) UN1-DS-GR, with identified modes of vibration obtained from the SSI-UPCX method, and deformed mode shapes, with linear interpolation.

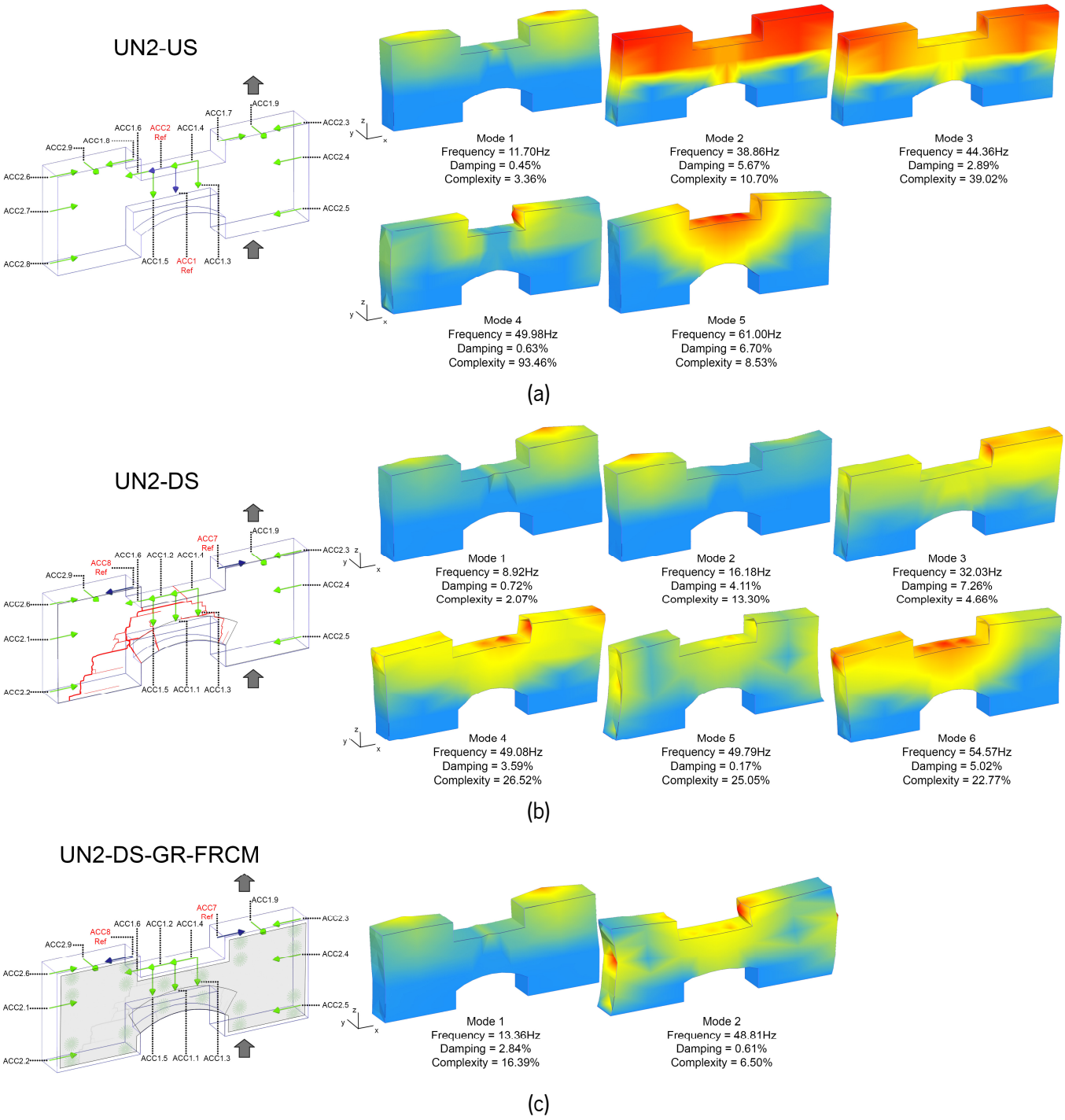


Figure 114. Disposition of accelerometers in the performed Setups for: (a) UN2-US; (b) UN2-DS, and (c) UN2-DS-GR-FRCM, with identified modes of vibration obtained from the SSI-UPCX method, and deformed mode shapes, with linear interpolation.

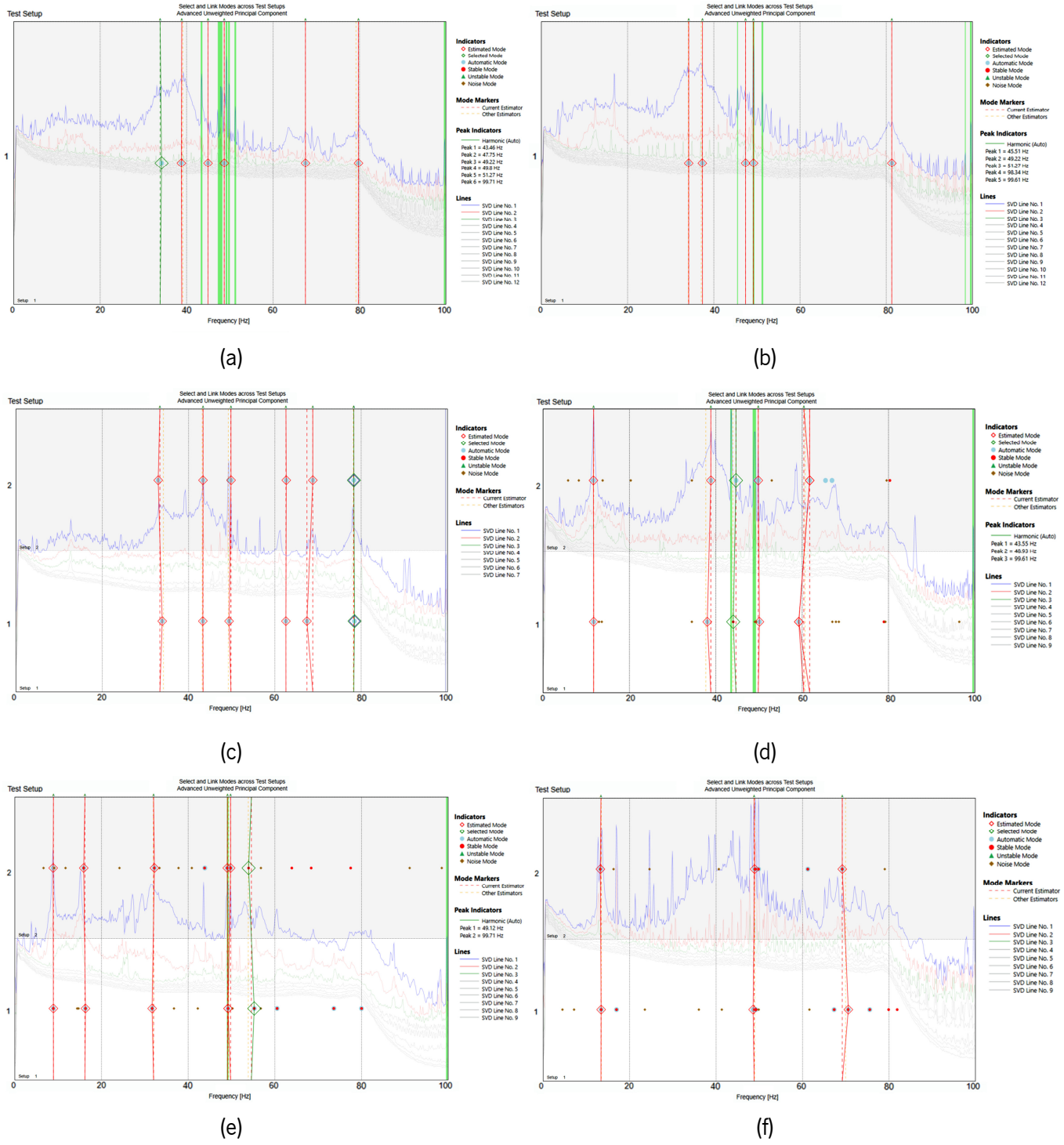


Figure 115. Data driven stabilization diagrams, with the poles selection of the SSI-UPCX method, for (a) UN1-US; (b) UN1-DS; (c) UN1-DS-GR; (d) UN2-US; (e) UN2-DS, and (f) UN2-DS-GR-FRCM. Note the Nyquist frequency of 100 Hz [SVS 2019].

Table 37. Frequencies, damping ratios and mode shape characteristics, under the SSI-UPCX method, for all the tested masonry assemblies [SVS 2019].

		Frequency [Hz]	Std. Frequency [Hz]	Damping [%]	Std. Damping [%]	Complexity [%]	Characteristics ①②③④⑤⑥⑦
UN1-US	Mode 1	33.88	0.19	6.93	0.46	13.46	IP Ip 1 ✓ Ip Ip
	Mode 2	38.87	0.13	4.65	0.19	1.86	IP Ip 1 ✓ Ip Ip
	Mode 3	44.96	0.11	7.97	0.58	41.76	IP Ip 1 ✓ ✓ Ip Ip
	Mode 4	48.70	0.04	2.88	0.23	24.56	IP Ip 1 ✓ ✓ Ip Ip
UN1-DS	Mode 1	34.18	0.18	7.92	0.50	11.34	IP Ip 1 ✓ Op Ip
	Mode 2	37.38	0.13	5.05	0.27	3.36	IP Ip 1 ✓ Op Ip
	Mode 3	47.37	0.38	4.37	0.88	45.37	IP Op 1 ✓ Op Ip
	Mode 4	49.18	0.01	0.19	0.01	25.61	IP Op 1 ✓ Op Ip
UN1-DS-GR	Mode 1	33.35	0.08	4.88	0.40	4.60	IP Ip 1 ✓ ✓ Ip Ip
	Mode 2	43.35	0.09	4.11	0.20	11.47	IP Ip 1 ✓ ✓ Ip Ip
	Mode 3	49.79	0.07	0.85	0.75	83.75	IP Op 2 ✓ Op Op
	Mode 4	62.56	0.16	6.61	0.55	10.61	IP Op 1 ✓ Ip Ip
UN2-US	Mode 1	11.70	0.01	0.21	0.33	4.24	OP Ip 1
	Mode 2	38.86	0.14	5.67	0.35	10.70	IP Ip 1 ✓ Ip Ip
	Mode 3	44.36	0.45	2.89	0.36	39.02	IP Ip 1 ✓ Ip Ip
	Mode 4	49.98	0.19	0.63	0.46	93.46	IP Op 2
	Mode 5	61.75	0.65	8.35	1.69	10.33	✓ Ip
UN2-DS	Mode 1	8.92	0.03	0.72	0.89	2.07	OP Ip 1
	Mode 2	16.18	0.29	4.11	0.68	13.30	OP Op 1
	Mode 3	32.03	0.11	7.26	0.41	4.66	IP Ip 1 ✓ Ip Ip
	Mode 4	49.08	0.07	3.59	0.27	26.52	IP Op 1 ✓ Ip Ip
	Mode 5	49.80	0.01	0.17	0.01	25.05	IP Op 2 ✓ Ip Ip
	Mode 6	54.57	0.87	5.02	1.70	22.77	IP Op 1 ✓ Ip Ip
UN2-DS-GR-FRCM	Mode 1	13.36	0.03	2.84	0.10	16.39	OP Ip 1
	Mode 2	48.80	0.01	0.61	0.02	6.50	IP Op 2 ✓ ✓ Ip Ip

① Type of mode for the piers. IP: In-plane, OP: Out-of-plane

② Type of mode for the piers. Ip: In-phase, Op: Out-of-phase

③ Type of mode for the piers. 1: 1st order, 2: 2nd order

④ Horizontal in-plane vectors in the spandrel

⑤ Vertical in-plane vectors in the spandrel

⑥ Type of mode for the spandrel and piers. Ip: In-phase, Op: Out-of-phase

⑦ Type of mode for the spandrel. Ip: In-phase, Op: Out-of-phase

Table 38. MAC values of principal in-plane and out-of-plane, in-phase modes between: (a) UN1-US; and UN1-DS; (b) UN1-US and UN1-DS-GR; (d) UN2-US and UN2-DS, and (e) UN2-US and UN2-DS-GR-FRCM. Note the color gradient and cell attributes in (c).

(a)

In-plane, In-phase modes

UN1-DS / UN1-US	MODE-1 (34.18 Hz)	MODE-2 (37.38 Hz)
MODE-1 (33.88 Hz)	1.00	-
	0.45	-
	0.60	-
MODE-2 (38.87 Hz)	-	1.00
	-	0.44
	-	0.96

(b)

In-plane, In-phase modes

UN1-DS -GR / UN1-US	MODE-1 (33.35 Hz)	MODE-2 (43.35 Hz)
MODE-1 (33.88 Hz)	1.00	-
	0.81	-
	0.44	-
MODE-2 (38.87 Hz)	-	1.00
	-	0.94
	-	0.74
MODE-3 (44.96 Hz)	0.99	0.99
	0.74	0.92
	0.29	0.96

(c)

COLOR MAP

1-0.8

0.8-0.65

0.65-0.5

0.5-0.4

0.4-0.3

0.3-0

Piers

All DOFs except base

Spandrel

(d)

Out-of-plane, In-plane, In-phase modes

UN2-DS / UN2-US	MODE-1 (8.92 Hz)	MODE-3 (32.03 Hz)
MODE-1 (11.70 Hz)	0.99	-
	0.99	-
	0.83	-
MODE-2 (38.86 Hz)	-	0.94
	-	0.94
	-	0.95
MODE-3 (44.36 Hz)	-	0.13
	-	0.00
	-	0.58

(e)

Out-of-plane, In-plane, In-phase modes

UN2-DS-GR-FRCM / UN2-US	MODE-1 (13.36 Hz)	MODE-2 (48.81 Hz)
MODE-1 (11.70 Hz)	0.66	-
	0.59	-
	0.13	-
MODE-2 (38.86 Hz)	-	0.00
	-	0.00
	-	0.03
MODE-3 (44.36 Hz)	-	0.28
	-	0.05
	-	0.06

In the AVT of the undamaged state (US) principal, in-plane modes, under mostly horizontal vectorial components, and in-phase for the piers and spandrels, for both assemblies UN1-US and UN2-US are estimated within the range of 33.4-45 Hz. The piers deflect under a single curvature, with highest amplitudes at the top. Yet, the presence of many similar in-plane modes is an indication of unavoidable imperfections in the mockups. For UN2-US, the first mode is an in-phase,

out-of-plane mode, concerning the piers, and is significantly lower, equal to 11.7 Hz, which demonstrates the lower out-of-plane bending stiffness of the assembly in the out-of-plane direction. Vertical, in-plane modes, in the spandrel, of high vectorial components, are found under higher frequencies, equal to 49Hz for UN1-US (Mode 4) and 61 Hz for UN2-US (Mode 5). Here, the vertical response of the spandrel is believed to be dominated by the high flexural stiffness of the timber lintel. Considering also the high difference in frequencies of the principal vertical modes between the two assemblies, it can be attributed to potential imperfections in the UN1-US mockup and to local variabilities in the material properties of the constituents. Finally, considering the damping ratios, those are found for principal in-plane responses, within the range of 1.9-8.0%, for the single identified out-of-plane mode is found equal to 0.5%, while for the principal vertical modes of the spandrel, within the range of 2.9-6.7%. Yet, as stated in Mendes 2012 and Ramos 2003, the experimental estimation of damping parameters, also proportional to the stiffness and mass, are considered indicators of the energy dissipation of a structure, yet, often of low resolution and particularly difficult to estimate in masonry structures.

Assessing the dynamic properties under the presence of damage, in UN1-DS and UN2-DS, in comparison to UN1-US and UN2-US, and despite the complexity in global modes, several aspects can be signified. First, for the deformed shapes in the principal in-plane modes of UN1-DS (Mode 1 and Mode 2), and despite the minor changes in frequency values, the original, in-phase, horizontal deformation of the spandrel in UN1-US, is being shifted to out-of-phase, after the flexural cracking in the spandrel and the rapid decrease of flexural stiffness. Damping values are also affected, by an increase of 14-170%. The damage related change in the degrees of freedom of the abovementioned modes can be numerically quantified by the low MAC values, of around 0.45, as shown in Table 38a. Also, considering Modes 3 and Mode 4, they appear altered, configured with an out-of-phase vectorial deformation for the piers and a vertical component in the spandrel, the latter of a low amplitude.

In addition, for UN2-DS, after the infliction of damage, the first out-of-plane mode (Mode 1) is maintained, correlated to the corresponding one of UN2-US, under a MAC value of 0.99, and shifted to a frequency lower by 24% (Table 38d). Here, the damping ratio is also increased by 60%. Furthermore, an additional out-of-plane mode arises (Mode 2), with an out-of-phase configuration for the piers and a higher damping ratio, which is indicative of the advanced fragmentations in the core of the spandrel and fixed pier. For the principal in-plane mode of UN2-US (Mode 2), it remains

unchanged, with a global MAC value of 0.95, but under a lower frequency by 18% (Table 38d). Here, the damping ratio appears also increased by an average of 28%. Such a difference in the configuration of the principal in-plane modes for UN1-DS and UN2-DS can be attributed to the differences in the lateral boundary conditions in the moving pier, during the testing under vertical uplift, and the resulted flexural failure in UN1-DS, versus the combined flexural and shear failure in UN2-DS, with the later more distributed in the spandrel and non-moving pier. Following, similar to UN1-DS, three new in-plane and out-of-phase modes arise in UN2-DS (Mode 4, Mode 5 and Mode 6), all with high vertical in-phase components in the spandrel.

At a final stage, by comparing the AVT of the repaired and retrofitted assemblies UN1-DS-GR and UN2-DS-GR-FRCM with those of UN1-US and UN2-US respectively, it can be concluded that the process of reintegration of stiffness in cracked areas with grouting injections and the addition of in-plane stiffness with the FRCM system has reflected significantly on the dynamic properties. Here, important aspects can be signified as: (a) the structural repair with grouting injections in UN1-DS-GR appears to have re-established the principal in-plane modes (Mode 1 and Mode 2) in the in-phase configuration, that of UN1-US, with high MAC values, equal to 0.81 for 0.94, with the respective modes of UN1-US (Table 38b). Yet the lower MAC values in the spandrel's degrees of freedom are attributed to the presence of higher amplitudes for the vertical components. Here the frequency of Mode 1 remains practically unchanged, while the one for Mode 2 is increased by 24%, signifying the increase of stiffness. The damping ratios are also decreased by 18-38%, compared to the respective ones of UN1-DS; (b) in UN2-DS-GR-FRCM, the FRCM retrofitting scheme, combined with prior grouting injections, has significantly contributed in the increase of the out-of-plane bending stiffness, with the corresponding frequency of Mode 1 found increased by 14%, and (c) the in-plane mode (Mode 2) is utterly transformed to a global in-plane bending mode of 2nd order, with a frequency increased by 52%, compared to the one of UN2-DS (Mode 3 in Figure 114b), which signifies the vast increase in the in-plane stiffness, provided by the FRCM system.

Here is noted that the evolution of frequencies in the matching modes of the assemblies at the undamaged state (US), the damaged state (DS) and the repair and retrofitted stage (R&R), for both assemblies UN1 and UN2, are depicted in Figure 116.

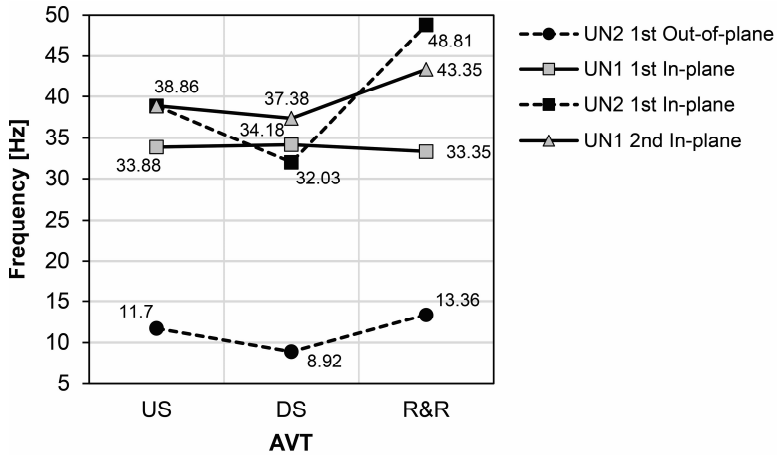


Figure 116. Evolution of frequencies for the undamaged state (US), the damaged state (DS), and the repair and retrofitted state (R&R) of the pier and spandrel masonry assemblies UN1 and UN2.

6.5.3. Application of mechanical strength models for masonry spandrels UN1 and UN2

Accounting for the collection of experimental data for the tested piers and spandrel, masonry assemblies UN1-US, UN1-DS-GR, UN2-US and UN2-DS-GR-FRCM, code evaluation procedures of the expected failure modes and capacities are performed, under the analytical expressions and framework of FEMA 274 1997, FEMA 356 2000, FEMA 306 1998 and NTC 2018, as described in Section 6.4.

First, according to FEMA 356 2000 and FEMA 306 1998, a hierarchical step-by-step evaluation of the in-plane capacities is performed, for the piers and spandrel, the later, both in un-cracked and cracked conditions, with the lower in-plane capacity determining the first response of the structural system. In addition, for the in-plane shear capacity of the spandrel, the capacity verification of NTC 2018 is applied. Furthermore, under the current framework, the concept of a mixed sequential failure, as observed during testing, with a consecutive flexural and shear failure in the spandrel, followed by a shear failure in the non-moving pier, can also be verified analytically, under the hypothesis that load trajectories are not significantly altered by prior failure modes. Thus, the hierarchical in-plane capacity is concluded in a two-step process, covering the assessment of the pier and spandrel, as independent structural elements.

First, the masonry piers, under a constant prestress state of 0.21 MPa, are considered partially fixed, and connected to the spandrel. Yet, their in-plane capacity can be verified independently, as a single macro-element, under the lateral force interaction with the spandrel. The corresponding strengths, as formulated in FEMA 356 2000, are considering a lateral in-plane

load application. Hence, focusing only on the non-moving pier, the calculated values of the in-plane shear capacities can be accounted, under the condition of a secondary response, considering the in-plane axial counteraction with the timber lintel and the deformed spandrel, during the evolution of the vertical uplift in the moving pier.

The aspect ratio of the pier b_P, defined as the length L_p, over the entire height h, is equal to 1.12. Yet, considering the lateral counteraction with the spandrel at the level of the spandrel's compressive toe, the effective length h_{eff} disregards the part of the pier over the extrados of the spandrel, and thus, the aspect ratio is equal to 1.07. Following the evaluation process in FEMA 306 1998, for weak pier-strong spandrel mechanisms, as described in Section 6.4, under a categorized moderately stocky pier (b_P>1.0), the predicted behavior corresponds to the relative comparison between in-plane strength, with respect to rocking, bed joint sliding, diagonal tension and toe crushing, here denoted as V_r, $V_{bjs,1}$, V_{dt} and V_{tc} respectively (Equation 88-Equation 92). The defined geometrical and mechanical parameters for all the tested assemblies are presented in Table 39. Accounting for the constant axial stress condition, which is implemented by adjusting the counterpressure from the hydraulic jacks, the non-moving pier is considered as partially fixed, thus the reduction factor α is taken equal to 0.75. Hence, for the piers from the different tested assemblies, the following can be concluded:

(a) For the non-moving pier in UN1-US, UN2-US and UN1-DS-GR, the rocking strength V_r and toe crushing strength V_{tc} are the lowest expected, here found equal to 77.56 kN and 81.52 kN respectively. Yet, accounting for the observed sliding failure in the pier, at the level of the spandrel, it appears dominant for the pier, together with a combination of diagonal or vertical shear cracking towards the compressive toe. Such a failure is mostly associated to the counteracting effect of the timber beam and the compressive toe of the spandrel, which causes the early shear sliding of the adjacent bed joint. Thus, under the hypothesis of a cohesionless frictional response in the bed joint, the reduced bed joint sliding strength V_{bjs2} can be considered as the principal failure, given by Equation 110, here found equal to 51.23 kN (See also Section 6.4 for abbreviations) [FEMA 306 1998].

$$V_{bjs2} = \frac{0.75\frac{P_{CE}}{A_n}}{1.5}A_n \qquad \text{Equation 110}$$

(b) The in-plane response of the non-moving pier in the retrofitted assembly UN2-DS-GR-FRCM is characterized by the reintegration of the cracked interface through injection grouting, and an additional in-plane capacity component, offered by the FRCM system. According to ACI 549.4R-13 2013 and CNR-DT 215/2018 2020 the tensile behavior of a FRCM system is best fitted with a bilinear curve with hardening, until sudden failure occurs, by slippage or rupture of the fiber mesh. Thus, the contribution to the in-plane capacity in the strengthened pier can be divided in an initial stage -1-, up to the point of cracking of the cementitious matrix, with the tensile Young's modulus $\mathrm{E_m}$ and tensile strength $\mathrm{f_{t,m}}$ of the structural render, and a second stage -2- that corresponds to the FRCM system cracked and idealized with the tensile Young's modulus $\mathrm{E_f}$ and tensile strength $\mathrm{f_{fv}}$ of the fiber mesh. For design purposes, the latter is limited by the slippage strain of the fiber mesh within the cementitious matric, which according to ACI 549.4R-13 2013 is set at 4‰ for shear actions. Instead, in CNR-DT 215/2018 2020, the design process leads to similar values, with the characteristic value of tensile stress limit for shear actions, denoted as $\sigma_{\mathrm{lim,conv}}$, derived from the respective tensile strain limit $\varepsilon_{\mathrm{lim,conv}}$, taken equal to 0.80 times the average ultimate tensile strain and divided with a safety factor of 1.5 for the Ultimate Limit State. In addition, an environmental corrective factor can be applied, equal to 0.80 for external exposure conditions. Here, nominal values of material properties are used, in order to derive to nominal capacity values. Yet, the recommended limit of 0.80 for the ultimate tensile strain under shear actions is accounted in the average response verification.

Under a hypothesis of a simultaneous shear failure for the two-layered render and the masonry pier, the updated in-plane strengths of bed joint sliding, diagonal tension and toe crushing for capacity stage -1- of the FRCM system, here denoted as $\mathrm{V_{bjs1,1}}$, $\mathrm{V_{bjs2,1}}$, $\mathrm{V_{dt,1}}$ and $\mathrm{V_{tc,1}}$ respectively, while the rocking strength $\mathrm{V_r}$ remains unchanged. The updated in-plane capacities are presented in Table 39. Here, the reduced bed joint sliding strength $\mathrm{V_{bjs2,1}}$, found equal to 53.73 kN, is the lowest, and can be considered as the principal failure, during stage -1- of the tensile behavior for the FRCM system.

Following the cracking of the cementitious matrix and masonry, the activation of the basalt fiber mesh is expected. According to CNR-DT 215/2018 2020, the design shear strength of the cracked FRCM system $\mathrm{V_f}$ is given by Equation 111, where γ_{RD} is a partial safety factor equal to 2, $\mathrm{n_f}$ is the number of layers of the fiber mesh, $\mathrm{t_f}$ is the equivalent

thickness of the fiber mesh activated in shear, l_f is dimension of the fiber mesh orthogonally to the shear force, taken by maximum, equal to the horizontal dimension of the pier or spandrel, and f_{fv} is the design value of tensile strength, accounting for the activation of the fiber mesh under shear actions, the type of environmental exposure, and divided with the safety factor of 1.5.

$$V_f = \frac{1}{\gamma_{RD}} n_f t_f l_f f_{fv} \qquad \text{Equation 111}$$

Accounting for the principal failure and resulted cracking at stage -1-, the updated nominal in-plane capacity of stage -2-, here denoted as $V_{bjs2,2}$, considers the frictional sliding strength of the masonry and the structural render, and the shear strength of the fiber mesh, found equal to 135.45 kN (Table 39). Hence shear sliding is no longer the dominant mode of failure for the non-moving pier. Here is noted that nominal values of strengths are calculated, thus, average material properties, without safety factors. Considering the similar lower values of compressive toe crushing and rocking strength for the non-moving pier, a possible combined failure mechanism is to be expected. In fact, as observed at the last steps of the vertical uplift testing for UN2-DS-GR-FRCM, the crack pattern at the surface of the render is a combination of a sliding crack in the proximity of the timber lintel and a diagonal stepped crack oriented towards the compressive toe, while rocking is eminent, with a maximum documented rotating uplift at the base, of almost 1 cm (Figure 110).

(c) The in-plane capacity of the spandrel for UN1-US, UN2-US and by extent to UN1-DS-GR is determined under flexural and shear actions, both in the elastic and cracked limit, according to Equation 93-Equation 100, from FEMA 306 1998. An additional shear capacity verification is provided by NTC 2018.

Defining geometrical and mechanical parameters for the spandrel, as shown in Table 40, the shear force at the elastic limit is the resultant of the shear stresses at the bed and collar joints of the spandrel's interface $T_{sp,un}$, and the shear contribution of the timber beam T_b, at the plane defined by the bearing length l_b. Following the hypotheses presented in Section 6.4, only the horizontal shear actions in the spandrel, over the beam and arch springing are considered, under the same height of involved courses, here found equal to 0.41 m. Under the equilibrium of sectional forces, at the barycenter of compressive stresses in the spandrel, the total moment of the elastic limit under flexure $M_{total,un}$ is equal to 6.82 kN/m. The

corresponding vertical shear force $V_{sp,un}$, at the interface, is dependent on the actual boundary conditions at both ends of the spandrel, and can expressed by Equation 112, where L is the free span of the spandrel and c is a boundary-end coefficient, equal to 0.5 and 1.0 for a fixed and a cantilevered beam respectively [Tomazevic 1999].

Accounting for the lateral restrain conditions for UN1-US and UN2-US (Table 32), values for c, equal to 0.75 and 0.5 are assigned respectively. Hence, the corresponding shear force for the elastic limit of the flexural strength is 7.57 kN and 11.36 kN for UN1-US and UN2-US respectively, while UN1-DS-GR is matched with UN2-US, under the equal application of boundary conditions. Thus, considering the total shear force in the spandrel during the laboratory tests, which is within the range of 40-58 kN, the flexural strength, until cracking, accounts only for a small percentage and confirms with the early formation of flexural cracks during the tests.

$$V_{sp,un} = \frac{M_{total,un}}{cL} \qquad \text{Equation 112}$$

Following, the shear stresses, under flexural cracking, progress only under the frictional resistance, with no cohesion, at the level of the bed joints and the base of timber beam, while the collar joints are excluded. Here, the shear planes within the masonry courses and the timber beam, account for an effective depth b_{effcr}, reduced an average slip Δs, which is considered here equal to 3 mm, according to the documented crack patterns. According to Equation 98-Equation 99 and Equation 101-Equation 102, the marginal shear component under flexural cracking is found equal to 1.61 kN and 2.42 kN for UN1-US and UN2-US/UN1-DS-GR respectively. Here is noted that the shear forces in the spandrel, as considered by Equation 112, are accounting for elastic conditions, which in fact cannot reflect changes in stiffness during cracking. Yet, Equation 112 is used also for cracked conditions, considering that those reflect at the inflection yield point of the first crack, and for the sake of comparison between cracked and uncracked state.

The shear strength of the spandrel under diagonal tension, involves the diagonal compressive strut only of masonry, with an aspect ratio equal to 2.0, and under a conservative hypothesis of zero axial stresses, while the presence of the timber beam only contributes against the collapse of the rocking spandrel. Here, the height of the masonry spandrel from both respective sides is considered, according to Section 6.4, since the springing of the arch

is participating in the trajectory of the compressive strut. According to FEMA 306 1998 and by applying Equation 100, the shear strength against diagonal tension is found equal to 56.5 kN and is considered unreduced for cracked conditions (Table 41). The calculated capacity is in optimum agreement with the ones of UN2-US and UN1-DS-GR, with a difference in the range of 2-3%. In addition, according to NTC 2018 and Equation 106, the respective capacity is found equal to 70.5 kN, as presented in Table 41. Here, the prediction of capacity is under a higher difference compared with the experimental one, being higher by 21-27%. For the spandrel in UN1-US, the shear capacity during testing is found lower by 39-46%, compared to UN2-US and UN1-DS-GR, which can be attributed to the lack of lateral restrain and the resulted decrease in lateral stiffness, and thus, the predicted shear strength presents a higher difference, of around 40%.

The strengthening of UN2-DS-GR-FRCM with an FRCM system, contributes to the flexural and diagonal shear capacity, under a two-stage response, the first until the cracking of the structural render and the second, under the tensile or shear activation of the fiber mesh. Here, a hypothesis of a simultaneous failure of the associated structural components and the summing of their respective capacities is adopted [ACI 549.4R-13 2013].

For the flexural strength, the structural render contributes only to the elastic limit, and under direct tensile actions in the half of the total height of the spandrel (Table 40). Thus, the total shear component of the flexural strength before cracking is equal to 14.8 kN, higher by 29%, compared to the UN2-US. Soon after, the marginal flexural capacity of the masonry is enhanced with the activation of the fiber mesh, under a flexural out-of-plane action. According to CNR-DT 215/2018 2020, the nominal limit for the tensile strain is equal to the ultimate tensile strain, here equal to 19‰, by considering only tensile actions with a sufficient bearing length and no debonding. Yet, considering the combination of tensile and shear actions in the spandrel, a limit of 0.80 times the ultimate tensile strain is also set for the fiber mesh. The nominal shear capacity is given by Equation 111 and Equation 112, not accounting of safety factors, and where l_f is the height of the fiber mesh activated in tension, here taken equal to the half of the average spandrel's height from the two sides. Thus, the flexural strength of the fiber mesh is of 9.22 kN/m, with a shear component of 15.37 kN (Table 40). Thus, the total shear force in the spandrel, under the flexural limit of the fiber mesh and for cracked conditions regarding masonry is equal to 17.79 kN, higher by 21%, compared to the elastic limit of the first stage. Such a secondary response after cracking, under a higher flexural strength, is bound

to move flexural cracking for the render in adjacent locations, as is also documented during the laboratory testing of UN2-DS-GR-FRCM (Figure 110).

Considering the behavior of the retrofitted spandrel under diagonal shear, and under the hypothesis of the same path for the compressive strut, the contribution of the structural render increases the diagonal shear strength prediction to 81.1 kN, higher by 44%, compared to the respective one of UN2-US (Table 41). Soon after the cracking of the structural render, and disregarding its shear contribution, the second stage of the diagonal shear response in the spandrel initiates, which accounts for the fiber mesh under a shear action, with a design shear strength given by Equation 111, and under a limit by the shear nominal strains equal to 15.2‰ (0.8x19.0‰) [CNR-DT 215/2018 2020]. Thus, the nominal shear strength component of the fiber mesh is found equal to 81.72 kN, with the total diagonal shear strength in the spandrel being equal to 138.18 kN, higher by 145%, compared to the calculated one for UN2-US. Further on, the analytical diagonal shear capacity of UN2-DS-GR-FRCM is higher by 56% compared to the respective one from laboratory testing, also considered under an acceptable margin, considering that the actual failure of the spandrel could not be reached, given the transition towards a rocking failure for the piers.

Table 39. Analytical formulations, with geometrical and mechanical parameters for prioritizing the in-plane strengths for the non-moving masonry piers of UN1-US, UN2-US, UN1-DS-GR and UN2-DS-GR-FRCM, according to FEMA 356 2000.

	UN1-US UN2-US UN1-DS-GR	UN2-DS-GR-FRCM	
	Masonry	Render[1]	Fiber mesh[2]
L_P (m)	1.20	1.20	1.20
h_{eff} (m)	1.07[3]	1.07	1.07
t (m)[4]	0.41	0.02[5]	3.2E-05[2]
b_P [6]	1.12	1.12	-
A_n (m^2)	0.49	0.02	3.2E-05[7]
P_{CE} (kN)	102.46[8]	5.00[9]	-
f_{ae} (MPa)	0.21[10]	0.21	-
f_t (MPa)	0.42[11]	2.09[12]	1700[2]
v_{te} (MPa)	0.62[13]	3.14[13]	-
v_{me} (MPa)	0.34	1.28	-
a	0.75[14]	0.75[14]	-
β	1	1	-
n	-	-	2
f_{me} (MPa)	8.80[15]	16.76[16]	-
f'_{dt} (MPa)	0.34[17]	1.28[17]	-
f'_m (MPa)	5.5	10.48	-
f_{fv} (MPa)	-	-	1064[18]
		[19]/[20]	[21](-)[22]/[20]
V_{dt} (kN)	211.19	33.12/244.31	81.72(21.79)/292.90
V_{tc} (kN)	81.52	4.08/85.61	-/85.61
V_{bjs1} (kN)	166.08	30.71/196.80	-/-
V_{bjs2} (kN)	51.23	2.50/53.73	81.72(21.79)/135.45
V_r (kN)	77.56	-/77.56	-/77.56

[1] GeoCalce F Antisismico 2019
[2] GeoSteel Grid 200 2019
[3] Effective height of pier, taken from the base until the level of extrados of the spandrel
[4] Thickness
[5] Two layers of render of 0.01 m of thickness each
[6] Aspect ratio equal to L/h
[7] Area of fiber mesh, per unit length (m^2/m) [GeoSteel Grid 200 2019]
[8] Measured force from two hydraulic jacks, and steel parts at the top one pier. The self-weight of the pier is not included for simplicity [FEMA 356 2000]
[9] Equivalent load in render, considering the applied vertical stress state of 0.21 MPa
[10] Vertical load P_{CE}, applied in the plan area of the pier A_n
[11] Average tensile strength of masonry from diagonal compression tests on wallets, Table 16
[12] Average tensile strength of M15 render taken equal to $2 \cdot f_f$, according to Lourenco and Gaetani 2022, where f_f is the average flexural strength from flexure tests on prisms (Table 10)
[13] Considered equal to $1.5 f_t$ [Angelillo et al. 2014]
[14] Pier is considered as semi-fixed
[15] Average compressive strength of masonry from uniaxial compression tests on wallets (Table 16)
[16] Average compressive strength of hydraulic lime-based render M15 from uniaxial compression tests on prisms (Table 10)
[17] Lower strength in diagonal tension, taken equal to v_{me} [FEMA 356 2000]
[18] Nominal tensile strength of the fiber mesh, under the effect of shear actions. For the design strength value, a safety factor and an environmental exposure coefficient for the ULS are applied. The Young's modulus is 70 GPa [CNR-DT 215/2018 2020 and GeoSteel Grid 200 2019]
[19] Nominal strength component of the structural render
[20] Total strength taken as the sum of nominal strengths of subsequent components, under the condition of simultaneous failure [ACI 549.4R-13 2013 and CNR-DT 215/2018 2020]
[21] Nominal strength component of the fiber mesh
[22] Design strength component of the fiber mesh [CNR-DT 215/2018 2020]

Table 40. Analytical formulations, with geometrical and mechanical parameters for the in-plane flexural strength in the spandrels of UN1-US, UN2-US, UN1-DS-GR and UN2-DS-GR-FRCM, according to FEMA 356 2000.

	UN1-US UN2-US UN1-DS-GR	UN2-DS-GR-FRCM	
	Masonry[1]	Render[2]	Fiber mesh[3]
L (m)	1.20	1.20	1.20
b_{effun} (m)	0.10[4]	-	-
Δ s (m)	0.003	-	-
b_{effcr} (m)	0.097	-	-
γ	0.5	-	-
f_t (MPa)	0.42[5]	2.09[6]	1700[3]
v_{te} (MPa)	0.62[7]	-	-
v_{bjun} (MPa)	0.29	-	-
v_{cun} (MPa)	0.23	-	-
v_{bjcr} (MPa)	0.05	-	-
f_{fe} (MPa)	-	-	1064[8]
b_w (m)	0.10	-	-
b_h (m)	0.05/0.01[9]	-	-
d_{sp} (m)	0.41[10]/0.41[11]	-	-
b_{sp} (m)	0.41	-	-
t (m)[12]	-	0.02[13]	3.2E-05[3]
n	-	-	2
NB	3	-	-
NR	3.42	-	-
η	1.71[14]	-	-
l_b (m)[15]	0.25	-	-
t_b (m)[15]	0.20	-	-
h_b (m)[15]	0.11	-	-
$d_{sp,lim}$ (m)[16]	0.27	0.37	-
$d_{b,lim}$ (m)[16]	0.46	-	-
$d_{sp,cr}$ (m)[16]	0.21	-	-
$d_{b,cr}$ (m)[16]	0.43	-	-
d_f (m)[17]	-	-	0.52
$T_{sp,lim}/T_{b,lim}$(kN)	8.87/14.28	T_r[2] (kN)	5.43
$M_{tot,un}$ (kN/m)	6.82[18]	M_r[2]	1.98
c[19]	0.75[20]/0.5[21]	c[19]	0.5[21]
$V_{L,un}$ (kN)[22]	7.57[20]/11.36[21]	$V_{L,un}$ (kN)[22]	14.67[21]
$T_{sp,cr}/T_{b,cr}$ (kN)	1.73/2.57	T_m[3] (kN)	21.96[23](5.86)[24]
$M_{tot,cr}$ (kN/m)	1.45[18]	M_m[3] (kN/m)	9.22[23](2.46)[24]
c[19]	0.75[20]/0.5[21]	c[19]	0.5[21]
$V_{L,cr}$ (kN)[22]	1.61[20]/2.42[21]	$V_{L,cr}$ (kN)[22]	17.79[21]

[1] Until the elastic limit (lim) and under cracked conditions (cr)

[2] GeoCalce F Antisismico 2019. Force and moment components are denoted as T_r and M_r respectively

[3] GeoSteel Grid 200 2019. Force and moment components are denoted as T_m and M_m respectively

[4] ½ of the brick's length, here equal to 0.20 m

[5] Average tensile strength of masonry from diagonal compression tests on wallets, Table 16

[6] Average tensile strength of M15 render taken equal to $2 \cdot f_f$, where f_f, according to Lourenco and Gaetani 2022, where f_f is the average flexural strength from flexure tests on prisms (Table 10)

[7] Considered equal to $1.5 f_t$ [Angelillo et al. 2014]

[8] Nominal tensile strength of the fiber mesh, under the combination with shear actions. For the design strength value, a safety factor and an environmental exposure coefficient for the ULS are applied. The Young's modulus is 70 GPa [CNR-DT 215/2018 2020 and GeoSteel Grid 200 2019]

[9] Bed joint thickness

[10] Spandrel clear height from the side of the timber lintel, without considering the height of the timber lintel

[11] Spandrel clear height from the side of the arch, without considering the height of the arch at the level of the springing

[12] Thickness

[13] Two layers of render of 0.01 m of thickness each

[14] Taken as NR/2

[15] l_b: bearing length of timber beam, t_b: width of timber beam and h_b: height of timber beam

[16] Distance from the horizontal plane of the force resultant to the point of the compressive resultant. The distribution of compressive stresses in the section of the spandrel, for a moment action, is considered triangular and uniform, for the elastic and cracked state respectively

[17] Effective depth in shear [ACI 549.4R-13 2013]

[18] Equilibrium of moments at the point of the compressive resultant

[19] Coefficient of the boundary conditions at the end of the spandrel; equal to 1 and 0.5 for cantilever and fixed beam respectively

[20] Spandrel of UN1-US, with the absence of lateral boundary conditions. Here the spandrel is considered semi-fixed on the end of the moving pier

[21] Spandrel of UN2-US and UN1-DS-GR with lateral boundary conditions. Here the spandrel is considered fixed at both ends

[22] Nominal limit shear force at the interface of the pier and spandrel, for uncracked (un) and cracked (cr) conditions (Equation 112)

[23] Nominal strength component of the fiber mesh

[24] Design strength component of the fiber mesh [CNR-DT 215/2018 2020]

Table 41. Analytical formulations, with geometrical and mechanical parameters for the in-plane shear strength in the spandrels of UN1-US, UN2-US, UN1-DS-GR and UN2-DS-GR-FRCM, according to FEMA 356 2000 and NTC 2018.

FEMA 356 2000	UN1-US UN2-US UN1-DS-GR	UN2-DS-GR-FRCM	
	Masonry[1]	Render[2]	Fiber mesh[3]
L (m)	1.20	1.20	1.20
d_{sp} (m)	0.41[4]/0.77[5]	0.41[4]/0.77[5]	0.52[6]/0.77[5]
b_a [7]	2.03	-	-
β	1.0	-	-
b_{sp} (m)[8]	0.41	-	-
t (m)[9]	-	0.02[10]	3.2E-05[3]
f_{ae} (MPa)	0.00	-	-
f_t (MPa)	0.42[11]	2.09[12]	1700[3]
v_{te} (MPa)	0.34[13]	-	-
v_{cun} (MPa)	0.23	-	-
f'_{dt} (MPa)	0.23	2.09[12]	-
f_{fe} (MPa)	-	-	1064[14]
A_f (m^2/m)	-	-	3.2E-05[15]
		[17]/[18]	[19](-)[20]/[18]
V_{spun} (kN)	56.47[16]	24.66/81.13	81.72(21.79)/138.18

NTC 2018	UN1-US UN2-US UN1-DS-GR
	Masonry[1]
l (m)	1.20
t (m)[8]	0.41
h (m)	0.41[4]/0.77[5]
b_s (m)[21]	1
μ	0.577[22]
h_b (m)	0.05
l_b (m)	0.046
Φ	1.09
f_{btd} (MPa)	0.86[23]
f_{vod} (MPa)	0.23[16]
σ_o (MPa)	0.00
$V_{t,lim}$ (kN)	129.92
V_t (kN)	70.46

[1] Shear strength for the masonry spandrel is considered unreduced after cracking
[2] GeoCalce F Antisismico 2019
[3] GeoSteel Grid 200 2019
[4] Spandrel clear height from the side of the timber lintel, without considering the height of the timber lintel
[5] Spandrel clear height from the side of the arch, also considering the height of the arch at the level of the springing
[6] Spandrel clear height from the side of the timber lintel, also considering the height of the timber lintel
[7] Aspect ratio equal to L_{sp}/d_{sp}. Here the average d_{sp} is considered
[8] Thickness of the spandrel
[9] Thickness
[10] Two layers of render of 0.01 m of thickness each
[11] Average tensile strength of masonry from diagonal compression tests on wallets, Table 16
[12] Average tensile strength of M15 render taken equal to $2 \cdot f_f$, where f_f, according to Lourenco and Gaetani 2022, where f_f is the average flexural strength from flexure tests on prisms (Table 10)
[13] Considered equal to $1.5 f_t$ [Angelillo et al. 2014]
[14] Nominal tensile strength of the fiber mesh, under the effect of shear actions. Is noted that for the design strength value, a safety factor and an environmental exposure coefficient for the ULS are applied. The nominal Young's modulus is 70 GPa [CNR-DT 215/2018 2020 and GeoSteel Grid 200 2019]
[15] Area of fiber mesh, per unit length (m^2/m) [GeoSteel Grid 200 2019]
[16] Shear strength of the spandrel considering the average height at the interface and the expected bed-joint bond shear strength under zero vertical stress equal to $0.375 v_{te}$
[17] Nominal strength component of the structural render
[18] Total strength taken as the sum of nominal strengths of subsequent components, under the condition of simultaneous failure [ACI 549.4R-13 2013 and CNR-DT 215/2018 2020]
[19] Nominal strength component of the fiber mesh
[20] Design strength component of the fiber mesh [CNR-DT 215/2018 2020]
[21] Slenderness ratio equal to h_{sp}/L_{sp}. Here the average height between two sides of the spandrel is considered and the recommended range $1.5>b\geq1.0$
[22] Corresponding to a friction angle of 30° [NTC 2018]
[23] Taken equal to $0.1 f_b$ from Table 9 [NTC 2018]

6.6. Conclusions

In general, masonry perforated walls, composed by piers and spandrels, connected to flexible floors, and subjected to in-plane monotonic or cyclic loads, can exhibit a variety of failure modes, under flexure, diagonal or sliding shear, rocking and compressive crushing, with some of which either predominant, but often under a hierarchical and sequential progression. Current building codes account for the coupling of spandrels with adjacent piers, and in-plane spandrel capacity models, besides the relative aspect ratios with the masonry piers, are dependent on the axial and flexural stiffness of masonry, the in-plane boundary conditions, the level of interlocking of brick units at the interfaces with the adjacent piers, the shear contribution at the bed and collar joint planes, as well as the presence of timber lintels, arches and strengthening elements [FEMA 306 1998, NTC 2018].

Considering the experimental works on the in-plane behavior of perforated masonry walls, the level of coupling, especially under the presence of timber lintels and the level of axial stresses in the spandrel are among the dominating parameters that control the response and improve both ductility and capacity [Augenti et al. 2016, Gattesco et al. 2015, Gattesco et al. 2008, Parisi et al. 2014 and Beyer and Dazio 2012]. In fact, the presence of axial stresses in the spandrel increases the shear capacity, under a predominant diagonal shear failure mode. Yet, a realistic representation of axial compressive stresses in the spandrel is proven a challenging task, as it variates throughout the evolution of the in-plane loading, without sufficient field data to serve as validation. In addition, for the experimental testing of perforated walls, being part of a façade, under uniform spans and pier's spacing, and relatively flexible diaphragms, a null or low, constant axial prestress is suggested.

In addition, experimental works in damaged piers and spandrel systems, strengthened with structural grouts, structural renders, with embedded fiber meshes, and horizontal tying actions by metallic ties and angles, have concluded on improving the overall in-plane displacement ductility, shear and flexural strength [Augenti et al.2016 and Gattesco et al. 2015].

The current experimental work aimed on assessing the in-plane capacity and damage due to subsidence, in real scale pier and spandrel masonry assemblies, under the mechanical and geometrical reference of historic solid brick and lime mortar masonry facades. The process of testing protocols involved a vertical differential uplift, applied in one of the piers, and under a

displacement control, in two twin brick masonry assemblies -UN1-US and UN2-US-, with the same vertical prestress and different in-plane boundary conditions. For both assemblies the response was highly ductile, nonlinear, with moderate hardening after yield and almost flattened at the last steps, with a severe loss of shear stiffness within the range of 0.6-0.8$V_{sp,max}$, attributed to the flexural failure in the spandrel, the loss of cohesion at crack interfaces and the splitting of interlocking bricks. Yet, the shear capacity, and displacement ductility in the spandrel was found higher, under a higher in-plane rotational restrain, which allows the progression of the compressive strut and, in accordance, the full evolution of the diagonal shear failure in the spandrel. At the last steps, a stepped, sliding crack was formed in the non-moving pier of both assemblies, which actually denotes that given the presence of strong coupling with timber lintels, the failure of the piers is also eminent and that strengthening schemes that involve both piers and spandrels need to be addressed.

Subsequently, both damaged assemblies -UN1-DS and UN2-DS- were subjected to repair and retrofitting techniques -grouting injections (UN1-DS-GR and UN2-DS-GR-FRCM) and a FRCM system with in-plane adhesive anchors (UN2-DS-GR-FRCM)- and retested, under identical boundary conditions. Both techniques were effective, under sufficient shear capacity and displacement ductility, while the measurement of their dynamic properties, by means of AVT, evidenced the increase in the in-plane stiffness.

In fact, the structural reintegration of the cracked interfaces with a high performance, lime-based fluid mortar, by means of grouting injections, was able to reach the shear capacity of the undamaged masonry, under high hardening stiffness and ductility margins. Crack patterns are organized under the same paths, but often were found to deviate in neighboring joints and bricks.

In the case of the comprehensive retrofit, with the FRCM system and adhesive anchors, the shear tested capacity of the spandrel was found higher by at least 50%, compared to the one of the unstrengthened assembly UN2-US, while no actual peak was reached, given the rocking of the adjoining piers. The corresponding displacement ductility was also improved by 56%.

The framework of mechanical prediction models, from current building codes, for in-plane strength correlation and prioritization in piers and spandrels, subjected to in-plane loading, was also investigated. Here, the analytical expressions and framework from FEMA 306 1998 offers a complete evaluation process for the relative and residual, nominal in-plane strength participation

in flexure, shear, rocking and compressive toe actions, for the piers and spandrel, while considering some adjustments in the formulas, the contribution of timber lintels and in-plane strengthening with a FRCM system could be accounted, under the hypothesis of simultaneous failure. Thus, by assuming stability in load path trajectories of consecutive failure modes, and comparing resulting strength amplitudes, the sequence of flexural and shear diagonal failure in the spandrel, followed by the shear stepped and diagonal sliding, and rocking in the non-moving pier could be matched with the documented ones during the laboratory tests of UN1-DS-GR, UN2-US and UN2-DS-GR-FRCM. Besides, the peak shear capacity in the spandrel, being the result of the dominant failure mode, was approximated analytically and was found almost identical to the experimental one. Important aspects identified, were the condition of fixed ends in the spandrel and the consideration of the lower diagonal shear strength of masonry, matched with the nominal bond strength at the bed joint level, under the effect of cohesion and friction, and in accordance with the vertical axial stresses.

CHAPTER 7. CONCLUSIONS AND FUTURE RESEARCH

CHAPTER 7. Outline

7.1. Introduction

7.2. Summary of conclusions

7.2.1. Implementation and processing aspects on field monitoring of induced ground-borne vibrations

7.2.2. Evaluation of structural damage and failure, under long-term fatigue loading

7.2.3. Quantitative interpretations from tests of differential settlements on piers and spandrel specimens, and the effect of repair and retrofit applications

7.2.4. Structural assessment of buildings of cultural heritage, under multitude actions and long-term effects from differential settlements and ground-borne vibrations

7.3. Future research

7.1. Introduction

The thesis focused on applied experimental testing, analysis, processing and analytical applications in simulated historic masonry assemblies, under the effect of soil settlements and fatigue from induced ground-borne vibrations generated from tunneling and underground railway operations. In addition, field monitoring applications in a cultural heritage building, subjected to induced ground-borne vibrations, served as a supporting process for the design and input of fatigue experimental testing, together with the applicability of data acquisition, instrumentation and post-processing of large size data series. The intended objectives were addressed, while important questions were also raised on the current framework of assessment for cultural heritage buildings, in the proximity of underground railways. Besides the processing and interpretation of experimental data for differential settlements and fatigue, e.g., the results on masonry inelastic behavior, stiffness degradation, resulting cracking and failure, were associated with a comprehensive literature review on: tunneling construction in soft ground, the nature of induced ground-borne vibrations, the configuration of historic masonry facades of the 19th-20th centuries in Europe, numerical applications and the overall assessment framework of both phenomena. Considering that detailed conclusions are presented in each of the respective chapters, a summary of essential conclusions and suggestions for future research are presented in the following sections.

7.2. Summary of conclusions

7.2.1. Implementation and processing aspects on field monitoring of induced ground-borne vibrations

The process of Structural Health Monitoring (SHM) of induced ground-borne vibrations in cultural heritage buildings, in the proximity of operating underground railways, aims at acquiring data of vibration amplitudes, induced frequency range and transfer functions, longitudinally and in elevation, under representative operational periods and probability distributions. Under a direct comparison with threshold values of kinetic quantities from current standards, expressed in velocity terms, safety under the serviceability limit state and associated probabilities of minor damage occurrence can be verified. Certain monitoring and post-processing decisions that reflect on the accuracy of the assessment, are highlighted:

- The necessity of the use of geophones, which provide a direct measurement of velocities;
- a sampling frequency of around ten times the highest frequency of the signal;
- the optimum choice of acquisition locations;
- the firm coupling of instrumentation to structural elements, and,
- performing acquisitions under no ground-borne vibrations, in order to provide a basis for post-processing and low-frequency, noise filtering.

Yet, the probability of structural damage and the assessment framework due to fatigue actions from induced ground-borne vibrations are not clearly established in current standards. In fact, corresponding vibration thresholds would be practically intolerable to occupants, regarding annoyance and disturbance levels. Nevertheless, for damaged cultural heritage buildings and ruins, induced vibration limits for structural damage are under much lower bounds, and thus, concluding on their safety can only be justified through oriented research and advanced structural analyses, focused on damage accumulation and instabilities.

7.2.2. Evaluation of structural damage and failure in masonry, under long-term fatigue loading

As notably stressed, aspects of durability, under long-term effects in historic masonry structures, have not been fully evaluated and many times not incorporated in the structural assessment framework. Under the effect of induced ground-borne vibrations of high amplitude,

e.g., >8 mm/s for an induced frequency range of 50-100 Hz, the possibility of fatigue induced damage, by means of cyclic softening and tensile crack growth in masonry, is eminent, even at a relatively low number of cycles ($\approx 10^5$). Considering the continuous or intermittent nature of induced ground-borne vibrations, the knowledge of residual material properties for masonry and their rate of deterioration over time, is of interest. Of particular use are the formation of fatigue stress and strain curves ($S - N_f$ and $\varepsilon - N_f$), according to the number of cycles until failure N_f. Despite the complex inelastic strain accumulation at the mortar-brick interface and that of the brick units, overall displacement measurements in areas of stress concentration and macro-crack formation, under the knowledge of static and fatigue stress levels, is substantial for monitoring fatigue. Here, it is noted that of particular interest is fatigue loading in masonry under diagonal compression actions, considering the low levels of tensile strength f_t. In particular, at masonry locations of tensile stress concentration, i.e., $\geq 0.70 f_t$, where the transition to macrocracking is already established, or is even closer to failure ($\geq 0.90 f_t$), where crack growth is considered highly unstable, fatigue loading at medium to low levels can lead to immense stiffness degradation and failure, at relatively low number of cycles.

Experimental fatigue loading protocols are configured as cyclic quasi-static sinusoidal loading, with the conversion from ground-borne vibrations to equivalent displacement or force amplitudes, formed through stiffness functions. First and foremost, static and fatigue stress combinations in masonry, to be replicated experimentally, should be defined under in situ observations. Thus, instead of assessing fatigue under constant stress levels, one should also account for progressively increasing static shear stress levels, in case of time-varying loading conditions, e.g., a dead load increase from structural interventions and a change of load paths from settlements, earthquakes or accidental actions.

Here is noted that for the assessment of fatigue loading and corresponding fatigue life in masonry specimens, the knowledge of static mechanical properties and stress-strain curves is essential, but if the variability in tensile strength and stiffness in masonry is high, the assignment of reference values is not advised. Instead, average values can be obtained under a sufficient number of specimens, all constructed and cured under the same conditions. As demonstrated from several tested brick masonry wallets -with and without render-, the normalized, average, ascended part of the quasi-static diagonal compression, stress-strain curve, represents an optimal response, formed under high correlation. Thus, together with the knowledge of the elastic stiffness

of the wallet of interest, obtained under a quasi-static preload, a sufficient estimation of the peak direct shear strength and strain, and the envelop fit curve can be obtained, e.g., with the formulation of Hoshikuma et al 1997.

Considering the outcomes of the fatigue diagonal compression experimental campaign, in simulated historic solid brick and lime mortar masonry wallets, with one-sided, lime-based rendering, the cyclic loading, corresponding to peak particle velocities higher than 8 mm/s, for a 50-100 Hz dominant frequency range, and under a high static diagonal compression, namely in the range of 0.6-0.9f_t, resulted to cracking and local shear failure at relatively low number of cycles, around 10^5-10^6. Here is noted that the shear stiffness evolution during a constant fatigue loading, and under a gradual increase in static loading, follows a somewhat steady decrease, besides the last, tertiary stage, which is considered to increase exponentially. In fact, normalized shear stiffness and strain average fatigue amplitudes, of two complete fatigue loading combinations, until failure, follow the same exponential, reverse power law, with a different multiplying coefficient. This, given the low number of data, can be hypothesized as a function of the static and fatigue stress combination. Thus, in field applications, the possibility of a fatigue induced structural cracking should be investigated, under a direct shear stress state and with the abovementioned ranges, in areas of shear stress concentrations, e.g., windowsills, arches, shear connectors, walls under in-plane actions, etc.

In addition, from the experimental fatigue tests resulting to failure, the constructed fatigue curves for the average direct shear strain ($\gamma_t - N_f$), and the shear secant stiffness ($G_{sec} - N_f$), were fitted with a reversed non-symmetrical sigmoid function of the Gompertz equation, under a high achieved correlation. Such a response, and under a deterministic path, is considered as a fatigue property, namely to a resulting fatigue life, for a specific type of masonry and under a fatigue loading combination. Yet, shear stiffness and tensile strength degradation, during various fatigue load combinations, under the hypothesis of equal fatigue properties, can be associated directly, when normalized with initial values, prior to fatigue. Thus, under end-to-end linear piecewise functions of normalized fatigue properties and normalized fatigue cycles, fatigue life estimates can be attempted for field applications, where failure has not yet reached. Alternatively, fatigue life curves, e.g., stress ($S - N_f$) or strain ($\varepsilon - N_f$) based, can be constructed, for various fatigue and static stress levels, and according to the current framework [Carpinteri and Paggi 2009, BD 91/04-14 and Dowling 2007]. Nevertheless, the statistical reliability of fatigue normalized functions needs

to be optimized with a sufficient number of experimental fatigue tests. One should also account the difficulty of obtaining statistical distribution parameters of fatigue data, under the effect of many variables, i.e., different masonry typologies, principal actions under tension, compression or bending, and at every stress level. Also, of importance is the association of fatigue curves with induced ground-borne vibration limits from standards, which can be established through secant stiffness trends, and according to applied static stress levels.

In fact, once the above-mentioned fatigue life properties are defined, field monitoring protocols of fatigue from induced groundborne vibrations in a cultural heritage building, associated to a specific masonry type, should include the following:

- A monitoring process of induced groundborne vibrations should conclude on the amplitude, frequency and spatial distribution of the input fatigue parameters. Also, acquiring the distribution of groundborne vibration amplitudes in various locations of the structure, focusing on plausible amplifications;
- material properties for the structural elements of interest should be established, either by experimental or in-situ testing. Considering field tests, the local stress state, the compressive and shear capacity can be established, with the use of minor destructive testing, e.g., single and double compressive and shear flat jack tests, mortar bed joint shear resistance tests, etc.;
- nonlinear static FE analyses should conclude on the stress-strain distribution, mainly identifying direct shear stress concentration areas. Here, the use of phased analysis techniques, following construction sequences and anticipated changes in structural elements and load paths, are of importance;
- a correlation of stress concentration areas, with those under high induced vibration amplitudes should conclude on the most prominent areas for in-situ monitoring acquisitions for fatigue;
- statistical formulations on the remaining life and expected failure, according to the Miner's rule and identified bins of vibration amplitudes, can result to safety factors, of either critical fatigue stress levels or cycles, and,
- long-term monitoring, with the installation of strain gauges, attached in masonry, covering high direct shear stress zones and existing crack patterns, which aim on following potential positive trends in strain softening, together with temperature compensation. Here is noted that from the experimental fatigue tests, the strain gauges were found beneficial, as they can capture

fatigue strain reversals and can exhibit positive or negative trends, following the evolution of macrocracks.

Considering the design and assessment approach of building codes for fatigue, reduction coefficients assigned for the material design fatigue strength, e.g., in EN 1992.1.1:2004, and for the ULS, is found equal to 1.8, accounting for the nominal strength, and are considered in line with the outcomes of the conducted fatigue shear tests.

Besides, for fatigue loading, the process of structural assessment in cultural heritage buildings should also include reduction coefficients, similarly to the assessment for creep, accounting for the stiffness degradation in masonry. Thus, considering the maximum decay in the values of shear modulus found in this work, a fatigue overall reduction coefficient, for the nominal shear modulus in the range of 1.5, applies.

7.2.3. Quantitative interpretations from tests of differential settlements on piers and spandrel specimens, and the effect of repair and retrofit applications

In general, the in-plane capacity of masonry perforated walls, composed by piers and spandrels, and connected to flexible floors, under the influence of in-plane earthquake forces or differential vertical settlements, is influenced by the coupling of spandrels with the adjacent piers, also acknowledged by current building codes. Among the main parameters for the in-plane capacity, overall ductility and sequential progression of failure modes are the geometric configuration of the spandrel, namely the aspect ratio with respect to the piers, the in-plane boundary conditions, by means of axial vertical prestress in the piers and horizontal prestress or restrain in the spandrel, the level of interlocking of brick units at the spandrel's interfaces with the adjacent piers, the shear bond at the bed and collar joints, the presence of timber lintels, arches and strengthening elements, as demonstrated in FEMA 306 1998, NTC 2018, Gattesco et al. 2015 and Beyer and Dazio 2012.

According to their relative influence, a hierarchical progression of different failure modes is expected, under flexure, diagonal or sliding shear, rocking and compressive crushing, both for the piers and spandrels, also accounting that load trajectories are not expected to alter significantly after each failure.

Considering the experimental works on the in-plane behavior of perforated walls, of simulated historic solid brick and lime mortar masonry, with equal size and spacing for piers, and tested under a vertical asymmetrical uplift, the in-plane capacity and respective damage, transitioned from an initial flexural failure in the spandrel interfaces, through vertical shear cracks, to a diagonal shear failure in the spandrel, mostly through a stepped sliding crack at the beds joints, to a final, sliding, shear crack in one of the piers, combined with rocking. The overall response is documented as highly ductile, nonlinear, with moderate hardening and almost flattened at the last steps.

Other aspects to be highlighted during testing are:

- The increased shear capacity and displacement ductility under the increase of in-plane rotational restrain for the moving pier;
- the avoidance of collapse for the spandrel, after its rocking failure, given the presence of the timber lintel;
- the yielding point of the structural system, identified at 0.6-0.8 times of the maximum shear capacity, is attributed to the flexural failure in the spandrel, the progressive loss of cohesion at crack interfaces and the splitting of interlocking bricks;
- the secondary sliding shear failure in one of the piers, as a result of the counteraction with the timber lintel and the compressive strut in the spandrel, denotes the need of strengthening schemes in masonry perforated walls that address the in-plane capacity and failure of both piers and spandrels.

The applicability and effectiveness of repair and strengthening schemes, namely grouting injections and a Fiber Reinforced Cementitious Matrix system (FRCM), with in-plane (in thickness) FRCM anchors, in masonry perforated walls, under prior extensive in-plane cracking, were investigated experimentally in the current research work. Both techniques were found effective in providing sufficient shear capacity and displacement ductility.

Solely by structural repairs of cracked interfaces, by means of grouting injections, with a high performance, lime-based fluid mortar, the measured shear capacity was fully reintegrated, also under higher hardening stiffness and ductility margins, compared to the undamaged masonry

assembly. Here, crack patterns followed similar paths, deviating slightly to neighboring joints and bricks.

In the case of the retrofit, with grouting injections and the FRCM system with FRCM anchors, the shear tested capacity and displacement ductility of the structural system was found higher by at least 50% and 56% respectively, compared to the undamaged masonry assembly, and considering that no actual peak was reached, due to the subsequent rocking of the adjoining piers.

Considering the complex interaction of unstrengthened piers and spandrels, under boundary conditions of rotational restrain for piers, and the framework of mechanical prediction models, namely the analytical expressions from FEMA 306 1998, for the relative and residual, nominal in-plane strength in flexure, shear, rocking and compressive toe actions, those were found in optimum agreement with experimental results, under differences within the range of 2-3%. Important aspects to consider in the analytical models are: the contribution of the timber lintels in shear plane actions, along their embedment length; the exemption of the arch height for the consideration of the compressive strut action, given its prior flexural failure; the adjustment of a corrective coefficient considering the level of lateral restrain conditions of the spandrel, and, the assignment for the lower diagonal shear strength of masonry, namely the nominal bond strength at the bed joint level, under the effect of cohesion, friction, and the vertical axial stresses.

In addition, the contribution of the FRCM system can be also accounted analytically, considering some adjustments in the formulas from FEMA 306 1998 and ACI 549.4R-13 2013 and CNR-DT 215/2018 2020, and under the hypothesis of simultaneous in-plane failure of structural systems, working together in a section.

7.2.4. Structural assessment of buildings of cultural heritage, under multitude actions and long-term effects from differential settlements and ground-borne vibrations

Under the perspective of structural assessment for cultural heritage buildings, and accounting for unavoidable computational restrictions, a fully integrated multi-hazard structural response is rarely conducted. For a structure in the proximity of underground railways, and under the effect of settlements and induced ground-borne vibrations, but also accounting other potential hazards, e.g., earthquakes, a combined process of structural assessment is particularly complex,

especially when homogeneous 3D FE models are used, with constitutive material models that do not account for cyclic deterioration.

Considering the modelling of a phased nonlinear response and a cumulative damage propagation, under the combined effect of settlements, fatigue and earthquakes, and under the commonly used smeared crack models for masonry, the use of corrective coefficients on the nominal material properties, accounting for fatigue strength, over a specific number of cycles, is considered acceptable. Yet, one should also account that fatigue actions are mostly localized, under the exact combination of static and cyclic actions, and thus, modelling of a progressive material deterioration due to fatigue, by means of reduced material properties, should be conducted only in partial FE models. For larger FE models, in order to follow the evolution of material cyclic softening due to fatigue, in many potential areas, and also account for changes in load paths, 3D material constitutive models with updated yield surfaces are needed, which account for the inelastic cumulative strains and damage under each cycle.

In fact, a 3D orthotropic smeared crack and crack band model, for cementitious materials, part of the material library in ATENA FE software, fully incorporates fatigue tensile damage [Červenka et al. 2021]. Here, for the total accounted tensile strain ε_{ij}, decomposed into an elastic ε_{ij}^{e}, plastic ε_{ij}^{p} and fracturing ε_{ij}^{f} strain, an additional fracturing strain increment $\varepsilon_{fatigue}$ is added after N_i cycles, which is a percentage of the failing strain after N_f cycles. Defined material parameters include the knowledge of S-N curves of the material, determined from experiments, and incorporated in Equation 113, with $\beta_{fatigue}$ a material constant, mostly defined within a range of static tensile stresses, R is the ratio between the minimum σ_{min} and maximum σ_{max} fatigue tensile stresses, and f_t is the static tensile strength. Thus, the need for determining experimentally probabilistic distribution functions for fatigue in masonry, accounting for different masonry typologies, material constituents, and a full range of static and cyclic stress combinations, is signified as essential in incorporating fatigue damage into multi-hazard assessment processes for cultural heritage buildings.

$$\frac{\sigma_{max}}{f_t} = 1 - \beta_{fatigue}(1 - R)\log N_f \qquad \text{Equation 113}$$

7.3. Future research

Among the aspects dedicated to future works, are the reproduction of the experimental results in masonry piers and spandrel specimens, under the effect of monotonic differential displacements, with nonlinear FE models, under updated boundary conditions and considering the material characterization tests. The aim is set on the comparison of the associated cracking and deformation, and validating the effectiveness of repair and retrofitting techniques. Additionally, numerical applications, under the effect of cyclic tensile fatigue loading will be attempted. In specific, the following strategy for numerical modelling is proposed:

1. FEM for tested assemblies UN1-US and UN2-US:

(a) A homogeneous FEM for the masonry assemblies and the steel frame, testing setup. Introduction of a movable base with interface elements and lateral restrain with springs;

(b) first updating of masonry stiffness and interfaces, according to the dynamic response, under a constant axial prestress in the piers;

(c) second updating of the boundary conditions for the piers, by calibrating the stiffness of interfaces and springs, according to the acquired data from the LVDTs, and,

(d) nonlinear static analyses under a vertical displacement uplift.

2. FEM for the tested assembly, after damage, followed by structural grouting (UN1-DS-GR):

(a) A homogeneous FEM for UN1-DS-GR, updated with interfaces, replicating cracks, filled with high performance grout;

(b) updating of the interface stiffness of reintegrated cracks, according to the dynamic response, under a constant axial prestress in the piers, and,

(c) nonlinear static analyses under a vertical displacement uplift.

3. FEM for the tested assembly, after damage, followed by structural retrofit (UN2-DS-GR-FRCM):

(a) A homogeneous FEM for UN2-DS-GR-FRCM, updated with interphases, replicating cracks, filled with high performance grout, and the FRCM system with FRCM anchors;

(b) first updating of the stiffness of the cementitious matrix and fiber mesh according to the dynamic response, under a constant axial prestress in the piers, and,

(c) Nonlinear phased and static analyses under a vertical displacement uplift.

4. FE analyses replicating tests on wallets DCf2, DCf3 and DCf4 under diagonal compression fatigue loading, accounting for a 3D orthotropic smeared crack and crack band model, which incorporates fatigue fracturing strain.

5. FE analyses combining the effect of settlements and fatigue from induced vibrations, accounting for a 3D orthotropic smeared crack and crack band model, which incorporates fatigue fracturing strain.

REFERENCES

[1] 27A (2019). Reinforcement for actions in-plane and out-of-plane in masonry by whidespread rendering with natural basalt fiber mesh and stainless steel, and GEOMALTA® certified EN 998 based on pure natural hydraulic lime NHL 3.5, Kerakoll Products, Kerakoll S.p.A., Italy.

[2] ABAQUS (2009). Abaqus 6.11 Theory Manual, Dassault Systèmes Simulia Corp., USA.

[3] Abrams, D., Noland, J., Atkinson, R., Waugh, P. (1985). Response of Clay-Unit Masonry to Repeated Compressive Forces.

[4] ACI 549.4R-13 (2013) Guide to Design and Construction of Externally Bonded Fabric-Reinforced Cementitious Matrix (FRCM) Systems for Repair and Strengthening Concrete and Masonry Structures, ACI, USA.

[5] Adell Argilés, J. M. (1992). 19th century brick architecture: rationality and modernity, Informes de La Construcción, 44(421), 5–15 (in Spanish). (doi.org/10.3989/ic.1992.v44.i421.1309)

[6] Alliche, A. (2004)Damage model for fatigue loading of concrete, International Journal of Fatigue, Vol. 26, pp. 915–921. (doi:10.1016/j.ijfatigue.2004.02.006)

[7] Almeida, A.P.P.J. Pereira, E. B., Barros, A.O. J. (2015). Assessment of overlay masonry strengthening system under in-plane monotonic and cyclic loading using the diagonal tensile test, Construction and Building Materials, Vol. 94, pp. 851-865. (doi.org/10.1016/j.conbuildmat.2015.07.040)

[8] Alshebani, M., Sinha, S., (1999). Cyclic biaxial stress-strain curves of masonry: a generalized approach. Structures and Buildings, 146(2), pp. 141-145.

[9] Amorosi, A., Boldini, D., Felice, G. D., Malena, M., & Sebastianelli, M. (2014). Tunnelling-induced deformation and damage on historical masonry structures, Géotechnique, 64(2), 118-130. (doi:10.1680/geot.13.p.032)

[10] Andersen, L., Jones, C. (2006). Coupled boundary and finite element analysis of vibration from railway tunnels—a comparison of two- and three-dimensional models. Journal of Sound and Vibration, 293(3-5), 611-625. doi:10.1016/j.jsv.2005.08.044

[11] Andrews, J., Buehler, D., Gill, H., Bender, W. L. (2013). Transportation and construction vibration – Guidance manual September, California Department of Transportation, Division of Environmental Analysis, Environmental Engineering.

[12] Angelillo M., Lourenço P.B., Milani G. (2014). Masonry behavior and modelling, Mechanics of Masonry Structures, CISM International Centre for Mechanical Sciences Volume 551, pp 1-26 (DOI 10.1007/ 978-3-7091-1774-3_1)

[13] Apolo, G. L., Martínez-Luengas, A. L. (1995). Técnicas de intervención en el patrimonio arquitectónico. Tomo I. Reestructuración en madera, Consultores Técnicos de Construcción, Spain (In Spanish).

[14] ASTM C469/C469M-14 (2014). Standard Test Method for Static Modulus of Elasticity and Poisson's Ratio of Concrete in Compression, ASTM International, West Conshohocken, PA. (www.astm.org)

[15] ASTM C67/C67M-20 (2020). Standard Test Methods for Sampling and Testing Brick and Structural Clay Tile, ASTM International, West Conshohocken, PA. (www.astm.org)

[16] ASTM E111-17 (2017). Standard Test Method for Young's Modulus, Tangent Modulus, and Chord Modulus, ASTM International, West Conshohocken, PA. (www.astm.org)

[17] Attewell, P. B. & Woodman, J.P. (1982). Predicting the dynamic of ground settlement and its derivatives caused by tunneling in soil. Ground Engineering 15(7), 13-22

[18] Attewell, P. B., Yeates, J., Selby, A. R. (1986). Soil movements induced by tunneling and their effects on pipelines and structures. Blackie, Glasgow.

[19] Augenti, N., Graziotti, F., Magenes, G., Parisi, F. (2016) Experimental researches on the seismic behaviour of masonry spandrels: An international perspective Research Report, EUCENTRE, Pavia, Italy. (ISBN: 978-88-6198-124-9)

[20] Bai, Y., Xu, Z.D. (2019). Structural dynamics. John Wiley & Sons, Inc.

[21] BD 91/04-14 (2004) Design Manual for Roads and Bridges, Volume 2 Highway Structures: Design (Substructures and Special Structures) Materials, Section 2 Special Structures, Part 14, Unreinforced Masonry Arch Bridges, Stationery Office, London.

[22] Benovolo L. (1971). History of modern architecture, Volume I: The tradition of modern architecture, M.I.T. Press, Cambridge, Massachusetts, USA.

[23] Bergdoll B. (2000). European Architecture 1750-1890, Oxford University Press, N.Y., USA.

[24] Beyer, K. (2012) Peak and residual strengths of brick masonry spandrels, Engineering Structures, Volume 41, pp. 533-547. (DOI: 10.1016/j.engstruct.2012.03.015)

[25] Beyer, K. and Dazio, A. (2012) Quasi-Static Cyclic Tests on Masonry Spandrels, Earthquake Spectra, Volume 28, No. 3, pp. 907–929. (DOI: 10.1193/1.4000063)

[26] Bickel, J. O., Kuesel, T. R. (1982). Tunnel engineering handbook. New York: Van Nostrand Reinhold Co.

[27] Binda L. ed. (2008). Learning from failure, Long-term behavior of heavy masonry structures, Southampton: WIT Press.

[28] Binda, L., Cantini, L., Cardani, G., Saisi, A. Tiraboschi, C. (2007). Use of flat-jack and sonic tests for the qualification of historic masonry, Conference Proceedings the 10th North American Masonry Conference, St. Louis, Missouri, USA.

[29] Binda, L., Ignoul, S., Schueremans, L., Verstrynge, E., Oliveira, D., Lourenco, P.B., Modena, C. (2008). Long term compressive testing of masonry - Test procedure and practical experience, Structural Analysis of Historic Construction: Preserving Safety and Significance, pp. 1357-1361. (doi:10.1201/9781439828229.ch155)

[30] Bormann, P., Wielandt, E. (2013). Seismic Signals and Noise. - In: Bormann, P. (Ed.), New Manual of Seismological Observatory Practice 2 (NMSOP2), Potsdam : Deutsches GeoForschungsZentrum GFZ, pp. 1–62. (doi: http://doi.org/10.2312/GFZ.NMSOP-2_ch4)

[31] Boroschek, R. L., Legrand, D. (2006). Tilt Motion Effects on the Double-Time Integration of Linear Accelerometers: An Experimental Approach. Bulletin of the Seismological Society of America, 96(6), 2072-2089. (doi:10.1785/0120050167)

[32] Boscardin, M. D., Cording, E. J. (1989). Building response to excavation induced settlement. Journal of Geotechnical Engineering, 115(1), 1–21.

[33] Bozzano, C., Podestà, S., Scandolo, L., Brignola A. (2013). Diagonal compression tests on two-part walls: the influence of headers, XV ANIDIS seismic engineering conference, Padua (in Italian)

[34] Brandt, A. (2011). Noise and vibration analysis signal analysis and experimental procedures, Wiley, West Sussex, UK.

[35] Brandt, A., Brincker, R. (2014). Integrating time signals in frequency domain – Comparison with time domain integration. Measurement, 58, 511-519. (doi:10.1016/j.measurement.2014.09.004)

[36] Breitenbucher, R., Ibuk, H. (2006). Experimentally based investigations on the degradation-process of concrete under cyclic load, Materials and Structures, Vol 39, pp.717–724. (DOI: 10.1617/s11527-006-9097-9)

[37] Brignola, A., Frumento, S., Lagomarsino, S., Podestà, S. (2009). Identification of Shear Parameters of Masonry Panels through the In-Situ Diagonal Compression Test, International Journal of Architectural Heritage, 3:1, 52-73. (DOI: 10.1080/15583050802138634)

[38] Brooks, J. J. (2015). Concrete and Masonry Movements, Chapter 5 - Elasticity of Masonry, Butterworth-Heinemann, pp. 95-136. (DOI: 10.1016/B978-0-12-801525-4.00005-4)

[39] BS 5228-2:2009+A1:2014 (2014). Code of practice for noise and vibration control on construction and open sites – Part 2: Vibration, British Standard.

[40] BS 7385-2:1993 (1993). Evaluation and measurement for vibration in buildings, Guide to damage levels from groundborne vibration, British Standard.

[41] BS EN 10080 (2005). Steel for the reinforcement of concrete - Weldable reinforcing steel – General, BSI British Standards.

[42] BS EN 1015-10:1999 (1999). Methods of test for mortar for masonry - Part 10: Determination of dry bulk density of hardened mortar, CEN, Brussels.

[43] BS EN 1015-11:1999 (1999). Methods of test for mortar for masonry - Part 11: Determination of flexural and compressive strength of hardened mortar, CEN, Brussels.

[44] BS EN 1015-2:1998 (1998). Methods of test for mortar for masonry-Part 2: Bulk sampling of mortars and preparation of test mortars, CEN, Brussels.

[45] BS EN 1015-3:1999 (1999). Methods of test for mortar for masonry - Part 3: Determination of consistence of fresh mortar (by flow table) +A1:2004, CEN, Brussels.

[46] BS EN 1052-1:1999 (1999). Methods of test for masonry - Part 1: Determination of compressive strength, CEN, Brussels.

[47] BS EN 12390-5:2019 (2019). Testing hardened concrete – Part 5: Flexural strength of test specimens, CEN, Brussels.

[48] BS EN 459-1:2010 (2010). European Standard: Building lime - Part 1: Definitions, specifications and conformity criteria, CEN, Brussels.

[49] BS EN 771-1:2011 (2011). Specification for masonry units – Part 1: Clay masonry units (+A1:2005), CEN, Brussels.

[50] BS EN 772-1:2011 (2011). Methods of test for masonry units. Determination of compressive strength +A1:2015, CEN, Brussels.

[51] BS EN 772-3:1998 (1998). Methods of test for masonry units - Part 3: Determination of net volume and percentage of voids of clay masonry units by hydrostatic weighing, CEN, Brussels.

[52] BS EN 998-2:2003 (2003). Specification for mortar for masonry - Part 2: Masonry mortar, CEN, Brussels.

[53] Burd, H.J., Dphil, M.A., Houlsby, G.T., Augarde, C.E., Liu, G. (2000). Modelling tunnelling-induced settlement of masonry buildings. Proc Instn Civ Eng Geothech Eng, 143, 17–29.

[54] Burland, J.B, Wroth, C.P. (1974). "Settlement of Buildings and Associate Damage," Proceedings of a Conference on Settlement of Structures, Cambridge, pp. 611-654.

[55] C 597-02 (2003). Standard Test Method for Pulse Velocity Through Concrete. ASTM International, United States.

[56] Camino Olea M. S. (2001). Construcción y ornamentación de las fachadas de ladrillo prensado, al descubierto, en la ciudad de Valladolid, PhD Thesis, E. T. Superior de Arquitectura, Universidad Politécnica de Madrid, Madrid, Spain (in Spanish).

[57] CAN/CSA S304.1-04 (2004). Design of Masonry Structures. Canadian Standards Association, Mississauga, Ontario, Canada.

[58] Cardoso, R., Lopes, M., Bento, R., D'Ayala D. (2014). World Housing Encyclopedia: A Resource on Construction in Earthquake Regions, Housing Report 92, Historic, braced frame timber buildings with masonry infill ('Pombalino' buildings), World Housing Encyclopedia, EERI and IAEE (http://www.world-housing.net/)

[59] Carozzi, F.G., D'Antino, T. and Poggi, C. (2018) In-situ experimental tests on masonry panels strengthened with Textile Reinforced Mortar composites, Procedia Structural Integrity, Vol 11, pp. 355–362. (DOI: 10.1016/j.prostr.2018.11.046)

[60] Carpinteri, A., Grazzini, A., Lacidogna, G., Manuello, A. (2014). Durability evaluation of reinforced masonry by fatigue tests and acoustic emission technique, Struct. Control Health Monit., Vol. 21, pp. 950–961. (doi: 10.1002/stc.1623)

[61] Carpinteri, A., Paggi, M. (2009). A unified interpretation of the power laws in fatigue and the analytical correlations between cyclic properties of engineering materials, International Journal of Fatigue, Vol 31, pp. 1524-1531. (doi:10.1016/j.ijfatigue.2009.04.014)

[62] Casas, J. R. (2009). A probabilistic fatigue strength model for brick masonry under compression, Construction and Building Materials, Volume 23, Issue 8, pp. 2964-2972. (doi.org/10.1016/j.conbuildmat.2009.02.043)

[63] Casas, J. R., (2010). Reliability-based assessment of masonry arch bridges. Construction and Building Materials, 25(2011), pp. 1621-1631.

[64] Cavalagli, N., Comanducci, G., Ubertini, F. (2017). Earthquake-Induced Damage Detection in a Monumental Masonry Bell-Tower Using Long-Term Dynamic Monitoring Data, Journal of Earthquake Engineering, 22(sup1), 96–119. (DOI: 10.1080/13632469.2017.1323048)

[65] CEB-FIP. Model Code 90 (1993). CEB/FIP Model Code for Concrete Structures, Euro-International Committee from Concrete (CEB), Thomas Telford Ltd., UK.

[66] Červenka, V., Jendele, L. and Červenka, J. (2021) ATENA Program Documentation Part 1, Theory, Červenka Consulting s.r.o.

[67] Chabat, P. (1886). La Brique et la Terre Cuite. Étude historique; fabraication et usages. Paris (In French).

[68] Chabat, P. (1989). Victorian brick and terra-cotta architecture in full color: 160 plates. New York: Dover.

[69] Cheng, C.Y., Dasari, G.R., Chow, Y.K., Leung, C.F. (2007). Finite element analysis of tunnel–soil–pile interaction using displacement controlled model, Tunnelling and Underground Space Technology, Volume 22, Issue 4, pp. 450-466. (https://doi.org/10.1016/j.tust.2006.08.002)

[70] Ching, D.K. F., Jarzombek M., Prakash V. (2017). A Global History of Architecture, Third Edition, John Wiley & Sons, New Jersey, USA.

[71] CNR-DT 215/2018 (2020). Guide for the Design and Construction of Externally Bonded Fibre Reinforced Inorganic Matrix Systems for Strengthening Existing Structures, CNR – Advisory Committee on Technical Recommendations for Construction, Rome.

[72] Como M. (2016). Springer Series in Solid and Structural Mechanics, Volume 5, Springer International Publishing AG, Switzerland (DOI 10.1007/978-3-319-24569-0)

[73] Concrete Material Use Strain Gauge (2021). Concrete Material Use Strain Gauge, Tokyo Measuring Instruments Laboratory Co., Ltd. (n.d.). https://tml.jp/e/product/strain_gauge/concrete.html.

[74] Corradi, M., Sisti, R., Borri, A. (2018). Effect of Thin Cement-Based Renders on the Structural Response of Masonry Wall Panels, Applied Sciences, Vol 8, pp. 98. (doi:10.3390/app8010098)

[75] Costigan, A., Pavía, S., Kinnane O. (2015). An experimental evaluation of prediction models for the mechanical behavior of unreinforced, lime-mortar masonry under compression, Journal of Building Engineering, Vol 4, pp. 283–294. (http://dx.doi.org/10.1016/j.jobe.2015.10.001)

[76] Cowper, G. R. (1966). The shear coefficient in Timoshenko's beam theory, Journal of Applied Mechanics, 33,335-340.

[77] CPC8 (1975). Rilem Technical Recommendations for the Modulus of elasticity of concrete in compression, TC14-CPC, E & FN Spon, London.

[78] D'Ambraa, C., Lignola, G. P., Prota, A., Sacco, E. and Fabbrocino, F. (2018) Experimental performance of FRCM retrofit on out-of-plane behaviour of clay brick walls, Composites Part B, Vol 148, pp. 198–206. (https://doi.org/10.1016/j.compositesb.2018.04.062)

[79] Day, R. W. (1999) Geotechnical and foundation engineering: design and construction. New York: McGraw-Hill.

[80] Diana user's manual. (2020). DIANA FEA, DIANA Documentation, Release 10.4, Retrieved March 11, 2021, from https://dianafea.com/manuals/d104/Diana.html, DIANA FEA BV.

[81] DIN 4150-3 (2016). Structural vibration in buildings – Effects on structures. Deutsches Institut für Normung.

[82] DIN 45669-2:1995-06 (1995). Mechanical vibration and shock measurement, Part 1 Measuring equipment, Part 2 Measurement procedure, Deutsches Institut für Normung.

[83] Dominguez J. (1993). Boundary Elements in Dynamics. Computation Mechanics Publications, Southampton.

[84] Dowling, N.E. (2007). Mechanical Behavior of Materials: Engineering Methods for Deformation, Fracture, and Fatigue, Pearson Prentice Hall: Upper Saddle River, NJ, USA, 2007.

[85] Drysdale, R. G., Hamid, A. A., and Baker, L. R. (1994). Masonry structures: Behaviour and design, Prentice-Hall, Englewood Cliffs, N.J.

[86] Dvorkin, E. N., Cuitiño, A. M., Gioia, G. (1989) A concrete material model based on non-associated plasticity and fracture. Engineering Computations, Vol 6(4), pp. 281–294. (https://doi.org/10.1108/eb023783)

[87] EN 1990 (2002). Basis of structural design, CEN, Brussels.

[88] EN 1992-1-1 (2004). Design of concrete structures - Part 1-1: General rules and rules for buildings, CEN, Brussels.

[89] EN 1996-1-1 (2005). Design of masonry structures - Part 1-1: General rules for reinforced and unreinforced masonry structures, CEN, Brussels.

[90] EN 1998-1 (2004). Eurocode 8: Design of structures for earthquake resistance - Part 1: General rules, seismic actions and rules for buildings, CEN, Brussels.

[91] EN 338 (2009) Structural timber - Strength classes, European Committee for Standardization, Brussels.

[92] EN 998-1 (2016). Specification for mortar for masonry - Part 1: Rendering and plastering mortar, CEN, Brussels.

[93] Esveld. C. (2001). 'Modern Railway Track', 2nd edition, MRT Productions, Zaltbommel.

[94] Ewing, B. D., Kowalsky, M. J. (2004). "Compressive behavior of unconfined and confined clay brick masonry." J. Struct. Eng., 130(4), 650–661.

[95] Facconi, L., Minelli, F., Vecchio, J. F. (2018). Predicting Uniaxial Cyclic Compressive Behavior of Brick Masonry: New Analytical Model, Journal of Structural Engineering, 144(2): 04017213. (DOI: 10.1061/(ASCE)ST.1943-541X.0001961)

[96] Fargnoli, V., Boldini, D., Amorosi A. (2013). TBM tunneling- induced settlements in coarse-grained soils: the case of the new Milan underground line 5, Tunn Undergr Sp Tech, 38, 336–47.

[97] Feenstra, P. H. (1993). Computational Aspects of Biaxial Stress in Plain and Reinforced Concrete, PhD thesis, Delft University of Technology.

[98] FEMA 274 (1997). NEHRP commentary on the guidelines for the seismic rehabilitation of buildings, ASCE for the Federal Emergency Management Agency, Washington, D.C., US.

[99] FEMA 306 (1998). Evaluation of earthquake damaged concrete and masonry wall buildings, ASCE for the Federal Emergency Management Agency, Washington, D.C., US.

[100] FEMA 308 (1998). Evaluation of earthquake damaged concrete and masonry wall buildings, ASCE for the Federal Emergency Management Agency, Washington, D.C., US.

[101] FEMA 356 (2000). Prestandard and Commentary for the Seismic Rehabilitation of Buildings, ASCE for the Federal Emergency Management Agency, Washington, D.C., US.

[102] Fernandes, M. F., Lourenço, B. P., Castro, F. (2009). Materials, Technologies and Practice in Historic Heritage Structures, Chapter 3, Ancient Clay Bricks: Manufacture, and Properties, Science Business and Media B.V. (DOI 10.1007/978-90-481-2684-2_3)

[103] FIB Model Code (2013) FIB Model Code for Concrete Structures 2010, International Federation for Structural Concrete, Lausanne, Switzerland.

[104] Forrest, J., Hunt, H. (2006). A three-dimensional tunnel model for calculation of train-induced ground vibration. Journal of Sound and Vibration, 294(4-5), 678-705. (doi:10.1016/j.jsv.2005.12.032)

[105] Franzius, J. N., Potts, D. M., Burland, J. B. (2006). The response of surface structures to tunnel construction. Proceedings of the Institution of Civil Engineers, Geotechnical Engineering 159, Issue GE1, 3–17.

[106] Gattesco, N. and Boem I. (2015) Experimental and analytical study to evaluate the effectiveness of an in-plane reinforcement for masonry walls using GFRP meshes, Construction and Building Materials, Vol 88, pp. 94–104. (http://dx.doi.org/10.1016/j.conbuildmat.2015.04.014)

[107] Gattesco, N., Macorini, L., Dudine, A. (2015) Experimental Response of Brick-Masonry Spandrels under In-Plane Cyclic Loading, J. Struct. Eng., 04015146. (DOI: 10.1061/(ASCE)ST.1943-541X.0001418)

[108] Gazonas, G.A., Scheidler, M.J., Velo, A.P. (2015) Exact analytical solutions for elastodynamic impact, International Journal of Solids and Structures, Vol 75–76, pp. 172–187. (http://dx.doi.org/10.1016/j.ijsolstr.2015.08.011)

[109] GB/T 50452 (2008) Technical specifications for protection of historic buildings against man-made vibration, China National Standards.

[110] Gentile, C., Guidobaldi, M., Saisi, A. (2016). One-year dynamic monitoring of a historic tower: damage detection under changing environment, Meccanica, 51(11), 2873–2889. (doi: 10.1007/s11012-016-0482-3)

[111] GeoCalce F Antisismico (2019). Repair and reinforcement of reinforced concrete and masonry natural geo-mortars for structural and anti-seismic reinforcement of walls, GeoCalce® F Antisismico, Kerakoll Products, Kerakoll S.p.A., Italy. (https://products.kerakoll.com/en/p/geocalce-f-antisismico)

[112] GeoCalce FL Antisismico (2019). Repair and reinforcement of reinforced concrete and masonry natural geo-mortars for structural and anti-seismic reinforcement of walls, GeoCalce® FL Antisismico, Kerakoll Products, Kerakoll S.p.A., Italy. (https://products.kerakoll.com/en/p/geocalce-fl-antisismico)

[113] GeoSteel Grid 200 (2019). Repair and reinforcement of reinforced concrete and masonry, Steel bars, fabrics and accessories for structural and anti-seismic reinforcement of concrete and masonry, GeoSteel 600, Kerakoll Products, Kerakoll S.p.A., Italy.

[114] GeoSteel Injector&Connector (2019). Repair and reinforcement of reinforced concrete and masonry, Steel bars, fabrics and accessories for structural and anti-seismic reinforcement of concrete and masonry, GeoSteel Injector&Connector, Kerakoll Products, Kerakoll S.p.A., Italy.

[115] Gere, J. M. and Timoshenko, S. (1972). Mechanics of materials. New York: Van Nostrand Reinhold Co.

[116] Ghangale, D., Colaço, A., Alves Costa, P., and Arcos, R. (2019). A Methodology Based on Structural Finite Element Method-Boundary Element Method and Acoustic Boundary Element Method Models in 2.5D for the Prediction of Reradiated Noise in Railway-Induced Ground-Borne

Vibration Problem, ASME. J. Vib. Acoust. June 2019; 141(3): 031011. (https://doi.org/10.1115/1.4042518)

[117] Giardina, G., Graaf, A. V., Hendriks, M. A., Rots, J. G., & Marini, A. (2013). Numerical analysis of a masonry façade subject to tunnelling-induced settlements. Engineering Structures, 54, 234-247. (doi:10.1016/j.engstruct.2013.03.055)

[118] Giardina, G., Marini, A., Hendriks, M. A., Rots, J. G., Rizzardini, F., & Giuriani, E. (2012). Experimental analysis of a masonry façade subject to tunnelling-induced settlement. Engineering Structures, 45, 421-434. (doi:10.1016/j.engstruct.2012.06.042)

[119] Giron-Sierra, J. M. (2018). Digital signal processing with Matlab examples, Volume 1: Signals and data, filtering, non-stationary signals, modulation, Springer. (doi: 10.1007/978-981-10-2534-1)

[120] Glinka, G. (1985) Calculation of inelastic notch-tip strain-stress histories under cyclic loading, Engineering Fracture Mechanics, Vol. 22.(5), pp. 839-854.

[121] Goh, K.H., Mair, R.J. (2014). Response of framed buildings to excavation-induced movements. Soils Found. 54 (3), 250–268.

[122] González-Redondo, E. G., Hernández-Ros, R. A. (2001). Classification of masonry structures used in domestic architecture of 17th-19th centuries in Madrid, Transactions on the Built Environment, Vol 55, WIT Press.

[123] González-Redondo, E. G., Hernández-Ros, R. A. (2003). Wooden framed structures in Madrid domestic architecture of 17th to 19th centuries, 1st International Congress on Construction History, Madrid, Spain(In Spanish).

[124] Graziotti, F., Magenes , G., Penna, A., Augenti, N. (2016) Experimental campaign on double-leaf stone masonry specimens at the university of Pavia and Eucentre Pavia, in Experimental researches on the seismic behaviour of masonry spandrels: an international perspective, Research report, EUCENTRE, Pavia, Italy. (ISBN: 978-88-6198-124-9)

[125] Hanson, C. E., Towers, D. A., Meister L. D. (2006). Transit Noise and Vibration Impact Assessment FTA-VA-90-1003-06 Report, U.S. Department of Transportation, Federal Transit Administration, Washington DC, USA.

[126] Hognestad, E. (1951). A study of Combined Bending and Axial Load in R.C. Members" University of Illinois Enginering Exp. Sta. Bull. No.399, (1951)

[127] Holmen, J. O. (1982). "Fatigue of concrete by constant and variable amplitude loading." Fatigue of Concrete Structures, ACI Special Publication 75, American Concrete Institute, Detroit, 71–110.

[128] Metro de Lisboa (2021). https://www.metrolisboa.pt/viajar/horarios-e-frequencias/, Metropolitano de Lisboa, E.P.E., Lisbon, Portugal. (In Portuguese)

[129] Hordijk, D. A. (1991). Local Approach to Fatigue of Concrete, PhD thesis, Delft University of Technology.

[130] Hoshikuma, J., Kawashima, K., Nagaya, K., and Taylor, A. W. (1997). Stress-strain model for confined reinforced concrete in bridge piers, J. Struct. Eng. (10.1061/(ASCE)0733-9445(1997)123:5(624), 624–633)

[131] Hu, Y., Shi, J., Cao, X., Zhi, J. (2021) Low Cycle Fatigue Life Assessment Based on the Accumulated Plastic Strain Energy Density, Materials, Vol 14, pp. 2372. (doi.org/10.3390/ma14092372)

[132] Hunt, H. E., Hussein, M. F. (2007). Ground-Borne Vibration Transmission from Road and Rail Systems: Prediction and Control. Handbook of Noise and Vibration Control, 1458-1469. (doi:10.1002/9780470209707.ch123)

[133] Hussein, M., Hunt, H. (2007). A numerical model for calculating vibration from a railway tunnel embedded in a full-space. Journal of Sound and Vibration, 305(3), 401-431. (doi:10.1016/j.jsv.2007.03.068)

[134] ICOMOS/ISCARSAH Committee (2005) Recommendations for the analysis, conservation and structural restoration of architectural heritage. www.icomos.org

[135] ISO 13822 (2010) Basis for design of structures - Assessment of existing structures, ISO, Geneva, Switzerland.

[136] ISO 4866:1990/Amd 2:1996 (2010). Mechanical vibration and shock — Vibration of buildings — Guidelines for the measurement of vibrations and evaluation of their effects on buildings — Amendment 2, International Organization for Standardization.

[137] Ispir, M., Ilki, A. (2013). Behavior of Historical Unreinforced Brick Masonry Walls under Monotonic and Cyclic Compression, Arab J Sci Eng (2013) 38:1993–2007. (DOI 10.1007/s13369-013-0567-4)

[138] ITA/AITES Report (2006). Settlements induced by tunneling in Soft Ground, Tunneling and Underground Space Technology, Vol 22, pp. 119–149. (doi:10.1016/j.tust.2006.11.001)

[139] JCSS (2011). Probabilistic Model Code Part 3: Resistance Models, 3.2 Masonry Properties, Joint Committee on Structural Safety, Technical University of Denmark.

[140] Jones, C. J., Thompson, D. J., Petyt, M. (2002). A model for ground vibration from railway tunnels. Proceedings of the Institution of Civil Engineers, Transportation, 153(2), 121-129. (doi:10.1680/tran.153.2.121.38918)

[141] Jukic, D., Kralikb, G., Scitovskia, R. (2004) Least-squares fitting Gompertz curve, Journal of Computational and Applied Mathematics, Vol 169, pp. 359–375. (doi:10.1016/j.cam.2003.12.030)

[142] Kaushik, H. B. , Rai, D. C., Jain, S. K. (2007). Stress-Strain Characteristics of Clay Brick Masonry under Uniaxial Compression, Journal of Materials in Civil Engineering, Vol. 19, No. 9, ASCE. (DOI: 10.1061/(ASCE)0899-1561(2007)19:9(728))

[143] Kita, A., Cavalagli, N., & Ubertini, F. (2019). Temperature effects on static and dynamic behavior of Consoli Palace in Gubbio, Italy, Mechanical Systems and Signal Processing, 120, 180–202. (DOI: 10.1016/j.ymssp.2018.10.021)

[144] Koltsida, I.S., Tomor, A.K., Booth C.A. (2018A). Experimental evaluation of changes in strain under compressive fatigue loading of brick masonry, Construction and Building Materials, Vol 162, pp. 104-112. (https://doi.org/10.1016/j.conbuildmat.2017.12.016)

[145] Koltsida, I.S., Tomor, A.K., Booth C.A. (2018B). Probability of fatigue failure in brick masonry under compressive loading, International Journal of Fatigue, Vol 112, pp. 233-239. (https://doi.org/10.1016/j.ijfatigue.2018.03.023)

[146] Konon, W. (1985) Vibration criteria for historic buildings. Journal of Construction Engineering and Management 111(3):208–215.

[147] Krakowiak, J. K., Lourenço, B. P., Ulm, J. F. (2011). Multitechnique Investigation of Extruded Clay Brick Microstructure, Journal of the American Ceramic Society, Vol. 94(9), pp. 3012-3022. (doi.org/10.1111/j.1551-2916.2011.04484.x)

[148] Lacroux, J., Détain, C. (1878). Constructions en briques. La brique ordinaire au point de vue décoratif, de la société Centrale des Architectes des oeuvres de M. César Daly, Paris (In French).

[149] Lake, L.M., Rarnkin, W.J., Hawley, J. (1992). Prediction and effects of ground movements caused by tunnelling in soft ground beneath urban areas, CIRIA Project Report 30, Construction Industry Research and Information Association, London.

[150] Lanas, J., Pérez Bernal, J.L., Bello, M.A., Alvarez Galindo, J.I. (2004). Mechanical properties of natural hydraulic lime-based mortars, Cement and Concrete Research, Vol 34, pp. 2191–2201. (doi:10.1016/j.cemconres.2004.02.005)

[151] Lee, J., Park, D., Kyung, D., Lee, D. (2013). Effect of Particle characteristics on K0 Behavior for Granular Materials. 377-380, 18th International Conference on Soil Mechanics and Geotechnical Engineering, ICSMGE 2013, Paris, France.

[152] Lourenco P.B. (1996) Computational strategies for masonry structures, PhD Thesis, Delft University of Technology, Civil Engineering Department , Delft University Press, Netherlands.

[153] Lourenço P.B. (1996). "Chapter 2: Modelling Masonry: A Material Description" Computational Strategies for Masonry Structures. Delft, Netherlands: Delft UP, 11-26.

[154] Lourenço P.B. (1998). Experimental and numerical issues in the modelling of the mechanical behavior of masonry, Structural Analysis of Historical Constructions II: Possibilities of Numerical and Experimental Techniques. Barcelona: International Center for Numerical Methods in Engineering.

[155] Lourenço P.B. (2002). Computations on historic masonry structures, Progress in Structural Engineering and Materials, Vol 4, pp. 301–319 (DOI: 10.1002/pse.120)

[156] Lourenço, B. P., Fernandes, M. F., Castro, F. (2010). Handmade Clay Bricks: Chemical, Physical and Mechanical Properties, International Journal of Architectural Heritage, Conservation, Analysis, and Restoration, Vol. 4, Issue 1, pp. 38-58. (DOI: 10.1080/15583050902871092)

[157] Lourenco, P.B. and Gaetani, A. (2022) Finite Element Analysis for Building Assessment, Advanced Use and Practical Recommendations, Routledge, Taylor and Francis Group.

[158] Lourenco, P.B., Rots, J.G., Blaauwendraad, J. (1995) Two approaches for the analysis of masonry structures: micro and macro modelling, HERON, Vol. 40, No. 4. (ISSN 0046-7316)

[159] Lourenco, P.B., Rots, J.G., Blaauwendraad, J. (1995) Two approaches for the analysis of masonry structures: micro and macro modelling, HERON, Vol. 40, No. 4. (ISSN 0046-7316)

[160] LUM B6 (1991). LUM B6 Diagonal tensile strength tests of small wall specimens, Recommendations for the Testing and Use of Constructions Materials, RILEM, pp. 488 – 489.

[161] LUMA6 (1991). Rilem Technical Recommendations for the Testing and Use of Construction Materials, LUMA6 Compressive strength of mortar, E & FN Spon, London.

[162] LUMA7 (1991). Rilem Technical Recommendations for the Testing and Use of Construction Materials, LUMA7 Flexural strength of mortar, E & FN Spon, London.

[163] Lumantarna, R., Biggs, T. D., Ingham M. J. (2014). Uniaxial Compressive Strength and Stiffness of Field-Extracted and Laboratory-Constructed Masonry Prisms, Journal of Materials in Civil Engineering, Vol. 26, No. 4. (doi: 10.1061/(ASCE)MT.1943-5533.0000731)

[164] Luso, E., Lourenço, P. B. (2017) Bond strength characterization of commercially available grouts for masonry, Construction and Building Materials, Vol 144, pp. 317–326. (http://dx.doi.org/10.1016/j.conbuildmat.2017.03.179)

[165] Luso, E., Lourenço, P. B. (2019) Mechanical Behavior of Two-Leaf Masonry Wall–Strengthening Using Different Grouts, Journal of Materials in Civil Engineering, ASCE. (DOI:10.1061/(ASCE)MT.1943-5533.0002712)

[166] Mair, R., & Taylor, R. (2001). 14 Elizabeth House: Settlement predictions. In J. B. Burland, J. R. Standing, & F. M. Jardine (Eds.), Building response to tunnelling: Case studies from construction of the jubilee line extension, pp. 195-216 London. London: Thomas Telford.

[167] Mair, R.J., Taylor, R.N. (1997). Bored tunneling in the urban environment: State-of-the-art report and theme lecture. 14th Int. Conf. soil Mech. Found. Eng., Rotterdam, Netherlands, p. 2353–85.

[168] Marques, A.I.M. (2020). Reabilitação de edifícios antigos. Redução da vulnerabilidade sísmica através do reforço de paredes. PhD. thesis, ULisboa/IST, Lisboa, Portugal.

[169] Mascarenhas, J. (1996) A study on the design and construction of Buildings in the Pombaline quarter of Linbon, PhD Thesis, Polytechnic Institute of Santarem, Portugal.

[170] Masonry Standards Joint Committee MSJC (2002). Building code requirements for masonry structures, ACI 530-02/ASCE 5-02/TMS 402-02, American Concrete Institute, Structural Engineering Institute of the American Society of Civil Engineers, The Masonry Society, Detroit.

[171] Melbourne, C., Tomor A.K., Wang, J. (2004). Cyclic load capacity and endurance limit of multi-ring masonry arches, Arch Bridges, ARCH´04, Barcelona.

[172] Melbourne, C., Wang, J., Tomor A. (2007) A new masonry arch bridge assessment strategy (SMART), Proceedings of the Institution of Civil Engineers - Bridge Engineering, Vol. 160(2), pp. 81-87. (DOI:10.1680/BREN.2007.160.2.81)

[173] Mendes, N. (2012). Seismic Assessment of Ancient Masonry Buildings: Shaking Table Tests and Numerical Analysis. PhD Thesis, School of Engineering, University of Minho, Guimaraes, Portugal.

[174] Meyerhof, G.G. (1953). Some recent foundation research and its application to design. The Structural Engineer 31, 151–167.

[175] Miner, M.A. (1945). Cumulative Damage in Fatigue. Journal of Applied Mechanics, 3, 159-164.

[176] Moreira, S. (2015). Seismic retrofit of masonry-to-timber connections in historical constructions, PhD thesis, University of Minho, http://hdl.handle.net/1822/38756.

[177] Muñoz R., Lourenço, B. P. (2016). Ancoragens em paredes de alvenarias: ensaios, projeto e aplicação, Seminário Reabilitação de Fachadas, University of Minho, Guimarães. (in portuguese)

[178] NA to BS EN 1996-1-1:2005 (2007). UK National Annex to Eurocode 6: Design of masonry structures - Part 1-1: General rules for reinforced and unreinforced masonry structures, BSI

[179] Namazi, E., Mohamad, H., (2013). Assessment of building damage induced by three-dimensional ground movements, J Geotech Geoenviron Engn ASCE, 139, 608–18.

[180] National Research Council (1977). Guidelines for Preparing Environmental Impact Statements on Noise. Washington, DC: The National Academies Press. (https://doi.org/10.17226/20340)

[181] NBE-AE (1988) REAL DECRETO 1370/1988, de 25 de julio, por el que se aprueba la Norma Básica de la Edificación: NBE-AE/88. Acciones en la edificación. (In Spanish)

[182] Netzel, H. (2006) Review of the limiting tensile strain method for predicting settlement induced building damage, Geotechnical Aspects of Underground Construction in Soft Ground - Proceedings of the 5th International Conference of TC28 of the ISSMGE, pp. 159-164.

[183] NHL 5 (2014). Cal hidráulica natural NHL 5, Ficha técnica, Declaração de desempenho, Ficha de dados de segurança, Secil, Lisbon. (In portuguese) (https://secilpro.com/produtos/tipos_aplicacao/reabilitacao-e-restauro/alvenarias-antigas/cal-hidraulica-natural-nhl-5)

[184] Nicholas, T. (2006). High Cycle Fatigue: A Mechanics of Materials Perspective. 1st ed. Oxford, UK: Elsevier Ltd.

[185] NTC (2018) Nuove norme sismiche per il calcolo strutturale. With Circolare from January 21, no. 7 (2019) from Ministry of infrastructure and transportation. Italy (in Italian).

[186] Ntotsios, E., Koroma, S.G., W.I. Hamad, Thompson, D.J., Hunt, H.E.M., Talbot, J.P., Hussein, M.F.M. (2015). Modelling of Train Induced Vibration, IMechE: The Stephenson Conference – Research for Railways, United Kingdom (https://www.researchgate.net/publication/299365488)

[187] O'Reilly, M.P., New, B.M. (1982). Settlements above tunnels in the United Kingdom - their magnitude and prediction. In: 3rd International Symposium, Inst. of Mining and Metallurgy, London, England, p.173-181.

[188] Oliveira, V. D. (2000). Mechanical Characterization of Stone and Brick Masonry, Report 00-DEC/E-4, University of Minho, Guimarães, Portugal.

[189] Oliveira, V. D. (2003). Experimental and numerical analysis of blocky masonry structures under cyclic loading, PhD thesis, University of Minho, Guimarães, Portugal. (http://hdl.handle.net/1822/180)

[190] Oppenheim, A.V., Schafer, R.W. (2014). Discrete-time signal processing Chapter 7, Harlow, Essex, UK: Pearson.

[191] Parisi, F., Augenti, N., Prota, A. (2014) Implications of the spandrel type on the lateral behavior of unreinforced masonry walls, Earthquake Engineering & Structural Dynamics, Vol. 43, pp. 1867–1887. (DOI: 10.1002/eqe.2441)

[192] Paulay, T., Priestley, M. J. N. (1992). Seismic design of reinforced concrete and masonry buildings, Wiley-Interscience, New York.

[193] Peck, R.B. (1969). Deep excavations and tunneling in soft ground. State of the art volume. Proc. 7th Int. Conf. soil Mech. Found. Eng., Mexico City, p. 225–90.

[194] Peterson, A. P. G. (1980). Handbook of Noise Measurement. General Radio Company, Concord, MA,USA.

[195] Pierdicca, A., Clementi, F., Fortunati, A., Lenci, S. (2019). Tracking modal parameters evolution of a school building during retrofitting works Bulletin of Earthquake Engineering, Volume 17, Issue 2, pp 1029-1052. (doi: 10.1007/s10518-018-0483-9)

[196] Pierdicca, A., Clementi, F., Isidori, D., Concettoni, E., Cristalli, C., Lenci, S. (2016). Numerical model upgrading of a historical masonry palace monitored with a wireless sensor network. International Journal of Masonry Research and Innovation, 1(1), 74. (doi: 10.1504/ijmri.2016.074748)

[197] Potts, D. M., Zdravkovic, L. (2001). Finite element analysis in Geotechnical engineering: Theory and application. London, United Kingdom: Thomas Telford.

[198] Potts, D.M., Addenbrooke, T.I. (2017). A structure's influence on tunnelling-induced ground movements, Proc Instn Civ Eng Geotech Eng, 125, 109–25.

[199] Prota, A., Marcari, G., Fabbrocino, G., Manfredi, G., Aldea, C. (2006) Experimental In-Plane Behavior of Tuff Masonry Strengthened with Cementitious Matrix-Grid Composites, Journal of Composites for Construction, Vol. 10, (DOI: 10.1061/(ASCE)1090-0268(2006)10:3(223))

[200] Puzrin, A.M., Burland, J.B., Standing, J.R. (2012). Simple approach to predicting ground displacements caused by tunnelling in undrained anisotropic elastic soil. Geotechnique; 62:341–52.

[201] Rail industry focus (2015). from https://www.railtechnologymagazine.com/Rail-Industry-Focus-/crossrail-tunnel-fit-out-on-track, Rail Technology Magazine.

[202] Ramesh, M., Azenha, M., Lourenço, P.B. (2019) Quantification of impact of lime on mechanical behaviour of lime cement blended mortars for bedding joints in masonry systems, Construction and Building Materials, Vol 229, 116884. (https://doi.org/10.1016/j.conbuildmat.2019.116884)

[203] Ramos L. (2007) "Damage identification on masonry structures based on vibration signatures". PhD Thesis. University of Minho, Portugal. (http://hdl.handle.net/1822/7380).

[204] Rampello, S., Callisto, L., Viggiani, G. and Soccodato, F. M. (2012). Evaluating the effects of tunneling on historical buildings: the example of a new subway in Rome / Auswertung der Auswirkungen des Tunnelbaus auf historische Gebäude am Beispiel einer neuen U-Bahnlinie in Rom. Geomechanik Tunnelbau, 5: 275–299. (doi: 10.1002/geot.201200017)

[205] Rankin, W. J. (1988). Ground movements resulting from urban tunneling; predictions and effects. Engineering Geology Special Publication 5: 79.

[206] REABILITA CAL CS (2019). Argamassa de consolidação de alvenarias antigas exclusivamente formulada com cal hidráulica natural, Ficha técnica, Declaração de desempenho, Ficha de dados de segurança, Secil, Lisbon. (In portuguese) (https://www.seciltek.com/documentos/reabilita)

[207] Renton, J. D. (1991). Generalized beam theory applied to shear stiffness, Int. J. Solids Struct., Vol 27(15), 1955-1967.

[208] RILEM TC 162-TDF (2002). RILEM TC 162-TDF: Test and design methods for steel fibre-reinforced concrete, Bending test, Final Recommendation, Materials and Structures, Vol. 35, pp 579-582.

[209] Roberts, T., Hughes, T., Dandamudi, V., Bell, B., (2006). Quasi-static and high cycle fatigue strength of brick masonry. Construction and Building Materials, 20(9), pp. 603-614.

[210] Roca, P., Molins C., Marí, A.R. (2005) Strength Capacity of Masonry Wall Structures by the Equivalent Frame Method, Journal of Structural Engineering, Vol. 131, No. 10. (DOI: 10.1061/(ASCE)0733-9445(2005)131:10(1601))

[211] Rodrigues, J. (2004). Identificação Modal Estocástica, Métodos de Análise e Aplicações em Estruturas de Engenharia Civil, PhD Thesis, Engineering Faculty of University of Porto, Portugal (in Portuguese)

[212] Ronca, P., Franchi, A., Crespi, P. (2005). Structural failure of historic buildings: masonry fatigue tests for an interpretation model, Structural Analysis of Historical Constructions - 2 Volume Set - Modena, Lourenço & Roca (eds). (https://doi.org/10.1201/9781482288377)

[213] Rots, J.C. (1988). Computational modelling of concrete fracture, PhD Dissertation, Delft University of Technology.

[214] Rouphael, T. J (2009). Chapter 7 - Uniform Sampling of Signals and Automatic Gain Control, RF and Digital Signal Processing for Software-Defined Radio, Newnes, pp. 199-234. (https://doi.org/10.1016/B978-0-7506-8210-7.00007-2)

[215] Rowe, R. K., Lo, K. Y., Kack, G. J. (1983). A method of estimating surface settlement tunnels constructed in soft ground, Can. Geotech. J. 20, No. 1, 11–22.

[216] Saisi, A., Gentile, C., Guidobaldi, M. (2015). Post-earthquake continuous dynamic monitoring of the Gabbia Tower in Mantua, Italy, Construction and Building Materials, 81, 101–112. (DOI: 10.1016/j.conbuildmat.2015.02.010)

[217] Saurenman, H.J., Nelson, J.T., Wilson G.P. (1982). Handbook of Urban Rail Noise and Vibration Control, Report DOT-TSC-UMTA-81–72. US Department of Transportation, Urban Mass Transportation Administration, Washington DC, USA.

[218] Shin, S.H., Kim, C.Y., Kim, K.Y., Jue, K.S., Hong, S.W. (2007). An optimized monitoring of critical buildings adjacent to tunnel construction in urban area, Proceedings of the 33rd ITA-AITES World Tunnel Congress - Underground Space - The 4th Dimension of Metropolises, 2, pp. 913-916.

[219] Silveira, D., Varum H., Costa, A., Carvalho, J. (2015). Mechanical Properties and Behavior of Traditional Adobe Wall Panels of the Aveiro District, J. Mater. Civ. Eng., 27(9): 04014253. (DOI: 10.1061/(ASCE)MT.1943-5533.0001194)

[220] SIPA (2011). Information System for Architectural Heritage, Parish Igreja dos Anjos, IPA.00003199 (in Portuguese) http://www.monumentos.gov.pt

[221] Siskind, D. E., Stagg, M.S., Kopp, J. W., Dowding C. H. (1980). Structure response and damage produced by ground vibration from surface mine blasting, United States Bureau of Mines, Report of Investigations No. RI. 8507.

[222] SN 604312A:1992 (1992). Effects of Vibration on Construction (Superseded), Swiss Standards Association.

[223] Son, M. (2015). Response analysis of nearby structures to tunneling-induced ground movements in sandy soils, Tunnelling and Underground Space Technology, Volume 48, 156-169. (http://dx.doi.org/10.1016/j.tust.2015.03.008)

[224] Suryanarayana, C. (2011) Experimental Techniques in Materials and Mechanics, CRC Press, Taylor & Francis Group, US.

[225] SVS (2019): ARTeMIS Modal Pro User Manual, Release 6.0.2.0, Structural Vibration Solutions, Aalborg, Denmark.

[226] Thompson, D. J., Jones, C., Gautier, P. (2009). Railway noise and vibration: Mechanisms, modelling and means of control. Amsterdam: Elsevier.

[227] Thorenfeldt, E., Tomaszewicz, A., Jensen, J. J. (1987). Mechanical properties of high-strength concrete and applications in design, In Proc. Symp. Utilization of High-Strength Concrete (Stavanger, Norway) (Trondheim, 1987), Tapir.

[228] Timoshenko, S. (1955). Strength of Materials, Part 1: Elementary Theory and Problems, 3rd edn. Van Nostrand, New York.

[229] TM E519/E519M-20 (2020). Standard Test Method for Diagonal Tension (Shear) in Masonry Assemblages, ASTM International, West Conshohocken, PA. (www.astm.org)

[230] TMS 402-11/ACI 530-11/ASCE 5-11 (2011). Building Code Requirements and Specification for Masonry Structures, Masonry Standards Joint Committee (MSJC), USA.

[231] Tomazevic, M. (1999). Earthquake-resistance design of masonry buildings, Imperial College Press, London, UK.

[232] Tomor, A., Verstrynge, E. (2013). A joint fatigue–creep deterioration model for masonry with acoustic emission based damage assessment, Construction and Building Materials, Vol 43, pp. 575-588. (http://dx.doi.org/10.1016/j.conbuildmat.2013.02.045)

[233] Vasconcelos, F. M. G. (2005). Experimental investigations on the mechanics of stone masonry: Characterization of granites and behavior of ancient masonry shear walls, PhD thesis, University of Minho, 2005. (http://hdl.handle.net/1822/17383)

[234] Vibration from Underground Railways Pipe-in-Pipe software – New Release (2013). Department of Engineering. http://www.eng.cam.ac.uk/news/vibration-underground-railways-pipe-pipe-software-new-release, University of Cambridge.

[235] Vinci, M. (2019) Metodi di calcolo e tecniche di consolidamento per edifici in muratura, Secondo il D.M. 17/01/2018 e Circolare 7/2019, Dario Flaccovio Editore. (In Italian - ISBN 9788857911038)

[236] Vintzileou, E., Miltiadou-Fezans, A. (2008) Mechanical properties of three-leaf stone masonry grouted with ternary or hydraulic lime-based grouts, Engineering Structures, Vol. 30(8), pp. 2265-2276. (https://doi.org/10.1016/j.engstruct.2007.11.003)

[237] Wang, X., Lam, C. C., Iu, V. P. (2019) Comparison of different types of TRM composites for strengthening masonry panels, Construction and Building Materials, Vol 219, pp. 184-194. (https://doi.org/10.1016/j.conbuildmat.2019.05.179)

[238] Wong, R., Kaiser, P. (1987). Prediction of ground movements above shallow tunnels. Proceedings of the international symposium on Prediction and Performance in Geotechnical Engineering, Calgary.

[239] Worden K. (1990). Data processing and experiment design for the restoring force surface method, part I: integration and differentiation of measured time data, Mechanical Systems and Signal Processing, Volume 4, Issue 4, pp. 295-319.

[240] Xia, H, & Calçada, R. (2013). Traffic induced Environmental Vibrations and Controls: Theory and Application. (Vol. 6619) New York: Nova Science Publishers Inc.

[241] Yang, Y. B., Hung, H. H., Kao, J. C., Lu, J. W., Leung, A. Y., Iu, V. P., Mok, K. M. (2010). 2.5D Finite/Infinite Element Approach for Simulating Train-Induced Ground Vibrations. doi:10.1063/1.3452242

[242] Yang, Y., & Hung, H. (2001). A 2.5D finite/infinite element approach for modelling visco-elastic bodies subjected to moving loads. International Journal for Numerical Methods in Engineering, 51(11), 1317-1336. (doi:10.1002/nme.208)

[243] Zheng, G., Lu, P., Diao, Y. (2015). Advance speed-based parametric study of greenfield deformation induced by EPBM tunneling in soft ground Computers and Geotechnics, 65, pp. 220-232.

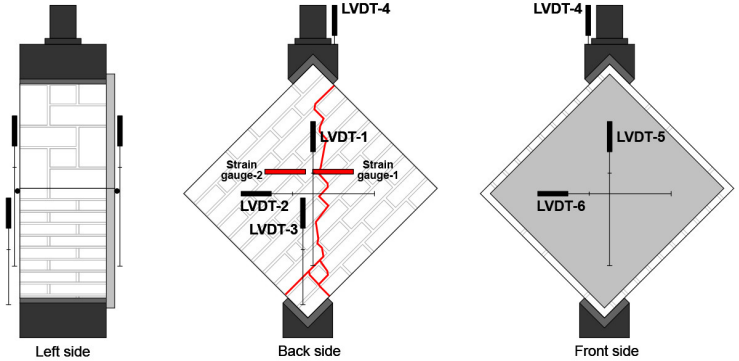
[244] Zucchini, A., Lourenco, P.B. (2006). Mechanics of masonry in compression: Results from a homogenization approach, International Journal of Computers and Structures, Vol. 85, pp. 193–204, Elsevier. (doi:10.1016/j.compstruc.2006.08.054)

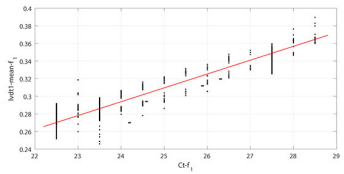
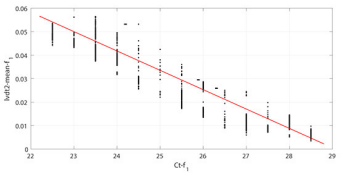
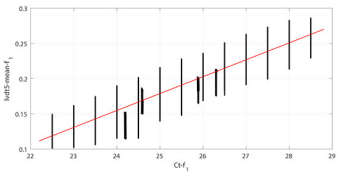
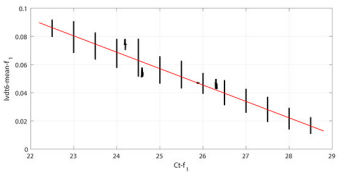
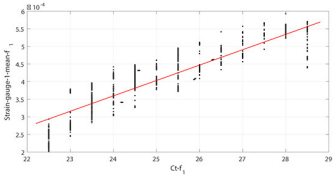
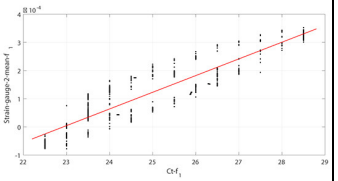
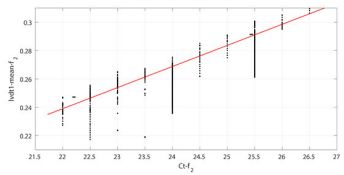
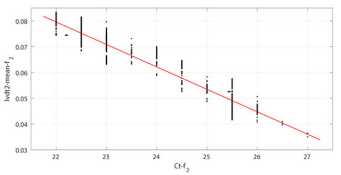
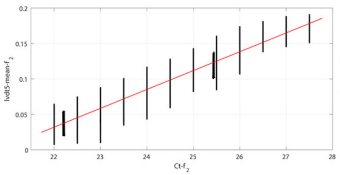
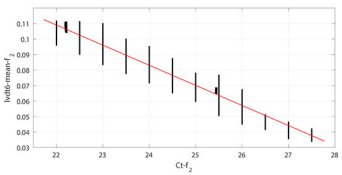
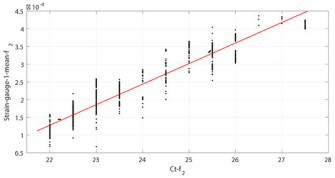
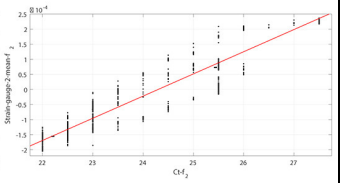
ANNEXES

ANNEX A

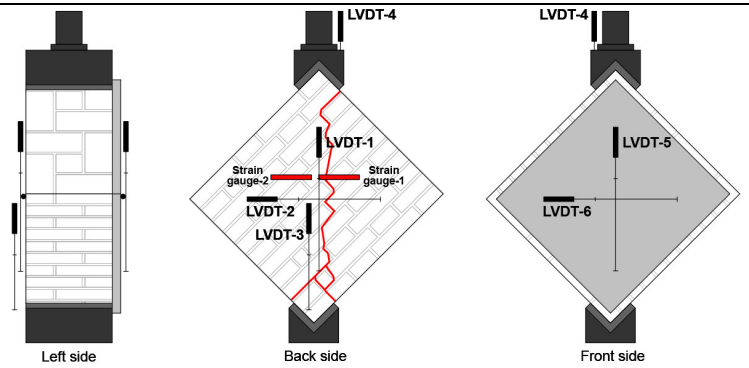
Table 42. Correlation of displacement and temperature data with linear trending, for wallet DCf2.Note the relative locations of strain gauges, LVDTs and cracks.

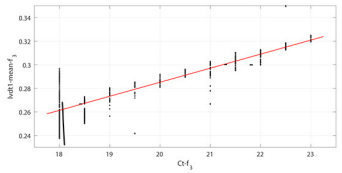
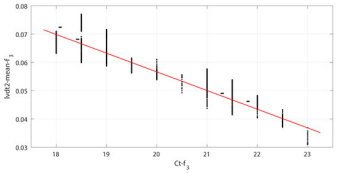
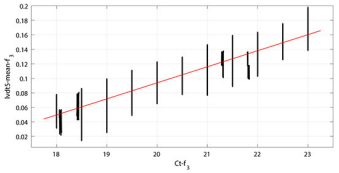
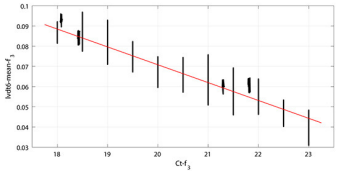
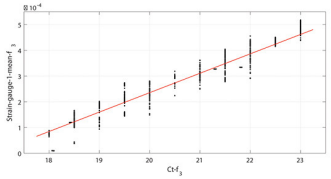
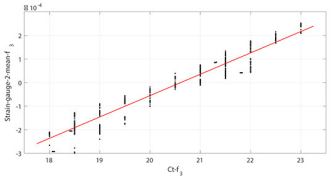
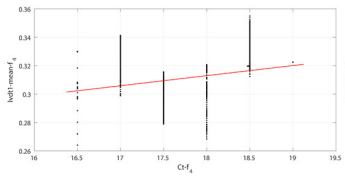
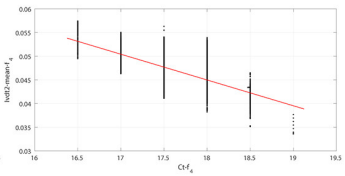
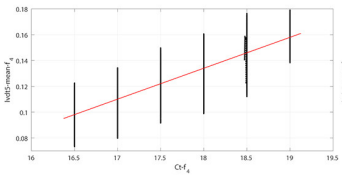
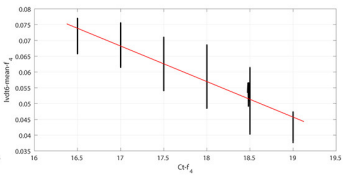
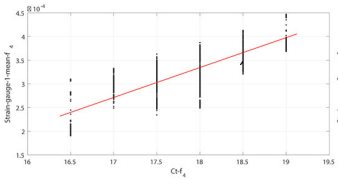
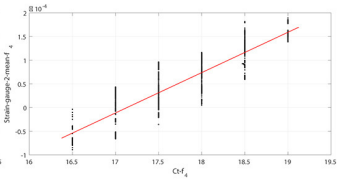
DCf2j



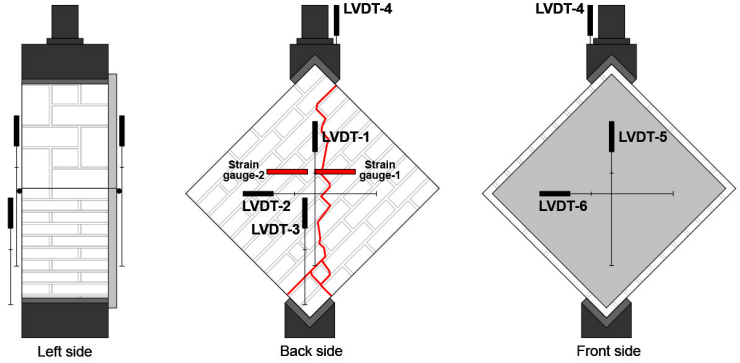
j	LVDT-1	LVDT-2	LVDT-5	LVDT-6	Strain gauge-1	Strain gauge-2
1						
	f(x) = p1*x + p2 p1 = 0.01572, p2 = -0.08357 SSE: 9.326 R-square: 0.8678 Adj. R-square: 0.8678 RMSE: 0.01132	f(x) = p1*x + p2 p1 = -0.008242, p2 = 0.2396 SSE: 2.166 R-square: 0.8887 Adj. R-square: 0.8887 RMSE: 0.005498	f(x) = p1*x + p2 p1 = 0.024, p2 = -0.4212 SSE: 17.55 R-square: 0.8934 Adj. R-square: 0.8934 RMSE: 0.0153	f(x) = p1*x + p2 p1 = -0.01164, p2 = 0.348 SSE: 1.076 R-square: 0.9698 Adj. R-square: 0.9698 RMSE: 0.00379	f(x) = p1*x + p2 p1 = 4.4e-05, p2 = -6.9e-04 SSE: 9.397e-05 R-square: 0.8382 Adj. R-square: 0.8382 RMSE: 3.54e-05	f(x) = p1*x + p2 p1 = 5.9e-05, p2 = -0.001357 SSE: 0.000166 R-square: 0.8436 Adj. R-square: 0.8436 RMSE: 4.704e-05
2						
	f(x) = p1*x + p2 p1 = 0.01488, p2 = -0.0884 SSE: 3.407 R-square: 0.9011 Adj. R-square: 0.9011 RMSE: 0.006799	f(x) = p1*x + p2 p1 = -0.008708, p2 = 0.2711 SSE: 0.6549 R-square: 0.9368 Adj. R-square: 0.9368 RMSE: 0.002987	f(x) = p1*x + p2 p1 = 0.02659, p2 = -0.553 SSE: 14.17 R-square: 0.8785 Adj. R-square: 0.8785 RMSE: 0.01376	f(x) = p1*x + p2 p1 = -0.01297, p2 = 0.3945 SSE: 1.672 R-square: 0.9363 Adj. R-square: 0.9363 RMSE: 0.004723	f(x) = p1*x + p2 p1 = 5.8e-05, p2 = -0.001148 SSE: 6.637e-05 R-square: 0.8811 Adj. R-square: 0.8811 RMSE: 2.975e-05	f(x) = p1*x + p2 p1 = 7.4e-05, p2 = -0.001787 SSE: 0.000153 R-square: 0.8379 Adj. R-square: 0.8379 RMSE: 4.517e-05

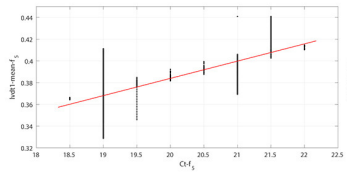
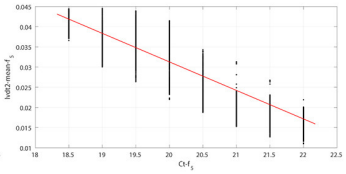
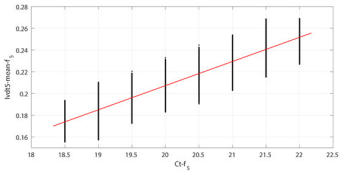
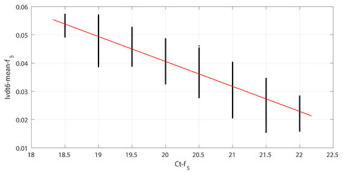
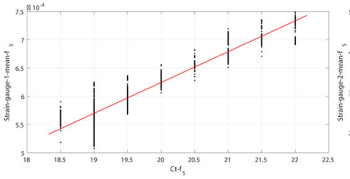
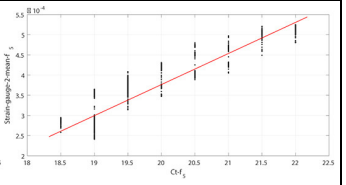
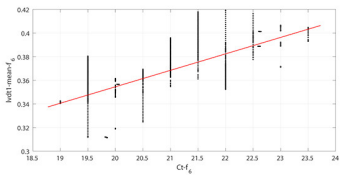
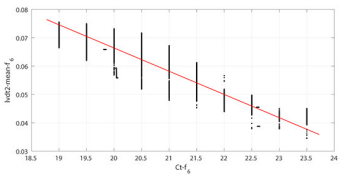
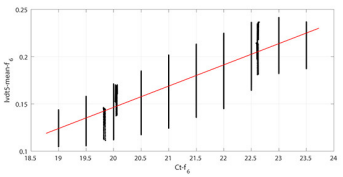
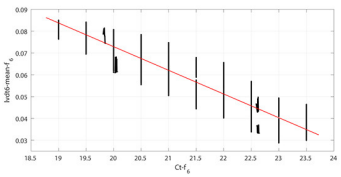
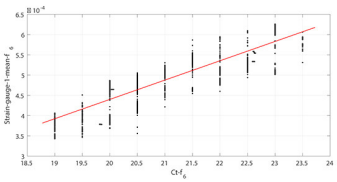
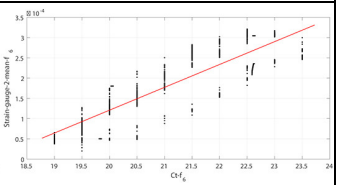
DCf2j



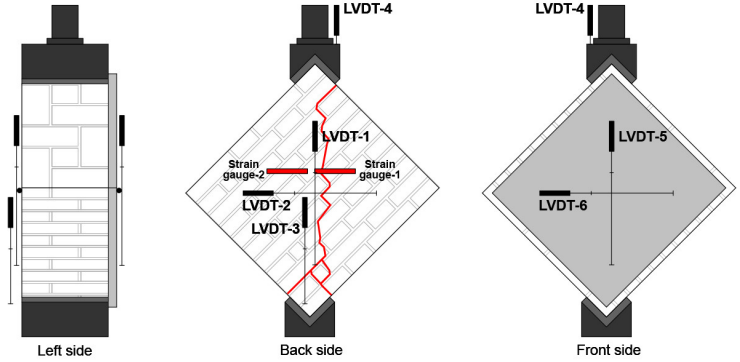
j	LVDT-1	LVDT-2	LVDT-5	LVDT-6	Strain gauge-1	Strain gauge-2
3						
	f(x) = p1*x + p2 p1 = 0.01192, p2 = 0.04671 SSE: 2.233 R-square: 0.9048 Adj. R-square: 0.9048 RMSE: 0.00548	f(x) = p1*x + p2 p1 = -0.006606, p2 = 0.1888 SSE: 0.464 R-square: 0.9332 Adj. R-square: 0.9332 RMSE: 0.002503	f(x) = p1*x + p2 p1 = 0.02214, p2 = -0.3489 SSE: 14.04 R-square: 0.842 Adj. R-square: 0.842 RMSE: 0.01369	f(x) = p1*x + p2 p1 = -0.008837, p2 = 0.2475 SSE: 1.304 R-square: 0.9013 Adj. R-square: 0.9013 RMSE: 0.004172	f(x) = p1*x + p2 p1 = 7.5e-05, p2 = -0.001274 SSE: 7.232e-05 R-square: 0.9233 Adj. R-square: 0.9233 RMSE: 3.105e-05	f(x) = p1*x + p2 p1 = 9.1e-05, p2 = -0.001868 SSE: 8.252e-05 R-square: 0.9383 Adj. R-square: 0.9383 RMSE: 3.317e-05
4						
	f(x) = p1*x + p2 p1 = 0.007106, p2 = 0.1851 SSE: 5.798 R-square: 0.1952 Adj. R-square: 0.1952 RMSE: 0.008912	f(x) = p1*x + p2 p1 = -0.005442, p2 = 0.1429 SSE: 0.6896 R-square: 0.5595 Adj. R-square: 0.5595 RMSE: 0.003049	f(x) = p1*x + p2 p1 = 0.02394, p2 = -0.2969 SSE: 11.57 R-square: 0.6026 Adj. R-square: 0.6026 RMSE: 0.01242	f(x) = p1*x + p2 p1 = -0.01125, p2 = 0.2595 SSE: 0.763 R-square: 0.8354 Adj. R-square: 0.8354 RMSE: 0.003191	f(x) = p1*x + p2 p1 = 6.3e-05, p2 = -8.0e-04 SSE: 6.714e-05 R-square: 0.6455 Adj. R-square: 0.6455 RMSE: 2.992e-05	f(x) = p1*x + p2 p1 = 8.5e-05, p2 = -0.001459 SSE: 6.658e-05 R-square: 0.7695 Adj. R-square: 0.7695 RMSE: 2.979e-05

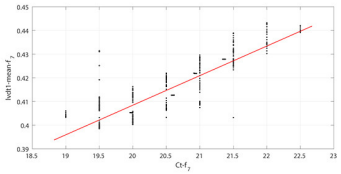
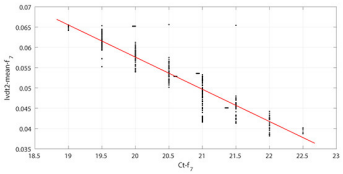
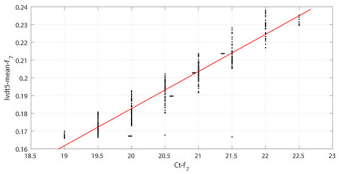
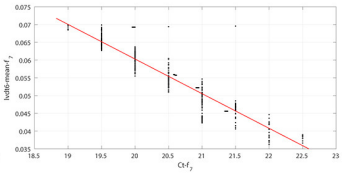
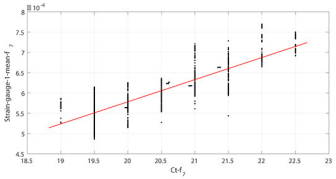
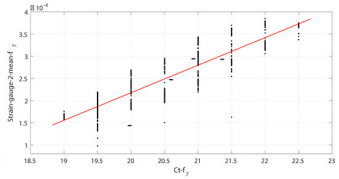
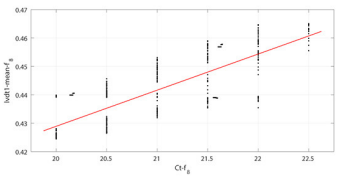
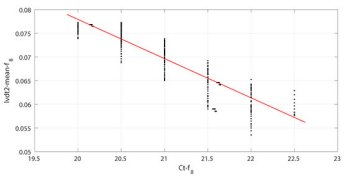
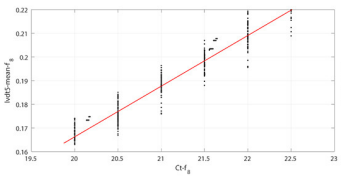
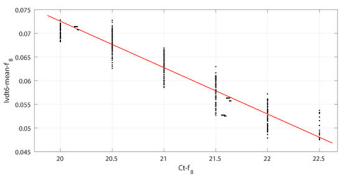
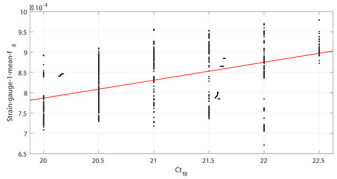
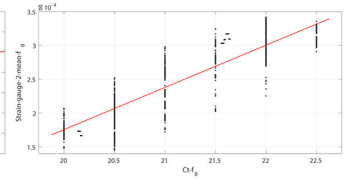
DCf2j



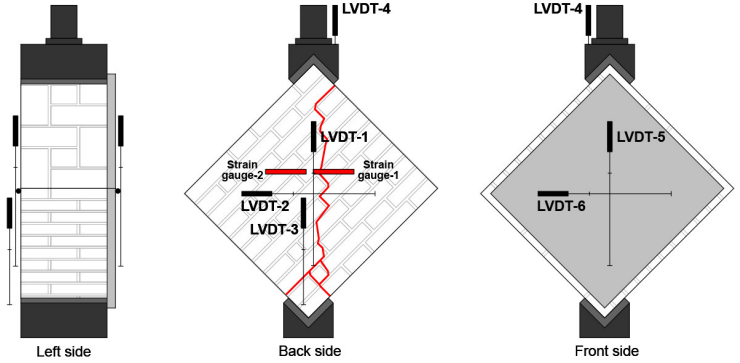
j	LVDT-1	LVDT-2	LVDT-5	LVDT-6	Strain gauge-1	Strain gauge-2
5						
	f(x) = p1*x + p2 p1 = 0.01009, p2 = 0.1797 SSE: 14.59 R-square: 0.3426 Adj. R-square: 0.3426 RMSE: 0.01412	f(x) = p1*x + p2 p1 = -0.005241, p2 = 0.137 SSE: 2.759 R-square: 0.4239 Adj. R-square: 0.4239 RMSE: 0.006194	f(x) = p1*x + p2 p1 = 0.01285, p2 = -0.05375 SSE: 36.86 R-square: 0.2535 Adjusted R-square: 0.2535 RMSE: 0.02217	f(x) = p1*x + p2 p1 = -0.005016, p2 = 0.1424 SSE: 5.133 R-square: 0.2708 Adjusted R-square: 0.2707 RMSE: 0.008275	f(x) = p1*x + p2 p1 = 3.2e-05, p2 = -2.0e-05 SSE: 0.0001849 R-square: 0.2925 Adj. R-square: 0.2925 RMSE: 4.965e-05	f(x) = p1*x + p2 p1 = 3.7e-05, p2 = -3.8e-04 SSE: 0.0004321 R-square: 0.196 Adj. R-square: 0.196 RMSE: 7.59e-05
6						
	f(x) = p1*x + p2 p1 = 0.01393, p2 = 0.07596 SSE: 4.005 R-square: 0.8397 Adj. R-square: 0.8397 RMSE: 0.007341	f(x) = p1*x + p2 p1 = -0.008192, p2 = 0.2302 SSE: 1.197 R-square: 0.8586 Adj. R-square: 0.8586 RMSE: 0.004001	f(x) = p1*x + p2 p1 = 0.02246, p2 = -0.3028 SSE: 15.9 R-square: 0.7747 Adj. R-square: 0.7747 RMSE: 0.01456	f(x) = p1*x + p2 p1 = -0.01086, p2 = 0.2901 SSE: 1.883 R-square: 0.8716 Adj. R-square: 0.8716 RMSE: 0.005012	f(x) = p1*x + p2 p1 = 4.8e-05, p2 = -5.1e-04 SSE: 7.711e-05 R-square: 0.7618 Adj. R-square: 0.7618 RMSE: 3.206e-05	f(x) = p1*x + p2 p1 = 5.6e-05, p2 = 0.001008 SSE: 0.0001175 R-square: 0.7461 Adj. R-square: 0.7461 RMSE: 3.958e-05

DCf2j



j	LVDT-1	LVDT-2	LVDT-5	LVDT-6	Strain gauge-1	Strain gauge-2
7	 f(x) = p1*x + p2 p1 = 0.0125, p2 = 0.1585 SSE: 3.23 R-square: 0.7343 Adj. R-square: 0.7343 RMSE: 0.006574	 f(x) = p1*x + p2 p1 = -0.00793, p2 = 0.2162 SSE: 0.4227 R-square: 0.8949 Adj. R-square: 0.8949 RMSE: 0.002374	 f(x) = p1*x + p2 p1 = 0.0209, p2 = -0.2353 SSE: 2.712 R-square: 0.902 Adj. R-square: 0.902 RMSE: 0.006024	 f(x) = p1*x + p2 p1 = -0.009755, p2 = 0.2554 SSE: 0.5527 R-square: 0.9079 Adj. R-square: 0.9079 RMSE: 0.002715	 f(x) = p1*x + p2 p1 = 5.4e-05, p2 = -5.1e-04 SSE: 6.271e-05 R-square: 0.7308 Adj. R-square: 0.7308 RMSE: 2.892e-05	 f(x) = p1*x + p2 p1 = 6.2e-05, p2 = -0.001024 SSE: 6.813e-05 R-square: 0.764 Adj. R-square: 0.7639 RMSE: 3.014e-05
8	 f(x) = p1*x + p2 p1 = 0.01272, p2 = 0.1745 SSE: 3.463 R-square: 0.6559 Adj. R-square: 0.6559 RMSE: 0.006807	 f(x) = p1*x + p2 p1 = -0.008283, p2 = 0.2436 SSE: 0.4667 R-square: 0.8571 Adj. R-square: 0.8571 RMSE: 0.002499	 f(x) = p1*x + p2 p1 = 0.02141, p2 = -0.2619 SSE: 1.245 R-square: 0.9375 Adj. R-square: 0.9375 RMSE: 0.004082	 f(x) = p1*x + p2 p1 = -0.0098, p2 = 0.2685 SSE: 0.4097 R-square: 0.9053 Adj. R-square: 0.9053 RMSE: 0.002341	 f(x) = p1*x + p2 p1 = 4.4e-05, p2 = -9.6e-05 SSE: 0.0002383 R-square: 0.2502 Adj. R-square: 0.2502 RMSE: 5.646e-05	 f(x) = p1*x + p2 p1 = 6.2e-05, p2 = -0.001073 SSE: 5.979e-05 R-square: 0.7266 Adj. R-square: 0.7266 RMSE: 2.828e-05

DCf2j



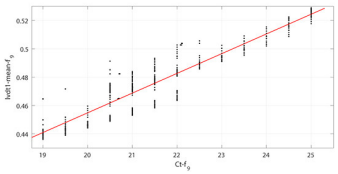
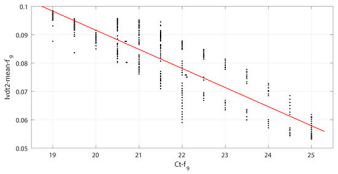
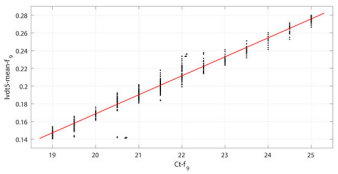
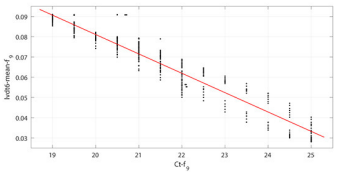
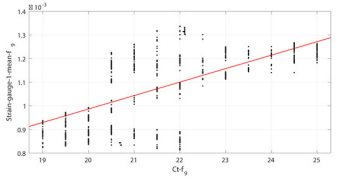
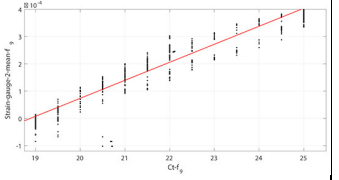
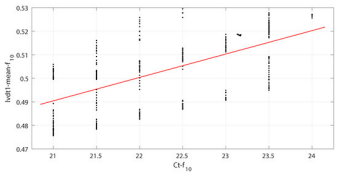
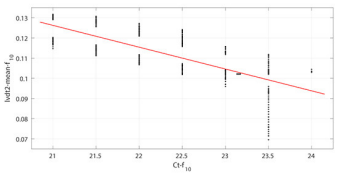
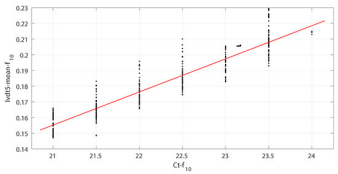
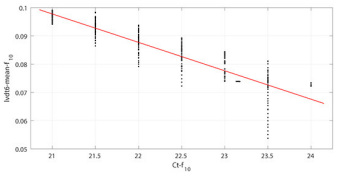
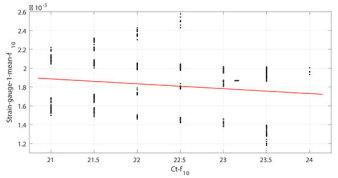
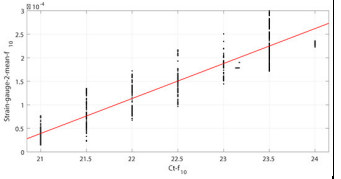
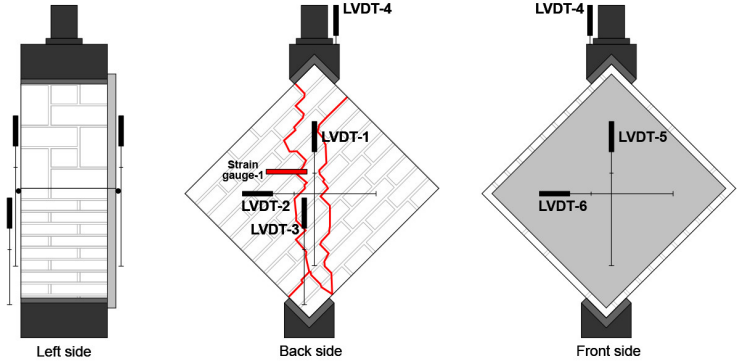
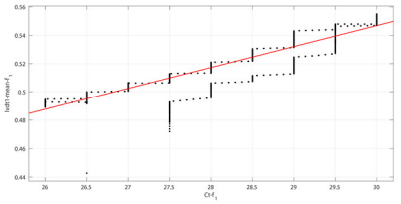
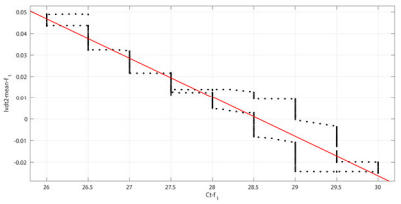
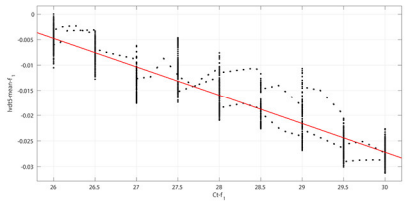
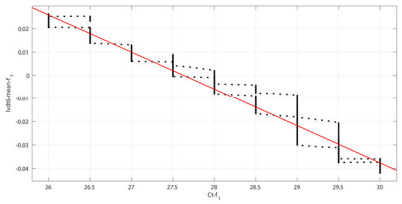
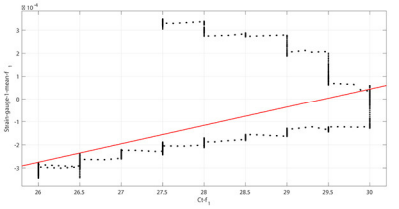
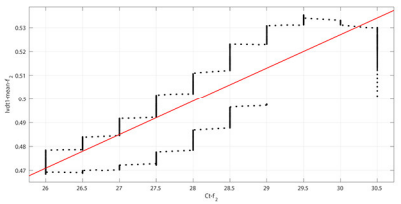
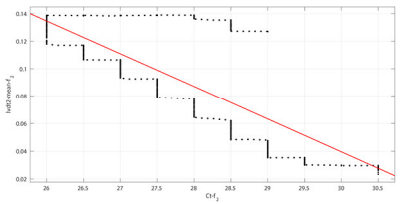
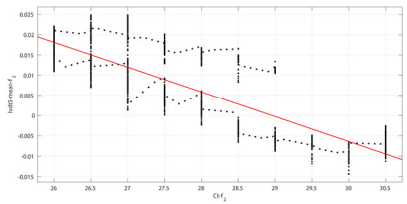
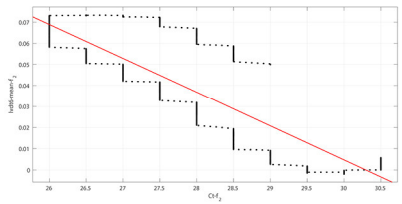
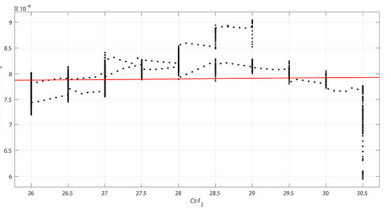
j	LVDT-1	LVDT-2	LVDT-5	LVDT-6	Strain gauge-1	Strain gauge-2
9	 f(x) = p1*x + p2 p1 = 0.01391, p2 = 0.1766 SSE: 5.227 R-square: 0.8951 Adj. R-square: 0.8951 RMSE: 0.008363	 f(x) = p1*x + p2 p1 = -0.006736, p2 = 0.2263 SSE: 2.883 R-square: 0.7839 Adj. R-square: 0.7839 RMSE: 0.00621	 f(x) = p1*x + p2 p1 = 0.02142, p2 = -0.2596 SSE: 3.434 R-square: 0.9685 Adj. R-square: 0.9685 RMSE: 0.006778	 f(x) = p1*x + p2 p1 = -0.009564, p2 = 0.2723 SSE: 1.561 R-square: 0.9311 Adj. R-square: 0.9311 RMSE: 0.00457	 f(x) = p1*x + p2 p1 = 5.7e-05, p2 = -1.5e-04 SSE: 0.001081 R-square: 0.4091 Adj. R-square: 0.4091 RMSE: 0.0001202	 f(x) = p1*x + p2 p1 = 6.6e-05, p2 = -0.001247 SSE: 0.00012 R-square: 0.8934 Adj. R-square: 0.8934 RMSE: 4.007e-05
10	 f(x) = p1*x + p2 p1 = 0.01093, p2 = 0.2597 SSE: 8.026 R-square: 0.5043 Adj. R-square: 0.5043 RMSE: 0.01036	 f(x) = p1*x + p2 p1 = -0.00699, p2 = 0.2684 SSE: 9.621 R-square: 0.2577 Adj. R-square: 0.2576 RMSE: 0.01135	 f(x) = p1*x + p2 p1 = 0.01755, p2 = -0.2091 SSE: 12.42 R-square: 0.629 Adj. R-square: 0.629 RMSE: 0.01289	 f(x) = p1*x + p2 p1 = -0.008393, p2 = 0.272 SSE: 3.054 R-square: 0.6119 Adj. R-square: 0.6119 RMSE: 0.006392	 f(x) = p1*x + p2 p1 = 4.4e-05 , p2 = 8.4e-04 SSE: 0.006654 R-square: 0.0199 Adj. R-square: 0.01989 RMSE: 0.0002984	 f(x) = p1*x + p2 p1 = 4.2e-05, p2 = -8.0e-04 SSE: 0.0003245 R-square: 0.2678 Adj. R-square: 0.2678 RMSE: 6.589e-05

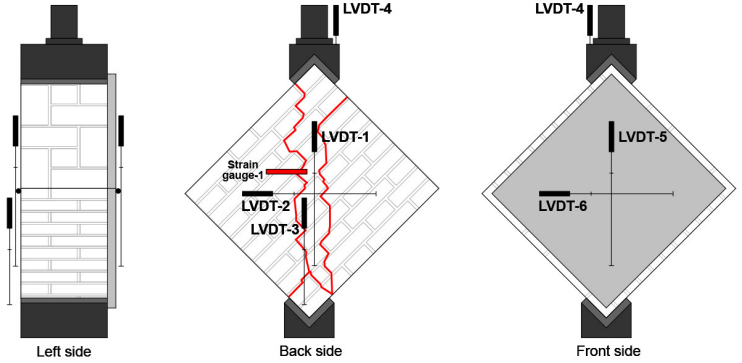
Table 43. Correlation of displacement and temperature data with linear trending, for wallet DCf3.Note the relative locations of strain gauges, LVDTs and cracks.

DCf3j



j	LVDT-1	LVDT-2	LVDT-5	LVDT-6	Strain gauge-1
1					
	f(x) = p1*x + p2 p1 =0.01478, p2 = 0.1033 SSE: 4.767 R-square: 0.8998 Adj. R-square: 0.8998 RMSE: 0.007141	f(x) = p1*x + p2 p1 = -0.01826, p2 = 0.5215 SSE: 2.526 R-square: 0.9628 Adj. R-square: 0.9628 RMSE: 0.005191	f(x) = p1*x + p2 p1 = -0.005615, p2 = 0.1412 SSE: 0.6644 R-square: 0.9029 Adj. R-square: 0.9029 RMSE: 0.002662	f(x) = p1*x + p2 p1 = -0.01587, p2 = 0.4385 SSE: 1.254 R-square: 0.9752 Adj. R-square: 0.9752 RMSE: 0.003657	Part-1 f(x) = p1*x + p2 p1 = 7.985e-05, p2 = -0.002352 SSE: 0.002242 R-square: 0.3447 Adj. R-square: 0.3447 RMSE: 0.0001565
2					
	f(x) = p1*x + p2 p1 = 0.01404, p2 = 0.106 SSE: 8.525 R-square: 0.8082 Adj. R-square: 0.8082 RMSE: 0.009542	f(x) = p1*x + p2 p1 = -0.02378, p2 = 0.753 SSE: 45.37 R-square: 0.6958 Adj. R-square: 0.6957 RMSE: 0.022	f(x) = p1*x + p2 p1 = -0.006125, p2 = 0.1773 SSE: 2.521 R-square: 0.7319 Adj. R-square: 0.7319 RMSE: 0.005186	f(x) = p1*x + p2 p1 = -0.01604, p2 = 0.4858 SSE: 15.7 R-square: 0.7503 Adj. R-square: 0.7503 RMSE: 0.01294	f(x) = p1*x + p2 p1 = 1.52e-06, p2 = 0.0007579 SSE: 0.0001223 R-square: 0.001986 Adj. R-square: 0.001975 RMSE: 3.612e-05

DCf3j



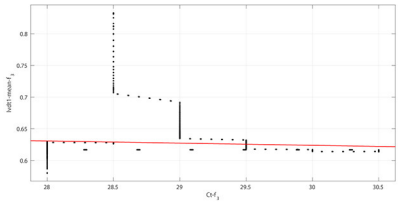
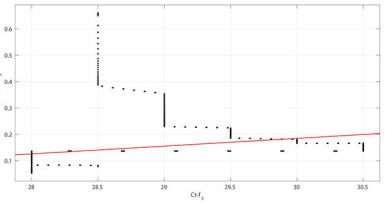
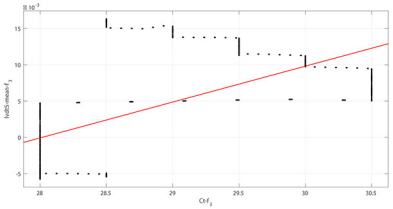
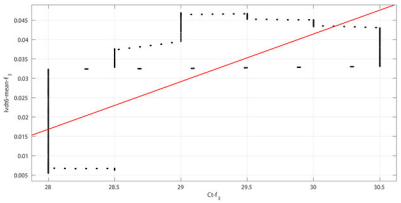
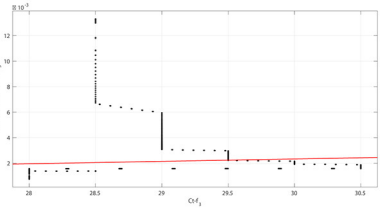
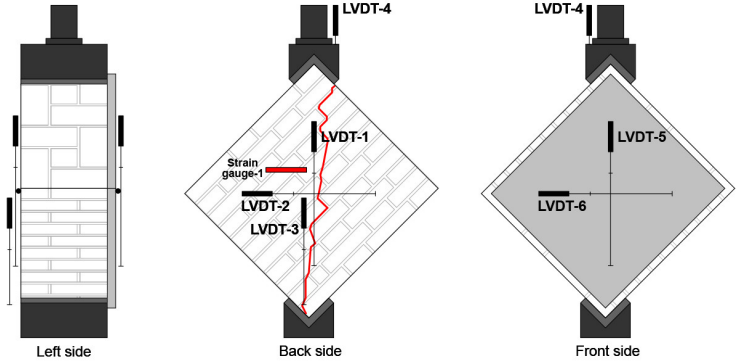
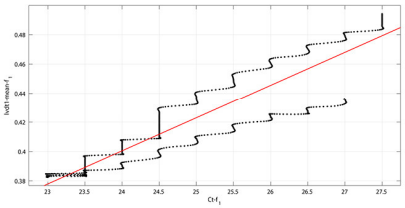
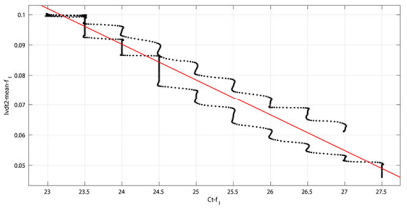
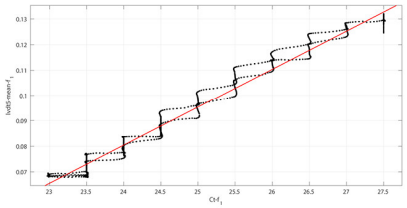
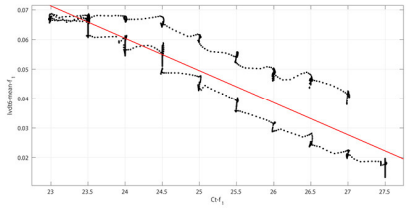
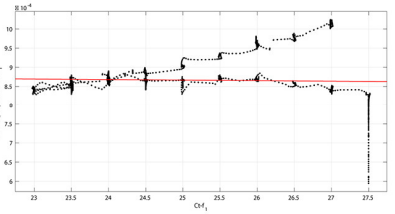
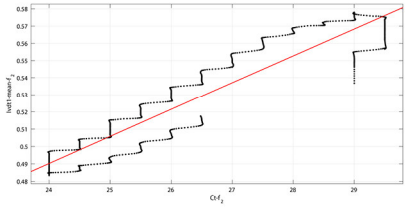
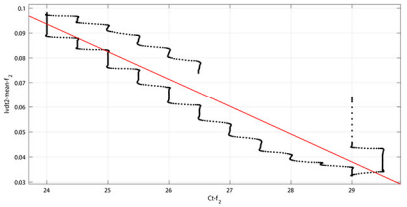
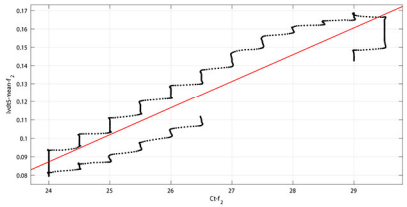
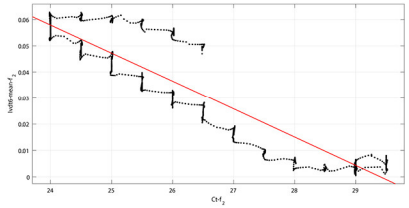
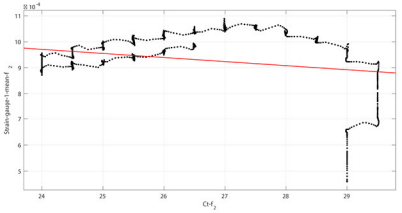
j	LVDT-1	LVDT-2	LVDT-5	LVDT-6	Strain gauge-1
3					
	f(x) = p1*x + p2 p1 = -0.003437, p2 = 0.727 SSE: 29.98 R-square: 0.01586 Adj. R-square: 0.01584 RMSE: 0.02614	f(x) = p1*x + p2 p1 = 0.0294, p2 = -0.6973 SSE: 297.7 R-square: 0.1062 Adj. R-square: 0.1062 RMSE: 0.08232	f(x) = p1*x + p2 p1 = 0.004948, p2 = -0.1386 SSE: 1.408 R-square: 0.4156 Adj. R-square: 0.4156 RMSE: 0.005661	f(x) = p1*x + p2 p1 = 0.01231, p2 = -0.3278 SSE: 4.816 R-square: 0.5628 Adj. R-square: 0.5628 RMSE: 0.01047	f(x) = p1*x + p2 p1 =0.0001876, p2 = -0.003302 SSE: 0.102 R-square: 0.01392 Adj. R-square: 0.0139 RMSE: 0.001523

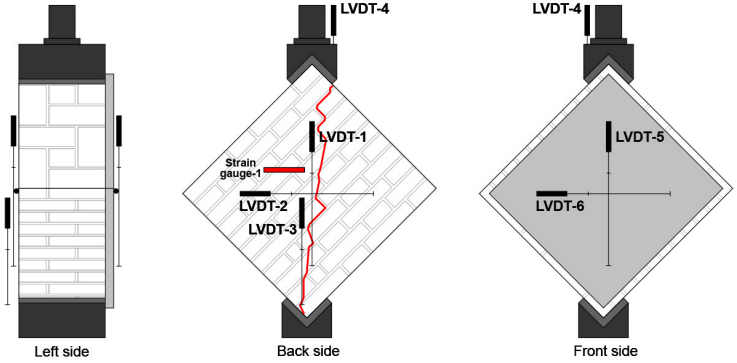
Table 44. Correlation of displacement and temperature data with linear trending, for wallet DCf4.Note the relative locations of strain gauges, LVDTs and cracks.

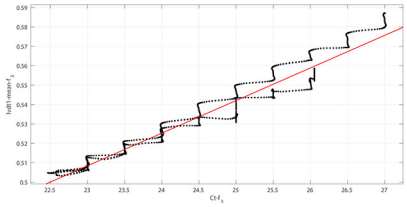
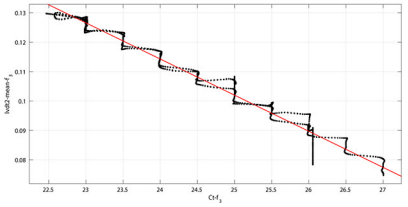
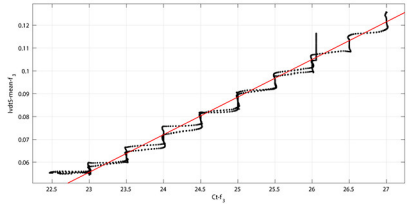
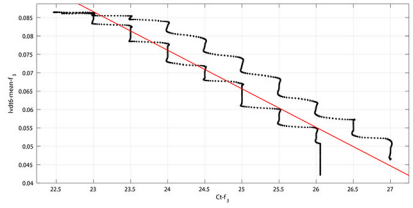
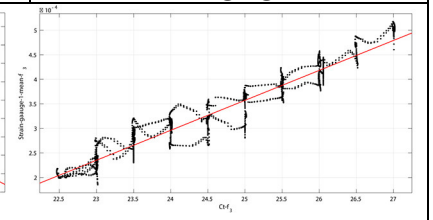
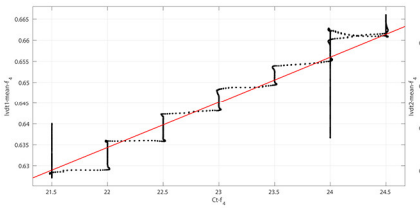
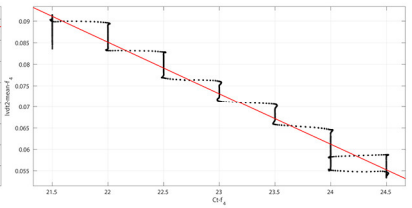
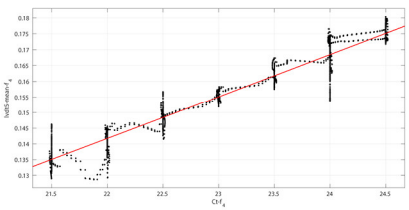
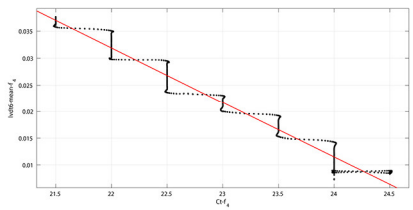
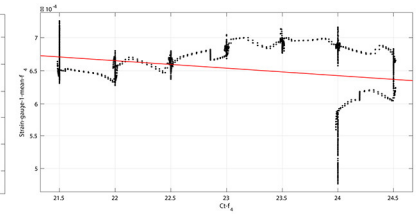
DCf4j



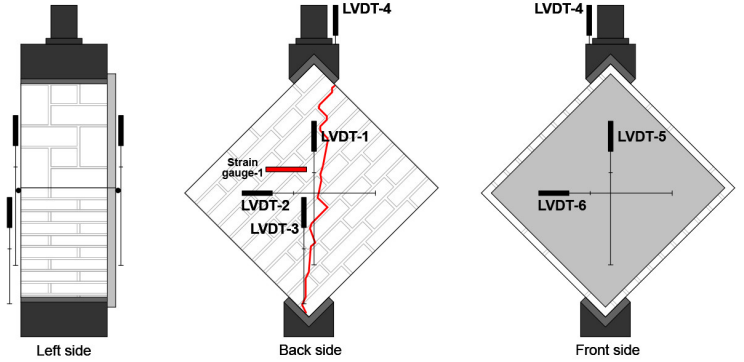
j	LVDT-1	LVDT-2	LVDT-5	LVDT-6	Strain gauge-1
1					
	f(x) = p1*x + p2 p1 = 0.02251, p2 = -0.1397 SSE: 14.33 R-square: 0.8624 Adj. R-square: 0.8624 RMSE: 0.01237	f(x) = p1*x + p2 p1 = -0.0118, p2 = 0.3733 SSE: 1.286 R-square: 0.9496 Adj. R-square: 0.9496 RMSE: 0.003713	f(x) = p1*x + p2 p1 = 0.01493, p2 = -0.2779 SSE: 0.8514 R-square: 0.9789 Adjusted R-square: 0.9789 RMSE: 0.003015	f(x) = p1*x + p2 p1 = -0.0109, p2 = 0.3221 SSE: 3.584 R-square: 0.855 Adjusted R-square: 0.855 RMSE: 0.006183	f(x) = p1*x + p2 p1 = -1.4e-06, p2 = 9.0e-04 SSE: 0.0002377 R-square: 0.001445 Adj. R-square: 0.001435 RMSE: 5.036e-05
2					
	f(x) = p1*x + p2 p1 = 0.01561, p2 = 0.1156 SSE: 9.375 R-square: 0.9011 Adj. R-square: 0.9011 RMSE: 0.01	f(x) = p1*x + p2 p1 = -0.01112, p2 = 0.3604 SSE: 4.202 R-square: 0.9117 Adj. R-square: 0.9117 RMSE: 0.006695	f(x) = p1*x + p2 p1 = 0.01466, p2 = -0.2647 SSE: 8.369 R-square: 0.8991 Adj. R-square: 0.8991 RMSE: 0.009474	f(x) = p1*x + p2 p1 = -0.0107, p2 = 0.3148 SSE: 5.883 R-square: 0.8724 Adj. R-square: 0.8724 RMSE: 0.007922	f(x) = p1*x + p2 p1 = -1.7e-05, p2 = 1.4e-04 SSE: 0.0008753 R-square: 0.1074 Adj. R-square: 0.1073 RMSE: 9.662e-05

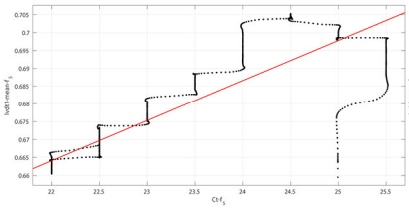
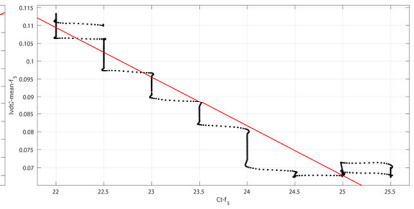
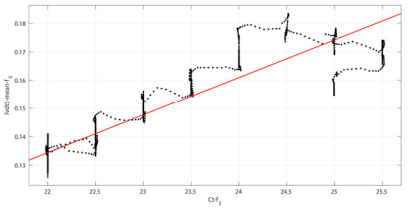
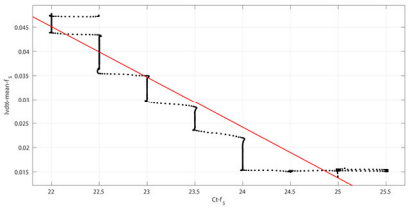
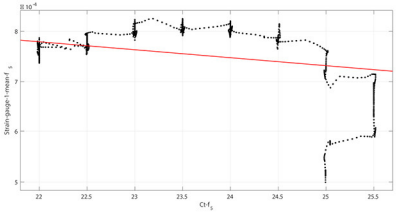
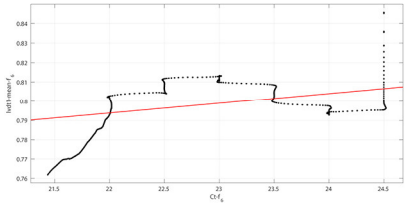
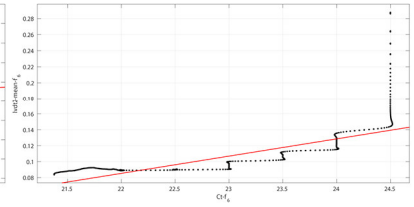
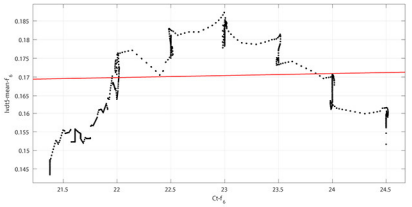
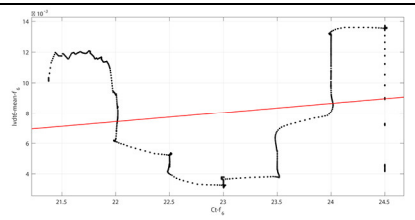
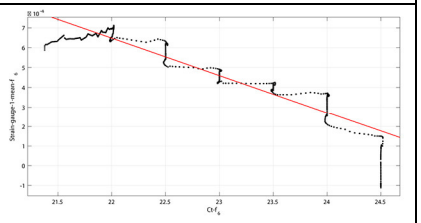
DCf4j



j	LVDT-1	LVDT-2	LVDT-5	LVDT-6	Strain gauge-1
3	 f(x) = p1*x + p2 p1 = 0.0168, p2 = 0.1221 SSE: 1.988 R-square: 0.9556 Adj. R-square: 0.9556 RMSE: 0.004617	 f(x) = p1*x + p2 p1 = -0.01229, p2 = 0.4093 SSE: 0.6772 R-square: 0.9715 Adj. R-square: 0.9715 RMSE: 0.002688	 f(x) = p1*x + p2 p1 = 0.01647, p2 = -0.3231 SSE: 1.093 R-square: 0.9743 Adj. R-square: 0.9743 RMSE: 0.003414	 f(x) = p1*x + p2 p1 = -0.11049, p2 = 0.3279 SSE: 2.146 R-square: 0.8869 Adj. R-square: 0.8869 RMSE: 0.004785	 f(x) = p1*x + p2 p1 = 6.1e-05, p2 = -0.001168 SSE: 4.83e-05 R-square: 0.9218 Adj. R-square: 0.9218 RMSE: 2.27e-05
4	 f(x) = p1*x + p2 p1 = 0.01081, p2 = 0.3965 SSE: 1.528 R-square: 0.894 Adj. R-square: 0.894 RMSE: 0.004048	 f(x) = p1*x + p2 p1 = -0.01197, p2 = 0.3485 SSE: 0.4115 R-square: 0.9747 Adj. R-square: 0.9747 RMSE: 0.002095	 f(x) = p1*x + p2 p1 = 0.01335, p2 = -0.152 SSE: 1.207 R-square: 0.9424 Adj. R-square: 0.9424 RMSE: 0.003589	 f(x) = p1*x + p2 p1 = -0.0102, p2 = 0.2563 SSE: 0.2507 R-square: 0.9787 Adj. R-square: 0.9787 RMSE: 0.001635	 f(x) = p1*x + p2 p1 = -1.1e-05, p2 = 9.1e-04 SSE: 0.0001813 R-square: 0.07224 Adj. R-square: 0.07223 RMSE: 4.397e-05

DCf4j



j	LVDT-1	LVDT-2	LVDT-5	LVDT-6	Strain gauge-1
5					
	f(x) = p1*x + p2 p1 = 0.01122, p2 = 0.4172 SSE: 3.803 R-square: 0.8061 Adj. R-square: 0.8061 RMSE: 0.006369	f(x) = p1*x + p2 p1 = -0.01387, p2 = 0.4146 SSE: 1.64 R-square: 0.9364 Adj. R-square: 0.9364 RMSE: 0.004183	f(x) = p1*x + p2 p1 = 0.01327, p2 = -0.1577 SSE: 3.454 R-square: 0.8649 Adj. R-square: 0.8649 RMSE: 0.00607	f(x) = p1*x + p2 p1 = -0.01046, p2 = 0.2753 SSE: 1.157 R-square: 0.9233 Adj. R-square: 0.9233 RMSE: 0.003513	f(x) = p1*x + p2 p1 =-1.6e-06, p2 = 1.1e-03 SSE: 0.0001781 R-square: 0.1494 Adj. R-square: 0.1494 RMSE: 4.359e-05
6					
	f(x) = p1*x + p2 p1 = 0.005104, p2 = 0.6815 SSE: 5.234 R-square: 0.1369 Adj. R-square: 0.1369 RMSE: 0.01164	f(x) = p1*x + p2 p1 = 0.02165, p2 = -0.391 SSE: 10.11 R-square: 0.6055 Adj. R-square: 0.6055 RMSE: 0.01607	f(x) = p1*x + p2 p1 = 0.0005412, p2 = 0.1579 SSE: 3.567 R-square: 0.00271 Adj. R-square: 0.002684 RMSE: 0.009549	f(x) = p1*x + p2 p1 = 0.0006, p2 = -0.00609 SSE: 0.5201 R-square: 0.02345 Adj. R-square: 0.02342 RMSE: 0.003646	f(x) = p1*x + p2 p1 =-1.9e-04, p2 = 4.8e-03 SSE: 0.0001549 R-square: 0.8833 Adj. R-square: 0.8833 RMSE: 6.292e-05